CZECH UNIVERSITY OF LIFE SCIENCES PRAGUE

Faculty of Engineering

Department of Mechanical Engineering

58th International Conference of Machine Design Departments 2017

Proceedings of 58th International Conference of Machine Design Departments – ICMD 2017

September 6th 2017 – September 8th 2017

Prague

Czech Republic

Editor in chief: David Herák

Online version is available at http://proceedings.icmd.cz/2017/

ISBN 978-80-213-2769-6

58th International Conference of Machine Design Departments 2017

September 6th 2017 – September 8th 2017

ICMD 2017

The 58th International Conference of Machine Design Departments is mainly focused on sharing professional experience and discussing new theoretical and practical findings. The objective of the conference is to identify the current situation, exchange experience, establish and strengthen relationships between universities, companies and scientists from the field of Machine Design.

Conference venue:

Hotel Modrá Stodola, Horoměřice, Czech Republic & Faculty of Engineering, Czech University of Life Sciences Prague, Kamýcká 129, Praha 6, Prague, 16521, Czech Republic

The 58th ICMD conference is organized under the auspices of dean of Faculty of Engineering **prof. Ing. Vladimír Jurča, CSc**

Chairman of the conference: David Herák, CZ

Scientific committee:

All manuscripts in conference proceedings have been reviewed by peer review process.

Reviewers:

Adamovský R.; Akangbe, O.L.; Beyhan M.; Dajbych O.; Dynybyl, V.; Demirel, B.; Demirel, C.; Gurdil A. K. G.; Herák D.; Hrabě P.; Chotěborský R.; Jurča V.; Kabutey A.; Kešner, A.; Mašek J.; Mizera, Č.; Napitupulu R.; Neuberger P.; Pandiangan S.; Petr, K; Petrů M.; Selvi K. C.; Sigalingging R.; Simanjuntak S.; Simanjuntak, E.; Sedláček, A.; Ševčík L.

ICMD 2017

ICMD conference is one of the oldest conferences, dealing with methods and applications in the machine design in Central Europe.

The main aim of the conference is to provide an international forum where experts, researchers, engineers, and also industrial practitioners, managers, and Ph.D. students can meet, share their experiences, and present the results of their efforts in the broad field of machine design and related fields.

Since 1960, when the first conference was organized in Melnik by Brno University of Technology, more than 56 years have passed. The main aim of the conference was providing an opportunity for professional experiences sharing in the field of machine design, gears and transmission mechanisms.

The heads of Mechanical Design Departments decided to organize these conferences annually first at the national and later at the international level and it is evident that the significance of the conference has grown.

Historically, the conferences were organized in different places by different mechanical design departments of Czech and Slovak technical universities.

In this year 2017 conference ICMD was organized by Department of Mechanical Engineering, Faculty of Engineering, Czech University of Life Sciences Prague and it was held in Czech Republic, Hotel Modrá Stodola, which is located on the border of Prague in small town Horoměřice (Horoměřice, Spojovací 918) from 6th September 2017 until 8th September 2017.

Department of Mechanical Engineering,
Faculty of Engineering, Czech University of Life Sciences Prague

The department is aimed at teaching of students in both theoretical and practical engineering related disciplines including technical documentation, applied mechanics, strength of materials, thermo-mechanics, hydromechanics and machine parts. The theoretical knowledge gained by the students enhances their ability to solve practical or technical engineering problems. The students also have the opportunity to study CAD application systems. The Department employees, in the field of science and research activities, focus on mechanical properties of agricultural materials, energy-intensive of agriculture and use of alternative energy sources. The Department Staff are also involved in national and international research projects or cooperation with foreign universities.

CONTENTS

OPERATIONAL PROBLEMS IN SLOW SPEED DIESEL ENGINES CAUSED BY USE OF POOR QUALITY FUELS WITH HIGH CAT-FINES CONTENT

Andrzej ADAMKIEWICZ[1], Jan Bohdan DRZEWIENIECKI[2]

[1]*Maritime University of Szczecin, Poland, e-mail: a.adamkiewicz@am.szczecin.pl*
[2]*Maritime University of Szczecin, Poland, e-mail: j.drzewieniecki@am.szczecin.pl*

Abstract
The article is focused on operational problems occurring in elements of slow speed, crosshead diesel engines such as piston – piston rings – cylinder liner assembly and fuel injection pumps caused by use of poor quality fuels with high content of catalytic fines. There are characterized common contaminants in these fuels with special attention to the most harmful the residual fuel catalytic particles so-called Cat-Fines, specified the maximum limits and described their influence on engine's tribological pairs. Furthermore, this paper considers the operational precautions and treatment of poor quality fuels with elaboration of specific procedures to prevent and reduce the influence of Cat-fines to tribological wear in engine elements and containing issues of condition monitoring of engine elements.

Key words: *diesel engines; tribological wear; residual fuels; catalytic fines.*

INTRODUCTION
Commercial demands towards ship managers to seek the ways to reduce operating costs combined with environmental legislation demands related to the global use of residual fuels and operation of vessels in certain areas called Emission Control Areas (ECA) create certain problems in safe and economical operation of vessels propelled by slow speed engines. Nowadays, reducing the costs of the ship's operation is primarily related to fuel oil consumption and it is achieved by reducing the actual ship's speed to the most economical speed or to so. very or extreme slow steaming. Furthermore, the fact that the reduction of sulphur content in residual fuels is proportional to a higher average amount of harmful catalytic fines (Cat-fines) used as a catalyst in the crude oil refining process, cause that vessels are bunkered with poor quality fuels. According to the reports by Hill (2013) and the author's research Study (2011, 2016), the reduced engine's load conditions and the steadily deteriorating quality of fuel oils, may lead to the possibility of the various operational difficulties. They can include, inter alia, the increased wear of the tribological pairs and their components mostly in the fuel system as described by Bejger al. (2015) and Henderson (2014) and in PRC assembly: piston - rings - cylinder liner as per research Study of author's (2017), McGeary al. (2004) and Satermeister al. (2013) and have decisive influence on their reliability. Therefore, it creates demands on implementation of operational precautions and improvement of efficiency in onboard fuel oil treatment which were the aims of this study. The results have been presented here as elaboration of specific procedures to prevent abnormal wear in elements of slow speed, crosshead diesel engines such as piston – piston rings – cylinder liner assembly and fuel injection pumps and to reduce the influence of use of poor quality residual fuels with high Cat-fines content on these elements by their condition monitoring.

MATERIALS AND METHODS
During normal operation, slow speed engines are supplied by residual fuels with sulphur content below 3.5% (HFO – Heavy Fuel Oil) and in Emission Control Areas (ECA) by low sulphur residual fuels (LSFO – Low Sulphur Fuel Oil). Besides, before entering the ports included in ECA fuel supply must be changed from residual into distillate low sulphur fuels (MGO – Marine Gas Oil) as it was described by authors (2011). The most common contaminants in these fuels are aluminum – silicon compounds and foreign substances or chemical waste, hazardous to the safety of the ship or detrimental to the performance of machinery. The limit values for different fuel grades presented in Marine Fuel Specification by Exxon Mobile Booklet (2016) indicate the minimum quality of fuel as supplied to the ship ensuring good operating results with commercially available fuels within these limits. However, engine's makers are giving with much lower limits for fuels expecting a positive influence on overhaul periods, by improving combustion as it is described in Wartsila Booklet (2007). Besides,

as results from various Insurers, Classification Societies and engine maker's reports described by Henderson (2014) and Hill (2013) during last years it was noticed an increase in engine damage due to poor quality of fuels containing catalytic fines, even though the fuels used by engines were within ISO 8217 specification limits and undergoing on board fuel treatment. It has shown that the most harmful contaminants are catalyst particles being the reason in nearly 90% of the cases. The residual fuel catalytic particles so-called Cat-fines are used as catalyst in the crude oil refining process called fluid catalytic cracking (FCC). The left over after this processing are the remnants which main components are formed in the catalysts alumina-silicates – hard ceramic compounds of aluminum and silicon having a diameter of 5-150μm, oval shape and the hardness near to grinding material. As per ISO 8217:2010 the limit for Cat-fines in bunkered fuels is 60mg/kg (ppm) once engine makers recommend that the inorganic particles of size less than 5μm in the fuel supplying to engine should be less than 20mg/kg and that the contents of catalytic fines should be less than 15mg/kg. This implies that the vessel's fuel treatment systems should be able to meet these requirements. According to own study and the results of majority of the fuel samples received and analyzed by DNV Petroleum Services, they were tested allowing Cat-fines max limit at 80mg/kg and the example is shown in fig. 1 where residual fuels bunkered on two occasions had Cat-fines content at the level above of 65mg/kg.

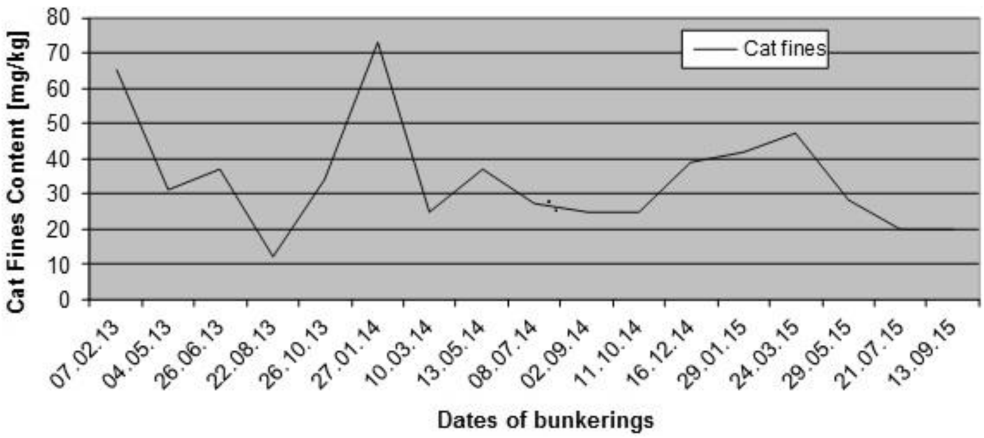

Fig.1 Cat fines content in bunkered residual fuels delivered in Fujairah over two years period of VLCC operation based on DNV Lab results of bunker samples [own study]

Cat-fines damage mainly occurs in large slow speed main engines because the larger fuel injection components allow sizeable Cat-fine particles get into the cylinders where lubricating oil is minimally applied to the liner surface, and doesn't wash them away. The minimum lubricating oil film thickness between the liner surface and piston rings at Top Dead Center (TDC) according to McGeary al. (2004) is down to 0.5μm. Consequently, even very small particles captured between the piston ring and cylinder liner will contribute to the wear in the TDC area. Cat-fines get embedded into engine components and cause abrasive wear to affected PRC assembly: cylinder liners – piston rings (fig. 2a, b) and fuel system: pumps and injectors (fig. 2c, d).As it results from author's research, the appropriate procedures of filtration of fuel oil on board leads to a significant reduction in their content but not to their elimination (6 mg/kg – tab. 1). The remaining in fuel catalytic particles due to their shape and size are not retained even through fine filters with a degree of filtration 10-30μm and still create a risk of increased abrasive wear. During laboratory analysis of worn elements, catalytic particles were found in surface layers of materials, and their average size as per Henderson (2014) was not exceeding 20μm. Generally, larger Cat-fines in the 10-25μm range, are considered most likely to become embedded in the engine parts, however, high amount of cat fines in the 5-10μm range is likely to increase wear rates as well.In compliance with Tier II NOx regulations and Energy Efficiency Design Index (EEDI) guidelines, diesel engines must operate under increased combustion pressures and reduced operating temperatures. These regulations together with poor quality fuels have led to an increase in cold corrosion which is according to elaboration carried out by CIMAC Working Group (2011) the most serious in modern engine designs that have been modified for low-load operation.

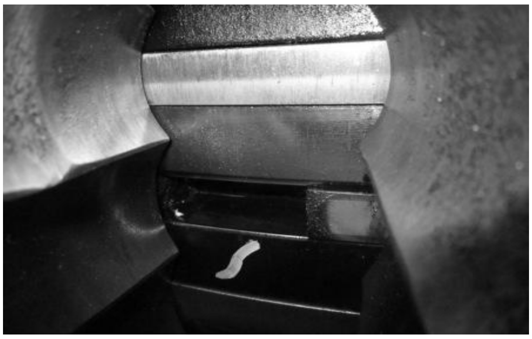

a) – abrasive wear of the 1st(upper) ring with visible scuffing wear marks on top and pilled out part of the 2nd(lower) ring. Cat-fines as hard grains causing abrasive wear down to the surface by continuous ploughing and scratching which displays vertical scratches, the size of which depends on the dimensions of the particles involved. These particles can also affect the sides of the rings as they jam in the ring groove, thereby causing "pitting" of the surface.

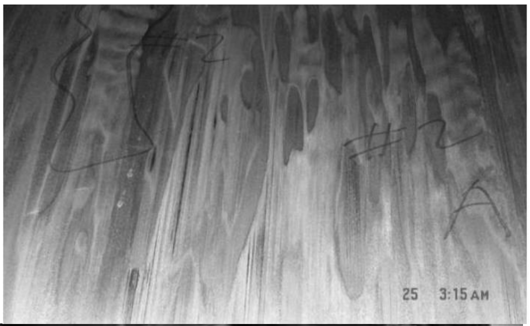

b) – cold corrosion caused due to the engine operation at “low loads” combined with the increased pressure and reduced temperatures within the engine cylindersthat created conditions below the dew point, allowing water to condense on the cylinder liner walls.That condensate combined with sulphur, forming sulphuric acid – corroding the liner surface and creating excessive wear of the liner material.

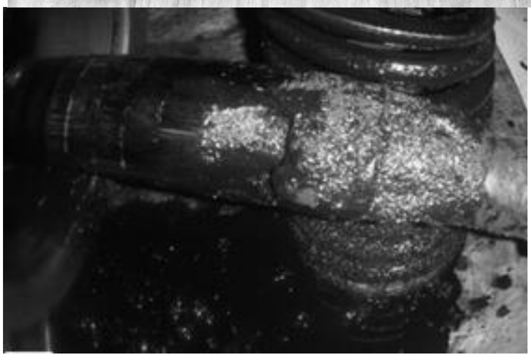

c) – solid fuel deposits covering Fuel Injection Pump’s (FIP) spring and plunger. Formation of deposits in FIP parts during engine stoppage due to poor quality fuel comes to deposition and hardened remaining of residual fuel in spring chamber and the lower part of plunger causing precision pair – plunger barrel (BP) is stuck. This leads to difficulties and/ or impossible to start the engine, and therefore require replacement of FIP with stuck parts and/ or its cleaning/ repair.

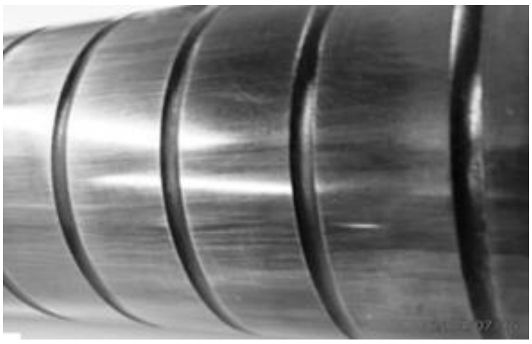

d) – abrasive wear in FIP plunger with visible scratches caused by fuel with Cat-fines. The presence of Cat-fines between small radial clearances of BP precision pairs causes scratches of running surfaces, difficulties in maintaining of an oil layer between them and leads to accelerated abrasive wear that may cause decrease of maximum combustion pressure, and therefore reduction in indicated power obtained from the cylinder, and even can lead to engine stoppage.

Fig. 2 Abnormal wear in slow speed diesel engine elements caused by poor quality fuels [own study]: a, b – piston rings and cylinder liners (PRC assembly) observed during inspection through scavenge ports; c, d –fuel oil injection pump (FIP) elements condition investigation due to pump’s failure

RESULTS AND DISCUSSION

As presented in the previous chapters, there is a strong need for implementation of operational precautions and improvement of efficiency in onboard fuel oil treatment once consuming poor quality fuels. Based on own research, the authors elaborated the following procedures to prevent/ reduce the influence of Cat-fines to tribological wear of engine’s elements:

Fuel oil storage and distribution on board:

1. Frequent draining of settling and service tanks to remove water and Cat-fines as they have tendency to settle at the bottom. They could be mixed when the sediment is churned up in rough weather and circulate in quantities beyond the capacity of on board fuel treatment plant.

2. Bunker tanks should be stripped as low as possible because new bunkers should preferably be placed to empty tanks, and blending of different fuels avoided. If blending is deemed necessary allowable proportion should be 20:80 and an adequate compatibility test performed.

Fuel oil treatment:

3. The most affective units which can deal with Cat-fines in fuel are purifiers that act as centrifugal force is utilized to accelerate the separation process among elements with different density.
4. If the purifier uses gravity disc (conventional purifiers), it is advisable to select one size larger gravity disc than that recommended by the manufacturer of the purifier. Correct gravity disc, along with steady feed temperature as close as possible to 98°C without fluctuation, determines the position of the oil-water interface (an unstable interface will spoil the efficiency of the plant).
5. Two purifiers should be used in parallel with minimum output and de-sludge at 30 min interval. This will ensure the longest possible retention in the centrifuges and enables optimal efficiency for removal of Cat-fines from very high content of 73 mg/kg to 6 mg/kg with efficiency above 85%. In the contrary, when only one purifier was in use Cat-fines content was reduce to 22 mg/kg – tab. 1.
6. Fuel oil fine and auto backwash filters should be operational and all fuel oil drains should not be reused but incinerated or consumed by auxiliary boiler.

Usage of poor quality fuel

7. The vessel should have sufficient fuel on board to avoid using of newly bunkered fuel without obtaining and acting on the results of fuel sample analysis sent after bunkering.
8. It is recommended that a proper Fuel System Check (FSC) is carried out by taking samples throughout the fuel system at intervals of 4-6 months. However, FSC Samples should also be taken whenever Al/Si as bunkered exceeds 40 mg/kg. Subsequently, the recommendation is to carry out proper testing of samples taken before and after the purifier(s), at the same time. The samples should be sent to accredited laboratories as DNV Petroleum Services for analysis – tab. 1.

Tab. 1 Juxtaposition of Fuel System Check (FSC) results for HFO samples taken before (D) and after purifier (E) for different residual fuels with high Cat-fines content (A) [own elaboration]

Date			Analysis Results – particles [mg/kg]							
Bunkering	Sampling	Sampling Point	Density [kg/m^3]	Water [%]	Sulphur [%]	V	Na	Al.	Si	Cat Fines [mg/kg]
07.02.13		A	989.2	0.06	3.52	54	38	33	32	65
	26.02.13	D	989.4	0.04	3.62	52	32	19	18	37
		E	989.1	0.05	3.63	53	30	11	11	22
27.01.14		A	989.7	0.1	3.41	89	20	34	39	73
	27.02.14	D	989.8	0.07	3.49	92	22	7	7	14
		E	989.8	0.09	3.42	95	22	3	3	6
29.01.15		A	990.5	0.14	3.29	43	21			42
	11.02.15	D	990.4	0.14	3.34	45	21			38
		E	990.9	0.05	3.39	45	11			6

Condition monitoring of engine elements:

9. As far is practical, the condition of cylinder liners and piston rings from scavenge ports should be visually inspected for any abnormalities which were detailed described by authors (2017).
10. Regular engine's performance (combustion pressure measuring) in regular intervals with trend analysis should be measured and analyzed to confirm condition of fuel system.
11. Application of further assessing methods of the condition and wear of PCR during operation of large slow speed engines by collection of cylinder drain oil (CDO) from under piston spaces including the measurement of Fe-content by spot or online methods (fig. 3) that were subject of research study by authors (2017), McGeary (2004) and elaborated by CIMAC (2011).

Regular intervals of testing with trend monitoring allow to control over abrasive wear caused by presence of Cat-fines in fuel indicated by presence of iron wear particles. In addition, a new method enabling to monitor specific levels of both metallic and corroded iron in cylinder oil, may protect and prevent against Cat-fines attack – fig. 3 and lead to diagnosis based on condition monitoring.

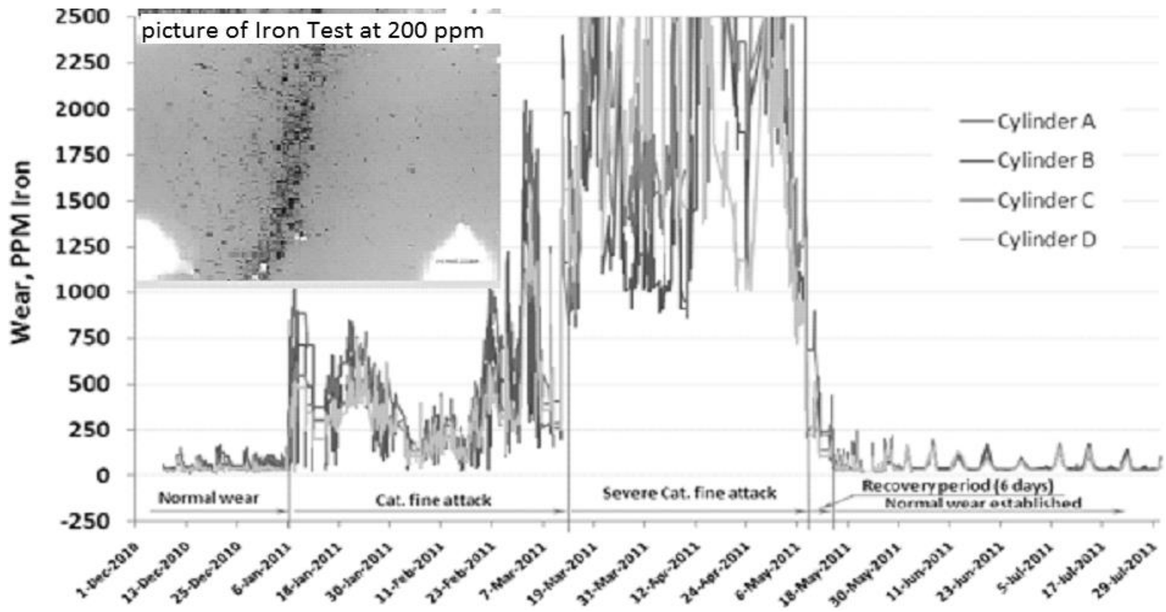

Fig. 3 Severe Cat-fines attack documented by means of Kittiwake online equipment measuring the content of iron wear particles it peaked to more than 2,500 mg/kg [8]. Before attack, the iron level was below 200 mg/kg (Cat-fines alert) as on the picture confirmed by Iron Test [own study]

Knowing the amount of iron in the cylinder scrape down oil related to wear trend in PRC as well as the remaining alkalinity reserve (TBN) – fig.4 is the essential requirement to adjust appropriate cylinder oil feed rate depended also on engine's load and sulphur content in fuel as well and to minimize the impact of the escalating challenge of cold corrosion reported by CIMAC Working Group (2011). The authors' study on interpretation of used oil analysis results and diagnosis of machinery condition, based on precise knowledge of the equipment and experience with operating conditions as the engineering staff on board the vessels backed up by the scientific knowledge and research listed in the author's article giving support from reported incidents and other complimentary information.

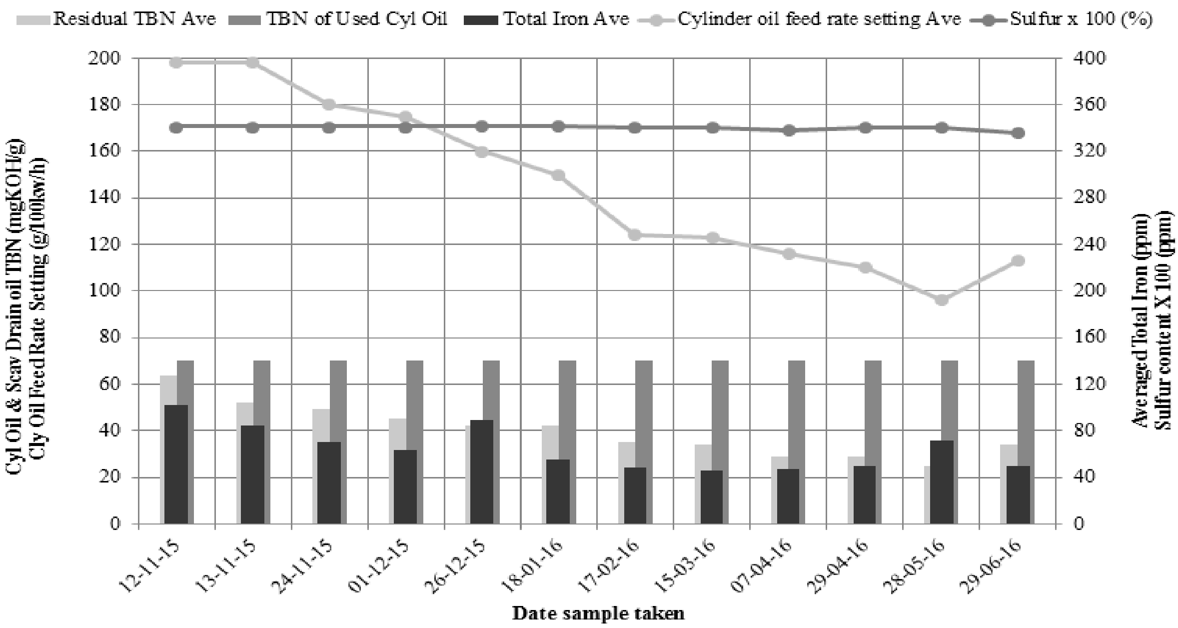

Fig. 4 Relationship of key values (time-series) among cylinder oil feed rate and total iron content in cylinder drain oil in relation to fuel sulphur content and alkalinity reserve [own study]

CONCLUSIONS

The mentioned in this article issues can lead to the following conclusions that can help to understand the core of the problem in operation of slow speed crosshead diesel engines supplied by poor quality fuels with high Cat-fines content, especially once they are running under "low load" condition, minimize cold corrosion appearance and prevent the escalation of engine damages and related both in delays in commercial operations and unnecessary additional costs and insurance claims as well:

- Bunkered poor quality fuels containing Cat-fines impurities even with very small particles are found to be responsible for wear cases in slow speed engines' tribological nodes such as piston – piston rings – cylinder liner assembly and precision pairs of fuel injection pumps. The problems which arise due to Cat-fines are often unexpected as they are not always evenly distributed in the fuel and are sometimes present even when they do not appear in the analysis results.
- In order to reduce the risk of encountering high wear rates, the Cat-fines content in the bunkered fuel must be reduced significantly by onboard fuel treatment system before entering the engine to meet recommended by engine maker's limits. The results should be confirmed by checking of Fuel System Check samples in accredited laboratories or implementation of on line analyzers. It should also include engine performance and Iron powder tests by on-site methods with trend monitoring which are not so precise as lab results but are immediate what is very crucial factor in evaluation of each cylinder conditions, combustion and lubrication, confirming which units are functioning correctly and pointing those require attention. The further study will also identify reasons of possible malfunction and help to find the remedy.
- Effective Onboard Fuel Management System could minimize and significantly reduce the risk of engine break-down and lengthy/costly repairs caused by off-spec bunkers if have been implemented and followed at all times. Therefore, ship managers should provide an internal review of their Bunker Handling and Management plans and enhance planned maintenance systems by in order to provide early identification of fuel related problems.

REFERENCES

1. Adamkiewicz A., Drzewieniecki J. (2017). Operational evaluation of piston-rings-cylinder liner assembly wear in marine main diesel engines. *Tribologia, 1*, 5-15.
2. Adamkiewicz A., Drzewieniecki J. (2016). The influence of fuel quality on tribological wear in slow speed diesel engines. *Wear Processes in the Transport Engineering* (pp. 1-10). Solid State Phenomena.
3. Bejger A., Drzewieniecki J. (2015).Analysis of tribological processes occurring in precision pairs based on example of fuel injection pumps of marine diesel engines. *Scientific Journal of the Maritime University of Szczecin, 41*(113), 9-16.
4. Adamkiewicz A., Drzewieniecki J. (2011). Operational problems in marine diesel engines switching on low sulfur fuels before entering the emission controlled areas. *Journal of Polish CIMAC, 6* (1), 9-17.
5. CIMAC Working Group, Marine Lubricants (2011). Used engine oil analysis – user interpretation guide. International Council on Combustion Engines. *CIMAC* No. 30.
6. *Exxon Mobile Booklet* (2012).Marine Fuel Specification.
7. Henderson K. (2014). Increasing engine damage caused by catalyst fines. *Marine Propulsion Report*.
8. McGeary T., Chew F. (2004). Investigations into abrasive and corrosive wear mechanisms of pistons and liners in large bore 2-stroke diesel engine. *CIMAC*, Paper no. 14.
9. Sautermeister F., Priest M., Lee P., Fox M. (2013). Impact of sulphuric acid on cylinder lubrication for large 2-stroke marine diesel engines. *Tribology International*; *59*, 47-56.
10. *Wartsila Booklet (2007).* Quality requirements and recommendations for heavy fuel oil used in RT Sulzer diesel engines.
11. Hill P. (2013).Rise in Claims Attributed to CatFines in Bunker FO.*www.braemarsa.com*

Corresponding author:
Eng. Jan Bohdan Drzewieniecki, Ph.D., Marine Chief Engineer Officer, Maritime University of Szczecin, Mechanical Engineering Faculty, Department of Condition Monitoring & Maintenance of Machinery, Willowa str. 2-4, 71-650 Szczecin, Poland, e-mail: j.drzewieniecki@am.szczecin.pl

AIR, GROUND MASSIF LOW-TEMPERATURE ENERGY SOURCES

Radomír ADAMOVSKÝ[1], Anna HEJLOVÁ[2]

[1]Department of Mechanical Engineering, Faculty of Engineering, Czech University of Life Sciences Prague
[2]Department of Mathematics, Faculty of Engineering, Czech University of Life Sciences Prague.

Abstract
The aim of this study was to analyze and compare the impact of two low-temperature energy sources, air and linear horizontal ground heat exchanger (HGHE), on the energy effect of a heat pump and their contribution to fulfilling the objectives of reducing fossil fuel consumption. The results of operational verification and statistical analysis showed that linear HGHE is a more favorable low-temperature energy source for heat pumps than air in terms of expected energy effects. The set of temperatures of the heat transfer fluid from a linear HGHE showed higher average and median values, and less variability in comparison with the corresponding set of air temperatures. Temperatures of the fluid in linear HGHE were positive over the entire heating period and more than 73% of the data were higher than the temperatures of air. A higher value of the energy effect of the linear HGHE expressed by a comparative coefficient of performance, ε_h of reversed Carnot cycle, also showed higher benefits of this low-temperature energy source with more significant impact on consumption of fossil fuels.

Key words: *low-temperature energy source; temperature; air; ground massif; heat pump; heating factor; Carnot cycle.*

INTRODUCTION
Water and air, and both ground and rock massifs are important and frequently used low-temperature energy sources for heat pumps. Exploitation of surface or underground water as low temperature heat source is very limited because of the nature of its availability, complex legislation, variability of water flow and instability in heating power. Installation of the energy system is easier and cheaper when using air. The environmental aspect of the use of air is also important. This system affects the heat balance of the surrounding environment minimally. The energy delivered from the air to the heat pump evaporator returns to the environment as thermal losses in the exchanger. Horizontal ground heat exchangers (HGHE) with different pipe configurations, most commonly linear and slinky types, installed at depths of 1 to 2 m are used in Europe to obtain thermal energy from the ground. In the rock mass, vertical heat exchangers, mainly in the form of single or double U-tubes, installed in boreholes of depths of 70 to 200 m, are used to obtain heat energy. The heat transfer fluid, which is heated and fed to the heat pump evaporator flows through both of the heat exchanger types.
By 2007, the most annually installed heat pump type in the Czech Republic were those for which the low-temperature source for the evaporator was ground or rock massif. In 2006 alone, 4.82% of installed heat exchangers were of air to air heat pumps, 38.07% of air to water, 53.79% of ground to water and 3.32% of water to water heat pumps. However, in subsequent years, sharp falls were recorded in the installation of ground to water heat pumps. In 2014, the shares in total heat pump installation of ground to water, water to water and air to water heat pump types were, respectively 19.58, 0.59% and 79.83% (Bufka, Rosecky, 2016). Similar trends in changes in the share of low-temperature energy sources for heat pumps were also reported by L u n d and B o y d (2015) in the global geothermal energy use report. The main reason why investors prefer air to water heat pumps is because of its significantly lower investment costs compared to other low-temperature sources. Furthermore, its installation is easy and simple. For this reason, manufacturers have payed exceptional care to innovations and expansion of the possibilities of using air to water heat pumps. Success has been particularly achieved in the use of air as a low temperature source. Contemporary heat pumps can work with air at temperatures -15 °C or lower without any problem and can be delivered as block, compact units already filled with refrigerant, which significantly simplifies installation.

The primary objective of using renewable energy sources is first of all to reduce fossil fuel consumption. The open question is how the above-mentioned low-temperature sources contribute to meeting the goals of reducing fuel and energy consumption.
Modelling of heat transfer fluid temperatures in HGHEs and VGHEs (Vertical Ground Heat Exchangers) was addressed by F l o r i d e s et al. (2013). In particular, they evaluated the effect of linear HGHE pipe spacing on the fluid temperature. Their results indicated that increase in the HGHE tube spacing caused decrease in the temperature of the heat transfer fluid. B a n k (2012) stated that the temperature of the HGHE heat transfer fluid varied between +5 and -5 ° C during operation. VDI (2001) recommended that the temperature of the heat transfer fluid from the heat pump into the ground loop should not differ by more than ± 12 ° C from temperature of ground mass without HGHE. The performance and economic comparison of low-temperature energy sources (VGHE, HGHE, air) for heat pumps were dealt with by P e t i t and M e y e r (1998) who pointed out that whereas VGHEs provided the best performance, HGHE achieved more favorable heating factor (COP) than VGHE compared to air and VGHE as well. Also HGHE appeared to be the most cost effective.
The aim of this article was to analyze and compare the influence of two low-temperature energy sources used in heat pumps on the energy effect of the heat pump and their contribution to meeting targets of reducing fossil fuel consumption. In terms of frequency of use, air and linear HGHE with configuration most commonly used in the Czech Republic were selected for analysis and comparison.

MATERIALS AND METHODS

Theoretical analysis
The energy effect of the ideal reversed Carnot cycle operating between the temperatures T_p and T_o at which we supply and dissipate the heat can be expressed by equations (1) and (2):

$$\varepsilon_c = \frac{T_p}{\left|T_p - T_o\right|} \tag{1}$$

$$\varepsilon_h = \frac{T_o}{\left|T_p - T_o\right|} \tag{2}$$

Factor ε_c (cooling) is used to express the energy effect during cooling and ε_h (heating) when expressing the effect during heating. It follows from both equations that the effects are dependent on the temperature difference between T_p and T_o. The smaller the temperature difference - which represents work input brought into the cycle - the greater the effect of the ideal Carnot cycle.
The use of the ideal Carnot cycle is advantageous in our case because it enables to express the energy effects only depending on the temperatures mentioned. At the considered constant temperature T_o, the energy effect evaluated when using the cycle for heating is dependent on temperature- T_p.

Materials and methods of measurement

The linear horizontal ground heat exchanger was made of a polyethylene tubing PE 100RC 40x3.7mm (LUNA PLAST a.s. Hořín, Czech Republic) resistant to point loads and cracking. It was not placed in a sand bed. Exchanger tubing with a total length of 330 m (41.473 m^2) is installed at a depth of 1.8 m in 3 loops with a spacing of 1 m. The length of each loop was 54.62 m. The heat transfer fluid flowing through the exchanger was a mixture of 33% ethyl alcohol and 67% water. The MTW 3 electronic heat meter (manufactured by Itron Inc., Liberty Lake, USA) was used to measure the total heat flow through the horizontal heat exchangers, recording the flow and temperature of the heat transfer fluid at the outlet t_{L1} and the inlet t_{L2} to the ground heat exchanger. The temperature of the ground massif t_g at a distance of 10 m from the linear HGHE was measured by the GKF 200 temperature sensor (manufactured by GREISINGER electronic GmbH, Regenstauf, Germany) and recorded by the ALMEMO 5990 measuring station. The subject of the evaluation and statistical analysis were the exit temperatures of the fluid from the linear HGHE t_{L2} and the ambient temperatures t_e, corresponding to the temperature T_p in equation (2). Ambient temperatures were measured at a height of 2 m above the ground surface and 20 m away from horizontal ground exchangers by the ALMEMO FHA646AG sensor (manufactured by AHLBORN Mess-und Regulungstechnik, Holzkirchen, Germany). All temperatures were recorded in quarter-hour intervals and an hourly average was calculated from these values. The test was conducted for 217 days in the heating period from 17 September 2012 to 22 April 2013, so the basic statistical set for the evaluation of individual low-temperature energy sources were 5,208 temperature values. The results were evaluated using STATISTICA (StatSoft, Inc. 2013) and MS Excel (Mošna, 2017). Basic descriptive characteristics of the location, variability and distribution of the data sets were determined. The energy effect of the comparative ideal reversed Carnot cycle expressed by the heating factor ε_h according to (2) was also evaluated, where a constant temperature T_0 = 55 °C was considered.

RESULTS AND DISCUSSION

Basic descriptive statistics of temperature data of two low-temperature energy sources are summarized in Tab. 1 and in box plots (Fig. 1).

Tab. 1 Basic statistical characteristics of the data sets

Characteristics	Low-temperature energy source	
	Air	Linear HGHE
Mean $\bar{x}$ (°C)	5.47	8.13
Standard deviation S (K)	6.35	4.51
Variation coefficient VK (%)	116.12	55.43
Minimum x_{min} (°C)	-15.80	1.67
Maximum x_{max} (°C)	28.60	17.82
Range R (K)	44.40	16.15
Median $\tilde{x}$ (°C)	5.10	6.37
Mode $\hat{x}$ (°C)	6.00	6.00
Lower quartile Q_1 (°C)	1.00	4.62
Upper quartile Q_3 (°C)	9.10	11.45
Interquartile range Q_3 - Q_1 (K)	8.10	6.83
Coefficient of skewness A (-)	0.55	-0.76

A considerable variance was observed in the air temperatures data set; the standard deviation S was greater than the arithmetic mean, and the variation coefficient VK thus exceeded 100%. On the other hand, the variance in the data of the linear HGHE was significantly lower; the standard deviation S was approximately half the arithmetic mean which corresponded to a VK of approximately 55%.

The high variation in air temperatures negatively affected the process of heat transfer in the evaporator particularly in terms of changes in differential temperatures of air supplied to the evaporator and the evaporation temperature of working fluid of the heat pump.

The box plot (Fig. 1) shows the medians, quartiles and extreme values and thus gives general information on the both data sets. Firstly, there is a clear difference in the range values R. It is also apparent that a half of the air temperature data are within the interval from 1.00 to 9.10 °C and half of the HGHE temperature data are within the interval from 4.62 to 11.45 °C. The values of the lower and upper quartiles Q_1 and Q_3 in the linear HGHE data are higher than the corresponding values in the air temperature data (by 3.62 and by 2.35 K, respectively). The interquartile ranges $Q_3 – Q_1$ in both data sets were not much different (about 1.3 K). In the air temperature data, the interquartile range represented only 18.24% of the range R, whereas the interquartile range in the linear HGHE data set corresponded to 42.29% of R. This comparison also demonstrated the lower temperature variability in the linear HGHE.

Both aspects, i.e. the position of the interquartile range towards higher temperatures and lower variability of temperatures, had a positive influence on the effect of the heat pump.

From the point of view of efficient use of low-temperature sources, the interval and temperature distribution between the lowest temperature x_{min} and the lower quartile Q_1, containing 25% of all temperature values, were also significant. In the air temperature data set, 25% of the data were within the interval from -15.80 to 1.00 °C; whereas in the linear HGHE temperature set within the interval from 1.67 to 4.62 °C. Low evaporation temperatures of the heat pump working medium, together with the high frequency of low-temperatures of air with high relative humidity caused freezing of the evaporator and consequently a more frequent defrosting of the equipment was necessary. Due to the increase in electric power consumption for reverse operation of the heat pump, the effect of the whole system decreased.

The large interval between upper quartile Q_3 and the highest air temperature x_{max} from 9.10 to 28.60°C can be explained by higher air temperatures at the beginning and at the end of the heating season. In the case of linear HGHE, this interval was significantly smaller, i.e. from 11.45 to 17.82 ° C.

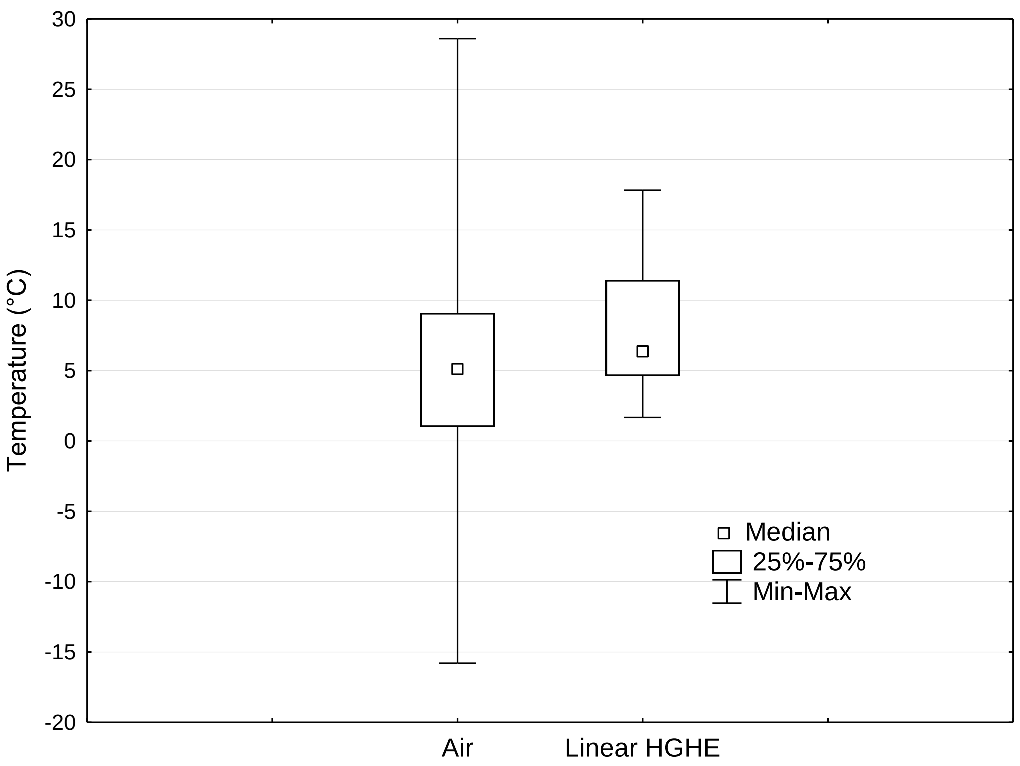

Fig. 1 Box-whisker plots of temperatures of the low-temperature sources

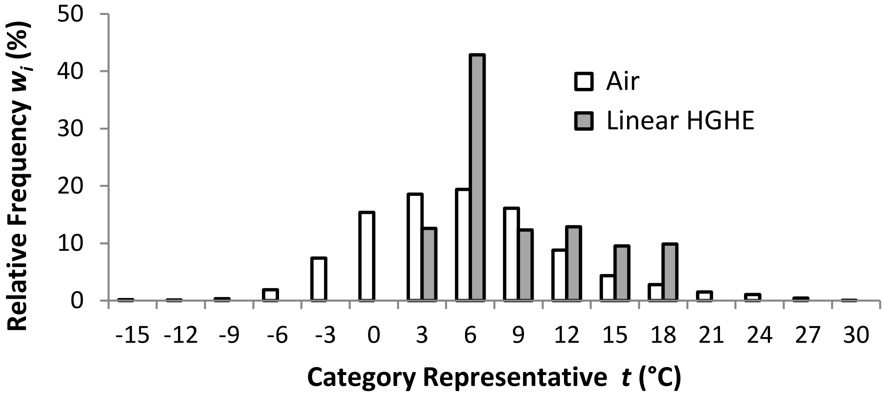

Fig. 2 Histograms of temperature relative frequencies in low-temperature sources

The distributions of the temperature data were further depicted in histograms (Fig. 2) generated from data sorted into intervals of length 3K. The mode $\hat{x}$ in both datasets was estimated as the center of the interval from 4.50 to 7.50°C with a frequency of 42.86% in the linear HGHE data set and a frequency of only 19.37% in the air temperature set. The histogram shape and the relations $\hat{x} \cong \tilde{x} \cong \bar{x}$, they both indicated a symmetric distribution of the air temperature data. On the other hand, the data of linear HGHE were mostly concentrated to the left of the mean and $\hat{x} < \tilde{x} < \bar{x}$ (see Fig. 2 and Tab. 1), hence the data distribution can be considered as left-handed asymmetric one. Nevertheless, a right-handed skewness has not been proven (see coefficient *A* close to zero in Tab. 1).
Temperatures of the heat transfer fluid in the linear HGHE were positive with the average value of 8.13°C which was about 3 K greater than stated by B a n k s (2012). With respect to HGHE pipe spacing, the temperature of the heat transfer fluid were in agreement with results presented by F l o r i d e s et al. (2013). When the temperatures of the heat transfer fluid in the linear HGHE and air systems throughout the measured period were compared, 73.6% of the HGHE temperatures were observed to be higher than the air temperatures. This corresponded to the significantly higher average of HGHE data than the average of the air data (confirmed by t-test on common level of 5%).
Higher temperatures of the heat transfer fluid are associated with higher heating factor ε_h (2). Therefore, the frequency of higher temperatures in the linear HGHE confirmed greater energy effects of this low-temperature source. For both low-temperature sources, the heating factors ε_h were calculated according to (2) and evaluated throughout the monitored heating period and especially in the reduced part where the air temperatures were less or equal to zero, which represented 20.12% of the data. The results, i.e. the heating factor averages ε_h and standard deviations *S*, are summarized in Tab. 2.

Tab. 2: Heating factors ε_h and standard deviations *S* during the whole heating period and from reduced data at ambient temperatures $t_e \leq 0$ °C

	Whole heating period		Reduced data, $t_e \leq 0$ °C	
	ε_h (-)	*S* (-)	ε_h (-)	*S* (-)
Air	6.75	1.00	5.71	0.22
Linear HGHE	7.07	0.74	6.59	0.28

The energy effect of air was influenced by higher air temperatures at the beginning and at the end of the heating period when almost 10% of the data exceeded the maximum temperature of the HGHE heat transfer medium. At negative air temperatures, the heating factor dropped below to the average value of 5.71±0.22. Mean values of heating factor ε_h of air were lower than at linear HGHE and that difference was more pronounced in the reduced data (t-tests also confirmed significant differences).
In the context of the recommendation of the German standard VDI (2001) cited earlier, the temperature differences t_{L1} of heat transfer fluid exiting the heat pump and the temperatures t_g of the ground

massif measured outside HGHE at the same depth of the massif were evaluated. The statistical analysis revealed that the average temperature difference $\Delta t_{\phi} = t_g - t_{L1}$ = 3.52±2.68 K, maximum difference Δt_{max} = 9.46 K. Hence, the temperature differences did not exceed the recommended range.

CONCLUSIONS

The results of the operational verification and analysis have shown that linear HGHE is a significantly more favorable low-temperature energy source for heat pumps than air in terms of the predicted energy efficiency benefit. The set of temperatures of heat transfer fluid of linear HGHE had less variability, the upper and lower quartiles and the median values were higher in comparison with the corresponding air temperatures. Fluid temperatures were positive throughout the heating period and more than 73% of the values were higher than corresponding air temperatures. The higher value of the energy effect in the linear HGHE, expressed by the heating factor ε_h of the comparative reversed Carnot cycle, demonstrated higher benefits of this low-temperature energy source. These favorable characteristics of a fluid temperature set from linear HGHE had a positive effect on the operation of the heat pump and on reduction of fossil fuels consumption both in the heating system and for the heat pump drive. The achieved results meet the objectives of the research papers presented in the introduction of the article. It is now necessary to seek ways to promote the application of low-temperature energy sources for heat pumps since they are more efficient than the currently widely used air.

ACKNOWLEDGMENT

The research work was carried out with the support of the company VESKOM Ltd. based in Prague, and at its experimental site in Prague - Dolní Měcholupy, Czech Republic.

REFERENCES

1. Banks, D. (2012). An Introduction to Thermogeology: Ground Source Heating and Cooling. 2nd Ed. Chichester, West Sussex, John Wiley & Sons, Ltd., 546
2. Bufka, A., & Rosecký, D. (2016). Renewable energy in 2014. Results the statistical survey. (In Czech). Prague: The Ministry of Industry and Trade of the Czech Republic.
3. Florides, G., Theofanous, E., Iosif-Stylianou, I., Tassou, S., Christodoulides, P., Zomeni, Z., Tsiolakis, E., Kaligorou, S., Messaritis, V., Pouloupatis, P., Panayitou, G. (2013). Modeling and assessment of the efficiency of horizontal and vertical ground heat exchangers. Energy, 58, 655-663.
4. Lund, J. W., Boyd, T. A. (2015). Direct Utilization of Geothermal Energy 2015 Worldwide Review, Australia. In Proceedings World Geothermal Congress 2015, Melbourne, Australia, 19-25 April 2015 (pp. 17-24).
5. Mošna, F. (2017). Statistical Tools of Excel. In Proceedings of 16th International Conference APLIMAT 2017, Bratislava, Slovakia, 31 Jan–2 Feb 2017 (pp. 1101-1106).
6. Petit, P.J., Meyer, J.P. (1998). Techno-economic analysis between the performances of heat source air conditioners in South Africa. Energy Conversion and Management, 39/7, 661–669.
7. VDI 4640- Part 2, Thermal use of the underground – Ground source heat pump systems. Verein Deutscher Ingenieure, Düsseldorf, (2001).

Corresponding author:
Prof. Ing. Radomír Adamovský, Dr.Sc., Department of Mechanical Engineering, Faculty of Engineering, Czech University of Life Sciences Prague, Kamýcká 129, Praha 6 - Suchdol, 165 00, Czech Republic, Phone: +420 22438 4176, e-mail: adamovsky@tf.czu.cz

VERIFYING A TRUCK COLLISION APPLYING THE SDC METHOD

Piotr ALEKSANDROWICZ[1]

[1]*Faculty of Mechanical Engineering, Institute of the Automation and Transport, University of Science and Technology in Bydgoszcz, Al. prof. S. Kaliskiego 7, Poland.*

Abstract
A car collision with a barrier or with another vehicle results in a necessity of repair and the costs are usually not low at all. It causes problems of abuse by reporting fake car collisions. The research methods presented in the article applying computer methods executed with the SDC method facilitate an efficient verification of car collisions which, in fact, did not occur. Research methods executed in the SDC convention use the static, dynamic analysis of vehicle damage as well as the analysis of characteristic damage. To automate the decision-making process during the crash verification with the SDC method, the author's IT tool to be applied in practise was also developed. The research with a set of real road traffic damage already at the stage of civil-law proceedings shows that insurance companies face a problem of a lack of effective computer methods which would allow for eliminating fake vehicle collisions.

Key words: *SDC method, vehicle collision verifying.*

INTRODUCTION

The repair costs, to be borne to restore the vehicle to its before-accident condition, are the cause of fake car collisions. Insurance companies see the problem of insurance crime, however, to manage claims, they do not introduce any computer methods applied in mechanical engineering in a form of simulation programs for vehicle collisions, databases of vehicle vector styling and IT tools aiding the decision-making process.

The possibilities of applying the proposed method to eliminate insurance frauds have been described in another paper (*Aleksandrowicz, 2017a*), and verifying vehicle collision with the SDC method requires dividing the process into three groups of computer research methods.

The first group includes a static analysis of damage inflicted during the collision of vehicles (S). The aim of applying the proposed procedures in that group is verifying the geometrical agreement of the damage of vehicles involved in the declared collision. The procedure uses the databases of vehicle vector stylings and their photographs (*http://www.autoview.at*).

The second group of research methods uses IT tools for a dynamic analysis of collisions and its aim is to verify whether such collision could have occurred in the circumstances reported. The analysis involves both verifying the vehicle crash itself and time and space relations between the participants of the collision reported to the insurance company. Dynamic analysis uses simulation programs offering a selection, adequate to the damage verified, of model and parameters of the crash and collision detection model as well as computations to determine whether time and space relations necessary for the contact between the simulation objects exist. Another paper (*Aleksandrowicz, 2017b*) discusses a selection of the applicable model of vehicle collision and collision detection while working with V-SIM4 program (*V-SIM4.0 – User manual, 2016*) used for a dynamic verification of vehicle collisions with the SDC method, whereas papers (*Kostek, 2017a,b et al.*) cover identifying impact parameters based on crash tests and a simulation of vehicle collision with a barrier to be applied in V-SIM4 program by road accident reconstruction and claims verification practitioners. Using software for a dynamic analysis, one should also consider an effect of uncertainty of the input data on computation results. With that in mind, it is most effective to use the modules of simulation programs which facilitate optimization calculations, e.g. with the Monte Carlo method, which has been covered in other papers (*Wach & Unarski, 2007a,b*).

The third, and the last, group of research methods includes an analysis of damage characteristic at the place of contact of vehicles during the crash or collision with a e.g. elements of roads infrastructure. Additionally, to provide a more detailed pattern of verifying the collision with the SDC method and the operation of the dedicated IT tool aiding the decision-making process

(*http://wim.utp.edu.pl/dok/wyklady/analiza_sdc.xlsm*), a demonstration film was recorded (*https://www.youtube.com/watch?v=91rYSnVrbs4&feature=youtu.be*).
This paper aims at demonstrating the SDC method developed to verify vehicle crashes and the author's IT tool facilitating a decision-making process to identify and to eliminate post-accident repair claim frauds.

MATERIALS AND METHODS

For the purpose of this paper, vehicle collisions were examined for 84 claims applying the following SDC method procedures. Further analyses involved the use of the computer program developed by the author; the program automates the decision-making process to eliminate post-accident repair claim frauds.
Static analysis can use research methods which compare real objects in a form of vehicles or their elements, photographs of damaged vehicles or vehicle vector stylings. Performing a transparent superposition involves superposing scaled photographs of both vehicles; one which is less transparent, which allows for a geometrical comparison of damage as in real-life objects, Fig. 1.
Vehicle vector stylings, on the other hand, are imported to the simulation program in the real scale and proportions and their shapes are the shapes of vehicles taking part in the collision reported; they can be used to perform geometrical measurements of the damage zones overlap, Fig. 2.

Fig. 1 Combinations of research procedures in the block of static analysis of the vehicles collision, transparent superposition.

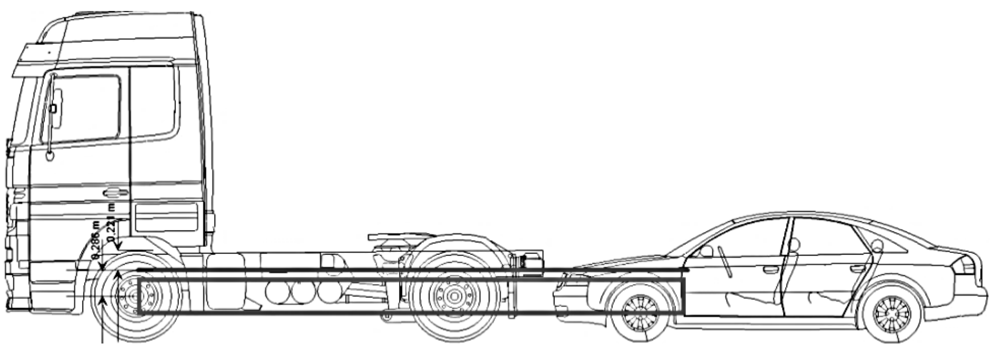

Fig. 2 Combinations of research procedures in the block of static analysis of the vehicles collision a comparison of damage zones in vehicle vector stylings.

Figures 3 and 4 demonstrate the results of the dynamic verification of a truck collision with a passenger car as well as with a tree (*https://www.youtube.com/watch?v=91rYSnVrbs4&feature=youtu.be*).

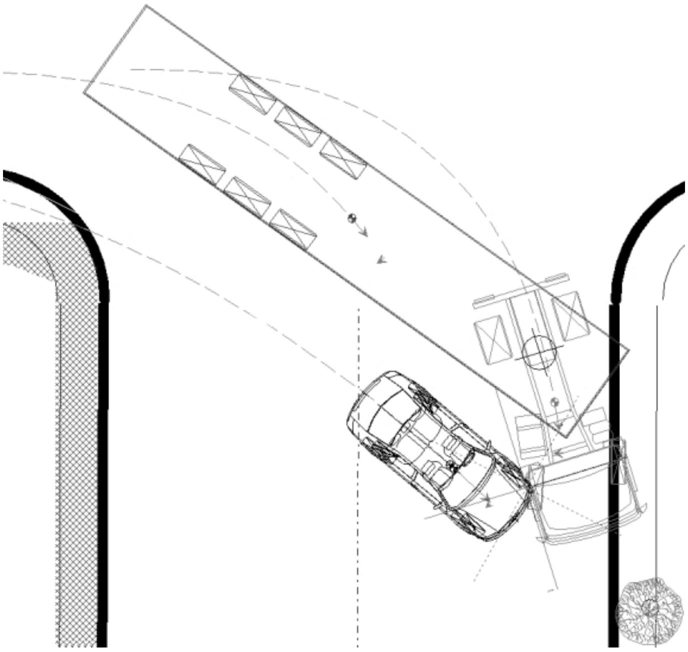

Fig. 3 Visualisation of dynamic verification performed in V-SIM4, a collision between a passenger car and a truck.

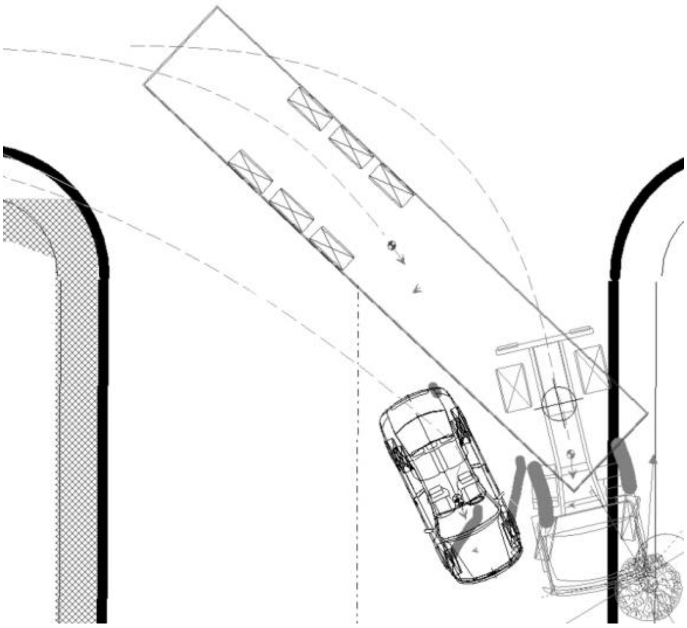

Fig. 4 Visualisation of dynamic verification performed in V-SIM4, a crash of a truck into the tree.

To verify characteristic damage of vehicles, data from inspections of vehicles or photographs taken at the resolution allowing for multiple magnification are used. The analysis aims at identifying the marks of contact between the vehicles in a form of shape mapping, paint layers, organic substances, etc.
Fig. 5a presents a sample mark of shape mapping of a truck hub cap on the passenger car fender as well as paint layers the colour of which correspond to the colour of that hub cap. Fig. 5b demonstrates traces of organic substance (bark) blocked in deformed, after the crash into a tree, structures of the left corner of road tractor cabin.

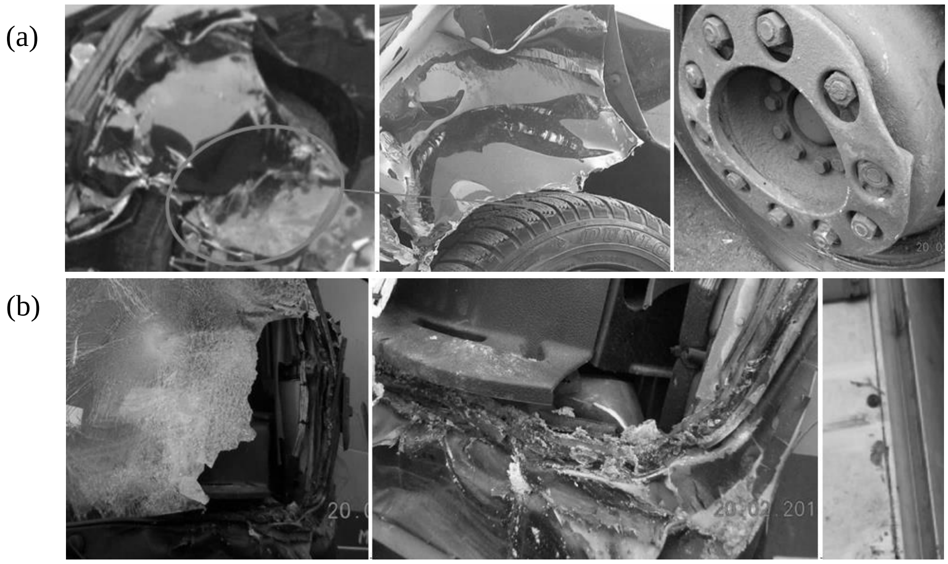

Fig. 5 Characteristic damage in a form of truck hub cap shape mapping on the passenger car fender and paint layers from that hub cap (a) and bark identified in the road tractor cabin (b).

In order to improve the research methods effectiveness, an IT tool has been elaborated to provide decision variants after entering the results of procedures S, D, C of a damage verified. Fig. 6 and Fig. 7 demonstrate the program dialog boxes (*http://wim.utp.edu.pl/dok/wyklady/analiza_sdc.xlsm*).

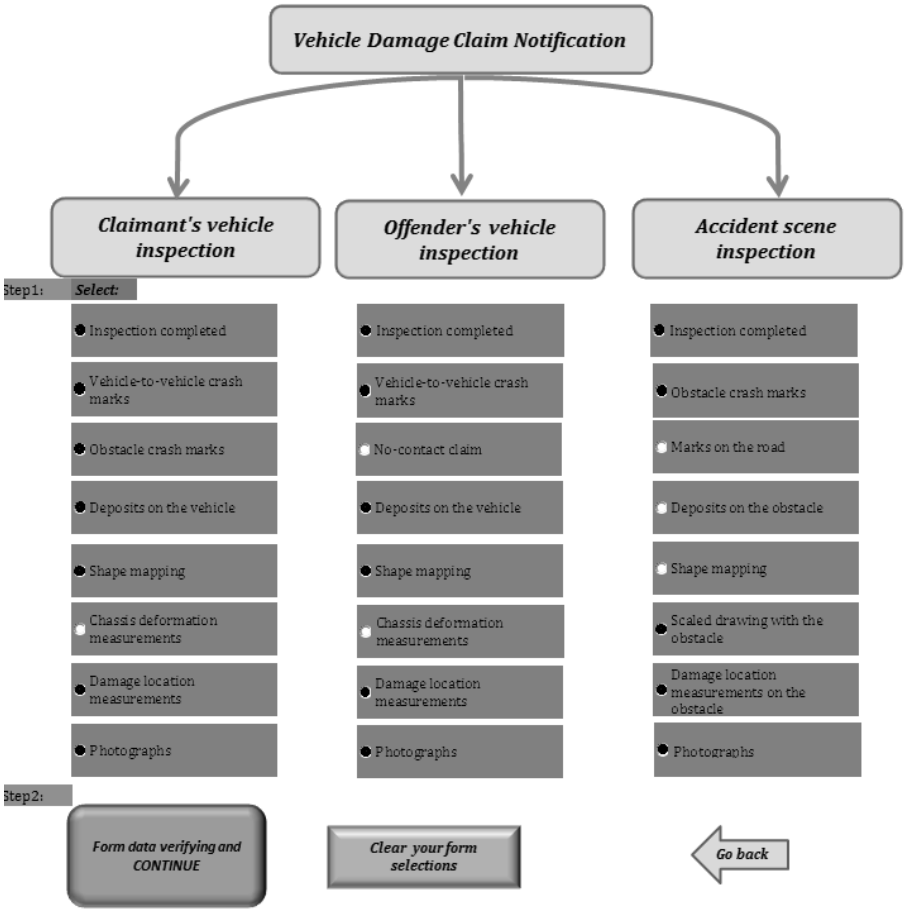

Fig. 6 Entering the input data in the dialog box.

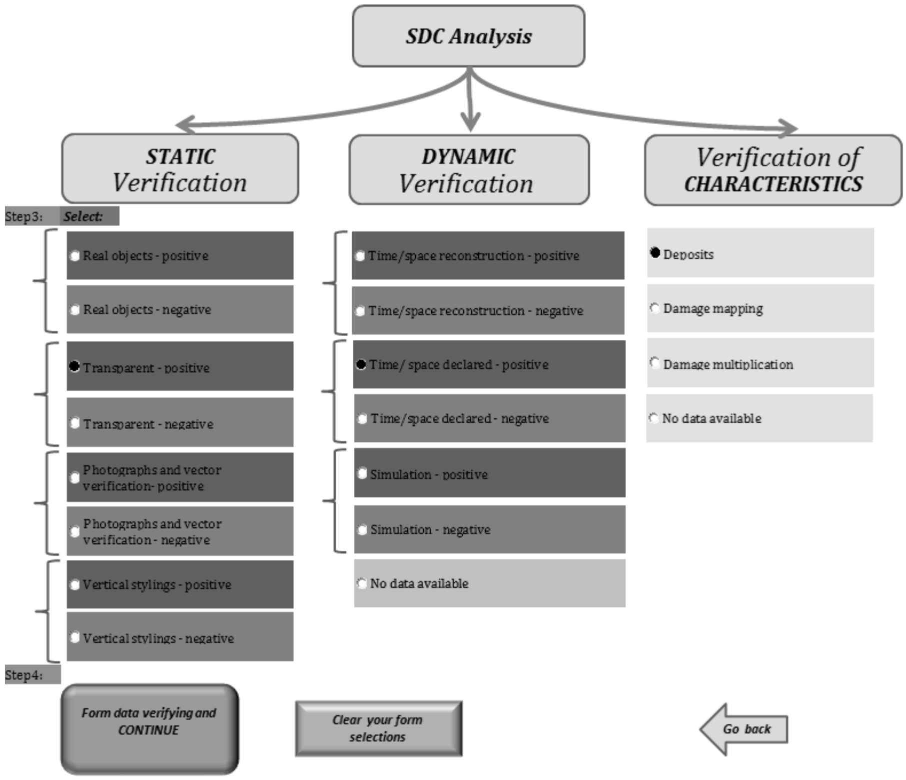

Fig. 7 Entering procedures S, D, C results in the dialog box.

RESULTS AND DISCUSSION

The research covered 84 claims of vehicle damage where the insurance companies refused to pay damages and the damages were claimed in court proceedings. To verify the decision of the insurance company in each case, the SDC method was applied. The analysis was performed applying procedure S, D, C and data was entered into the program to support decision-making. Letters P and N, positive or negative, stand for the result of each procedure, as compared with the total result received with the SDC method, for the results, see Fig. 8

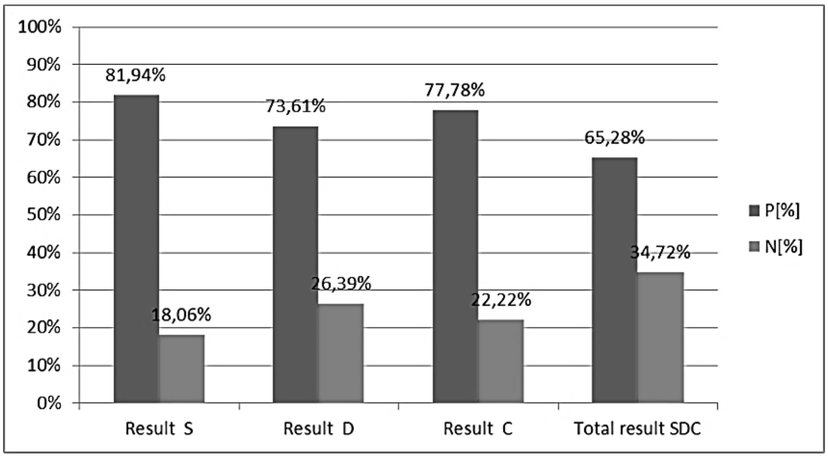

Fig. 8 Results of the study applying the SDC method.

The results of the examination with the SDC method have shown that only 34.72 % of the claims were correctly verified by insurance companies, and payment for the other 65.28 % should have been made already at the stage of claims management, without court proceedings.

CONCLUSIONS

Motor insurance crime is a very important social problem. For example, the issue of motor insurance frauds, as compared with the situation in the Czech Republic and in Germany, is presented in another paper (*Rábek, 2013*). However, in practice, a comprehensive claims verification such as in the proposed SDC convention together with decision-making process automation to eliminate fake collisions does not occur.

Bearing that in mind, it is the author's intention to encourage the application of such new approach in the SDC convention to verify car collisions using the program developed for that purpose to automate the decision-making process. The program offers decision variants to the operator and it has been specially developed following the MS Excel standard described in another paper (*Walkenbach, 2014*), thanks to which it can be applied by a high number of users with that popular software package.

The verification results point to serious problems of insurance companies verifying frauded damage claims both at the claims management stage and at the stage of disputes settled by the court, whichgenerates unquestionable losses for the parties to the proceedings.

Verifying claims with the proposed SDC method and the program developed to aid decision making is a new research, development and improvement area.

It is the author's intention to demonstrate the results of further research in successive articles.

REFERENCES

1. Aleksandrowicz, P. (2017). Analysis of vehicle collisions with the SDC method. In *EM2017 23rd International Conference Engineering Mechanics* (pp. 78-81).
2. Aleksandrowicz, P. (2017). Verifying the application of the models of crash and collision detection of incompatible vehicles. In *EM2017 23rd International Conference Engineering Mechanics* (pp. 82-85).
3. Kostek R., Aleksandrowicz, P. (2017). Effect of contact parameters on the pattern of vehicle collisions with a round pillar. In *EM2017 23rd International Conference Engineering Mechanics* (pp. 490-493).
4. Kostek R., Aleksandrowicz, P. (2017). Identification of the parameters of vehicle contact with a rigid barrier from a crash test. In *EM2017 23rd International Conference Engineering Mechanics* (pp. 494-497).
5. http://wim.utp.edu.pl/dok/wyklady/analiza_sdc.xlsm
6. http://www.autoview.at
7. http://www.cyborgidea.com.pl
8. https://www.youtube.com/watch?v=91rYSnVrbs4&feature=youtu.be
9. Rábek, V. (2013). Frauds in the field of the motor vehicle insurance. *Paragraph on the Road. Court Expertise Institute Cracow*, (7), pp. 43-68.
10. V-SIM4.0 – User manual (2016). *CIBID Cracow*.
11. Wach, W., Unarski, J. (2007). Determination of collision location – uncertainty analysis by means of Monte Carlo simulation, *16th EVU Annual Meeting Proceedings* (pp. 73-93).
12. Wach, W., Unarski, J. (2007). Uncertainty of calculation results in vehicle collision analysis, *Forensic Science International 167* (3), pp. 181-188.
13. Walkenbach, J. (2014). Excel 2013 PL. Programing in VBA. Vademecum of Walkenbach. *Helion Gliwice.*

Corresponding author:
Ing. Piotr Aleksandrowicz, Ph.D., Machine Maintenance Department, Institute of the Automation and Transport, University of Science and Technology, Al. prof. S. Kaliskiego 7, 85-796, Bydgoszcz, Poland, phone: +48 52 3408242, e-mail: p.aleksandrowicz@utp.edu.pl

MEASURING CUSTOMER COMFORT OF THE SIDE DOOR SELF-EQUIPMENT FOR THE AUTOMOBILE INDUSTRY

Pavel BARTONÍČEK[1], Ivan MAŠÍN[2]

[1]*Department of Machine Parts and Mechanism, Faculty of Mechanical Engineering Liberec*
[2]*Department of Machine Parts and Mechanism, Faculty of Mechanical Engineering Liberec*

Abstract
The article deals with the assessment of the customer comfort of controlling the side-cars-door and the creation of measuring devices for its objectification. The aim is to describe to the reader different approaches and the creation of a customer assessment methodology in the automotive industry. The collected data helps the automotive industry to innovate existing parts, construct new ones, reduced claim and production costs. The result is satisfaction customer's needs with a focus on a particular customer group.

Key words: *Energy measurement, speed measurement, automotive industry, quality, customer comfort.*

INTRODUCTION

Automobile manufacturers are looking for an opportunity to reach out to the customer, offering him added value. They use process and existing methods such as Customer design for X - DFX (1), Failure Mode and Effects Analysis - FMEA described by H u a n g (1996) , Advanced Product Quality Planning-APQP mentioned by S t a m a t i s (2003),. The automotive industry often used Lautes Denken methods used by Z h a o , B r o w n, K r a m e r , & X u (2011). For repeatability, all processes need to be checked to guarantee product quality. Car manufacturers follow the ISO 9001: 2015 standard, which establishes a link between company management, quality management system, customer requirements, allocation of competences, and more accurate targeting of market expectations. Newly, the introduction of a risk management system. These standards are defined and controlled in the Czech Republic by means of the Czech Accreditation Institute. The Czech Accreditation Institute (ČIA) provides the accreditation of persons, certification of authorities according to ČSN EN ISO/IEC 17021-1: 2016 or the quality management system. Means of law 505/1990 collections. the measurement, measuring equipment and systems are defined. Next it determines gauges, catalogs them, recommends calibration periods, defines the measurement process.

This article focuses on the preparation of technical measuring instruments. These specialized measuring devices evaluate the door closing speed and the total energy needed to close, open or progress the door control. We will explain the analogy of both approaches to evaluation and measurement of customer comfort. In the examples, it demonstrates the weaknesses and strengths of both methods in detecting manufacturing or user defects. The aim is the creation of a measuring device that describes a subjective customer assessment using measurable physical parameters. Another objective is to create a methodology that guarantees the repeatability and comparability of measurements. The obtained data are used by the automotive industry at the stage of development, production control and claims analysis. The priority is to reduce claims and production costs and to meet customer needs with a focus on a specific customer group focusing especially on a particular customer group.

MATERIALS AND METHODS

The principle of measuring the closing speed is the measurement of the time at which the measured object will run between two points on a defined path. By deriving the path by time, then determine the velocity according to the formula (1),

$$v = \frac{ds}{dt} = \dot{s} \tag{1}$$

Where the path s (m), time t (s), the resulting closing velocity v (m / s). The measuring device Fig. 1 is composed of a detection head and an evaluation unit. The detection head includes two industrial inductive sensors detecting presence of metallic material. Sensors are located exactly 50mm apart on a clearly defined linear path. Inductive sensors have been used, because passenger cars are mostly made of metallic materials. The evaluation unit contains a microprocessor that performs the evaluation of the measured value and the resulting closing speed is displayed on the display. Measuring device for energy measurement of the side door of a passenger car is based on the idea of measuring the total energy needed to close the door. One of the ways to measure energy is represented by equations (2), where m (kg) is the total weight of the door, v (m / s) is the speed of the moving door when closing or opening, Ec (J) is the resulting total energy.

$$E_c = \frac{1}{2} m \times v^2 \tag{2}$$

The measuring device Fig. 5 works on the principle of measuring the force supplied by the operator and accumulated in the spring. This stored energy is used for closing the door of a passengers car. The device also includes a tensometric sensor that measures the force supplied by oparator to the spring. The measurement result is the whole energy needed to close the passenger car door. Equation (3) describes the measurement principle of the instrument.

$$E_c = \frac{1}{c}\left[F_1 \times F_0 - F_0^2 + \frac{1}{2}(F_1 - F_0)^2\right] \tag{3}$$

Constant C (N / mm) the spring stiffness is determined by calibration from repeated measurements on the test standard. Force F_1 (N) is the tension force required to close the side door of the vehicle to overcome the effects listed in the table Tab..The force F_0 (N) is the force of the biased measuring arm. The resulting total energy E_c (Nm) is the energy needed to close the car door.

RESULTS AND DISCUSSION

Customer reviews are influenced by a subjective perception that assigns a negative or positive emotional charge to individual actions. Automobile manufacturers seek to gain and transform the customer's view into a measurable physical quantity that will help innovate the product in the PLM lifecycle management process in order to maintain its competitiveness. One example is the control of the car's side door system. Here the customer claims the difficulty of closing the door. To evaluate the subjective customer opinion, the automotive industry uses two methods. One is based on the measurement of the energy needed to control the door, the other method only monitors the closing speed of the door in the last phase of the movement. The measuring method of closing velicity of passengers car is based on an experiment empirically verified by the fact that the closing doors of the personal car need the greatest speed to overcome the door locking mechanism and compression of the door seal that seals the vehicle immediately before closing the door. Therefore, it is not necessary to measure the speed throughout the closing process, but just measure the impact speed of the door immediately before closing them, ie approximate the circular path of the door in the measured section as a straight line.

Fig. 1 Measuring of closing velocity

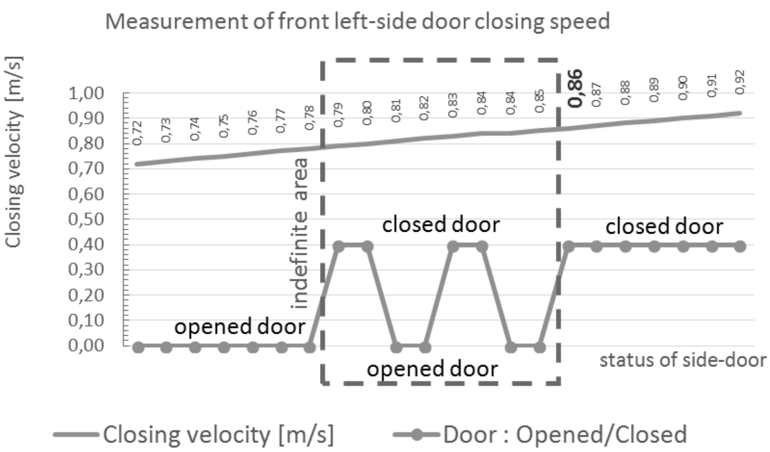

Fig. 2 Result of closing speed experiment

The measurements were made on the front-left door of Škoda Octavia car in the door handle area. The door has been repeatedly closed to find the smallest value of the door closing speed. The measurement was repeated several times to determine the accuracy of the measured value. The results of the measurements were recorded in the graph Fig. 2.The experiment showed an anomaly during the closing speed measurement close to the true closure speed (0.86 m/s). In this "undefined area", the side-car-doors may be during repeated measurement opend or closed randomly in spite of the same value of closing speed. An "undefined area" was defined at a rate of 0.78 m / s and 0.85 m / s. Another measure was found that the closing speed is affected by the delay between the two measurements and is dependent on the relaxation of the main seal Fig. 3.

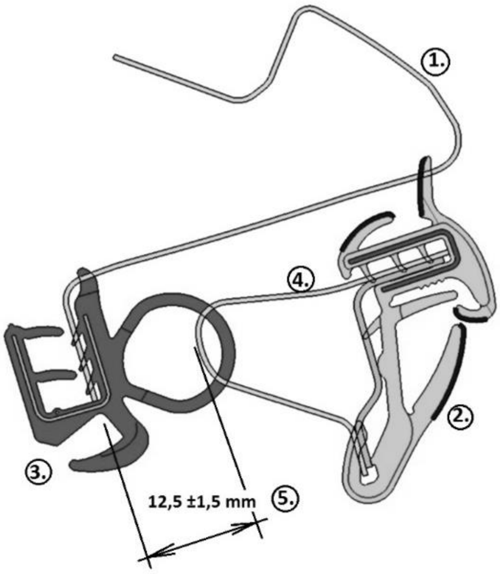

Fig. 3 Cur through the side door

Fig. 4 Detail of the main sealing of the door

The side doors, position 4. at Fig. 3. are adjacent to the side of the car (position 1.) and are sealed at the point of contact by the main sealing (position 3.), which has cut off venting hole in regular intervals. Relaxing the seal means the fully inflated seal time Fig. 4 to a state where it does not exhibit deformation. Based on this experiment, a method of measuring the closing speed was set up and a pause between iterations was set, resulting in a "undefined area" reduction and higher measurement accuracy. The following measurements determined the side effects on the closing velocity Tab. 1.

Tab. 1 Effect on the door closing speed

Influencing effect	Vehicle part	Parameter / unit
Position of the door latch and lock	Lock of the lock	position at Y and Z axis / (mm)
Facing the door to the side of the car	Door hinges	position at Z axis / (mm)
The gap between the door and the side	Door, sidebars	position at Y axis / (mm)
Flexible of main seal	Main door seal	hardness / (N/mm)

The measuring of closing energy method is based on the measurement of the total energy needed to close the door. The measuring device Fig. 5. consists of a spring (which accumulates the force required to close the door). Then the strain gauge (measures the force). The measuring device measures the total energy required to close the door when the spring is released.

Fig. 5 Measurement of closing energy

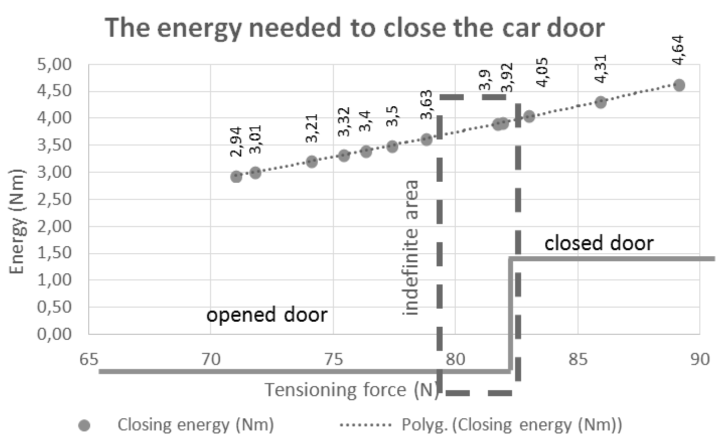

Fig. 6 Result of closing energy experiment

The experiment showed that there is also a "undefined region" (Fig. 6), in which one door is open and one closed at one closing energy value. Its size is influenced by other phenomena in addition to the phenomena mentioned Tab. 1. (see Tab. 2)

Tab. 2 Side effect on the door closing energy

Influencing effect	Parameter / Unit
Setting the measuring arm in the car	distance in X axis / (mm)
Preload of the spring before the measurement begins	force / (N)
The accuracy of meas.depends on the quality of the operator	Repeatability of measurement

CONCLUSION

The results of the experiments were used to make a comparison between the two measuring methods, ie the side-door-closing speed and the closing energy needed to close the passenger side door Fig. 7. The measurement did not show a linear dependence between the closing energy measurement and the closing speed.

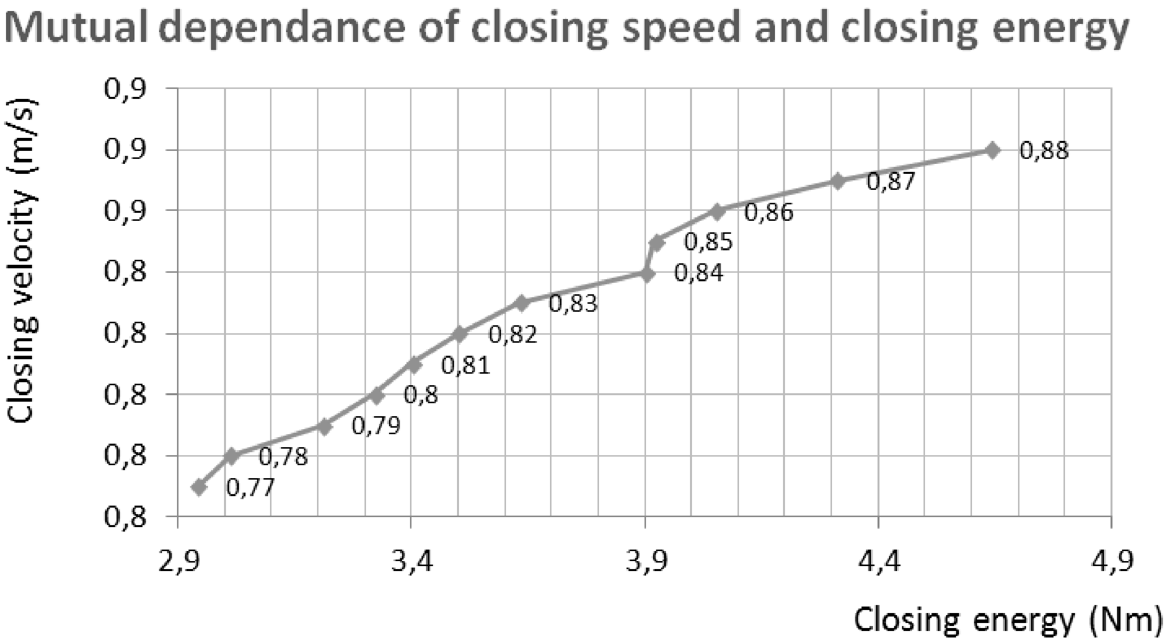

Fig. 7 Result the comparison of closing speed and closing energy

The energy measurement method has proven to be disadvantageous for several reasons:

- Higher dependence on the operator precision, setting of the measuring arm and continuous and gradual increase of the tensioning force F_1 (N).
- The wider indefinite area represents approximately 10.4% of the measured value. Repeated measurements have failed to reduce the measurement and thus improve the measurement.
- The repeatability of measurement due to non-linearity Fig.7 is worse when measuring the closing energy compared to the closing speed measurement.
- Because the telescopic arm is rubbing, the measurement inaccuracy increases.
- The total measurement time of the car is including installation for about 1.5 hours, which puts great demands on the operator's concentration.
- The measuring range depends on the spring tension F_0 (N) of the measuring arm, ie the measurement in the range of 10-25 cm opening the side door.

The closing speed measurements showed the following benefits over the closing energy measurements:

- Greater sensitivity and scalability of measurement allows for faster analysis.
- Repeatability of measurement result approx. ± 0.03 m/s
- Closer indefinite area, here is 0.07 m/s, which is about 8% of the measured value, but empirical experience can achieve another narrowing of an "indeterminate area" to about 4% of the measured value.
- Lower operator requirements
- Easier installation of measuring equipment, complete car can be measured in about 1/4 hours
- Measuring range, 5cm.

The purpose of this article was to make a comparison between closing energy and closing speeds, methods that evaluate customer comfort in the automotive industry. Exploration has shown that snap rate measurement is better suited for quick fault detection, which is quick, easy on the operator and allows faster analysis. Measurement of the closing energy is an elegant way of measuring the otherwise subjective feeling of the customer because it evaluates the energy input in a larger open-door-range (about 5 times greater) than when measuring the closing speed.

ACKNOWLEDGMENTS
This study was supported by a car manufacturer Škoda Auto a.s., Technical University of Liberec namely Doc. Ph.D. Ing. Petrů and Prof. Ing. Ševčík, CSc. and Institute of Industrial Engineering IPI, namely Doc. Dr. Ing. Mašín

REFERENCES

1. Huang, G. Q., (1996). Design for X, Current engineering imperatives. USA: Springer-Science-Business Media *ISBN: 978-94-011-3985-4.*
2. Stamatis, H.D., (2003), Failure Mode And Effect Analysis from Theory to Execution. USA: Quality press *ISBN: 978-0-87389-598-9.*
3. Zhao, Y., Brown, R., Kramer, R., & Xu, X. (2011). Information Modeling for Interoperable Dimensional Metrology. USA: Springer. *ISBN: 978-1-4471-2166-4*
4. Green, A., (1989). Verbal Protocol Analysis in Language Testing Researc. GB: University of Cambridge. *ISBN: 978-0-52158-635-1*
5. Czech Accreditation Institute (ČIA). (2017). Retrieved from: http://www.cia.cz
6. Czech office for standards, metrology, and testing. Law no. 505/1990. Collection . (2017) Retrieved from: http:// www. unmz.cz/ fies/metrologie/úplná%20pracovní%20znění %20předpisů/ zm3-2015.pdf.

Corresponding author:
Ing. Pavel Bartoníček, Technical University of Liberec, Faculty of Mechanical Engineering, Studentská 2, Liberec, Czech Republic, 461 17, email: pavel.bartonicek@gmail.com

CHARACTERISTIC PARAMETERS FOR PROPULSION SYSTEMS COOPERATING WIH SHAFT GENERATOR ON FEEDER CONTAINER SHIPS

Cezary BEHRENDT[1]

[1]*Institute of Marine Propulsion Plants Operations, Maritime University of Szczecin, Poland*

Abstract
The paper presents the obtained parameters of specific propulsion systems cooperating with shaft generators, used at feeder container ships. Based on the collected technical and operational data for container ships of various load capacity, constructed between 2000 and 2015, and by applying different analytical and statistical methods the parameters have been determined. Shaft generators' power has been established in relation to the power of main engines. The ratio of shaft generator power to main engine power has been also determined as well as the speed developed by container ships depending on the propulsion system power and on the relation to the generators' power to the power of main engines. Feeder container ships have been selected as a subject of the analysis taking into consideration the environmental and economic aspects. This type of ships is the most frequently operated in the sea regions where strict rules and provisions on exhaust gas emission apply. They transport container to and from ports serving ships of high bearing capacity. The parameters obtained may be applied to specify the ratio for exhaust gas emission, to compare fuel consumption for various methods of generating electricity and to assess the possibilities to use the waste heat recovery systems along with turbogenerators.

Key words: *feeder container ship, energetic systems, characteristic parameters*

INTRODUCTION

The problem of proper selection of shaft generator power and the electricity generation methods refers in particular to container ships due to a high demand for electricity as a result of a large number of the refrigerated containers being transported thereby.
Generating electricity using shaft generators driven by the main engine is one of the alternative methods to reduce fuel consumption and the cost of electricity generation.
The efficiency of that solution results from the generally known advantages such as:

- the reduction of fuel cost and cost of lubricating oils used in the process of electricity generation due to higher efficiency of the main engine when compared with auxiliary diesel engines for power generator units;
- improvement of the environment by the reduction of exhaust gas emission and remaining petroleum waste.

These effects however include certain defects. The main ones are:

- the requirement to stabilize the frequency of current generated by the generator in every operational condition of the propulsion system (variable rotational speed of the generator driven by the main engine);
- using a shaft generator to reduce the ship speed as a part of the main engine power is transferred to the generator as opposed to the propeller. The speed decrease depends on the shaft generator power and is within the range from 5% to 10% of the operational speed (*Balcerski* 1998, *Behrendt* 1997).

The power of shaft generators installed on ships depends on the type and purpose of the ship.
The rule is that a shaft generator should fully cover the demand for electricity for cargo ships while sea voyage.
The power of shaft generators equals to from 115% to 120% (*James M., Wolfe P.E., Morgan M. & Fanberg P.E.* 2014, *MAN Diesel & Turbo* 2013) of the design power resulting from the electric balance. Such a power surplus is assumed due to the fact that:

- the sum of powers of working electrical equipment and machines is a random variable;
- the generator is loaded with starting current of electric motors;

- along with time the generator efficiency decreases as well as electric motors supplied by it.

Increasingly common on ships are used waste heat recovery systems in order to maximize the amount of steam generated in waste heat boilers. The steam is used to cover the demand for heat on a ship and to drive turbogenerators (*Behrendt* 2016, *Hagesteijn G.P.J.J., Hooijmans P.M, v.d. Meij K.H., Greening D. & Yu L.* 2014, *MAN Diesel & Turbo* 2012, *Mitsubishi Energy Recovery System for Container Vessels* 2015). The power of a turbogenerator depends mainly on the main engine power and its power load. Due to high speeds developed by container ships and hence the main engine power, this type of ships is in particular suitable to install the waste heat recovery systems.
A traditional method for determining a demand for electricity, applied by naval design offices, consists of preparing an electric balance in which electric motors' powers are summed up. Based on this, marine generators' power is specified.
The paper aim is to present the characteristic parameters for propulsion systems of feeder container ships which would specify the relations of shaft generators' powers to the main engine power, ship speed, deadweight capacity, the number of crewmembers, the number of transported containers. For that purpose, technical and operational data of the ships has been gathered. The data refers to the feeder container ships of various dimensions, constructed between 2000 and 2015. The data has been processed.
Similar methods of determining characteristic parameters for propulsion systems have been applied for other ships' types (*Balcerski A., Bocheński D.* 1998, *Matuszak Z., Nicewicz G.* 2013).

MATERIALS AND METHODS

On the grounds of an analysis of science studies (*Schiff & Hafen 2000-2015*, *Pohl K.* 2009) the author was enabled to prepare Table 1. The table includes technical and operational data of the container ships constructed in shipyards located around the world between 2000 and 2015. Due to a limited size of the paper, Table 1 includes data regarding chosen the ships constructed in 2000 only. The full table consists of data referring to 87 container ships.

Tab1. Technical and operational parameters of selected feeder container ships

Ship name/ Year of built/ Country of built	Dead weight	Container no/ Refrigerated Container no	Vessel Speed	ME* Type / Power	Propeller Type	SG* Power	No and BT* Power	No and DG* Power
	D	n/n_1	v	N_{SG}	FPP*/CPP*	N_{PZ}	N_S	N_{SZP}
	[dwt]	[-]	[kn]	[kW]	[-]	[kW]	[kW]	[kW]
Geuldiep/ 2000/ Spain	4.100	240/100	13	MaK 6M32/ 2.880	CPP	240	1x290	2x160
Marcape/ 2000/ China	5.100	550/40	16	MaK 9M32/ 3.960	CPP	780	1x450	3x300
Annegret/ 2000/ Germany	9.631	813/50	20	MAN 9L48/60/ 9.450	CPP	1000	1x750	3x300
Apollon/ 2000/ Korea	11.950	901/176	17	Wartsila 8L46B/ 7.800	CPP	900	1x700	2x600
Isolde/ 2000/ Germany	34.026	2442/400	21	MAN L70MC/ 19.180	CPP	1400	1x1100	3x780
* ME- Main Engine, FPP-Fixed Pitch Propeller, CPP-Controllable Pitch Propeller, SG-Shaft Generator, BT-Bow Thruster, DG-Diesel Generator								

When analyzing the data in Table 1 and the remaining data, it may be stated as follows:

- deadweight capacity of feeder container ships is of highly variable. The smallest ships' deadweight capacity is 4,000 DWT, while the largest ones, given the service possibilities of destination ports, have the deadweight capacity of 40,000 DWT;
- the maximum number of transported containers varied from 200 to 3,000 items. Each ship could transport refrigerated containers the number of which equaled to from 40 to 500 items;
- operational speeds of the ships were within the range of 13-24 kn and were lower than the speeds developed by container ships transporting a cargo to large cargo ports; their maximum operational speed may equal to 28 kn;
- the power of the main engines varied within the range of 2.000 and 25.000 kW; the power is mainly dependable on the developed speed ships' capacity;
- every propulsion systems of the analyzed container ships were equipped with shaft generators the powers of which were sufficient to cover the demand for electricity of the ships and the transported refrigerated containers during a sea voyage;
- every container ship was equipped with a bow thruster/bow thrusters which enhanced maneuverability, especially in small harbors;
- the most ships were furnished with the CPP (Controllable Pitch Propeller); this stabilizes the frequency of current generated by the shaft generator in variable operational conditions. This technical solution is characteristic for feeder container ships.

Collected technical and operational data of feeder container ships allowed, using statistical analysis, to determine various characteristic parameters.

RESULTS AND DISCUSSION

The data in Tab. 1 allowed to determine numerous characteristic parameters. Certain, selected ones are presented and discussed in this section.
Figure 1 presents a function showing a relation of shaft generator power to the power of the main engine.

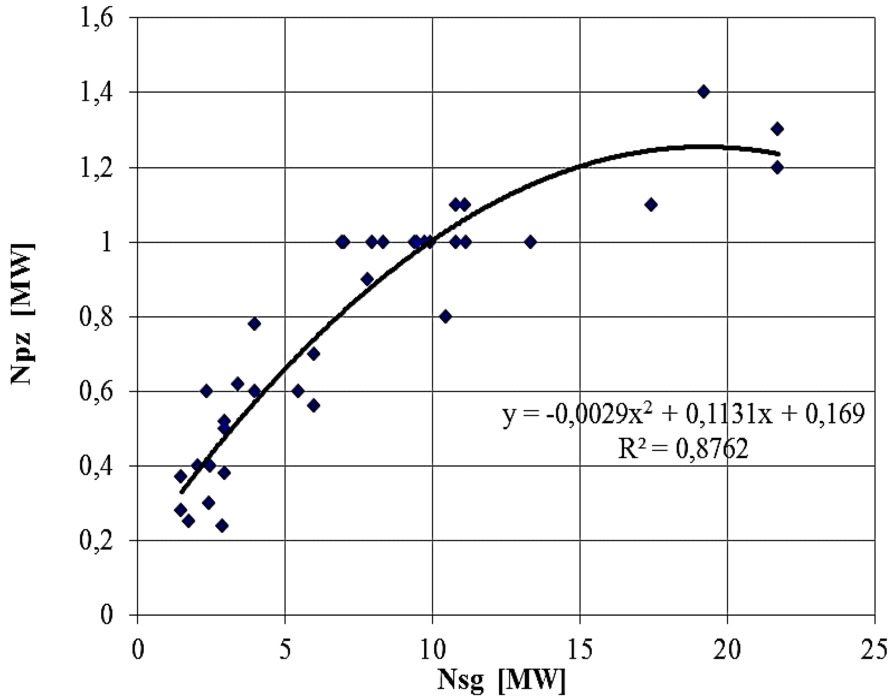

Fig.1 Relation of shaft generator power to the power of the main engine on feeder container ships

As the analyses have not shown any significant differences in the powers of the generators installed on the containers ships within the analyzed period, the graph does not differentiate the points so that they correspond to the individual shipbuilding years.
The obtained formula 1 enables to calculate the power of a shaft generator N_{pz} as a function of main engine power N_{sg}:

$$N_{pz} = -0{,}0029N_{sg}^2 + 0{,}1131N_{sg} + 0{,}169 \qquad [MW] \qquad (1)$$

Where: N_{sg} [MW] - main engine power

A mathematical relation (formula 2) has been also determined to compute the ratio of the power of a shaft generator N_{pz} to the main engine power depending on the main engine power N_{sg}:

$$\frac{N_{pz}}{N_{sg}} = 24{,}773N_{sg}^{-0{,}45} \qquad [\%] \qquad (2)$$

Formula (1) and (2) are applicable for :

$2\ MW \leq N_{sg} \leq 25\ MW$

Due to modern software and applications, it is possible to draw a dependency chart in a 3D coordinate system. As independent variables, main engine power N_{SG} and the relation of shaft generator power N_{pz} to main engine power has been selected. The dependent variable is ship speed v.

The relation $v = f\left(N_{sg}, \frac{N_{pz}}{N_{sg}}\right)$ is presented in Figure 2.

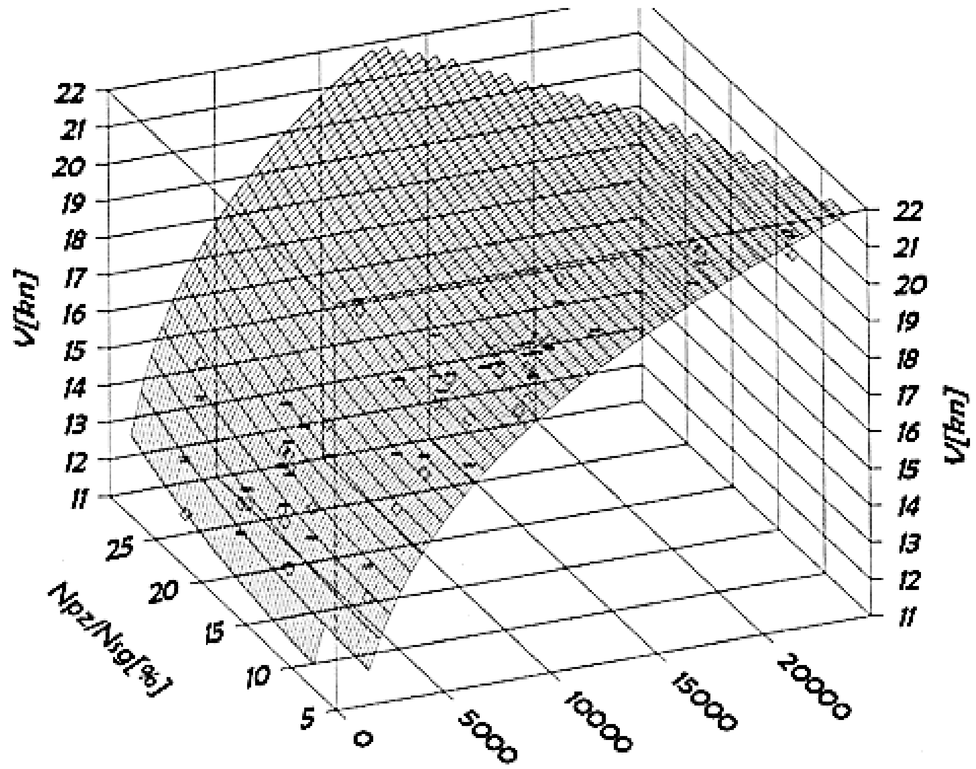

Fig. 2 Speed of container ships in connection to the power of main engine and the relation of shaft generators

The plane presented in Figure 2 may be calculated using formula 3:

$$v = 0{,}8735 + 0{,}2195 \ln N_{sg} + 2{,}8034e^{-5}\left(\frac{N_{pz}}{N_{sg}}\right)^{2,5} \quad \text{[kn]} \qquad (3)$$

The formula 3 is applicable for:

$5\% \le \dfrac{N_{pz}}{N_{sg}} \le 25\%, \qquad 2000 \le N_{sg} \le 25000$ kW

The formulas specifying selected parameters for feeder container ships, characterize with large values of the squared correlation coefficient (formula 1, R^2=0,8762, formula 2, R^2=0,8804 and formula 3, R^2=0,9053).

Statistical method presented in the paper was first time used to determine various characteristic parameters of feeder container ships. Similar methods of determining characteristic parameters for propulsion systems and energetic systems have been applied for other ships' types (*Balcerski A., Bocheński D.* for technological and energetic systems of fishing vessels and dredgers, *James M., Wolfe P.E., Morgan M. & Fanberg P.E.* for ships' electrical power plants, *Matuszak Z., Nicewicz G.* for marine electric power plants of container ships and drilling platforms, *Behrendt C.* for ships' propulsion system cooperating with shaft generator).

According the research analysis method presented in the paper allowed to determine numerous characteristic parameters chosen and dedicated to ships' types. Achieved formulas characterize with large values of the squared correlation coefficient.

Characteristic parameters are used on preliminary stage of ships' design and energetic analysis.

CONCLUSIONS

- The practical applications of the obtained formulas can be as follows:
  - determining energy efficiency indicators for all devices and machinery in the engine room according to the guidelines and requirements of the International Maritime Agency *(Lloyds Register);*
  - forecasting exhaust gas emission for various methods of generating electricity and in various operational conditions;
  - determining feeder container ship speed at recommended operation together with slow stimming;
  - determining cooperation conditions for propulsion systems and shaft generator at the design stage;
  - comparing actual demand for electricity with possible to have it generated using a turbogenerator;
  - determining configuration of waste heat recovery systems to achieve maximum steam capacity;
  - determining electric energy demand in function of refrigerated container quantity and ships' speed;
  - determining influence ratio of the power of a shaft generator to the main engine power depending on the main engine power and their influence on the ships' speed.
- Applied presented method of determining characteristic parameters for propulsion systems for other ships' types.

ACKNOWLEDGMENTS

This research outcome has been achieved under the research project no. 2/S/IESO/2014 financed from a subsidy of the Polish Ministry of Science and Higher Educations for statutory activities of Maritime University of Szczecin.

REFERENCES

1. Balcerski A., Bocheński D. (1998). *Układy technologiczne i energetyczne jednostek oceanotechniczych / Technological and energetic systems of ocean vessels*. Gdańsk : Gdańsk University of Technology.
2. Behrendt C. (1997). Service Investigations of a Ship Propulsion System Cooperating with Suspended Electric Generator, *Polish Maritime Research, No 2 (12)*, 29-31.
3. Behrendt C. (2016). An Analysis of Monitoring Requirements for Waste Heat Resource in Marine Power Systems, In *57-th International Conference of Machine Design Departments ICMD2016*, (pp.189-194), Book of Proceedings.
4. Hagesteijn G.P.J.J., Hooijmans P.M, v.d. Meij K.H., Greening D. & Yu L. (2014). Traditions Broken in Modern Container Ship Design. In *Conference Design & Operation of Container Ships* (pp. 36-46*)*, Book of Proceedings.
5. Implementing a Ship Energy Efficiency Management Plan (SEEMP), Guidance for shipowners and operators (2012). *Lloyds Register, (version 2.0).*
6. James M., Wolfe P.E., Morgan M. & Fanberg P.E. (2014). Statistical Analysis for Shipboard Electrical Power Plant Design. *The Glosten Associates, Inc.publication*. http://www.sname.org/HigherLogic/System/DownloadDocumentFile.ashx?DocumentFileKey=dad4cc49-da68-4274-a622-916100d514a4 [accesed May 02.2017]
7. MAN Diesel & Turbo (2012). *Quantum 9000. Two-stroke LNG by DNV and MAN Diesel & Turbo*, Publication no. 5510-0108, MAN Diesel & Turbo, Copenhagen, Denmark.
8. MAN Diesel & Turbo (2013). *Propulsion Trends in Container Vessels Two-stroke Engines*. Publication No 5510-0040-02ppr. Copyright©MAN Diesel & Turbo, Copenhagen, Denmark.
9. Matuszak Z., Nicewicz G. (2013). Analysis of marine electric power plants loads. In *ICMD2013 Conference Modern Methods of Construction Design Proceedings.* (pp.273-281), Springer International Publishing Switzerland 2014.
10. Mitsubishi Energy Recovery System for Container Vessels (2015). *Mitsubishi Heavy Industries Ltd, Nagasaki Shipyard & Machinery Works, Marine Machinery Design Department* http://pdf.nauticexpo.com/pdf/mitsubishi-heavy-industries-ship-ocean/energy-recovery-system-container-vessels/32135-20215.html [accesed Apr.14.2017].
11. Produced Ship List (2000-2015). *Schiff & Hafen*. DVV Media Group GmbH.
12. Pohl K. (2009). The Container Ships from Szczecin. Szczecin: Grapus Sp. z o.o.

Corresponding author:

Assoc. Prof. Cezary Behrendt, Ph.D. Eng, Institute of Marine Propulsion Plants Operations, Faculty of Marine Engineering, Maritime University of Szczecin, Wały Chrobrego 1-2, 70-500 Szczecin, Poland, phone: +48 91 4809479, e-mail: c.behrendt@am.szczecin.pl

DESCRIPTION OF THE BEARING CHECK PROGRAM FOR COUNTERSHAFT GEARBOXES

Michal BELORIT[1], Slavomír HRČEK[2], Tomáš GAJDOŠÍK[3], Ján ŠTEININGER[4]

[1]*Department of Design and Mechanical Engineering, University of Zilina*
[2]*Department of Design and Mechanical Engineering, University of Zilina*
[3]*Department of Design and Mechanical Engineering, University of Zilina*
[4]*Department of Design and Mechanical Engineering, University of Zilina*

Abstract
The article deals with the description of countershaft gearboxes and their basic dividing. Generally explains the program created in the environment of Microsoft excel and Matlab for controlling of designated bearings in this type of transmissions.

Key words:*countershaft gearbox, check program, rolling bearings.*

INTRODUCTION

Transmission is important mechanical component of almost every vehicle. Especially of the ones, that are fitted with an internal combustion engine. Because in spite of great amount of these engines usage, it has disadvantages such as incapability of production torque from zero engine speed, the maximum power is reached only at the specific engine speed and the fuel consumption depends on the operating engine point. These drawbacks can be compensated by an application of a conveniently designed transmission and a clutch (Lukáč, et al., 2016).
The countershaft gearboxes fall into the category of geared transmissions. And its main functions in automobiles are to change the torque and the speed of an engine in the way a vehicle is able to move in external conditions, to allow idle running of an engine and to enable reverse motion of a vehicle (Zdeněk, Žďábský, 2012). This category is possible to divide into three more groups, depending on the count of meshing gear pairs, which the power flows through, when the speed gear is shifted. It is termed the number of the ratio stages and according to it there are those groups (Naunheimer, et al., 2011):

- Single-stage transmission
- Two-stage transmission
- Multi-stage transmission

In the Fig. 1 below are plotted schematic examples of countershaft gearboxes. Single-stage means that the power flows from an input shaft to an output shaft, which could be also a countershaft, through one geared pair. In two-stage gearboxes the power goes from input to a countershaft and then to an output shaft, so there are two geared pairs simultaneously in action. The same analogy works for multi-stage transmissions (Naunheimer, et al., 2011).

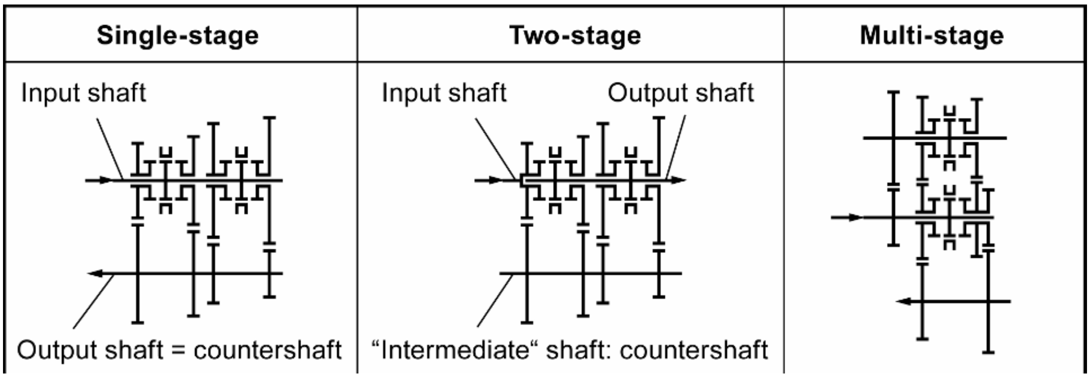

Fig. 1 Examples of countershaft gearboxes(Naunheimer, et al., 2011)

The countershaft gearboxes are also marked as gear sets with fixed axles and mainly consist of an input, output shaft and a countershaft, that are rotating in a rigid position in a gearbox. They are fitted in bearings, which are dynamically loaded throughout the transmission operating run. And they have important meaning for achieving the required durability and functionality of whole gearbox. That is why it is necessary to advisable designate rolling bearings in respect of a duty cycle and all known operating conditions (Hrček&Bucala, 2014).

MATERIALS AND METHODS

The program for control of rolling bearings was created only for the specific configuration of two-stage countershaft gearboxes. It considers that the axis of all shafts are lying in the same plane X-Z and that it is maximally twenty speed gearbox. The schematic view shown in the Fig. 2 is applicable just in the situation, when minimally two gears are mounted on the countershaft.

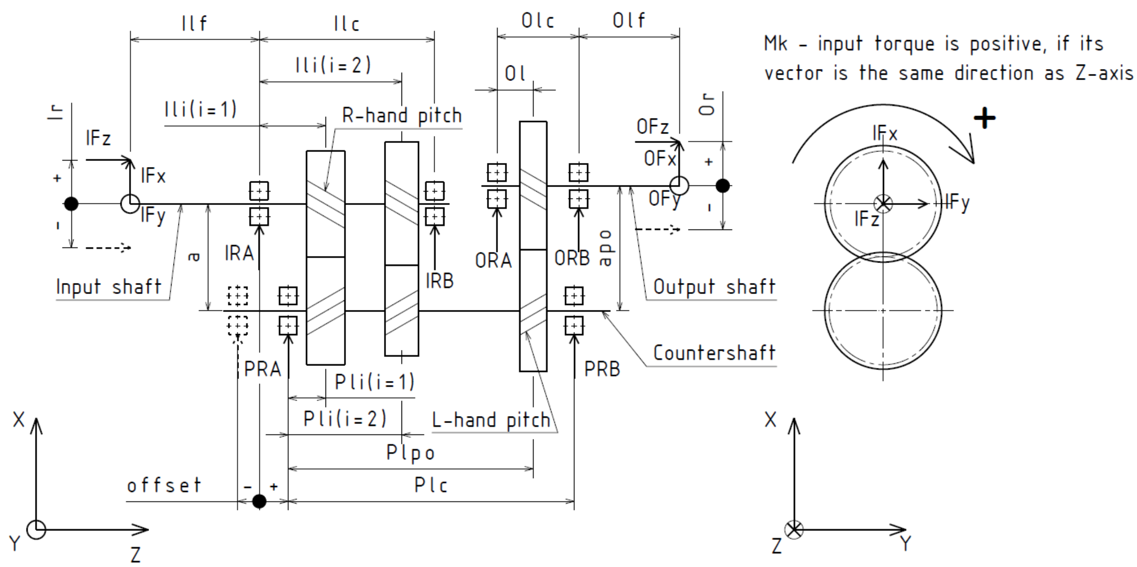

Fig. 2 The main schema of the inspected countershaft gearbox[Authors]

In the case there is mounted only one gear wheel, the countershaft becomes an output shaft and the program operates with configuration of a simple gearing plotted in Fig.3 below.

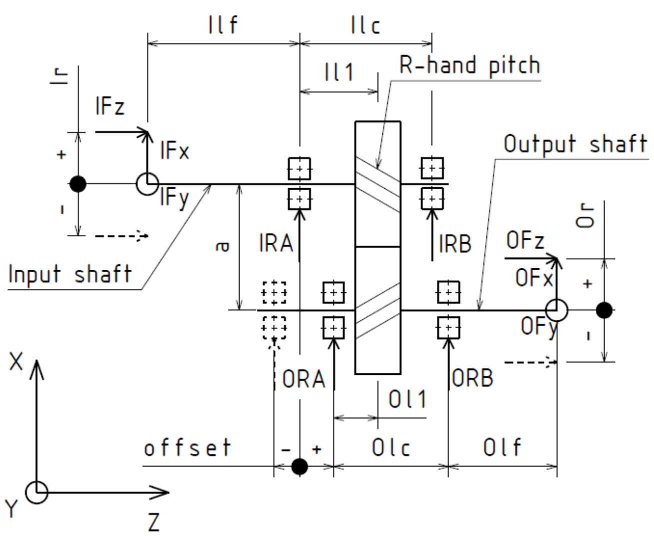

Fig. 3 The schema of a simple gearing[Authors]

RESULTS AND DISCUSSION

The program itself is compounded of two parts. One of them is created in the software Microsoft excel and the piece of it is shown in Fig. 4. The excel sheet contains the schematics mentioned above, according to which is needed to fill four tables of input data. These data includes information about relative positions of gears, bearings and shafts. Their basic geometric dimensions required for the calculation of forces distribution, duty cycle for every single speed gear and bearing characteristics. Even the database was created, that stores test array of bearings and their parameters declared by manufacturers. So the definition of each rolling bearing is executed by choosing the particular one from the drop-down list. This causes loading of all necessary specifications from the database. The list can be filtered by criterion of contact type between a rolling element and a groove of bearing rings, namely point or line contact. Next step is to set which bearings do or do not carry axial loading. It is important especially for the calculation of equivalent dynamical load (Kohár, et al., 2016).

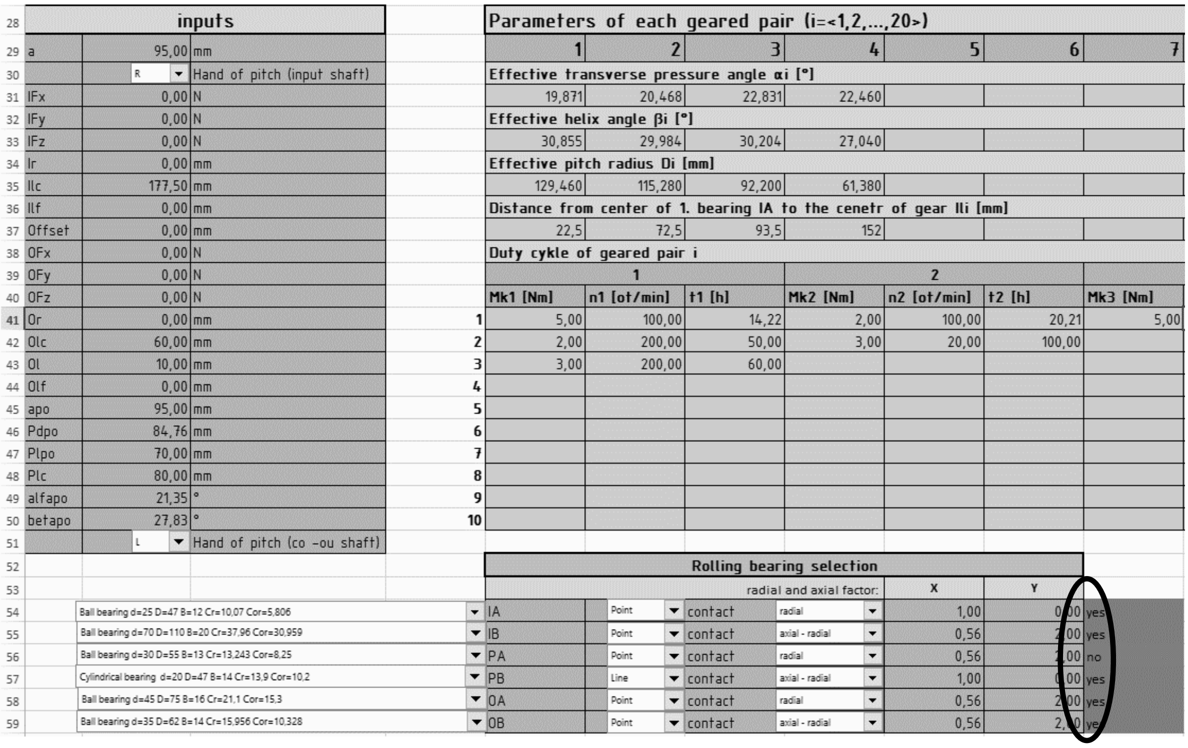

	inputs		
29	a	95,00	mm
30		R	Hand of pitch (input shaft)
31	lFx	0,00	N
32	lFy	0,00	N
33	lFz	0,00	N
34	lr	0,00	mm
35	llc	177,50	mm
36	llf	0,00	mm
37	Offset	0,00	mm
38	OFx	0,00	N
39	OFy	0,00	N
40	OFz	0,00	N
41	Or	0,00	mm
42	Olc	60,00	mm
43	Ol	10,00	mm
44	Olf	0,00	mm
45	apo	95,00	mm
46	Pdpo	84,76	mm
47	Plpo	70,00	mm
48	Plc	80,00	mm
49	alfapo	21,35	°
50	betapo	27,83	°
51		L	Hand of pitch (co -ou shaft)

Parameters of each geared pair (i=<1,2,...,20>)							
	1	2	3	4	5	6	7
Effective transverse pressure angle αi [°]							
	19,871	20,468	22,831	22,460			
Effective helix angle βi [°]							
	30,855	29,984	30,204	27,040			
Effective pitch radius Di [mm]							
	129,460	115,280	92,200	61,380			
Distance from center of 1. bearing IA to the cenetr of gear lli [mm]							
	22,5	72,5	93,5	152			
Duty cykle of geared pair i							
	1			2			
	Mk1 [Nm]	n1 [ot/min]	t1 [h]	Mk2 [Nm]	n2 [ot/min]	t2 [h]	Mk3 [Nm]
1	5,00	100,00	14,22	2,00	100,00	20,21	5,00
2	2,00	200,00	50,00	3,00	20,00	100,00	
3	3,00	200,00	60,00				
4							
5							
6							
7							
8							
9							
10							

	Rolling bearing selection							
					radial and axial factor:	X	Y	
54	Ball bearing d=25 D=47 B=12 Cr=10,07 Cor=5,806	IA	Point	contact	radial	1,00	0,00	yes
55	Ball bearing d=70 D=110 B=20 Cr=37,96 Cor=30,959	IB	Point	contact	axial - radial	0,56	2,00	yes
56	Ball bearing d=30 D=55 B=13 Cr=13,243 Cor=8,25	PA	Point	contact	radial	0,56	2,00	no
57	Cylindrical bearing d=20 D=47 B=14 Cr=13,9 Cor=10,2	PB	Line	contact	axial - radial	1,00	0,00	yes
58	Ball bearing d=45 D=75 B=16 Cr=21,1 Cor=15,3	OA	Point	contact	radial	0,56	2,00	yes
59	Ball bearing d=35 D=62 B=14 Cr=15,956 Cor=10,328	OB	Point	contact	axial - radial	0,56	2,00	yes

Fig. 4 Excel file with input data [Authors]

After filling of all needed inputs comes the second part of the program. It was created in the environment of software Matlab of company Mathworks. Here is written a function whose code includes conditions and all essential equations. Running of the function executes the code and starts loading the data from the excel file and calculating. It calculates forces in gearings, speed of shafts, reactions in supports (only of statically determinate beams), medium radial and axial load, equivalent dynamic bearing load, calculated dynamic load rating and so on. There is the connection between the Matlab function and the Excel file, so the results are written back into this file. The most important output is the calculated dynamic load rating of each bearing. Because according to the criterion (1)

$$C \leq C_r \tag{1}$$

where C is the calculated dynamic load rating (kN), C_r is the basic dynamic load rating (kN), is evaluated if the chosen bearing is suitable for required conditions. In the excel file is the column, emphasised in Fig. 4, that gives information whether the criterion for each one bearing is met or not. This way the bearing check program works (Kohár, 2015).

It is also possible to use the program for the designation of bearings. But in this state it is too complicated because it requires to stepwise select bearings and after each selection to run the program, until the program says the bearings are satisfying.

CONCLUSION

The program, that is able to calculate a countershaft gearbox of any configuration and then evaluate the applicability of the assigned bearings or designate convenient bearings from the list on its own, would be really useful and desirable. It could save the time of this operation and eliminate an aberration. So the next developing of the program will be focused on the designation process and augmentation of the gearbox variants.

ACKNOWLEDGMENT

This study was supported by Slovak Research and Development Agency under the contract no. APVV-14-0508 – Development of new methods for the design of special large-size slewing rings.

We support research activities in Slovakia / project financed from EU funds.
This article was created by the project "ProHiSpeB - prototype of telematics axle bearing for high speeds" on the basis Operational Programme Research and Development funded by the European Regional Development Fund.

REFERENCES

1. Hrček, S., Bucala, J. (2014). Thermalsimulationsof Plasmabitelectronicsystemprotectivehousings. In *Modernmethodsofconstruction design* (pp. 71-76). Cham: Springer.
2. Kohár, R., Brumerčík, F., Lukáč, M., Nieoczym, A. (2016). Numericalanalysisofrollerbearing. In *Appliedcomputer science* (pp. 5-16).
3. Kohár, R. (2015). Úvod do štrukturálnejoptimalizácie. In *Wspomaganekomputerovomodelowanie, analiza i projektowanieelementówmaszyn i mechanizmów* (pp. 95-103). Lublin: PolitechnikaLubelska.
4. Lukáč, M., Brumerčík, F., Krzywonos, L. (2016). Driveabilitysimulationofvehiclewith variant tireproperties. In *Communications : scientificlettersofthe University of Žilina* (pp. 34-37).
5. Naunheimer, H., Bertsche, B., Ryborz, J., Novak, W. (2011). Automotivetransmissions. *Springer Heidelberg Dordrecht London New York.*
6. Tropp, M., Lukáč, M., Nieoczym, A., Brumerčík, F. (2106) Hydrauliccircuits in transport and mechatronicsystems. In *Logi : scientificjournal on transport and logistics* (pp. 143-149)
7. Zdeněk. J., Žďábský, B. (2012). Automobily (2) – Převody. *Avid.*

Corresponding author:
Ing. Michal BELORIT, Department of Design and Mechanical Engineering, Faculty of Mechanical Engineering, University of Zilina, Univerzitná 8215/1, 010 26 Žilina, Slovak Republic, e-mail: michal.belorit@fstroj.uniza.sk

AXLE WEIGHING SYSTEM

Marek BISTÁK[1], Štefan MEDVECKÝ[1], Slavomír HRČEK[1]

[1]*Department of Design and Machine Elements, Faculty of Mechanical Engineering, University of Zilina*

Abstract
The paper presents the layout of the axle weighing system. The implementation of this equipment resulted from the requirement to measure and verify the mass of vehicles dispatching different kinds of loads from the several workplaces. In the past, the control measurement had been carried out by one above-ground weighbridge mounted at one workstation, but the increasing number of temporary workplaces resulted in the operational weighing of vehicles needs.
There were established the following standard criteria in the development - the cost of the entire project, operation of the equipment, the weight and mobility of the equipment.

Key words: *Axle weighing scale, Strain gauge, Vehicle*

INTRODUCTION

The axle weighing system is used for measuring the weight of motor vehicle, truck or semi-trailer. It consists of the axle weighing scales (2pcs for the weighted axle of the vehicle) and the evaluation unit. The axle scale consists of an aluminium weighing bridge installed on four or six strain gauge sensors. The measuring range is 3t, 6t, 10t, 12t, or 20t. The ramps provide the smooth passage through the axle scale. The evaluation unit is placed in a portable case for reasons of safety and mobility. During the measurement, it processes the generated electrical signal from the scales with which the evaluation unit is connected via cables with a length of up to 10 m or via WiFi. The resulting weight value is shown on the display and then printed as a measurement record.
There is used the static or dynamic method for the vehicle weighing. The static method requires the scale must be placed under each wheel of the vehicle. The gravity of each wheel is measured at the time interval of 10 seconds. For weighing by the dynamic method, two scales are placed on the fixed floor at a distance according to the axle wheel gauge. The vehicle must pass through the wheels of each axle through the axle weighing scales at a speed of up to 5 km.h-1 at the time interval of 30 or 60 seconds. The resulting mass of the vehicle is determined from the time course. (Málik, 2013)

MATERIALS AND METHODS

Development of the axle weighing system

The following requirements must be taken into account in the development of the axle weighing system:

- the measuring range of the axle weighing scale - 9 tons per wheel,
- maximum scale dimensions with ramps (W x L x H) 500 x 1200 x 70 [mm],
- measurement of the 2, 3 – axle vehicles up to 40 tonnes,
- usability of stock materials
- productivity in the company's production capabilities,
- mobile and simple handling
- the cost of the whole project

RESULTS AND DISCUSSION

The variant layout

The variant of the weighing system is proposed for these requirements. It consists of the axle weighing scale disposition and control unit.

The road axle weighing scale displacement

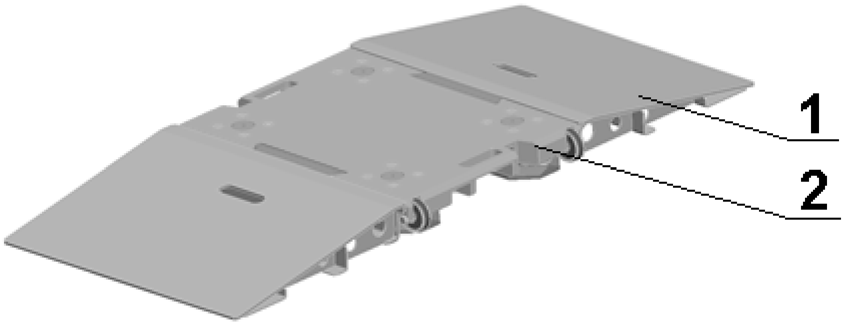

Fig. 1 Axle weighing scale

The weigh bridge of the axle weighing scale is the aluminium plate with dimensions of 500 x 400 x 40 mm. The relief grooves in order to reduce weight, two sliding locks for insuring the ramps against shifting and two handles are provided in the plate. On the right side of the scale, two traversing wheels are attached for its simplified manipulation. Four strain gauge housings are attached to the bridge using screw connections. (Kohár, 2015)

The weighing bridge was tested by the Ansys Workbench program. The crossing of the truck's rear wheel through the scale was simulated. The steering force generated by the wheel was 120,000.0 N. The bridge was fixed by fixed support. The result was total deformation of the plate 0,7 mm and equivalent stress 72 MPa. The resulting value of the simulated deflection fulfilled the condition of the maximum allowable deflection l/250 = 1,1 mm. (Kohár, et al., 2016)

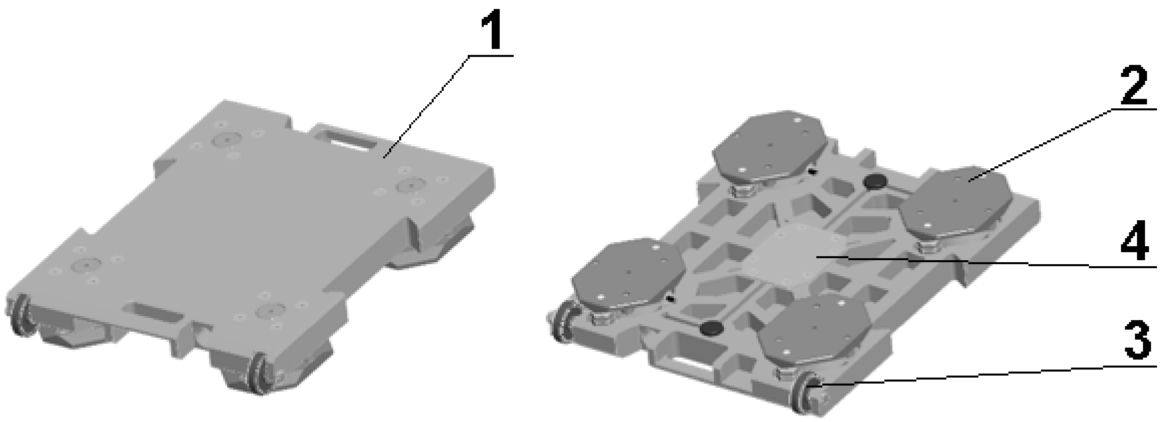

1- bridge, 2- strain gauge housings, 3- wheel, 4- sheet (connecting block cover)

Fig. 2 Axle weighing scale displacement

The weighing system

The weighing system consists of four strain gauge housings. The each strain gauge housing pedestal has UTILCELL M420-2.5t strain gauge sensor operating in the piezoelectric principle. The strain gauge is secured against movement in the direction of the "x" and "y" axes using three screws deployed with a 120º rotation. The height of the pedestal against the floor is adjusted by the height of its top cover. It is set using two bolts, each with two nuts. A steel roller for one-point load force transfer is located between the strain gauge measuring area and the cover.(Tropp et al., 2016)

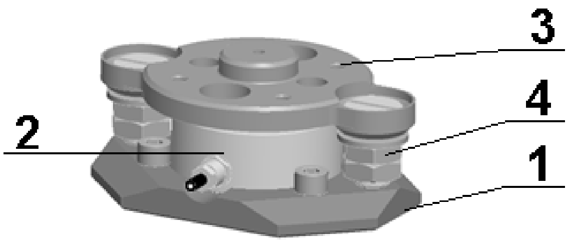

1- pedestal, 2- strain gauge M420, 3- cover,
4- adjusting bolt with nuts and support

Fig. 3 Strain gauge housing

Technical parameters of the axle weighing scale

Tab. 1 Technical parameters of the proposed axle scale

Description	Unit/characteristics
Weighing [kg]	9 000
Accuracy – division[kg]	5
Nominal sensitivity [mV/ V]	2 ± 0,1 %
Function	weighing (static, dynamic)
Velocity of weighing [s]	≤ 10
Dimension of weighing area W x L [mm]	500 x 400
Dimensions of scales with ramps W x L x H [mm]	500 x 1200 x 70
Scale weight [kg]	42
Construction design	steel / aluminium
Operating temperature standard [°C]	-10 ÷ 40
Operating temperature limits [°C]	-50 ÷ 80
Data transfer	Via cable
Location	mobile
Protection	IP 68

Evaluation unit

The complex evaluation unit consists of the UTILCELL Matrix Digital electronics (communication with PC via USB port), I/O Card with 6 digital inputs and a small cash register printer. This apparatus is located in a safety case from firm and flexible copolymer resistant to mechanical shocks. The top of the unit covers the design panel. (Lukáč, et al., 2016)

Fig. 4 Evaluation unit

CONCLUSIONS

The axle weighing scale as a whole fulfills all the requirements specified by the contracting entity. The advantage of this scale is the mobile construction, easy assembly and its favorable acquisition price. It can weigh a vehicle with 2, 3 axles, the total weight of which does not exceed 40t.

ACKNOWLEDGMENT

We support research activities in Slovakia / project financed from EU funds.
This article was created by the project "ProHiSpeB - prototype of telematics axle bearing for high speeds" on the basis Operational Programme Research and Development funded by the European Regional Development Fund.

REFERENCES

1. Málik, L. a kol. (2013). Konštruovanie II: Časti a mechanizmy strojov. Žilina. EDIS - publishers ŽU.
2. Medvecký, Š. a kol. (2005). Konštrukčné inovácie na základe bionických princípov, Sedmihorky. In: Sborník 46. Konferencie katedier častí a mechanizmov strojov.
3. Utillcell snímač síl M420. http://www.utilcell.com/content/snimac-sil-m420/
4. Utillcell MATRIX digital. http://www.utilcell.com/content/matrix-matrix-digital/
5. Kohár R., Brumerčík F., Lukáč M., Nieoczym A. (2016). Numerical analysis of roller bearing. *Applied computer science, 12(1),* 5-16.
6. Kohár R. (2015). Úvod do štrukturálnej optimalizácie. In: Wspomagane komputerovo modelowanie, analiza i projektowanie elementów maszyn i mechanizmów. (pp. 95-103). Lublin: Politechnika Lubelska.
7. Lukáč M., Brumerčík F., Krzywonos L. (2016). Driveability simulation of vehicle with variant tire properties. *Communications: scientific letters of the University of Žilina, 18(2),* 34-37.
8. Tropp M., Lukáč M., Nieoczym A., Brumerčík F. (2016). Hydraulic circuits in transport and mechatronic systems. *Logi : scientific journal on transport and logistics, 7(1),* 143-149.

Corresponding author:
Ing. Marek Bisták, Department of Design and Machine Elements, Faculty of Mechanical Engineering, University of Zilina, Univerzitna 2, Žilina, 01026, Slovakia, e-mail: marek.bistak@fstroj.uniza.sk

CHEMICAL MARKER AS A SAFE METHOD IN RESEARCH

Sylwester BOROWSKI[1], Sławomir ŻAK[2]

[1] *Faculty of Mechanical Engineering, UTP University of Science and Technology,*
[2]*Faculty of Chemical Technology and Engineering, UTP University of Science and Technology.*

Abstract
In the study there is presented the method of biologically active preparations' marking with n-hexane. Application of the marker allowed efficient conducting of studies concerning irregularity of the preservative's distribution. The material obtained as a result of the experiments' conducting – biomass may be with success applied for normal technological processes in biogas plants and as fodder.

Key words: *biomass, preservatives, marker.*

INTRODUCTION

Studies concerning production of fodders and substrates, should answer the question whether the obtained product is of good quality and what elements of the applied technological process have an impact on that quality.
Many researchers are evaluating the impact of applied technology on the end effects. Zbytek et al. (2016) in his publication analyzes the technologies available on the market, whereas Zastempowski, Borowski & Kaszkowiak (2013) in their publication, they analyzed several selected issues related to the collection of biomass. Zastempowski & Bochat (2014) whether Flizikowski et al. (2015) they focused on the issues involved in constructing machines used during harvesting and processing of biomass. The problem of applied technology is also evident in economic articles (Bojar, 2001).
In the studies performed by the authors concerning the quality of humid hay harvested with the use of a biologically active preservative, the quality of the obtained fodder was determined on the basis of its testing at the assumed time following harvesting. The applied preservative Inoculant 1155, in its composition has lyophilisate of *Bacilus spp* bacteria, which after being added to the harvested hay multiplicated and spread in the harvested mass. For their existential needs they use humidity from hay, and following its utilization (dehumidification of hay) they die. So, it is a natural and fully safe preservation method. However, research of the number of bacteria in individual places of the „silo" several days following harvesting, does not give full information on the preparation's distribution immediately after harvesting, what in case of chemical preparations' use is a very essential information (Bernes et al., 2008, Dulcet et al., 2006).
The condition of correct application of the preservative is supplying of its precisely determined volume to the harvested biomass in such a way as to receive its smooth mixing. As a result of smooth preservative's distribution in the harvested biomass, worsening of its quality may take place. It is particularly evident in case of harvesting biomass of decreased humidity or in places where relocation of silage juices is not possible (Dulcet, Mikołajczak & Olszewski, 2002, Rotz, 2003). There are always losses of it at the time of the preservative's adding at the time of harvesting. Apart from the possible, toxic impact on environment in case of use of chemical preservatives, losses also influence the increased costs of preservation. The use of the chemical preservatives may also adversely influence the plants' growth, what as an effect may result in the yield's decrease (Dulcet et al., 2006, Dulcet, Mikołajczak & Olszewski, 2002).
The literature analysis of the issues concerning harvesting of fodders with the use of additives showed, that in case of some studies there occurred the problem of assessing the evenness of the formulation's mixing with the harvested material. The assessment was conducted on the basis of the analysis of collected samples through:
- pH measurements of quantitative marking of formulation's used in the studies (Dulcet, 2001, Wrzos, 1980),
- analysis of the obtained fodder's quality (Dulcet, 2001, Maškova Holubowa & Luňaček, 1991).

Other methods used for the assessment of evenness of mixing of the formulation with the harvested material are the fluorimetric analysis and irradiation with isotopes. However, these methods, are rela-

tively difficult to be used, and fodders remaining after studies conducted in such a manner may not be fit for feeding (Koch, 1985, Wittenberg 1997).
The purpose of this study is presentation of the method of marking biologically active preparations with the use of n-hexane and the obtained results of the studies.

MATERIALS AND METHODS

In the studies there was used the solid granulated preparation Inoculant 1155 of Pioneer of the following physical properties: bank mass 1040 kg · m^{-3}, relative humidity 2,5 %, average diameter of granules 0,87 mm. The preparation was applied in the volume of 0,1 % (1 kg per ton of humid hay). The preparation comprises lyophilisate of natural bacteria *Bacilus spp.* and calcium carbonate. The guaranteed number of live bacteria is 1 · 108 cfu · g^{-1}.
For the needs of the experiment, the microbiological preparation Inoculant 1155 was marked with a contact method ensuring high efficiency (fig. 1). The marker's odour was passed through the preparation's bed till the moment of the indicator's saturation (Kondo et al., 2001).

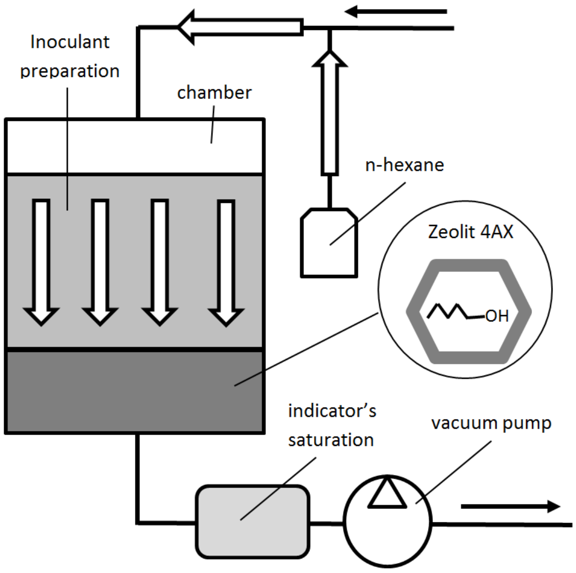

Fig. 1. Marking of Inoculant preparation with the use on n-hexane with the use of the contact method.

The applied marker creates a physical bond with the preparation (fig. 2) which disintegrates under the influence of an extraction solvent.

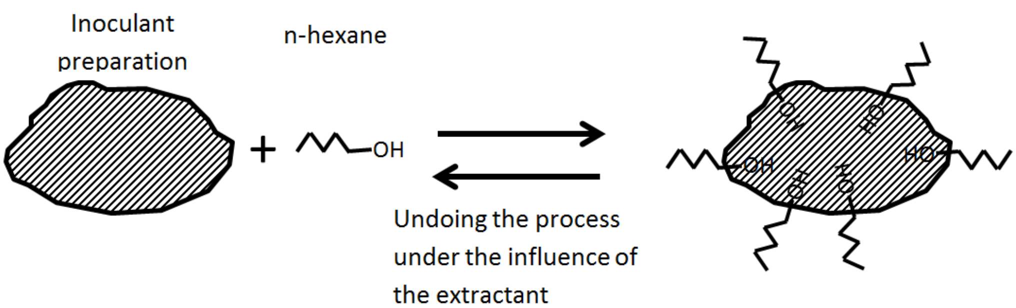

Fig. 2. Scheme of the marker molecules' connections with a microbiological preparation.

In order to obtain repeatable results, the algorithm of procedure was developed. The taken sample, after separation of coarse impurities is subject to be dried to solid mass in order to mark the content of water. Then, the dried mass is homogenised just to be fragmented to the level below 150,0 µm. A

fragmented sample is subject to extraction (extraction solvent – 150,0 ml) in the arrangement liquid (acetone) – solid body in the temperature of 20±1,0OC with the use of centrifuge for 24 hours in a tightly closed conical flasks of capacity of 250,0 ml. Having spinned the solid bodies on the centrifuge, take with a microsyringe from the decantate 2,0-3,0 μl of acetone sample for the purposes of analyte's marking with the use of the gas chromatograph and a mass spectometer.
For the tests there was used the gas chromatograph HP 5890 series II Hewlett Packard (column HP-1, of the length – 30,0 m, diameter φ – 0,53 mm, phase Hypersil ODS Shandon) with detector AED and ECD and a mass spectometer (MS 5972 series Mass Selective Detector – column: Pona of the length 25,0 m, diameter φ – 0,33 mm). The analysis was conducted in the mode of temperature programming: 20-120OC/10 min., 120-180OC/20 min. and 180-260OC/20 min.

RESULTS AND DISCUSSION
For the purposes of the developed method's verification, preliminary studies have been conducted. Pursuant to the assumed algorithm, the quantitative marking of the external standard was conducted. The level of n-hexane's recovery obtained in the studies amounted to 89,1 - 94,6% at the time of that alcohol's retention TR – 11,2 - 11,4 min. The obtained results are presented in figure 3.

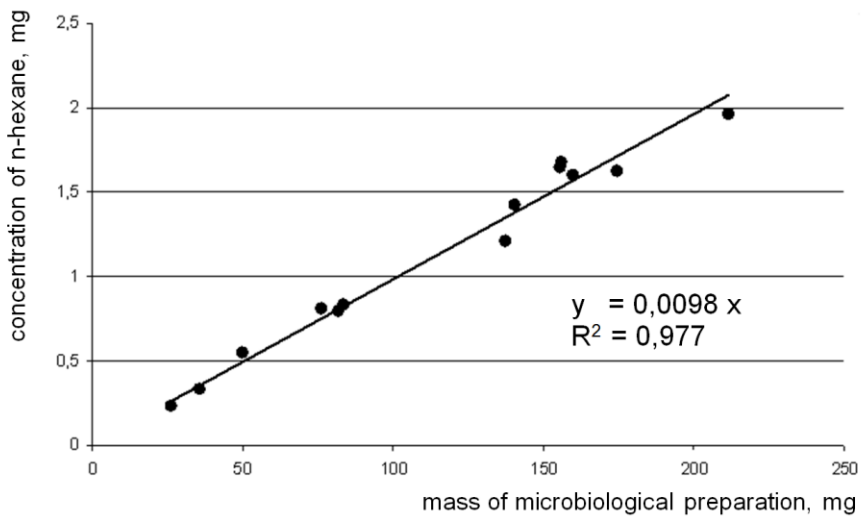

Fig. 3. Dependency of the concentration of n-hexane marked in the preliminary studies.

As a result of the conducted analysis, the recourse equation (1) at the significance level p = 0,05 has been determined. It is a linear function and is characterized by high determination coefficient $R^2 = 0,977$, what proves good determination of the functional dependencies.

$$y = 0,0098 \cdot x \qquad (2)$$

CONCLUSIONS
Application of the new method of microbiological preparation's marking with the use of h-hexane makes it possible to obtain information of the microbiological preparation's distribution directly following harvesting. This method allows conducting of the experiment in the conditions identical to those occurring in agrarian practice.
Application of the marker allows application of quick methods of analysis with the use of gas chromatograph and mass spectometer. It is an environment-friendly method, and fodder that remained after taking of samples is safe for microorganisms occurring in fermentative bed and for animals.

REFERENCES

1. Bernes G., Persson Waller K., & Jensen S.K. (2008). Hay and silage as vitamin sources in organic sheep production. [in:] Hopkins A., Gustafson T., Bertilsson J., Dalin G., Nilsdotter-Linde N., Spörndly E. Biodiversity and Animal Feed. Future Challenges for Grassland Production. Proc. of the 22nd General Meeting of the European Grassland Federation, June 2008, Uppsala, pp. 565-567.
2. Dulcet E., Kaszkowiak J., Borowski S., & Mikołajczak J. (2006). Effects of Microbiological Additive on Baled Wet Hay. Biostystems Engineering 95(3), pp. 379-384.
3. Dulcet E., Mikołajczak J., & Olszewski T. (2002). Technique of application of preservatives in wet hay harvest (Technika zastosowania konserwantów przy zbiorze wilgotnego siana). Wydawnictwa Uczelniane ATR w Bydgoszczy,
4. Rotz C.A. (2003). Advances in Dairy Technology 15, pp. 227-239.
5. Dulcet E. (2001). Modern techniques for harvesting green fodder and methods of silage. (Nowoczesne techniki zbioru zielonek i metody ich zakiszania.) Wydawnictwa Uczelniane ATR w Bydgoszczy
6. Wrzos W. (1980). Report of qualification test of dispenser used in green feed preservation „Apol-2/100" (Sprawozdanie z badań kwalifikacyjnych dozownika do konserwacji zielonek „Apol-2/100"). IBMER XXII/720, Warszawa.
7. Maškova H., Holubowa V., & Luňaček M. (1991). Zemědělska Technika 5/6, pp. 259-265.
8. Koch H., & Spiels M. (1985). Deutsche Flanzenschutzd. 37, Braunschweig, pp. 187-190.
9. Wittenberg K.M. (1997). Microbal and nutrive changes in forage during harvest and storage as hay. Proc. XVIII international Grassland Congres, Canada, June 1997, pp. 265-270,
10. Kondo K., Lee X.P., Kumazawa T., Sato K., Watanabe-Suzuki K., Seno H., & Suzuki O., (2001). Sensitive Determination of n-Hexane and Cyclohexane in Human Body Fluids by Capillary Gas Chromatography with Cryogenic Oven Trapping J. AOAC Int., 84(1), pp. 19-23.
11. Zbytek Z., Dach J., Pawlowski T., Smurzynska A., Czekala W., & Janczak D., (2016). Energy and economic potential of maize straw used for biofuels production [in:] Demetrescu I., Oh K., Kaushik NK. & Butu, A., MATEC Web of Conferences Volume: 60 Edited by: 3rd International Conference On Chemical And Biological Sciences Book Series
12. Zastempowski M., Borowski S., & Kaszkowiak J. 2013. New solution in harvesting plants for power purposes. 5th International Conference TAE Trends in agricultural engineering, Prague 2013, pp.673-676.
13. Zastempowski M., & Bochat A. (2014). Modeling of cutting process by the shear-finger cutting block. ASABE Applied Engineering in Agriculture. Vol. 30, No. 3, pp. 347-353.
14. Flizikowski J., Topolinski T., Opielak M., Tomporowski A., & Mrozinski A. (*2015)* Research And Analysis Of Operating Characteristics Of Energetic Biomass Micronizer, Eksploatacja I Niezawodnosc-Maintenance And Reliability *17(1) pp. 19-26.*
15. Twaruzek M., Dorszewski P., Grabowicz M., Szterk P., Grajewski J., Kaszkowiak J. (2016). Effect Of Additives On The Fermentation Profile, Microbial Colonization And Oxygen Stress Of Alfalfa Silages Journal Of Elementology 21(4) Pp. 1161-1172
16. Bojar W. (2001). The cost budgeting in the crop production connected with organisational schemes [in:] Juliszewski T. Farm Work Science Facing Challenges Of The Xxi Century pp. 45-50.

Corresponding author:
Sylwester Borowski, Ph.D., Faculty of Mechanical Engineering, UTP University of Science and Technology, Al. prof. S. Kaliskiego 7, 85-796 Bydgoszcz, Poland, phone: +48 52 3408132, e-mail: sylwester.borowski@utp.edu.pl

ASSESSMENT OF OPTIONS FOR APPLICATIONS TICN-MP + MOVIC DEPOSITED ON THE CONVEX-CONCAVE GEARING WORKING IN INTERACTION WITH THE ECOLOGICAL LUBRICANT

Miroslav BOŠANSKÝ[1], Juraj RUSNÁK[2]

[1] *Institute of Transport Engineering and Designing, Faculty of Mechanical Engineering STU in Bratislava*
[2] *Department of Machine Designing, Faculty of Engineering SAU in Nitra*

Abstract
The additional article deals with the assessment of the possibility of applying the coating TiCN-MP + MOVIC deposited on the convex-concave gearing made of material C55E4 working in interaction with the ecological lubricant Biohyd MS46 and BioGear S150., where, based on scuffing FZG tests according to STN 65 6280 norm, are experimentally appreciated possibilities of its application.

Key words: *Non Standard C-C gears, Scuffing, FZG Test, Coat, ecological oils*

INTRODUCTION

Considerable share on the pollution of environment has mobile equipment used for the implementation of a wide variety of construction and ground works. Mobile machinery directly affects the quality of the environment. They are a potential source of pollution of soil, water and air. Noise and vibrations emitted by the machine have negative impact on humans, also other living organisms in the vicinity of the source (*Gulan, 2005*). Risk is also leak of working fluids into the environment, which can cause ecological accident, as most of operating fluids used in mobile working machines is of petroleum origin. One of the ways, how to prevent widespread contamination of soil or water, is the use of ecologically easily biodegradable lubricants and oils. Use of biodegradable lubricants is recommended wherever it is necessary to minimize possible effects of the machine actions on the environment. Some countries, such as Germany and Sweden require the use of biodegradable oils in all applications working in environmentally sensitive areas, such as the area of protection of water resources (*Staša*, 2012). But, biodegradable oils, in most cases do not reach the performance parameters of mineral oils.

MATERIALS AND METHODS

With increasing loading of gears are increased also contact pressures of gearing, friction and temperature, whereby at creation of tooth side damage plays size of contact pressures an important role. The higher resistance against disturbances can be achieved by increasing the surface carry capacity of the tooth side. Arrangements, by which we can achieved it, are mainly change of the geometry of gearing, the use of higher quality oils and materials, respectively increasing the surface hardness of tooth sides, where can be also included application of thin hard coatings. Regarding the change of geometry, (*Orokocký, 2004, Bošanský et al, 2012, Vereš et al, 2006*) they present favorable results in terms of contact pressures, specific slips and wear of convex-concave gearing compared with involute gearing.

Currently there is deposition of coatings in gears in practice not widely used, despite the fact, that in field of their application were proceeded several studies (*Michalczewski et al, 2013, Lümkemann et al, 2014, Tuszynski et al, 2015*),whereby were solved particularly TiN, TiCN, TiAlN, CrN and other thin hard coatings with a top layer with a low coefficient of friction. From used methods deposition of coating layers analysis results, that the application in gears is due to less heat affecting of the basic material, PVD method most appropriate.

From of convex-concave gearing analysis (*Bošanský et al, 2012, Vereš et al, 2006*), we chosed for application coating TiCN-MP+MOVIC (MoS_2), as an appropriate combination of hard layer TiCN-

MP and softer layer with a low coefficient of friction MOVIC. Coating TiCN-MP is often used to increase hardness and sliding properties of tools for forming and machining of steel with lower strenght limit and also is used for surface treatment of callipers. Coating show high hardness and good sliding properties. MOVIC coating is a coating based on MoS_2. It's a sliding coating with a low friction coefficient applied mainly in shaping machines and screw taps. It can be applied separately, directly to the surface of component, or to any hard coating. Basic parameters are listed in the tab. 1 (*Liss, 2015*). This coating was applied by PVD method on tested gears, which were made of material C55E4. Demanded surface hardness of the tooth sides was achieved by laser hardening, the parameters of which are mentioned in (*Míšaný, 2015*).

Tab. 1 Properties of the coatings deposited on the test gear

	Nano hardness [GPa]	Thickness [µm]	Coefficient of friction with steel	Maximum operating temperature [°C]
TiCN-MP	32	1 to 4	0,2	400
Movic (MoS_2)	20	0,5 to 5	0,1	400
TiCN-MP+ MOVIC	32	1,5 to 5,5	0,15	400

The scuffing experiment was carried out by standard Niemann test with closed power flow on the scuffing (Fig. 1).

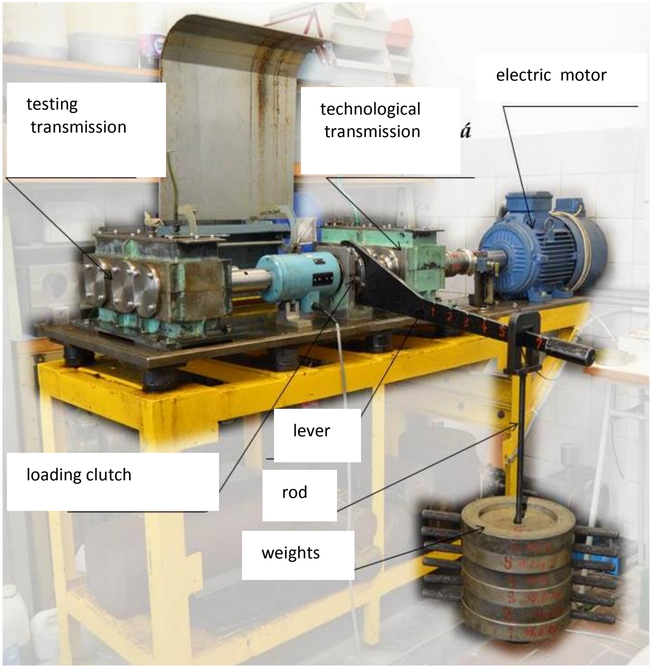

Fig.1 Niemann stend

In this experiment were used two types of biodegradable oils. Hydraulic oil OMV Biohyd MS46, its basic specifications are listed in tab. 2 and gear oil OMV BioGear S150, its basic specifications are listed in tab. 3.

Tab. 2 Technical data of Biohyd MS 46 oil

Property	OMV Biohyd MS 46	Unit
Viscosity grade ISO VG	46	-
Viscosity at 40°C	46	$mm.^2s^{-1}$
Viscosity at 100°C	9,2	$mm.^2s^{-1}$
Viscosity index	187	-
Density at 15°C	915	$kg.m^{-3}$
Pour point	-51	°C
Ignition point	237	°C

Tab. 3 Technical data of Biohyd S 150 oil

Property	OMV Biogear S150	Unit
Viscosity grade ISO VG	150	-
Viscosity at 40°C	150,7	$mm.^2s^{-1}$
Viscosity at 100°C	21,4	$mm.^2s^{-1}$
Viscosity index	167	-
Density at 15°C	947	$kg.m^{-3}$
Pour point	-27	°C
Ignition point	224	°C

Scuffing occurs according to DIN 51354 and STN 65 6280 with the degree of load, when the difference of the sum of the wheel weight losses and pinion in two consecutive degrees is greater than 10mg. Degree, at which seizing reflects, is considered as damaging level and thus is limit level previous encumber one. For gears weighing were used Mettler Toledo PR2003 scales, able to be encumbered up to 2100 g and with sensitivity of 1 mg. Due to the fact, that they were evaluated for scuffing and also gears were coated, where weight loss was also affected by the loss of the coating, thus next evaluation criterion were measuring of surface roughness. Measurement was carried out by contact roughness gauge Taylor-Hobson Surtrnic 3+. According to the evaluation of surface roughness it is a damaging step marked the one in which value of surface roughness Rz_{DIN} reach limit 7μm.

RESULTS AND DISCUSSION

Weight losses of test gearings for the various loading stages are shown in Fig. 2 and Fig. 3. By continuous exposure to loading occurred increase of weight loss, which was caused by scuffing the soft top coat, thus in the early levels of loading occurred to wearing of the upper lubricate coating MOVIC, as Fig.. 4 confirmed.

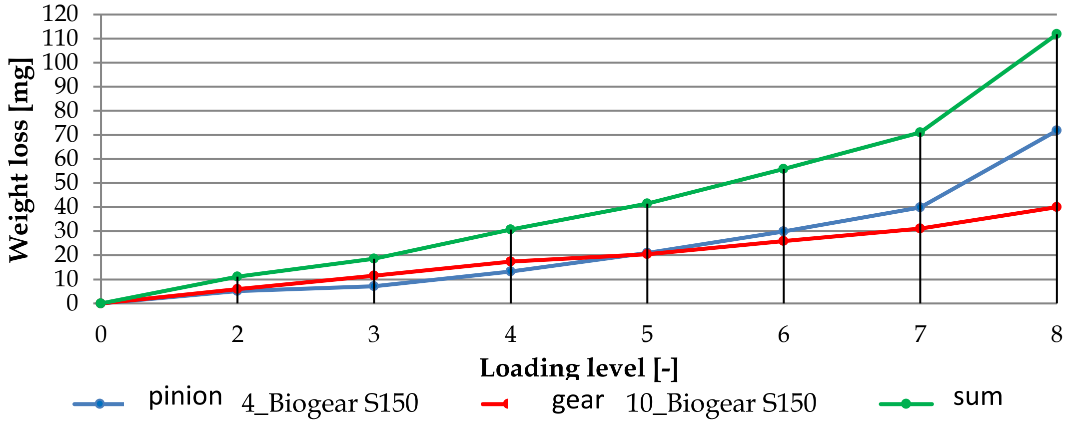

Fig. 2 Dependence of weight loss of gearing with coat TiCN-MP+MOVIC -lubricated by OMV Biogear S150 oil

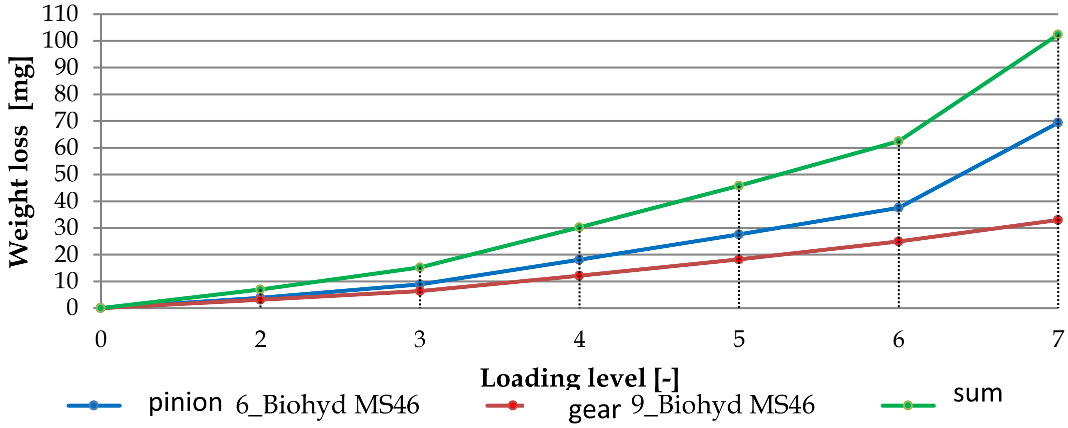

Fig. 3 Dependence of weight loss of gearing coated TiCN-MP+MOVIC -lubricated by OMV Biohyd MS46 oil

In the figure is clearly visible gray MOVIC coat and under it begins to emerge bronze-brown spots of coat TiCN-MP.

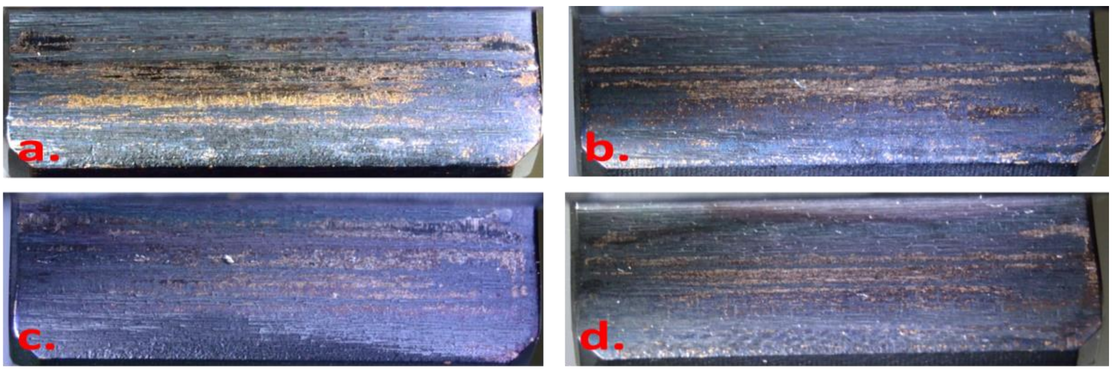

Fig.4 *Surface wear of the tooth side after fourth level of loading*

a/c pinion in interaction with OMV Biohyd MS46 / OMV Biogear S150 oil
b/d wheel in interaction with OMV Biohyd MS46 / OMV Biogear S150 oil

At next levels of loading has occurred wearing of coating across the whole dedendum area. This is evident from Fig. 5, where is wearing of bronze-brown coating TiCN-MP visible as a dark gray area (hardened base material buffed to a mirror shine).

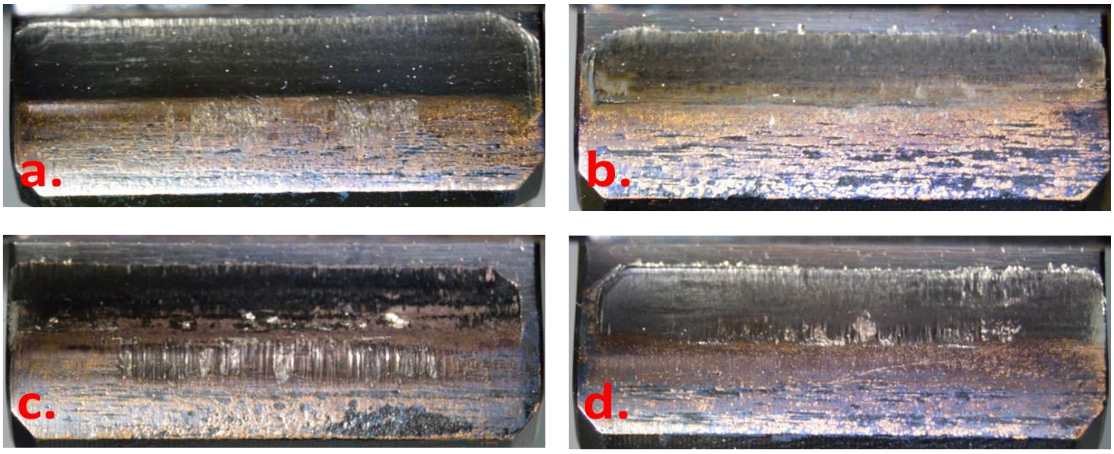

Fig.5 *Surface wear of the tooth side after 1.loading level*

a/c *pinion in interaction with OMV Biohyd MS46 / OMV Biogear S150 oil*
b/d *wheel in interaction with OMV Biohyd MS46 / OMV Biogear S150 oil*

CONCLUSIONS

Based on evaluation of the scuffing with Niemann test from the loss of material point of view came to scuffing already at 7. level in the interaction with the OMV Biohyd MS46 oil and at the 8. level in the interaction with OMV BioGear S 150 oil, in terms of roughness at 11. and 12. level (*Míšaný, 2015*). At these levels came to partial coating wear in the dedendum of the tooth. Already, based on these results, can be stated better adhesion of the coating TiCN-MP + MOVIC in convex-concave gearing than it was with DLC film deposited as well in a convex-concave gearing, at which came to due to (*Zápotočný, 2014*) scuffing from the weight loss point of view already at 5. level with OMV Biohyd MS46 oil and at the 7. level with OMV BioGear S150 oil, while at 4. level already came to rub off of DLC coating. In the context of comparative tests were also carried out tests for coatings TiN and MoS_2. From the achieved results it can be stated, there´s better carry capacity of multi coating compared with single layer coating MoS_2 (*Fedák 2008*).

ACKNOWLEDGMENT

The research work reported here was made possible by grant projects VEGA 1/0227/15.

REFERENCES

1. Bošanský, M., & Fedák, M. (2009): Tvrdé povlaky ako alternatíva tepelného spracovania ozubených prevodov, *Acta technologica agriculturae*, Nira 2009
2. Bošanský. M., Vereš, M., Tököly, P., & Vanya, A**.** **(**2012) *Neštandardné ozubené prevody* Vydavateľstvo STU Bratislava 2012, 11590 p., ISBN 978-80-227-3713-5

3. Bošanský, M., Vanya, A., Čaplovič, Ľ., Hudáková, M., & Sondor, J. (2013) Evaluation of Properties of Selected Coatings on Aisi Grade 18Ni(250) Maraging Steel in Terms of their use in Gears, *Advanced Materials Research* Vol. 746 (2013) pp 179-185 Trans Tech Publications, Switzerland
4. Bošanský, M., Vanya, A., & Vereš, M. (2013) Evaluation of properties of Selected Coatings on Steel C60E in Terms of their Use in Gearing. *Advanced Materials Research Vol. 716* (2013) pp 166-171 Trans Tech Publications, Switzerland.
5. Fedák, M. (2008) *Povlaky ako možnosť zvýšenia únosnosti ozubených kolies - Dizertačná práca.* Bratislava : Strojnícka fakulta STU v Bratislave, 2008
6. Gulan, L. (2005). Tendencie vývoja konštrukcií mobilných pracovných strojov., 2/2005.
7. Liss, a.s. , (2015) Katalog povlaku, Platit. [Online], 25. jún 2015.
8. Lümkemann, A., Beutner, M., Morstein, M., Köchig, M., Wengler, M., Cselle, T., & Karpuschewski, B. (2014) A New Generation of PVD Coatings for High-Performance Gear Hobbing. Preprint from A Coatings Conference, Thessaloniki, Greece, Oct.1- 3, 2014, Platit
9. Michalczevwski, R., et al.,. (2013) New scuffing test methods for the determination of the scufing resistance of coated gears. *Tribology- Fundamentals and advancements.* ISBN: 978-953-51-1135-1, 2013, Vol.12, Issue.4.
10. Míšaný, J. (2015) Vplyv prevodového ústrojenstva stavebného stroja a možnosti zvýšenia jeho únosnosti so zameraním na zníženie ekologického zaťaženia pôdy. *Dizertačná práca*. Bratislava : s.n., 2015.
11. Orokocký, R. (2004). Zvyšovanie odolnosti ozubených prevodov v interakcii s ekologickými mazivami Dizertačná práca. Bratislava : s.n., 2004.
12. Staša, R. (2012). Ekologické maziva na bázi esteru splňují vysoké technologické a ekolgické požadavky. *Tribotechnika.* ISSN 1 338-0524, 2012, 3/2012.
13. Tuszynski,W., Kalbarczyk, M., Michalak, M., Michalczewski, R., & Wieczorek, A. (2015) The Effect of WC/C Coating on the Wear of Bevel Gears Used in *Coal Mines. Materials Science (Medžiagotyra).* Vol. 21, No. 3. 2015 ISSN 1392–1320
14. Vereš, M.- Bošanský, M.- Gaduš, J. (2006) *Theory of Convex – Concave and Plane Cylindrical Gearing*, Vydavateľstvo STU Bratislava 2006, 180 p., ISBN 80-227-2451-3,
15. Zápotočný, J. (2014) Určenie kvalitatívnych a kvantitatívnych charakteristík deponovaných povlakov v systéme povlak bok zuba z tribotechnického hľadiska. *Dizertačná práca.* Bratislava : s.n., 2014.

Corresponding author:

prof. Ing. Miroslav Bošanský, PhD., Institute of Transport Technology and Designing, Faculty of Mechanical Engineering, Slovak University of Technology in Bratislava, Námestie slobody 17, 81231 Bratislava, Slovakia, e-mail: miroslav.bosansky@stuba.sk

THE APPLICATION OF NEW RULES OF GPS IN STRUCTURAL PRODUCT REQUIREMENT

Jozef BRONČEK[1], Mário DRBÚL[2], Michal STPUPAVSKÝ[1], Norbert RADEK[3]

[1] *Department of Machine Elements and design, University of Žilina*
[2] *Department of Machining and Manufacturing Technology, University of Žilina*
[3]*Center of Laser Technologies of Metals, Kielce University of Technology*

Abstract
The approach of the constructer and designer of the products and its components is based on the restrictions which are conditioned by model layout of geometric elements. The designer has to know the principles of GPS perfectly in order to be able to order geometric and proportional tolerances correctly. Moreover, he should have inevitable requirements and experience of tolerances production and measurement. When the designer orders important parameters and proportions, their boundary deviations and tolerances, he gives primary impulse to the way in which these parameters will be produced and controlled afterwards. The aim of the contribution is to show how a designer can noticeably contribute to the optimisation of control operations by the application of new requirements according to the standard EN ISO 1101.

Key words: *GPS; documentation; geometrical tolerances, designer.*

INTRODUCTION

The basic rule of the design realisation in the technical documentation is the relationship demarcation between length size and its deviation (which are the results of production and can be found out by measuring), and geometrical tolerances. The geometrical tolerances determine the characteristics of every geometrical feature, i. e. size, shape, direction and position. The definition of the tolerance zone from the point of view of its shape and size, and of its assignment to the assessed shape of geometrical feature has to be unambiguous, so that the regulation of every geometrical tolerance was unambiguous. The way of the control of tolerated feature depends on the definition of the tolerance zone. This is the reason why it is important to understand correctly the definitions of individual geometrical characteristics unambiguously stated by standards and to learn how to order them on drawings correctly (*Broncek, Handbook of Designer 1, 2015; Draganovska, Materials Science Forum, 2014; Broncek, Materials Science Forum, 2015*). But deciding about optimal tolerances is not easy. Firstly, the tolerance always has to have a relation to the function of part, and secondly, the stated tolerances have to be manufactorable. Thirdly, we have to be able to do unambiguous and repeatable measurement of all tolerances. The designer has to know perfectly the principles of GPS in order to be able to order geometrical and dimensional tolerances. Moreover, the designer should be aware of necessary requirements and experiences related to manufacturing and measurement of tolerances.
Geometrical product specification (GPS) is overall term for a group of international standards and determines basic relations between size tolerances and geometrical tolerances. GPS include the standards which are related to construction requirements, but also to their proper manufacturing process and product verification for the assessment of correct shape, or more precisely for the assessment of the correct geometry. One of the basic standards of GPS is the standard EN ISO 1101 which is the standard of geometrical tolerance and which determines basic requirements for use of geometrical tolerance when creating technical drawing documentation. In the framework of the inspection, the standard was completely restructured and fundamentally extended with new parts (e.g. the part about filters, filtration in GPS). New concepts, terms and definitions (e.g. theoretically exact feature TEF, connected feature, or specification element) are applied in the revised edition of the standard of the year 2017. These concepts, terms and definitions were not used in the previous editions of the standard, but nowadays they are valid for the definitions of geometrical features in the set of GPS standards. In the following part of the article, we would like to briefly introduce several changes and examples which are

included in this standard and which are related mainly to its application when ordering geometrical tolerances on drawings.

The main changes introduced by the standard EN ISO 1101 are:

- Tools for a specification of the tolerated feature filtration have been added and a line type for an illustration has been selected.
- Tools for tolerance of associated features have been added.
- Tools for shape characteristics specification by determination of referential feature and specified parameter assignment have been added.
- Tools which specify restrictions of the tolerance zone have been added.

The aim of the contribution is to show how a designer can noticeably contribute to the optimisation of control operations by the application of new requirements according to the standard EN ISO 1101.

MATERIALS AND METHODS

The GPS specification for GPS characteristics has to be stated in the technical documentation of a product. The GPS characteristics enable the determination of the deviations (of texture, shape, orientation and location) and the proportions having regard to the ideal features. The deviations of texture and shape are determined from one non-ideal feature. The deviations of orientation and location are situational characteristics which are determined from two non-ideal features. The proportion is a proper characteristic which is determined from one non-ideal feature. Figure 1 shows the GPS characteristics of shape for plane surface. The shape of characteristic is expressed as basic characteristic which is a situational characteristic between non-ideal feature and ideal feature, i. e. maximal distance between the smoothed feature and the plane.

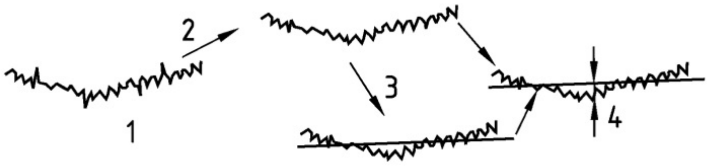

Key
1 non-ideal feature
2 filtration
3 association
4 basic characteristic

Fig. 1 Example of determining GPS characteristics

The workpiece or feature is to be considered acceptable/good when the specification is fulfilled. Only that which is explicitly required in the technical product documentation shall be taken into account. The actual GPS specification stated in the technical product documentation defines the measurand. On a drawing, the geometrical tolerances are indicated in a tolerance indicator (tolerance frame vertically divided into two or more parts). The data in the tolerance frame are always ordered from left to right and the content of individual parts is explained in Figure 2.

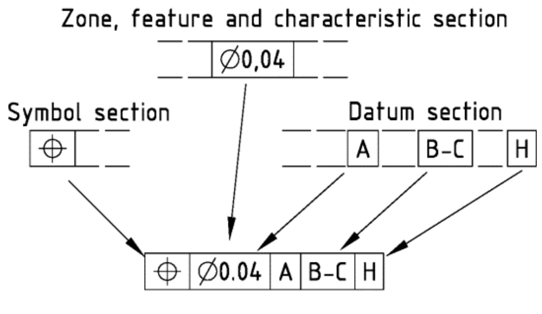

Fig. 2 Example of data arrangement in tolerance indicator

Table 1 shows the tolerance features which can be used in the second part of the tolerance indicator, in a different grouping and order for a zone, for a tolerated feature and characteristic. All specification features are optional besides those of them which determine the width of the tolerance zone. In the following part of the article, we briefly state the analysis of certain requirements which are used to control specific functions of the products. Filter specification stated in the part of the tolerance indicator is optional specification feature. The ordering of the filtration of tolerated feature is marked by specification combination which is composed of two elements. The first element of the order marks the type of the specified filter and the second element contains the nesting index, value of boundary wavelength λc or filter characteristics. The boundary wavelength λc and the filter type describe the features of the filter (characteristics of the filter or transfer function).

Tab. 1 Specification elements in the tolerance zone, feature and characteristic section of tolerance indicator [1]

Tolerance zone					Tolerance feature				Characteristic		Material condition and state
Shape	Width and extent	Combination	Specified offset	Constrain	Filter type	Filter indices	Associated. toleranced feature	Derived feature	Association	Parameter	
ϕ	0.02	CZ	UZ+0,2	OZ	G	0.8	C	A	C CE CI	P	M
$S\phi$	0.02-0,01	SZ	UZ-0,3	VA	S	-250	G	P	G GE GI	V	L
	0.1/75		UZ+0.1:+0,2	> <	Etc.	0.8 -250	N	P 25	X	T	R
	0.1/75x75		UZ+0.1:-0,3			500	T	P 32-7	N	Q	F
	0.2/ϕ4		UZ-0.1:-0,3			-15	X				
	0.2/75x30°					500 -15					

According to the norm ISO 16610-21, the boundary wavelength represents 50% of the transfer characteristic. It means that the value of depicted frequency is considered to be permeable for boundary wavelength exactly 50%. The difference is principally given by 3 different characteristics of the filter, i.e. the bottom permeability, the top permeability and the filter permeability band. When we want to measure a shape, we use mainly the filtration with the bottom. The transmission band (band pass filter) has to be marked by the basic length of filters (in mm) which are separated by a hyphen "-". For the same filter type (G- Gauss' filter) a long-wave pass filter 0,25 is written first and then short-wave pass filter 8 is written afterwards (Figure 3). The tolerated features are all lines at the surface which are parallel to the datum A.

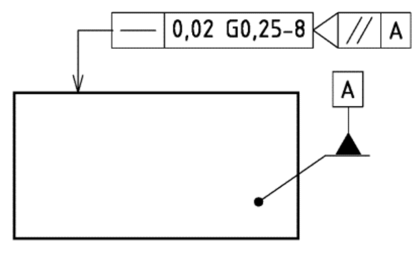

Fig. 3 Example of the specification for geometrical shape deviation – linearity with the given band pass filter for a filter type – Gaussian filter

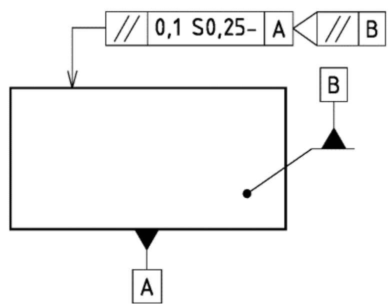

Fig. 4 Example of the specification of linearity tolerance zone when using long-wave spline filter

The example of the collinearity tolerance zone order when using long-wave spline filter is visualized on Figure 4. The specification S in the part of the tolerance indicator indicates that the spine filter is ordered. The value 0,25 represents the bound 0,25 mm. We are talking about a long-wave pass filter, because the hyphen "-" follows the value. While using this filter, the wavelengths shorter than cut-off value are removed. This is the reason why the specification refers to the feature which has been fil-

tered with a 0,25 mm long wave spline filter. The plane cross point indicator placed beside the tolerance indicator marks, that the specification is related to the line features parallel to the datum B. It means that every individual filtered line has to be parallel to the datum A and has to be located in the tolerance zone defined as the space between two lines 0,1 mm apart. The nesting index for open features, e. g. straight line, plane, cylinder in an axial direction, is stated in mm. The nesting index for closed features, e. g. cylinder in a peripheral direction, is stated in UPR – undulations per revolution. The units shall not be indicated.
Figure 5 shows the example of the specification for shape geometrical deviation – circularity. The specification G in the tolerance indicator element marks that ordered Gaussian filter and indication N determine the specification of the smallest circumscribed referential element/feature. The tolerated feature is considered to be closed and nesting index is stated in the values of UPR (undulation per revolution), because we are talking about the circularity specification. The value of 50% stands for 50% UPR and because a hyphen "-" follows the value UPR and it is a long-wave pass filter which removes short wavelengths (higher UPR numbers). This is the reason why the specification order is related to the feature which has been filtered with the help of 50 UPR Gaussian long-wave pass filter. The notation in the tolerance indicator element shows that every individual filtered circumferential profile line has to be located in the tolerance zone defined as the space between two concentric circles with 0,02 mm radius difference.
When we order the requirement for the feature which is open in two directions, e. g. a plane, we can order filters (various) for each direction. The plane cross-line indicator for a direction mark, in which the first stated filter should be used, is stated as the tolerance indicator. In order to separate two filter indications "x" is used. The second filter, which is related to the closed feature, is applied in the perpendicular direction to the first filter direction. For the function which is open in one direction and closed in the second direction, e. g. cylinder, the filter indicator for open direction has to be directed before filter indicator determined for the closed direction.

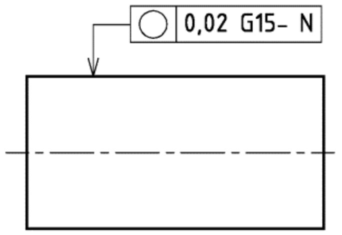

Fig. 5 Example of a specification for shape geometrical deviation – roundness specification

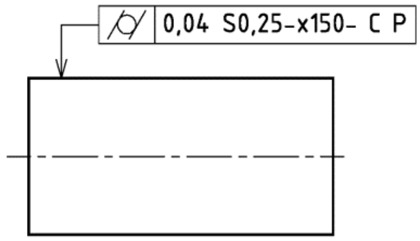

Fig. 6 Example of shape geometrical deviation specification – cylindricity specification

Figure 6 shows the example of the specification of shape geometrical deviation – cylindricity specification which is related to the profile point height (indicator P) in regard to the referential cylinder. The referential cylinder is associated by the method minimax (indicator C – Chebyshev) after the application of a long-wave spline filter with boundary values 0,25 mm in the axial direction and 150 UPR in the circumferential direction.
In the mechanical engineering enterprises, there is a standard requirement that the constructional solution has to be appropriate even from the technological point of view. Analogically, the requirement on the metrologicality of the construction should be applied to the construction, too. It means that the measuring operations when the quality control are realisable and appropriate from the point of view of the accuracy of the measurement and from the economical point of view. The designer can considerably contribute to the optimisation of the control operations by applying new requirements according to the standard EN ISO 1101. The decision, which measuring method or which measuring device will be applied for the given control operation, is based on the requirements which are included in the technical (manufacturing) documentation. The way how the constructer orders important parameters and proportions, their boundary deviations and tolerances gives the primary impulse to how these parameters will be controlled (*Kohar, Communications, 2014; Fabian, Communications, 2014; Martinec,*

2015; Mazinova, 2015; Stupavsky, Materials Science Forum, 2014). This enables the designer to predetermine the form and the content of the control operations. These statements are confirmed in the following part with the help of specific example.

RESULTS AND DISCUSSION

The aim of the experimental measurement was to measure and evaluate the deviation of proportions and geometrical shape deviations on a functional surface of a rotary component with the diameter ϕ 46,545 mm (Figure 7). The forging made of the material 16MnCr5 is an intermediate product for the component manufacture. The surface of the component should be modified by a nitriding and shaped by grinding afterwards. The ordered tolerance of proportions – or diameter is ±0,025 mm and shape deviation tolerance is ordered by cylindricity 0,02 mm.

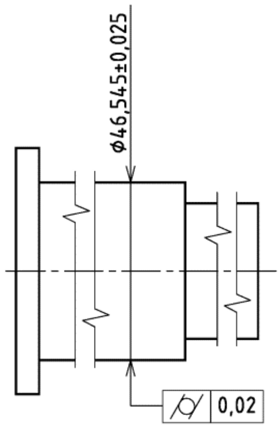

Fig. 7 The order of the proportions requirement and the specification for shape geometrical deviation - cylindricity

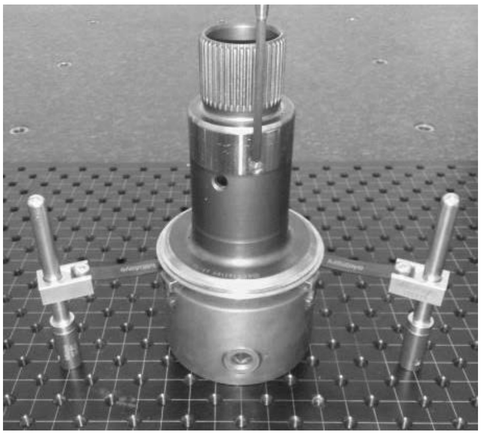

Fig. 8 The picture of 3D coordinate measuring machine CMM

The experiments were realized on the 3D coordinate measuring machine (CMM) from the company Zeiss with the help of the passive scanning probe which cooperates with the software Calypso. The evaluation of the measurement results gained on the machine CMM, which were measured on the same workpiece and under the same measurement conditions, can be considerably different which depends on the use of different methods of the results evaluation of the measurement by measuring software. The external diameter was measured by continuous method by scanning of the profile surface. An ideal geometrical feature – cylinder was affiliated to the gained profile by selected approximation method.

Tab. 2 Selected results from measurement of the proportion and geometrical deviation of cylindricity

Name	Actual dimension (mm)	Nominal dimension (mm)	Difference (mm)
Dimension specification			
Cylinder diameter method GG	46.5204	46.5450	-0.0246
Cylinder diameter method GN (E)	46.5305	46.5450	-0.0145
2-point diameter max.	46.5343	46.5450	-0.0107
Cylindricity specification			
Cylindricity method G	0.0115	0	0.0115
Cylindricity method N	0.0122	0	0.0122
Cylindricity method C	0.0112	0	0.0112

The approximation methods: the smallest squares method – G, the packaging surface method – E and two-point method were used to evaluate the proportions. The proportions were removed from the referential feature by the methods G and E, and the referential feature was used in a two-point method to determinate its centre. The geometrical deviation of cylindricity was evaluated from the surface profile we had taken by these methods: the smallest squares method – G (LSCY), the smallest circumscribed cylinder method (MCCY) and the minimal zone method (MZCY). Table 2 shows certain results from the protocol of the measurement of the proportions and cylindricity. The implementation of individual measurement principles serves to the comparison of the results of measurement for the examination of the pertinence of correct requirement order according to the appropriate method.

CONCLUSIONS

From the analysis of processed values data follows, that different results were achieved by the application of individual approximation methods of geometrical features affiliation. The smallest external diameter deviation values were recognised when using two-point method (method of tangent features). While the evaluation of shape geometrical feature – cylindricity that the smallest geometrical deviation values were recognised when applying the minimal zone method MZCY. By the conclusion reflection about (the objectivity) the appropriateness of the use of particular measurement method we are able to state that, while the selection of the particular method for referential geometrical feature determination (reference circle), we have to take into consideration mainly the supposed function of the evaluated surface.

The established results point to the fact, that measurement and evaluation methods influence the final measured value. This is the reason, why it is important that the designer orders appropriate method of measurement and evaluation of measured parameter values on the drawing documentation to the order of parameter specification.

ACKNOWLEDGMENT

This study was supported by the grant project No. KEGA 031 ŽU-4/2016 and International project APVV No. SK-PL-2015-0008.

REFERENCES

1. Bronček, J., Kučera,L., Žarnay, M., Poljak, S., Čillík, L. (2015). Handbook of Designer 1. EDIS - ŽU v Žiline.
2. Draganovská, D., Ižarijová, G., Brezinová J., Guzanová M. (2014). The study of parameters of surface roughness by the correlation analysis. *Materials Science Forum, 818, 15-18.*
3. Bronček, J., Fabian, P., Radek, N. (2015). *Materials Science Forum. 818, 209-212.*
4. Kohar, R., Hrcek, S., Dynamic Analysis of a Rolling Bearing Cage with Respect to the Elastic Properties of the Cage for the Axial and Radial Load Cases. (*2014) Communications - Scientific Letters of the University of Zilina, 16, No. 3A, 74-8.*
5. Fabian, P., Janekejech, P., Kyselová, M.: (2014). Simulation of Roundness, Hardness and Microstructure of Bearing Rings with thin Cross Sections by using SYSWELD, *Communications - Scientific Letters of the University of Zilina, vol. 16, 124-129.*
6. Martinec, T., Mlynec, J., Petru, M. (2015) *Robotics and Computer-Integrated Manufacturing, vol. 35, 42-54.*
7. Mazínová, I. (2015). GPS – Do we know what we prescribe? In. 5*6 International Conference Machine Design Departments* (pp. 205-212).
8. Stupavsky, M., Broncek, J. (2014). *Materials Science Forum, 818, 15-18. 276-279.*
9. EN ISO 1101:2017 *Geometrical product specifications (GPS) - Geometrical tolerancing - Tolerances of form, orientation, location and run-out.*
10. ISO 16610-21:2012 *Geometrical product specifications (GPS) – Filtration – Part 21: Linear profile filters. Gaussian filters.*

Corresponding author:
doc. Ing. Jozef Bronček, Ph.D., Department of Design and Mechanical Elements, Department of Mechanical Engineering, Faculty of Mechanical Engineering, University of Žilina, 01026 Žilina, Slovakia, phone: +421 513 2929, e-mail: jozef.broncek@fstroj.uniza.sk

APPLICATION OF SIMULATION SOFTWARE TO OPTIMIZE CONSTRUCTION NODES OF ULTRASONIC WELDING MACHINES

Marcel ČAČO[1], Rastislav TRIBULA[2], Peter ŠČERBA[3], Róbert KOHÁR[4]

[1]*CEIT technical innovation, s.r.o., Slovakia, e-mail: marcel.caco@ceitgroup.eu*
[2]*CEIT technical innovation, s.r.o., Slovakia, e-mail: rastislav.tribula@ceitgroup.eu*
[3]*CEIT technical innovation, s.r.o., Slovakia, e-mail: peter.scerba@ceitgroup.eu*
[4]*University of Žilina, Slovakia, e-mail: Robert.Kohar@fstroj.uniza.sk*

Abstract
The whole lifecycle of a construction node and the whole technical system attempts to be optimized. An engineer decides whether the construction node or the whole technical system need optimization or when and by which optimization tools will be the optimization performed. Virtual simulation software belongs to the tools that help the engineer to make a decision. Within the virtual environment, there can be performed simulations that analyze the whole technical systems in detail. It is possible to proceed to such virtual simulations and analyzes during different stages of the technical system lifecycle and they may help us to reveal and precisely identify structural shortcomings, weak spots and elements. By means of such simulations, the engineer can solve a problem in the technical system construction in a faster, better and cheaper way.

Key words: *technical system; construction node; optimization; virtual simulation.*

INTRODUCTION

New kinds of software are being developed daily. They have to find and accurately identify possible construction deficiencies. Such software enables to simulate different impacts and loads on the construction elements, construction nodes or on the whole technical system and thereby save time and money. Such software analyzes enable to verify the selected parameters of the technical system at any time in the construction process, thus ensuring proper selection of optimization.

Thermoplastics are widely used due to their good mechanical and construction properties, mainly in the area of consumer goods, electrical engineering and automotive industry. Their great construction advantage is that they can be very reliably connected by means of welding. Ultrasonic welding belongs to effective welding methods of plastics. Practical application of ultrasonic welding for hard plastics was finished in year 1960. The patent for the ultrasonic method for welding rigid thermoplastic parts was awarded to Robert Soloff and Seymour Linsley in 1965 (Weber, 2007).

Success of the company depends primarily on the ability of meeting the requirements of the market respectively customer requirements. For this reason, customer satisfaction has become a measure of success (Žarnay, et al., 2000). Perspective future of automation of the ultrasonic welding of differently sized plastic parts leads the company CEIT Technical Innovation s.r.o. (Central European Institute of Technology s.r.o.) to optimize the already produced welding machines and to produce unified assembly units for incorporation into ultrasonic welding machines.

To perform a good welding joint, it is necessary to observe the main parameters of the ultrasonic welding. The values of the ultrasonic welding parameters vary according to the welded material.

The main parameters of the ultrasonic welding are: tip welding deflection amplitude A_o (mm), compressive force F_p (N), frequency f (Hz), welding time t (s) (Sobotová, 2005). Correct understanding of quintessence of physical phenomena and their effective use in technical systems also provides solid platform for innovation (Bultey, Yan, Zanni, 2015).

MATERIALS AND METHODS

The technical node for gripping the sonotrode shall ensure all the requirements coming from the ultrasonic welding technology. The technological procedure of ultrasonic welding involves the welding head supply to the welding joint. Transmission of ultrasonic vibrations into the welding joint is performed for the required time and under constant pressure and, if necessary, to ensure cooling of

the welding joint. The transfer of physical quantities necessary to carry out the ultrasonic welding has a negative impact on the whole construction node of welding heads or sonotrodes gripping.
When designing the construction nodes of sonotrode gripping, the greatest possible repeatability of these nodes was taken into account for the design of other technical systems for the ultrasonic welding. The following step was to create a database, including these construction nodes, for a faster production of technical systems. In this regard, the 3D design models of construction nodes for sonotrodes gripping were subjected to simulations in the virtual world. There were designed two gripping variants on Fig. 1. Both variants were subjected to simulations.

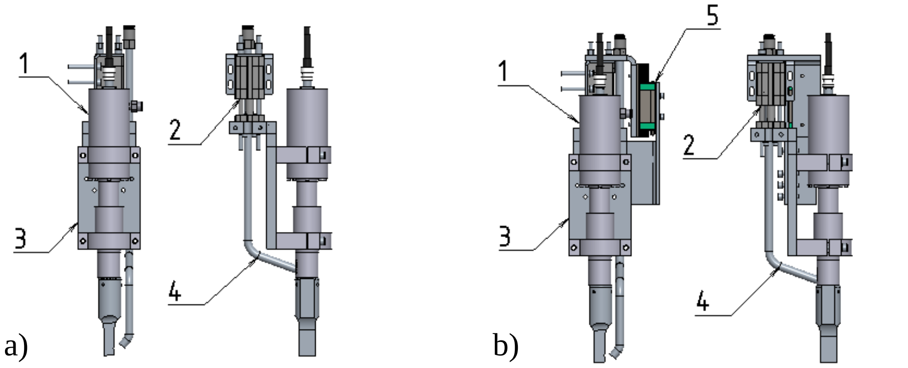

Fig. 1 a) Welding head gripping, Variant no.1; b) Welding head gripping, Variant no.2; (1) Sonotrode, (2) Linear conduct, (3) Pneumatic cylinder, (4) Cooling tube, (5) Gripping construction

For the purposes of the software in which the simulations were performed, both variants were simplified as much as possible and the 3D models were relieved of the excess elements that met only the secondary functions. Within the simulations, there were taken into account the gravitational force and the compressive force acting in the opposite direction as the gravitational force. The compressive forces during the ultrasonic welding range from 0,2 MPa to 10 MPa. They are selected according to the welded material properties and the type of material used. We will count with the greatest possible load of 3 MPa on the welded polymer.

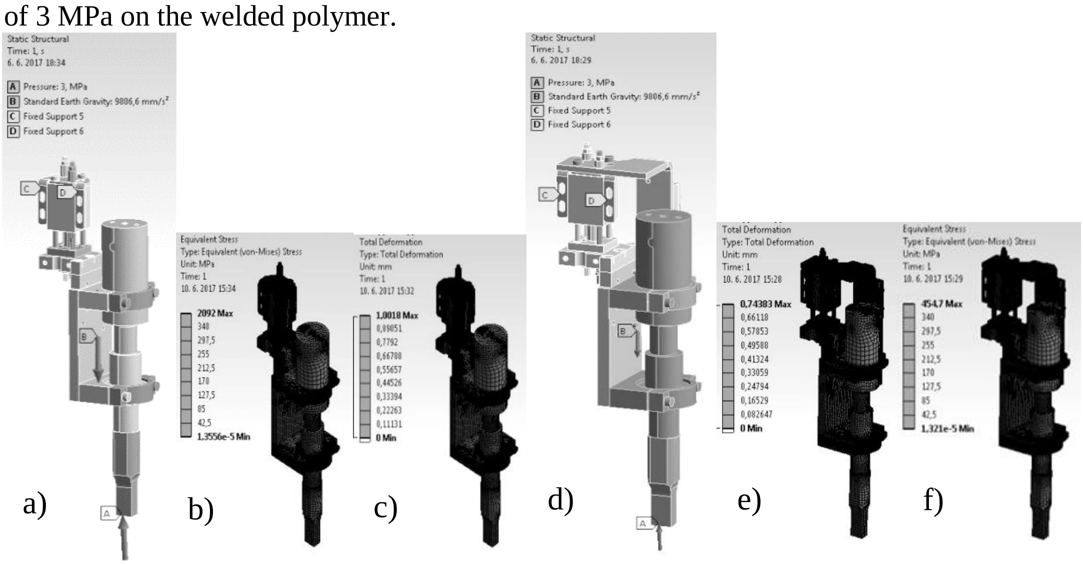

Fig. 2 a) Gripping and loadings, Variant no.1; b) Deflection of the sonotrode head, Variant no.1; c) Maximum stress in Variant no.1; d) Gripping and loadings, Variant no.2; e) Deflection of the sonotrode head, Variant no.2; f) Maximum stress in Variant no.2;

Variants have a similar construction type and some construction elements are repeated. Both variants are gripped to surfaces C, D, loaded by the gravitational force B and the compressive force A in the welding joint. These simulations show that the sonotrode has 1.0018 mm deflection of the welding head in the welding joint on the gripping, Variant no.1, and 0.744 mm deflection on the gripping, Variant no.2. In both designed constructions, too much stress is formed in the same construction unit and exceeds the used material´s strength limit of R_m 340 MPa. In Variant no.1, there is the stress of 2092 MPa and 454,7 MPa (Figure 2) in Variant no.2.

We need the construction node to ensure that deflection of the sonotrode head in the welding joint is at maximum 1 mm and the mechanical stress in the construction does not exceed 340 MPa. An analysis of the impacts of forces necessary during the ultrasonic welding technological process on the technical node has revealed the technical node construction deficiencies that prevent to repeatedly perform welding joints of the required quality. The simulations performed have exactly determined the unsatisfactory construction unit and also the specific place in which the unsatisfactory unit is overloaded on Fig. 3.

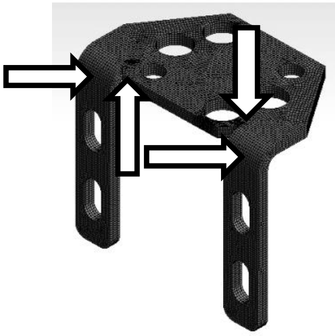

Fig. 3 Unsatisfactory construction unit (unsatisfactory construction places are marked with arrows).

This construction unit occurs in both original variants of the sonotrode gripping and proved to be unsatisfactory in both variants during simulations. When considering strength, both variants are unacceptable and the construction needs to be modified.

RESULTS AND DISCUSSION

The simulation results led to the design of Variant no.3 in which all the shortocomings of the previous variants should have been removed. The same simulations were performed also on the construction of this variant. When designing the construction node, Variant no.3, we tried to use as many construction units as possible from the previous variants, which complied with the requirements of the ultrasonic welding technological process when considering strength and functionality.

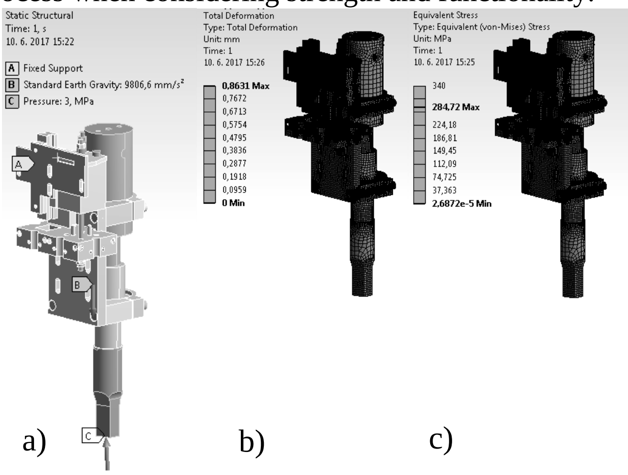

Fig. 4 a) Gripping and loadings, Variant no. 3; b) Deflection of the sonotrode head, Variant no.3; c) Maximum strength in Variant no. 3;

The construction node is gripped to surface A, loaded by the gravitational force B and compressive force A in the welding joint. The gripping area, the strength and the direction of their action are shown in the figure Fig. 4. The simulation shows that on the gripping, Variant no.3, the sonotrode has 0.863

mm deflection in the welding joint and the maximum voltage of 284.72 MPa is being formed in the construction with 3 MPa load.
When considering the forces used during the ultrasonic welding technological process, this construction node fully complies with the construction requirements for the use in the technical systems of the ultrasonic welding machines.

Tab. 1 Gripping analysis

Gripping	Deflection mm	Stress MPa	R_m MPa	Satisfactory Yes/No
Variant no.1	1,0018	2092	340	No
Variant no.2	0,744	454,7	340	No
Variant no.3	0,863	284,74	340	Yes

CONCLUSIONS

The biggest problem with the designed technical systems of the ultrasonic welding machines has been to design a sufficiently stiff, but also the most variable sonotrode gripping. The simulation software helped us to identify the unsatisfactory element and its deficiencies in the construction node in a relatively short time. This led us more effectively towards design of a new, suitable construction node. This saved us time and money that can be saved or used within the optimization process.

ACKNOWLEDGMENT

This work was created by the implementation of the project „Low cost logistic system based on mobile robotic platforms for industrial use", „ITMS: 26220220092 " suppported by the Operational Programme Research and Development and by the European Fund for Regional Development.

„We support research activities in Slovakia / This project is being co-financed by the European Union"

REFERENCES

1. Žarnay, M., Čilík, L., Bronček, J., Jurák, L., Takács, R., Žarnay, R. (2000). Technologickosť konštrukcií strojov. Žilina, ŽU – EDIS, ISBN: 80-7100-664-5.
2. MEDVECKÝ, Š. (2006). Konštruovanie 1. Žilina, ŽU – EDIS, ISBN: 978-80-8070-640-91.
3. ČILLÍK, L., ŽARNAY, M. (2001). Metodika konštruovania. Žilina, ŽU – EDIS, ISBN: 80-7100-934-2.
4. Bultey, A., Yan, W., Zanni, C. (2015). A proposal of a systematic and consistent Substance-Field Analysis. Procedia Engineering, Vol.131, p. 701-710. doi:10.1016/j.proeng.2015.12.357
5. Sobotová, L. (2005). Poznatky o zváraní plastov ultrazvukom a jeho využitie v praxi. Transfer inovácií, 8/2005, ISBN: 80-7093-6.
6. Weber, A. (2007, November 30). Weldind Still Ensures High-Strength Joints. Assembly Magazine. Retrieved from http// www.assemblymag.com/articles/85017-welding-still-ensures-high-strength-joint
7. The internal documentation of CEIT Technical Innovation, s.r.o.

Corresponding author:
Ing. Marcel Čačo, CEIT Technical Innovation s.r.o, Univerzitná 8413/6, 010 08 Žilina, Slovak Republic, phone: +421 41 513 7424, e-mail: marcel.caco@ceitgroup.eu

COMPARISON OF DEFORMATION ENERGY OF PARTICULAR OIL-BEARING CROPS

Cimen DEMIREL[1], Abraham KABUTEY[2], David HERAK[2], Gurkan A. K. GURDIL[1]

[1]*Department of Agricultural Machinery, Faculty of Agriculture, Ondokuz Mayis University, Samsun, Turkey*
[2]*Department of Mechanical Engineering, Faculty of Engineering, Czech University of Life Sciences Prague, Kamycka 129, 165 21 Prague, Suchdol, Prague 6, Czech Republic*

Abstract
The study focused on the description of the empirical and theoretical relationship between the force and deformation as well as the deformation energy of bulk oilseeds of oil palm, sunflower, rape and flax. Each of the bulk material initial height of 60 mm was loaded using the universal compression machine and pressing vessel of diameter 60 mm at a maximum force of 200 kN and speed of 5 mm/min. The tangent curve model was used to describe the experimental data. The amounts of numerical deformation energy of oil palm and sunflower bulk materials at a force of 200 kN were1245.55±20.41 (J) and 675.94±5.55 (J) whiles that of the analytical were 1283.96±29.55 (J) and 823.31±123.20 (J). At an optimal force of 163 kN for rape and flax bulk oilseeds, the amounts of experimental and analytical model of deformation energy were 718.27±29.41 (J) and 690.55±45.71 (J) then 600.96±4.62 (J) and 566.82±5.31 (J).

Key words: *bulk oilseeds; compression loading; empirical data; mathematical model*

INTRODUCTION

Oil is usually extracted from oil-bearing materials by mechanical expression or solvent method (*Owolarafe, et al., 2008*). Compression test of bulk systems also requires that the materials be placed in an enclosure to withstand the resulting pressure or compressive force (*Raji & Favier, 2004*). The knowledge of the required amount of energy of the oil-bearing materials during compression is useful in developing the appropriate equipment design and optimized processing conditions for greater oil recovery from oilseeds (*Chapuis, et al., 2014*). From the literature, the use of a mathematical model for the estimation of the energy in compression test has been reported for some bulk oilseeds (*Herak et al., 2011; Sigalingging et al., 2014, 2015*). Adequate information in this subject area is still needed to developing a more detailed mathematical model for energy requirement of oil-bearing materials during compression loading test and mechanical screw press. The objective of this study was to determine the numerical and analytical deformation energy of some bulk oilseeds/kernels of oil-bearing crops under compression loading.

MATERIALS AND METHOD

Sample and moisture content

The moisture content of the bulk oil palm kernels and the bulk oilseeds of sunflower, rape and flax was determined using the standard oven method with a temperature setting of 105 °C and drying time of 17 h (*ISI, 1996*). The initial and final weights of the bulk materials before and after oven drying were determined with the electronic balance (Kern 440–35, Kern & Sohn GmbH, Balingen, Germany). The determined amounts were 8.57, 4.79, 4.62 and 7.32 % on a wet basis according to equation (1) (*Blahovec, 2008*).

$$MC_{w.b.} = \left[\left(\frac{m_a - m_b}{m_a}\right)100\right] \tag{1}$$

where: $MC_{w.b.}$ is the moisture content on a wet basis (%), m_a is the mass of the bulk samples in the initial state and m_b is the mass of the bulk samples after drying or heat treatment (g).

Compression test of bulk oilseeds/kernels

The bulk oil-bearing materials were compressed at a maximum force of 200 kN and speed of 5 mm/min using the universal compression testing machine (ZDM 50, Czech Republic) and pressing vessel of diameter 60 mm. The initial pressing height of the bulk samples was measured at 60 mm where they were repeated three times. The obtained amounts of the force and corresponding deformation were further processed using the MathCAD 14 software (*Mathsoft, 2014; Marquardt, 1963; Pritchard, 1998*).

Deformation energy

The deformation energy was calculated using equation (2) (*Herak et al., 2012*).

$$D_E = \sum_{n=0}^{n=i-1}\left[\left(\frac{F_{n+1}+F_n}{2}\right)(x_{n+1}-x_n)\right] \tag{2}$$

where D_E is the deformation energy (J), $F_{n+1}+F_n$ and $x_{n+1}-x_n$ are values of the force (N) and deformation (mm), *n* is the number of observed values and *i* is 1, 2, 3………..$i_{\max}$ observations.

Percentage oil yield

The percentage oil yield of the bulk oilseeds/kernels was calculated using equation (3) (*Deli et al., 2011*).

$$OY(\%) = \frac{O_w}{O_m}100 \tag{3}$$

where OY is the oil yield (%), O_w is the mass of oil (g) and O_m is the mass of bulk oilseeds/kernels (g)

Theoretical fitted curves and deformation energy

The theoretical dependency between the force and deformation curves of the bulk oil-bearing materials was described using the tangent curve function as indicated in equation (4) (*Herak et al., 2011; Sigalingging et al., 2014, 2015*).

$$\mathrm{F}(\mathrm{x},\mathrm{A},\mathrm{B}) = \mathrm{A}\cdot(\tan(\mathrm{B}\cdot\mathrm{x}))^{\mathrm{n}} \tag{4}$$

Where F is the compressive force (kN), x is the deformation of bulk material (mm), A is the force coefficient of mechanical behaviour (kN), B is the deformation coefficient of mechanical behaviour (mm^{-1}) and n is the value of the fitting function (-). The integral of equation 4 is the deformation energy (J).

RESULTS AND DISCUSSION

The results of the numerical and analytical evaluation of the bulk oilseeds of oil palm, sunflower, rape and flax are presented in Tab. 1 and 2 as well as Fig. 1 to 3 respectively. For rape and flax bulk oilseeds, the optimal force without the ejection of the seedcake through the pressing vessel holes was observed at a maximum force of 163 kN. However, the initial maximum force of 200 kN for oil palm and sunflower bulk oilseeds/kernels was without any ejection process. The ejection process is characterized by the serration behaviour on the force and deformation curve (Fig. 1). Both the smooth curve pattern and serration effect exhibited by the oil-bearing crops are important for analyzing the energy requirement for the output oil (*Divisova et al., 2014*).

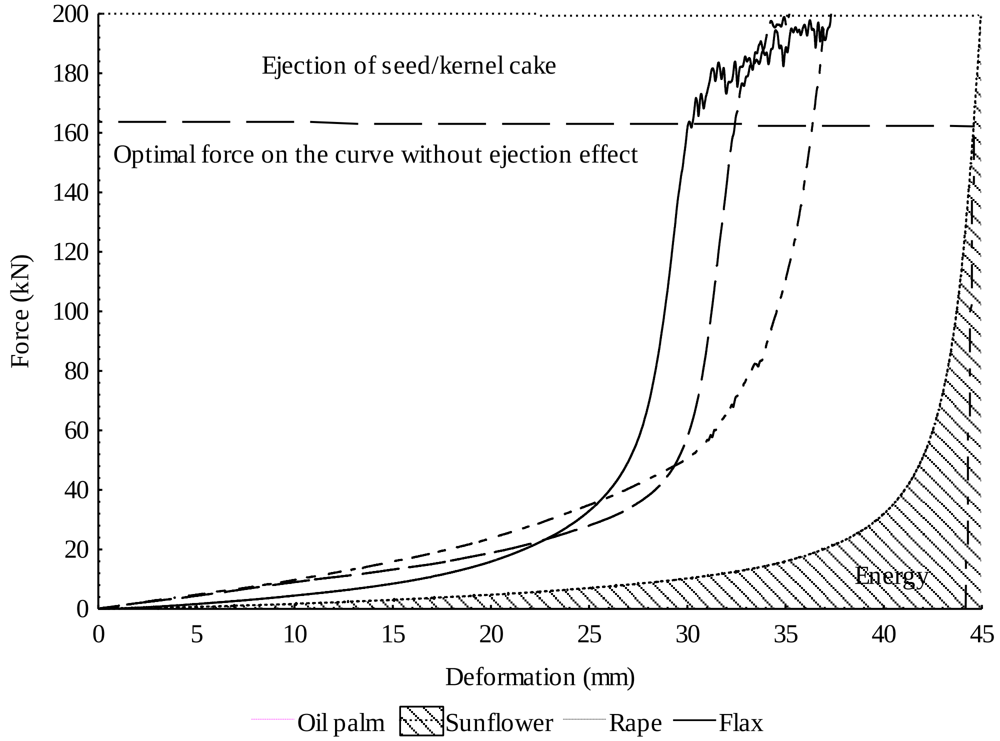

Fig. 1 Force and deformation curves of bulk oilseed or kernel of oil palm, sunflower, rape and flax

The empirical amounts of deformation energy of oil palm, sunflower, rape and flax bulk materials were 1245.55±20.41 (J), 675.94±5.55 (J) 718.27±29.41 (J) and 600.96±4.62 (J). Similarly, the analytical deformation energy values based on the tangent curve model of the above-mentioned bulk oilseeds/kernels in that order were 1283.96±29.55 (J), 823.31±123.20 (J), 690.55±45.71 (J) and 566.82±5.31 (J) (Tab. 1). Flax bulk oilseeds indicated the lowest deformation energy at a speed of 5 mm/min. These amounts are described graphically in Fig. 2. Following in that order the oil yield amounts were 27.32±0.79 (%), 21.08±0.59 (%), 23.04±0.15 (%) and 14.19±0.61 (%).

Tab. 1 Evaluation of numerical and analytical deformation energy of different bulk oilseeds

Bulk oilseeds/kernels	Force (kN)	Deformation (mm)	Deformation energy (J)	
			Numerical	Analytical
Oil palm	200	39.53±2.21	1245.55±20.41	1283.96±29.55
Sunflower		45.36±0.37	675.94±5.55	823.31±123.20
Oil palm	*163	38.91±0.20	1133.72±15.44	1151±31.51
Sunflower		44.97±0.37	604.77±8.57	634.20±60.91
*Rape		33.03±0.56	718.27±29.41	690.55±45.71
*Flax		29.68±0.52	600.96±4.62	566.82±5.31

* Optimal force without seedcake ejection from the pressing vessel holes.

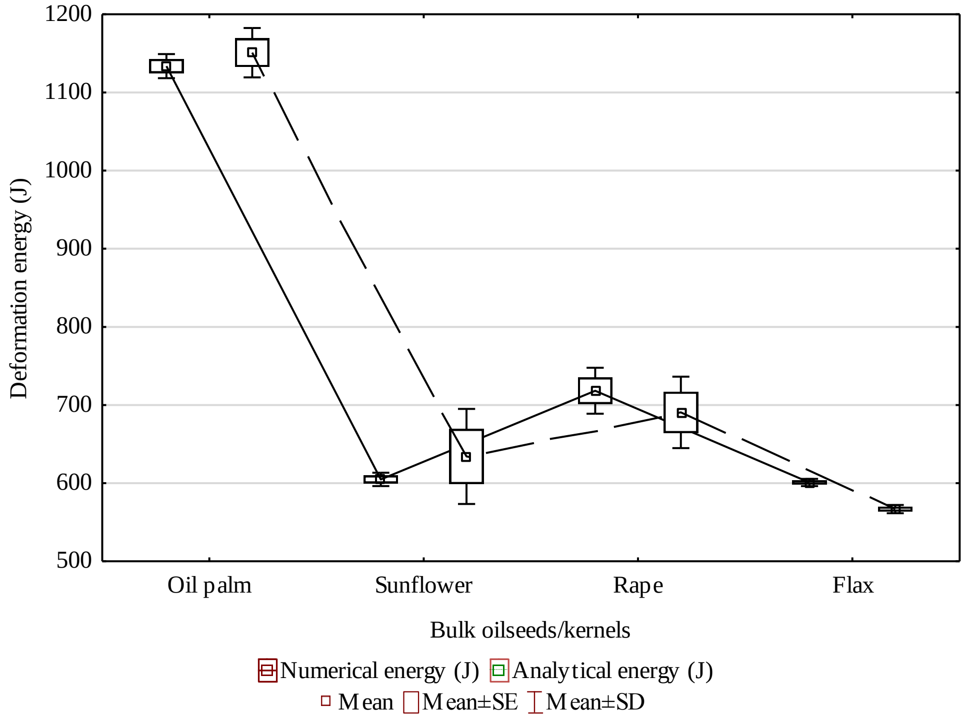

Fig. 2 Relationship between the numerical and analytical deformation energy of bulk oilseeds at force 163 kN

The statistical analyses of the tangent curve mathematical model are given in Tab. 2. The results were significant where the values of $F_{critical}$ were higher than F_{ratio} for all determined coefficients. Further, the amounts of P_{value} were also higher than the alpha level of 0.05.

Tab. 2 Tangent model coefficients and statistical analyses at force 200 and 163 kN

Bulk oilseeds/kernels	A (kN)	B (mm^{-1})	n (-)	F_{ratio} (-)	$F_{critical}$ (-)	P_{value} (-)	R^2 (-)
				At force 200 kN			
Oil palm	19.577 ±1.161	0.038 ±0.002	1	0.002 ±0.003	3.858 ±0.001	0.969 ±0.030	0.999 ±0.001
Sunflower	7.573 ±0.241	0.034 ±0.001	1	0.067 ±0.024	3.860 ±0.001	0.799 ±0.039	0.996 ±0.001
				At force 163 kN			
Oil palm	19.460 ±1.166	0.038 ±0.002	1	0.004 ±0.006	3.860 ±0.002	0.952 ±0.034	0.999 ±0.001
Sunflower	6.781 ±0.095	0.034 ±0.001	1	0.025 ±0.013	3.860 ±0.002	0.878 ±0.031	0.999 ±0.001
Rape	11.373 ±1.124	0.046 ±0.001	1	0.011 ±0.017	3.864 ±0.005	0.934 ±0.064	0.992 ±0.002
Flax	7.170 ±0.517	0.046 ±0.001	2	0.057 ±0.028	3.868 ±0.004	0.816 ±0.048	0.996 ±0.001

F_{ratio} is the value that compares the joint effect of variables (-), $F_{critical}$ is the critical value that compares a pair of models (-), P_{value} is the significance level within a statistical hypothesis test (-), R^2 is the coefficient of determination of fitted data (-).

The coefficients of determination (R^2) of the tangent model were between 0.992 and 0.999 indicating the accuracy of the mathematical model for describing the empirical data of bulk oilseeds under compression loading (Fig. 3).

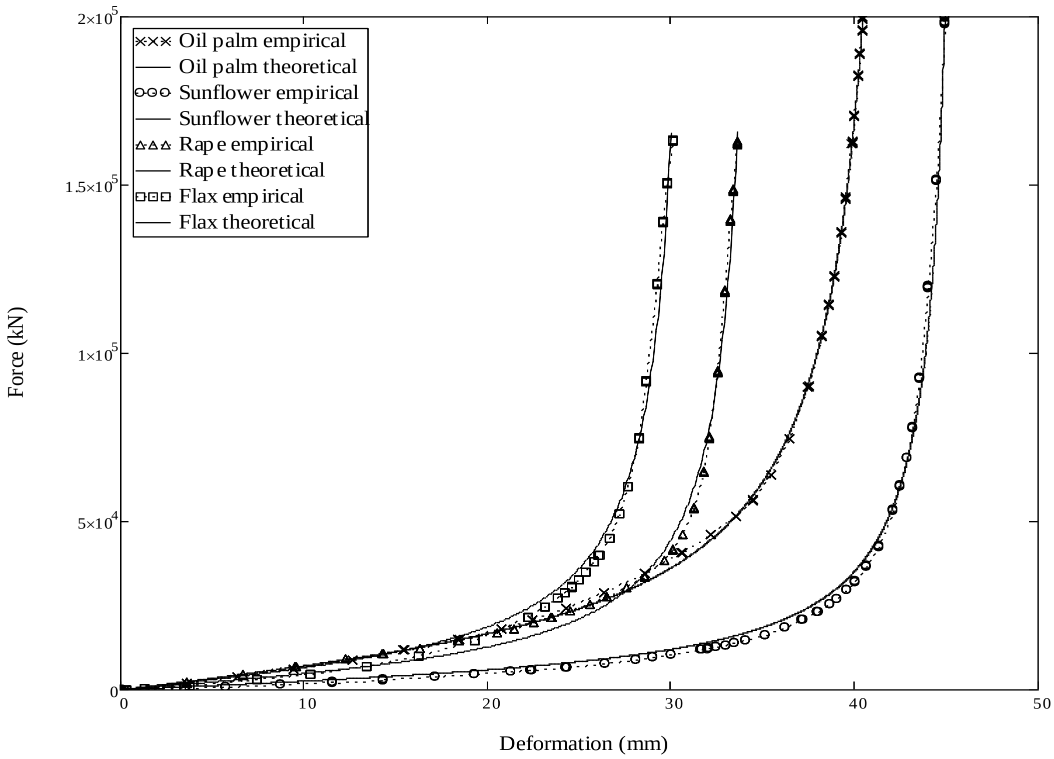

Fig. 3 Empirical and theoretical descriptions of force and deformation of some bulk oilseeds

The present results were in agreement with other published studies focused on the mechanical behaviour of bulk oilseeds or kernels under compression loading (*Herak et al., 2011; Sigalingging et al., 2014, 2015*). However, research is still needed for developing a general model which takes into account the effects of speed, moisture content, heat treatment temperature and friction which thus influence the pressing process. This knowledge can be transferred to the non-linear pressing involving a mechanical screw press or expeller for optimizing the energy requirement and oil recovery efficiency.

CONCLUSION

A good fit was obtained between the experimental data of the different oil-bearing seeds/kernels and predicted data based on the tangent curve model. The coefficients of determination (R^2) of the tangent model were between 0.992 and 0.999. However, the incorporation of other pressing factors in the tangent curve model is required to describe the mechanical behaviour of bulk oilseeds under compression loading.

REFERENCES

1. Blahovec, J. (2008). *Agromaterials Study Guide*. Czech University of Life Sciences Prague.
2. Chapuis, A., Blin, J., Carre, P. & Lecomte, D. (2014). Separation efficiency and energy consumption of oil expression using a screw-press: The case of Jatropha curcas L. seeds. *Industrial Crops and Products*, 52:752-761.
3. Deli S., Farah Masturah M., Tajul Aris Y. & Wan Nadiah W. A. (2011). The effects of physical parameters of the screw press oil expeller on oil yield from nigella sativa l. seeds. *International Food Research*, 18:1367-1373.
4. Divisova M., Herak D., Kabutey A., Sleger V., Sigalingging R. & Svatonova T. (2014). Deformation curve characteristics of rapeseeds and sunflower

seeds under compression loading. *Scientia Agriculturae Bohemica*, 45(3):180-186.
5. Herak, D., Kabutey, A., Sedlacek, A. & Gurdil, G.A. (2011). Tangent curve utilization for description of mechanical behaviour of pressed mixture. *Research in Agricultural Engineering*, 57(1):1-18.
6. Herak D., Kabutey A., Sedlacek A. & Gurdil G.A. (2012). Mechanical behaviour of several layers of selected plant seeds under compression loading. *Research in Agricultural Engineering*, 58(1):24-29.
7. ISI (1996). *Indian standard methods for analysis of oilseeds*, IS:3579. New Delhi: Indian.
8. Marquardt, D.W. (1963). An algorithm for the least-squares estimation of nonlinear parameters, SIAM. *Journal of Applied Mathematics*, 11(2):431-441.
9. Mathsoft (2014). *Inc. Parametric Technology Corporation*, 140 Kendrick Street, Needham, MA 02494 USA.
10. Owolarafe, O.K., Osunlek, A.S., Odejobi, O.A., Ajadi, S.O., & Faborade, M.O., (2008). Mathematical modelling and simulation of the hydraulic expression of oil from oil palm fruit. *Biosystems Engineering*, 101:331-340.
11. Pritchard, P. J. (1998). *Mathcad: A tool for engineering problem solving*. McGraw-Hill Science Engineering, New York, USA.
12. Raji, A.O. & Favier, J.F. (2004). Model for the deformation in agricultural and food particulate materials under bulk compressive loading using discrete element method. I: Theory, model development and validation. *Journal of Food Engineering*, 64:359-371.
13. Sigalingging, R., Herak, D., Kabutey, A., Mizera, C. & Divisova, M. (2014). Tangent curve function description of mechanical behaviour of bulk oilseeds: A review. *Scientia Agriculturae Bohemica*, 45(4):259-264. Standard Institute.
14. Sigalingging, R., Herak, D., Kabutey, A., Dajbych, O.; Hrabe, P. & Mizera, C. (2015). Application of a tangent curve mathematical model for analysis of the mechanical behaviour of sunflower bulk seeds. *International Agrophysics*, 29(4):517-524.

Corresponding author:
Cimen Demirel, Department of Agricultural Machinery, Faculty of Agriculture, Ondokuz Mayis University, Samsun, Turkey, phone: +90 554 702 45 81, e-mail: cimen.demirel@omu.edu.tr

CORE DRILLING MACHINE FOR PERFECTLY VERTICAL DRILLS

Martin DUB[1], Martin JANDA[1], Jiří MRÁZEK[1], Martin KAVKA[1], Vojtěch DYNYBYL[1]

[1]*Czech Technical University in Prague, Department of Designing and Machine Components, Technická 4, 166 07, Prague, Czech Republic*

Abstract
The article is focused on the design of new drilling machine for building perfectly vertical drills. The need of the vertically accurate drills is given by the necessity of inverted pendulum installation into the water dams. The machine is designed with emphasis on mobility and installation dimensions in the dam corridors.

Key words: *drilling machine; core drilling; water dam; inverse pendulum; monitoring.*

INTRODUCTION

The security of water dams is very actual topic. The pendulums are used for monitoring of water dam tilt. These tilts can reach quite high values due to the temperature difference or amount of retained water. The fixed point of the pendulum is usually placed nearby the top of the dam and the weight is nearby the foundation joint of the dam. For more precise measurement the inverse pendulums are used in combination with classic pendulums. The inverse pendulums are installed through the foundation joint of the dam. This allows to separate the movements of the dam due to the temperature, water etc. and the movements caused by the changes in the subsoil. For this purpose, it is necessary to build very accurate vertical drill through the dam concrete, foundation joint and the subsoil rock (Webster, 1998). The verticality of the drill is required 0.1%, i.e. 1 mm deviation for 1 m of the drill. The designed drilling machine was further used in cooperation with company CHEMCOMEX Praha, a.s. for the new technology development within the project TA04020433.

MATERIALS AND METHODS

The drilling machine is designed as a two-column with a drill head on the lifting portal. The CAD model can be seen in Fig. 1.

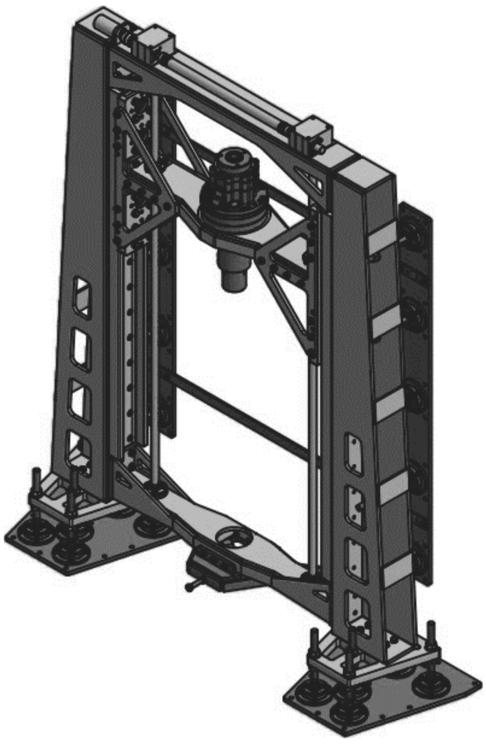

Fig. 1 The CAD model of the designed drilling machine

The drilling machine is designed for the bore diameter 137 mm and the tight drilling column is used. The necessary torque for the drilling is approx. 2000 Nm and revolutions 190 rev/min. These parameters are satisfied by the hydraulic drill head JANO RH 250. The stroke of the drill head is realized by means of the motion screws and lifting gearboxes. The input power is realized by the hydraulics again. The linear movement is secured by the rails and track runner bearings.

It has to be supposed that the connecting surfaces in the dam corridor are not ideally flat, see in Fig. 2. The correct setting up of the drilling machine is essential for the verticality of the built drill. For this purpose, the special adjustable struts with spherical joint were designed, see Fig. 2. These struts can compensate the imperfections both on the floor and on wall of the corridor. This system allows the correct setting up of the drilling machine into the vertical position. Whole adjustable system is in Fig. 3.

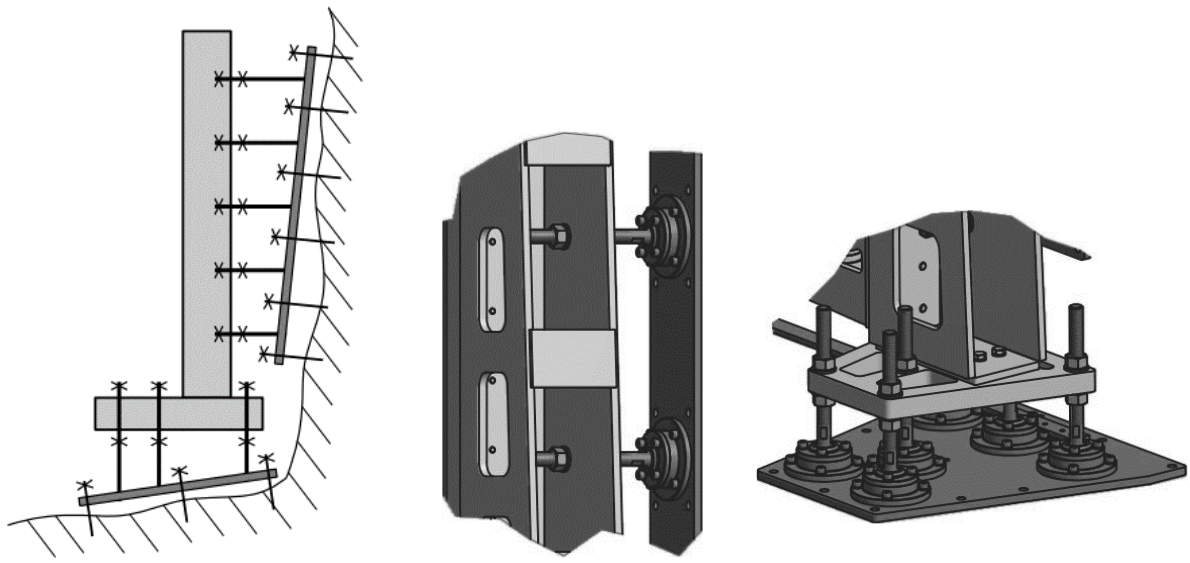

Fig. 2 Scheme of the non-ideal surface for the drilling machine connection and designed solution by means of the struts with spherical joints (Kavka, 2015)

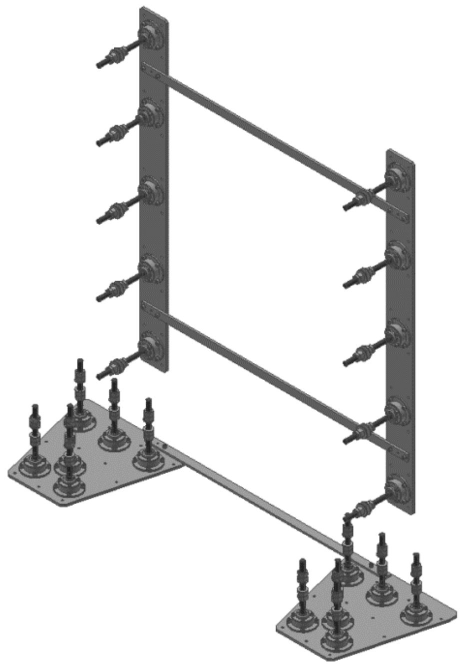

Fig. 3 Adjustable system for compensation of imperfections of the floor and wall (Kavka, 2015)

RESULTS AND DISCUSSION

The drilling machine was manufactured according the introduced design. The first testing took place on the testing polygon on the premises of the company CHEMCOMEX Praha, a.s. Complex drilling tests were carried out. Furthermore, the verticality of the test drill was measured by the special measuring pendulum. Measured data were evaluated with very good result of verticality.

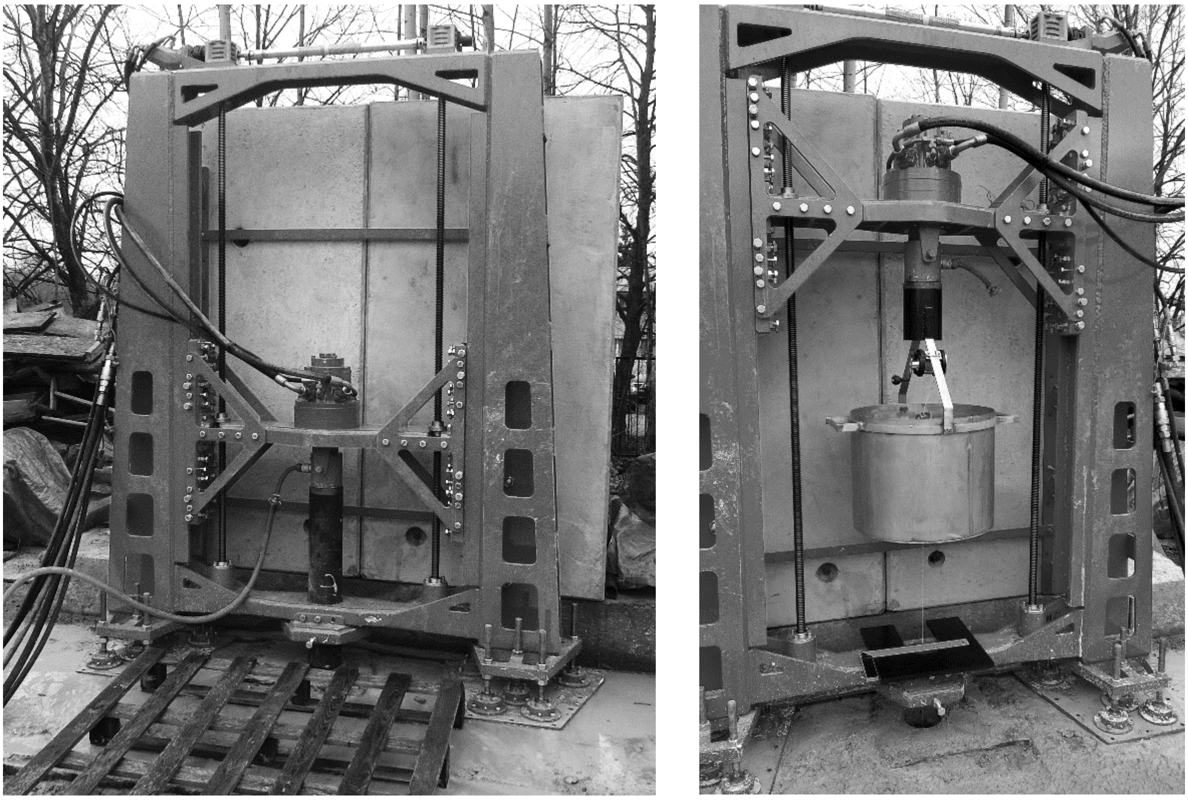

Fig. 4 Drilling machine on the testing polygon and special measuring pendulum mounted on the drill head

After necessary test of the drilling machine, it was moved to the Orlík dam, see Fig 5. The main goal was to build the 10.5 m deep drill of diameter 137 mm through the foundation joint of the water dam and keep up the given verticality 0.1%. At first, the drilling machine had to be mounted to the floor and wall using above mentioned adjustable system. The axis of the drill head was established into the coincidence with vertical. The problem with the rinse water had to be also solved due to the environmental and technical reasons.

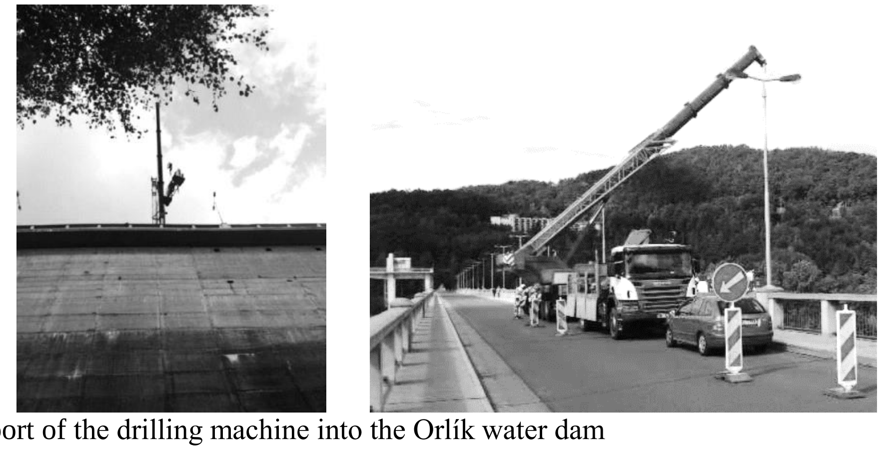

Fig. 5 Transport of the drilling machine into the Orlík water dam

The drill in the Orlík dam was built into the deep of 10.5 m. The first 2.8 m of the drill was built in the concrete structure of the dam and the rest of the drill is located in the rock base. The drill was continuously monitored by means of the special measuring pendulum to keep up the given verticality with very good results. Drilling machine in the corridor of the Orlík water dam can be seen in Fig. 6.

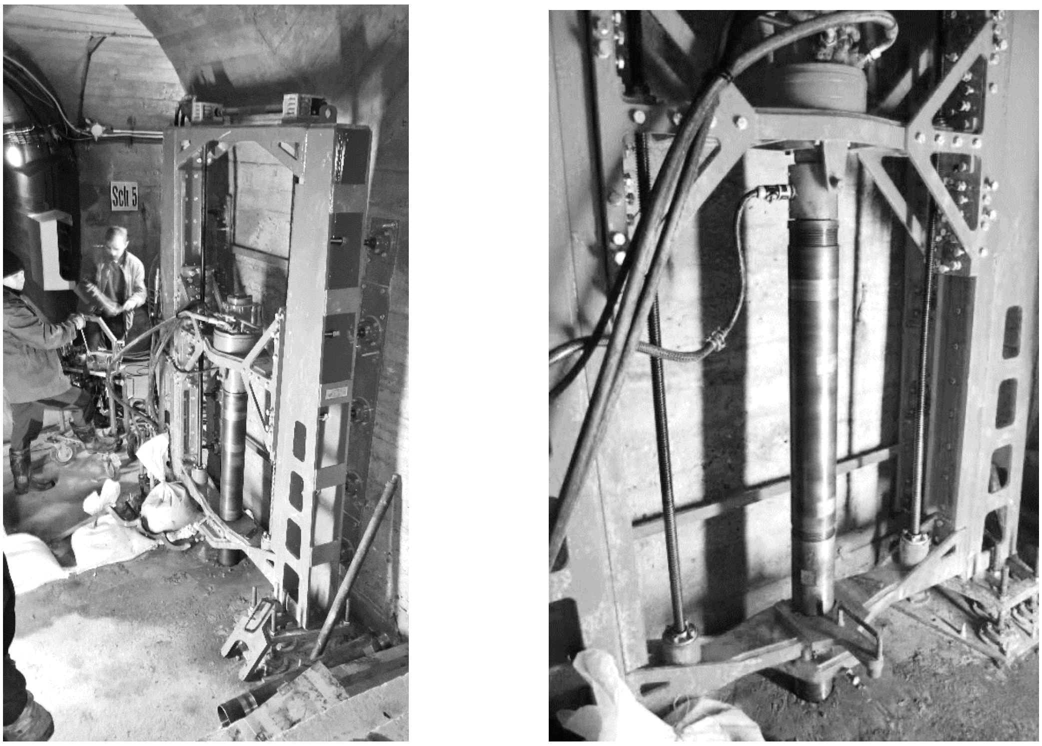

Fig. 6 Drilling machine during the drilling in the corridor of Orlík water dam

CONCLUSION

This contribution describes the design the new design of the special drilling machine. This machine is capable to build accurately vertical drill by means of core drilling technology. These vertical drills are requested nowadays due to the installations of inverted pendulums for the water dams. Further, the testing of the drilling machine, its transport to the Orlík water dam and own drilling in the dam is described.

REFERENCES

1. Webster, J. G. (1998). The Measurement, Instrumentation and Sensors Handbook. *CRC Press*.
2. Kavka, M. (2015). Structural design of compact device for deep drilling in the body of the dam. *Diploma thesis*.

Corresponding author:
Ing. Martin Dub, Ph.D., Czech Technical University in Prague, Department of Designing and Machine Components, Technická 4, 166 07, Prague 6, Czech Republic, phone: +420 728 120 299, e-mail: martin.dub@fs.cvut.cz

APPLICATION OF LINEAR DRIVE TESTING METHODOLOGY

Vojtěch DYNYBYL[1], Vít KLÍMA[1], Jiří MRÁZEK[1]

[1]*Department of Mechanical Design and Machine Parts, Faculty of Mechanical Engineering, CTU in Prague*

Abstract
This article is devoted to the developing of the methodology of testing of operational parameters of linear drives. Article is mainly focused on the testing of timing belt driven linear positioner. The main comparative parameters were appointed and methods for measuring will be explained. Selected methods will be explained on real-executed experiment. The results of the experiment will be discussed and analyzed.

Key words: *Linear positioner, testing of linear drives, timing-belt, experimental stand*

INTRODUCTION

This article discusses a development and further application of methods for measurement of the operational parameters of a linear drive. Article is mainly focused on the timing belt driven linear positioners and is based on master thesis elaborated by the author (*Klíma,2016; Gates Metcrol Inc,2006; FORBO Siegling GmbH,2015*).
Methodology was developed as a tool for comprehensive and objective evaluation of operational parameters of commercially produced linear positioners. That could be used for finding of the performance standard of linear positioning applications for further projects in this field.

The main comparative parameters were appointed as:

a)	Maximal load capacity of Linear Positioner (hereinafter LP)	[N]
b)	Two-sided stiffness of LP	[N/mm]
c)	Accuracy of positioning	[mm]
d)	Efficiency of linear drive	[-]

MATERIALS AND METHODS

Basic principles of the parameters measuring

Measuring methods for the above mentioned comparative parameters were developed. These methods allow repeatable experiments in laboratory conditions. Methods require precise measurement of appointed characteristically values. These values are necessary for determination of real operational parameters of linear drive. These methods will be in this chapter described and explained individually (*Klíma,2016*).

Accuracy of Positioning

Accuracy of linear positioning is a crucial attribute in real industrial service and application of the linear drive. The accuracy depends not only on the linear positioner itself, but on every component inserted into the drive system. In our case is necessary to considerate the influence of stiffness and deformation of every element in the drive system (clutches, torque sensor, drive shafts, etc.). Positioning error is thereafter calculated as the difference between theoretically expected and the experimentally measured real values of strokes (*Klíma,2016*).

Efficiency of Linear Drive

The Efficiency of the linear positioner can be calculated as ratio of input and output mechanical work. These works are determined on the experimentally measured data. Input mechanical work is calculated as torque of the drive electromotor multiplied by its angular rotation. Output mechanical work is calculated similarly as the action force of platform multiplied by its velocity value. These values are divided and this quotient is the requested efficiency (1) (*Klíma,2016*).

$$\eta_{\text{ system}} = \frac{P_{out}}{P_{in}} = \frac{W_{out}}{P_{in}} = \frac{F_r.s}{T_m.\alpha} = \frac{F_r.s}{T_m.\alpha.r_m.2.\pi} \qquad (1)$$

Where:

$\eta_{\text{ system}}$	- Efficiency of linear positioner	[-]
$P_{\text{ out}}$	- Power at the system output (positioning platform)	[W]
$P_{\text{ in}}$	- Power at the system input (driven shaft of positioner)	[W]
$W_{\text{ out}}$	- Mechanical work at the system output	[J]
$W_{\text{ in}}$	- Mechanical work at the system input	[J]
F_r	- Force generated by LP in the direction of positioning	[N]
s	- Stroke of LP	[mm]
T_m	- Torque at the drive shaft of LP	[N.mm]
α	- Revolution angle of drive shaft	[rad]
r_m	- Revolutions of drive shaft	[rev]

Experimental Stand

The experimental stand was designed as energetically open system without energy recuperation. This solution is suitable for our relatively simple experiment. Individual sensors have been built into experimental system according to the diagram below (*Klíma,2016*).

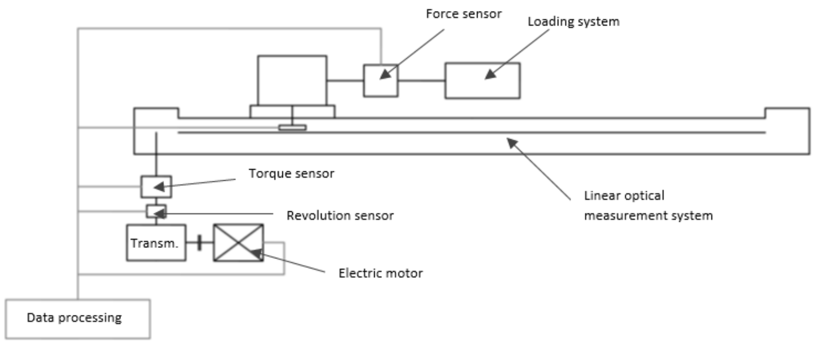

Fig. 1 Schematic chart of experimental stand (*Klíma,2016*)

The Screw-jack system ZIMM Z-5-SL with maximal stroke of 350 mm and maximal generated force of 5kN was chosen as the loading system. This screw-jack was used for experimental testing of load capacity and two-side stiffness of the linear drive. This screw-jack was driven by servo-motor FESTO EMMS-AS-70-S-RM (*Klíma,2016*).

Tab. 1 Used sensors

Measured Value	Sensor
Torque at drive shaft of LP	HBM T20WN
Action force of platform	HBM S9
Position of platform	JCXE 1- 450 mm
Safety end-switches	SAIP-CLS-111

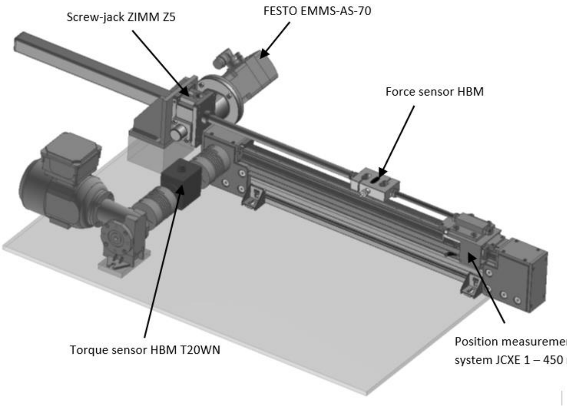

Fig. 2 3D Visualisation of experimental stand with student project linear drive (*Klíma,2016*)

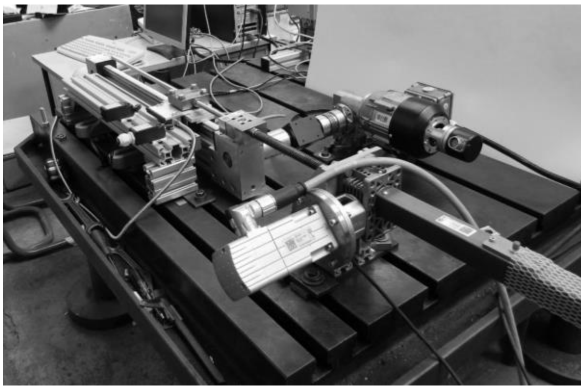

Fig. 3 Application of experimental stand in the department laboratory (*Klíma,2016*)

Practical application of selected methods
Developed experimental stand was realised and selected methods were verified in practice. Measurements of real load capacity and two-sided stiffness were realised on the student designed linear positioner. Target of this experiment was the verification of design parameters (*Klíma,2016*).

RESULTS AND DISCUSSION
Determining of Loading Capacity of Linear Positioner
At first phase of experiment was necessary to find the accurate value of loading force which can be transmitted by the platform of the linear drive. The external loading force was generated by screw-jack while the drive shaft of linear positioner was fully locked. The size of the force was increased from zero to maximal transmittable load in steps of 50 N. After skipping the belt through locked pulley was the experimental phase finished and the maximal stable transmissible force was recorded and plotted to graph (Fig.4) (*Klíma,2016*).

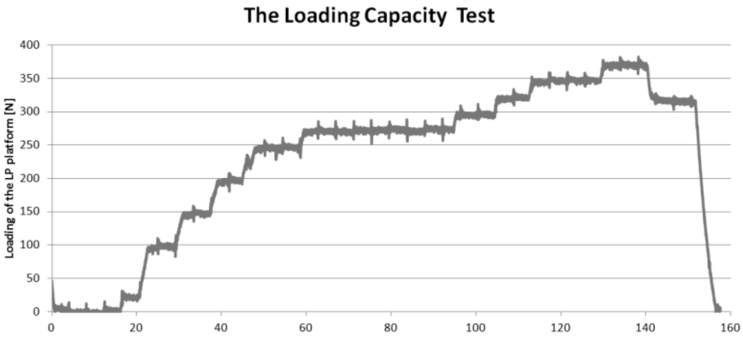

Fig. 4 Maximal transmissible force of tested linear drive (*Klíma,2016*)

According to the graph above we could say the maximal loading capacity of tested LP in the direction of positioning is equal to 350 N. When the external load reaches the level of 375 N, the deformation of position significantly increases. In this point the linear positioner wasn't able to positioning under loading and the reaction force had been reduced to zero (*Klíma,2016*).

Two-sided Stiffness of Linear Positioner
In previous part was determined the maximal loading force to value of 300 N. Twelve suitable stroke positions were chosen for measuring the two-sided stiffness. This stiffness calculation was based on the immediate change of platform position under the influence of the loading force (*Klíma,2016*).

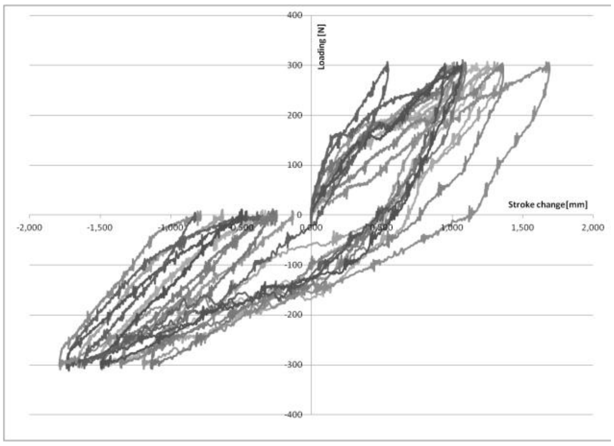

Fig. 5 Curves of the stroke changes under the loading force (*Klíma,2016*)

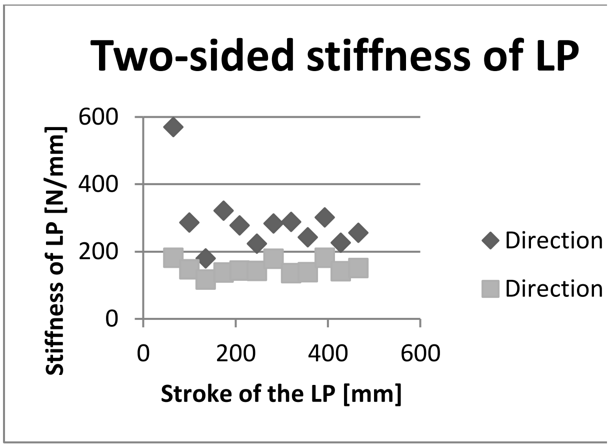

Fig. 6 Two-sided stiffness of linear positioner (*Klíma,2016*)

In the graph above can be seen the influence of the pre-loading force to the stiffness of LP during the first measuring cycle. On the hysteresis curves area of decreasing of stiffness is in the loading level about 180 N. This area indicates the compensation of the backslash in the timing belt mechanism (backslash between the teeth of belt and the drive pulley). This phenomenon does not occur in the first measurement cycle after pre-loading of the positioner. The difference between position of the platform at start of the loading sequence and the position after relief from loading sequence is obtained positioning error (*Klíma,2016*).

CONCLUSION

Functionality of developed methods for testing of linear drives was experimentally verified with application on the real linear drive system. Maximal operational parameters were discovered and compared with expected values. The measured results match the real-life behaviour of system and clarified effects and phenomenon incurred during the experiment. The weak points of the structural design of student project were appointed. Areas of future development in order to improve the operational parameters were recommended (*Klíma,2016*).

REFERENCES

1. Klíma, V., (2016). Testing of Linear Actuators, Design of Linear Drive, (Diploma Thesis). Prague. *CTU in Prague*.
2. GATES Mectrol,Inc. (2006). Timing Belt Theory Handbook. Salem
3. FORBO Siegling GmbH. (2015). Siegling Proposition Timing Belts Calculation Methods. Hannover

Corresponding author:
Ing. Vít Klíma , Department of Mechanical Design and Machine Parts, Faculty of Mechanical Engineering, CTU in Prague, Technická 4, Praha 6, Prague, 166 07, Czech Republic, phone: +420 22435-2415, e-mail: vit.klima@fs.cvut.cz

THE BEARING SYSTEM FOR THE CALIBRATOR OF SCHENBERG DETECTOR

Carlos FRAJUCA, Paulo Fernandes JUNIOR

Sao Paulo Federal Institute – Sao Paulo-SP-Brazil

ABSTRACT
This paper presents some topics for the "Mario Schenberg" gravitational waves detector calibrator, focused on the bearing system. This device must symmetrically rotate two objects, with mass and at a radius as large as possible, at a speed of 96,000 rpm, and therefore falls into the high-speed machines category. The guidelines and solutions proposed in this paper constitute a contribution to this class of engineering problems and were based on an extensive literature search, contacts with experts, the tutor's and author's experience, as well as on experimental results. A hybrid bearing that combines a radial passive magnetic bearing with an axial sliding bearing, here called MPS (Magnetic Passive and Sliding, was proposed. A reduced physical prototype was built and tested. Although the prototype has been tested at speeds below 12,000 rpm, the proposed guidelines were partially validated.

Keywords: Gravitational Waves Calibrator, Mario Schenberg Detector, High Rotation Machine, Passive Magnetic Bearing, Magnetic Sliding Bearing..

INTRODUCTION

Since Einstein's prediction of gravitational waves in 1916, scientists around the world are attempting to detect it, first signal were found. There are few gravitational wave detectors in the world. Brazil participates in this international effort with its resonant mass detector called "Mario Schenberg", built by the research group Graviton and installed at the University of São Paulo. To carry out the calibration of the Mario Schenberg detector an external device is necessary (Calibrator) capable of generating a periodic tidal signal. This device, here designated by the acronym DCMS (Device for Calibration of the Mario Schenberg detector), should rotate symmetrically two equal objects with the largest mass and at the largest possible radius, at a frequency of 1,600 Hz or 96,000 rpm (ANDRADE , 2006; PADOVANI, 2012; RUIZ, 2014; SANTOS, 2013). Figure 1 shows a basic schematic of this device.

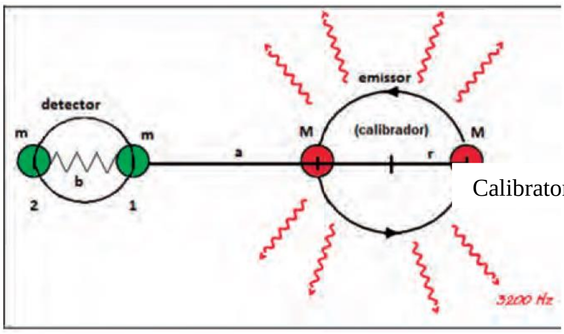

Fig. 1 Schematic illustration of the gravitational signal generator Source: Adapted from Padovani (2012).

The DCMS fits into the well-known class of engineering problems called "High Speed Rotary Machines High Speed " (WATSON, 1999). The project and the manufacture of these machines bring important challenges that involve several areas of Engineering.
According to Choi (2015), such problems include mechanical, electrical and magnetic losses, extreme mechanical stresses arising from high centrifugal forces, heating, power limitations of electronic circuits, increasing complexity of control algorithms and complex linked issues to the dynamics of rotors and vibrations.
The present work is part of a broader study aimed at obtaining guidelines for the whole project of the

DCMS (FERNANDES, 2015). In this preliminary work the main challenges to be overcome for the construction of such a device were discussed. This involved studies related to:
A) Protection structure: To ensure protection against the risks inherent in high speeds and at the same time eliminate aerodynamic drag, it was proposed to operate the DCMS inside a vacuum chamber shielded with ballistic materials;
B) Bearing: After careful comparative studies among several types of bearings presented in the literature, the hybrid passive magnet permanent magnet model developed in Pavani (2014) was adopted;
C) Design of the rotor: In order to withstand the high centrifugal load resulting from the high rotations, a system has been proposed for curing the rotating objects with carbon fiber, supported by a disc-shaped structure made of a composite of carbon fiber in epoxy resin;
D) Drive: It was proposed direct drive of the rotor (direct drive) with a reluctance motor controlled by an advanced electronic control algorithm;
E) Rotor Dynamics: Important guidelines have been proposed to avoid, or at least mitigate, the vibrations that cause instabilities in the rotor and often prevent the reach of high speeds.

MATERIALS AND METHODS

Selection of bearing type: The selection of bearings is generally focused on reducing the energy losses due to friction and wear, thus minimizing maintenance, increasing life and reducing equipment failure (HARNOY, 2003 apud PAVANI, 2014).
Among the most critical challenges encountered in the construction of the DCMS is the development of a DCMS high-speed rolling bearing that exhibits the least possible mechanical loss and rigidity sufficient to maintain the stability of the rotor, which is capable of attenuating vibrations, constructive and operational simplicity, among other requirements.
According to Pereira (2005), it is desirable in any rotary machine that the bearings be more flexible than the rotor shaft. The reasons for this are:
A) The low stiffness of the bearings reduces the transmission of the dynamic loads to its foundation, Service life of bearings and reducing structural vibrations;
B) Low bearing rigidity allows damping to operate more efficiently, attenuating the rotor's amplitude at critical speeds.
According to Borisavljevic (2011), in addition to operating practically without friction, the magnetic bearings operation, at extremely high speeds, and have the ability of the suspended rotor to rotate around its center of mass and not necessarily around its geometric center, thus allowing a rotor and high speed range. Whitley (1984) confirms that, in order for the rotor to benefit from a more flexible bearing system, such as magnetic bearings.
After careful analysis of the advantages and disadvantages presented by the different types of bearings, it was concluded that magnetic bearings are best suited for the high speed required by DCMS.
In Ruiz (2014) a study on the DCMS was carried out, recommending the use of magnetic bearings with variable reluctance drive which, according to Lembke, 2005, would have the following advantages:
- High reliability;
- Low losses, even at very high speeds;
- No wear, since there is no mechanical contact between the bearing parts;
- Absence of acoustic and vibrational noise;
- Greater simplicity when compared to active magnetic bearings;
- Report of tested bearings in vacuum pumps with speeds above 90000 rpm.

Permanent magnet passive magnet bearings (PMPMs) exhibit the most extreme simplicity, reliability and durability, requiring no supplies of external energy (YONNET, 1978), nor cooling systems for its operation. Considering its simplicity, PMPM was chosen. However, PMPMs need stabilization in at least one direction (EARNSHAW, 1842). This often requires the use of complex active systems.
The MPS (Magnetic Passive and Sliding) bearing: Pavani (2014) presents a simpler strategy for the axial stabilization of an MMP. The MMP proposed by the authors is intended for applications where axial forces are very small or constant, as in the case of DCMS. This bearing combines a radial MMP and an axial sliding bearing (strut) by pivots. The radial MMP consists of two pairs of cylindrical permanent magnets in axial attraction. In each pair, one of the magnets is attached to the end of the shaft

and the other to a fixed base. The rotor is self-centered in the radial direction by the action of the attraction between the magnets of each pair. Due to the negative rigidity in axial direction, the proposed bearing contains a spacer (steel ball or PVC pivot) between the magnets. By adjusting the spacing between the magnets, it is possible to minimize the axial force resulting from the attraction of the two bearings. According to the authors, the lower the resultant force, the lower the friction losses and the wear of the surfaces in contact (Figure 2).
This bearing, here called the MPS (Magnetic Passive and Sliding), presents a number of advantageous features for the DCMS, such as extremely constructive and operational simplicity, compact dimensions, no maintenance, very low friction, durability and reliability, this hybrid bearing concept was adopted for DCMS.
Magnetic bearings and brushless motors: The advantages of the use of brushless electric motors and magnetic bearings at high speeds. However, these two solutions implies an important challenge. As explained in RUIZ, 2014, the rotor / stator air gap should be as small as possible to ensure the efficiency of an electric motor. On the other hand, if the rotor is suspended by a PMPM, the rotor can move from its axis of rotation when facing vibrations and other instabilities (LI, 2012).
The engine air gap designed in Ruiz (2014) was specified in 0.25 mm, however the smallest one obtained in the experiments of this work was 0.75 mm, due to the collisions of the rotor with the stator.
The landing bearings: The limited rigidity of magnetic bearings requires the use of auxiliary landing bearings intended to contain temporary rotor oscillations within the limit established by the radial clearance (Figure 2). These bearings can be constructed with ball bearings ceramic elements (hybrids). Cage bearings are not recommended because of their lower resistance to repeated shocks with the rotor (KÄRKKÄINEN, 2007). Figure 2 shows the application of the emergency bearings.

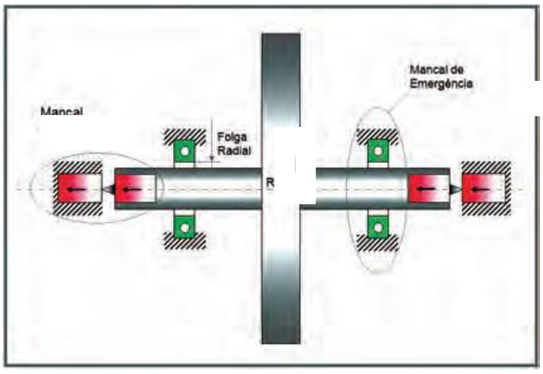

Fig. 2 joint bearings emergency bearings with the MPS bearings

According to Halminen et al. (2015), it is recommended a good alignment between the bearings, since large misalignment may cause serious damage to the bearings and to the rotor. Since DCMS should operate in a vacuum, the bearings must be lubricated with lubricants such as, for example, those made on the basis of Fluorinated polymers, including polytetrafluoroethylene (PTFE) known commercially as Teflon (NISHIMURA, 1999).

RESULTS AND DISCUSSIONS

In order to confirm the feasibility of obtaining a DCMS with the use of the above MPS bearing described, as well as identifying the various problems to overcome in order to obtain the DCMS, a prototype was built containing a rotor supported by bearings MPS and an electric motor for its drive.
At this stage of the research, it was not 96,000 rpm, specified for the DCMS.
The bearings: Two identical MPS bearings were constructed with based on the principle presented in Pavani (2014). Each two cylindrical magnets ($Nd_2Fe_{14}B$, Ø14x14 mm) in axial attraction, and a polymer pivot (PVC), the centralizing device provides greater ease and speed in replacing of the pivots.
The Bearing bases allow easy installation and removal of magnets and adjustment of the distance between bearings, which allows you to adjust the air gap in the bearings. Per ease of construction they were implemented in wood.

The drive: The drive of the rotor was made by a variable reluctance type motor consisting of a single-piece core made of sweet iron, containing 4 lugs, each acting as a magnet motor pole. For the activation of this core, the stator of a commercial 12-pole magnetic motor (coils) was used. These 12 coils were interconnected in order to compose 3 phases of 4 coils. The phases of the stator are energized sequentially, based on signals generated by reflective type photo detectors that detect the passage of stamped references on the side face of the flywheel.
Upon detecting a reference, the photo detector transmits a low voltage signal to the power board which sends it properly amplified to the corresponding phase of the motor, synchronized with the angular position of the rotor.
The rotor: The prototype rotor consists of the axle, flywheel and core (rotor) of the engine. The motor core and the two neodymium magnets were coupled to the shaft by means of interference fit. At particularly high speeds, as required in the DCMS, a number of considerations are required so that the inertia wheel (flywheel) does not disintegrate due to high centrifugal forces. The studies in this respect will be presented in later work. As already mentioned in this work, it will not be considered a particularly high rotation and therefore a simple wheel in polymeric material is employed.

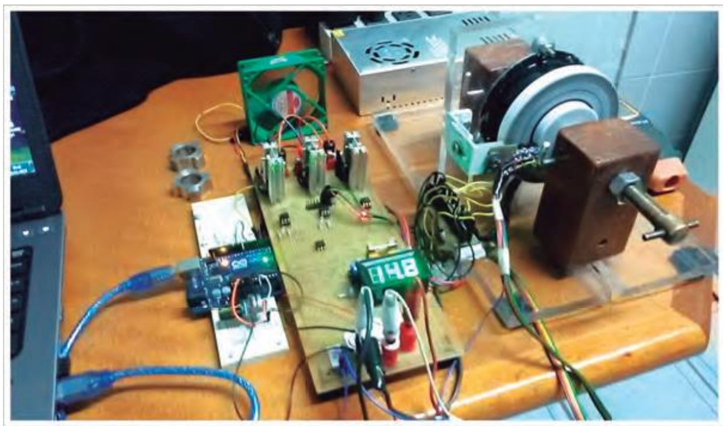

Fig. 3 shows the test bench with the assembled prototype assembly.

By adjusting this clearance to a minimum value and other adjustments, it was possible to achieve higher speed. This experimental result was in agreement with the statement made in Pavani (2014): "The smaller this resultant force, the less friction and the wear of the surfaces in contact". The following are the main experiments directly related to the bearings.
Tests of new materials for the pivots: In order to investigate the performance of other materials for the pivots, 5 different polymers (Nylon, Polyacetal, Teflon, PVC and hard rubber) were tested. First the 5 pivots were tested for the maximum rotation reached. Afterwards they were submitted to the rotation of 2,000 rpm for two hours, all under the same conditions. The wear was evaluated with the aid of a profile projector. The results are set forth in Table 1.

Tab. 1 - Performance of the different polymers used as pivots

Polimer	Maximum rotation speed (rpm)	Wear (mm) 2000 rpm/120min
PVC	2.7	0.05
Nylon 6	2.95	0.03
Teflon	2.9	0.10
Rubber	2.6	0.05
Poliacetal	2.7	0.07

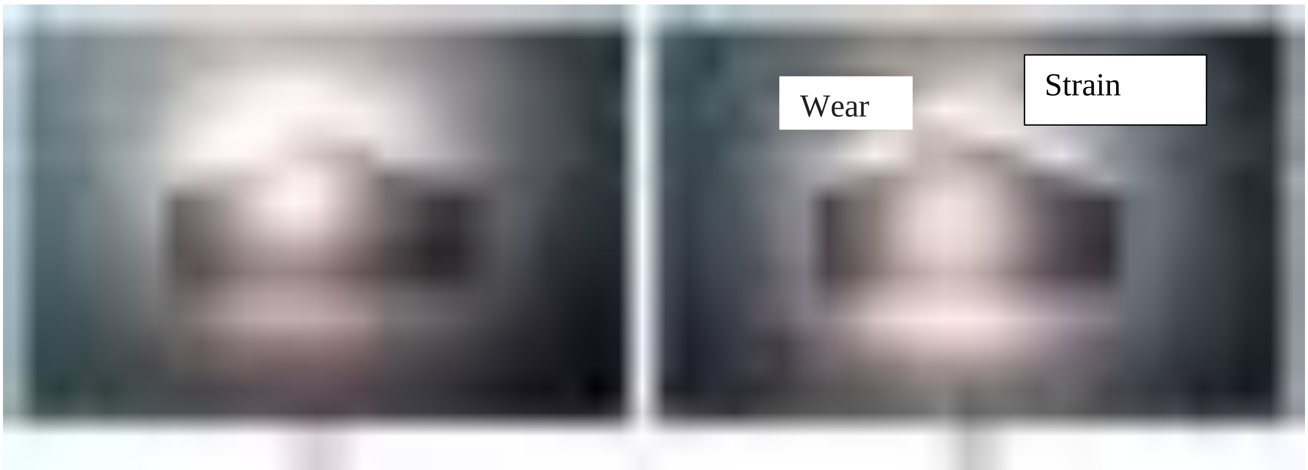

Fig. 4 images obtained on the profile projector. (A) Pivot before the test; (B) Pivot after the test.

Minimum rotor / stator air gap: Aiming to discover the smallest possible air gap, some experiments were performed with motor cores of different diameters. The minimum air gap that still allowed rotation without physical contact of the rotor with the stator was 0.75 mm.

CONCLUSIONS

This work is part of a study that aims to obtain guidelines for the DCMS project. In this larger study, challenges were discussed regarding the protection structure, the bearings, the rotor design, the drive and aspects involving the rotor dynamics. The present work focused on the bearings.

Considering the advantageous features such as extreme simplicity, compact size, the absence of maintenance, very low friction and reliability, and perfect adaptation to DCMS, the hybrid magnetic bearing model presented in Pavani (2014) was adopted in this work.

A small scale physical prototype was built and the bearing performance was investigated experimentally. New materials were investigated for the pivots and the best result was obtained with nylon 6. A magnetic device has been successfully developed to precisely balance the pulling forces of the two bearings. These two solutions, together with the adjustment of a minimum clearance in the bearings, provided very low friction and wear. Graphite powder lubrication has improved performance. Although limited, the radial stiffness of this magnetic bearing proved sufficient to maintain rotor stability.

This bearing model was very promising for DCMS. Even using a relatively simple and relatively small prototype, rotations near 12,000 rpm were achieved.

Certainly much higher rotation speed can be achieved with a larger prototype, made with more rigid and precise elements and more advanced materials, being driven by a more powerful engine controlled by a more advanced digital / electronic system. Obtaining speeds closer to those required for the DCMS (96,000 rpm) requires more studies not only on the bearings but on the whole DCMS assembly. Attaining greater rotation speed the studies carried out in the larger work become more relevant: design of the rotor to resist centrifugal forces, rotor dynamics, structure design and others.

REFERENCES

1. Andrade, L. A. Desenvolvimento de Osciladores em 10 GHZ de Ultrabaixo Ruído de Fase e Análise de seus desempenhos nos Transdutores Paramétricos do Detector de Ondas Gravitacionais Mário Schenberg. Sao Jose dos Campos: PhD Thesis – INPE, 2006.
2. Borisavljevic, A. Limits, Modeling and Design of High-Speed Permanent Magnet Machines. Delft: PhD Thesis Technical University of Delft, 2011.
3. Choi, W.; Li, S.; Sarlioglu, B. Core Loss Estimation of High Speed Electric Ma-

chines: An Assessment. Wisconsin Electric Machines and Power Electronics Consortium (WEMPEC), Madison, 2015.
4. Earnshaw, S. On the nature of the molecular forces which regulate the constitution of lumiferous ether. Trans. Camb. Phil. Soc, p. 97-112, jul. 1842.
5. Fernandes, P.; Frajuca, C.; Horikawa, O. Diretrizes para o projeto do dispositivo para calibração do detector Mario Schenberg. Sao Paulo: Máster dissertation - IFSP, 2015.
6. Halminen, O. Et Al. Active magnetic bearing-supported rotor with misaligned cageless backup bearings: A dropdown event simulation model. Mechanical Systems and Signal Processing, v. 50-51, p. 692–705, 2015.
7. Kärkkäinen, A. Dynamic Simulations of Rotors During Drop on Retainer Bearings. Lappeenranta: PhD Thesis Lappeenranta University of Technology, 2007.
8. Li, P.; Sahinkaya, M. N.; Keogh, P. S. Active Recovery Of Contact-Free Levitation In Magnetic Bearingsystems. Proceedings of the ASME 2012 International Design Engineering Technical Conferences & Computers and Information in Engineering Conferences & Computers and Information in Engineering Conference IDETC/CIE, Chicago, 12-15 Ago. 2012.
9. Nishimura, M.; Suzuki, M. Solid-lubricated ball bearings for use in a vacuum — state-of-the-art. Tribology International, v. 32, n. 11, p. 637–647, Nov. 1999.
10. Padovani, D. M. Desenvolvimento de um experimento para medir a velocidade da interação gravitacional. Sao Paulo: Máster disseration, 2012.
11. Pavani, R. A.; Horikawa, O. Compact Magnetic and Sliding Hybrid Bearing for Low Axial Load Applications. 22nd International Conference on Magnetically Levitated Systems and Linear Drives (MagLev 2014), Rio de Janeiro, v. 1, set. 2014.
12. Pereira, J. C. Introdução à Dinâmica de Rotores. 1. ed. Florianópolis: Universidade Federal de Santa Catarina , v. 1, 2005. ISBN APOSTILA - Introdução a Dinamica de Rotores Prof. José Carlos Pereira Florianópolis, janeiro de 2005 Universidade Federal de Santa Catarina Departamento de Engenharia Mecânica Grupo de Análise e Projeto Mecânico.
13. Ruiz, W. Experimento Para Medir A Velocidade Da Interação Gravitacional Utilizando Um Motor De Relutância Variável. Sao Paulo: Master dissestation, IFSP, 2014.
14. Santos, K. A. M. D. Protótipo de Experimento para medir velocidade de interação gravitacional. Sao Paulo: Master dissertation - IFSP, 2013.
15. Watson, J. The Control of High-Speed Machines. Computing and Control Engineering Journal, Burgess Hill, Dez. 1999. 245.
16. Whitley, S. Review of the gas centrifuge until 1962. Part II: Principles of high-speed rotation. Rev. Mod. Phys, Chester, v.56, n. 1, p. 67-97, Jan. 1984.
17. Yonnet, J. P. Passive magnetic bearings with permanent magnets. IEEE Transactions On Magnetics, Saint Martin D´Heres, V. Mag-14, n. 5, p. 803-805, set. 1978.

Corresponding author:
Carlos Frajuca, Ph.D., Department of Mechanical Engineering, Sao Paulo Federal Institute, Rua Pedro Vicente 625, Sao Paulo, SP, 01109010, Brazil, phone: +55 11987229644, e-mail: frajuca@gmail.com

HYDROSTATIC DRIVER FOR TOOL CARRIES MT8

Tomáš GAJDOŠÍK[1], Mária TOMÁŠIKOVÁ[2]

[1]*Department of Mechanical Engineering, University of Žilina, tomas.gajdosik@fstroj.uniza.sk*
[2]*Department of Mechanical Engineering, University of Žilina, maria.tomasikova@fstroj.uniza.sk*

Abstract
The article introduces the tool carrier and justifies the need to solve its drive by a hydrostatic transmission. Subsequently, a block diagram for the hydrostatic transmission and its control is described in the paper. The article describes the components for hydrostatic transmission which are supplemented by charts of calculated operating characteristics of the hydro generator and the hydraulic motors. In conclusion, the article deals with the calculation of the traction force characteristics on the machine wheels and the calculation of gear ratios and hydrostatic transmission ratios.

Key words: *Hydrostatic transmission, traction force, hydro motor, hydro generator*

INTRODUCTION

Tool carriers are mobile machines which are developed for work mostly in sloping mountain and underground terrain. They can work in slopes up to 40 degrees. They are mainly driven by diesel engines. These machines have a wide track and a position of center of gravity is not too high for better stability on the slopes. Their advantage is the possibility of aggregating of various devices from grasses to low or high grasslands, through pickers and manipulators to sweepers and tanks. Attachments are attached to the front or rear by a three-point hinge and they can be driven by an output shaft.

The reason for the new concept of the drive is to replace the components of the mechanical drive and we will achieve the increase in the moral value, the competitiveness of the product and increasing of the machine variability.
The basic requirements were 35 degrees slope accessibility, two driving modes - road / work, 4x4 switchable 4x2, maximum speed 25 km / h, working 12 km / h and use of hinged hydraulic motors in particular. (Hrček S. & Bucala J., 2014)

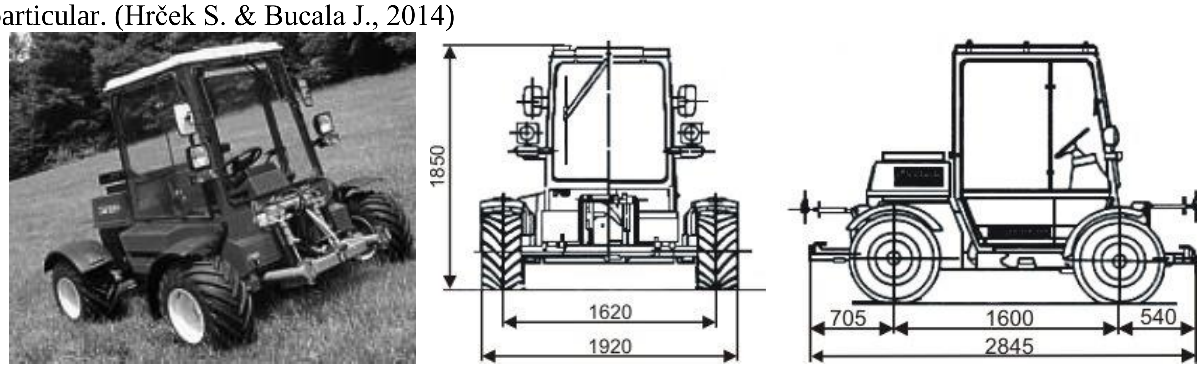

Fig. 1 Tool carries MT 8-222 and its basic dimensions

MATERIALS AND METHODS

Block scheme of hydrostatic drive with control

The Fig. 2 shows block diagram which was prepared from the requirements. All basic mechanical, hydraulic and electronic components of the hydrostatic drive of the wheels and their steering and their interrelationships are shown in this scheme. (Kohár R., Brumerčík F., Lukáč M. & Nieoczym A., 2016)
The black continuous line shows the power line of the hydrostatic transmission. The black interrupted line shows hydrostatic overflow line. The blue continuous line is the control circuit. The blue interrupted line is the overhead line of the control circuit and the green continuous line is electric wiring, which connects control and actuator components of the drive. (Kohár R., 2016), (Lukáč M., Brumerčík F. & Krzywonos L., 2016)

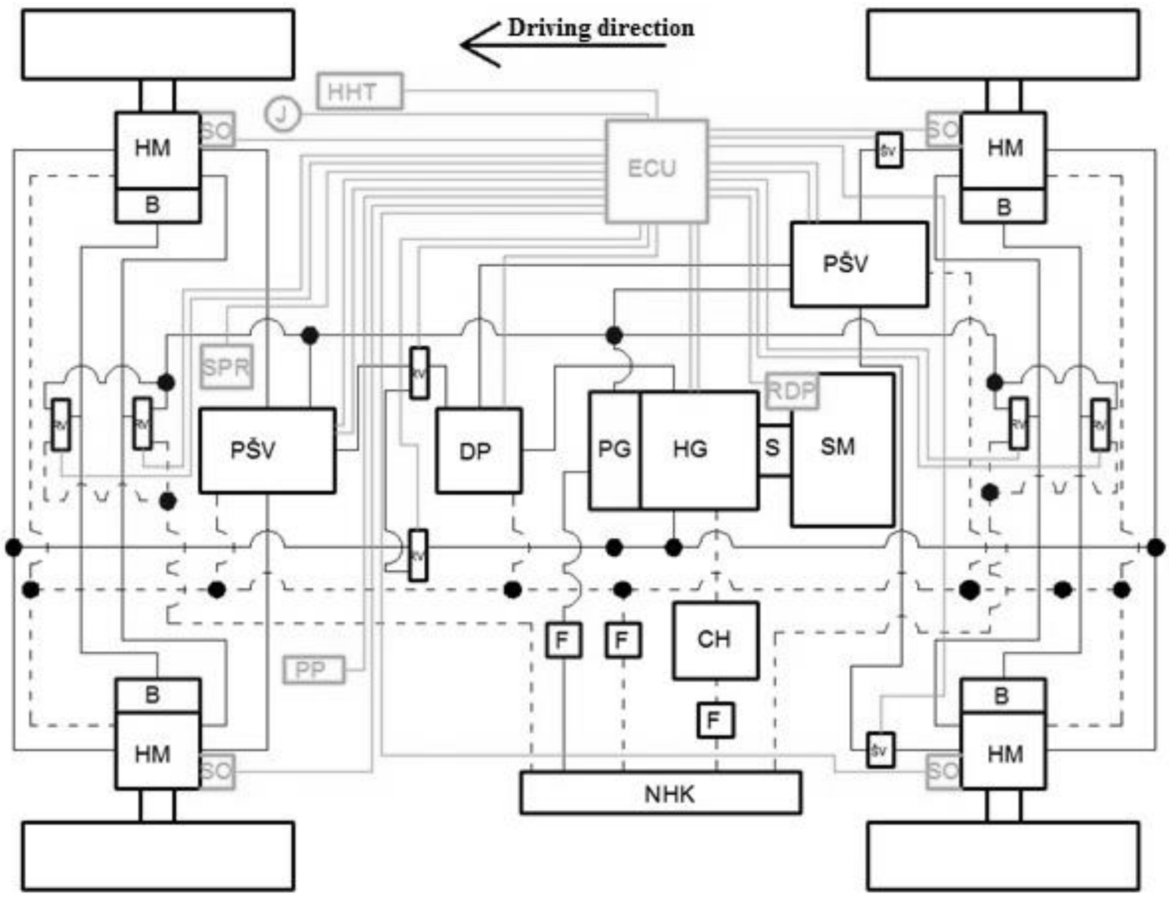

Fig. 2 Block diagram of the hydrostatic drive of the drive wheels with electronic control.

Tab. 1 Explanation of parts, which are used in block scheme

Hydraulic parts		**Mechanical parts**		**Electric parts**	
DP	Flow divider	B	Brake	ECU	Electronic control unit
F	Filter	S	Clutch	HHT	Control terminal
HG	Hydro generator	SM	Engine	J	Joystick
HM	Hydro motor			PP	Acceleration / deceleration pedal
CH	Cooler			RDP	Fuel Dosing Controller of SM
NHK	Hydraulic fluid reservoir			SO	Speed sensor
PŠV	Proportional throttle valve			SPR	Steering position sensor
RV	Control valve				
ŠV	Throttle valve				
PG	Additional hydro generator				

Components and projective parameters of hydrostatic transmission

The power unit is straight-three engine with 1649 cm^3 displacement with maximum power P = 25.4 kW at 3000 rpm and a maximum torque of 94 Nm at 1700 rpm. Tires size- 31x15,5-15 have a static radius 350 mm and the effective circumference 2235 mm. The calculation of the tractive force of the machine at its maximum required weight of 2000 kg, depending on the coefficient of engagement μ on the different surface types, was made before the design of the hydrostatic transmission. (Tropp M., Lukáč M., Nieoczym A. & Brumerčík F.,2016)

The maximum of tractive force of machine is calculated by equation 1:

$$F_{T1max} = m_{max}.g.\mu = 2000.9{,}81.0{,}9 = 17658\ (N) \qquad (1)$$

Subsequently, calculations of rolling resistance, climbing and total loss force at the 35 degrees climbing angle and various types of fieldwork were also done. The maximum traction force required was 17700 N which is based on these calculations. (Kučera Ľ. & Gajdošík T., 2014)
The calculation of the corner power of hydro generator for driving mode – work (2) and driving mode-road (3) was performed in the 4x4 drive was performed from the required tractive force.

$$P_{R1} = \frac{F_{T1max} \cdot v_{1max}}{3600} = \frac{17700.12}{3600} = 59\ (kW) \tag{2}$$

$$P_{R2} = \frac{F_{T2max} \cdot v_{2max}}{3600} = \frac{8500.25}{3600} = 59{,}027\ (kW) \tag{3}$$

The total transmission range with hydrostatic transmission efficiency $\eta_{HSP} = 0{,}85$ will be:

$$R_P = \frac{P_{R1}}{P_{SMmax} \cdot \eta_{HSP}} = \frac{59}{25{,}4.0{,}85} = 2{,}732 \tag{4}$$

On the basis of the corner power calculation, an axial piston axial piston hydro generator was selected and used with a maximum displacement volume of 40 cm3 / rev, a theoretical flow of 144 l / min at 3600 rpm, a theoretical output of 76.8 kW at a pressure difference of 32 MPa, a torque of 63,7 Nm at a pressure difference of 10 MPa. The minimum system pressure is 1.5 MPa and the maximum working pressure is 35 MPa. (Kučera Ľ., Gajdošík T. & Bucala J., 2014)
From the known values of the hydro generator and the combustion engine was made a graph of the hydro generator power which is dependent on the torque of the combustion engine and the angle of the inclined plate of the hydro generator (Fig. 3) and then the graph of the complete characteristic of the hydro generator (Fig.4) was made also.

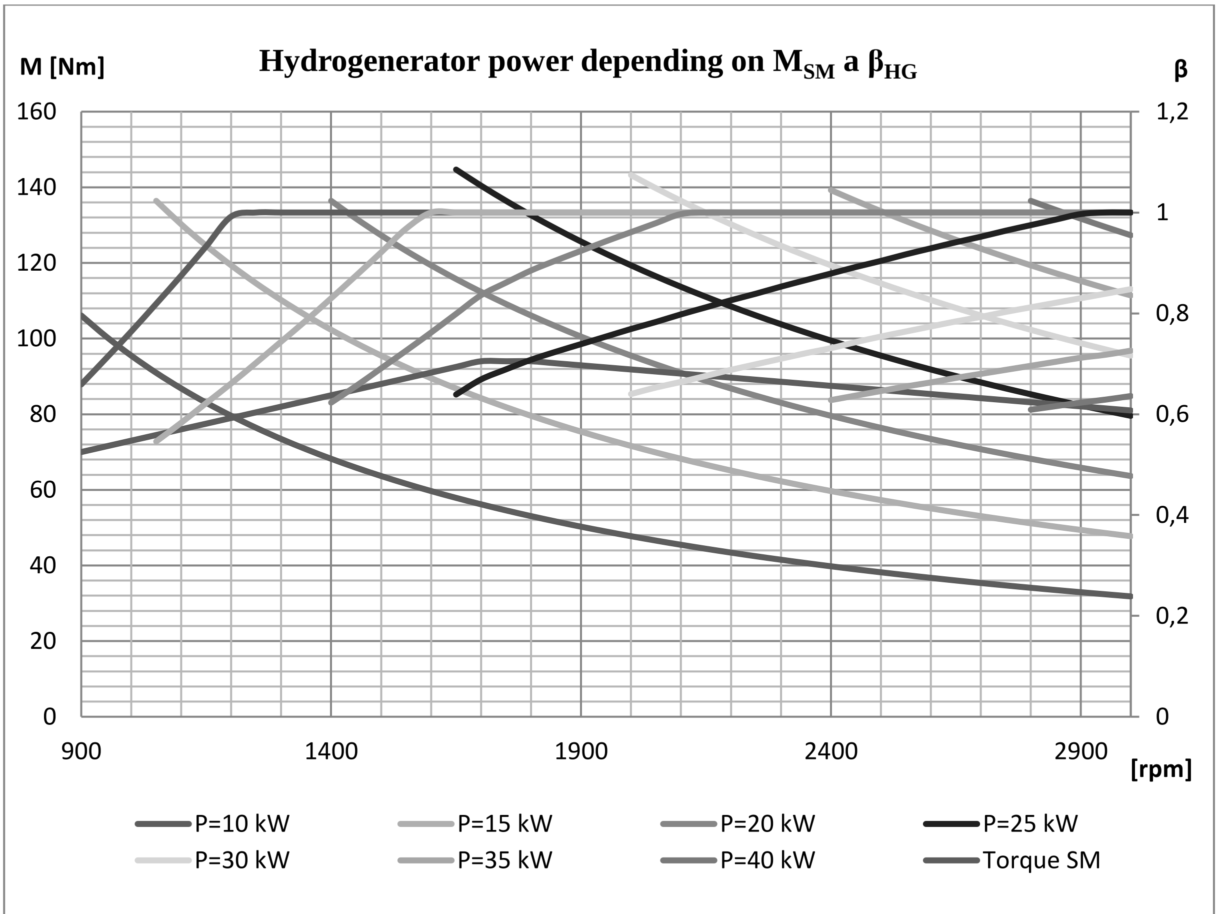

Fig. 3 Hydrogenerator power is depending on M_{SM} a β_{HG}

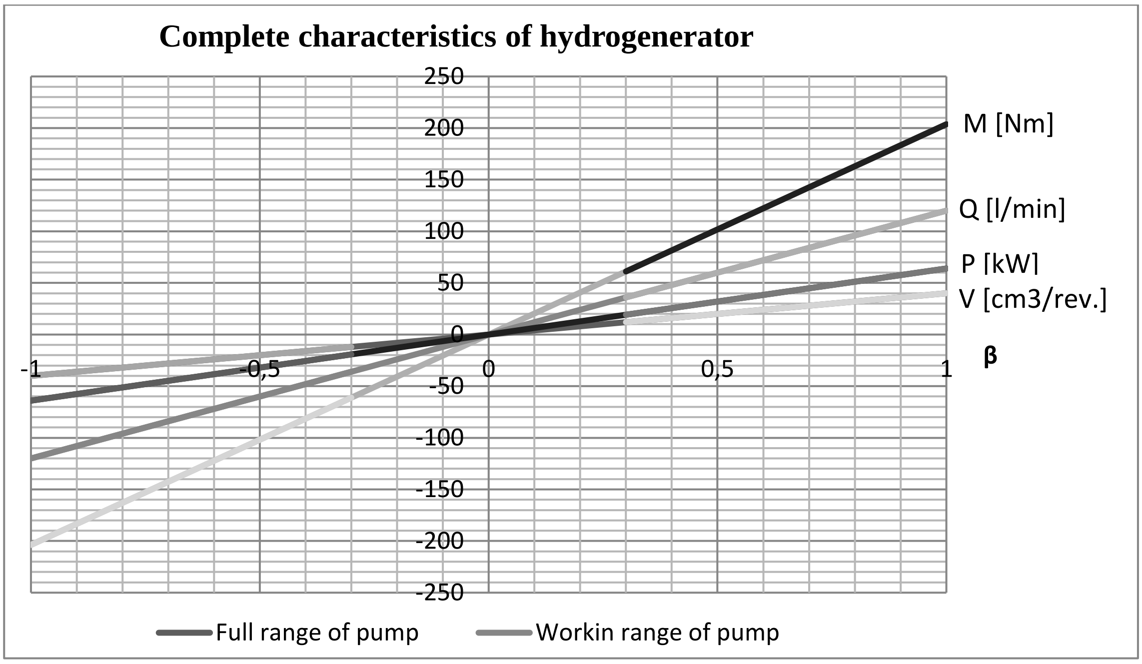

Fig. 4 Complete characteristic of hydro generator

The 2-displacement motors with brake and with placement in swivel joints were used as steerable wheel motors. The displacement is 322/166 cm^3/rev., maximum power is 22 kW, maximum speed id 250/275 rpm and maximum pressure is 40 MPa. The graphs in FIG. 5 and 6 show the dependence of the torque of the hydraulic motor on speed. From the graphs it is also possible to calculate the flow rate at the given speed and the given slope of the inclined plate of the hydro generator and the corresponding pressure in the system.

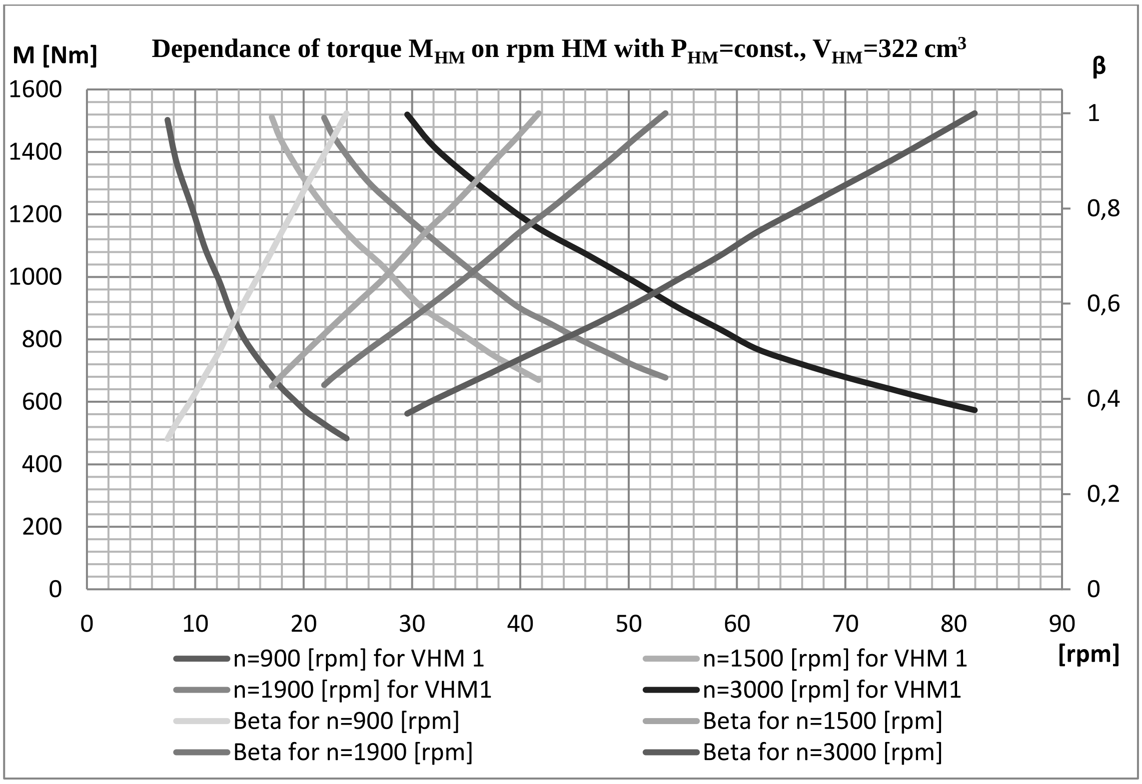

Fig. 5 Dependence of torque M_{HM} on rpm with power= constant, displacement= 322 cm^3

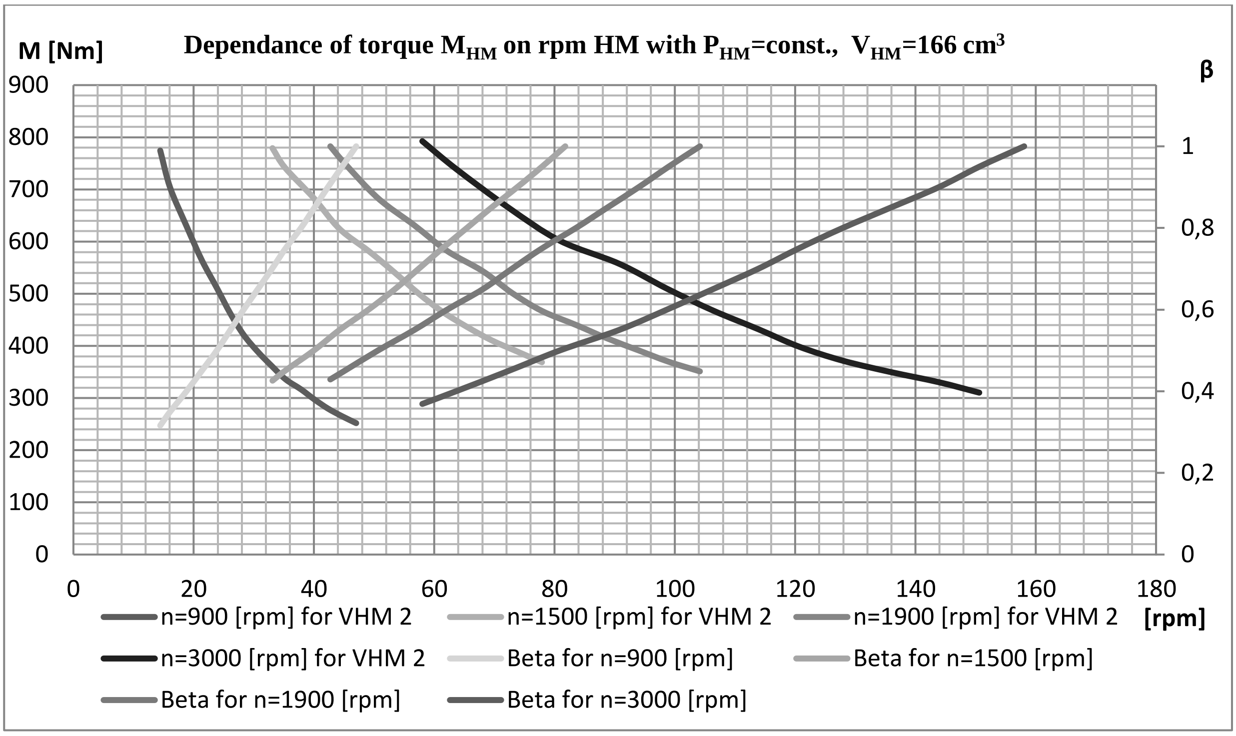

Fig. 6 Dependence of M_{HM} torque on rpm with power= constant, displacement= 166 cm^3

RESULTS AND DISCUSSION

Tractive force characteristics

In this part of paper is description of calculation of traction parameters for driving mode- work, especifically for the A1 point in graph (Fig. 7). (Kučera Ľ. & Gajdošík T., 2013)

- The calculation of the minimum value of regulatory parameter- β_{HGmin} of hydro generator at the maximum possible speeds (n_{HGmax}=3000 rpm and torque M_{sm}=81 Nm) :

$$\beta_{HG} = \frac{M_{SM}.20.\pi.\eta_{mech.HG3000}}{\Delta p.V_{HGmax}} = \frac{81.20.\pi.0{,}927}{320.40} = 0{,}369 \tag{5}$$

- The calculation of displacement of the hydro generator at the maximum engine speed.

$$Q_{HGmaxA3000} = \frac{V_{HGmax}\cdot\beta_{HGmin}\cdot n_{HG}\cdot\eta_{QHG3000}}{1000} = \frac{40.0{,}369.3000.0{,}927}{1000} = 41{,}063\ (l/min) \tag{6}$$

- Displacement from the hydro generator is divided between four hydro motors. The calculation of hydraulic motor speed at the maximum hydro generator speed and also the first working displacement of the hydraulic motor (V_{HM}=0,322 l/rev.) :

$$n_{HM2maxA23000} = \frac{Q_{HMmaxA3000}\cdot\eta_{QHM3000}}{V_{HM2max}} = \frac{10{,}265.0{,}927}{0{,}322} = 29{,}565\ (ot/min) \tag{7}$$

- The calculation of machine speed at the direct ride on plane:

$$v_{1maxA13000} = \frac{RC.n_{HM1maxA13000}\cdot 60}{1000} = \frac{2{,}253.29{,}565.60}{1000} = 3{,}996\ (km/h) \tag{8}$$

- The calculation of torque and tractive force at the one wheel:

$$M_{HM1maxA13000} = \frac{\Delta p.V_{HM1max}\cdot\eta_{mech.HMV13000}}{20.\pi} = \frac{320.322.0{,}927}{20.\pi} = 1519{,}682\ (Nm) \tag{9}$$

$$F_{T1maxA13000} = \frac{M_{HM1maxA13000}}{SR} = \frac{1519{,}682}{0{,}35} = 4341{,}951\ (N) \tag{10}$$

- The calculation of total tractive force:

$$F_{T\_total} = 4.F_{T1maxA13000} = 4.4341{,}951 = 17367{,}804\ (N)$$

All the working points of the diagrams in Fig. 7 and Fig. 8 were calculated by the same process.

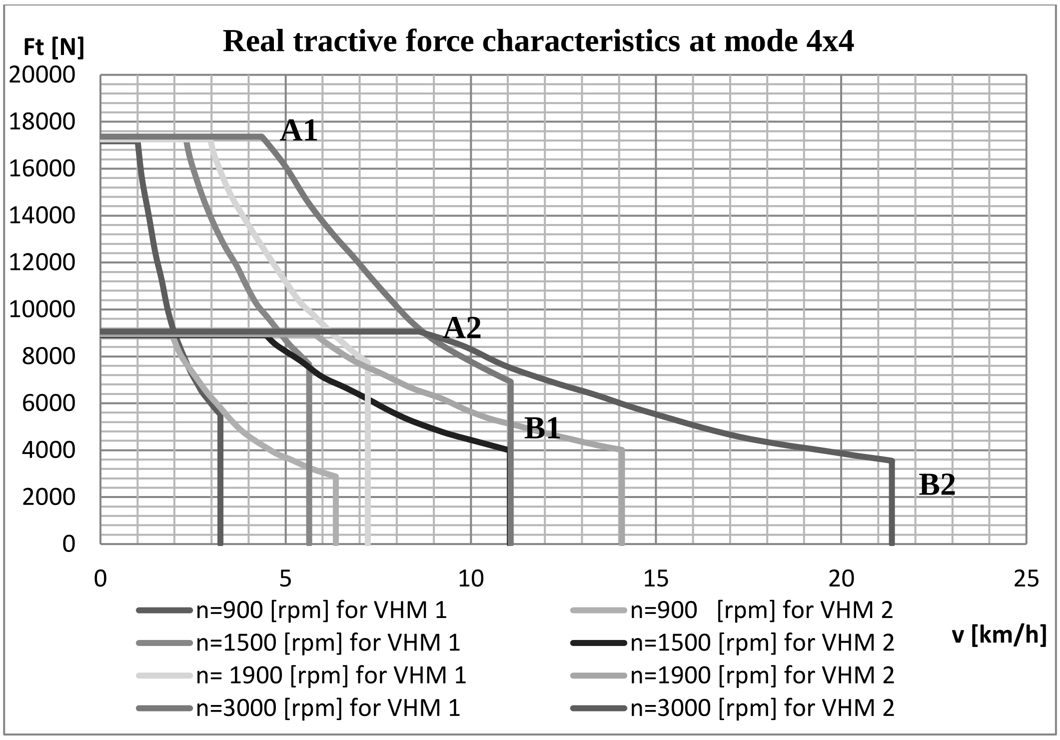

Fig. 7 Real tractive force characteristics at mode- 4x4

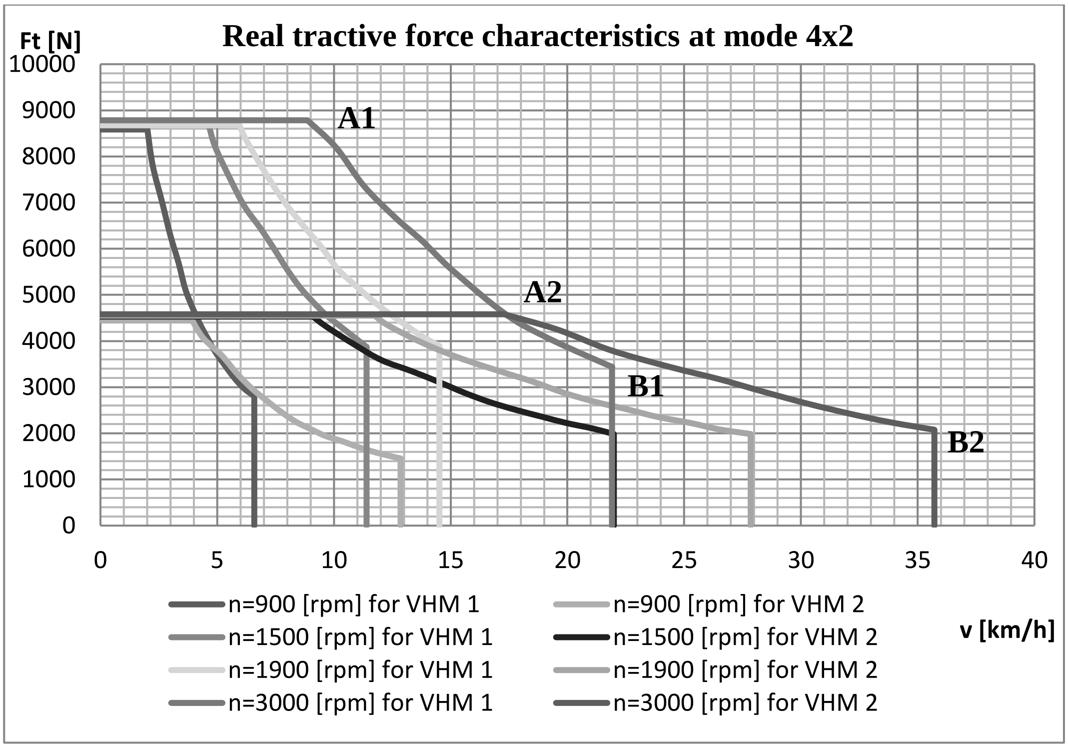

Fig. 8 Real tractive force characteristics at mode- 4x2

Transmission ratios:

- The calculations of the maximum and minimum kinematic ratio at the first displacement of the hydraulic motor (V_{HM1}):

$$i_{h1max} = \frac{4.V_{HM1max}}{V_{HGmax} \cdot \beta_{HGmin} \cdot \eta_{QHM} \cdot \eta_{QHG}} = \frac{4.0{,}322}{0{,}04.0{,}369.0{,}927.0{,}927} = 101{,}547 \quad (11)$$

$$i_{h1min} = \frac{4.V_{HM1max}}{V_{HGmax} \cdot \beta_{HGmax} \cdot \eta_{QHM82} \cdot \eta_{QHG3000}} = \frac{4.0{,}322}{0{,}04.1.0{,}953.0{,}921} = 36{,}686 \quad (12)$$

- The kinematic range of the transmission system at the first working displacement of the hydraulic motor is:

$$R_{K1} = \frac{i_{h1max}}{i_{h1min}} = \frac{101{,}547}{36{,}686} = 2{,}768 \quad (13)$$

- The calculation of maximum and minimum torque ratios for the first working displacement of the hydraulic motor:

$$\bar{\iota}_{h1max} = \frac{4.V_{HM1max} \cdot \eta_{mech.HM29} \cdot \eta_{mech.HG3000}}{\beta_{HGmin} \cdot V_{HGmax}} = \frac{4.0{,}322.0{,}927.0{,}927}{0{,}369.0{,}04} = 74{,}987 \quad (14)$$

$$\bar{\iota}_{h1min} = \frac{4.V_{HM1max} \cdot \eta_{mech.HM82} \cdot \eta_{mech.HG3000}}{\beta_{HGmax} \cdot V_{HGmax}} = \frac{4.0{,}322.0{,}953.0{,}921}{1.0{,}04} = 28{,}262 \quad (15)$$

- The calculation of torque gear range:

$$R_{M1} = \frac{\bar{\iota}_{h1max}}{\bar{\iota}_{h1min}} = \frac{74{,}987}{28{,}262} = 2{,}653 \quad (16)$$

The same process was used to calculate the maximum and minimum kinematic and torque transmission ratio of the drive with the second working displacement of the hydraulic motors.

Hydrostatic drive control system

The control system provides complete control over wheel speed control and forward / reverse steering. It provides the option of selecting driving modes via the hand-held terminal in the operator's cab. The machine operator selects only the type of driving mode, the travel direction (forward / reverse) and the driving speed using the accelerator pedal. Speed sensors are built into hydraulic motors measure the speed of rotation of each driven wheel, continuously. The control unit compares these speeds and reduces the flow to this wheel (via the control valve) if it is necessary (increasing the speed of one-wheel relative to others - slipping) until the wheel speed is again balanced. The system also checks the position of the sloping HG plate and controls the fuel dose for engine which is depending on the load. (Tomášiková M., Tropp M., Krzysiak Z. & Brumerčík F., 2015)

CONCLUSIONS

The article describes the design calculation of a hydrostatic drive for a special working machine working on slopes. The article also describes the selection of the basic components of the hydrostatic drive. After designing the components of the hydrostatic drive are made a few process: process for calculating of the drive parameters and also the process of calculating the machine stroke parameters which is projected into graphs. The final calculation of kinematic and torque transmission ratios and ranges is described at the end of the article. The benefits of this are the unconventional solution of the wheel drive system, the removal of the morally obsolete mechanical wheel drive, the increase in the possibility of variability, arrangement and axle concepts.

ACKNOWLEDGMENT

This study was supported by Slovak Research and Development Agency under the contract no. APVV-14-0508 – Development of new methods for the design of special large-size slewing rings.

REFERENCES

1. Hrček S. & Bucala J.: Thermal simulations of Plasmabit electronic system protective housings. In: Modern methods of construction design. - Cham: Springer, 2014. - ISBN 978-3-319-05202-1. - S. 71-76.
2. Kohár R., Brumerčík F., Lukáč M. & Nieoczym A.: Numerical analysis of roller bearing. In: Applied computer science. - ISSN 1895-3735. - Vol. 12, no. 1 (2016), s. 5-16.
3. Kohár R.: Úvod do štrukturálnej optimalizácie. In: Wspomagane komputerovo modelowanie, analiza i projektowanie elementów maszyn i mechanizmów. - Lublin: Politechnika Lubelska, 2015. - ISBN 978-83-7947-135-5. - S. 95-103.
4. Lukáč M., Brumerčík F. & Krzywonos L.: Driveability simulation of vehicle with variant tire properties. In: Communications : scientific letters of the University of Žilina. - ISSN 1335-4205. - Vol. 18, no. 2 (2016), s. 34-37.
5. Tropp M., Lukáč M., Nieoczym A. & Brumerčík F.: Hydraulic circuits in transport and mechatronic systems. In: Logi : scientific journal on transport and logistics. - ISSN 1804-3216. - Vol. 7, no. 1 (2016), s. 143-149.
6. Kučera Ľ. & Gajdošík T.: The vibrodiagnostic of gear. In: Modern methods of construction design. Cham: Springer, 2014. - ISBN 978-3-319-05202-1. – S. 113-118
7. Kučera Ľ., Gajdošík T. & Bucala J.: The vibrodiagnostic of demaged gears of planetary gearboxes. In: Communications: scientific letters of the University of Žilina, 2014. – ISSN 1335-4205. – Vol.16, no. 3A, s. 67-73
8. Kučera Ľ. & Gajdošík T.: The vibrodiagnostic of gears. In: 54th International conference of machine design departments: book of proceedings 10th – 12th September, 2013. - ISBN 978-80-7372-986-8. –S 93-98
9. Tomášiková M., Tropp M., Krzysiak Z. & Brumerčík F.: Suspension of transport equipment. In: Logi : scientific journal on transport and logistics. - ISSN 1804-3216. - Vol. 6, no. 2 (2015), s. 48-55.

Corresponding author:
Ing. Tomáš Gajdošík, Ph.D., University of Žilina, Univerzitná 1, Žilina, Slovakia, 010 26, tomas.gajdosik@fstroj.uniza.sk

ENERGY EFFICIENCY OF OFFSHORE SUPPORT VESSEL

Bartosz GŁOWACKI[1], Cezary BEHRENDT[2]

[1] G-DESIGN, ul.Wrzosowa 9b, 72-123 Pucice, Poland
[2] Institute of Marine Propulsion Plants Operations, Faculty of Marine Engineering, Maritime University of Szczecin, Poland

Abstract
The paper presents the identified problems related to the development of energy efficiency assessment methodology for support vessels in terms of oil rigs. Based on the operational data, collected at an Anchor Handling Tug Supply vessel, such an assessment has been carried out. The function (technical support for oil rigs) of the vessel has also been taken into consideration. In order to assess the energy efficiency, the Energy Efficiency Operational Indicator has been applied. This indicator was developed and implemented by the International Maritime Organization, but the authors have adjusted it to the characteristic and the specification of the analyzed vessel. This is the first elaboration regarding Offshore Support Vessels which include Anchor Handling Tug Supply vessel.

Key words: *offshore support vessel, energy efficiency, energy efficiency indicator*

Introduction

The offshore support vessels market is subject to dynamic changes and the volume of new orders for the construction of new vessels is dependent on the oil prices [http://www.portalmorski.pl].
It also affects the employment rate for offshore supply vessels which is correlated with the cost of services provided by them. The forecast increase of orders in the period of 2005-2020 for new vessels and offshore supply vessels started to fluctuate, and the number of orders for the services has dropped [http://www.dbs.com.sg]. The employment rate of OSV (Offshore Support Vessel) in 2016 is presented in Table 1. In the case of division of the OSVs into PSV (Platform Supply Vessel) and AHTS (Anchor Handling Tug Supply Vessel), their use depends on their dimensions.

Tab. 1 Employment rate for OSV operating at the North Sea in 2016 [10]

OSV type	Employment rate %
PSV (medium)	71
PSV (large)	80
AHTS (medium)	29
AHTS (large)	55

The Employment of the vessels and the number of orders for services provided by the OSVs will be consequently related to the prices of the offered services and obtainable technical options. The prices are affected mainly by fuel cost which equals to 50-80% of vessel total operational and maintenance costs. Therefore, only companies and vessels that manage the energy efficiently will survive on the market. The improvement of the energy efficiency should affect not only the service price but mainly should minimize the negative impact on the environment caused by the fuel combustion process. This matter has been raised by the IMO (International Maritime Organization) since a very long period and the following resolutions enforce the implementation of the SEEMP (Ship Energy Efficiency Management Plan) at ships. The analysis presented below is aimed at the assessment of the energy efficiency of a selected AHTS vessel during its operation. The analysis has been based on the operational data, measured and collected at the vessel. The authors have applied also the indicator implemented by the IMO, namely the EEOI, which is used to specify the energy efficiency for ships. It is also applied during drawing up the SEEMP.

MATERIALS AND METHODS

The vessel selected for the purpose of the analysis is the *Kingdom of Fife*. This vessel is classified as AHTS vessel. This type of vessel is a variant of PSV vessel that has been modified. Among the most significant changes one may find:

- Increased power of the main engine;
- Assembly of a dynamic positioning system;
- Assembly of lifts and auxiliary winches;
- Assembly of a high-pull anchor and towing winch.

Due to the structural changes made, from typical supply vessel (PSV), a versatile vessel was constructed (ATHS). It offers both transport and supply services and is capable of the buoy and anchor handling, general assistance duties and towing (also for Royal Navy [http://www.maritimejournal.]).
The technical and operational data of the vessel in question is presented in Table 2 [http://www.briggsmarine.com]

Tab.2 Technical and operational data for AHTS – the *Kingdom of Fife*

Parameter	Value
Type	AHTS
Year Built	2008
Length Overall	61,20 m
Breadth	13,50 m
Max. draft	4,75
Deadweight	1266 BRT
F.W. Capacity	246 m^3
Speed	13,7
Main Engine Type	2 x Caterpillar C286-6
Generators	2x438 KVA
Thrusters	Caterpillar 392 kW
Output	2 x 2030 kW
Fuel	MDO F76
Fuel Conversion Ratio	3,5
Fuel Consumption per Day	12 t
Max Speed	13,7 kts

The *Kingdom of Fife*, presented in Figure 1, is not equipped with a software to monitor energy efficiency. It is understandable since the regulations imposing on shipowners the obligation to apply energy efficiency monitoring systems came into force in 2013. Whereas, the vessel was constructed in 2008. Therefore, it was not covered by the IMO requirements. The lack of an opportunity to evaluate the current vessel energy efficiency has prompted the authors to address the problem. The efficiency has been assessed on the grounds of the data being collected for 28 days (this is a period of working time of one crew). The operational data was collected every day at midday and at the start and the end of maneuvers and operational tasks (loading, buoy handling, navigation without load) performed by the vessel.

Fig. 1 AHTS vessel – Kindom of Fife at operation at the North Sea (*photo Briggs Marine)*

The engine room is modern and fully automated. It is supervised by two engineer. The vessel is serviced by external companies but day-to-day failures are repaired by the officers upon the prior agreement with the shipowner. The engine room is presented in Figure 2.


Fig. 2 Engine room of the *Kingdom of Fife* (*photo Briggs Marine*)

For the purpose of the operational effectiveness assessment of the AHTS vessel, the EEOI has been applied. It has been modified and adjusted in order to make such an assessment of the vessel when a specific operational task was being performed, not for the entire voyage *[Głowacki, B., Behrendt, C., 2015]*.
The EEOI calculation method for a current operation, taking into consideration the current energy load and freight being onboard, is presented by formula 1:

$$EEOI = \frac{FC_i C_F}{m\ D} \qquad [tCO_2/tNm] \tag{1}$$

where:
FC_i – mass of fuel consumed by main and auxiliary engines during a single task performance[t],
C_F - conversion rate expressed as a relation of CO_2 mass generated during used fuel combustion process [t_{CO2} / t_{fuel}],
m – mass of freight onboard [t],
D – distance expressed in nautical miles that the vessel travelled during the performance of a specific task [Nm – nautical mile].
As it may be noted, formula 1 relates also the amount of consumed fuel with the amount of CO_2 emitted to the atmosphere.

RESULTS AND DISCUSSION

The energy efficiency has been determined using the test results of consumed fuel and the work time of main engines and the auxiliary engines. The main engines generally work when the vessel navigate without load and performs operational tasks (loading and unloading supplies, buoy and anchor handling and towing, etc.). Since the main hydraulic pumps are suspended on the main engines, it has been noted that the main engines were working for 2-4 hours during unloading process in a port. It is related to the employment of the hydraulic deck cranes and their higher demand for power. The data included in Table 3 refers to the work time of the internal-combustion engines assembled at the vessel. The data has been collected based on the entries in the engine room log book. The internal-combustion engines at the vessel are the only devices fed with marine fuel. The *Kingdom of Fife* is not equipped with an oil-fired boiler and every heating process for the purpose of social heating (heating of cabins, water) and technical heating (warming the engines and tanks) is performed by electric heat exchangers.

Tab. 3 Work of main engines and power generators in the analyzed period

Engine	Use
Period of monitoring	28 days
Number of monitoring hours	672 h
Main engine No. 1 work time (ME 1)	295 h
Main engine No. 2 work time (ME 2)	297 h
Power use rate for main engine No. 1 (ME 1)	44%
Power use rate for main engine No. 2 (ME 2)	44%
Power use rate for diesel generators No. 1 and No. 2 (DG1 i DG2)	(63%) (37%)
Bow Thruster work time (BT)	97 h

Based on the data in Table 3, Figure 3 has been drawn up. It shows the main engine work hours on individual days during the vessel operation. When analyzing Figure 3, it may be noted that the main engines are in operation for 24 hours per day only when the vessel is on the move to a specific port or activity area. During buoy and anchor handling etc. the main engines are operated the most frequently for 8-12 hours. Between 5 p.m. and 6 p.m., when the vessel is at the destination, the main engines are not in the operation and the vessel does not carry out any tasks. This is proven by the data in the engine room log book. At that time, the crew prepares the vessel to the next assignment and inspects the technical condition of the marine devices and machines. Certain small repairs and service works are also performed. The 9-10 hour periods, presented in Figure 3, of the main engines work refer to the activities carried out at the destination point consisting in deployment and picking up the navigation buoys.

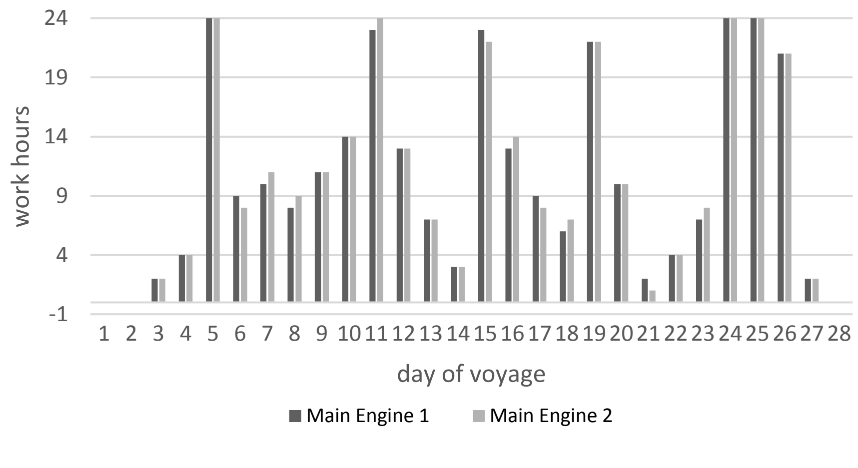

Fig. 3 Work hours of main engines during operational tasks

The energy efficiency assessment of an AHTS vessel using the EEOI is not very reliable since the distance travelled by the vessel during a buoy deployment or an anchor weighting is minimal. This affects negatively the EEOI value as the value depends on the travelled distance. The energy efficiency assessment by the EEOI for individual tasks completed by the vessel is possible only for towing a buoy or an anchor under the condition that the distance travelled is measurable. The data collected during these activities may be compared to the historical data at similar water areas. One should strive to obtain the least value of the EEOI. The comparison of the historical values with the present ones shall enable the vessel energy efficiency to be assessed.
The data in Table 4, regarding the fuel consumption of the vessel in question, has been developed on the grounds of the entries in the engine room log book and navigation data (time, distance travelled). The freight transported by the vessel during the 28 days equaled to 20 tones, which is not a significant value when compared to the amount of fuel (350 tones). For the purpose of the EEOI calculation for particular operational tasks, the mass of fuel and freight onboard have been assumed as the transported cargo mass.

Tab. 4 Fuel consumption of the *Kingdom of Fife* during operational tasks

Task	Working device	Fuel consumption t/h
Stay at port	DG1 or DG2	0,0279
Loading at port	DG1 or DG2	0,0355
Navigation without load	ME1, ME2, DG1,	0,281
Buoy deployment	ME1, ME2, DG1, BT	0,194

ME1- Main Engine No1, ME2- Main Engine No2, DG1 – Diesel Generator No1, DG2 – Diesel Generator No2, BT – Bow Thruster

Table 5 presents the data specifying the voyage stages and operational tasks performed by the vessel and the EEOI values calculated using formula 1.

Tab. 5 Operational data of the *Kingdom of Fife* during operational tasks

Task	Duration	Fuel consumption	Cargo mass	Distance	EEOI
	h	t	t	Nm	tCO_2/tMm
Stay at port	48	1,352	167,31	0	Not determined
Loading at port	8	0,284	312,71	0	Not determined
Buoy deployment	9	1,704	310,59	0	Not determined
Navigation without load No 1	29,5	8,298	311,863	300	$0{,}31 * 10^{-3}$
Navigation without load No 2	36	11,35	295,05	343	$0{,}377 * 10^{-3}$
Navigation without load No 3	91	19,28	252,12	650	$0{,}378 * 10^{-3}$

As per the analysis, the energy efficiency assessment of an AHTS vessel by the EEOI, recommended by the IMO, is problematic to be carried out during the most of operational tasks. In order to apply formula 1, it is necessary to hold an information on the distance travelled by a vessel. This information is unmeasurable during the operation of the dynamic positioning system and buoy and anchor handling (weighting and dropping) when engines (main and auxiliary) are heavily loaded. The EEOI for the ATHS vessel may be determined for such tasks as navigation without load and transport of buoys and anchors. The analysis included in the paper and identified problem should enable further development of the works related to drawing up the SEEMP for this type of vessels. The previous guidelines and analyses regarding the energy efficiency of vessels and ships [*PRS Nr 103/P, 2016, MEPC.1/circ.684 2010, MEPC. 203(62) 9, 2011*] have not referred to this type of vessels. The authors are experienced in assessing the energy efficiency for special vessels [Głowacki, B., Behrendt, C. 2015], which should enable further research to be carried out. Effective energy management of AHTS vessels, in relation to the large number of them being in operation [*Herdzik, J. 2012*], will contribute to the limitation of the harmful exhaust gas emission to the atmosphere and to the reduction of the maintenance costs and prices for services provided.

CONCLUSIONS

The matter of the EEOI determination and the SEEMP development for vessels is currently leading in the shipbuilding industry. It is related both to the desire to the reduction of fuel consumption and the mitigation and minimization of the threats to the environment resulting from the vessels operation.
As the analysis showed, the methods to determine the EEOI and to draw up the SEEMP should be developed for each vessel type taking into consideration their function.

ACKNOWLEDGMENT

This research outcome has been achieved under the research project no. 1/S/IESO/2014 financed from a subsidy of the Polish Ministry of Science and Higher Educations for statutory activities of Maritime University of Szczecin
We wish to express our gratitude to Briggs Marine of the UK and Mr. Jacek Bednarczyk (Second Engineer Officer) for sharing the technical and operational data of the *Kingdom of Fife*.

REFERENCES

1. Głowacki, B., Behrendt, C. (2015) Energy Efficiency Operational Indicator – Assessment Tool of the Energy Efficiency for Fishing Cutters, *TRANSCOM 2015, Universit of Zilina,*
2. Herdzik, J. (2012) Dynamika rozwoju konstrukcji statków obsługujacych platformy wiertnicze i wydobywcze, *Logistyka 5/2012*, (pp.443-450)
3. MEPC.1/circ.684 (2010), Guidelines for voluntary use of the ship energy efficiency operational indicator (EEOI).
4. MEPC.203(62) (2011) Inclusion of regulations on energy efficiency for ships in MARPOL Annex VI.
5. PRS Nr 103/P – Wytyczne dotyczące efektywności energetycznej statków, Gdańsk 2016
6. http://www.dbs.com.sg/treasures-private-client/aics/templatedata/article/industry/data/en/GR/072016/Offshore_Support_Vessels.xml (acessed 20.06.2017r).
7. http://www.maritimejournal.com/news101/vessel-build-and-maintenance/vessel-launch/briggs_raises_its_game_with_three_new_vessels (accesed 10.06.2017r.)
8. http://www.briggsmarine.com/marine/vessel-charter/anchor-handling-vessels-ahvs/kingdom-of-fife/ (accesed 20.06.2017)

Corresponding author:
Bartosz Głowacki, M.Sc., G-DESIGN, ul.Wrzosowa 9b, 72-123 Pucice, Poland, phone: +48 91 88 12 347, e-mail: biuro@g-design.pl, www.g-design.pl;
Assoc. Prof. Cezary Behrendt, Ph.D. Eng., Maritime University of Szczecin, Mechanical Faculty, Institute of Marine Propulsion Plants Operation, Wały Chrobrego 1-2, 70-500 Szczecin, Poland, phone: +48 91 4809479, e-mail: c.behrendt@am.szczecin.pl

INFLUENCE OF CHOSEN PARAMETERS ON ELECTRICAL MACHINES BEARINGS EXPLOITATION

Radoslaw GORDON[1]

[1]*Department of Mechanical Engineering,*
Maritime University of Szczecin

Abstract

This article focuses on the occurrence of bearing degradation in motors powered by alternating current of the inverters drive system with different carrier frequencies using the IGBT switching method based on PWM signal modulation. Due to wide application of inverters to control multi-phases motors (usually three-phase current motors), this article highlights the matter of the occurrence that current flows and voltage drops in the circuit: shaft - bearings - ground, their influence on bearing damages and suggestions for counteractions.

Key words: *bearing degradation, bearings currents, electrical machines,*

INTRODUCTION

Due to its simple design, efficiency and low price, synchronous and asynchronous motors are gaining a predominant position in the electrical machinery market. The main disadvantage of such motors was the speed regulation resulting from the fact that motor rotation speed depends mainly on two parameters: frequency and number of poles. Speed of asynchronous cage motor is calculated by equation (1)

$$n_0 = \frac{f{*}60}{p} rev/min \tag{1}$$

Where n_0 is synchronous rational speed (rev/min), f is power supply frequency (Hz), p is number of motor poles (-).

Synchronous rotational speed is the speed at which the stator flux rotates and it is called the synchronous speed, and it depends on number of poles of the motor and the power supply frequency.
The problem with frequency regulation has been eliminated with the common use of cheap inverter systems, both in new solutions and as a replacement of the controls of the operating motors as well. Because of use of alternating current, between the rotor and the grounded stator the leakage currents are generated. Those currents flow through the shaft and then through the bearings and causes their degradation. The disadvantage of frequency converters is that they generate not only the given carrier frequency but at the output they generating also many harmonic frequencies being the result of switching transistors. The motor is powered by three-phase voltage CMV (Common Mode Voltage). Voltage discharges through the lowest resistance between the rotor and the motor housing, usually through the oil filter. The main sources of bearing currents (Hadden, T., Jiang, J.W (2016)) deriving from capacitive voltages that are inducted on the motor shaft and high frequency currents made by CMV.

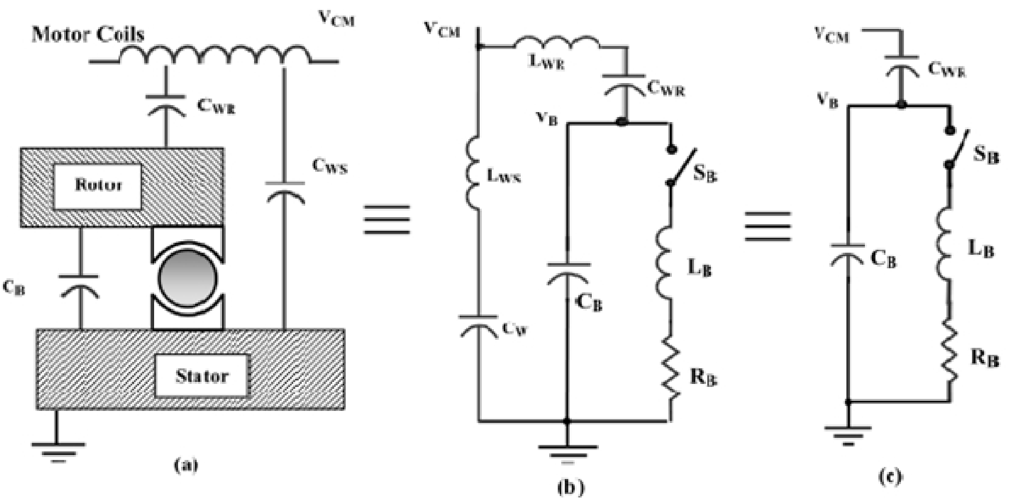

Fig. 1 Simplified electrical motor bearing current model (Hadden, T., Jiang, J.W (2016)).

Because of the fact that in short time periods the voltages and currents can reach very high values on the bearings, microscopic cavities and pits on the bearing spheres and its raceways are being formed (Willwerth, A. (2014)).

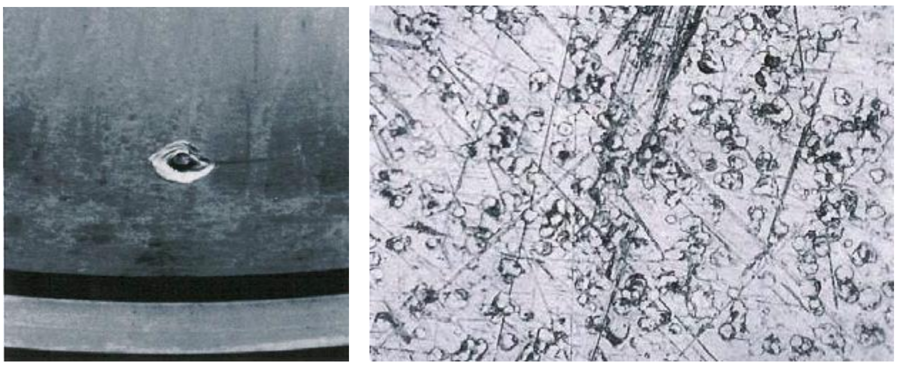

Fig. 2 Pit (0.1 -0.3 mm) and group of pits (1-5 micrometers) in the raceway of the bearings produced during the bearing current flow (Baldor. (2014)).

MATERIALS AND METHODS

Inverter control circuit consists of Analog Devices ADSP-21065L 66MHz Harvard Architecture 32-bit processor (40 digital I/O pins), which realizes control algorithm and the Altera Flex FPGA which was programmed as IGBT modulator (Abramowicz, K. (2014)). Algorithm was able to control the output voltage with carrier frequencies from 3 to 15kHz and the angular speed of the motor from 25 to 300 rad / s. The tested engine was Bessel RSH 80-4b Insulation class F, 4 poles. Supply voltage 400V, rated current is 2.5A, Synchronous speed 1500u / min, phase shift 0.53. Bearing with SKF6204-2Z bearings (Deep groove ball bearings, single row), maximum 9000 rpm and AC6204-GL SMB (max 1100 rpm) with plastic balls (high resistance). Measurements were performed by Tektronix Oscilloscope and low-voltage probe.

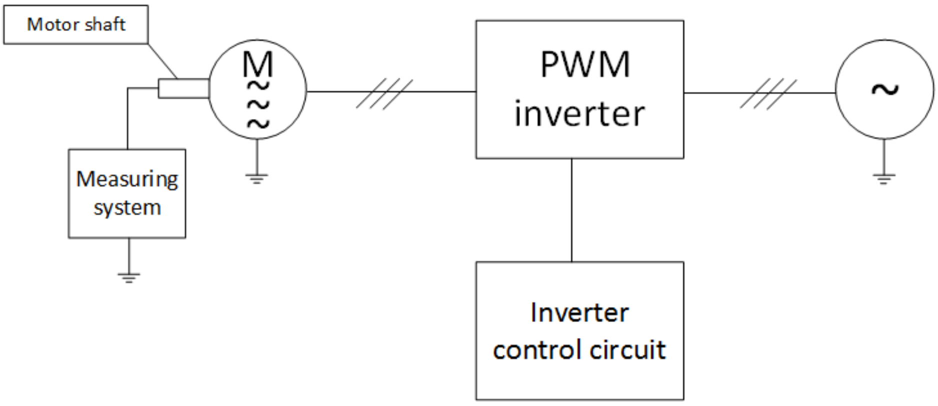

Fig. 3 Block diagram CMV and bearings currents measurement system (own fig.)

RESULTS AND DISCUSSION

The results were adjusted for selected frequencies and angular velocities. Figures 3 and 4 show the registered measurements for carrier frequencies of 6kHz and 12.5kHz of angular speed of 150rad/s, 4.5kHz and 10.5kHz, and angular speed of 300rad/s.

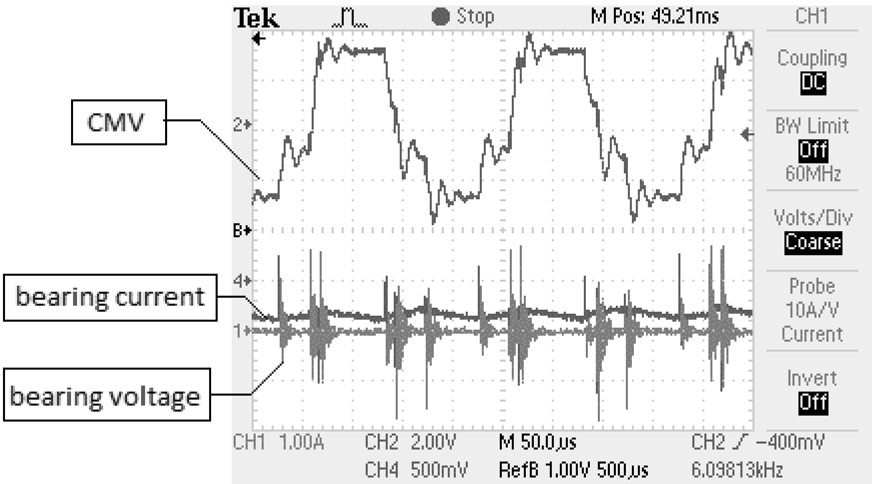

Fig. 4 Measured data for f= 6kHz angular speed 150 rad/ s (Abramowicz, K. (2014)).

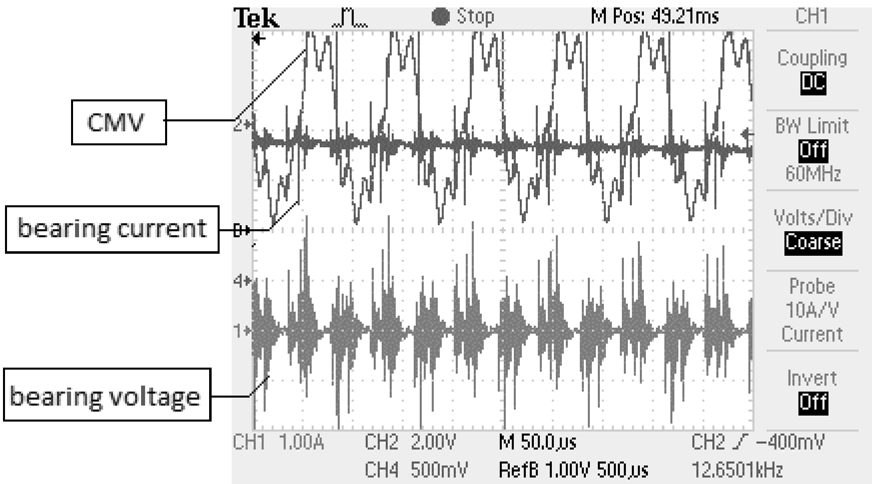

Fig. 5 Measured data for f=12,6kHz angular speed 150 rad/s (Abramowicz, K. (2014)).

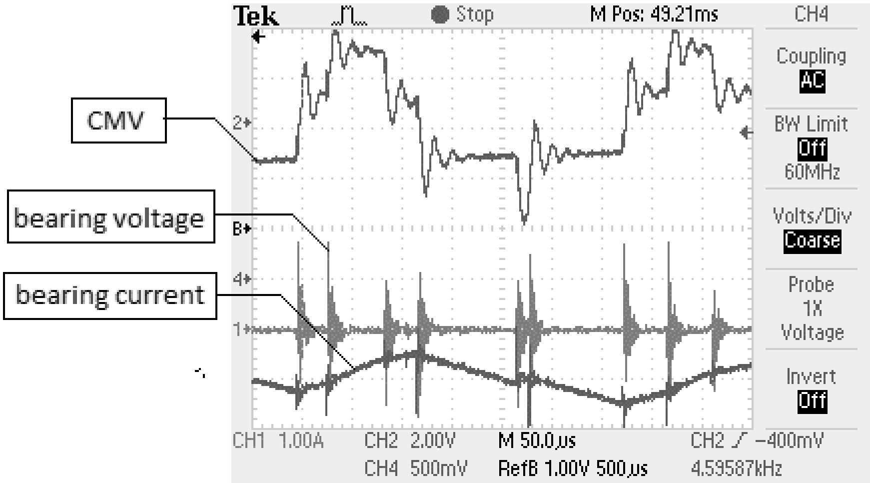

Fig. 6 Measured data for f= 4,5kHz angular speed 300 rad/s (Abramowicz, K. (2014)).

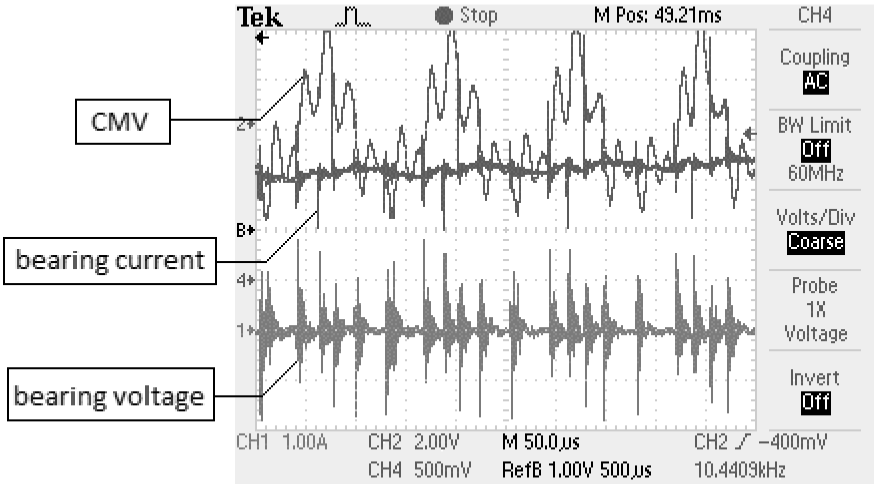

Fig. 7 Measured data for f= 10,5kHz angular speed 300 rad/s (Abramowicz, K. (2014)).

Blue line shows CMV, green line is bearing current, orange line shows the bearing voltage. The values of bearing currents as a function of the different frequencies are shown in the bar charts of Figures 8 and 9.

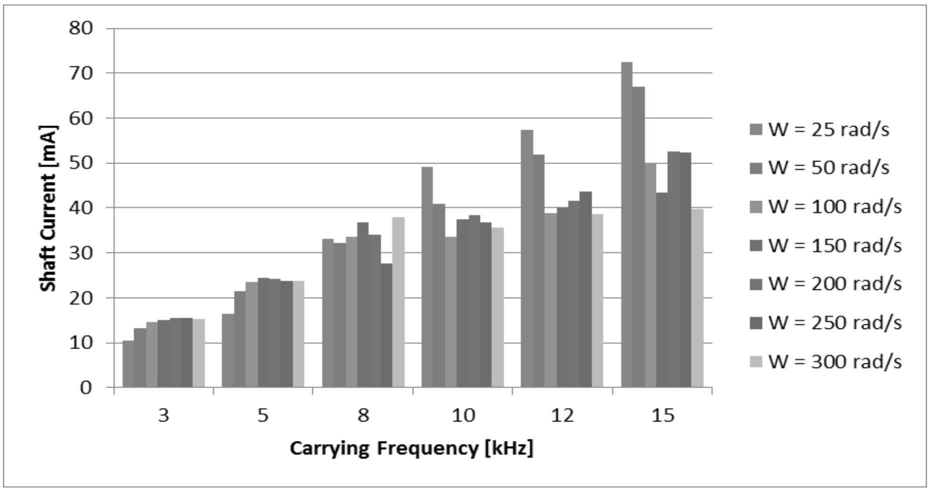

Fig. 7 Currents values measured for bearings SKF6204-2Z (Abramowicz, K. (2014)).

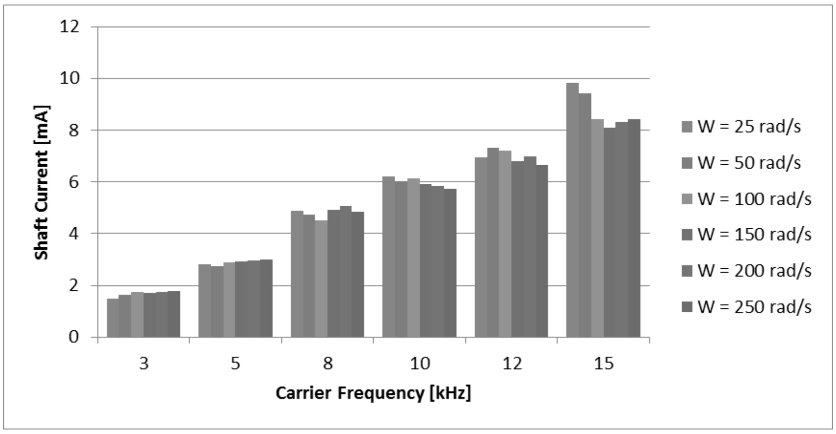

Fig. 8 Currents values measured for bearings AC6204-GL SMB (Abramowicz, K. (2014)).

CONCLUSIONS

Flowing currents cause micro damages to the bearings which may degrade them after some time. The progress of degradation is depending on many factors. This article depict fact that decreasing the carrier frequency of the inverter output voltage considerably reduces the degradation process. The use of plastic bearings can significantly reduce the impact of the bearing current on the damage. When replacing bearings, it would be advisable to use ceramic or plastic bearings which would increase the life of the bearings in case of low power electrical motors.
Other possibilities of limiting the common mode voltage and bearing currents are grounding the motor shaft with brushes and use filters and multilevel inverters in order to reduce the occurrence of higher harmonic frequency.
In many cases, for example of ships equipped with electrical main drives diagnostic bearings vibroacoustic systems are a must in spite of bearing currents possible damages (Tarnapowicz, D. (2016)).
Additionally, shielding of inverter - motor cable has matter to shaft currents and supply currents what is presented in (Kempski, A.(2005)).

ACKNOWLEDGMENT
This study was supported by program 1/S/2016/IEiAO

REFERENCES

1. Abramowicz, K. (2014). Reluctance machine control and measurement methods, Szczecin.

2. Tarnapowicz, D. (2016). The application of vibrometers in monitoring of the electric motor bearings condition on the marine ships. Conference DIAGO.

3. Kempski, A. (2005). Elektromagnetyczne zaburzenia przewodzone w układach napędów przekształtnikowych. Zielona Góra: Oficyna Wydawnictw Uniwersytetu Zielonogórskiego.

4. Willwerth, A. (2014). Profilaktyczna ochrona łożysk. Inżynieria i Utrzymanie Ruchu. Warszawa. (pp.2-3)

5. Hadden, T., Jiang, J.W., Bilgin B, Yang,Y., Sathyan, A., Dadkhah, H., Emadi, A., (2016). A Review of Shaft Voltages and Bearing Currents in EV and HEV Motors, McMaster Institute for Automotive Research and Technology (MacAUTO), McMaster University, ON, Canada 2FCA USA LLC, MI, USA, (pp.1581). IEEE.

6. Baldor. (2014). CommonModeBearingCurrents.pdf. (pp.15-26).

Corresponding author:
Msc.Ing. Radoslaw Gordon., Department of Mechanical Engineering, Maritime University of Szczecin, Waly Chrobrego 1-2 Szczecin, Polska, phone: +48509113573, e-mail: R.Gordon@am.szczecin.pl

CONSTRUCTION DESIGN AUTOMATICALLY ADJUSTABLE MECHANISM FOR CRANE FORKS

Stanislav GRAMBLIČKA[1], Róbert KOHÁR[1], Rudolf MADAJ[1]

[1]*Department of design and mechanical elements, Zilina 010 26, Slovakia*

Abstract
The article deals with the design of the part construction automatically adjustable mechanism for crane forks. In order to solve in the creation of solutions, the TRIZ method was used. Thanks to which managed to construct the optimal design solution. Automatically adjustable mechanism comprises a and at the same time provides the load-bearing part of the for crane forks. Design proposal and its creation was based on the entry requirements so as to be able to in terms of safety and in terms of functionality to serve its fundamental role in the operation.

Key words: *structural design; mechanism; optimization; a defensive role calculation.*

INTRODUCTION

The issue of construction and structural design of crane forks has led to entirely new dimensions thanks to current possibilities of software tools and manufacturing technology. Currently include crane forks for essential accessory lifting techniques. Its primary function is to facilitate and simplify handling of heavy loads. The current trend in the field of development of techniques is directed to the continuous improvement of individual elements of the product. The crane fork is currently supplied on the market in multiple versions and parameters, which allow for the aid of a crane transport materials and semi-finished products on pallets in production and storage areas. Some of the key structural elements ensures safety and stability while loading and moving materials. The current trend in development and innovation covers also this area of technology, it results from the continuous increase in the claims of the final consumer but also the growing competition in the market. Therefore, it is necessary to constantly work on improvements, whether structural or mechanical parts of this type of equipment. It is necessary to constantly improve production technology and to consolidate manufacturing costs in accordance with the resulting in the desired effect. When creating the design was based on the use of proven methodology triz, which forms the basis for the creation of new innovative solutions and allows the right mix of innovative principles under given conditions. This well-known methodological princip was applied in particular in the optimization of the weight of the construction of the mechanism for meeting certain strength, stiffness and functional properties of the mechanism. The solutions apply to the system the correct combination of options of the material used, manufacturing technologies and the use of appropriate computer software techniques. Our ultimate solution was preceded by several draft variants from which after thorough analysis and evaluation of chosen the very best. (Jedlinski, Caban, Krywonos, Wierzbicki, & Brumercik, 2016)

Fig. 1 The design of the crane forks of the load capacity 2000 kg

MATERIALS AND METHODS

The methodological procedure of Triz in the creation of the design:

- Select the area or object of innovation and an automatically adjustable mechanism of concrete hanging eye
- Data collection and subsequent evaluation of information about the upgraded facility, which are necessary for further solution
- Functional cost analysis of the upgraded object, where was carried out the analysis of the elements, structures, functions and parameters of the mechanism.
- Advanced diagnostics functionality, costs, and problems individual elements of the mechanism and their links to other parts of the structure
- Innovation object for the purpose of reducing the weight and thereby the total production costs
- Development of the object for the purpose of improving the strength properties and its functionality
- Selection and verification of variants
- Dizajn, test, CAD a CAM (Martikan, Brumercik, & Bastovansky, 2015)

The nature of the construction is weld – frame part and then mounted – automatic adjusting mechanism, whose task is the automatic positioning of the centre of gravity of the lifting of the preparation in two basic working positions. The first working position of the loading of the preparation is in the condition unloaded by using the transported load and the second working position is in a state loaded with the transported load.

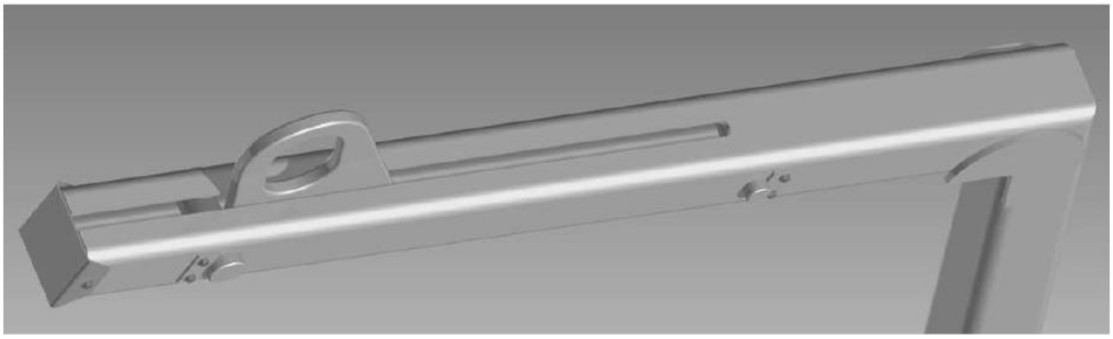

Fig. 2 The detail of the construction of the automatic setting mechanism of the crane forks

Construction of a suspension mesh has the character of the welded part, which is formed by a steel plate and two steel bolts. Steel plate is of a material 11 500 S235J0 (Shigley, Mischke, & Budynas, 2010). The thickness of the plates is 25 (mm). After made a plate, it is necessary to additionally process edges in the sense create rounded edges all the external and internal peripheral edges of the both sides of the radius 5 (mm).

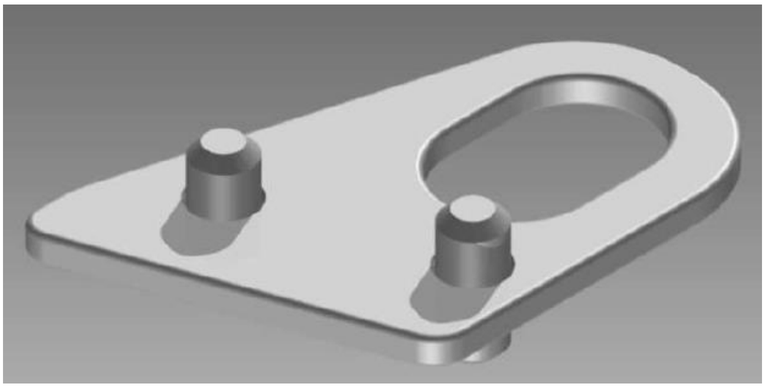

Fig. 3 The detail of the construction of a suspension mesh

In places the assumption of the occurrence of the concentration of the voltages was softened by the network. Load force FZ was to simulate touching the hook on the inner surface of the eye. Its location was realized on the part of the hole of the mesh, where it is to the point of contact of the hook. The action of the reaction forces is shown in the area of the edges of the both pivots of each of the parties. In these places is expected of the reaction forces coming from the total burdensome forces. (Sága, Vaško, Kocúr, Tóth, & Kohár, 2006)

The input attributes a strength of the analysis:

- The size of the total force FZ = 22 (kN)
- The size of the reaction force in the stub RA = 5,5 (kN)
- Material steel 11 500 (S235J0)
- Ultimate tensile strength Rm = 470 (MPa)
- The characteristic stress Re = 245 (MPa)
- Allowed voltage Thrust/Pressure σD = 140 (MPa)

RESULTS AND DISCUSSION

After the preparation of the design of the mesh, it was necessary to verify the accuracy of the optimized solutions in terms of strength and stiffness. The preparation of the model and subsequent calculation was implemented in the environment of the program Autodesk Inventor Profesional. The formation of a 3D model is managed more closer to reality. The Model is an assembly consisting of welded link parts, which are formed of a plate and two cylindrical pins. Attachment of the mesh or boundary conditions i entered as the zero offset of the respective nodes. The result of the analysis is that the largest concentration of the tensions is precisely in the area of the upper part of the plate mesh, where there is a contact surface of the eye and the hook. (Sága, Vaško, Kocúr, Tóth, & Kohár, 2006)

Tab. 1 The resultes of the analysis

Material	Displacement mm	Stress von Mises MPa
Steel 11 500 (S235J0)	0.0662	118,5

The resulting maximum tension is 118,5 (MPa), which is suitable because of the total permitted tension according to the selected type of material. Another result of the analysis is the total displacement, which is again the largest in the area of the top part of the plate mesh, where the maximum calculated value in the program achieves less than 0.07 (mm) which is from the point of view of the standard (DIN EN 13155 A2) is admissible and compliant. In the overall solution of the system is also necessary to mention the fact that the final effect depends also on the accuracy of manufacture and also at the final operating environment. (Sága, Vaško, Kocúr, Tóth, & Kohár, 2006)

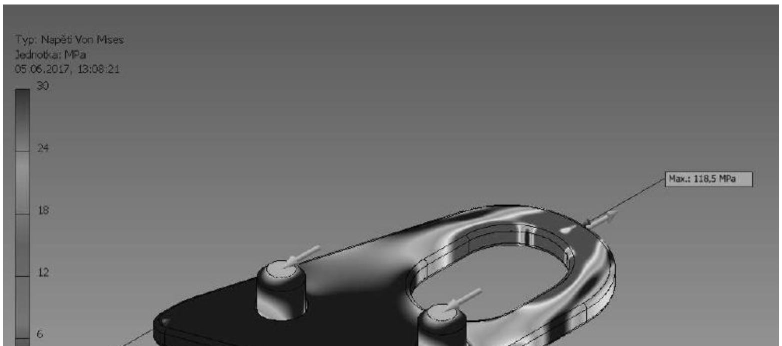

Fig. 4 The calculation of over tensions in the program Autodesk Inventor Profesional (Tension von Mises)

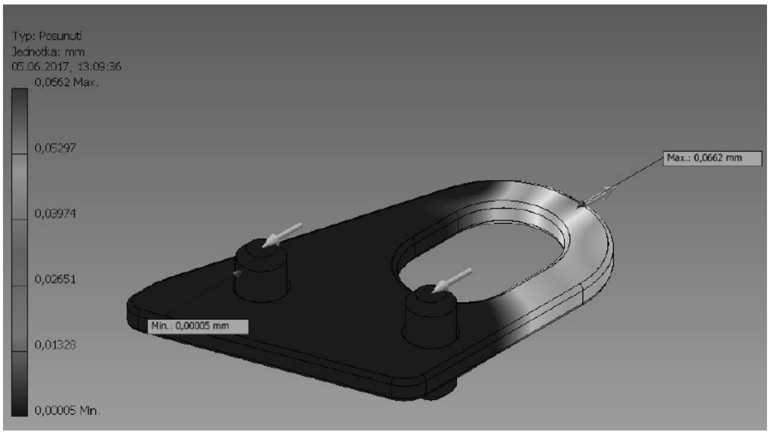

Fig. 5 The calculation of the overall displacement in program Autodesk Inventor Profesional

CONCLUSIONS

According to the input parameters was achieved by matching the design solution. In the design of optimized solutions part of the automatic setting mechanism of optimizing the suspension of the eye. The subject of optimization was the material for better mechanical properties, in addition has occurred in the formation to optimize the thickness of the material used, and from a value of 30 mm for the final 25 mm which contributed to the saving of weight and total production costs of the mechanism. Another subject of the optimization was the modification of the peripheral edges part of the mesh from bevel edges on edges the rounded and it from the outside and from the inside of the eye. The rounded edges allow you to reduce risk of increased concentration of tension in the edges area and this leads to prevention of the occurrence of permanent deformation of the component. In addition, we achieved improvements in the field of surface treatment of pins and in particular the precision of the production, which was especially needed due to a reduction in skin friction occurs when you move the mesh in the frame of crane forks in search of the right position of the centre of gravity.

ACKNOWLEDGMENT

The research is supported by the following institutions with project Cultural and Educational Grant Agency of the Ministry of Education, Science, Research and Sport of the Slovak Republic under the contract no. 040ŽU-4/2016 - Modernization of teaching with Rapid Prototyping Technology.

REFERENCES

1. Sága M., Vaško M., Kocúr R., Tóth Ľ., Kohár R.: *Aplikácia optimalizačných algoritmov v mechanike telies*. Vedecko - technická spoločnosť pri Žilinskej univerzite. Žilina 2006, 240s.
2. Shigley J.E., Mischke CH.R., Budynas R.G.: *Konstruování strojních součastí*. VUT-Brno: VUTIUM vydavateľstvo, 2010, 1159s.
3. Jedlinski L., Caban J., Krywonos L., Wierzbicki S., Brumercik F: *Application of vibration signal in the diagnosis of IC engine valve clearance*. Journal of Vibroengineering, Vol. 17, No. 1 (2015), pp. 175-187.
4. Martikan M., Brumercik F., Bastovansky R.: *Development of mechatronic deformation system*. Applied mechanics and materials, Vol. 803 (2015), pp. 173-178.
5. Brumercik F., Lukac M., Krzywonos L.: *Driveability simulation of vehicle with variant tire properties. Communications*, Vol. 18, No. 2 (2016), pp. 34-37.
6. http://www.triz.sk/

Corresponding author:
Ing. Stanislav Gramblička, Department of design and mechanical elements, Faculty of Design and Machine Elements, Slovak University of Zilina, Univerzitná 1, Zilina, 010 26, Slovak Republic, phone: +421415132922, e-mail: stanislav.gramblicka@fstroj.uniza.sk

DESIGN AND CONSTRUCTION OF A HYDRAULIC BRIQUETTING MACHINE FOR HAZELNUT HUSK AGRICULTURAL RESIDUE

Gürkan Alp Kağan GÜRDİL, Bahadır DEMİREL

Department of Agricultural Machinery and Technologies Engineering, Faculty of Agriculture, Ondokuz Mayis University, Samsun, Turkey

Abstract
Briquetting is the most widely-used waste compaction technology. Briquette quality is evaluated mainly by briquette density. Briquette density is very important for the impact of technological parameters compacting pressure, burning speed, briquette stability, etc. Briquettes made by hydraulic briquetting presses are of the highest quality. This developed hydraulic briquetting system is manufactured in Terme Industrial zone Samsun Turkey. The objective of the present study is to give theoretical analyses of parameters which have an impact on briquette quality. Hazelnut husk briquettes were dried up to 13 – 15 % moisture content and they were grinded into (2-5)-(7-10) mm size and were pressed under 160 MPa pressure. The physical-mechanical properties of the briquettes were investigated.

Key words: *briquetting; hydraulic press; physical parameters, design.*

INTRODUCTION

Biomass defined as different materials of biological origin mainly plant material and animal wastes (*Sampson, et al., 1993; Trebbi, 1993*), used primarily as domestic energy source is naturally abundant and present a renewable energy opportunity that could serves as an alternative to fossil fuel. Behind coal and oil, biomass is the third largest energy resource in the world (*Bapat, et al., 1997*) having dominated the world energy consumption until the mid-19th century (*Tumuluru, et al., 2010*). Utilization of agricultural residues is often difficult due to their uneven and troublesome characteristics. The process of compaction of residues into a product of higher density than the original raw material is known as densification. Densification has aroused a great deal of interest in developing countries all over the world lately as a technique for upgrading residues as an energy source (*Bhattacharya, et al., 2002*). Briquetting is the most widely-used waste compaction technology (*Biath & Ondruska, 2012*). High-density, compressed biomass simplifies the logistics of handling and storage, improves biomass stability, facilitates the feeding of solid biomass fuels into energy utilization devices and offers higher energy density, cleaner burning solid fuels that in some cases can approach the heating value of coals (*Klass, 1998*).
The objective of study is to develop of a hydraulic briquetting machine with horizontal pressing in order to enable material back up for hazelnut husks. This developed hydraulic briquetting system is manufactured in Terme Industrial zone Samsun Turkey. The objective of the present study is to give theoretical analyses of parameters which have an impact on briquette quality. Hazelnut husk briquettes were dried up to 13 – 15 % moisture content and they were grinded into (2-5)-(7-10) mm size and were pressed under 160 MPa pressure. The physical effects of the briquettes were investigated.

MATERIALS AND METHODS

A Hydraulic type briquetting machine with a horizontal pressing course, designed and constructed in Terme industrial zone of Samsun was used for briquetting the hazelnut husk residues. Briquetting pressure range of this machine is adjustable from 0 to 320 MPa by a manometer on it.
Piston and cylinder of the machine is bedded horizontally thus the briquetting is done in a horizontal course. The pump of the machine has a tank of 25 L capacity of hydraulic oil with a 1.2 $m^3.s^{-1}$ flow rate. Stroke of the piston is 310 mm and the velocity of the stroke is adjusted to 10 $mm.s^{-1}$ at 160 MPa briquetting pressure.
Machine dimensions are 1280x1155x740 (AxBxC) mm. Operation of the machine is controlled by a start-stop button embedded on it. Hydraulic pump functions by a 15 kW powered 3-phase electrical engine with a star delta starter. The mold for the briquette was not heated. As a support block for the

pressing a rectangle shaped metal plate is placed at the end of the course having 125x105x30 mm dimensions. Movement of this plate is done manually. Main parts are given in Figure 1, the mold in Figure 2 and finally manufacturing stages of this machine are given in Figure 3, below.

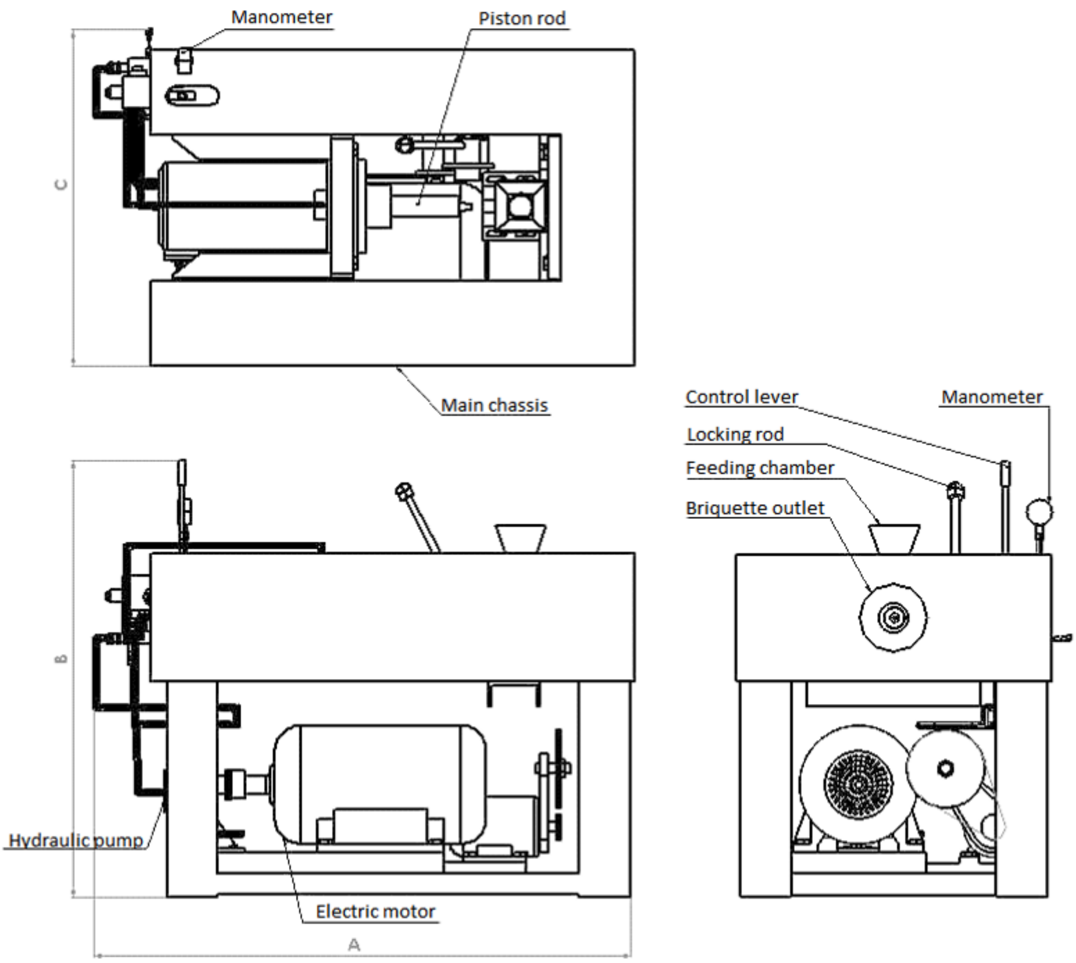

Fig. 1 Main parts of the briquetting machine

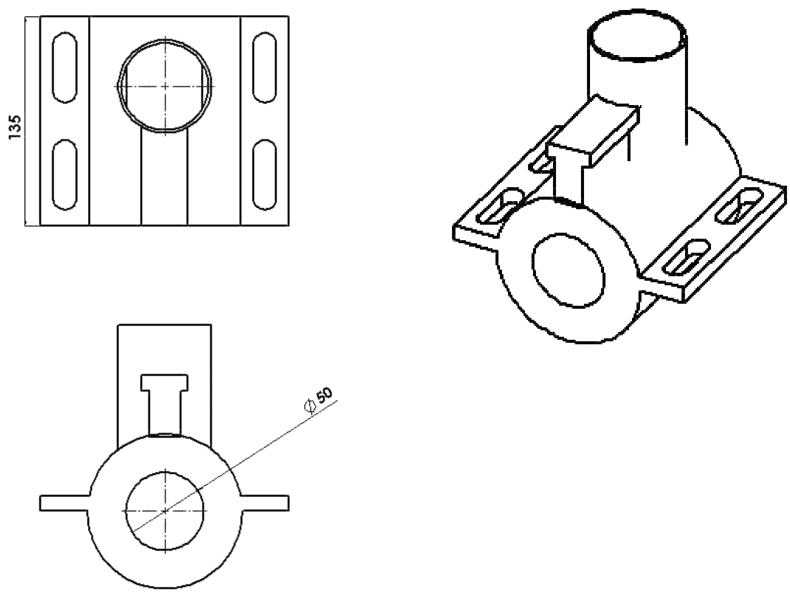

Fig. 2 The mold

Fig. 3 Manufacturing stages

Briquetting of Hazelnut Husk Agricultural Residue

The residues were first dried in normal conditions under the sun and their moisture contents were decreased down to 13-15 %. Then the dried material was ground by a knife-hammer mill till the required particle sizes were obtained (2-5; 7-10 mm). Their moisture contents were controlled again and they were briquetted under 160 MPa briquetting pressures.

The briquetting pressure was chosen as 160 MPa showed that the briquettes were enough solid and durable both physically and in shape. This working pressures also matches with the studies defined in *Krizan, et al., (2015), Zhang & Guo (2014) and Sun, et al., (2014)*. Feeding of material was done batch wise during the briquetting process in order to avoid occlusion. The material prepared for briquetting was poured into the cylindrical mold and they were squeezed by a piston in the mold and the briquettes were obtained. Pressing process continued 20 seconds more after the completing of squeezing in order to avoid expansion in the produced briquettes. Full cylindrical shape briquettes having 50 mm diameter and 80 to 110 mm varying lengths were produced by this process.

RESULTS AND DISCUSSION

As mentioned the residues obtained after harvesting of hazelnut were briquetted under 160 MPa briquetting pressure with 13-15 % moisture content and with two different particle sizes (2-5 mm and 7-10 mm). Then the solid biofuel properties of these briquettes at each application were analyzed. Samples of full cylindrical shaped briquettes for each application are given in Figure 4, below.

M: 13-15 %

PS: 2-5 mm	PS: 7-10 mm
P: 160 MPa	P: 160 MPa

Fig. 4 Briquettes produced from different particle sizes

Volume mass of the material and the briquettes with compression ratios are given in Table 1. The highest compression ratio (7.03) was achieved at 160 MPa briquetting pressure, 13-15 % moisture content of the material and with 7-10 mm particle sizes.

Tab. 1 Compression ratios of the hazelnut husk briquettes

P (MPa)	M (%)	PS (mm)	Volume mass of material (kg.m^{-3})	Volume mass briquettes (kg.m^{-3})	Compression ratio
160	13-15	2-5	176.79	1143.23	6.47
		7-10	142.90	1005.43	7.03

Tumbler Index

Tumbler index is an indicator of resistance of briquettes against the forces they face during loading, discharging, transporting procedures. Thus it is an indicator of solidness of briquettes (*Zhang & Guo, 2014; Niedziolka, et al., 2015*).

Tab. 2 Effect of particle size on tumbler index

	Tubler Index (%) $\overline{X} \pm S_{\overline{x}}$
PS (mm)	
2-5	78.92 ± 3.57
7-10	73.23 ± 3.16
Sig.	**<0.01**

The highest Tumbler Index (78.92 ± 3.57) was achieved with the briquettes made from 2-5 mm particle sizes at 160 MPa briquetting pressure and at 13-15 % moisture content of material. The difference between the Tumbler Indexes of the briquettes at different particle sizes was found to be statistically significant (P<0.01). The reason for this was estimated as that the hazelnut husk has ligneous structure so, the briquettes made from a higher particle sized material can be more brittle. The remaining briquettes after Tumbler Index tests are given in Figure 5.

M: 13-15 %

PB: 2-5 mm
P: 160 MPa

PB: 7-10 mm
P: 160 MPa

Fig. 5 The remaining hazelnut husk briquettes after Tumbler Index tests

The results of Tumbler Index tests showed that the main abrasion and breakdowns realized at the both ends and at the middle part of the briquettes. The reason for that can be the batch squeezing procedure depending on the material feeding which ends up with layered structure. The breaking mainly occurred in that layer borders.

Shatter Index

The resistance of briquettes against impacts during loading and discharging processes are tested by Shatter Index. In this test the briquettes were intentionally dropped down 10 times from a height of 1 m above ground level. The results of Shatter Index tests are given in Table, below.

Tab. 3 Effect of particle size on Shatter Index

	Shatter Index (%)
	$\bar{X} \pm S_{\bar{x}}$
PS (mm)	
2-5	91.27 ± 1.68
7-10	91.17 ± 1.82
Sig.	**0.947**

The difference between the Shatter Indexes of the briquettes produced from two different particle sizes was not found to be statistically important. The views of briquettes after Shatter Index testes are given in Figure 6.

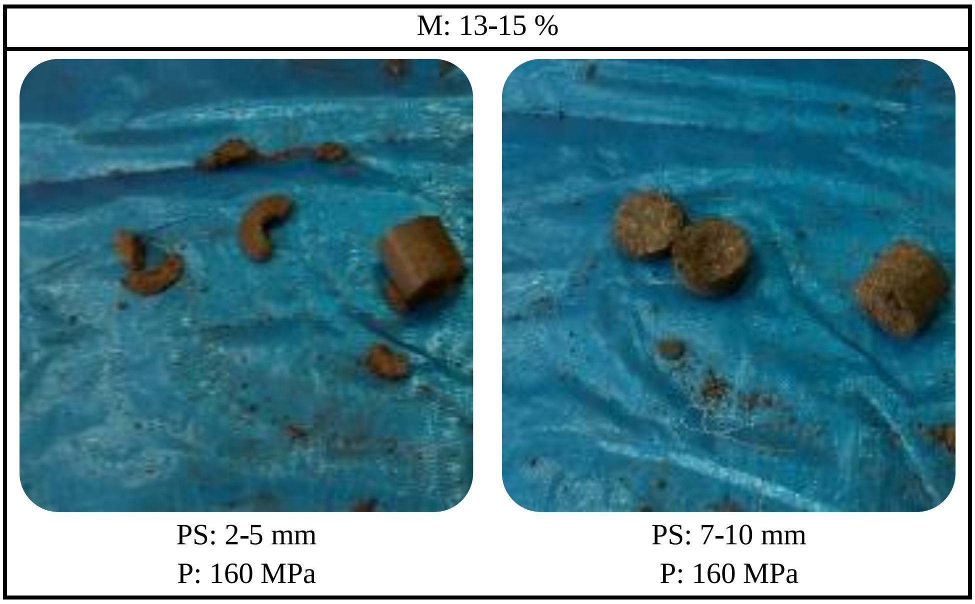

Fig. 6 Shatter tests of briquettes

The tests showed again that all the breakings and split ups happened at the both ends and in the middle of the briquettes due to batch squeezing of the material.

CONCLUSIONS

In this study a particular hydraulic type briquetting machine with a horizontal course was designed and developed for the briquetting of hazelnut husk agricultural residues in order to be evaluated as solid biofuel. Effect of two different particle sizes were analysed on the physical-mechanical parameters of briquettes which are produced under 160 MPa pressure and at 13-15% moisture content. The results showed that the developed hydraulic type briquetting machine is very suitable for briquetting of hazelnut husk agricultural residues. After all the tests it’s found that the effect of particle size on volume mass of material, volume mass of briquettes, compression ratio, Tumbler Index were statistically important but, its effect on Shatter Index was not found to be important. These kinds of researches will help to improve the design and function of briquetting machines for the future and by this way for the energy deficiency of the world by converting agricultural residues to energy sources.

ACKNOWLEDGMENT

This study was supported by BAP unit of Ondokuz Mayis University with the project number ZRT.1904.12.013 and by TÜBİTAK (THE SCIENTIFIC AND TECHNOLOGICAL RESEARCH COUNCIL OF TURKEY) with the project number 112O454.

REFERENCES

1. Bapat, D. W., Kulkarni, S. V. & Bhandarkar, V. P. (1997). Design and operating experience on fluidized bed boiler burning biomass fuels with high alkali ash. Proceedings of the 14th International Conference on Fluidized Bed Combustion, New York: Vancouver ASME, 165–174.
2. Bhattacharya, S.C., Leon M.A., Rahman, M.M. (2002). A Study on improved biomass briquetting. Energy for Sustainable Development, 6(2), pp. 67–71.
3. Biath, P., Ondruska, J. (2012). Idealized compression ratio for a screw briquetting press. Acta Polytechnica, 52(3), 13-16.
4. Francis, O. O. (2013). Development of an appropriate biomass brıquetting machine for use in rural communities. Department of Agricultural and Bioresources Engineering Faculty of Engineering, University of Nigeria, Nsukka (pp. 158).
5. Klass, D. L. (1998). Biomass for renewable energy, fuels, and chemicals. Academic Press.
6. Križan, P., Šooš, L., Matúš, M., Beniak, J., Svátek, M. (2015). Research of significant densifcation parameters influence on final briquettes quality. Wood Research 60(2), 301-316.
7. Niedziołka, I., Szpryngiel, M., Jakubowska, M.K., Kraszkiewicz, A., Zawislak, K., Sobczak, P., Nadulski, R. 2015. Assessment of the energetic and mechanical properties of pellets produced from agricultural biomass. Renewable Energy, 76, 312-317.
8. Sampson, R. N., Wright, L. L., Winjum, J. K., Kinsman, J. D., Benneman, J., Kursten, E., Scurlock, J. M. O. (1993). Biomass management and energy. Water, Air, and Soil Pollution, 70(1–4), pp. 139–59.
9. Sun, B., Yu, J., Tahmasebi, A., Han, Y. (2014). An experimental study on binderless briquetting of chinese lignite: effects of briquetting conditions. Fuel Processing Technology, 124, 243–248.
10. Trebbi, G. (1993). Power-production options from biomass: The vision of a southern Euorpean utility. Bioresour. Technol., 46, 23-29.
11. Tumuluru, J. S., Wright, C. T., Kenny, K. L., and Hess, J. R. (2010). A review of biomass densification technologies for energy application. A report prepared for the U. S. Department of Energy by the Idaho National Laboratory, Biofuels and Renewable Energy Technologies Department, US.
12. Zhang, J., Guo, Y. (2014). Physical properties of solid fuel briquettes made from caragana korshinskii kom. Powder Technology, 256, 293–299.

Corresponding author:

Bahadır Demirel, Ph.D., Faculty of Agriculture, Department of Agricultural Machinery and Technologies Engineering, Ondokuz Mayis University, Samsun, 55139, Turkey, phone: +90 362 312 19 19, e-mail: bdemirel@omu.edu.tr

UTILIZATION OF RHEOLOGICAL MODEL FOR DESCRIPTION OF MECHANICAL BEHAVIOUR OF RAPE BULK SEEDS UNDER COMPRESSION LOADING

David HERAK[1], Ales SEDLACEK[1]

[1]*Department of Mechanical Engineering, Faculty of Engineering, Czech University of Life Sciences Prague*

Abstract
The article is focused on the description of mechanical behavior of rape bulk seeds under compression loading with aid of simple rheological model. A single pressing vessel with inner diameter 80 mm with initial pressing height 80 mm of bulk rape seeds were used for determination of deformation characteristics under compression loading up to 100 kN. Determined mechanical behavior of rape bulk seeds was described by rheological model with one branch and rheological model with two branches. Based on this study it follows that model with two branches more precisely described the compressive stress and time response than the model with one branch.

Key words: *viscosity; modulus; elasticity; strain; stress; time.*

INTRODUCTION

For optimal design of technology for oil seeds pressing it is necessary to fully understand to the inner processes occur during compression of bulk seeds as well as mathematically describe dependency between compressive force and bulk seeds deformation (*Karaj, & Muller, 2011*). There are several already published methods which can be used for description of deformation curve (*Herak, Kabutey, & Sigalingging, 2016; Kabutey, Herak, Choteborsky, et al., 2013; Rajabipour, Zariefard, Dodd, & Norris, 2004*). However these methods are mostly based on tangent curve utilization, using reciprocal slope transformation or application of Darcy laws. Unfortunately these methods don't respect viscoelasticity behavior of pressed bulk seeds which currently comes to the fore especially in oil processing models for example based on finite element method used in industrial engineering (*Petru, Novak, Herak, & Simanjuntak, 2012; Saeidirad, Rohani, & Zarinfneshat, 2013*). Mechanical behavior of rape bulk seeds under compression loading was deeply investigated in already published studies and gained knowledge is widely used in industrial practice (*Divisova, Herak, Kabutey, et al., 2014; Mohsenin, 1970*). Nevertheless the lack of information about viscoelasticity properties of rape bulk seeds still exists and they are highly desirable for mathematical models development. Thus the aim of this study is to describe mechanical behavior of rape bulk seeds under compression loading with aid of simple rheological model.

MATERIALS AND METHODS

Samples of bulk Rape seeds (*Brassica napus* L.) obtained from Czech Republic were used for the experiment. The general physical properties of the oilseed crop are given in Tab. 1. To determine the relationship between compressive force and deformation characteristic curves, a compression device (Labortech, model 50, Czech Republic) was used to record the course of deformation function. A single pressing vessel with inner diameter D = 80 mm (Fig. 1) was used. Initial pressing height H = 80 mm of bulk seeds were tested with a compression speed v = 1 mm·s^{-1} under temperature of 20 °C. The compressive force F was between 0 and 100 kN. The experiment was repeated three times. The measured characteristics between compressive force F (kN) and deformation x (mm) were transformed into dependency between compressive stress σ (MPa) and strain ε (-).

Tab. 1 Physical properties of bulk rapeseeds; data in the table are means ± SD

Moisture content (%)	Mass (g)	Porosity (%)	Coefficient of variation of compressive force (%)
6.9 ± 0.1	269± 0.4	42.85 ± 0.49	8.0 ± 0.3

Description of the mechanical behavior of rape bulk seeds was carried out by applying rheological model with one branch and rheological model with two branches presented in Fig. 1. One branch model was assembled as serial linked spring and dashpot, where spring was loaded by compression loading and dashpot by tension loading. Compressive speed was assumed as a constant and deformation rate γ (s^{-1}) was calculated by eq. (1).

$$\gamma = \frac{v}{H} \tag{1}$$

Mechanical behavior of one branch rheological model was described by general differential equation eq. (2).

$$\dot{\varepsilon} = \gamma = \frac{\dot{\sigma}}{\eta} - \frac{\sigma}{E} \tag{2}$$

where E (MPa) is moduli of elasticity and η ($MPa\cdot s^{-1}$) is coefficients of dynamic viscosity. Formula for description dependency between compressive stress and time (3) was determined by solving eq. (2) with consideration of boundary conditions (σ = 0 MPa; t = 0 s) that in zero time is also zero compression stress.

$$\sigma_I = \gamma \cdot \eta \cdot (e^{\frac{E}{\eta} \cdot t} - 1) \tag{3}$$

Two branch model (Fig. 1) was also derived from eq. (3) and it is described by eq. (4),

$$\sigma_{II} = \gamma \cdot \eta_1 \cdot \left(e^{\frac{E_1}{\eta_1} \cdot t} - 1\right) + \gamma \cdot \eta_2 \cdot (e^{\frac{E_2}{\eta_2} \cdot t} - 1) \tag{4}$$

where E_1 (MPa), E_2 (MPa) are moduli of elasticity for the models branches; η_1 ($MPa\cdot s^{-1}$) and η_2 ($MPa\cdot s^{-1}$), are coefficients of dynamic viscosity of the models branches, t (s) is time of compression; σ_I (MPa), σ_{II} (MPa) are compressive stress. The stress strain characteristics for rheological models was analyzed using Mathcad 14 Software (MathCAD 14, PTC Software, Needham, MA, USA), which uses the Levenberg-Marquardt algorithm for data fitting (*Marquardt, 1963*).

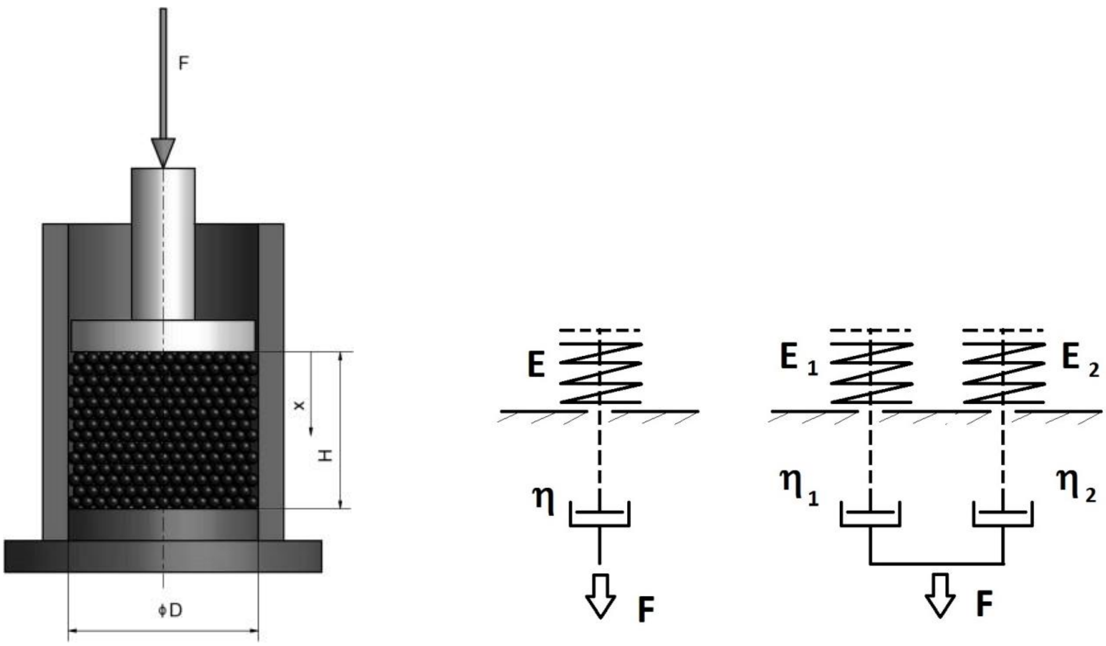

a) **b)** **c)**

Fig. 1 a) Scheme of pressing equipment; b) Scheme of one branch model; c) Scheme of two branches model

RESULTS AND DISCUSSION

The amounts determined from individual experiments are shown in Fig. 2. Measured amounts were fitted by one branch model (3) and two branches model (4) whose coefficients are shown in Tab. 2. Graphical displaying of measured amounts and fitted functions are also displayed in Fig. 2. From the determined coefficients of determination it was found that fitted functions described the measured amounts accurately. The amounts of the coefficients of determination in all experiments were close to one (Tab. 3). From analysis of the images of individual experiments it was clear that the fitted curves (3 and 4) described accurately measured amounts over the whole range of deformation. From the statistical analysis ANOVA which was calculated for the level of significance 0.05, it was seen (Tab. 3) that the values of F_{crit} (critical value compares a pair of models) were higher than F_{ratio} values (value of the F-test) for all measured experiments and amounts of P_{value} (significance level at which it can be rejected by the hypothesis of equality of models) were higher than significance level 0.05. This shows that one branch model as well as two branches model are statistically significant as measured data and models (3 and 4) can be used for fitting of measured amounts

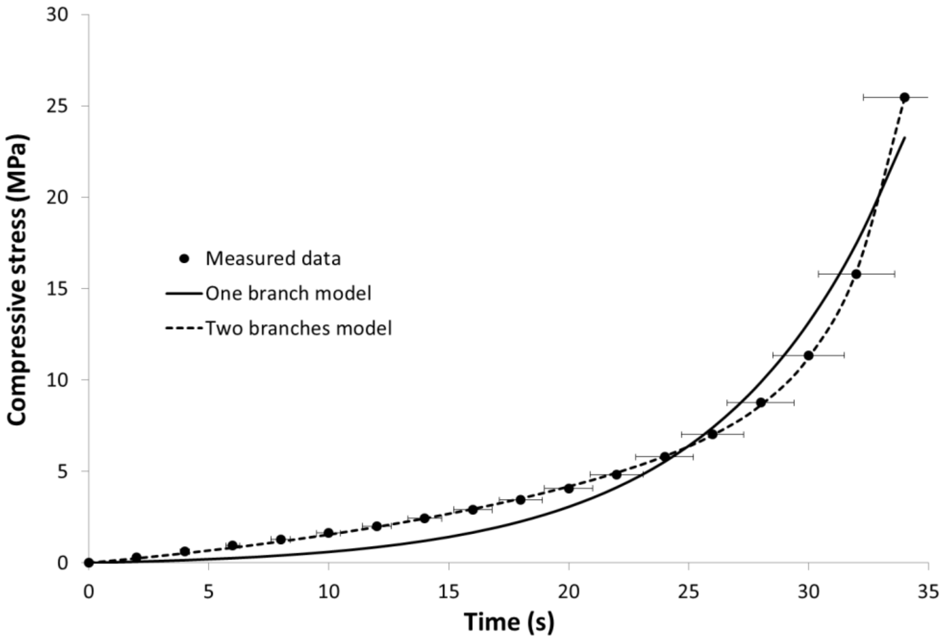

Fig. 2 Dependency between compressive stress and strain

Tab. 2 Determined coefficients of rheological models

One branch model		**Two branches model**			
E **(MPa)**	***η*** **(MPa·s^{-1})**	***E₁*** **(MPa)**	***η₁*** **(MPa·s^{-1})**	***E₂*** **(MPa)**	***η₂*** **(MPa·s^{-1})**
2.196	15.583	9.455	183.637	$3.737 \cdot 10^{-4}$	$9.033 \cdot 10^{-4}$

Tab. 3 Coefficients of statistical analysis

	F_{ratio} (-)	P_{value} (-)	F_{crit} (-)	R^2 (-)
One branch model	0.0345	0.854	4.1491	0.92
Two branches model	0.0005	0.994	4.1491	0.99

Based on the variability of rape bulk seeds which was confirmed by the coefficient of variation values (Tab. 1), the model with two branches (4) more precisely described the compressive stress and time response (Fig. 2) than the model with two branches (3), which showed deviation of the deformation curve as confirmed by the coefficient of variation values (Fig. 2). From this conducted study it follows that the determined curves using rheological models were in accordance with results of already published studies and that the obtained values of viscoelasticity properties of rape bulk seeds can be used as background for development of further models (*Herak, Kabutey, Divisova, & Simanjuntak, 2013; Blahovec, 1996.; Petru, Novak, Herak, & Simanjuntak, 2012; Rajabipour, Zariefard, Dodd, & Norris, 2004*) and it is clear that determined rheological model can be also used for description of mechanical behaviour of other oil bulk seeds.

CONCLUSIONS

- Mechanical behavior of rape bulk seeds under compression loading was determined in this study.
- With aid of two simple rheological models based on serial linked spring and dashpot deformation characteristic of rape bulk seeds was mathematically described.
- Rheological models were compared to each other and based on this study it follows that model with two branches more precisely described the compressive stress and time response than the model with one branch.

ACKNOWLEDGMENT

This study was supported by CULS FE IGA 2017:31130/1312/3111

REFERENCES

1. Divišová, M., Herák, D., Kabutey, A., Šleger, V., Sigalingging, R., & Svatoňová, T. (2014). Deformation curve characteristics of rapeseeds and sunflower seeds under compression loading. *Scientia agriculturae bohemica*, *45*(3), 180-186.
2. Herak, D., Kabutey, A., & Sigalingging, R. (2016). Mathematical Description of Non-linear Mechanical Behaviour of Materials Under Compression Loading, Case Study: Spruce Bulk Wood Chips. In *The Latest Methods of Construction Design* (pp. 405-409). Springer International Publishing.
3. Herak, D., Kabutey, A., Divisova, M., & Simanjuntak, S. (2013). Mathematical model of mechanical behaviour of Jatropha curcas L. seeds under compression loading. *Biosystems Engineering, 114(3)*, 279-288.
4. Kabutey, A., Herak, D., Choteborsky, R., Dajbych, O., Divisova, M., Boatri, W., et al. (2013). Linear pressing analysis of Jatropha curcas L seeds using different pressing vessel diameters and seed pressing heights. *Biosystems Engineering, 115(1)*, 42-49.
5. Blahovec, J. (1996). Stress relaxation phenomena in vegetable tissue. Experimental results. Journal of Material Science, 31, 1729e 1734.
6. Karaj, S., & Muller, J. (2011). Optimizing mechanical oil extraction of Jatropha curcas L. seeds with respect to press capacity, oil recovery and energy efficiency. *Industrial Crops and Products, 34*, 1010-1016.
7. Marquardt, D. W. (1963). An algorithm for the least-squares estimation of nonlinear parameters. *SIAM Journal on Applied Mathematics, 11 (2),* 431-441.
8. Mohsenin, N. N. (1970). Physical properties of plant and animal materials (Vol. 1). New York: Gordon and Breach.
9. Petru, M., Novak, O., Herak, D., & Simanjuntak, S. (2012). Finite element method model of the mechanical behaviour of Jatropha curcas L. seed under compression loading. *Biosystems Engineering, 111(4),* 412-421.
10. Rajabipour, A., Zariefard, M. R., Dodd, G. T., & Norris, E. R. (2004). Tensile strength and relaxation of tomato skin by a loop technique. *International Agrophysics, 18*, 1-5.
11. Saeidirad, M. H., Rohani, A., & Zarinfneshat, S. (2013). Predictions of viscoelastic behavior of pomegranate using artificial neural network and Maxwell model. *Computers and Electronics in Agriculture, 98*, 1-7.

Corresponding author:
Prof. Ing. David Herák, Ph.D., Department of Mechanical Engineering, Faculty of Engineering, Czech University of Life Sciences Prague, Kamýcká 129, Praha 6, Prague, 16521, Czech Republic, phone: +420 22438 3181, e-mail: herak@tf.czu.cz

ROLLING ELEMENT BEARING TEST RIG DEVELOPMENT

Jakub CHMELAŘ[1], Pavel MOSSÓCZY[2], Vojtěch DYNYBYL[3]

[1]*Department of Designing and Machine Components, FME, CTU in Prague*
[2]*Department of Designing and Machine Components, FME, CTU in Prague*
[3]*Department of Designing and Machine Components, FME, CTU in Prague*

Abstract
The article describes a concept of bearing test rig intended for a simulation of induced dynamic loading to roller bearings. Tested bearing can be preloaded by static radial force and then harmonic axial or radial dynamic force can be applied. Tested bearing is inserted into a housing that allows its free motion in radial direction of static loading and a limited motion in the other directions. Thanks to housing fixture design a roller bearings with free axial play can be used, in order to isolate the effect of axial vibration on outer race. The article is provided with figures illustrating the concept.

Key words: *Bearing; Test rig; Design.*

INTRODUCTION

In order to fully understand the behaviour of, on first sight simple systems, such as rolling element bearings, it is necessary to conduct an extensive testing and data evaluation for defined load cases in controlled environment (Dynybyl, 2009). There are multiple levels, where behaviour of bearings can be studied. The lowest level testing focuses on general phenomena occurring in bearings and is mostly conducted in laboratories. Usually specialised test devices are used, e.g. spiral orbital tester test for the study of tribological problematics of rolling contact or pulsatory tensile test rig for study of structural properties of bearing materials. The other step is component level testing, where bearing is tested as assembled component. Most frequent tests on this level are fatigue life tests under static loading (Harris, 2006), where the time to bearing failure is of main interest under tested conditions. Among other investigated parameters, we can find a bearing drag torque or bearing critical speed. Highest level of testing is operational testing, where bearing is inserted into a real or simulation model of a real application and various parameters are observed. Such tests are usually very valuable, because can show a real response of bearing to simulated operational conditions in context of the simulation model. The drawback is a high cost of such tests.

MATERIALS AND METHODS

Described roller element bearing test rig will be used for a study of roller bearings under dynamic loading conditions. Tested bearing will be preloaded with radial static force. A dynamic force component will be applied either into same radial direction or into an axial direction to simulate challenging operational conditions. For a simulation, linear vibrators will induce a harmonic dynamic force.

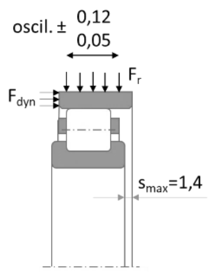

Fig 1. Studied roller bearing with free axial play of outer ring
and its predicted axial oscillation during dynamic loading.

Loading parameters are specified in next chapter. During testing, following values of bearing will be observed: Temperature of outer and inner ring, by surface acoustic waves generating and sensing device (SAW) a response to roller transition over observed region will be measured. (Brücker et. al.,A status of lubrication layer below the contact of most loaded elements will be estimated from measured signal and an orbiting speed of elements will be calculated too. Expected outputs from the tests are the record of temperature gradient between rings, the lubrication status identification for various operating conditions under pure static radial loading and with added dynamic components, either in radial or axial direction. In addition, the slide-to-roll ratio parameter of elements will be calculated with respect to loading character and a speed.

Requirements

Based on a brief test description a set of design and performance requirements for a test rig were defined. These were during design process multiple times revaluated to meet the low budget criterion and re-use in-house available resources and components.

Tested bearing requirements
Roller bearing with line contact (roller profile modification allowed)
Static radial load shall induce at least 2 GPa high contact pressure on inner ring. (Computed by KISSsoft)
Bearing shall have non-located outer ring – free axial play

Selected bearing type: N306 (see Fig. 1)
Bore diameter: 30 mm;
Outer diameter 71 mm;
Width: 19 mm
No of rollers: 12;
Axial play: max. 1,4 mm

Static loading device requirements
Loading device should provide loading force with magnitude 10 kN
Sensor of actual static radial force – range 10 kN
Connection of loading device with tested bearing shall eliminate undefined, off-axis loading
Loading force continuous control preferred

Dynamic loading device requirements
Loading device shall provide harmonic loading character
The frequency shall be at least 100 Hz
Dynamic force amplitude at least 90 N

Drive requirements:
AC motor, controlled by variable frequency drive (VFD),
Nominal speed 1500 rpm
Motor power 4 kW

RESULTS AND DISCUSSION

Defined requirements were in next step used as references for test stand concept development.

Mechanical Design Description

One of the main requirements for most of testing devices is a simple and fast change of the tested sample. On presented rig, see Fig 2 and Fig 3 with links, it was decided to place the tested bearing (1) on the end of the main shaft (2). The advantage is not only a good accessibility, but also the availability of free space for a direct axial loading of bearing, that would have been difficult to apply for different configurations.

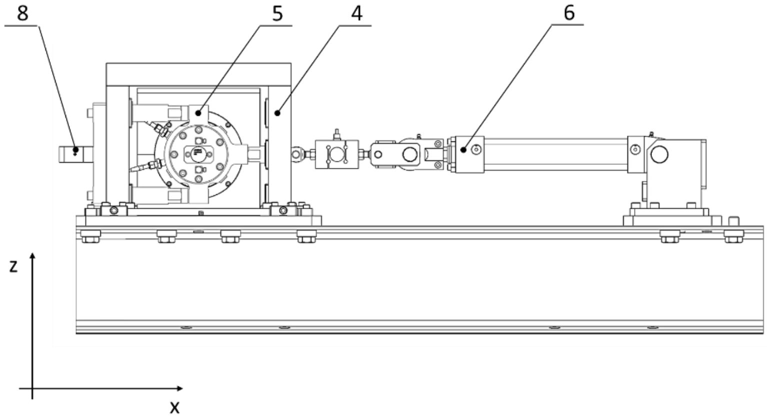

Fig. 2 Test rig front view with highlighted tested bearing housing

The dynamic loading would cause an excitation of all components of the test rig, therefore, two bearings that support center shaft are a heavy-duty tapered roller bearings in a stiff back-to-back configuration (3). The preload will be applied during the assemblage. Housings where both support bearings are located consist of rigid massive steel blocks, so high dynamic stability of structure is assured.

For the study of applied dynamic loading, a roller bearing with non-locating outer ring was selected (1). The location of outer ring must be assured by design of rig. According to a Fig 3, in the front section of the test rig, there is apparent a closed frame structure (4) equipped by bushings. These serve as guiding surfaces for three rods that provide a location of tested bearing housing (5). The guides allow housing free positioning in the direction (x) of applied force by hydraulic actuator (6). The motions in the other directions (y, z) are restricted and can be partly controlled by the selection of fits of the bushings and guiding rods. Estimated motion amplitude is based on fitting and manufacturing tolerance between 0,05 - 0,1 mm.

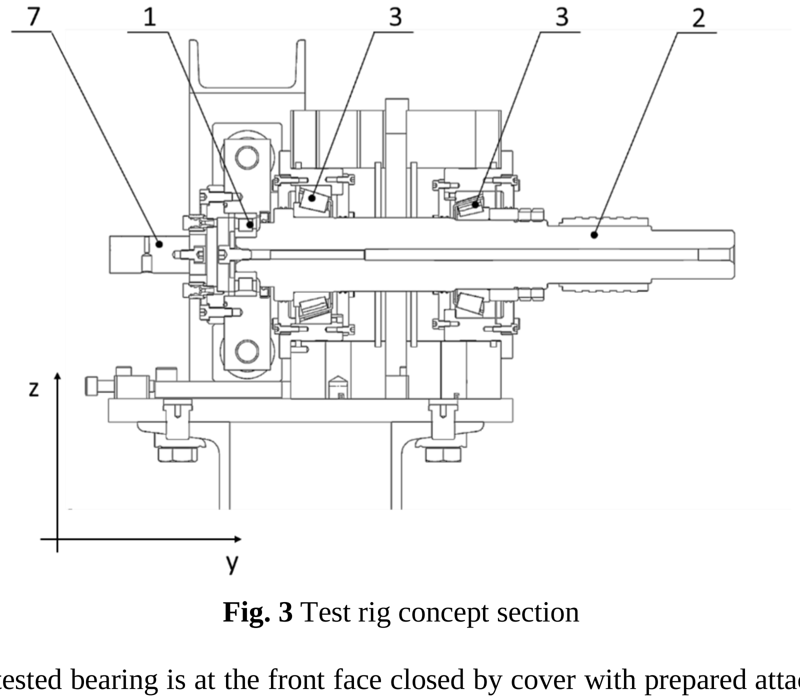

Fig. 3 Test rig concept section

The housing for tested bearing is at the front face closed by cover with prepared attachment points for dynamic loading exciter (7), also there are located input and output fittings for oil lubrication. The other side of housing has built in a rod sealing preventing the leakage of lubricant from chamber with bearing.

A radial surface of the housing is drilled with threaded thru holes that could be used for a direct attachment of sensors to outer ring of bearing. Dynamic exciter for a radial direction (8) has an attachment point on the lever that connects guiding rods.

Loading Apparatus

Static loading

Static loading mechanism consist of a hydraulic actuator, force gauge and two spherical joints. The system is designed to provide loading force with a magnitude up to 10 kN. The applied force is sensed in a force gauge and during test cycle is maintained at a preset value. Spherical joints are used to avoid any unrequested off axis loading that would induce an additional loading both tested bearing and force gauge.

Dynamic loading

To meet a requirement for a relative high frequency loading the option of pneumatic linear vibrator K15 was selected. Parameters of vibrator are summarized in a Tab. 1. Tests will be designed to use only one vibrator at a time. Attachment points are prepared according to Fig. 2 on the lever that connects guiding rods and Fig. 3 on the front cover of tested bearing housing. The attachment is by a screw.

Tab. 1 Parameters of pneumatic linear vibrator

Operating pressure [bar]	Frequency [Hz]	Peak force [N]
2	75	28
4	93	59
6	110	83

CONCLUSION

A bearing experimental test rig was introduced in this paper. It is intended for testing of roller bearings under an oscillatory dynamic loading. Tested bearing is attached to the end of the center shaft. An innovative tested bearing housing was introduced, allowing its free motion (limited only by inserted bearing radial clearance) in an axis of loading and constrained in the other directions. Test rig is equipped by a static radial loading mechanism, which can induce a force up to 10 kN that is equivalent to 2 GPa of contact pressure on inner ring of tested bearing. Pneumatic linear vibrator with excitation frequency up to 100 Hz will be used for dynamic loading of bearings. It can be attached either to the bearing housing front cover in order to induce axial vibrations or to the lever that connects guiding rods to induce radial vibrations. Test rig will be equipped by sensor based on excitation and sensing of surface acoustic waves allowing detection of lubrication state during operation (Brückner et.al, 2015). Currently test rig design concept is in patent approval process (Patent application No. 2017-270, 2017)

REFERENCES

1. Dynybyl, V. (2009). Výkonová metrologie: Experimentální podpora vývoje a inovací mechanismů ve strojírenství (Vyd. 1. ed.). Praha: České vysoké učení technické v Praze.
2. Harris, T. A., & Kotzalas, M. N. (2006). Essential concepts of bearing technology. CRC press.
3. Brückner, C., Stich, S., & Behrens, J. M. (2015) Determination of a bearings operating conditions during the working process by means of BeMoS®.
4. Chmelař, Dynybyl. (2017) Patent application No. 2017-270, Industrial Property Office. Application date 16.05.2017.

.

Corresponding author: Ing. Jakub Chmelar, Dep. of Designing and Machine Components, FME, Czech Technical University in Prague, Technicka 4, Praha 6, Prague, 166 07, Czech Republic, phone: +420 737 866 916, e-mail: Jakub.Chmelar@fs.cvut.cz

ANALYTICAL BEARING MODEL FOR ANALYSIS OF INNER LOAD DISTRIBUTION AND ESTIMATION OF OPERATIONAL LUBRICATION REGIME

Jakub CHMELAŘ[1], Vojtěch DYNYBYL[2]

[1]Department of Designing and Machine Components, FME, CTU in Prague
[2]Department of Designing and Machine Components, FME, CTU in Prague

Abstract
A mathematical model of roller bearing is presented in this paper. Calculation of load distribution and displacement is based on current standard ISO/TS 16 281. Bearing operating lubrication regime analysis is involved. It is based on lambda parameter consisting of EHD layer thickness value that is calculated from equation for wide elliptical contact and a composite surface roughness value. Model was successfully verified against commercial KISSsoft software.

Key words: *Bearing, Roller Bearing; Lubrication; EHD; Bearing mathematical model.*

INTRODUCTION
Identification of bearing properties during operation is very important step for analysis and implementation. Since well-known classical engineering equations for calculation of bearing life does not provide a detail insight a demand for a more complex model arises. The complex model shall provide information about actual load distribution between rollers, which is based on internal geometry such as radial clearance or roller profile modification. Additionally information regarding lubrication quality based on lubricant rheological parameters, mating surface texture and operating conditions are of interest. Such model based on current theoretical findings is presented in this paper.

MATERIALS AND METHODS
Analysis of load distribution on rolling elements within the roller bearing was carried out using method described in standard (International Organizatipon for Standardization [ISO], 2008). For roller bearings, method assumes Hertz line contact. Calculated load distribution is valid for low to medium speeds and quasi-static loading. Dynamic effects such as centrifugal and inertial forces are neglected. Another as-sumption concerns the deformation of outer ring/race where stiff supporting structure is considered and calculated deformations are only within the area of contact. For presented analysis, unidirectional radial load with small moment load is applied.

Roller load distribution
Deflection of j-th rolling element was calculated from radial deflection or inner ring according to (1)

$$\delta_j = \delta_r \cos(\varphi_j) - \frac{s}{2} \tag{1}$$

Where s is a total operational radial clearance, usually obtained from catalogues and modified in order to cover its changes due to temperature deformations. Coordinate φj (rad) is an angular coordinate of j-th roller. For an analysis, roller was divided into 41 equally length laminas. This allows including a roller profile modification into calculation and load distribution over the roller. For current analysis, a logarithmic profile modification described as function of coordinate x_k (mm) from roller center was used (2). The modification is depicted on the Fig. 5.

$$P(x_k) = 0.00035 \cdot Dwe \cdot \ln\left[1/(1-(\frac{2 \cdot x_k}{Lwe})^2)\right] \tag{2}$$

The deformation of each lamina including roller profile modification is calculated according to (3). If the result is negative, zero substitutes it.

$$\delta_{jk} = \left\langle \delta_j + x_k \cdot \tan\psi_j - 2P(x_k) \right\rangle \tag{3}$$

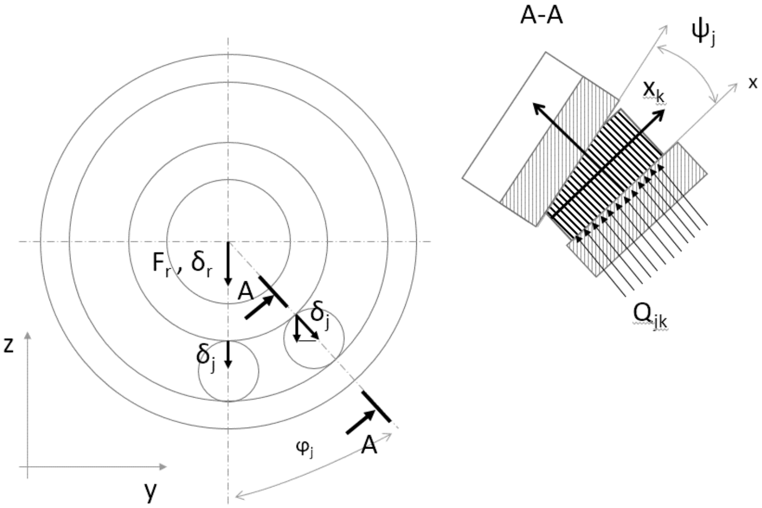

Fig. 1 Coordinates of bearing model (ISO, 2008)

Radial load F_r (N) and/or moment M_z (Nm) are supported by rolling elements. The fraction of load per lamina of each rolling element is calculated according to equation (4). In the analysis, rollers are substituted by 1D springs. Each spring has a stiffness covering the roller itself and its contacts with both races.

$$Q_{jk} = c_s \delta_{j,k}^{10/9} \tag{4}$$

The spring stiffness c_L distributed between laminas becomes c_s. For rollers and races made of steel c_L is expressed in eq. (5), where Lwe (mm) is length of body and n_s is number of laminas. Other possible values of c_L (N / mm) can be found in the literature (Harris & Kotzalas, 2006). Exact value for considered geometry and materials can be also obtained by means FEM analysis.

$$cs = \frac{c_L}{n_s} = \frac{35948 \cdot L_{WE}^{8/9}}{n_s} \tag{5}$$

Last step of an analysis is an iterative solution of static force and momentum equilibrium equations (6) and (7) for δ_r (mm) and ψ_j (rad) respectively.

$$Fr - cs \cdot \sum_{j=1}^{Z} \left(\cos(\varphi_J) \sum_{k=1}^{ns} \delta_{j,k}^{10/9} \right) = 0 \tag{6}$$

$$M_Z - cs \cdot \sum_{j=1}^{Z} \left(\cos(\varphi_J) \sum_{k=1}^{ns} x_k \cdot \delta_{j,k}^{10/9} \right) = 0 \tag{7}$$

Contact Pressure calculation

Contact pressure distribution on rollers was based on Hertz contact theory for line contact (Harris & Kotzalas, 2006). For each lamina and roller respectively, contact half width b (mm) and contact pressure P_{jk} (MPa) were calculated according to equations (8) and (9), where R and E are defined by eq. (14) and (15); w_s is length of lamina.

$$b_{jk} = \sqrt{\frac{8 \cdot (Q_{jk} / w_s) \cdot R_x}{\pi \cdot E'}} \tag{8}$$

$$P_{jk} = \frac{2 \cdot (Q_{jk} / w_s) \cdot R_x}{\pi \cdot b_{jk}} \tag{9}$$

Lubrication layer thickness

Minimal thickness of lubrication layer is calculated from equation (10) published by Dawson and Higginson. U, G and W are dimensionless groups; R_x (mm) is mutual curvature of bodies in contact, perpendicular to rolling direction. Radius Ry (mm) for roller bearing with profile modification could be estimated by circle curve fitting to profile modification. h0 (mm) is minimal lubrication layer thickness in contact (Wheeler, et al., 2016). Following equation is modified for wide elliptical contacts, where Rx / Ry > 3. From asymptotic analysis it could be proved, that the last bracket with exponent in (10) becomes 1 for Rx / Ry > 20

$$h_0 = 3.63 \cdot R_y \cdot \overline{U}^{0.68} \cdot \overline{G}^{0.49} \cdot \overline{W}^{-0.073} \cdot (1 - e^{-0.70(Rx/Ry)^{0.64}}) \tag{10}$$

Equation (10) was obtained by curve fitting of numerical solutions of Reynolds equation for elliptical contact in wide range of conditions. Presented form is modified for wide contacts with ellipticity parameter Rx / Ry > 2.5. For details, see (Wheeler, et al., 2016). Main assumptions for such equation are: model of smooth contact, fully flooded lubrication regime, contact pressure maintained below 2 GPa and isothermal conditions within lubrication layer. It also assumes Newtonian behavior of lubricant. Wheeler et. al found and described in study (Wheeler, et al., 2016), that such semi-analytical equation, tends to overestimate minimal lubrication layer thickness about a 6 % comparing to full numerical solution. Therefore, in the model, minimal thickness was reduced by 6 %. In addition, most semi-analytical equations tends to deviate in operational conditions where high loads and low speeds occurs. Therefore, it is necessary to pay attention when assessing a lubrication regimes laying in areas where transition from boundary lubrication to EHD comes about. For accurate results, full numerical solution of Reynolds equation is recommended (Wheeler, et al., 2016). The application of (10) for line contact is further limited to pure radial loading or very light off-axis moment loading that does not considerably influence the load distribution over the length of element. For one-sided skewed load distributions on the roller, lubrication layer height would have to be verified by complete numerical model of contact. Dimensionless groups used in equations consist of following parameters:

Speed parameters: $\overline{U} = \dfrac{U \cdot \eta_0}{E'R_y}$ (11)

Material parameters: $\overline{G} = \alpha^* \cdot E'$ (12)

Load parameters: $\overline{W} = \dfrac{W^{\backslash}}{E'R_y^2}$ (13)

R_x (mm) is mutual curvature of bodies in: $\dfrac{1}{R_y} = \dfrac{1}{R_{1y}} + \dfrac{1}{R_{2y}}$ (14)

E' (N/mm^2) is a mutual elastic modulus: $\dfrac{2}{E'} = \dfrac{1-\nu_1^2}{E_1} + \dfrac{1-\nu_2^2}{E_2}$ (15)

Where, η_0 is a lubricant dynamic viscosity at atmospheric pressure (MPa.s); α^* is a viscosity-pressure coefficient (1/MPa),

U is entraining speed of lubricant to the contact: $U = \dfrac{u_1 + u_2}{2}$ (mm/s) (16)

For roller bearing, with assumption of pure rolling, entraining speed could be calculated from kinematic analysis (Spikes, 2015). The cage/retainer revolution speed, the unknown, is subtracted from the rotation of inner and outer ring, so the rolling elements remain steady state and only rotate around their axis. This transformation allows writing two equations for roller peripheral speeds: at inner race and outer race. The unknown retainer speed is then removed by combination of equations and the peripheral speed of roller can be easily calculated. Entraining speed (16) is for roller bearing calculated acc.to (18)

$$U = \frac{R_i \omega_i}{2} \left(\frac{R_i + Dwe}{R_i + Dwe/2} \right) \tag{17}$$

Lambda parameter
Generally, in roller bearings, lubrication film thickness is of similar order as surface roughness. Therefore there is defined a lambda parameter, that compares minimal lubrication thickness to composite surface roughness. This is provided by equation (18), where s_x^2 is root mean square (RMS) value of roller and race surface roughness, h0 is minimal lubrication layer thickness calculated according to (10).The RMS value s_x can be estimated from Ra surface parameter as 1.25Ra.

$$\Lambda = \frac{h_0}{\sqrt{s_{race}^2 + s_{roller}^2}} \tag{18}$$

Based on extensive experimental research following values of lambda were found to correspond with lubrication regimes: $\Lambda < 1$ the load is supported mainly by surface asperities, both bodies are in direct contact, asperities are deformed, surfaces are loaded by shear stress if sliding occurs. For $1 < \Lambda < 3$ the mixed lubrication regime is present, meaning that applied load is yet partly supported by lubricant thin film, but still direct contact between bodies exist. When $\Lambda > 3$, the lubrication layer separates both contact bodies, the load is supported only by lubricant and local deformation of the bodies influence the lubrication layer thickness. The load is except minor traction shear mainly in normal direction (Harris & Kotzalas, 2006).

RESULTS AND DISCUSSION

Bearing model
The verification of bearing model was based on comparison results provided by software KISSsoft (KISSsoft, 2013) accompanied by a module for bearing calculation according to standard ISO (2008).

For a purpose of verification, a radial roller bearing N306 was used. The geometry is summarized in the **Tab 1**.

Tab. 1 Summary of N306 parameters

Parameter	Designation	Value	Dimension
Inner bore diameter	d	30	mm
Outer race diameter	D	72	mm
Width of bearing	B	19	mm
Number of rollers	Z	12	
Roller element diameter	Dwe	11	mm
Roller element active width	Lwe	11	mm
Inner ring race diameter	Di	43,5	mm
Radial internal clearance (SKF Group, 2013)	Pd	0,0325	mm
Basic dynamic load rating	C	58 500	N
Young modulus	E	210 000	N/mm^2
Poisson ratio	ν	0,3	

The verification of radial deflection and moment load was done for three radial load cases defined as P/C = 0,05; 0,1 and 0,2. Light moment loading was also applied, in order to have same load case as defined in KISSsoft for tested case. As you can see in Tab. 2 the deviation between radial deflection results obtained by the code implemented in this paper and the results obtained by KISSsoft was below 0.1 %. Similar situation is for misalignment assessment, where the error topped 6 %. The error might be introduced by different considered roller geometry in the KISSsoft calculation that would influence the angle.

Tab. 2 Bearing model verification – radial and angular displacement

P/C	Radial load [N]	Moment load [Nm]	Current model [μm]	KISSsoft [μm]	|Error| [%]	Current model [mrad]	KISSsoft [mrad]	|Error| [%]
0,05	2 925 N	0.05	28,226	28,222	0.015	0.017	0.017	0
0,1	5 850	0.13	34,73	34,731	0.003	0.032	0.034	6
0,2	11 700	0.35	45,198	45,203	0.011	0.066	0.069	4

Results of load distribution verification are stated in Tab. 3. Due to symmetrical loading of elements, only half of loaded elements were compared. Actual distribution is depicted in a Fig .2. Pressure distribution per lamina on the maximally loaded roller is depicted on the Fig. 3, numerical values of maximal pressure on inner race and outer race are evaluated in Tab. 4 and compared with results obtained from KISSsoft as verification. Absolute error indicates almost perfect fit.

Tab. 3 Bearing load distribution verification Load P/C=0.2

Roller #No	Current model [N]	KISSsoft [N]	|Error| [%]
5	576	577	0.17
6	3592	3590	0.05
7	4901	4905	0.08

Tab. 4 Max contact pressure verification Load P/C=0.2

Property	Current model [N/mm^2]	KISSsoft [μm]	|Error| [%]
Inner race	2140	2143	0.13
Outer race	1719	1721	0.12

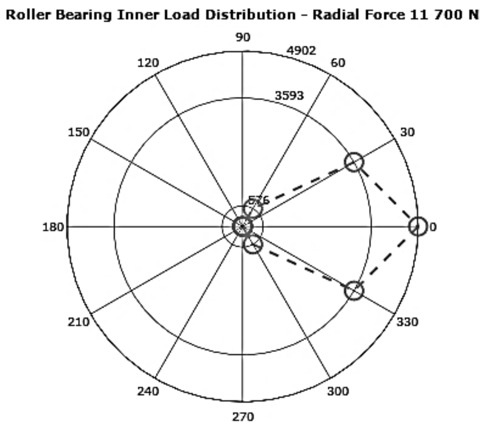

Fig. **2** Roller load distribution

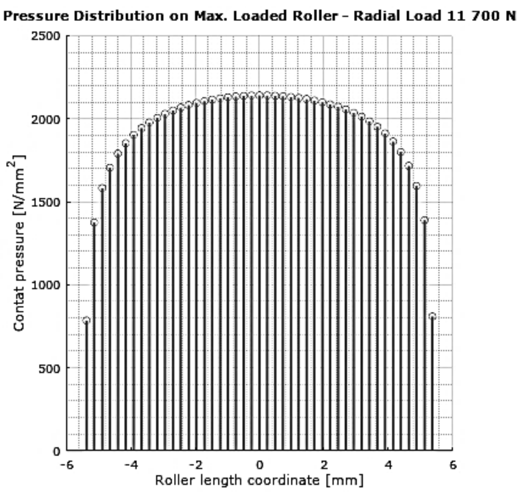

Fig. **3** Roller contact pressure distribution

Lubrication

Lambda parameter is calculated for every element – race contact. The result is graphically presented on the Fig.4. It is obvious, that less favourable lubrication conditions occur on the inner race contact, where lambda parameter for speed 2500 rpm indicates boundary lubrication $\Lambda = 2.2$. Lubrication regime on the outer race is analysed in the boundary regime too, but due to lighter loads, the lambda for most loaded element reaches $\Lambda = 2.8$.

Tab. 5 Summary of parameters used for lubrication calculation

Parameter	Designation	Value	
Lubricant dynamic viscosity at atm. pressure	η_0 (60°C)	32.10^{-9} (32)	MPa.s (cP)
Viscossity-pressure coefficient	α^* (60°C)	$17\ .10^{-3}$	MPa^{-1}
Race (inner / outer) surface roughness	Ra	0,08	μm
Roller surface roughness	Ra	0,03	μm
Equivalent radius of profile modification	Ry	1414	mm
Bearing inner race speed	n	2500	rpm

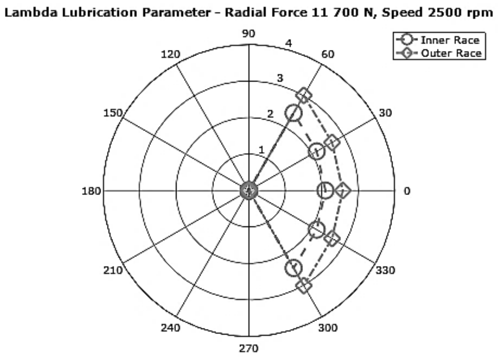

Fig. 4 Lambda parameter distribution

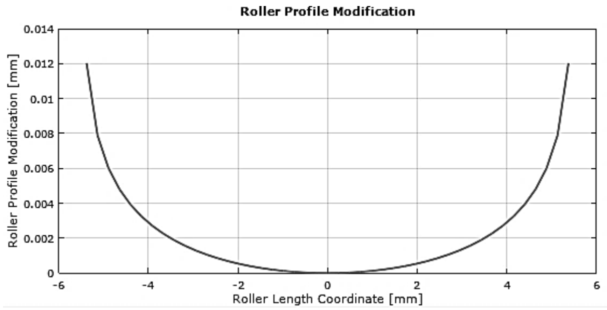

Fig. 5 Roller profile modification

CONCLUSIONS

Paper presents a mathematical model of a roller element bearing based on a method described in the standard (ISO, 2008) extended by calculation of lubrication layer thickness for every loaded element. Model calculates load distribution on rollers, contact pressure distribution on the roller. It is possible to apply a radial and moment load. Model was successfully verified against commercial CAE software KISSsoft. Lubrication is calculated according to semi-analytic equation for wide elliptical contact presented by Hamrock and Dowson (10). Lambda parameter (18) for estimation of lubrication regime by comparing lubrication layer thickness with surface composite roughness is calculated and results are presented as polar figure Fig 4. Lubrication calculation is limited by symmetrical load distribution on the roller element. Presented model will be further extended to cover other operating conditions.

REFERENCES

1. International Organizatipon for Standardization. (2008). Rolling bearings – Methods for calculating the modified reference rating life for universally loaded bearings (ISO/TS 16281:2008).
2. Harris, T. A., & Kotzalas, M. N. (2006). Essential concepts of bearing technology. CRC press.
3. Wheeler, J. D., Vergne, P., Fillot, N., & Philippon, D. (2016). On the relevance of analytical film thickness EHD equations for isothermal point contacts: Qualitative or quantitative predictions?. Friction, 4(4), 369.
4. Spikes, H. (2015). Basics of EHL for practical application. Lubrication Science, 27(1), 45-67.
5. KISSsoft, A. G. (2013). KISSSoft Release 03/2013 User Manual. Bubikon, Switzerland.
6. SKF Group, (2013) Rolling Bearings, Catalogue, S. G.. PUB BU/P1 10000/2 EN. SKF.

Corresponding author: Ing. Jakub Chmelar, Dep. of Designing and Machine Components, FME, Czech Technical University in Prague, Technicka 4, Praha 6, Prague, 166 07, Czech Republic, phone: +420 737 866 916, e-mail: Jakub.Chmelar@fs.cvut.cz

EXPERIMENTAL METHODS WITH STRAIN GAUGES FOR STUDY PURPOSES

Lukáš JANČAR[1], Václav MOSLER[2], Zdeněk FOLTA[3]

[1]VŠB – Technical University of Ostrava, Czech Republic, e-mail: Lukas.jancar.st@vsb.cz
[2]VŠB – Technical University of Ostrava, Czech Republic, e-mail: vaclav.mosler.st@vsb.cz
[3]VŠB – Technical University of Ostrava, Czech Republic, e-mail: zdenek.folta@vsb.cz

Abstract
Article deals with preparation of technical experiment for study purposes, where students can get to know strain gauges basics. Especially it deals with mechanical and thermal properties, reinforcement and linearity of strain gauges.

Key words: *Strain gauges; Technical experiment; Study.*

INTRODUCTION

During teaching of the lectures Technical experiment (Machine parts and mechanisms department - doc. Ing. Zdeněk Folta, 2015) a request to create practical stand for students was made. The stand should serve as a place to realistically verify the properties of strain gauges in the form of an experiment. There was no already existing stand with sufficient properties found on the market, so it was necessary to design it out of the scratch. The new stand was created with emphasis on easy and smart use, clear to students, and with use of the present standard software and ways of measurement (Mádr, 1991). The aim of the article is to show the concrete technical solution of the stand and how it can be used.

MATERIALS AND METHODS

The goal of the exercise at the proposed workplace is to verify the theoretical knowledge of the properties of strain gauges, namely: linearity, temperature dependence and amplification in various combinations (Škopán & Mynář, 1989). The workspace consists of 7 beams fixed to the structure as shown in Fig. 1. Each beam is provided with one or two strain gauges of different characteristics and a connector for connecting a measuring card, as is shown in Fig. 2. Resistive paper, resistive foil and semiconductor strain gauges are used. The beams have the same shape and are equipped with a set of holes for hanging the weights. Beams are made of various materials, steels 11 373 and 17 421 are used. The output of the measured beam is evaluated using the Mikrotechna M1000 device and LabView software.

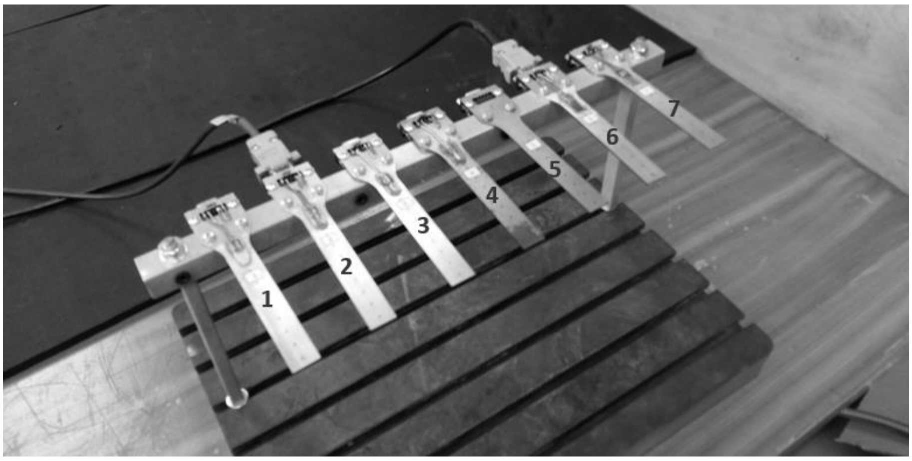

Fig. 1 Created experimental stand

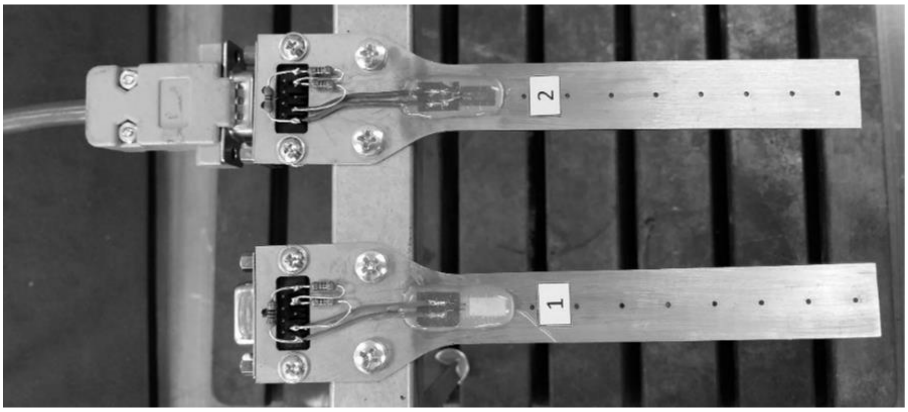

Fig. 2 Location of the strain gauge and its connection

The practice on the stand itself consists of several parts. The first is to determine the bending stress theoretically and practically. One of the holes in one of the beams hangs the metal cylinder of the defined weight and the output voltage U_m is measured, from which the bending stress in the strain gauge location is calculated according to the formula (1). Then the theoretical calculation of the bending stress according to the formula (2) is performed and the two results are compared. The result is to determine what is causing the measurement mismatch and finding unreliable values.

$$\sigma = \frac{4 \cdot U_m \cdot C \cdot E}{k \cdot n \cdot A \cdot p \cdot 1000} \; [MPa] \tag{1}$$

$$\sigma_o = \frac{M_o}{W_o} \; [MPa] \tag{2}$$

The second part of the measurement is the determination of the strain gauge linearity. Three beams are compared, one of which is fitted with a paper resistive strain gauge, a second with foil resistive gauge and a third with semiconductor strain gauge. The weight is gradually suspended in the holes in the beams and the signal strength and the bending moment are determined. The result is evaluation of dependence between bending moment and signal and its linearity. In Fig. 3 is a graphical representation of the signal running by gradually suspending the weight into all the holes of the beam fitted with a semiconductor strain gauge.

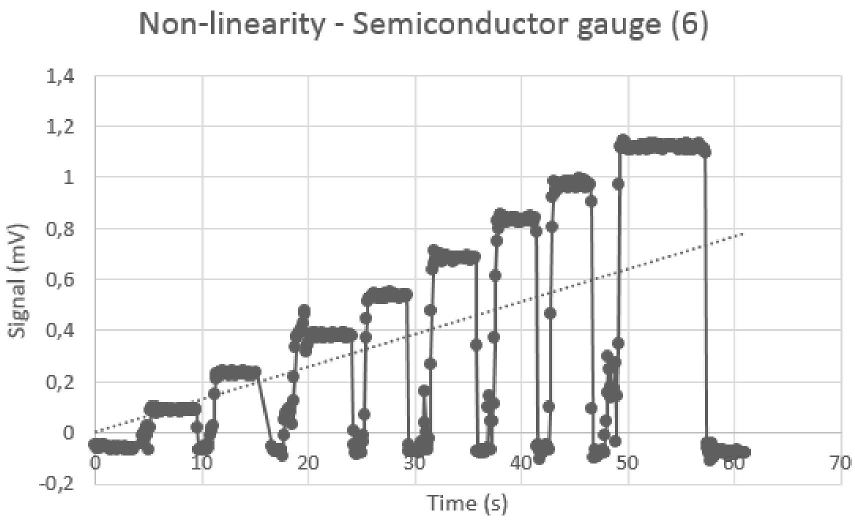

Fig. 3 Signal running - semiconductor gauge

In the third part, students have the opportunity to try amplifying the signal with a strain gauge bridge. The values measured on the beam with one active strain gauge added to the bridge by three resistors and a beam with two active strain gauges are compared. The fourth part deals with the determination of the modulus of elasticity of beam materials. It is measured on two beams fitted with the same strain gauges, one of which is made of structural steel, the other is of stainless steel. From the measured value of the signal, the modulus of elasticity of both beams is calculated from the formula (1) and the magnitudes of the signals can be compared for identical strain gauge connection, but other beam material. The last part of the measurement demonstrates the temperature dependence of different types of strain gauges with and without thermal compensation, it means when using only one or a two strain gauges in the bridge. Measurement is carried out similarly as in the previous steps, only artificially increasing the temperature of the strain gauge by heating to about 40 ° C. This is achieved by warming the strain gauge with warm air. The resulting values are tentative, but they can illustrate the temperature dependence of both types of strain gauges connection. The resulting signal waveform during warming and start of back cooling is shown in Fig. 1 (paper resistive strain gauge), Fig. 2 (foil resistive strain gauge) and Fig. 3 (two foil resistive strain gauges in the bridge).

RESULTS AND DISCUSSION

The stand described above allows to students get to know with strain gauges properties in a practical way, to understand connection options and calculation of physical values, like strain, force or deformation.

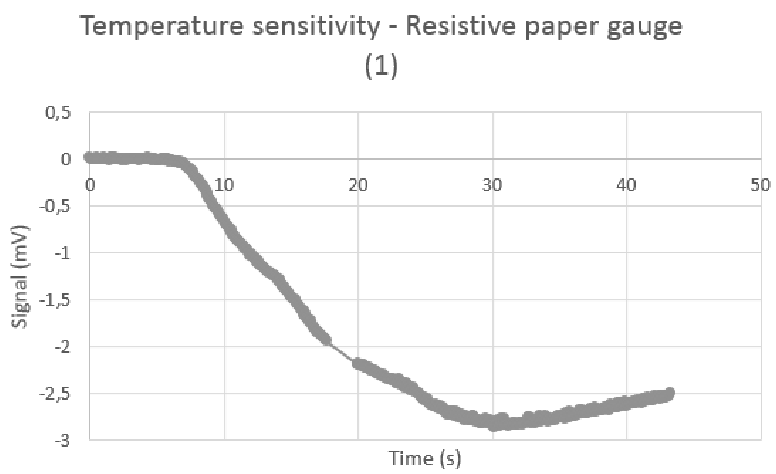

Fig. 4 Temperature sensitivity for resistive paper gauge

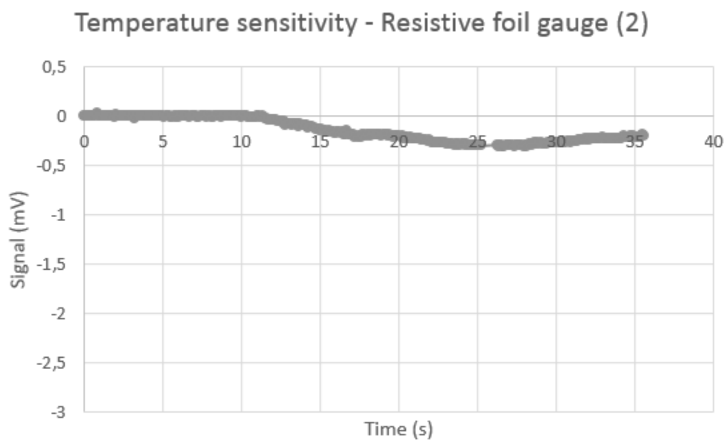

Fig. 5 Temperature sensitivity for resistive foil gauge

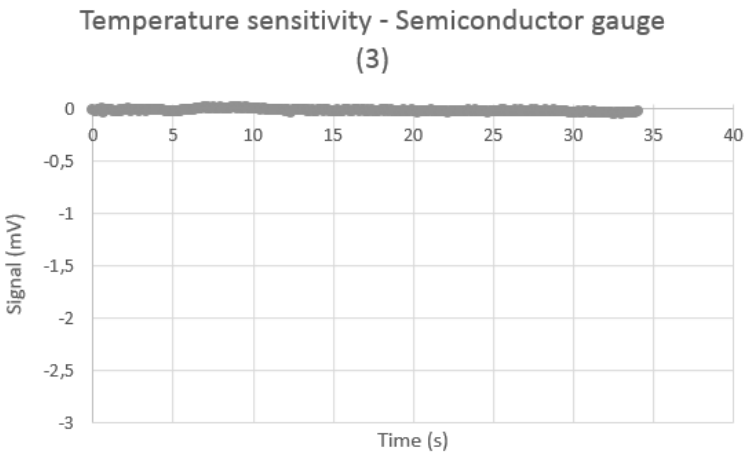

Fig. 6 Temperature sensitivity for semiconductor gauge

CONCLUSIONS

The benefits of creating the stand are mainly better understanding of the subject being taught, the ability to get in touch with individual elements used in the measurement, and to see a particular engagement with one's own eyes. It is also a great benefit for students to try working with measuring devices and applying acquired knowledge on a particular real experiment. The stand itself is not a discovery, but the application of the measuring methods used today (Olmi, 2015) to a compact test stand. Experiment uses current measurement sensors and evaluation techniques (Janíček, 1989).

REFERENCES

1. Janíček, P. (1989). *Technical experiment.* Brno: VUT.
2. Mádr, V. et al. (1991). *Physical measurement.* Prague: SNTL.
3. Machine parts and mechanisms department - doc. Ing. Zdeněk Folta, P. (2015). *Experimental methods in field: Lectures.* Ostrava: VŠB - TU Ostrava.
4. Olmi, G. (2015). *Load Cell Training for the Students of Experimental Stress Analysis.* Exp Techniques. doi:10.1111/ext.12175.
5. Škopán, M., & Mynář, B. (1989). *Experimental methods and machine testing.* Brno: VUT.

Corresponding author:
Ing. Lukáš Jančar, Department of Machine Parts and Mechanisms, Faculty of Mechanical Engineering, VŠB – Technical University of Ostrava, 17. listopadu 15/2172, Ostrava - Poruba, 70833, Czech Republic, phone: +420 597 324 313, e-mail: lukas.jancar.st@vsb.cz

THE METHODS OF PREPARING PETROLEUM - DERIVED WASTE TO BURN IN MARINE BOILERS

Robert JASIEWICZ[1]

[1]*Martime University of Szczecin, Poland*

Abstract

The paper presents a valuation of the potential use of petroleum - derived waste of various physical and chemical properties as well as morphology as fuel for oil - fired ship boilers. In order to use, as boiler fuel, petroleum - derived waste from various sources at a ship, it is necessary to prepare the waste ensuring that its morphology will enable proper combustion and atomization. Petroleum - derived waste has been a subject of treatment process on a real object.

The morphology was changed by means of a process of gravitational sedimentation, and static and dynamic homogenization. Then, the changes of the fluid structure were analyzed for individual treatment methods and for serial connection of homogenizers (static and dynamic). In order to determine how waste sedimentation and homogenization process conditions affect its morphology, the physical and chemical properties of same were measured. The application of the joint above mentioned methods for waste treatment resulted in the improvement of the atomization and combustion processes in the boilers, petroleum – derived waste utilization due to which the energy included therein may be recovered. Another result is the mitigation of environment pollution and the reduction of standard fuel consumption.

Key words: *petroleum - derived waste, morphology, homogenization, physical and chemical properties*

INTRODUCTION

The pursuit of cost reductions in shipping has caused the development of ship engines adjusted to burning fuel waste of inferior physical – chemical composition. The fuels, owning to their higher viscosity, density, and more mineral and catalytic contaminations must be subjected to a proper preparation process in order to be burnt in ship engines. The petroleum - derived waste is as a result of technological processes, operating of engine rooms and cleansing among others of marine fuel oils and lubricating oils.

The waste is a large operational problem for ship crews, in particular, with the regards to the methods of storage, treatment, utilization. The petroleum - derived waste is also a threat to the environment.

MARPOL 73/78 Convention is the basic legal act concerned with the problem of pollution of seas by the shipsand determine technical guidelines and recommendations related with i.e. the management of petroleum pollutants. According to the applicable recommendations of MARPOL Convention 73/78 the methods for waste oil management are as follows:

- storing generated waste oil in dedicated tanks on ships, its dehydration and discharge ashore in ports or specialised receiving units,
- waste oil utilisation in ship incinerators,
- energetic utilization in marine boilers (*MARPOL, 2011; Szczepanek, Kamiński, 2013*).

One of the ways to dispose of petroleum - derived waste recommended by MARPOL Convention 73/78 is to burn the waste in marine boilers. This method creates an opportunity to manage the waste and to mitigate environment pollution as well as use its chemical energy for own use, leaving a favorable effect in the form of the reduction of fuel consumption by an oil-fired boiler.

In order to use, as boiler fuel, petroleum - derived waste it is necessary to prepare the waste ensuring that its morphology will enable proper combustion and atomization.

The petroleum - derived waste morphology shall be defined as a structure consisting of a continuous phase, solid particles in the form of asphaltene and resin conglomerates and water. The petroleum - derived waste contains a lot of water and asphaltenes and resinous agglomerates dimensions, therefore the burning velocity of the petroleum - derived waste is slower and changeable in proportion to fluid flammable particles (*Jasiewicz, 2013; Rajewski, Balcerski, 1996*). The burning process of petroleum - derived waste can be improved by homogenization and size reduction of asphaltene- resinous particles with water, which result in smaller particles of 5 – 30 μm and their uniform diffusion throughout the fuel volume . Such a preparation of oil waste creates emulsion boosts burning process thanks to greater evaporation and better mixing with air (*Behrendt, Jasiewicz, 2015; Rajewski, Balcerski, 1996*).

MATERIALS AND METHODS

In order to determine how waste sedimentation and homogenization process conditions affect its morphology, the physical and chemical properties of same were measured. Carried out also a dimensional analysis of the distribution of both the asphaltene and resin particles. For that purpose an analysis of the particle size distribution of insoluble particles in n-heptane has been made by means of laser diffraction using Mastersizer 2000 (Malvern Instruments) analyser. by laser diffraction method and water droplets diameter by microscopic image analysis. All the research was carried out in the Fuel Research, Hydraulic Fluids and Environmental Protection Centre of the Maritime University of Szczecin.

RESULTS AND DISCUSSION

The petroleum - derived waste can be described as a compound structure of 3 elements: fuel, water and proper waste. Depending on the source, oil waste is a mixture of various fuels and oils of different physical-chemical properties, high water intensity and a great amount of impurities. Dispersed phase is composed of poliparticle hydrocarbons of a high ratio C:H, huge agglomerates of asphaltene – resinous (100 – 200 μm in diameter), tar, paraffin, coke and ash particles (from the final refining process), also inorganic impurities, such as: sand, rust particles, sludge and thick – drop water or water from a separate phase (*Behrendt, Jasiewicz, 2015; Jasiewicz, 2013; Rajewski, Balcerski, 1996*).

Table 1 contains selected physical-chemical properties of examples petroleum - derived waste.

Tab. 1. Selected physical-chemical properties of examples petroleum - derived waste

Physico-chemical properties	**Unit**	**Petroleum - derived waste number**					
		1	2	3	4	5	6
Density at 15^0C	kg/m^3	950	895	970	875	901	921
Kinematic viscosity at 50 ^{0}C	mm^2/s	53.6	15	89	7	11.2	28,7
Water content	% mass	18	5	2,4	0.5	10.8	16
Flash point	^{0}C	103	75	120	73	94	112

The analysis of physical-chemical properties of selected petroleum - derived waste proved that the waste comes from various sources and has a wide range of physical – chemical properties such as: density, viscosity, water content and flash point. Consequently, in the tank there is a mixture of fuel of different properties, huge water amount and a lot of solid impurities. Figure 1 presents the selected microscope photographs of the waste oil morphology from various sources, marked with sample numbers according to table 1.

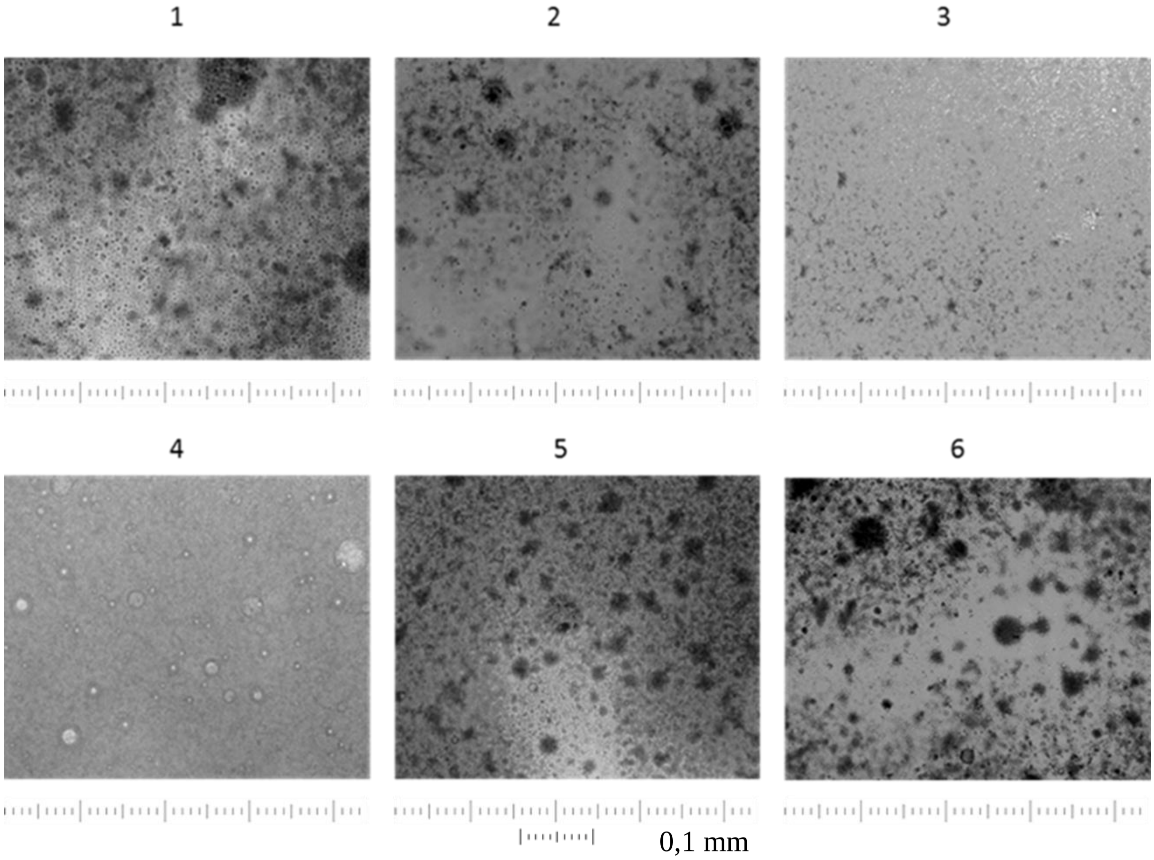

Fig.1. The petroleum - derived waste morphology from various sources, [own elaboration]

After the analysis of the asphaltene-resinous partitions for particular waste it was observed that the waste contained the largest number of pollution partitions of the diameter in the range from 63 μm to 300 μm. The analysis of the petroleum - derived waste microscope photographs presented in figure 1 shows that the water drop distribution is in the range from 10 μm to 400 μm. The water volume and the dispersion degree is variable along with following receipts of waste from different sources.

The experimental research is aimed at defining the impact of the previously mentioned homogenizing devices on the oil waste structure, particularly on the uniformity of the structure, and on the size – reducing of solid impurities in the form of asphaltene – resinous, and on the possibility of producing fuel – water emulsion. For that purpose an analysis of the particle size distribution of insoluble particles in n-heptane has been made by means of laser diffraction using Mastersizer 2000 (Malvern Instruments) analyser.

The analysis comprises four stages of the oil waste preparation for burning process:

- particle size distribution from the petroleum - derived waste sample accumulated in the oil waste tank (gravitational sedimentation),
- particle size distribution from the petroleum - derived waste sample subjected to homogenization process using the homogenising shredder pump (dynamic homogenizer),
- particle size distribution from the oil waste sample subjected to homogenization process using static homogeniser,
- particle size distribution from the oil waste sample subjected to homogenization process using homogenising shredder pump and static homogeniser working in serial system.

The measuring range of device goes from 0,02 to 2000 μm. Due to the application of Fraunhofer and Mie theories in the results analysis, the device complies with ISO 13320 norm pertaining to the analysis of particle size by means of laser diffraction method (*Malvern Instruments Ltd., 2007*). The figure 2,3,4,5 shows the distribution of size of particles insoluble in n-heptane for example of petroleum - derived waste sample for respective processes of preparing oil waste to burn in boiler on a vessel.

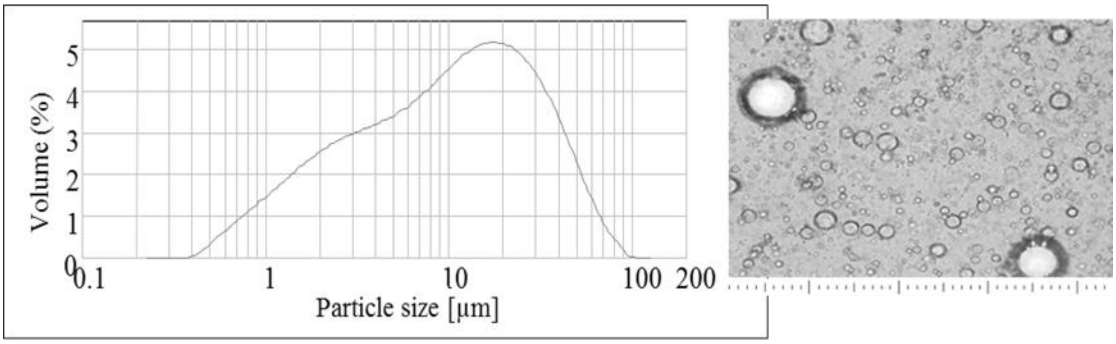

Fig.2. Particle size distribution from petroleum - derived waste sample accumulated in the oil waste tank (gravitational sedimentation)

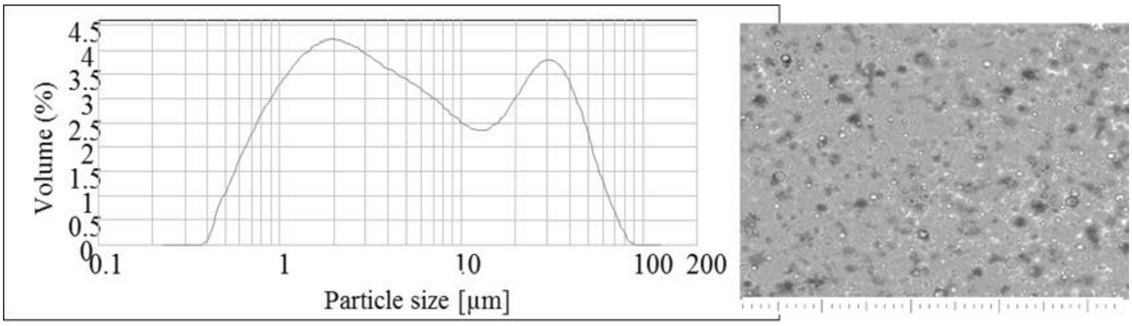

Fig.3. Particle size distribution from petroleum - derived waste sample subjected to homogenization process using homogenising shredder pump

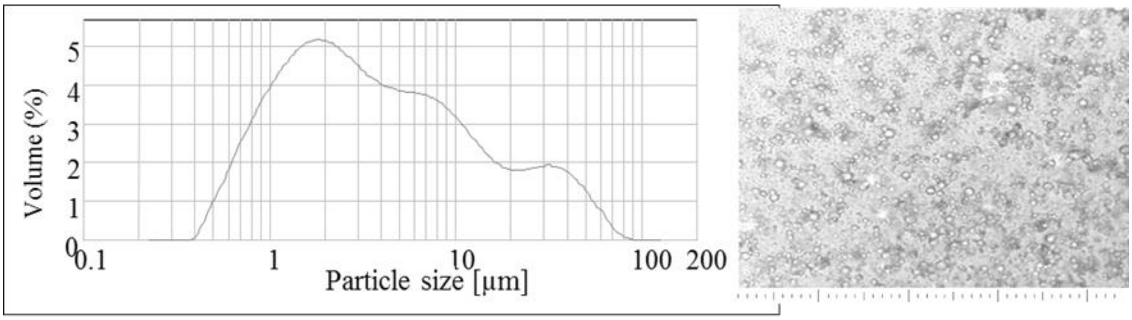

Fig.4. Particle size distribution from petroleum - derived waste sample subjected to homogenization process using static homogeniser

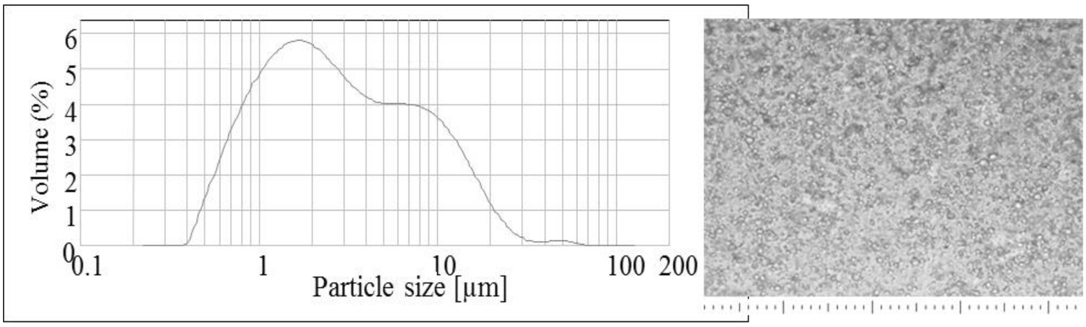

Fig.5. Particle size distribution from petroleum - derived waste sample subjected to homogenization process using homogenising shredder pump and static homogeniser working in a serial system

The application of series arrangement (homogenising shredder pump and static homogeniser) in the petroleum - derived waste preparation process for burning, has the highest impact on the structural change of the waste compared to a single device use.

The table 2 shows the statistics parameters of the particle size distribution for respective processes of preparing of sample petroleum - derived waste to burn in boiler. The statistics of the distribution are calculated from the results using the derived diameters D [m,n] - an internationally agreed method of defining the mean and other moments of particle size, whenD(v, 0.5) is the size in microns at which 50% of the sample is smaller and 50% is larger. This value is also known as the Mass Median Diameter (MMD), D(v, 0.1) is the size of particle below which 10% of the sample lies, D(v, 0.9) gives a size of particle below which 90% of the sample lies, D[3,2] is the surface area mean diameter. This is also known as the Sauter mean (*Horiba Scientific, 2012*; *Malvern Instruments Ltd., 2007*).

Tab.2. The statistics parameters of the particle size distribution for respective processes of preparing petroleum - derived waste sample to burn in boiler

Parameter	**Gravitational sedimentation**	**Homogenizing shredder pump**	**Static homogenizer**	**Series arrangement**
D(0.1) [μm]	1.619	0.962	0.925	0.832
D(0.5) [μm]	10.432	4.708	3.414	2.627
D(0.9) [μm]	37.550	36.306	25.169	11.740
D[3.2] [μm]	4.359	2.566	2.554	1.909
D[4.3] [μm]	15.619	12.378	8.590	4.834

The figure 2 and table 2 shows the changes of the petroleum - derived waste morphology when subjected to homogenizing devices operating alone or in line. The statistics parameters of the particle size distribution changes, table 2 shows size - reducing of asphaltene – resinous conglomerates for respective processes of preparing petroleum - derived waste to burn in boiler. The series arrangement brings about crushing of asphaltene – resinous conglomerates to 2 -11 μm dimensions and produces fuel – water emulsion, thus improving the burning process in the boiler.

As a result of comparing those process, one can conclude that the combination of gravitational sedimentation, the homogenising shredder pump and static homogeniser provides the best homogeneous structure of petroleum - derived waste.

CONCLUSIONS

The petroleum - derived waste comes from various sources and has a wide range of physical–chemical properties such as: density, viscosity, water content. The morphology of petroleum - derived waste from different sources is variable. In order to use, as boiler fuel, the petroleum - derived waste from various sources at a ship, it is necessary to prepare the waste ensuring that its morphology will enable proper combustion and atomization. The petroleum - derived waste homogenization by using homogenizing equipment, impacts its morphology change.

The application of series arrangement (homogenising shredder pump and static homogeniser) in the oil waste preparation process for burning, has the highest impact on the morphology change of the waste compared to a single device use. The petroleum - derived waste which underwent homogenization by means of static homogenizer are more homogeneous than the homogenising shredder pump. The application of series arrangement homogenising shredder pump and static homogeniser with the gravitational sedimentation in the oil waste preparation process for burning, has the highest impact on the morphology change of the waste compared to a single device use.

This method creates an opportunity to manage the waste and to mitigate environment pollution as well as use its chemical energy for own use, leaving a favorable effect in the form of the reduction of fuel consumption by an oil-fired boiler.

ACKNOWLEDGMENT

This research outcome has been achieved under the research project No 2/S/IESO/ 2014 financed from a subsidy of the Polish Ministry of Science and Higher Education for statutory activities of the Maritime University of Szczecin.

REFERENCES

1. Behrendt C. Jasiewicz R. (2015). Specification of waste oil generated at ships in terms of its use as fuel. *Logistyka*. nr 3, CD 1 pp. 1928-1935
2. Horiba Scientific (2012) . A guidebook to particle size analysis. *HORIBA Instruments, Inc*. USA
3. Jasiewicz R. (2013). The influence of oil waste homogenizing on its morphology to improve burning conditions in marine auxiliary boilers. *Scientific Journals Maritime University of Szczecin*. 36(108) z. 2 pp. 51–55
4. MARPOL (2011) Consolidated edition 2011. *IMO*. London, United Kingdom
5. Malvern Instruments Ltd. (2007). Mastersizer 2000 Essentials. User Manual. United Kingdom. Chapter 6, Page 5-4 to 5-6.
6. Rajewski P, Balcerski A (1996). Problems of management of oil-treatment sludge produced at operation of modern marine power plants. *International Conference. Analysis and utilisation of oily wastes. Auzo'96*. Gdańsk, Poland pp.278-282
7. Szczepanek M, Kamiński W. (2013). Risk analysis of sea environmental pollution by used lubricanting and hydraulic oils i the Baltic Sea fishing fleet. *Contrbition on the Theroy of Fishing Gears an Related Marine System*

Corresponding author:
Ing. Robert Jasiewicz, Ph.D., Department of Marine Machinery and Equipment, Institute of Marine Propulsion Plants Operation, Faculty of Marine Engineering, Maritime University of Szczecin, ul. Wały Chrobrego 1-2, 70-500 Szczecin, Poland, + 48 91 48 09 521, e-mail: r.jasiewicz@am.szczecin.pl

58th ICMD 2017
6 - 8 September 2017, Prague, Czech Republic

THE EFFECTS OF THE WRONG LUBRICATION METHOD OF THE GEAR TRAIN

Květoslav KALÁB[1]

[1]Department of Machine Parts and Mechanisms, Faculty of Mechanical Engineering, VŠB-Technical University of Ostrava, Czech Republic.

Abstract
In the article it is presented the remanufactured gearbox of the ball mill drive in the cement works. The first stage of the gearbox gear trains is wrong lubricated in operation. And the consequences of this error in lubricating are shown and analyzed in the article.

Key words: *lubrication, gear train, pitting, bearing.*

INTRODUCTION
In the framework of the raw material mill exchange in the cement plant was purchased the remanufactured gearbox TS with output of 800 [kW] and rated gear ratio of 6.3. It was the older gearbox, widely deployed in the Czechoslovak industry in the 1970s and 1980s. Repairs to the gearbox included replacement of shafts, covers, bearings, seals, new gear and bearing lubrication, and more.The gearbox in question is shown in Fig. 1.

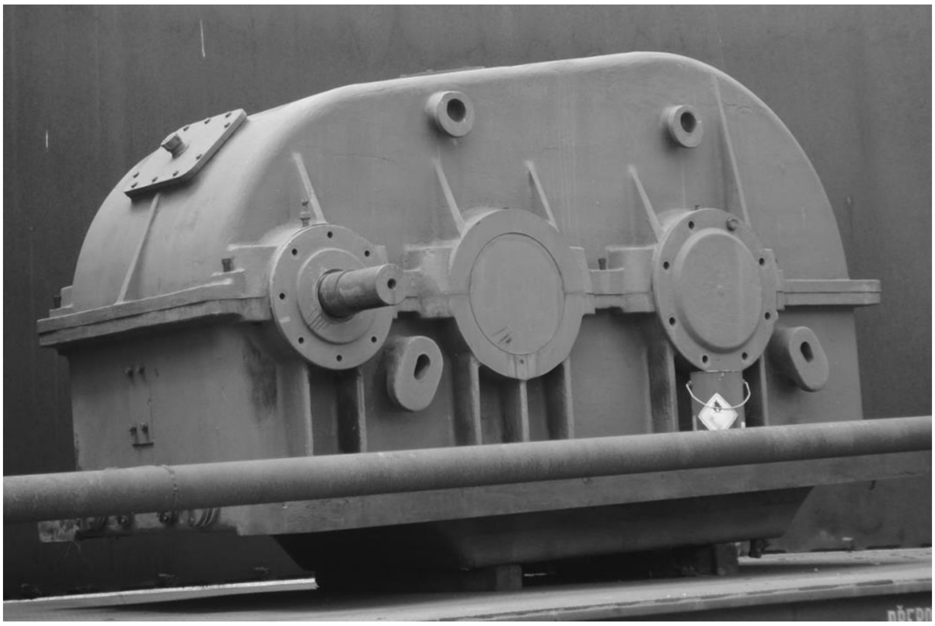

Fig. 1 Gearbox TS before repassing

MATERIALS AND METHODS
The gearbox repairs concerned the complete disassembly, pressing out shafts, removing rust from all parts, the repair of the shafts and the lids, the complete replacement of the bearings, the seals and the fasteners, machining dividing plane, machining bearing seats in the gearbox, design a new way of the lubrication of the first stage of the gear trains - circulation-system (the second stage of the gear trains is oil-bath lubricated), the restoration of the interior and exterior coats of the case body, coating and conservation, the complete assembly and testing (pressure test and run), as shown in the Fig. 2,3,4.

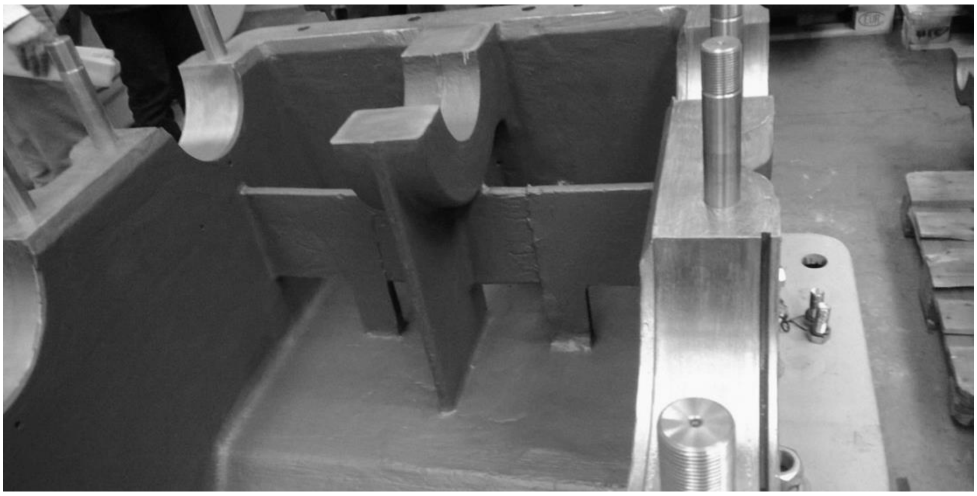

Fig. 2 Gearbox after repassing

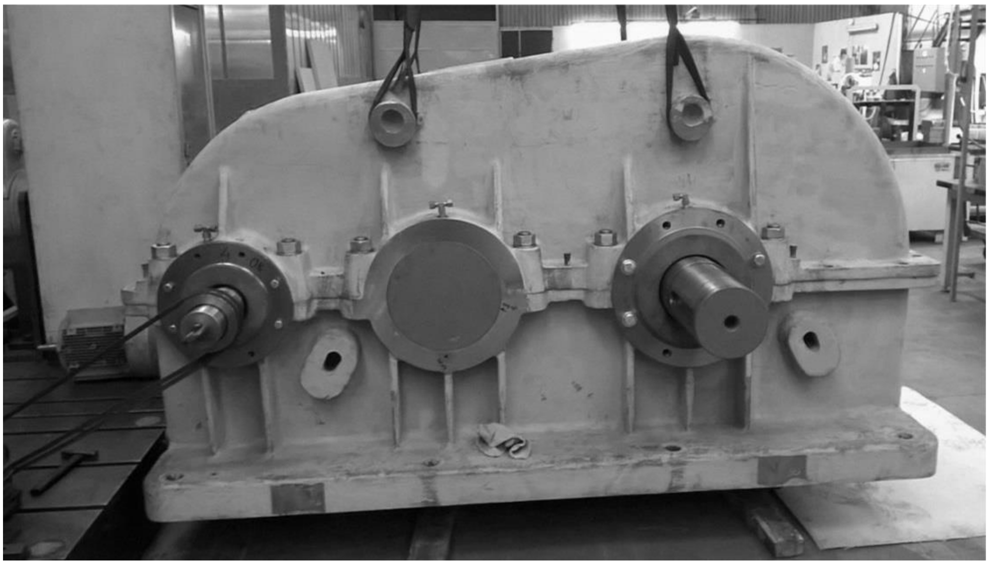

Fig. 3 Gearbox testing

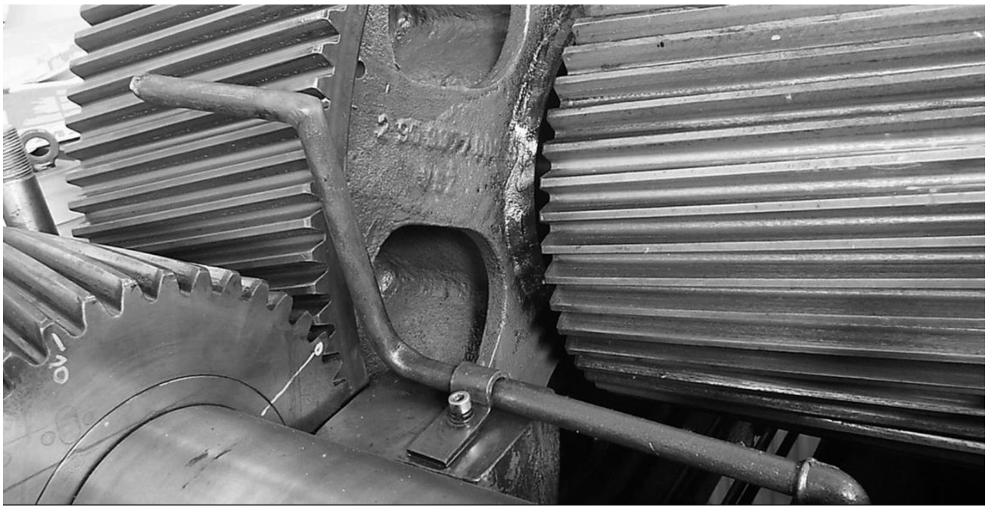

Fig. 4 Forced lubrication of the first stage of the gear trains

RESULTS AND DISCUSSION

Installation of the gearbox into the ball mill drive in cement works is shown in the Fig. 5. The gearbox was operated in the opposite direction of rotation. The lubricant was pushed out of the first stage of the gear trains and sprayed on the viewing window as shown in the Fig. 6 and Fig.7

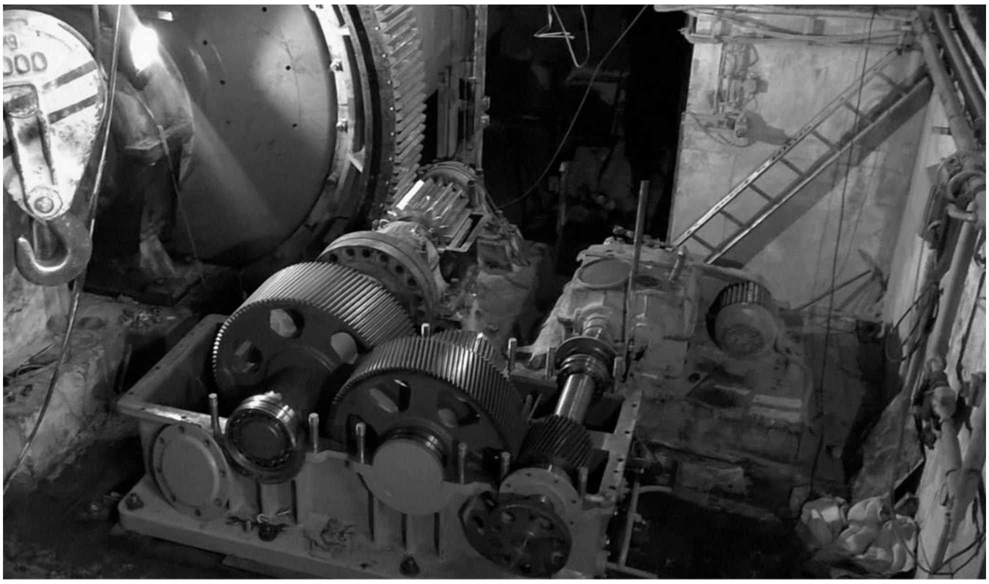

Fig. 5 Installation of the gearbox

Fig. 6 Splash lubrication with the opposite direction of rotation

Fig. 7 Viewing window sprayed with the grease

Due to the wrong lubrication of the gear, a pitting gear was formed, which caused considerable vibration. During operation, the gear unit in question was monitored and diagnosed each month. Diagnostic measured data of the vibrations and bearing condition are presented in Tab. 1,2,3.

Fig. 8 Pitting gear

Tab. 1 Envelope Vibration Acceleration ENV [gE], 500-10 kHz filter

Measurement number	ENV3	ENV4	ENV5	ENV6
1	14,95	13,1	4,94	4,93
2	15,82	10,17	10,91	6,59
3	**20,83**	14,28	12,56	7,83
4	**20,82**	14,13	8,74	5,64
5	**24,14**	17,75	11,34	10,22
6	**26,66**	13,04	13,63	7,63
7	**26,05**	18,02	13,59	10,72
8	**43,21**	**30,62**	19,71	13,79
9	**60,35**	**42,28**	**28,54**	18,81

Tab. 2 Effective value of vibration speeds in axial direction [mm/s]

M.n.	Prv3A	Prv4A	Prv5A	Prv6A	Prv7A	Prv8A
1	3,41	3,64	4,20	4,13	4,12	4,29
2	4,47	4,44	7,93	5,59	5,84	4,58
3	6,31	4,26	8,89	7,72	9,42	7,24
4	5,69	4,70	9,94	9,54	12,64	8,30
5	6,62	4,83	10,16	7,32	11,33	8,91
6	7,91	6,43	11,43	8,74	8,74	9,69
7	7,34	5,94	10,65	9,46	9,21	6,95
8	7,30	7,40	9,61	8,97	11,75	8,92

Tab. 3 Effective value of vibration speeds in vertical direction [mm/s]

M.n.	Prv3V	Prv4V	Prv5V	Prv6V	Prv7V	Prv8V
1	4,99	4,30	4,13	3,24	3,77	4,29
2	5,49	4,82	8,37	3,50	3,86	4,67
3	6,25	5,33	5,82	5,90	4,81	4,86
4	6,73	5,63	6,55	6,25	4,78	5,46
5	7,21	5,55	8,03	7,59	4,19	4,99
6	9,07	7,29	9,64	7,21	4,63	5,65
7	10,50	7,83	9,76	7,53	7,05	7,65
8	10,69	9,44	10,11	8,03	7,10	6,67

CONCLUSIONS

Measured data shows the progress of bearing damage and transmission. The condition of bearings and gearboxes was rated according to ČSN ISO 10816-1. The evaluations are summarized in the Tab. 4,5.

Tab. 4 Classification of bearing conditions according to ČSN ISO 10816-1

Measurement number	Bearing condition
1	acceptable
2	acceptable
3	unacceptable
4	unacceptable
5	unacceptable
6	unacceptable
7	unacceptable
8	unacceptable
9	unacceptable

Tab. 5 Classification of gearbox vibration conditions according to ČSN ISO 10816-1

Measurement number	Gearbox vibration condition
1	satisfactory
2	satisfactory
3	satisfactory
4	unacceptable
5	unacceptable
6	unacceptable
7	unacceptable
8	unacceptable

Damaged input shaft bearing on the engine side is shown in Fig. 9

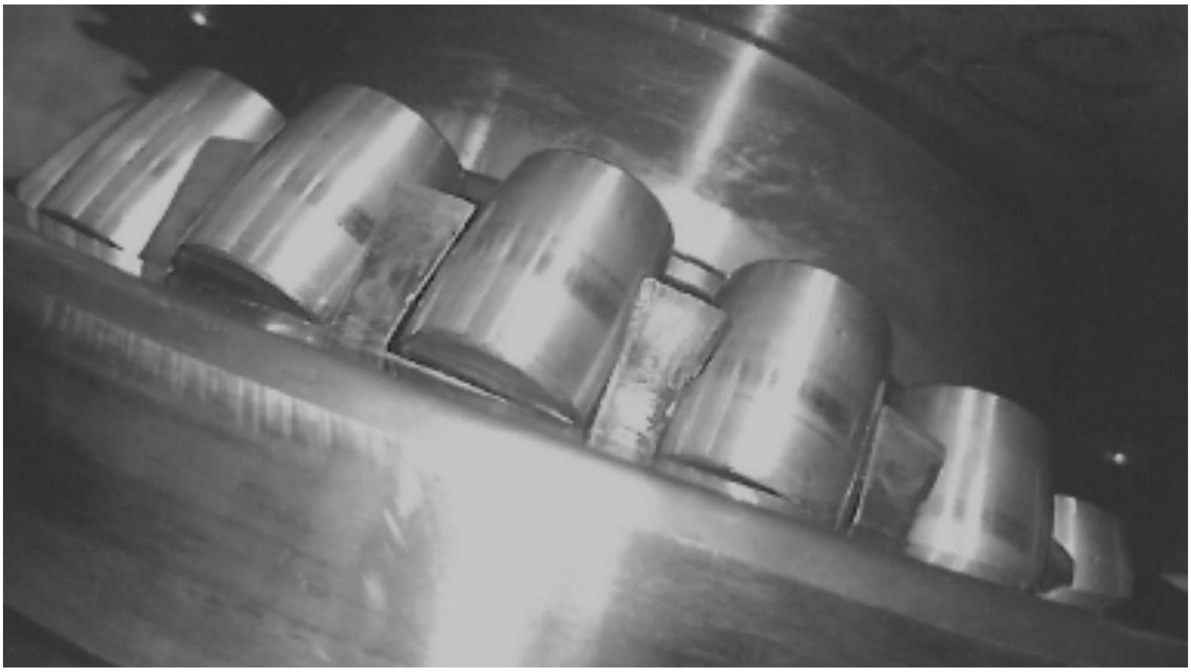

Fig. 6 Damaged input shaft bearing on the engine side

The wrong way of lubricating the gears damage not only gearing itself but also bearings, shafts, seals. Practically it destroy the entire transmission.

ACKNOWLEDGMENT
This article was supported by PSP Engineering Přerov, a. s.

REFERENCES

1. ČSN ISO 10816-1 Mechanical vibration - Evaluation of machine vibration by measurements on non-rotating parts. *ČNI Praha, 1998*

Corresponding author:

doc. Ing. Květoslav Kaláb, Ph.D., Department of Mechanical Engineering, Faculty of Mechanical Engineering, VŠB-Technical University of Ostrava, 17. listopadu 15/2172, Ostrava - Poruba, 70833, Czech Republic, phone: +420 597323090, e-mail: kvetoslav.kalab@vsb.cz

TESTING EQUIPMENT FOR COMPLEX ANALYSIS OF SCREW FASTENERS

Jan KANAVAL[1], Eliška CÉZOVÁ[1], Vít KLÍMA[1], František STARÝ[1]

[1]Department of Designing and Machine Components, Faculty of Mechanical Engineering, Czech Technical University in Prague

Abstract
This contribution describes analytical evaluation and experimental verification of the friction and force conditions in the prestressed bolted connections. In the case of using standard fasteners (bolts and nuts) there were evaluated mainly influence of advanced coatings using and lubricants into the threaded surfaces of bolted joints. To achieve the set goals modular design testing stand was designed. Achieved analytical findings and experimental verification will allow to refine the technological processes of assembly of bolted joints, which will have a major impact on the strength, durability and reliability of the screw connections (fasteners). Discovered knowledge are not currently available for design engineers during the designing of bolted joints. Design engineers typically use only recommendation of retailers and manufacturers when designing of bolted joints. In industrial practice, it is now very often required to calculate the screws according to the standard VDI 2230. Standard VDI 2230 specifies a procedure for the strength calculation of prestressed screw connections. The calculation is usually done on a personal computer using the KissSoft program.

Key words: *prestressed bolted connection; advanced coatings and lubricants; friction and force conditions; modular designed testing stand, Standard VDI 2230, KissSoft program.*

INTRODUCTION

In the process of tightening threaded fastener assemblies, especially for critical bolted joints, involves controlling both input torque and angle of turn to achieve the desired result of proper preload of the bolted assembly. Understanding the role of friction in both the underhead and threaded contact zones is the key to defining the relationship between torque, angle, and tension. There can be as many as 200 or more factors that affect the tension created in a bolt when tightening torque is applied. Fortunately, torque-angle signature curves can be obtained for most bolted joints. By combining the torque-angle curves with a few simple calculations and a basic understanding of the engineering mechanics of threaded fasteners, you can obtain the practical information needed to evaluate the characteristics of individual fastener tightening processes. The torque-angle curves can also provide the necessary information to properly qualify the capability of tightening tools to properly tighten a given fastener. These findings were described by Shoberg (2010).

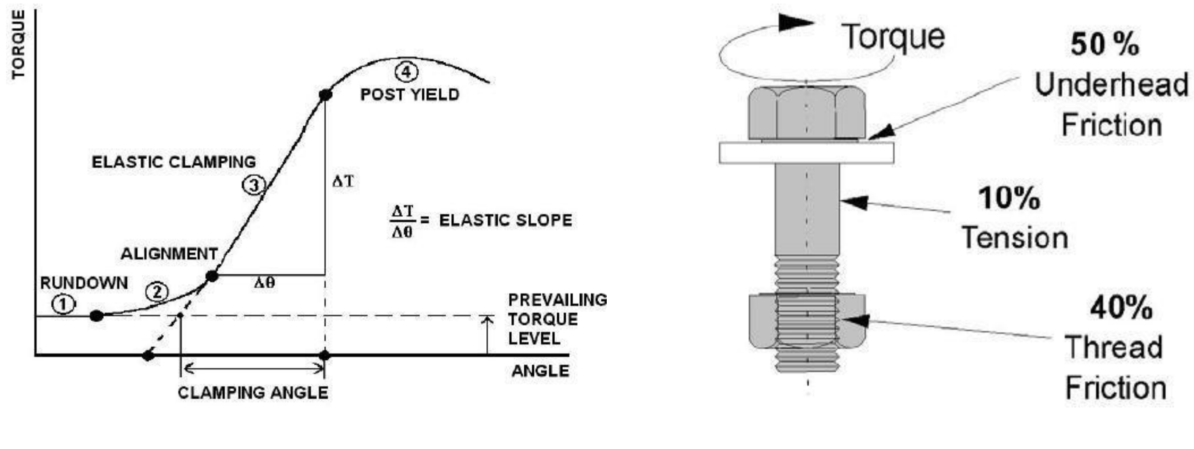

Fig. 1 Measured Torque-angle curve. Four Zones of the Tightening Process, (on the left side). Where Does the Torque Go? (on the right side). These figures were presented by Shoberg (2010).

There is defined the concept of controlled tightening of the screw connection in the technical support of the company Bossard. This method of tightening the screw connection respects the variable value of the friction coefficient in the thread and the reduction of prestress of the screw connection after assembly. Actual tensile bolt prestress after controlled tightening ensures correct functioning of screw joints during operation. The tensile prestress value of the bolt must be greater than the minimum value in terms of the correct operation of the screw connection and at the same time tensile prestress value of the bolt must by less than the maximum permissible value in relation to the achieve the yield strength of the bolt. (See Fig. 2)

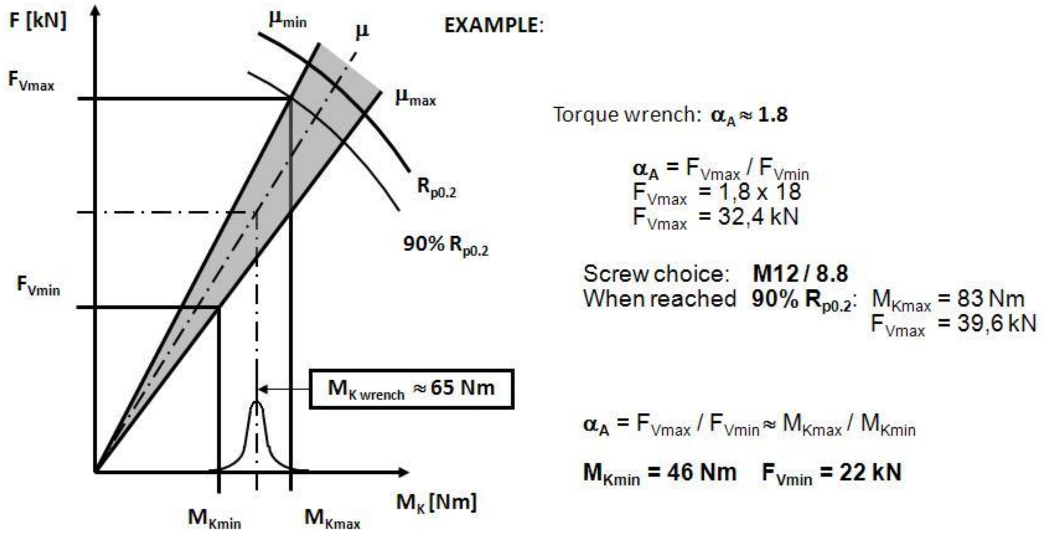

Fig. 2 Controlled tightening process of the prestress screw joints. The calculation procedure of the bolted joints and these diagrams are presented in the (technical support of the Anochrome Group Ltd. company; guideline VDI 2230; technical support of the Bossard CZ s.r.o. company).

Due to the contact of multiple surfaces with real surface roughness, the tension axial prestress is reduced after the screw connection is assembled. This phenomenon is caused by plastic deformation of individual contact surfaces. Reduction of the axial tensile stress is dependent on the number of contact surfaces of the screw joint and on their surface roughness. (See Fig. 3)

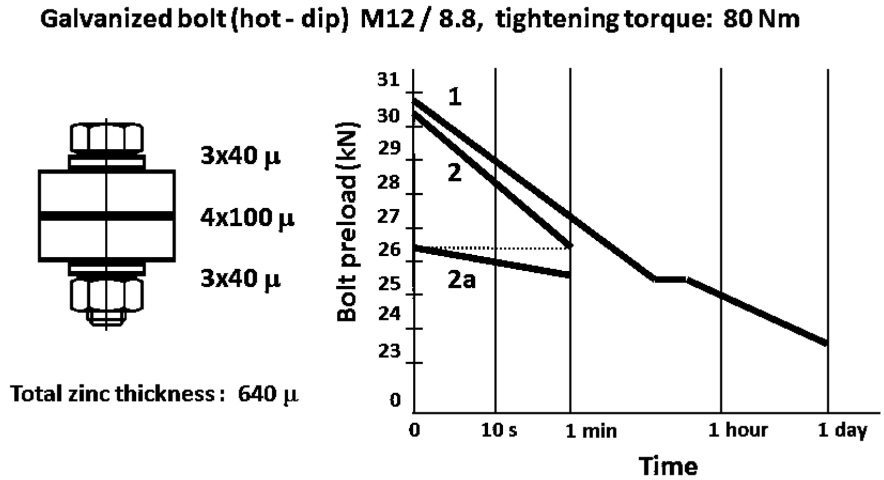

Fig. 3 Tension axial prestress reduction of the screw joint after assembly in time. This fact is also presented in the (guideline VDI 2230; technical support of the Bossard CZ s.r.o. company).

MATERIALS AND METHODS

The simple testing equipment for evaluation of threaded contact friction between the bolt and the nut was designed and manufactured at Department Designing and Machine Components of the Czech Technical University in Prague and simple experiments there were realized too. The results of these experiments are shown in table 1.

Fig. 4 Simple Testing Equipment for Evaluation of Threaded Contact Friction, (on the left side), HBM Torque Sensor T20WN, 200 Nm, (on the right side). These photographs were taken by the corresponding author (2015, 2016).

These simple realized experiments verified the chosen measurement methodology. The aim of the experiments was to determine the magnitude of the friction coefficient in the thread depending on the surface (coating) of the screw and the nut. The experience gained in this way was used to design testing equipment for complex screw joint testing. (See Fig. 5) The test equipment is currently being implemented by the prepared structural design.

On this testing equipment can be detected:

1) The value of the friction coefficient in the thread.
2) The value of the friction coefficient under screw head (under nut).
3) The tension axial prestress reducing after the screw connection is assembled.
4) To evaluate the characteristics of individual fastener tightening processes (Torque-angle curves).
5) Verifying the strength of the screw connection.

Tab. 1 Table Presenting Measured and Calculated Values for Bolt Size M12. This table was prepared by the corresponding author (2016).

Table Presenting Measured and Calculated Values for Bolt Size M12
(Bolt: stainless steel A2-80, Nut: stainless steel A4-80, coating - Delta Seal Black)

Hinge mass: 2,86kg

Nut friction moment M_p: 0Nmm

Weight mass (including hinge) m [kg]	Tensile force Q_o [N]	Wrench torque moment M_{kk} [Nmm]	Wrench torque moment without nut friction moment M_k [Nmm]	Calculated thread friction angle φ' [°]	Calculated thread friction coefficient f'[1]	Calculated friction coefficient f [1]
0	0	0	0	0	0	0
161,51	1584,41	1000	1000	9,50769	0,16748	0,14504
220,46	2162,71	1750	1750	11,32404	0,20026	0,17343
240,14	2355,77	2500	2500	13,8561	0,24666	0,21362
245,51	2408,45	2500	2500	13,62506	0,24239	0,20991
			Sample average μ:	12,08	0,214	0,186
Statistic evaluation			Sample standard deviation σ:	2,06	0,04	0,03

Technical parameters of this testing equipment:

Maximum testing torque moment	185 Nm
Maximum testing tension axial force	100 kN
Maximum testing rotation speed	97 min^{-1}
Maximum testing stroke	300 mm

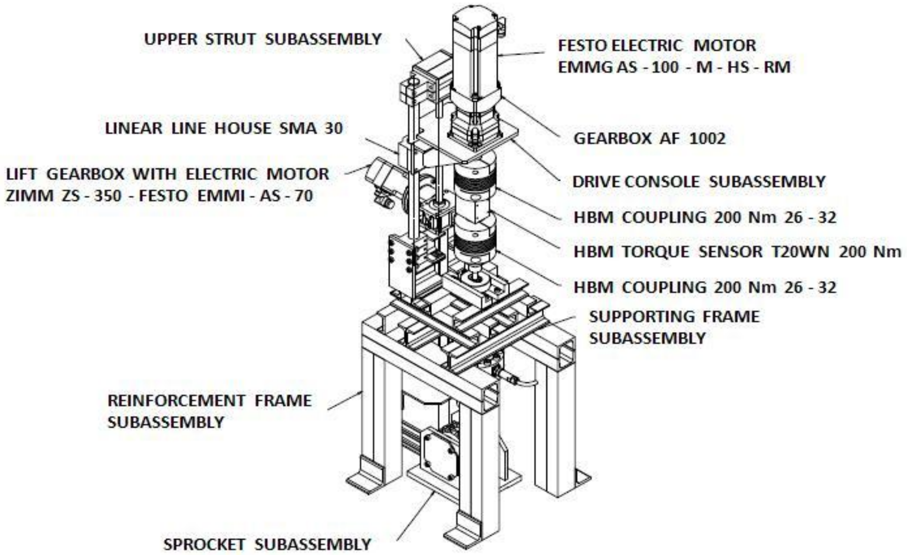

Fig. 5 Testing Equipment for Complex Analysis of Screw Fasteners. This image was processed by the corresponding author (2017).

RESULTS AND DISCUSSION

Aim of the experiments was to determine the magnitude of the friction coefficient in the thread depending on the surface (coating) of the screw and the nut. Measured data are presented in the Tab. 1 (only one example). Experimentally determined value of the friction coefficient in the thread (0,214) corresponds to the value reported in the technical literature.

CONCLUSIONS

The simple realized experiments verified the chosen measurement methodology. The experience gained in this way was used to design testing equipment for complex screw joint testing.

ACKNOWLEDGMENT

This study was supported by Student grants competition of the Czech Technical University in Prague, Faculty of Engineering, no. SGS16/145/OHK2/2T/12

REFERENCES

1. Shoberg, R. (2010). Engineering fundamentals of threaded fastener design and analysis. MI 48335, USA: RS Technologies, a Division of PCB Load & Torque, Inc.
2. Torque tension control. Technical support. Wolverhampton WV10 8HN, UK: Anochrome Group Ltd. Available at the web address https://www.anochrome.com/technical/torque-tension, (2017-06-20).
3. Guideline VDI 2230. (2003). Systematic calculation of high duty bolted joints. Part 1. Joints with one cylindrical bolt.
4. Technical support. Bossard CZ s.r.o. Brno: Available at the web address https://www.bossard.com/cs/aplikacni-inzenyrstvi/technické-zdroje.aspx, (2017-06-20).

Corresponding author:
Ing. Jan Kanaval, Ph.D., Department of Designing and Machine Components, Faculty of Mechanical Engineering, Czech Technical University in Prague, Technická 4, Praha 6, Prague, 166 07, Czech Republic, phone: +420 22435 2407, e-mail: jan.kanaval@fs.cvut.cz

STRUCTURAL ANALYSES OF AN AUTOMOTIVE DRY CLUTCH WITH QUARTER ASSEMBLY MODEL APPROACH

Mustafa Umut KARAOĞLAN[1], Gökçem ÇAPAR[2], Zeki Can KAYNAK[3], Serdar AKBULUT[4], Nusret Sefa KURALAY[5]

[1]*Department of Mechanical Engineering, Dokuz Eylul University, Izmir/TURKEY*
[2]*Department of Mechanical Engineering, Dokuz Eylul University, Izmir/TURKEY*
[3]*Department of Mechanical Engineering, Dokuz Eylul University, Izmir/TURKEY*
[4]*Department of Mechanical Engineering, Dokuz Eylul University, Izmir/TURKEY*
[5]*Department of Mechanical Engineering, Dokuz Eylul University, Izmir/TURKEY*

Abstract
This study aim calculating stress distribution, determination of the spring force with release travel and calculating releasing displacement on clutch assembly by using finite element method. Quarter clutch model is used for those analyses. Solid model of clutch assembly is performed by Solidworks 2016® and structural analysis is achieved by Ansys Workbench 15®. Structural analysis is performed in four steps which their first, second and third steps are related with assembly operation and fourth step is simulate spring deformation of clutch assembly. Spring forces are calculated with quarter clutch assembly model. Numerical results are compared with experimental result of diaphragm spring for validation of finite element analysis. Embossed diaphragm spring design is examined to reduce stress on clutch parts. Finite element results show the embossed spring design effect the clearance between pressure plate and clutch disc.

Key words: *Automotive dry clutch; quarter model; diaphragm spring; finite element method*

INTRODUCTION

Automotive dry clutches which are also named friction clutches, actuated externally by internal combustion engine to transmit torque from engine to gearbox with friction forces. External actuation performed via pushing clutch pedal. Kuralay (2008) reported of elastic deformation on diaphragm spring occurs during disengagement that produce release forces between pressure plate and friction disc of clutch. Clutch working operation is defined by reaction forces occurred by deformation of diaphragm spring. By applying preload, conical diaphragm spring is almost flattened. Clutch release takes place by force exerted by pressure bearing from diaphragm spring's flattened position. In power transmission, periphery of diaphragm spring applies pressure to pressure plate. This pressure is generated by connection between pressure plate and clutch via strap links.

Diaphragm spring's cone angle, width and other dimensions determine the values of reaction forces and load-deflection curve characteristic. Equivalent stress distributions and deformations of clutch assembly are connected with diaphragm spring's force-displacement behavior. Therefore, in the literature Topaç (2009) and Li-Jun (2008) are studied the effects of diaphragm springs' force-displacement behavior are studied by Pisaturo (2016) comprehensively. Other investigations are focused on one clutch component individually by Shukla (2016), and clutch assembly model by Purohit (2014) to determine structural behavior of clutch system which is consisted the determination of stress distribution and elastic deformation.

In the studies, structural behavior of vehicle clutches are examined by Vitnor (2016) with finite element (FE) method which is constructed to cover full assembly model. In this study, quarter assembly model is used to save time. Besides other literature works, preload conditions are included in FE analysis and structural behavior of clutch are investigated for assembly operation also.

Embossed diaphragm spring design is developed by Danev (2014) instead of diaphragm springs used in conventional vehicle clutches. Stresses and deformations of embossed diaphragm springs are examined comparatively with conventional ones. Evaluation of the improvement of friction clutch function and diaphragm spring stiffness are implemented.

MATERIALS AND METHODS

Quarter model of assembly is used for FE analysis instead of full clutch model. Quarter model was separated symmetrically which strap link and contact surface of release fork on release bearing assembly is located in the middle of model. Solid model of clutch assembly and their components are shown in figure 1. In order to determine the structural behaviour during the preloading and releasing operations a FE model has been implemented by using a commercial software named Ansys Workbench 16®. Proper mesh elements as Solid 92, Solid 95 and Solid 45 were used to simulate the quasi-static testing. Totally, 110709 elements and 219130 nodes of mesh were used on quarter model in the FE analysis. Body sizing on diaphragm spring, pressure plate and strap link, face sizing on pressure plate bottom surface and contact surfaces of diaphragm springs were applied for the accuracy of the results.

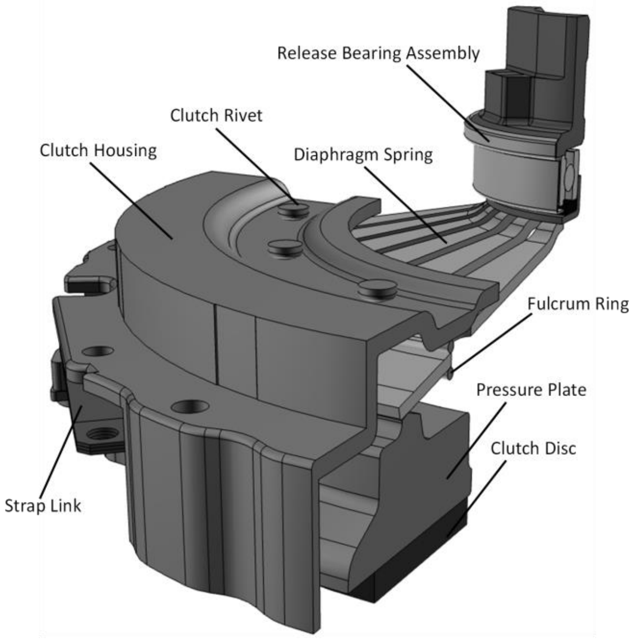

Fig. 1. Quarter Clutch Assembly Model

Diaphragm springs are designed in two different types as conventional (non-embossed) and embossed. This types of springs are separately applied on quarter clutch model for finite element analysis. A slice of embossed diaphragm spring is illustrated in Fig. 2 with emboss location and characterization dimensions. As shown in the Fig. 2, depth of emboss is 3 mm and representing λ is width, δ is length of emboss, ε is the distance from outside diameter to emboss starting location. Embossed model dimensions present as; λ is 3 mm, δ is 29.5 mm and ε is 38 mm.

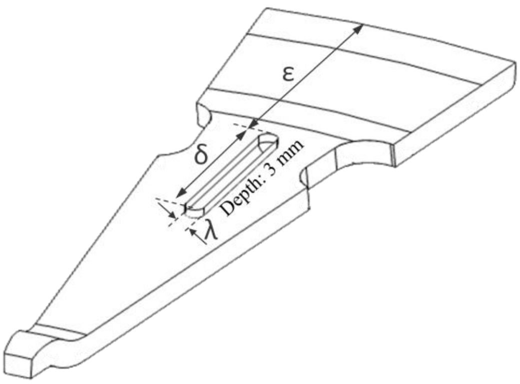

Fig. 2. Embossed Diaphragm Spring Dimensions

Diaphragm spring is manufactured from 50CrV4 steel alloy. Tension tests are implemented by test rig for four 50CrV4 steel alloy specimen. Average of test data was used in FE analysis. For plastic deformation, material's stress-strain diagram was determined by the test results to observing accurately elastoplastic behavior of diaphragm spring in FE method. Release bearing housing was produced GGG70 ductile cast iron. Bearing material is defined as SUJ2. Remaining clutch members' materials are accepted as structural steel alloy which hardening and hot tempered operations are implemented on them. Mechanical properties of materials which including young's modulus (E), poisson's ratio (ν), yield stress (S_y), tensile stress (S_{ut}) and density (ρ) are given in Table 1.

Tab.1. Clutch materials and properties

Material	E [GPa]	ν -	S_y [MPa]	S_{ut} [MPa]	ρ [kg/m^3]
Structural Steel	200	0.3	300	460	7850
50CrV4	227.5	0.3	1340	1370	7850
GGG70	176	0.275	420	700	7200
SUJ2	208	0.3	1370	1570	7830

Finite element method is used for understanding structural features of the clutch components. An advantage of FE method is that it can solve the mechanical problems with arbitrary structures and boundary conditions. Boundary conditions are taken as frictionless support at sections of quarter assembly model in FE method. Bolt holes of outside clutch housing and outside surfaces of intersection between clutch housing and flywheel are taken as fixed support. In clutch modeling, relations between components are classified as frictionless and frictional. To shorten analyze time, some of undersize contact faces, contacts are accepted as frictionless contact. Clutch housing-fulcrum ring, fulcrum ring-clutch rivets, diaphragm spring-fulcrum ring, diaphragm spring-pressure plate and strap link-rivets areas are assumed as frictionless contact. Pressure plate-strap link, strap link-rivets connections are defined as frictional contact. There is frictional contact between inner plates of strap link. In frictional contact surfaces, coefficient of friction is taken as 0.15 for metal-metal contact.

In Fig. 3, quarter assembly model of clutch components and analysis inputs of preloading and releasing displacements are presented. FE analysis is evaluated in four steps as shown in the graphic. First step represents preload operation for diaphragm spring which is applied on pressure plate. Preload operation of diaphragm spring actuates 6 mm from outer surface of it to the opposite direction of flywheel. Second step represents fixing operation between cover and pressure plate by using strap link connection. Strap link (green) is pressed 16.8 mm after first step to cover and bolted. Third and the last step is related with the releasing operation of bearing assembly. In third step, release bearing is travelled to new location of diaphragm spring contact surface with any resistant because of the deflection of the diaphragm spring after preload operation. Release bearing displacement is 20 mm until it reaches to diaphragm spring contact. Last step shows the loading of diaphragm spring for releasing operation.

The reason of separation third and fourth steps is to prevent connection fails with exact contact forming and investigation of releasing process individually.

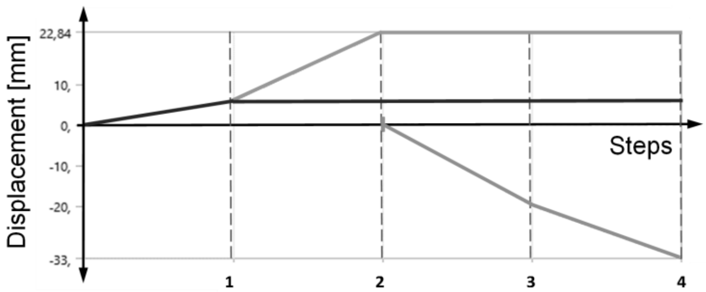

Fig. 3. Inputs of Clutch Model Components (Upper Line: Strap Link, Middle Line: Pressure Plate, Bottom Line: Release Bearing)

Force characteristic curve of conventional diaphragm spring is achieved by using force probe on lower fulcrum ring after finite element analysis was solved. Experimental and finite element results are good agreement especially in preloading time. Comparison of conventional diaphragm spring characteristics by experimental and numerical method is defined validation for the study.
Release bearing assembly was taking into consider individually. Reaction forces on the contact surface of diaphragm spring was determined by force probe in FE analysis. Reaction forces acts on release bearing assembly occurs during the last step which represents releasing operation.

RESULTS AND DISCUSSION
Except from the release bearing assembly, rest of components evaluated in quarter clutch model. Maximum stress on diaphragm spring reach at the top level of stress value in first step of FE analysis. Maximum stress level is reached in the middle of first step time. Maximum stress on diaphragm spring is shown in Figure 4 for both conventional type and embossed type.

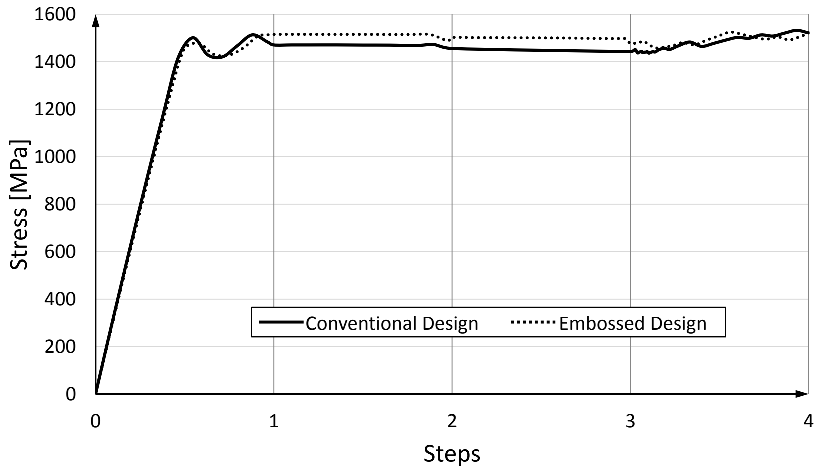

Fig. 4. Maximum Equivalent Stress on Diaphragm Spring

Preload operation causes increasing maximum stress of diaphragm spring on first step. Yield stress of diaphragm spring material is exceeded during preloading in up to 1370 MPa. Plastic deformation on diaphragm spring is occurred in first step. Until the last times of first step, maximum stresses of conventional and embossed spring types are similar. Strap link connection and release bearing free movement do not affect the stress in second and third step. Similar characteristics are occurred on springs in releasing operation. It is obvious that, equivalent stress are not tremendously changed on diaphragm springs at releasing. After the separation of clutch disc from pressure plate at the end of last step, stress distribution of diaphragm springs shown in the Figure 5.

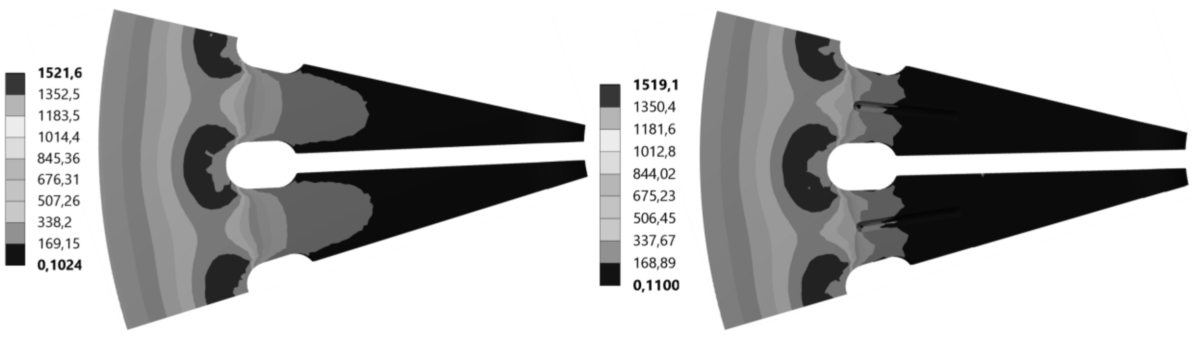

Fig. 5. Stress Distributions of Conventional (left) and Embossed (right) Diaphragm Springs at the end of releasing

Conventional diaphragm spring has maximum 1521.6 MPa and embossed diaphragm spring has 1519.1 MPa maximum stress. Stress distribution shows similar in both types. The advantage of embossed type diaphragm spring is having less stress on the spring fingers relatively.
Clutch housing is an important component of clutch assembly which less deformation and stress are desired on it for long service life without any failure such as cranking or fatigue. Maximum stress on clutch housing is shown in Figure 6. Clutch model with conventional type was always caused more stress on it. In preload operation stress was reached up to 200 MPa in conventional type. At the end of strap link connection on clutch housing, equivalent stress was reached about 295 MPa in conventional design and 270 MPa in embossed design. Release bearing motion that is reverse direction of preloading and strap link connection effects on decreasing stress in last step. It is clear that embossed design is useful for clutch housing because of less stress occurred.

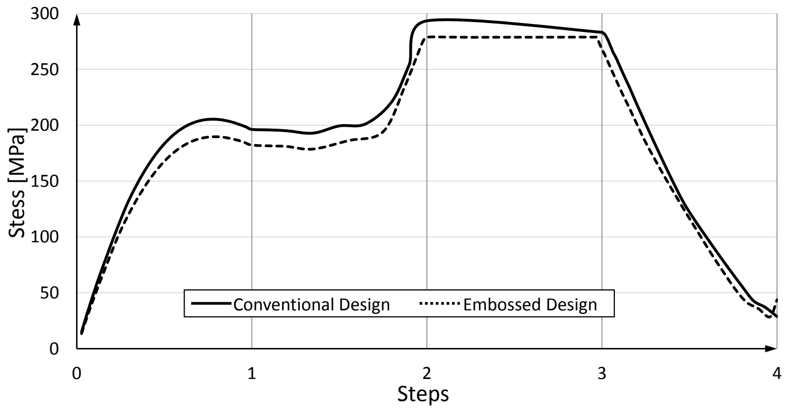

Fig. 6. Maximum Equivalent Stress on Clutch Housing

Strap link also is exposed the situation of exceeding yield stress and deforming plastic. Reasonable plastic deformations can occurred on trap link for connection of housing and pressure plate.
Fulcrum ring holds diaphragm spring with clutch cover. The deformation of diaphragm spring occurs due to fulcrum ring acting as support. Especially in releasing operation, compression stresses occur on fulcrum ring. Maximum stress on fulcrum ring is shown in Figure 7.

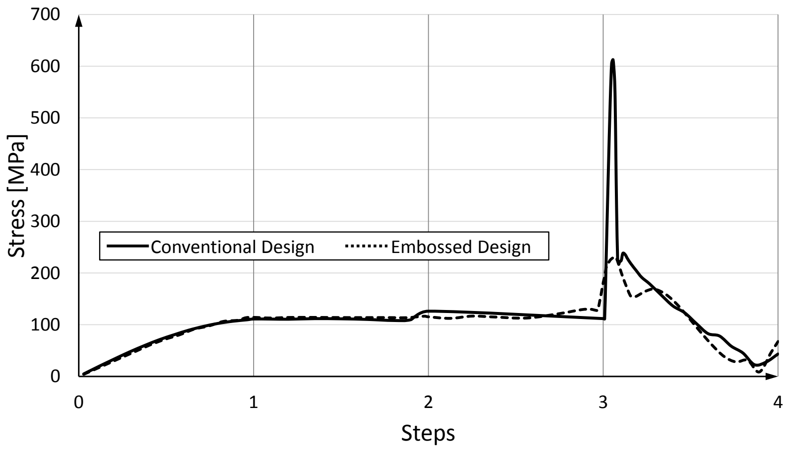

Fig. 7. Maximum Equivalent Stress on Fulcrum Ring

After solution of the analysis steps, disengagement of clutch was simulated by using FE method. Disengagement deflection means clearance between pressure plate and clutch disc on clutch system. End of the third step time represents engagement of clutch by achieving preloading and assembly operation. Clearance characteristics changed linearly during the disengagement. Pressure plate and clutch disc have 6.5 mm displacement until engagement was achieved. Deformations of quarter model of clutch system was assumed zero for initial condition of releasing at the end of third step to calculate releasing clearance between pressure plate and clutch disc. After finishing the solution time pressure plate deflection 9.10 mm for embossed and 8.99 mm for conventional diaphragm spring designs. Deflection difference between pressure plate deflections at the end of fourth step and 6.5 mm initial condition of preloading is defined clearance.

CONCLUSIONS

In this study, structural behavior of the automotive clutch system simulated during both preload operation for assembly and releasing operation. Load-deflection curves of conventional diaphragm spring was achieved by FE method and it was compared with the experimental results which we can assume that as validation for the study. Full model of release bearing assembly was investigated individually. Reaction forces on the contact surface that was occurred during fourth step time against diaphragm spring deformation, was used input force. Maximum stress on release bearing assembly is in the safe area for clutch assembly with conventional diaphragm spring. Simulation of clutch system was implemented for assembly and operation times in four analysis steps. FE results indicate that using embossed diaphragm spring in clutch assembly was improved maximum stress occurred on clutch housing and fulcrum ring. Emboss application was caused increasing on diaphragm spring stiffness. Releasing clearance was determined for two types of spring alternatives. It was calculated 2.99 mm for using conventional diaphragm spring. Emboss effect was increased the clearance up to 3.10 mm. So it is definitely clear that pressure plate clearance can be increased by using embossed diaphragm spring in clutch system. Also this study presents an alternative simulation approach that includes all components of assembly in quarter model for clutch systems by using FE method.

REFERENCES

1. Kuralay, N.S. 2008. *Motorlu Taşıtlar; Temel ve Tasarım Esasları, Yapı Elemanları, Cilt 1; Tahrik ve Sürüş Sistemleri.* İzmir: TMMOB Makina Mühendisleri Odası, Yayın No: MMO/2008/484; 315s. (In Turkish)
2. Topaç, M.M., Hamurişçi, Y., Kuralay, N.S. 2009. Determination of Elastic Deformation of an Automotive Clutch Cover Under Pedal Force By Using Finite Element Method, *Engineer and Machinery*, 50(590). (In Turkish with an abstract in English)
3. Pisaturo, M., Senatore, A. 2016. Simulation of Engagement Control in Automotive Dry-Clutch and Temperature Field Analysis Through Finite Element Model, *Applied Thermal Engineering, Vol: 93*, s. 958-966. DOI: 10.1016/2015.10.068.
4. Shukla, S., Elisala, A., Rao, G.V.R.S. 2016. Design Optimization of Diaphragm Spring with Various Load Condition, *Global Journal for Research Analysis, Vol: 5*, s. 184-187.
5. Li-jun, Z., Liu, T., Bao-yu, S. 2008. Optimum Design of Automobile Diaphragm Spring Clutch. *IEEE Vehicle Power and Propulsion Conference*, 3-5 September, Harbin.
6. Purohit, R., Khitoliya, P., Koli, D.K. 2014. Design and Finite Element Analysis of an Automotive Clutch Assembly, *Procedia Materials Science, Vol: 6*, s. 490-502.
7. Vitnor, S., Kavade, M. 2016. Finite Element Analysis of Friction Plate of Diaphragm Spring Clutch for TD-3250 Vehicle, *International Journal of Science and Research, Vol: 5*, No: 4, s. 1771-1775. ISSN: 2319-7064.
8. Danev, D., Kjosevski, M., Simeonov, S. 2014. Increasing Stiffness of Diaphragm-Spring Fingers as a Part of System Approach Improvement of Friction Clutch Function, *International Journal of Automobile Engineering Research and Development, Vol: 4*, No: 1, s. 11-22. ISSN: 2277-4785.

Corresponding author:
Ing. Mustafa Umut KARAOĞLAN, Ph.D., Department of Mechanical Engineering, Faculty of Engineering, Dokuz Eylul University, Tinaztepe Campus Buca/Izmir, Turkey, phone: +90 232 301 9249, e-mail: mustafa.karaoglan@deu.edu.tr

INFLUENCE OF COMPOSITION OF BIOGAS ON SELECTED ENGINE OIL VALUES

Jerzy KASZKOWIAK[1], Sylwester BOROWSKI[2], Piotr DORSZEWSKI[3], Marietta MARKIEWICZ-PATALON[4]

[1]Faculty of Mechanical Engineering, UTP University of Science and Technology, Poland.
[2]Faculty of Mechanical Engineering, UTP University of Science and Technology, Poland.
[3]Faculty of Animal Breeding and Biology, UTP University of Science and Technology, Poland.
[4]Faculty of Mechanical Engineering, UTP University of Science and Technology, Poland.

Abstract
The period between the changes of the engine oil constitutes one of the costs of their exploitation. In the article there is presented the analysis of the selected properties of the engine oil depending on time of operation and composition of biogas. It has been found, that for equally loaded combustion engine, the periods of the engine oil use to a high degree depend on the fuel's quality.

Key words: *combustion engine, biogas, engine oil.*

INTRODUCTION

For the combustion engines, it is the diesel oil and and gasoline that all the time constitute the most popular driving units in the mobile device. Looking for alternative energy carriers results in the fact, that more and more often there are used gasolines of renewable origin. One of them is biogas, which can be made both of the specially cultivated plants, as well as different types of organic (Czekała et al. 2016). These may be both agricuktural wastes (to być zarówno odpady rolnicze (liquid manure, dung) as well as wastes from food processing plants, odpady z pochodzące z zakładów przetwórstwa spożywczego, maintenance storages or markets (Guangqing L., et al. 2009). The other possibility is particularly valuable, as apart from the wastes utilization it does not require designing for cultivation of energy crops areas which could be used for food production (Bilcan, A., Le Corre, O. & Delebarre, A. 2003). Moreover, availability of cultivated plants is connected with seasonality and changeable supply while the wastes are available in a balanced manner for the whole year (kosiba et al. 2016). More and more often, for production of biogas there are also used biological products of sea origin – algae (Mussgnug et al. 2010). Depending on substrates from which biogas is made of, it may differ in chemical composition, volume and type of impurities. The range of changes in the biogas' composition depending on the type of the used substrate is presented in table 1.

Tab 1. Approximate composition of biogas depending on the source of origin (own study)

Gas/source of origin	*Agrarian biogas plant (corn, beets)*	*Sewage treatment plant*	*Municipal wastes*
Methane	*45-75%*	*64-75%*	*45-55%*
CO_2	*25-55%*	*20-35%*	*25-30%*
CO	*≤0,2%*	*≤0,2%*	*≤0,2%*
H_2S	*10-30000 ppm*	*≤8000 ppm*	*≤8000 ppm*
N_2	*0,01-5%*	*3-4%*	*10-25%*
O_2	*0,01-2%*	*0,5%*	*1-5%*

Biogas is characterised by the compositions changeability, what results both from heterogeneous substrate used for its production as well as treatment's effectiveness. The pollution of biogas, both mechanical as well as the presence undesirable chemical substances influences both the quality of the engine's operation (power, turning moment) as well as its permanence. Prior to be used for the combustion engines' feeding, biogas is purified (Annika F. et al 2004). Also the economical costs of biogas generation are of an higher and higer importance. As a consequence, it influences cost-effectiveness of the use of biogas as fuel (Zbytek Z. et al. 2016). In the entities generating biogas and using it for combustion engines‘ feeding, the engine oil is most often subject to constant control, and the decision on its replenishment or change is taken on the basis of the results of analyses and not the time of operation. In the conducted studies there were attempts to determine to what degree pollutions included in biogas impact its properties.

MATERIALS AND METHODS

Four combustion engines with spark ignition, with pressure charging, of the power 380 kW each were tested. They propelled electric power generators of the power of 340 kW, loading of which changed to a very low degree (±5%). The engines were in a very good technical condition. Prior to the tests, there were operated for not longer than 2 years. Before starting of the cycle of the tests, in all the engines the engine oil, air and oil filters were changed. The engine oil was controlled every 500 hours of operation. There were tested the folowing: viscosity of the oil (at 100 ^{0}C), the acid value (TAN), the contents of silicon and iron in oik. Biogas with which the engines were supplied, was made of wastes from the municipal wastes treatment plant. Its composition was controlled with the biogas analyser BIOTEX MultiPoint. Biogas, prior to its supplying to the engine, was cleaned from both mechanical as well as chemical impurities. The tests were conducted up to 3000 hours of each engine’s operation. The average composition of the gas obtained following its cleaning (mean values for the period of tests) is presented in the tabel 2. The composition of biogas supplying engines that were tested, had very good parameters, in particular high contents of methane and low contents of suplhur. For the purposes of the tests, the mean contents of the biogas componenets was calculated for each period (500 hours). Because of earlier experiments as well as available results of other authors‘ tests, particularly big attention was paid to the contents of the sulphur compounds in biogas (Anika et al. 2004). The composition of biogas for individual periods is presented in the table 3. In the course of the studies there occurred a short-term increase of the contents of hydrogen sulphide in biogas (in the period of 500-1000 hours of the conducted tests). Following completion of the period of tests, once again the engine oil was changed in all the engines.

Tab. 2. Mean values of the selected compounds in biogas in the period of the conducted tests

Biogas component	*Mean contents prior to purification*	*Mean contents following purification*
Methane	*65,25%*	*65,25%*
Hydrogen sulphide	*59 ppm*	*17 ppm*
Carbon dioxide	*35%*	*35%*
Ammonia	*0 ppm*	*0 ppm*

Tab.3. Mean contents of the selected compounds in biogas in individual periods of tests

Biogas component	*Methane [%]*	*Hydrogen sulphide [ppm]*
0-500 hours	*65,22*	*12,00[a]*
500-1000 hours	*65,23*	*41,00[b]*
1000-1500 hours	*65,26*	*14,00[a]*
1500-2000 hours	*65,27*	*11,00[a]*
2000-2500 hours	*65,23*	*12,00[a]*
2500-3000 hours	*65,28*	*11,00[a]*

The tested oil paramters and the contents of hydrogen sulphide in biogas were subject to the statistical analysis with the use of the Tukey’s test at the significance level 0,05.

RESULTS AND DISCUSSION

The mean results of the tested properties of oil obtained at the time of tests are presented in table 4.

Table 4. Mean results of oil tests

Working time [h]	*Viscosity [cSt(100^{0}C)]*	*Acid number [mg KOH g^{-1}]*	*Content of silica [ppm]*	*Contents of iron [ppm]*
0-500	*14,33^{a}*	*3,25^{a}*	*64,50^{a}*	*4,25^{b}*
500-1000	*14,28^{a}*	*3,26^{a}*	*66,75^{a}*	*4,80^{b}*
1000-1500	*13,85^{b}*	*2,45^{a}*	*83,75^{b}*	*5,50^{b}*
1500-2000	*13,80^{b}*	*2,10^{b}*	*88,75^{b}*	*3,50^{a}*
2000-2500	*13,83^{b}*	*2,06^{b}*	*57,75^{a}*	*3,00^{a}*
2500-3000	*14,15^{a}*	*2,16^{b}*	*75,70^{a}*	*6,25^{c}*

Viscosity, contents of silica and iron in oil did not exceed the admissible values. Only the acid number reached the values considered to be the border ones (Piec 2012). A slight drop in the oil's viscosity after 1000 working hours was observed. After the next 1500 hours of work, the increase of the viscosity values was observed. Viscosity prior to the period of lowering and after the repeated increase, had the values not essentially differing statistically. The drop in viscosity at the time of exploitation of engines powered with liquid fuels most often means diluting of oil as a result of unburnt oil's getting into oil. In case of engines powered with gas fuels, it most often proves chemical reactions taking place in oil and reducing its properties. The rise of viscosity most often proves of a considerable volume of pollutants and the gelation processes. The acid number at 1500 hours of work dropped to the level of 2,45 and was slightly dropping till the end of the research cycle. The values of the acid number for 4, 5 and 6 of the measurement, did not statistically differ and were at the same time statistically lower than for the measurements 1, 2 and 3. The drop of the acid number may in engines powered by the biogas be caused most of all with the increase of the sulpur contents in fuel. It may paradoxically result in the increase of the corrosion wear and tear. The measured contents of silica in the 3 and 4 measurement, had the value essentially statistically lower than for the measurement 1 and 2. The measurements 5 and 6 also had the value not differing statistically from the measurements 1 and 2. The increase of the contents of silica was most probably caused by the increased presence of sulphur in fuel and as a consequence – in oil. The increase of the contents of iron proves the progressing processes of wear and tear (Knopik et al. 2016).

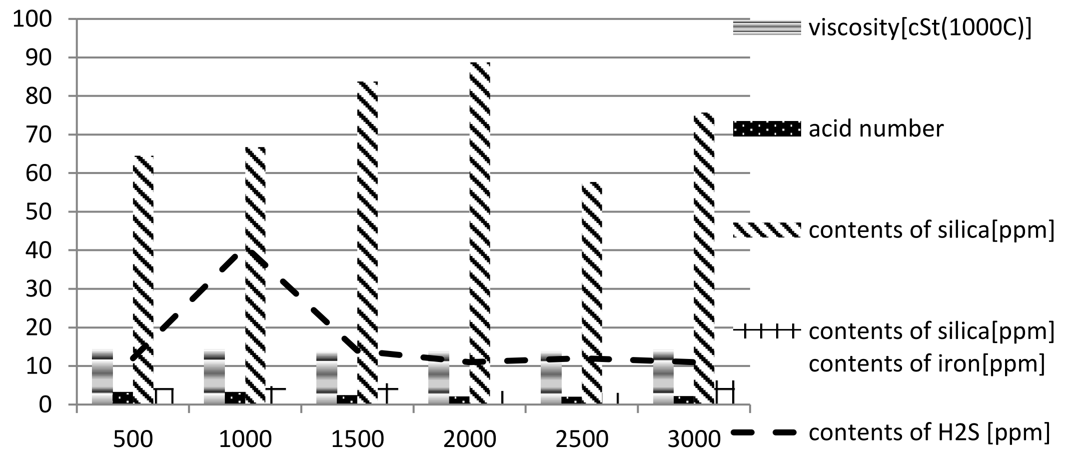

Fig. 1 Diagram of changes of the selected features of oil and biogas

The subsequent drop in the contents of iron in oil is most probably caused by the effective operation of the oil filtering system.
The contents of methane did not essentially statistically change, however the contents of the hydrogen sulfide increased more than three time for the run of 1000 hours. The difference was statistically essential.

CONCLUSIONS

At the time of the tests‘ conducting it was found, that the examined oil parameters essentially statistically changed following operation for 1000 – 1500 hours. It coincided with the increase of the hydrogen sulfide in biogas. The improvement of the parameters occurring after the subsequent 500 hours in spite of the fact that the level of oil was not supplemented, most probably resulted from effective operation of the oil filtering system

REFERENCES

1. Annika F., Andersson, T., Karlsson, A.,. Svensson. H., Ejlertsson. J., Occurrence and Abatement of Volatile Sulfur Compounds during Biogas Production (2004) *Journal of the Air & Waste Management Association* Vol. 54 , No. 7,
2. Bilcan, A., Le Corre, O. Delebarre, A. (2003), Thermal efficiency and environmental performances of a biogas-diesel stationary engine *Environmental Technology* Vol. 24 , No. 9,
3. Czekała, W., Bartnikowska S., Lewicka A., Bugała A., Zbytek Z., Lewicki A., (2016) Economic and energy efficiency of the solid biofuels produced from digested pulp *3RD International Conference on Chemical and Biological Sciences* Amsterdam
4. Guangqing L., ,Ruihong Z.,, , Hamed M. El-Mashad, Renjie D., (2009) Effect of feed to inoculum ratios on biogas yields of food and green wastes *Bioresource Technology* Vol. 100, No 21
5. Knopik, L., Migawa, K. & Kolber, P. (2016). Statistical analysis of parameters of rail vehicles. *22nd International Conference on Engineering Mechanics Location: Svratka, CZECH REPUBLIC*, 286-289
6. Kosiba J., Uhrinova D., Jablonicky J., Majdan R., (2016) Alternatívne palivá a pohony motorových vozidiel Nitra 2016
7. Mussgnug, J.H., Klassen, V., Schlüter, A., Kruse, O., (2010)Microalgae as substrates for fermentative biogas production in a combined biorefinery concept *Journal of Biotechnology* Vol. 150, / 1,
8. Piec P., (2012) Diagnostics the wear intensity of engine oil during operation *Tribologia Vol. 6*
9. Robinson N., Hons B. S. C.:(2000) Monitoring oil degradation with infrared spectroscopy – Wearcheck Division of Set Point Technology ISSUE 18.
10. Zbytek, Z., Dach, J., Pawłowski, T., Smurzynska, A., Czekała, W., Janczak , D., (2016) Energy and economics potential of maize straw used for biofuels production *3RD International Conference on Chemical and Biological Sciences* Amsterdam

Corresponding author:
Jerzy Kaszkowiak, PhD.: Faculty of Mechanical Engineering, UTP University of Science and Technology, Poland., Al. Prof. Kaliskiego 7, 85-796 Bydgoszcz, e-mail: kaszk@utp.edu.pl

UTILIZATION OF NUMERICAL SIMULATION FOR STEEL HARDNESS DETERMINATION

Adam KEŠNER[1], Rostislav CHOTĚBORSKÝ[1], Miloslav LINDA[2], Monika HROMASOVÁ[2]

[1]Department of Material Science and Manufacturing Technology, Faculty of Engineering, Czech University of Life Sciences Prague, Kamýcká 129, 165 21 Prague – Suchdol, Czech Republic
[2]Department of Electrical Engineering and Automation, Faculty of Engineering, Czech University of Life Sciences Prague, Kamýcká 129, 165 21 Prague – Suchdol, Czech Republic

Abstract
Agricultural tools must meet the requirements for durability and abrasion wear resistance. Steel hardness is one of the most important mechanical properties of agricultural tools. Low cost production of agricultural tools is nowadays a necessary factor in maintaining the competitiveness of producers. I is one of reasons, why numerical simulation is used to design of the heat treatment of steel for agricultural tools. Mathematical models allow cost reductions and time consumption if is it compared to the practical experiment. The hardness of 51CrV4 steel was determined in this work. Numerical inverse methods were used to simulation of steel hardness. The results of the model were verified by an experiment. The results show good relationships between measured hardness and numerical simulation.

Key words: *hardness; agriculture tools; heat treatment; steel.*

INTRODUCTION

Agricultural tools must meet the high customer requirements for abrasion wear resistance, hardness and toughness (Rose, Sutherland, Parker, Lobley, Winter, Morris, Twining, Ffoulkes, Amano, Dicks 2016; Votava 2014; Nalbant, Tufan Palali 2011). These requirements are obtained by setting various parameters of the heat treatment of steels for agricultural tools (Fernandes, Prabhu 2008; Lee, Mishra, Palmer 2016; Shaeri, Saghafian, Shabestari 2012). Heat treatment parameters are determined by experience in many companies (Votava 2014; Rose, Sutherland, Parker, Lobley, Winter, Morris, Twining, Ffoulkes, Amano, Dicks 2016). Numerical models of heat treatment of steel can reduce production cost if it is compare with experimental heat treatment of steel in experiments (Sinha, Prasad, Mandal, Maity 2007; Babu, Prasanna Kumar 2009; Teixeira, Rincon, Liu 2009).
Numerical simulation must be set with the exact boundary conditions (heat flux, specific heat capacity, thermal conductivity) for accurate heat treatment (Liu, Xu, Liu 2003; Şimşir, Gür 2008). The inovation of boundary and material conditions is described in articles (Kešner, Chotěborský, Linda 2016a, 2016b, 2017).
Microstructure of steel is the most important for steel hardness after its heat treatment (Li, Luo, Yeung, Lau 1997; Zdravecká, Tkáčová, Ondáč 2014). Results of some authors show that abrasion wear resistance is advisable to provide a combination of bainitic and martensitic microstructure (Das Bakshi, Shipway, Bhadeshia 2013a; Ohtsuka 2007; Das Bakshi, Shipway, Bhadeshia 2013b).
The size of the heat flux is variable in time during the heat treatment. For this reason, standard procedures for calculating the course of heat treatment in steel cannot be used. Numerical inversion methods of heat treatment can be used to design heat conduction and the associated calculations of the microstructural phases of individual steel properties such as hardness (Teixeira, Rincon, Liu 2009; T Telejko 2004; T. Telejko 2004).
The aim of this work was to design an algorithm that is able to predict the final steel hardness after its heat treatment and thair verification with experimental data.

MATERIALS AND METHODS

Low alloyed 51CrV4 steel was chosen for the experiment of this work. The tablature chemical composition is shown in Tab. 1.

Tab. 1 Chemical composition of steels 51CrV4 (wt. %)

material	C	Mn	Si	P	S	Cr	Ni	Cu	Al	Mo	V
51CrV4	0.53	0.89	0.26	0.012	0.025	1.02	0.08	0.13	0.028	0.02	0.12

Steels samples were prepared from rod in size 25 mm x 10 mm x 50 mm. The heating temperature 800 °C was used for all samples. The cooling parameters were designed to achieve a combination of bainite and martensite structures for austempering – see Tab. 2. Salt bath of 50 wt.% $NaNO_2$ + 50 wt.% $NaNO_3$ was used for cooling steel samples.

Tab. 2 Cooling parameters for austempering

	cooling 1			cooling 2			cooling 3		
sample	temp.	medium	time [s]	temp.	medium	time [s]	temp.	medium	time [s]
V1	300	salt bath	40	300	air	1000	20	air	to 20°C
V2	300	salt bath	40	20	water	to 20°C	X	X	X
V3	400	salt bath	40	400	air	1200	20	air	to 20°C
V4	400	salt bath	40	20	water	to 20°C	X	X	X

The algorithm was compiled for numerical simulation of final hardness in ElmerFem software. The entire cooling process has been included in the algorithm. The processing diagram of the algorithm procedure is shown in Fig. 1. The size of the model object was taken from experimental samples (25 mm x10 mm). The mesh was created with interest points in the center of the object 12.5 x 5 mm and close to surface 22 mm x 5 mm. The input parameters of the numerical simulation are the same as for experimental – see Tab. 2. The material constants of thermal capacity and thermal conductivity was taken from literature (Kešner, Chotěborský, Linda 2017).
Solution of numerical simulation was carried out in step Δt, when every step has been created in file **.vtu*, where the change of temperature was stored in the individual parts of the object. Thus it was created in „M“ files, it showing the number of steps of the simulation.

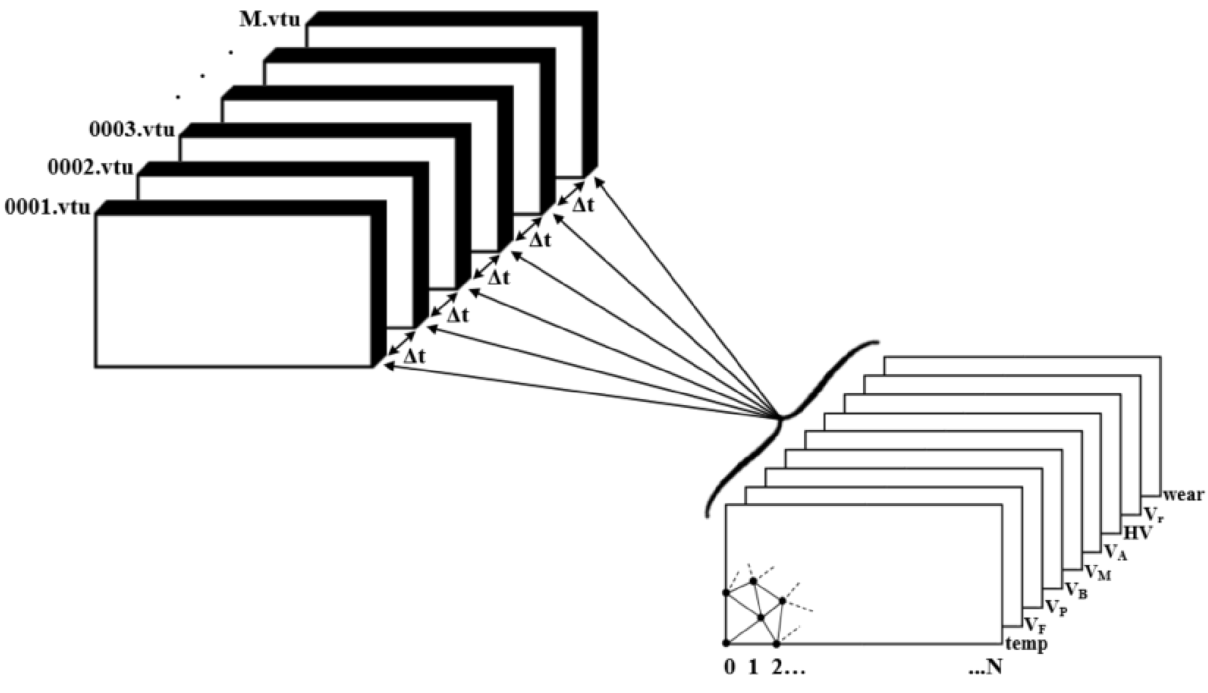

Fig. 1 Flow chart for determinate volume of phase and hardness

Volume of ferrite *Vf*, perlite *Vp*, bainite *Vb* and martensite *Vm*, hardness $HV_{0.3}$ / kgf mm^{-2} and cooling rate *VR* were calculated according to the cooling curve at each calculation step. The conditions for the formation of the individual phases were taken from the TTT diagram and were included in the algorithm calculation. The volume fraction of each phase was calculated at each timestep (equations 1 to 5). Vickers hardness was calculated according to the volume fraction of the phases (equation 6) and the chemical composition of the steel which was found in the material database (Chotěborský, Linda 2015).

$$VR = \left(\frac{0.8-C}{0.8}\right)^{-1} + \left(\frac{0.8-C}{0.8}\right)^{-1} \tag{1}$$

$$Vf = \sum_{i=1}^{n} -Kf \times Nf \times t^{Nf-1} \times e^{-Kf \times t^{Nf}} \times (1 - VR) \tag{2}$$

$$Vp = \sum_{i=1}^{n} -Kp \times Np \times t^{Np-1} \times e^{-Kp \times t^{Np}} \times (1 - Vf) \tag{3}$$

$$Vb = \sum_{i=1}^{n} -Kb \times Nb \times t^{Nb-1} \times e^{-Kb \times t^{Nb}} \times (1 - Vf - Vp) \tag{4}$$

$$Vm = 1 - e^{-\beta \times (Tm_{start} - T)} \times (1 - Vf - Vp - Vb) \tag{5}$$

$$HV = V_P \times HV_P + V_B \times HV_B + V_M \times HV_M \tag{6}$$

where *Kf, Kp, Kb* – overall rate constant of feritic, pearlitic and bainitic transformation that generally depends on temperature (-), *Nf, Np, Nb* – Avrami’s exponent for feritic, pearlitic and bainitic transformation that depends on temperature (-)

Parameters *Ni* and *Ki* were taken from the work (Kešner, Chotěborský, Linda 2016a) for algorithm calculation. The average cooling rate $t_{8\text{-}5}$ (between 800 °C and 500 °C) was determined from simulation. The log VR is included as soon as the sample temperature drops below 500 °C in the hardness equation. Vickers hardness was measured and analyzed from the sample surface to its center with a distance of 0.2 mm.

RESULTS AND DISCUSSION

The accuracy of hardness results depends on the correct estimation of the volume fraction of the individual microstructure phases. The results of hardness determination are shown in Fig. 2. Statistical analysis of measured and simulated hardness was determined of the F-test for significance level α=0.05. Results showed a minimal significant difference between simulated and measured hardness.

The hardness results were fitted with a linear trend. Samples V1, V3 and V4 showed the same direction of linear trend. Differences in the direction of the linear trend were found for sample V2. The simulation of hardness shows small differences in hardness. Experimental hardness results show a decreasing tendency of hardness from the surface of the sample to its core. This deviation may be due to an inaccurate estimate of the volume fravtion of the microstructure phases in the sample cross-section area. Experimental and simulation estimated hardnesses show a slight increase of hardness from the core to surface of the sample in sample V3. However linear trends show the same direction, it is assumed that the hardness increases towards the core of the sample. This may be due to the formation of a different microstructure in the sample cross-section area.

The smallest difference between experimental and simulated hardness (4 HV) was found in sample V3. The biggest hardness difference (38 HV) was found at the core of sample V2.

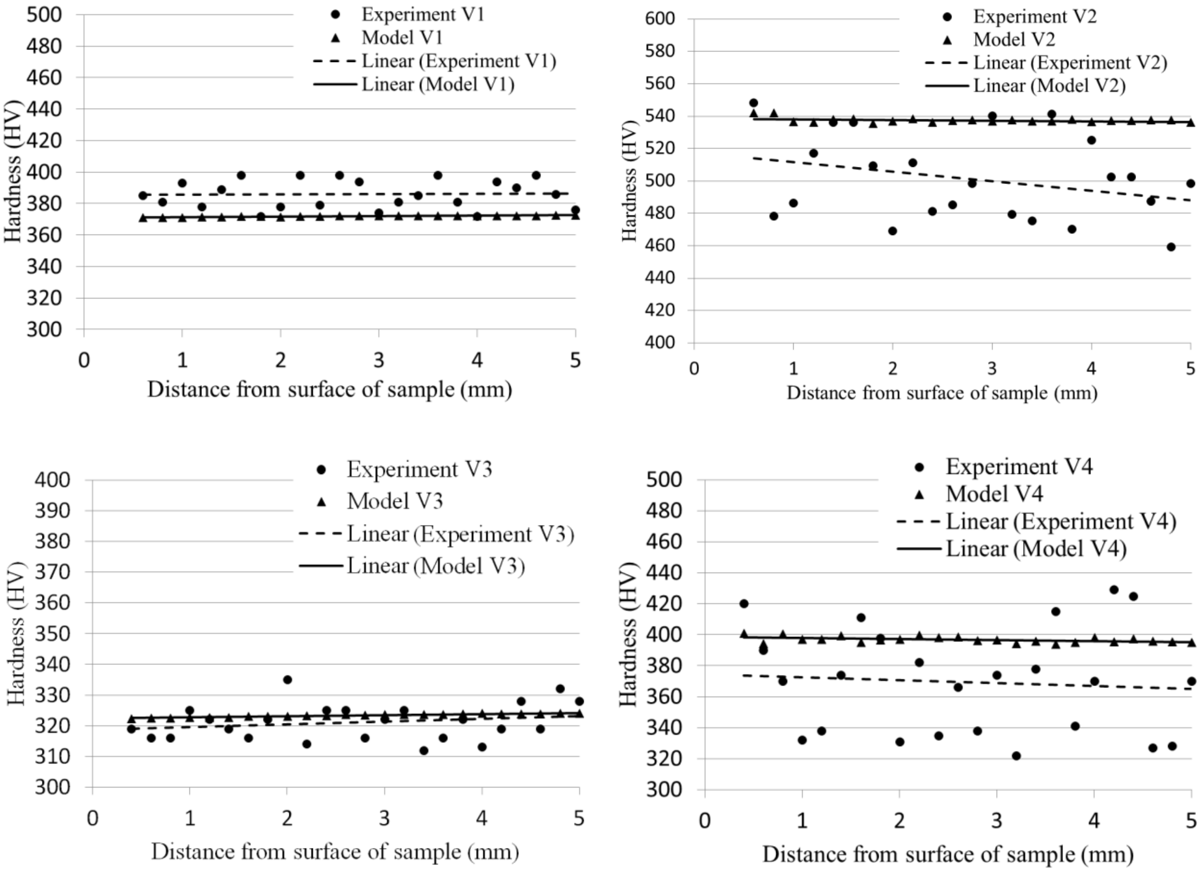

Fig. 2 Comparison of the experimentally measured and mathematically calculated hardness for 51CrV4 steel

A lot of authors (Votava, Kumbár, Polcar 2016; Narayanaswamy, Hodgson, Beladi 2016; LIU, SONG, CAO, CHEN, MENG 2016) describe experimental data of abrasion resistance and hardness in their works only as a supplement. Hardness is an important mechanical properties for agricultural tools (Herian, Aniołek, Cieśla, Skotnicki 2014; Jankauskas, Katinas, Skirkus, Alekneviciene 2014; Das Bakshi, Shipway, Bhadeshia 2013a). Hardness should be considered in the design of agricultural tools. (Chotěborský, Linda 2015) are concerned with the design of microstructure and hardness for a specific agricultural tools and assembly. Their procedure is identical as the procedure which is described in this work. The results of the model hardness and measured results show good agreement for steel of agricultural tool. For this reason, it can be concluded that the procedure described in these works can be used to design a heat treatment of an agricultural instrument where hardness is required.

CONCLUSIONS

A simulation was designed to estimate the hardness after heat treatment for low alloyed steel 51CrV4. The experiment was done to verify the results of a mathematical model of simulation. Microstructure is important for the correct estimation of hardness after heat treatment. The statistical test showed an agreement between model hardness and experimental hardness. The highest difference of hardness was found to be 38 HV between experimental hardness and simulated hardness. The procedure described in this paper can be used to estimate hardness after heat treatment.

ACKNOWLEDGMENT

This study was supported by by Internal grant 31140/1312/3114 agency of Faculty of Engineering, Czech University of Life Sciences in Prague.

REFERENCES

1. Babu, K., & Prasanna Kumar, T.S. (2009). Mathematical Modeling of Surface Heat Flux During Quenching. *Metallurgical and Materials Transactions B, 41*, 214–224.
2. Das Bakshi, S., Shipway, P.H., & Bhadeshia, H.K.D.H. (2013). Three-body abrasive wear of fine pearlite, nanostructured bainite and martensite. *Wear, 308*. 46–53.
3. Fernandes, P., & Prabhu, K. N. (2008). Comparative study of heat transfer and wetting behaviour of conventional and bioquenchants for industrial heat treatment. *International Journal of Heat and Mass Transfer, 51,* 526–538.
4. Herian, J., Aniołek, K., Cieśla, M., & Skotnicki, G. (2014). Shaping the structure during rolling and isothermal annealing, and its influence on the mechanical characteristics of high-carbon steel. *Materials Science and Engineering: A, 608,* 149–154.
5. Chotěborský, R., & Linda, M. (2015). FEM based numerical simulation for heat treatment of the agricultural tools. *Agronomy Research, 13*(3), 629–638.
6. Jankauskas, V., Katinas, E., Skirkus, R., & Aleknevicienе, V. (2014). The method of hardening soil rippers by surfacing and technical-economic assessment. *Journal of Friction and Wear*, 35*(4)*, 270–277.
7. Kešner, A., Chotěborský, R., & Linda, M. (2016a). A numerical simulation of steel quenching. *Proceeding of 6th international conference on trends in agricultural engineering 2016,* 300–305.
8. Kešner, A., Chotěborský, R., & Linda, M. (2016b). Determination of the heat flux of steel for the heat treatment model of agricultural tools. *Agronomy Research*, *14,* 1004–1014.
9. Kešner, A., Chotěborský, R., & Linda, M. (2017). Determining the specific heat capacity and thermal conductivity for adjusting boundary conditions of FEM model. *Agronomy Research, 15,* 1033–1040.
10. LEE, E., MISHRA, B., & PALMER, B.R. (2016). Effect of heat treatment on wear resistance of Fe–Cr–Mn–C–N high-interstitial stainless steel. *Wear, (368–369)*, 70–74.
11. Li, H. Y., Luo, D. F., Yeung, C. F., & Lau, K. H. (1997). Microstructural studies of QPQ complex salt bath heat-treated steels. *Journal of Materials Processing Technology, 69*, 45–49.
12. Liu, C.C., Xu, X.J., & Liu, Z. (2003). A FEM modeling of quenching and tempering and its application in industrial engineering. *Finite Elements in Analysis and Design,* 39(11), 1053–1070.
13. Liu, H., Song, Z., Cao, Q., Chen, S., & Meng, Q. (2016). Microstructure and Properties of Fe-Cr-C Hardfacing Alloys Reinforced with TiC-NbC. *Journal of Iron and Steel Research, International, 23*(3), 276–280.
14. Nalbant, M., & Tufan Palali, A. (2011). Effects of different material coatings on the wearing of plowshares in soil tillage. *Turkish Journal of Agriculture and Forestry*, *35*(3).
15. Narayanaswamy, B., Hodgson, P., & Beladi, H. (2016). Comparisons of the two-body abrasive wear behaviour of four different ferrous microstructures with similar hardness levels. *Wear, 350–351*, 155–165.
16. Ohtsuka, H. (2007). Effects of a High Magnetic Field on Bainitic and Martensitic Transformations in Steels. *Materials transactions, 48*(11), 2851–2854.
17. Rose, D.C., Sutherland, W.J., Parker, C., Lobley, M., Winter, M., Morris, C., Twining, S., Ffoulkes, CH., Amano, T., & Dicks, L.V. (2016). Decision support tools for agriculture: Towards effective design and delivery. *Agricultural Systéms.*
18. Shaeri, M.H., Saghafian, H., & Shabestari, S.G. (2012). Effect of heat treatment on microstructure and mechanical properties of Cr–Mo steels (FMU-226) used in mills liner. *Materials & Design, 34,* 192–200.
19. ŞIMŞIR, C., & GÜR, C.H. (2008). A FEM based framework for simulation of thermal treatments: Application to steel quenching. *Computational Materials Science, 44*(2), 588–600.
20. Sinha, V.K., Prasad, R.S., Mandal, A., & Maity, J. (2007). A Mathematical Model to Predict Microstructure of Heat-Treated Steel. *Journal of Materials Engineering and Performance, 16*(4), 461–469.
21. Teixeira, M.G., Rincon, M.A., & Liu, I.-S. (2009). Numerical analysis of quenching – Heat conduction in metallic materials. *Applied Mathematical Modelling*.

22. Telejko, T. (2004). Application of an inverse solution to the thermal conductivity identification using the finite element method. *Journal of Materials Processing Technology*.
23. Telejko, T. (2004). Analysis of an inverse method of simultaneous determination of thermal conductivity and heat of phase transformation in steels. *Journal of Materials Processing Technology*, 155–156, 1317–1323.
24. Votava, J. (2014). Usage of abrasion-resistant materials in agriculture. *Journal of Central European Agriculture*, *15*(2), 119–128.
25. Votava, J., Kumbár, V., & Polcar, A. (2016). Optimisation of Heat Treatment for Steel Stressed by Abrasive Erosive Degradation. *Acta Universitatis Agriculturae et Silviculturae Mendelianae Brunensis*, *64*(4), 1267–1277.
26. Zdravecká, E., Tkáčová, J., & Ondáč, M. (2014). Effect of microstructure factors on abrasion resistance of high-strength steels. *Research in Agricultural Engineering*, *60*(3), Czech Academy of Agricultural Sciences.

Corresponding author:
Ing. Adam Kešner, Department of Material Science and Manufacturing Technology, Faculty of Engineering, Czech University of Life Sciences Prague, Kamýcká 129, Praha 6, Prague, 16521, Czech Republic, phone: +420 22438 3271, e-mail: kesner@tf.czu.cz

SELECTED PROBLEMS EXPLOITING THRUSTERS ON DYNAMIC POSITIONING VESSELS

Marcin KOŁODZIEJSKI[1], Zbigniew MATUSZAK[2]

[1]Prosafe Offshore, Greenwell Road, East Tullos Inustrial Estate Aberdeen AB12 3AX, United Kingdom
[2]Faculty of Marine Engineering, Maritime University of Szczecin, Szczecin, Poland

Abstract
The aim of this project is to investigate the problems associated with current controllable pitch thrusters that are operated on dynamic positioning vessels. Work covers some component parts of a thruster and examines their failure mechanism. The paper is highlighting ways of improvement of thrusters' reliability during their operation.

Key words: *tunnel thruster; azimuth thruster.*

INTRODUCTION

Contemporary thrusters are used throughout the marine and offshore industry as a means of vessel propulsion, manoeuvring and dynamic positioning. Thrusters are available in two formats (*Kołodziejski, M. & Matuszak, Z., 1997*):
- fixed pitch propellers that are powered by DC electric motors, thrust is adjusted by means of variable speed and direction of electric motor. This kind of machinery is rather rarely met on offshore installations and that is why it will not be subject of this project;
- controllable pitch propellers that are powered by AC electric motors. They are running with approximately constant speed, thrust is adjusted by changing of pitch.
Both types of thrusters have a propeller of either fixed pitch or controllable pitch construction, however the controllable pitch assembly has been favoured due to its speed of response and is the subject of this study.
Vessels operators have increasingly expressed concern over the number of failures that have been experienced on dynamic positioning vessels. The overwhelming majority of failures require the thruster to be removed from its location in the vessel hull and brought to the surface for repair. This entails the implementation of an underwater removing mechanism if incorporated in the design, or for the vessel to go into dry dock (*The International Marine Contractors Association, Report No GM-01768/02-0695-2167: Failure Modes of CCP Thrusters*).

Tunnel thrusters

Tunnel thrusters are rigidly mounted inside a tunnel which runs athwartship in the bow or stern of a vessel. Figure 1a shows a diagram of a tunnel thruster. Tunnel thrusters are most commonly driven by an AC constant speed motor. There two types of drive configuration, an **L**- drive and an **Z**-drive An L-drive has the AC motor situated directly above the thruster unit and its drive shaft is located vertically into the thruster which is in turn located to the propeller shaft via a bevel gear arrangement, hence the drive system is an 'L' shape when viewed from the side.
A **Z**-drive is similar to an L-drive except that the AC motor is not situated vertically above the thruster hence a horizontal shaft is required which is connected to the vertical drive shaft via another bevel gear, giving a 'Z' shape arrangement. The vertical drive shaft is located in the thruster unit together with bearings and is connected to the pinion of the lower gear with a crowned tooth coupling. The drive is then transmitted through the pinion and gear and into the propeller shaft. The propeller shaft rotates the hub which in turn rotates the blades. The propeller shaft is supported with bearings and is hollow to allow the pitch control mechanism to run along its length. The lower gearbox id flooded with oil and is sealed in front of the propeller hub and protector with rope guards. The pitch control is actuated by a horizontal piston which operates a sliding yoke mechanism. By moving the position of the blade locating shoe the pitch of the propeller blades is altered. The blades are sealed with single O-

ring. There is a mechanical linkage feedback mechanism which allows a potentiometer to continuously provide the blade pitch angle to control the processor.

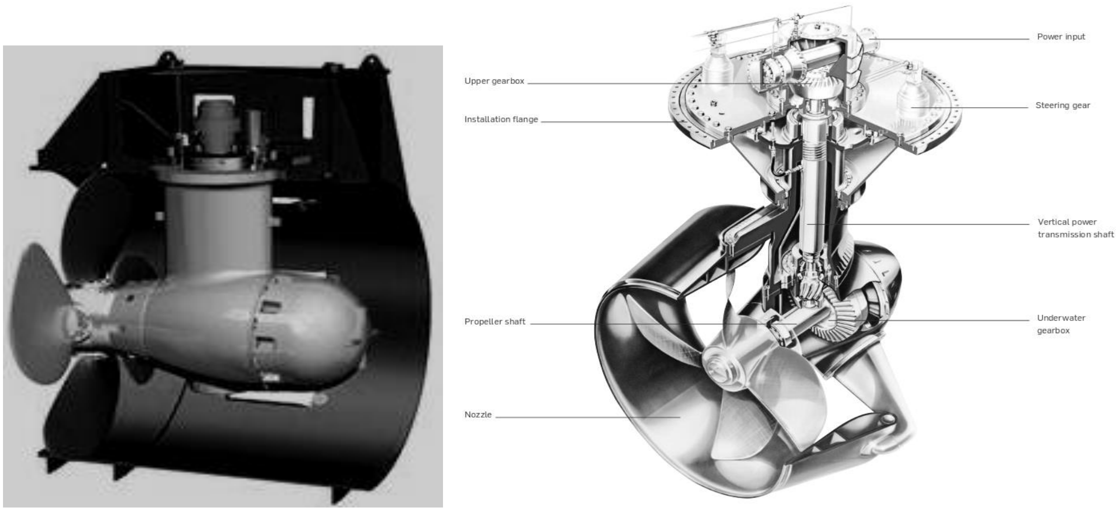

a) b)

Fig. 1 a) Tunnel thruster (*https://www.marinelink.com/news/introduce-steerable359425 [access 5.04.2017*]); b) Schematic diagram of an azimuth thruster (*https://proyectosnavales.com/2015/10/07/ azipod-mermaidpod-esipod-y-otros-pods/ [access 5.04.2017]*).

Azimuth Thrusters

Azimuth thrusters are essentially the same as tunnel thrusters with similar subsea design with one major difference, the ability to rotate through 360 degree about the drive shaft centre line. Figure 1b presents diagram of azimuth thruster. Azimuth thrusters are mounted on the underside of the vessel's hull or pontoons, and their position optimised for performance and minimum interference. They are usually driven in the same way as tunnel thrusters with an AC motors and an 'L' or 'Z' drive configuration. The thruster is normally rotated by two or more hydraulic motors which turn the upper steering gear. The main mechanical difference in operating conditions for an azimuth thruster compared to a tunnel thruster is its lack of circumferential rigid mounting around the propeller blades and its increased exposure to the rigours of a marine environment. The combination of these two elements contributes towards the greater susceptibility of azimuthing thrusters to failure.

Retractable azimuth thrusters

The main drawback with azimuth thrusters is the increase in the draught of the vessel due to the thrusters protruding below the vessel. To overcome this a retractable azimuth thruster was designed and manufactured. The unit is identical to a non-retractable azimuth thruster with the exception of the capability to be pulled up into the vessel's hull. The thruster is lowered via either hydraulic actuators or screw rods, and the thruster has a telescopic drive shaft to accommodate the change in position. On the base of the thruster nozzle there is the plate that fits into the hull to create a smooth hull form for when the vessel is not utilising it. The increased number of moving parts and the lengthened drive shaft leads to a retractable thruster being a little more prone to failure and most of them cannot be repaired from inside the hull when the thruster is retracted.

MATERIALS AND METHODS

Mechanical components and their possible failures

Drive shaft and crowned tooth coupling

The drive shaft runs vertically down the thruster transmitting torque from AC motor to the propeller shaft via a bevel gear. The shaft is held in place with bearings and connected to the bevel gear pinion with a crowned tooth coupling. The shaft is hollow and runs in an oil flooded environment.

The crowned tooth coupling should last the design life of the thruster if the maintenance procedures are followed. There have been incidents of the coupling being subjected to excessive wear due to lack of lubrication. This has been caused by insufficient application of grease to the coupling. The coupling is susceptible to vibration induced problems, which is enhanced by misalignment, hence it is crucial that the manufacturer aligns the system correctly and keeps vibration to a minimum. It is also subjected to a very rapid acceleration due to start-up on zero pitch. The thruster must be at zero pitch when the motor is started, if not then the coupling undergoes an enormous loading very rapidly. Zero pitch is sometimes hard to adjust and it may wander with time.

The drive shaft and coupling require little attention as they are generally reliable components. Their maintenance must not be neglected as this will lead to failure. It is essential that when the thruster is opened up during repairs the drive shaft is inspected for cracking. This should be part of the detailed checking procedure undertaken at every thruster overhaul and repair.

Bearings

The possibility of a bearing failure is often reduced by the frequency of thruster repairs and the ensuing re-builds for other reason. When the thruster is re-built new or refurbished bearings are installed as the original ones are usually damaged or displaced during dismantling. This then leads to the scenario of many vessels never reaching their bearing design life, hence artificially reducing the failure rate. However bearings have failed and do require the attention.

A thruster has several bearing which support the drive and propeller shafts. They are all of roller bearing construction but differ in size enormously, from the small lower drive shaft bearing to the very large upper steering gear bearing. Adequate lubrication is essential to sustain bearing life, yet there have been several incidents of bearing failure where sufficient lubrication was applied. It is also necessary to note that when a bearing fails it can damage other components from metal fragments, or even entire rollers, circulating the system.

There have been several cases of bearing failing as they approach, but have not exceeded, their design life. Bearing are often changed because the thruster is being overhauled for another reason, providing an ideal opportunity for expert inspection of the bearings that are replaced to compare wear and damage with known utilisation. By acknowledging that there is fault in a particular design the remaining vessels with similar designs can be informed and preventative action taken

Insufficient axial float of the propeller shaft may cause friction welding problems on some thrusters. Axial float corresponds to axial movement of the propeller shaft fore and aft. If the axial flow is not adequate then the locating bearings of the propeller shaft are subjected to the thrust loading rather than the thrust bearing. This can result in bearing running very hot causing friction welding to occur. The axial float of the shaft must be adequate to ensure that each bearing receives no more than its designated loading. Bearings have also failed due to too much axial float, so this parameter is critical and must be corrected at the outset. The shaft float requires careful design and correspondingly meticulous quality control during manufacture.

Bearing can overheat and run hot due to a lack of lubrication or if subjected to an oscillating load which is perpendicular to the plane of rotation. If the thruster has a significant vibration problem it can manifest itself as a bearing failure. If bearings overheat the contact surface will break down, otherwise known as pitting, causing metal fragments to circulate the system.

The biggest factor in all thruster failures is the seepage of water into a thruster unit. When a bearing runs in oil contaminated with seawater a range of problems occur. Water in oil creates a kind of water-oil sludge which tends to settle where the circulation is poor. Bearings which are in such locations are prone to gathering sludge and then rely on it to provide lubrication. The sludge is a poor lubricant and is detrimental to the running of the bearing. A bearing running with insufficient lubrication will run hot and begin to break down. Once a bearing has lost its surface hardness the break down is rapid and severe, and is accelerated by corrosion. Corrosion is caused by the seawater in the oil that attacks the bearing causing ‘black bearing’, which is the result of the combination of corrosion and overheating. To reduce the number of bearing failures the water ingress has to be stopped. Once this has been achieved the frequency of thruster failures due to bearing failures will decrease dramatically.

Gears

The failure of the bevel gear in the lower gearbox has a major influence on vessel downtime. They are susceptible to overloading, pitting, cracking and having teeth broken, all of which leads to catastrophic failure and costly repairs. As with bearing the prominent factor in gear failure is water ingress and its associated problems. The bevel gear is located in the lower gearbox and transmits the drive from the vertical drive shaft to the horizontal propeller shaft. It has helical teeth and the ratio is critical to the design of the thruster as it governs the size of the lower gearbox, which is significant for the hydrodynamic drag. To obtain maximum efficiency the motor speed wants to be high whereas the propeller blade speed wants to be low, hence the lower gearbox must optimise thrust efficiency and minimise drag.

Pitting of gears

Pitting of the surface of the gears is the most common cause of gear failure. Although the gears may not physically break they will require replacement which is costly and time consuming, compounded by the long lead times required to obtain new gears. The pitting of the gears is caused by inadequate lubrication and the generation of hot spots. The combination of heat and pressure between the meshing gears leads to the break down of the surface causing pitting. The lack of lubrication can be due to water in the oil or insufficient oil circulation, and usually combination of both. If the water is present in the unit it tends to gather at the base of the gear box and as the gear rotates it passes through this water and then meshes with the pinion, hence it meshes with water and oil causing hot spots to develop. Over time this repeated excessive and high pressure will cause pitting to occur. Pitting will occur on gears over a period of time, especially when run in marine environment and prone to water contamination. However, it should not manifest itself before the design life of the gears has been reached. In some thruster units it has appeared only a few months after installation. The primary solution to the problem is to remove the water from the oil and prevent the water from leaking into the lower gearbox. In addition to this the gear alignment must be accurate and the vibration levels of the lower gearbox must be negligible, as these factors will accelerate any rear wear problems. There have been a few incidents of heavy pitting where there was no indication of water ingress, the reason for this is unknown and requires further investigation. All these leads to the question why is there inadequate lubrication, and why is water allowed to enter the thruster and remain undetected? The poor lubrication can be easily blamed on water in the oil but it is a fundamental design fault in all thrusters. There is inadequate provision for complete circulation of the oil with the gears running in old, stagnant, un-filtered and water contaminated oil. Perhaps the oil needs additional pumping around the gears and a low take off point to properly monitor its condition. There is no point in analysing oil from the header tank when it is nothing like the oil around the gears where real damage occurs. The dichotomy between oil quality at the sampling tap and around the gears is enormous, and one which leads to neglect and failure. This is design fault which should be addressed immediately and rectified on all thrusters. Without comprehensive oil circulation around the gears and good oil sample analysis it is clear that a thruster failure will tend to always be diagnosed as inadequate lubrication even if this is only a secondary cause.

Broken teeth

Gear teeth can break due to fatigue or overloading which is usually caused by under design and occasionally due to material fault which went undetected. There have been several incidents of teeth breaking resulting in thruster failure and in some cases damage to other components through the broken teeth circulating the system. If the lower gearbox is subjected to high levels of vibration, fatigue problems will arise in the gears. Vibration can be transmitted down the drive shaft from the motor, or from the varying hydrodynamic forces as the thruster moves in the waves. This could lead to gear failure in the form of broken teeth through shock loading. However, the most common cause of broken teeth is due to a power overload. Gears that are under designed are likely to fail as they are not capable of withstanding the forces involved. This situation will arise when the vessel specification and workload are under estimated. An overload situation will also arise if the thruster is started with the blades not at zero pitch. This will put a huge load on the thruster and consequently the gears. If The blades strike floating debris the subsequent loading on the gears can be considerable and this has caused teeth to break.

RESULTS AND DISCUSSION

Problems associated with lubrication of thrusters' components

If a thruster is correctly designed, installed, and operated, then its reliability depends heavily on oil quality. Without sufficient lubrication and cooling the subsequent effects on the thruster can be catastrophic. It is of paramount importance when running thrusters to keep the oil clean and free of contamination. It follows that the design should enable competent engineers on board to maintain oil quality with relative ease. If the on board maintenance is carried out according to the manufacturers instructions and water ingress takes place, the responsibility rests on the manufacturers. The oil system on a thruster is vastly different from a normal mechanical device as the lubricating oil and hydraulic oil is the same. In other words oil that lubricates the meshing gears teeth also controls the hydraulic components. This inherently leads to problems as the oil chosen is a compromise between hydraulic oil and gear oil. The oil is contained in a local tank which is pressurised by a small header tank well above the water line at the deepest draft to give an overpressure in the gearbox. The oil is fed from the local tank to the thruster, circulated around the unit, and then returned to the tank through filters to remove any dirt. Overpressure provided by header tank is supposed to refrain water from leaking to the thruster unit through the seal. Water and oil do not mix, and once water has gained access to an oil lubricated system the water forms a kind of sludge which has a tendency to settle where circulation is poor. The sludge has no beneficial lubrication properties and only causes damage to the thruster. The water reduces the oil's capacity to lubricate and cool, allowing hot spots to develop on gears and bearings which leads to their eventual failure. It also causes hydraulic causes as the sludge can cause control valves to stick leading to control problems. The water usually enters the thruster through the propeller shaft seal despite the over pressure. The oil will normally become dirty from its operation in the lower gear box. The meshing gear will produce tiny metal fragments, the water introduces salt into the oil, and any oil degradation from overheating will also produce solid particles. Dirty oil offers substandard lubrication and cooling, increases wear rates, and causes hydraulic valves to stick. The reduced ability of the oil to function correctly leads to, or increases the risk of, the failure of other components. If the oil is overheated it will break down and its lubrication property will diminish. Excessive heating of the oil can be caused by the misalignment of components generating hot spots, poor circulation through the gearbox, and insufficient cooling. The first two are the most common causes and better circulation of the oil is an area which has been identified as requiring improvement. The fundamental problem with the oil is its susceptibility to water contamination. This has to be prevented by improving sealing. However, until a suitable sealing arrangement is produced the water should be removed using separators and filtration devices. It is also essential to improve the circulation of the oil as the water is often allowed to gather in the thruster and it never really surfaces for extraction analysis and replacement. By taking the oil from the bottom of the thruster the water would be forced out allowing it to be removed. This is a practical modification that needs urgent action for all thrusters. A continuos water content check is required to monitor the level of water in the oil as at present the oil sample analysis is not frequent enough or not true reflection of the oil in the thruster. In general the results of the oil analysis are relied upon far too heavily in assessing the condition of the thruster, and this has been proved through high failure rates with the oil analysis being satisfactory. The filtration of solid particles is essential to prolong the thruster life. It is a simple and easy operation to maintain filters. It is crucial that all filters are monitored closely and replaced regularly. If unusually high quantities of dirt are found they should be investigated. However, the filters rely on good oil circulation for the particles to reach them. The oil temperature should also be monitored carefully, but just checking the oil temperature outside the gearbox is not sufficient and temperature monitoring should be carried out in the lower gearbox as well. This is because the failures caused by overheating will occur here and the sooner information is received with regards a potential problem, the sooner it can be solved. Temperature monitoring within the lower gearbox is definitely a means by which catastrophic failures can be prevented. The problems of all sensors however is that they themselves are the purveyors of bad news.

CONCLUSIONS

To reduce the thrusters' failures the water ingress has to be stopped. Once this has been achieved the frequency of damages of bearings and gears will decrease dramatically. The requirement is to remove the water from the system, not only in an attempt to directly reduce the number of failures but also to aid clarification of the failure cause. It is very easy to lay the blame for a failure with water ingress, however once this has been removed from the equation failures must be attributed to another cause. Water ingress in some ways a convenient excuse for thruster failure, providing the manufactures with a cause without highlighting any design errors. By removing the water the lubrication will improve and the pitting of gears will be lowered. In conjunction with this oil circulation needs to be adequate to give good lubrication and cooling to the meshing gears. The only other way to reduce pitting is to upgrade the material specification. It is also essential that that the gears are aligned correctly to ensure that they mesh in the designed pattern, as incorrect meshing leads to excessive abrasive wear and eventually broken teeth. Any vibration problems should be addressed immediately as they will shorten the fatigue life of the gears. The running in of a thruster unit is critical to ensuring reliability. After every re-build they must be run in at a low load for a sustained period of time and the temptation to run to full power to resume work should be ignored. The longer the running in time the longer the life of the thruster. An extra day of running in will reduce the chance of thruster failure before a scheduled docking (*Matuszak, Z., 2010*).

ACKNOWLEDGMENT

„This research outcome has been achieved under the research project *Badanie efektywności energetycznej siłowni okrętowej w aspekcie niezawodnej i bezpiecznej eksploatacji* No 5/S/IESO/14 financed from a subsidy of the Ministry of Science and Higher Education for statutory activities”.

REFERENCES

1. Kołodziejski, M., & Matuszak, Z., (1997). Comments about the dynamic positioning vessels service. Second International Conference on Marine Technology, (Odra ‘97) Szczecin 13-15 May 1997, 343-349.
2. Matuszak, Z., (2010) Estimation of the availability of the power-propulsion and technological system of a fishing vessel at selected operational model. *Eksploatacja i Niezawodnosc – Maintenance and Reliability*, vol. 45, no. 1, 49-58. DOI: dx.doi.org/10.17531/ein.
3. The International Marine Contractors Association, Report No GM-01768/02-0695-2167: Failure Modes of CCP Thrusters.
4. https://www.marinelink.com/news/introduce-steerable359425 [access 5.04.2017].
5. https://proyectosnavales.com/2015/10/07/azipod-mermaidpod-esipod-y-otros-pods/ [access 5.04.2017].

Corresponding author:
Ing. Marcin Kołodziejski, Ph.D., Prosafe Offshore, Greenwell Road, East Tullos Inustrial Estate Aberdeen AB12 3AX, United Kingdom, e-mail: magosiak@box43.pl
prof. Ing. Zbigniew Matuszak, Ph.D., Faculty of Marine Engineering, Maritime University of Szczecin, ul. Wały Chrobrego 1-2, Szczecin, Poland, e-mail: z.matuszak@am.szczecin.pl

NUMERICAL ANALYSIS FOR OPTIMIZATION OF PRESSURE VESSEL

Marek KOVÁŘ[1]

[1]*Department of Textile Technologies, Technical University of Liberec*

Abstract
This study deals with creating s finite element model (FEM) of filter for future optimization. The filter is composed of two parts. These parts are pressure vessel and filter partition. Finite element analysis (FEA) is a good tool for predicting the state after load in a pressure vessel. FEA can find out hidden danger unachievable by analytical solution. On one hand, numerical solution can show critical part of the product, on the other hand can show over-size areas. First point of interest is thickness of pressure vessel. Thickness reduction will result in weight loss. The aim of this study is a verification numerical solution by analytical solution and to select over-size areas for future optimization.

Key words: *finite element analysis, thin-walled pressure vessel, filter, MSC Marc.*

INTRODUCTION

Pressure vessels are used in many different kind of industry. Thin-walled pressure vessel can perform the function as diving bottle, overpressure chamber, distillation tower or filter. They are metal containers. They are fulfilled by liquid or gas under pressure. Construction of the pressure vessel is welded from sheet plate usually. Material of sheet is galvanized metal, stainless steel or steel. They have two configurations and that horizontal position and vertical position. Problematic of pressure vessel is describing in (*Megyesy, Buthod 2008*; *Moss, Basic 2013*). The key of the pressure vessel is durability before damage by high pressure. This study is a pressure vessel like a part of the filter. They requirements are placed on the speed of filtration and weight of the device. The effort of many companies is to reduce weight and make filtration more efficient.
Filtration is process of separate between fluid and solid phase. This topic is describing in book (*Perlmutter 2015*). Suspension is conducted through the filter which stopped solid pollution and the liquid continues. Base part of the filter is filtering layer. It was created from textile, sieve or porous plate. The result must have the quality required by the customer. The subject of this problem is in (*Cheremisinoff 1989*). Liquid is generally used in process of filtration like a final product or can be used as supporting product for the next production. Filtrate liquid are used in wide spectrum of industry application as chemical industry, automotive, oil industry, glass production or food production. The incentive to crate this work has given (*Mutava* 2016)

MATERIALS AND METHODS

Design of the filter is shown on Figure 1. FEA will be restricted only on pressure vessel. Filter partition will be included in future study. The vessel was rolling from the sheet with 3 mm thickness. Full length of the vessel is 1072 mm. It is assumed from two parts. The first part is a cylinder with diameter 219 mm and the second part is hemispheric. The next part is the lid. Head part of the lid has diameter 262 mm. The filter has vertical configuration. Filling hole was on the side and the emptying hole was on the bottom of hemisphere. Due to the dimension, the vessel was considered like a thin-walled in FEA. Material of the vessel and lid was chosen as stainless steel 1.4301. This steel can easily be cold rolled, drawn and stamped. This steel can easily be welded by any conventional joining technique, except the oxyacetylene torch. The material has a Young´s modulus of 200×10^3 MPa, tensile strength of 1275 MPa, Yield strength 965 MPa and Poisson ratio of 0.3. The alloy steel was assumed to be isotropic linear-elastic in FEA. Construction pressure on the vessel was set on 1.3 MPa and operational pressure was set on 1 MPa.

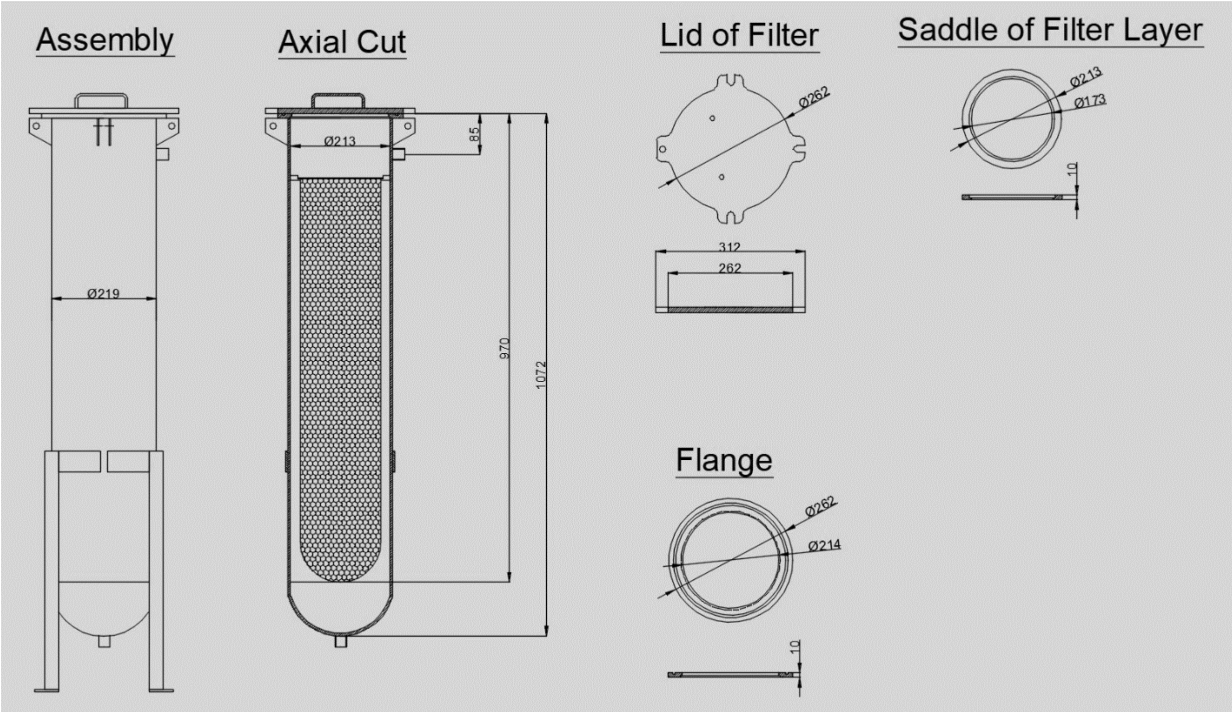

Fig. 1 Design of filter

Analytical solution was made only for cylinder part of a vessel at a sufficient distance from the stress change points.
Maximal axial stress can be calculated by equation (1)

$$\sigma_a = \frac{p \cdot r}{2 \cdot h} \tag{1}$$

where p is operation pressure (Pa), r is the mean radius of the vessel (mm) and h is wall thickness of the vessel (mm).
Maximal tangential stress can be calculated by equation (2)

$$\sigma_t = \frac{p \cdot r}{h} \tag{2}$$

where describe of member is the same for the equation (1).
Equation (3) is the Von Mises criterion for plane stress

$$\sigma = \sqrt{\sigma_1^2 - \sigma_1\sigma_2 - \sigma_1^2} \tag{3}$$

where subscript σ_1 replace with σ_a and σ_2 replace with σ_t.
History of creating a computing model was captured on figure 2. Simplification was made in drawing the model. Some parts were neglected. The model was drawled in software Autodesk Inventor 2018 (Figure 2a). This created model was imported in FEMAP for to create meshes. Solid model was reduced to mid-surface (Figure 2b). The lid was meshed separately. The vessel was contained in square shell an element with constant thickness 3 mm. The lid was meshed as solid with hex linear elements. Both meshed models are imported in MSC Marc software (Figure 2c). There was set boundary condition. The vessel was fixed on the ring which represents rack. Vessels lid was assembled to the vessel by glued contact. Inner pressure was made by face load and set on 1 MPa.

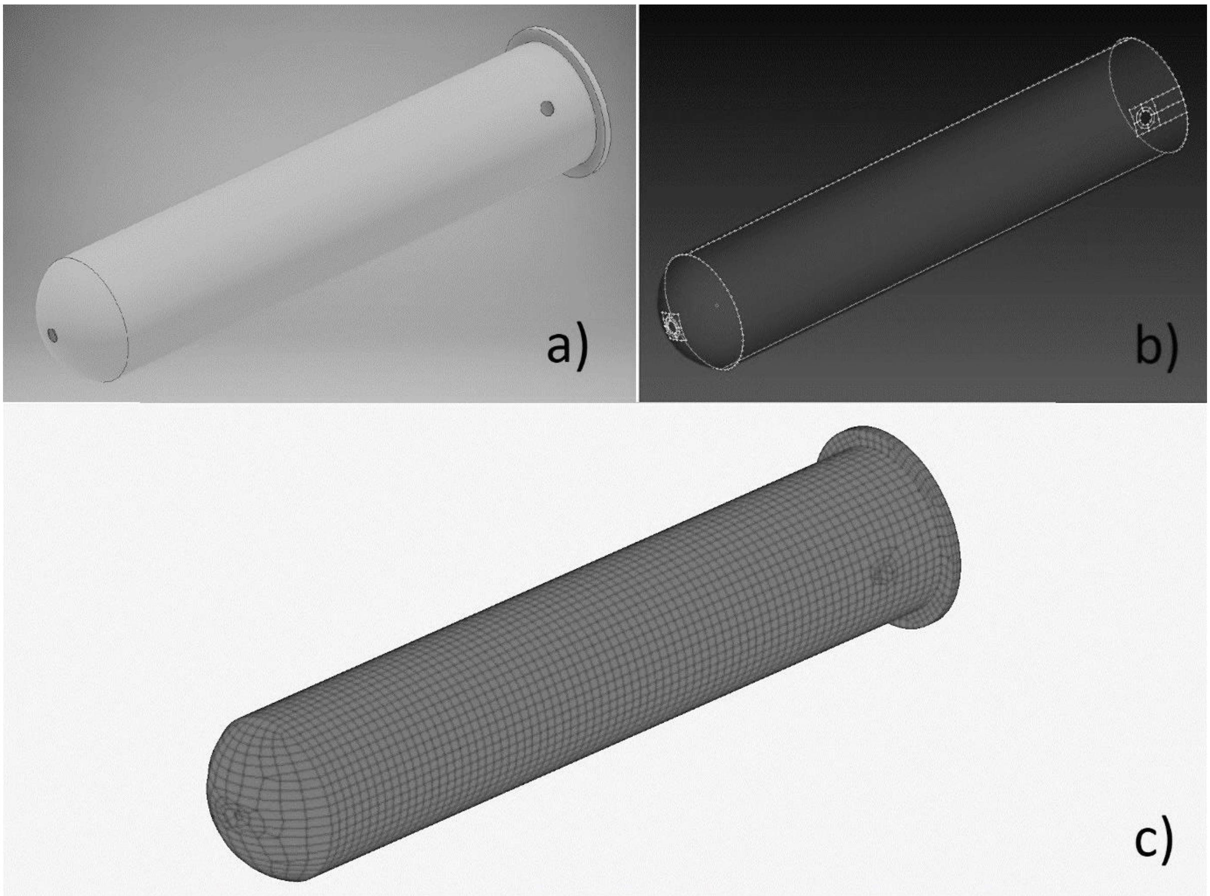

Fig. 2 FEM model creating sequence

RESULTS AND DISCUSSION

The results of analytical solution are shown in table 1. Difference was 0.83 % between analytical solution and numerical solution.

Tab. 1 Comparison analytical and numerical solution

Method	Von Mises Stress MPa
Analytical	31.61
Numerical	31.35

The FEA results were illustrated in Picture 3. Lowest Von Misses stress was determined on the hemisphere. The value of stress was 26 MPa. Maximum Von Misses stress was 83.01 MPa. This critical area was around filling hole. The lid was another area with stress concentrates. Stress concentrated in center of lid with maximal value 50.72 MPa. This solution was designed as worst situation of the pressure vessel. There is the space for considers to make a more detailed model. Welded flange is added in design of filters. Join was replaced as glued contact. It can lead up to growing stress in analyzing area. Flange can result in an increase a durability against pressure. The vessel is more durable with every other part.

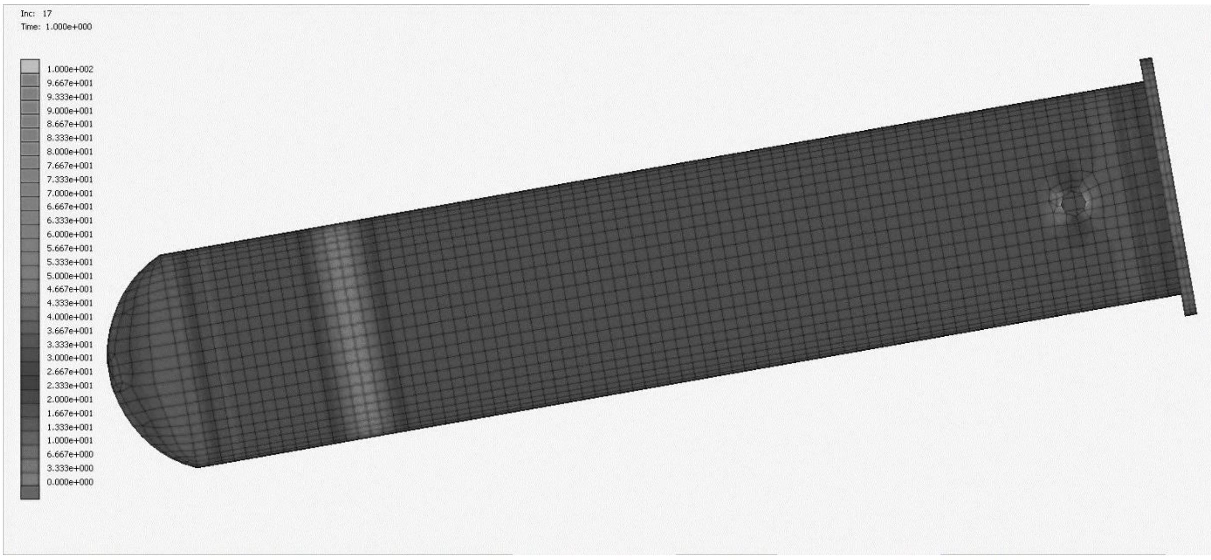

Fig. 3 Von Mises stress on pressure vessel

CONCLUSIONS

The aim of this analysis was to make the first study on concrete filter. The first part of the article was showed a comparison between analytical and numerical solution. The difference was 0,83 % between this solution. This result was only for cylinder part of the vessel. Analytical solution was hard used around hole or surface curvature. This results were captured easier by numerical solution. Finding of over-size or under-size areas lead up to better construction of the technical part. Pressure vessel can have had lower weight with same safety in this particular case. Analyses showed two critical areas. The first critical area was around filling hole. Less significant critical area was in the centre of the lid. On the other side, bottom hemisphere is over-size of the vessel. Significant thickness reduce can be done at the hemisphere end of the vessel. Next reduce of thickness can be done on cylindrical part of vessel. It is necessary to focus on the location around the filling hole. There is need to add more wall thickness or some reinforcement part. Critical location on the lid can be solved by the growing size of thickness or change shape of the lid. If hemisphere lid is used, the stress will dramatically reduce. Future studies will deal with find out the optimal shape of a vessel of the filter.

ACKNOWLEDGMENT

The results of this project LO1201 were obtained with co-funding from the Ministry of Education, Youth and Sports as part of targeted support from the "Národní program udržitelnosti I" program

REFERENCES

1. Megyesy, E. F., Buthod, P. (2008). *Pressure Vessel Handbook*. 14 th ed. Oklahoma: PV Pub.
2. Moss, D. R., Basic. M. (2013). *Pressure vessel design manual*. 4th ed. Boston: Elsevier/Butterworth-Heinemann
3. Perlmutter, B. A. (2015). *Solid-liquid filtration: practical guides in chemical engineering*. Oxford, [UK]: Butterworth-Heinemann.
4. Cheremisinoff, N. P., Azbel, D. *Liquid filtration for proces & pollution control*. Matawan, N.J.: SciTech
5. Mutava, J. et al. Finite Element Strucutral Analysis of a Thick-walled Pressure Vessel. In 2016 *Proceedings of Suitable Research and Inovation Conference,* [S.l.], p. 174-185.

Corresponding author:
Ing. Marek Kovář, Department of Textile Technologies, Faculty of Textile Engineering, Technical University of Liberec, Studentská 2, Liberec 1, 46001, Czech Republic, phone: +420 48535 3257, e-mail: Marek.Kovar@tul.cz

NEW CONCEPT OF SHIP'S POWER PLANT SYSTEM WITH VARYING ROTATIONAL SPEED GENSETS

Maciej KOZAK

Department of Mechanical Engineering, Maritime University of Szczecin

Abstract
A variable speed genset is an engine driven electrical power generating system that uses proper technology to control engine speed to provide performance enhancement, fuel savings, reduced emissions and noise reduction while providing power to the load at a specified voltage and frequency. The presented system consists of asynchronous generators and a DSP controller. Numerical simulations along with experimental results obtained in laboratory desk bench were presented.
Key words: *electronic governor, parallel operation, power distribution, load sharing, VSI, variable speed generators.*

INTRODUCTION

Currently most generators installed onboard of seagoing vessels operate with a fixed rotational speed which results in constant voltage frequency on terminals (mostly 60 Hz and 50 Hz). With high rotational speeds combustion engines produce higher exhaust gases emissions. The manufacturers have started to reduce the speed on engines just to meet new emission standards. In these solutions there is a need of maintaining higher, constant revolutions when operating with low loads. This has always been a major concern with regard to the glassing of the cylinders, engine lifespan, and consumption of lubricating oil.

In recent years manufacturers are creating and testing engines (Diesel, dual-fuel or gas feeded) that allow efficient operation under low RPM’s. This feature makes gensets more environmentally friendly because of low fuel consumption along with lower exhaust gases emission. Variable speed function of the engine is dependent on electrical generator load and power consumed. There are two main types of variable speed gensets. These are based on power electronics and based on a mechanical, constant speed transmission.

The constant speed transmission employs a mechanical solution that uses a standard synchronous alternator and a variable speed engine.

Power electronics based designs use an engine driven generator along with power transistor (or controllable thyristors) inverters in back-to-back intermediate circuit connection, power electronics filters and a control scheme to create resulting voltage and current waveforms comparable to that generated by a fixed speed synchronous genset. Line side inverter performs constant voltage and frequency output during most load conditions and may also provide fault protection. In the solution with AC voltage output of line side inverter and varying rotational speed there is problem of rapid load changes which may cause a voltage collapse. The drawback of lower RPM’s of combustion engine is the lack of power reserve so in such solution some other means of power reserve must be provided. The article presents new concept of system consisted of variable speed Diesel engines propelling asynchronous squirrel-cage electrical generators which are feeding IGBT’s inverter DC intermediate circuitry.

MATERIALS AND METHODS

The main advantage of varying RPM’s generator is average fuel saving from 6% (huge cruise ships) (*Lundh, Garcia-Gabin, Tervo & Lindkvist, 2015*), to about 20-30% (small, specialized diesel-electric vessels) thus reduced emissions as fuel is burned more cleanly. Moreover, very important factor on the vessel mounted genstes is reduced noise and vibrations level (>6dB) what in the case of all-electric ship with 6 medium speed gensets results in notably noise reduction. Another advantage of such system is decreased combustion engine wear resulting in doubling time to overhaul. According to average load requirement the driving Diesel engine can be optimally sized, with peak loads supplied from external electrical energy storage unit (batteries, super or ultra capacitors). With use of direct current ship electrical distribution system overall weight and space of the equipment decreases of about 30%. As real-world applications of offshore PSV ships like "Dina Star" or "Edda Ferd" show excellent results of using variable speed generators and DC current distribution systems along with power electronics controllable converters the attempts to improve such a system are being undertaken.

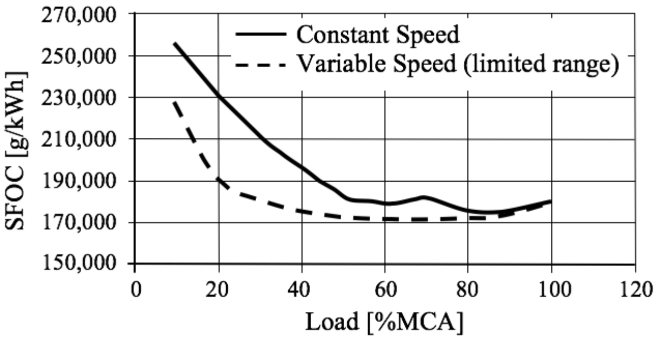

Fig. 1 Comparison of SFOC of variable speed operation efficiency against constant speed operation. (*Kozak, Gordon & Bejger, 2016*)

As it can be seen in the Fig. 1 the efficiency of presented system is notably better than one of the constant RPM's especially under medium and low load values. This is not surprising as the typical Diesels engines are designed to operate at minimal load at level of about 60%. The problem arises when load demand excesses a little bit power of one genset and to complete operation two generators must be put into parallel operation. The dynamic changeover of load between the gensets is recognized as the best mean for removing cylinder surface carbon deposits but it is not providing

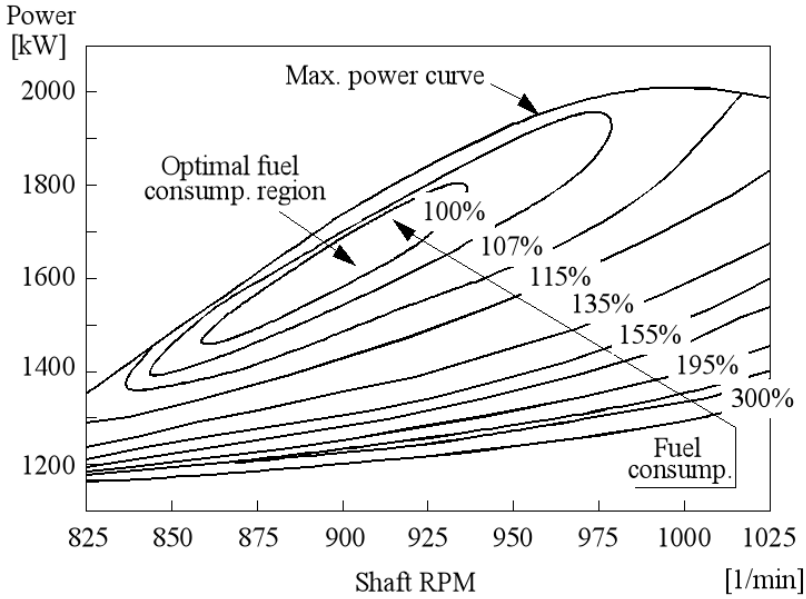

Fig. 2 Marine fuel consumption and exhaust gases emission reduction. (*Kozak, Bejger, Gałaj & Gawdziński, 2016*)

Ship electric load variability implies changing in time power generation, hence variable operation points for the generators. It is well-known that the SFOC (specific fuel oil consumption) function of a diesel generator depends solely on the generator output power and some loses. Generators fuel consumption function can be approximated by second order polynomials (*Kanellos, Tsekouras & Hatziargyriou, 2014*). This function can be expressed as:

$$FC_j(P_j) = a_{0j} + a_{1j}P_j + a_{2j}P_j^2,\ P_{jmin} \leq P_j \leq P_{jmax} \quad (1)$$

where P_j is the power of j-th unit.

Specific fuel oil consumption function (denoted as F_{SFOC}) is useful for the determination of the point of operation of a generator. SFOC determines generator fuel consumption per kilowatt hour. A typical SFOC is shown in Fig. 1. SFOC for given engine can be calculated as

$$F_{SFOCj}(P_j) = FC_j(P_j)/P_j = a_{0j}/P_j + a_{1j} + a_{2j}P_j\ ,\ \ P_{jmin} \leq P_j \leq P_{jmax} \qquad (2)$$

SFOC of combustion engine is a decreasing function of the produced power P. In the point where the most economical operation is achieved curve slope changes and increases until next maximum power.

In the case of ship propelled by electrical motors optimization of the electric power generation should be performed along with the optimization of the electric propulsion power. This problem comprises problems of power generating unit priority and optimal power distribution. Unit designation decides which gensets should be to be used. Power management system calculates optimal time of operation during the examined time period, while the load sharing between each generator is calculated by optimal power dispatch. Since the electrical generators are at most operating at constant speed, power distribution capabilities are limited.

To overcome aforementioned limitation a method of proper power distribution with use of control signals coming from electronic governor and DC system consisted of induction generators co-working with VSI inverter was developed. Main difference between proposed system and existing technical solutions is use of simple electrical machine as electrical generator. Onboard of few vessels similar systems consists of self-excited generators with series connected controlled rectifiers. As an emergency power reserve battery with boost-buck converters is provided.

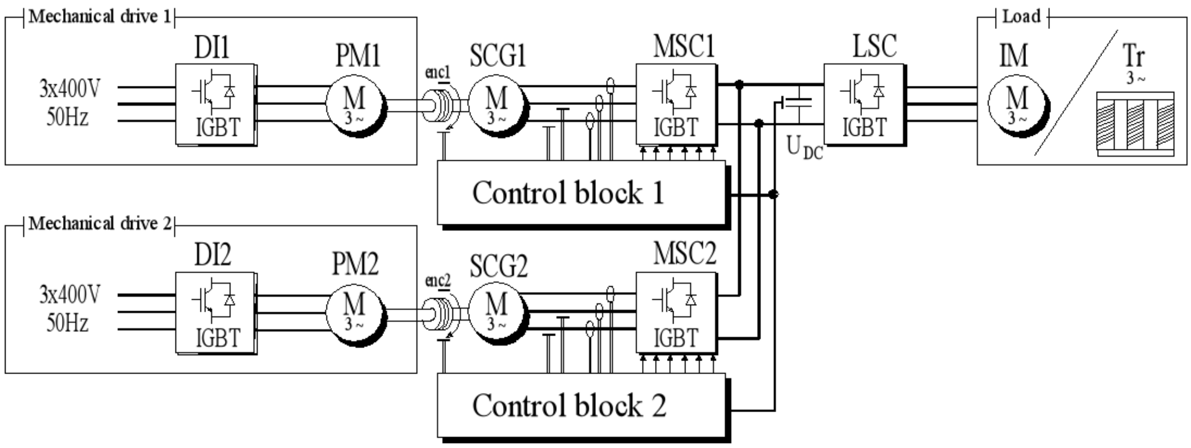

Fig. 3 Block scheme of proposed system. (*Kozak, Gordon & Bejger 2016*)

Proposed strategy of electrical generators control is based on assumption every inverter unit assigned to it's own generator can act as individual generator power management system "Slave" which cooperates with "Master" unit. While Modbus RTU communication network is assured, system can easy cooperate with combustion engine governor and control unit to maintain optimal point of combustion engine work thus to achieve best work parameters. As alternating voltage sources there are used asynchronous squirrel cage generators marked as SCG. Both generators are driven by prime movers (PM) fed by drive inverters (DI). This kind of connection allows convenient driving of generator sets in wide range of RPM's. As it can be seen in Fig. 3. both inverters are in back-to-back connection (with DC intermediate circuits) which can be extremely useful in case of both direction power transfer. In proposed solution electrical energy is distributed with means of direct current, but most of consumers need inverters to work properly, so in there can be add line side converter (LSC).

Proposed system consists of two real-time controlled inverters where digital signal processor can be programed with use of VisualDSP++ 5.0 programming high-level language. FPGA (field-programmable gate array) is programmed by Altera Quartus II software. FPGA digital circuit controls switching strategy of IGBT (insulated gate bipolar transistor) transistors in space vector pulse width modulation (SVPWM) and provides handling of analog to digital sensors. DSP circuitry calls FPGA in software interruptions and reads values of measured current and voltages for control purposes. After calculation loop is done DSP sends voltages data in α-β coordinates to execute by FPGA, which enables switching of IGBT transistors. FPGA software inherently cares of power electronics dead time so every change of power devices state must be preceded by short (usually few of μs) delay.

Proper operation of individual load inverters is ensured while direct current link voltage is maintained at desirable level. In tested system, DC voltage was set on 700V and it was kept almost constant by machine side inverters.

Considering Diesel engine governor inputs and outputs as main control unit the RPM's and engine mechanical torque would be the best choice of control signals. Such signals are inputs of electrical power management system with means of Modbus protocol.

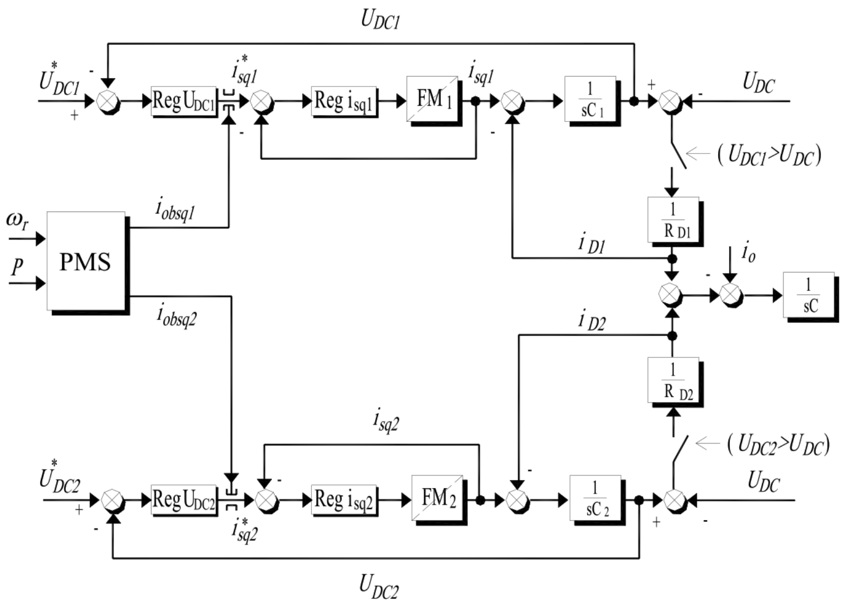

Fig. 4 Control system of proposed system.

The core of presented system are signals of available power P and rotational speed ω_r of working in parallel generators incoming into PMS (power management system). The data is proportional to incoming available power of each genset and consist of limited power and rotational speed of generators. Based on incoming data DSP is performing real-time calculations of power distribution between generators. There are Diesels engines torque maps (*Seung-Hwan, Jung-Sik, Joon-Hwan & Seung-Ki, 2015*) with optimal fuel consumption regions and forbidden areas in the form of tables embedded into software code. The data fill of tables would come from information provided by engines manufactures. The algorithm of power distribution seeks for optimal Power/RPM's ratio with use of (1) and (2) closest to optimal region of SFOC for each genset. In the case of two-way communication between PMS and EEG (engine electronic governor) power management system is capable to transmit RPM's control commands. Because of complexity of design and used algorithms it is worth to note that not only one configuration exists and finding the best parameters can be achieved in many ways. In proposed system knowledge of total electrical load of generators is crucial to work out proper Diesel engines control signals.

In the case of very simple to maintain asynchronous squirrel cage generator (SCG), task of excitation and stable work, is far more complicated than in other type of self-excited generators. Firstly, DC link capacitors have to be charged from external source. With energy stored in capacitors of intermediate circuit generator is put into operation and initially takes energy from energy banks for machine magnetization purposes. Decoupled control of magnetizing and active current is provided by means of programmed machine side inverter. After voltage build-up the DC busbar voltage is maintained by outer-loop control algorithm.

As control method algorithm the field oriented control (FOC) was chosen as perfectly fit to such a task. In a manner of this method there can be independently controlled active and reactive currents.

Active current i_{sq} control loop in d-q coordinates provides constant DC link voltage U_{DC} value, while reactive current i_{sd} is set to value motor magnetizing current.

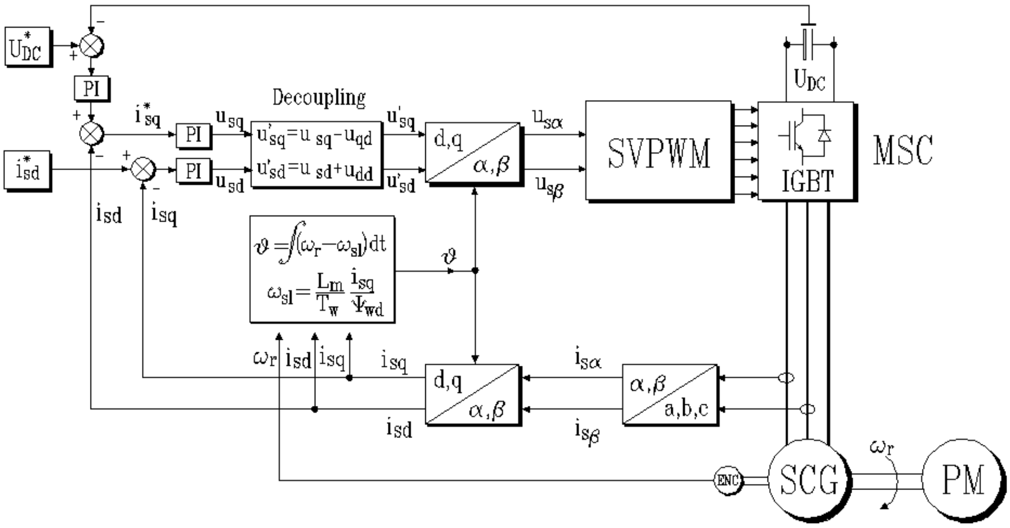

Fig. 5 Scheme of squirrel cage asynchronous generator FOC control *(Kozak, Gordon, Bejger 2016).*

The core of FOC is use of transformations calculated in real-time. Using of space vector properties there's possibility of projection sinusoidal balanced three phase quantities as easy to control constant values of currents, voltages and fluxes. For example space vector $\overline{x}_S$ representing aforementioned quantities can be expressed by two-phase magnitudes called x_α and x_β in the real-imaginary complex plane.

RESULTS AND DISCUSSION

To verify assumptions made, proposed system was simulated. All simulations including discretized asynchronous generators models were prepared in VisualDSP++ language. Control algorithms and procedures were coded in a manner that gave possibility to move straight the source code into DSP processor. Some parameters tuning was applied and simulations results were obtained.

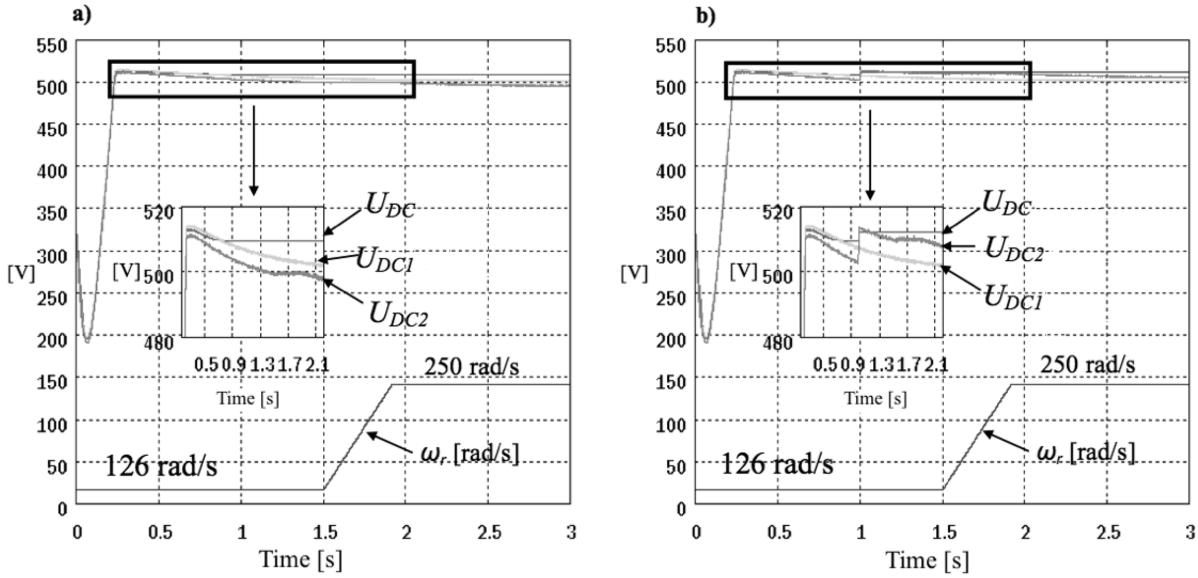

Fig. 6 Simulation results of start-up and parallel operation of two squirrel cage generators.
a) without power sharing algorithm enabled b) with automatic power sharing enabled.

For purpose of further researches laboratory test bench was created. System consists of two generators with outputs of power 1kW and 4kW respectively. Both of them are tied up to IGBT inverters controlled by one FPGA/DSP unit. LEM current and voltages transducers perform measurements. Field programming array FPGA works in DSP interrupts. In an interrupt call DSP is sending voltage waveforms of 16-bit length to FPGA. In the same time DSP reads values from analog-digital converters that are fed with data by LEM transducers. In FPGA space vector modulation program is executed in an endless loop. Auctioneering diodes are soldered on separate PCB along with electrolytic capacitors bank.

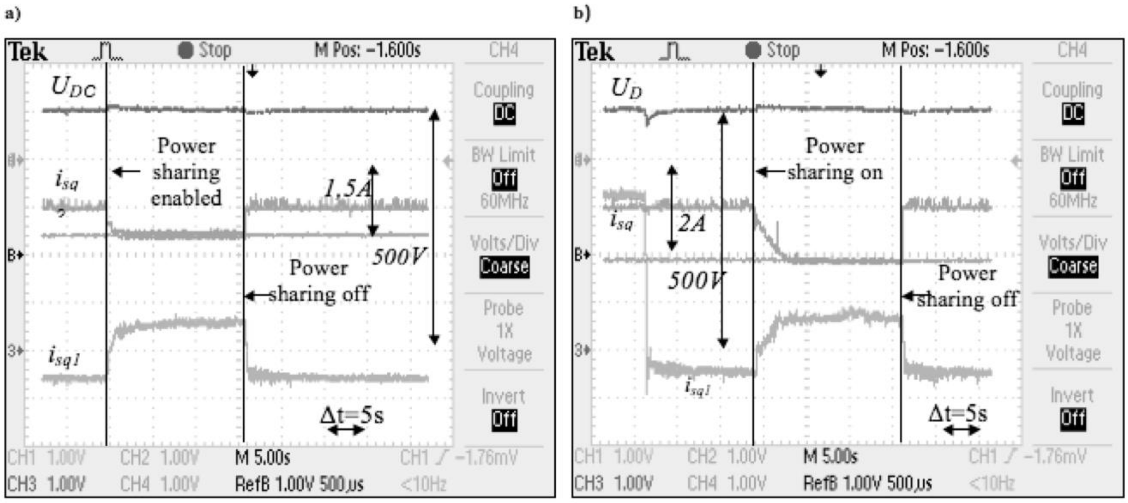

Fig. 7 Experimental results of power sharing in parallel connection of two asynchronous generators. a) current limit set to 1,5A b) current limit set to 2A

As a load commercial inverter was attached to DC link. To maintain power sharing, voltage of one generator was slightly raised and resulting generator current was limited to value incoming from external source (EEG). Next generator in parallel provided power for remaining load. This kind of system gives possibility to connect another generator and easy control of power distribution, current flow.

CONCLUSIONS

Presented system allows easy and stable distribution of electrical power and long-term cooperation of different electrical sources such as electric generators working in parallel with changing in wide range of angular speeds. Proposed algorithms and methods are still under development by adding new generators (e.g. reluctance machine), applying and testing new control algorithm cooperating with external control signals (electronic governor).

ACKNOWLEDGMENT

This study was supported by programme 1/S//2016/IEiAO by Maritime Academy of Szczecin

REFERENCES

1. Kozak M., Gordon R., Bejger A. (2016). Control of squirrel-cage electric generators in parallel intermediate dc circuit connection. *Maritime Academy of Szczecin Scientific Journals (SJ)*, *45*(117), 17-22.
2. Kanellos F. D., Tsekouras G. J., & Hatziargyriou N. D. (2014). Optimal Demand-Side Management and Power Generation Scheduling in an All-Electric Ship. *IEEE transactions on sustainable energy, 5(4),* 1166-1175.
3. Seung-Hwan L., Jung-Sik Y., Joon-Hwan L. & Seung-Ki S. (2015). Design of Speed Control Loop of a Variable Speed Diesel Engine Generator by Electric Governor. In *Industry Applications Society Annual Meeting, 2008. IAS '08. IEEE.*
4. Lundh M., Garcia-Gabin W., Tervo K. & Lindkvist R. (2015). Estimation and Optimization of Vessel Fuel Consumption. *IFAC-PapersOnLine, 49(23),* 394-399.

Corresponding author:
PhD. Eng. Maciej Kozak., Department of Mechanical Engineering, *Maritime University of Szczecin*, Waly Chrobrego 1-2, 70-500 Szczecin, Poland, tel .+48914809697, e-mail: m.kozak@am.szczecin.pl

DETERMINATION OF DIAGRAMS FOR DETERMINING OF SHAPE FACTOR α

Ivo KŘÍSTEK[1], Jiří HAVLÍK[2]

[1] *Department of Machine Parts and Mechanisms, VŠB-TU Ostrava*
[2] *Department of Machine Parts and Mechanisms, VŠB-TU Ostrava*

Abstract
Creating charts to determine the shape factor α. Experimental determination curves diagrams comparing the previously used charts and monograms. The beginning of the development of appropriate calculation methods for determining courses of stress concentration factor for individual notches, with the previously used charts.

Key words: *Diagram, Coefficient, Tension*

INTRODUCTION

Diagrams and monograms (**Fig. 1**) serve to determine a shape factor that causes stress concentration and thus negatively affects the life of machine parts. These diagrams have been known since the early 20th century. All stress concentration coefficients listed in diagrams, nomograms or calculated by formulas have been determined in the last century. At this time, we can use modern computational methods, such as FEM. However, the designer have not always opportunity, apply methods like FEM analysis. But no one knows how they were designed or acquired in the past.

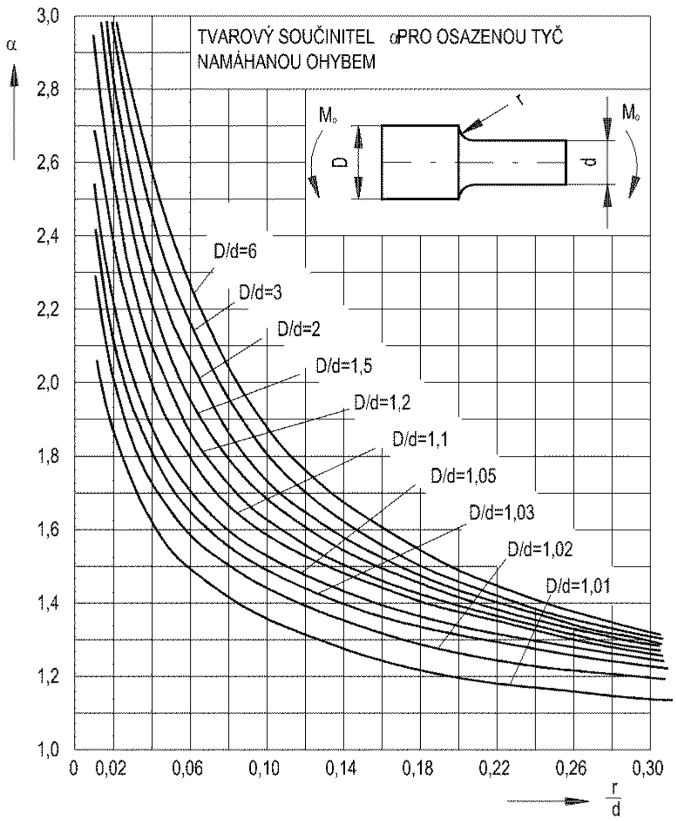

Fig. 1. Diagram of the stress concentration coefficient for the bending stress

Dependence of the determination of the shape factor depends on the size of the shaft and on the transition between the individual diameters. The smaller radius, has the higher pike tension, and vice versa. How, did the slope of each curve arise when there were no computational programs?

MATERIALS AND METHODS

As already mentioned, the value of the shape factor depends on the dimensions of the shaft and the transition between the diameters. According to known monograms, the slope of the curve is different for each parameter.

But, how can you get it, for different dimension of shaft? For determination of curves we use calculation, where we use MKP software (Ansys). Where the dimensional values of the shaft (radius r), we assigned parametrically. Four samples were selected, with other transition values (value radius r), but with the same D/d value and value r/d. The radius was variable – **Fig. 2**.

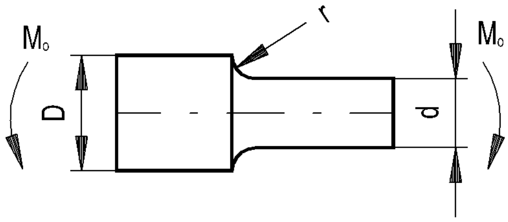

Fig. 2. Scheme of the test sample

Example of parameters for each sample you can see in the Tab. 1.

Tab.1 Example of parameters for calculation

	d	D	D/d	R	R/d
Sample 1	29	32	1,10	0,6	0,02
				1,8	0,06
				3	0,10
				4	0,14
				5,2	0,18
				6,4	0,22
				7,5	0,26
				8,7	0,30
Sample 2	32,7	36	1,10	0,6	0,02
				1,8	0,06
				3,2	0,10
				4,5	0,14
				6	0,18
				7,3	0,22
				8,5	0,26
				9,8	0,30

Use an empirical relationship (1) for calculate the bending concentration tension in the critical location on the shaft

$$\sigma_O = \frac{M_O}{W_O} \cdot \alpha \qquad (1)$$

For shape concentration factor α we use formula (2):

$$\alpha = \frac{\sigma_O \cdot W_O}{M_O} \qquad (2)$$

Where *Mo* is bending moment (Nm), *Wo* is cross section bending module (mm^2), σ_o is bending tension (MPa) and α is shape concentration factor (-).

We used the FEM software Ansys, we determinated the maximum voltage peak of tension at the transition point - between diameters. After that for each sample we determinate the value of the shape coefficient α was determined for the individual calculations that were entered into the graph and, with the help of the trend line, the curves for each sample were drawn. Samples in the graph, have a label "*S*", for example (S1 = sample 1) - **Fig. 3**

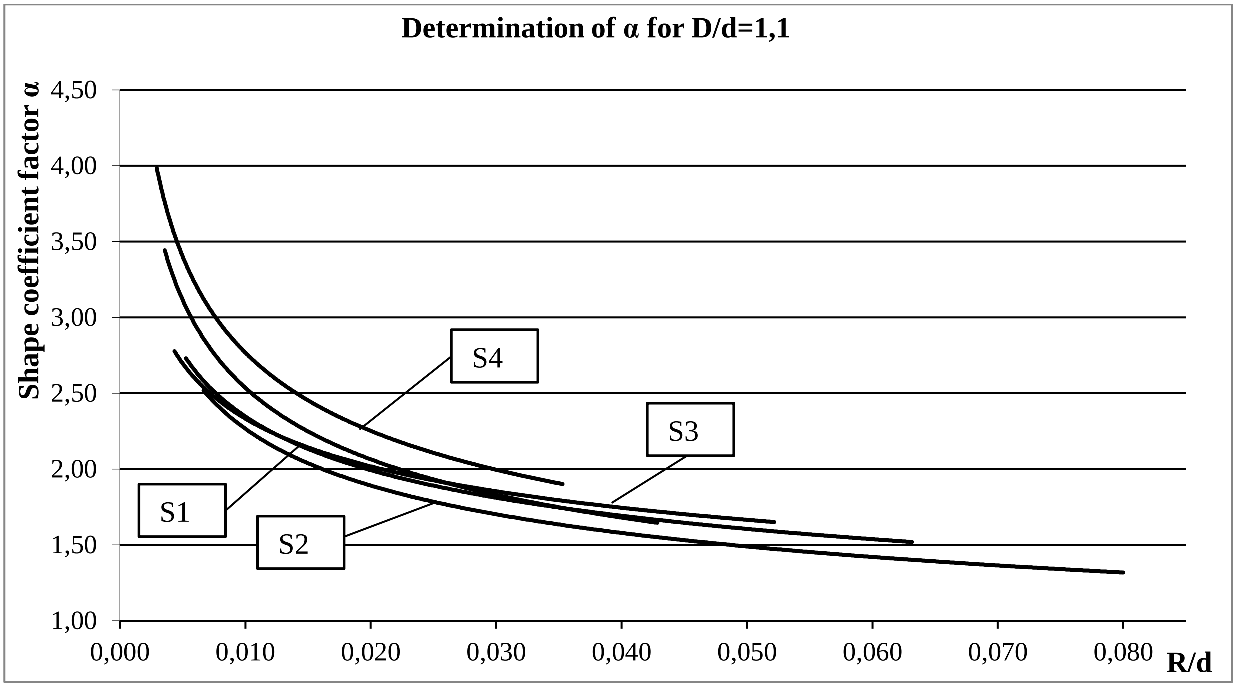

Fig. 3. Determination of shape coefficiente α for D/d=1,1

The graph (**Fig. 3**) shows, that each test sample has a different waveform. For each sample, we applied the same parameter of bending moment. And for each calculation we got a different maximum value of voltage peak in the transition between the diameters. Sample with small radius *r* is more sensitive (bigger tension) than a sample with bigger diameters. When we conected the values of the outermost curves, we find that it is a bounded area. This area depends on the number on the samples. For this reason, we toke the arithmetical value from this area, and we got a curve for parameter D/d=1,1 – **Fig. 4**.

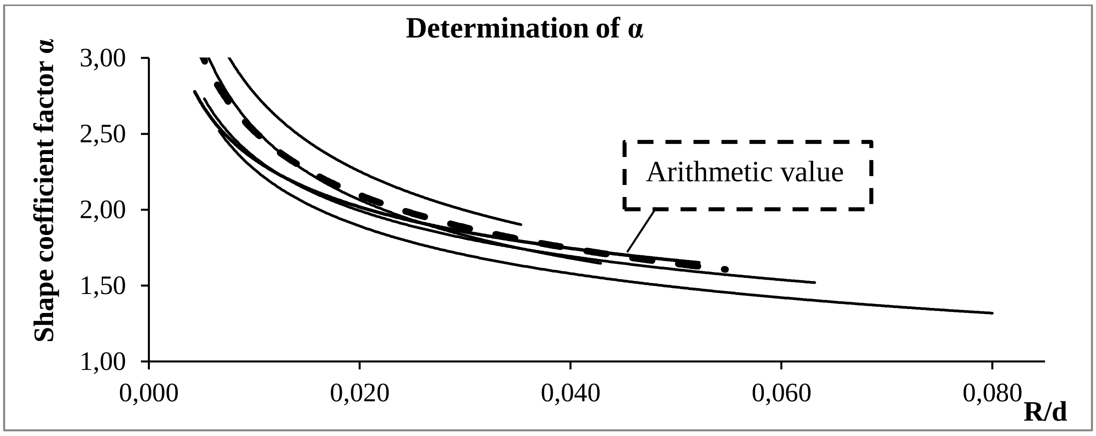

Fig. 4. Determination of shape coefficiente α for D/d=1,1

RESULTS AND DISCUSSION

We can see the common historical monogram (**Fig.5**).

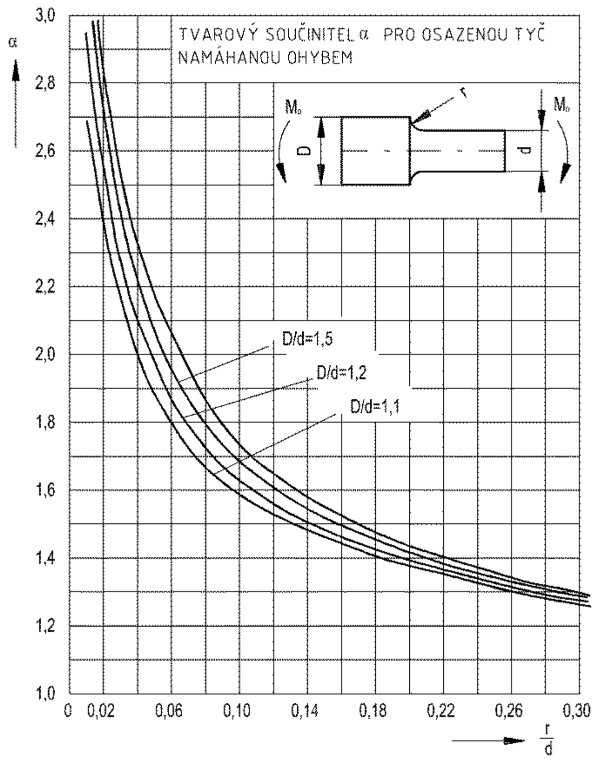

Fig. 5. Diagram of the stress concentration coefficient for the bending stress – chose curves

And compare with created monogram, we can see same similar slope of curves – **Fig. 6**.

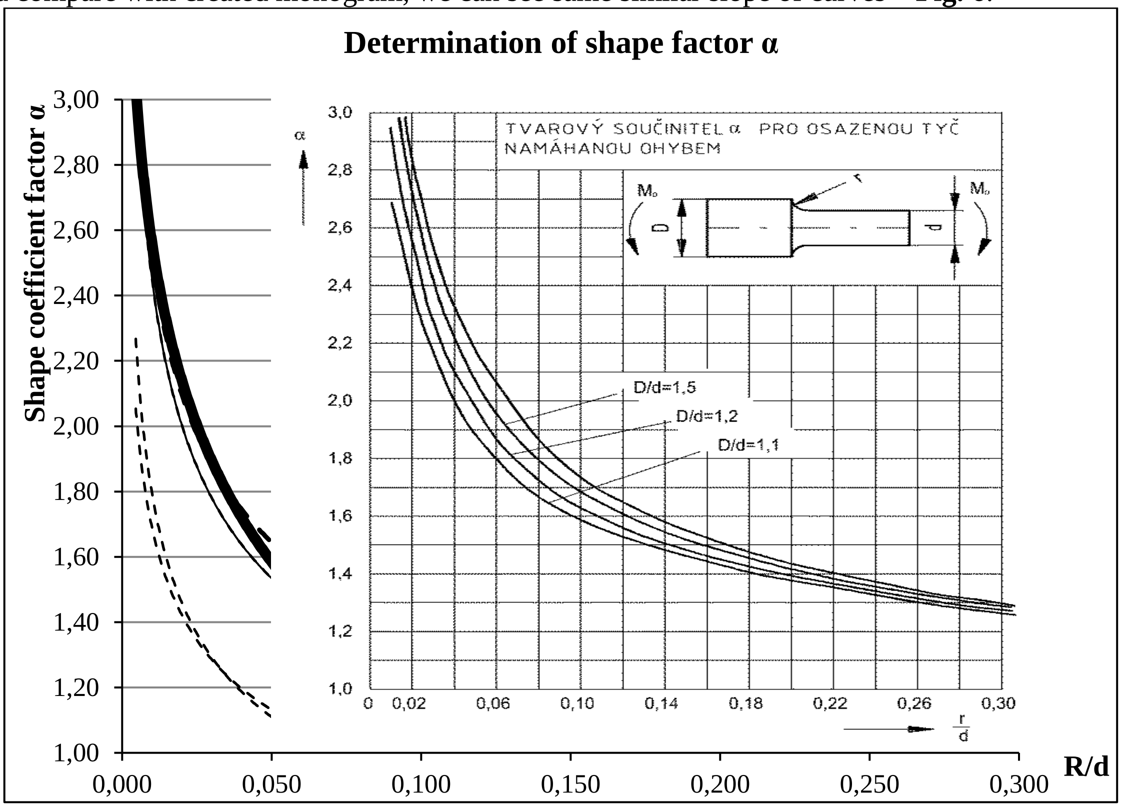

Fig. 6. Comparison of diagram D/d=1,1

As already mentioned, each parameter D/d has a different slope of the curve. For better understanding, now we compare the historical monogram, where are curves for values of the parameter D/d = 1.1, 1.2 with identical r / d. For the method of calculation, the values of samples were similar to historical. Parameter D/d = 1.1, 1.2 with identical r / d parameters. For each value of D/d we chose four samples, like in previous chapter. Once the individual variables had been determined. We made calculation with MKP analyses, and we got the maximum tension in the transition area. As in the calculation method, the values of the shape factor α for the individual calculations were plotted and plotted for each test sample, as the previous example.

We got a graf – **Fig 7** (for samples D/d=1,1) each sample with the same parameter D/d has a different slope of curve. You can see, that is the boundary area, which depends on the on number of samples, for this reason we use the arithmetic value from this area and we get the slope of curve for parameter D/d.

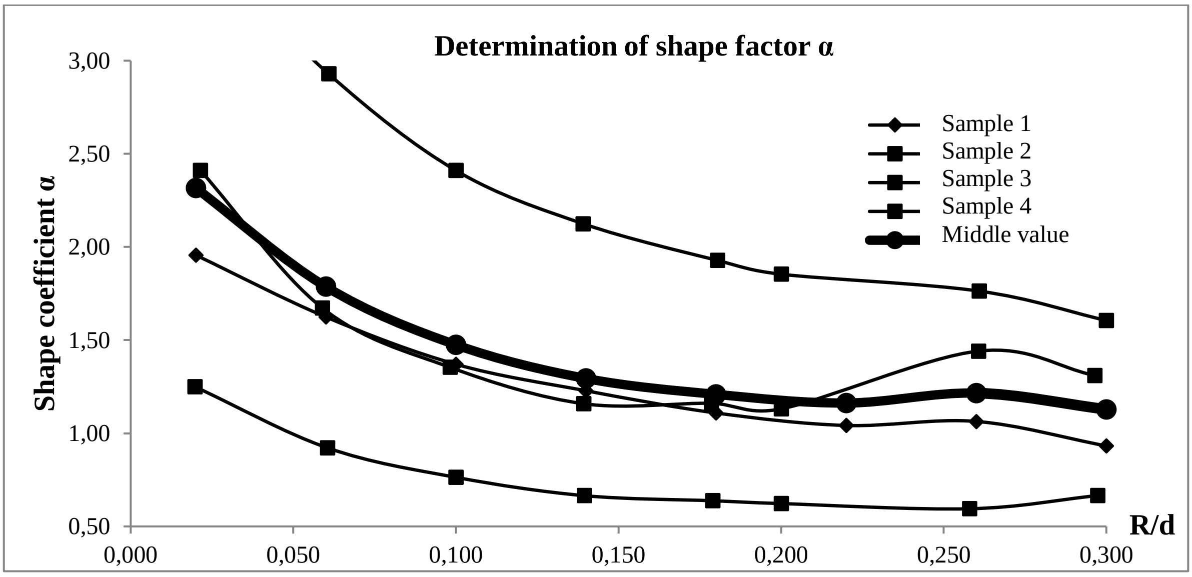

Fig. 7. Determinaton for shape factor α for D/d=1,1

Now, we can compare graphs. We can see some differencis between historical graft and crated graphs.

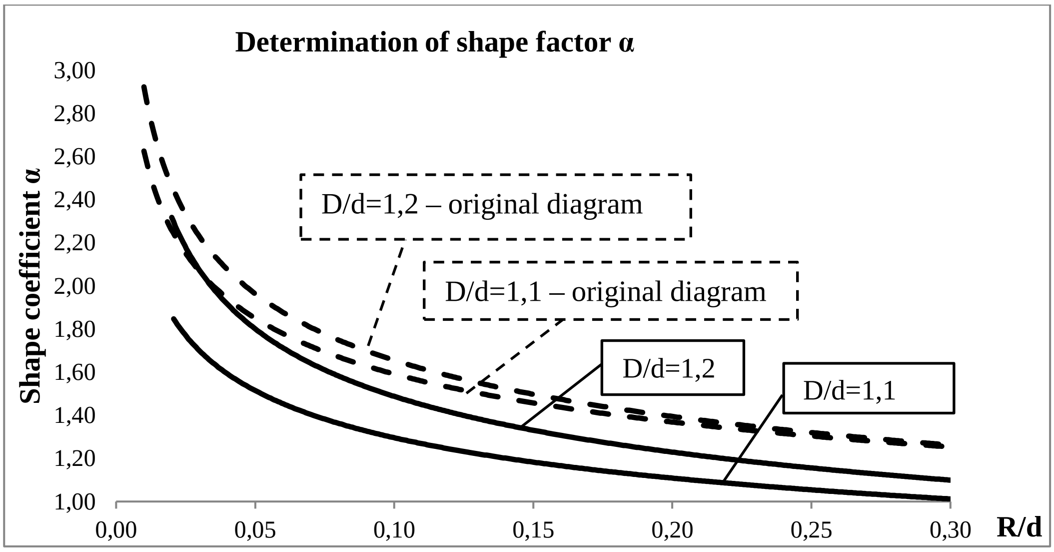

Fig. 8. Compare the diagrams

CONCLUSIONS

Comparison of the experimental determination of curves for a given D/d ratio with previously used diagrams with the same D/d ratio (**Fig. 8**), shows some similarity between these curves that determine the shape coefficient *"α"*. The shapes of curves are similar, but you can see, that are not the same value of shape factor *"α"*. For example, for value R/d on the curve D/d=1,1you can get a different value of *"α"*. As mentioned above, it is not known how the curves originated, without using the necessary method in history. This experiment shows the possible way of determining curves using modern computational methods that were not so common in the past.
These examples show the way, how can you determinate the shape factor *"α"* for danger place on the shaft (transition between diameters).
But on the shaft, exist another places, where is the tension is very dangerous for the lifetime of the shaft, for example, hole through, grooving and groove for pen. According to similar way I will try make shape concentration factor "α"for each concentration place on the shaft, and compare with the historical diagrams.

REFERENCES

1. Moravec, V., & Pišťáček, D. (2011). *Pevnost a životnost dynamicky namáhanýh strojních součástí* (2. vyd.). Ostrava: VŠB - Technická univerzita Ostrava.
2. Dejl, Z. (2000). *Konstrukce strojů a zařízení I: spojovací části strojů : návrh, výpočet, konstrukce*. Ostrava: Montanex.
3. Růžička, M. I., Hanke, M., & Rost, M. (1989). *Dynamická pevnost a životnost* (dotisk). Moravské tiskařské závody, n. p. Olomouc, závod Ostrava, provoz 22 Nový Jičín: České vysoké učení technické v Praze

SOFTWARE

4. ANSYS Workbench R14

Corresponding author:
Ing. Ivo Křístek : Department of Machine Parts and Mechanisms, Faculty of Mechanical Engi-neering, VŠB-TU Ostrava, 17.listopadu 15, Ostrava, 708 33, Czech Republic, phone: +420 721 310 011, e-mail: ivo.kristek@vsb.cz

COMPARISON OF BENDING PROPERTIES FOR WINDED AND WRAPPED COMPOSITES

Petr KULHAVÝ[1], Petr LEPŠÍK[1]

[1] *Technical University of Liberec, Faculty of Mechanical Engineering, Liberec, Czech Republic*

Abstract
The aim of presented work is by using the three point bending test compare two kind of theoretically identical composite rods manufactured by different ways. In technical practice we could find applications of pre-impregnated fibres so called "prepreg" especially by the wrapping technology, which is generally helical layering of one wide tape. The main disadvantage is limitation of using this technology only for straight shapes. Therefore a simultaneous deposition of larger number of thinner fiber filaments, called winding has been used to enhance this technology also for curved shapes and parts with various cross-sections. The aim of this work is to experimentally compare flexural strength of two almost identical composite rods, one wrapped and second winded. Subsequently in the ACP module of ANSYS their models as a tool for verification of the obtained data were created. Significant differences in the behavior of those rods created by two manufacturing methods have been found.

Key words: *composite; winding; wrapping; bending; prepregs.*

INTRODUCTION

Reduction of costs, improving quality and using of modern CAD technologies are the key points in the future of composite parts. Composite materials are used especially because of their low weight, very high strength and offer also solution for applications subjected to fatigue loadings. By changing the material from metal to composite It is possible to reduce the weight of vehicles with 40 to 60 per cent (*Harry, 2012*). The most effective replacement of conventional materials by composites is possible with the appropriate combination of manufacturing technologies, stack up of individual layers, dispersion and matrix. Plastics materials reinforced by long fibers are widely used because of their high strength and modulus to density ratio (*Suganuma, 2007*). Compared to metallic structures, composite laminates offer some unique engineering properties while presenting interesting but challenging problems for analysts and designers (*Kherredine, 2012*). During the creation of a composite part we have to consider lot of aspects (grease, pressure, temperature, imperfect vacuum, real thickness of plies) and this all significantly affect the final mechanical parameters. Instead of using classical dry fibres, this work describes using presaturated material so called prepreg. The main benefit of using pre-impregnated fibers instead of filaments is the simplification (or even elimination) of consequent technologies like saturation and curing in form. The aim of this article is to compare behavior of theoretically identical parts created from preimpregnated fibres by two different methods.

MATERIALS AND METHODS

Nowadays technologies like winding of fibers, tape wrapping, laminating of fabric layers and some other operations are often used for manufacturing the so called advanced composites (*Allen, 2004*). Methods based on epicyclic winding or helical wrapping (Fig. 1) are generally used for manufacturing of thin-walled composite parts with circular or oval profiles. Those methods are usually used for so-called "wet" case, when a bundle of dry placed fibers is subsequently impregnated with resin. Another way is to use of the pre impregnated materials. Because of their significantly different behavior (sticky, such as double-sided tape), their use is generally limited primarily to manufacturing straight bars. One of used technologies is wrapping. It means a helical layering of one wide tape on a straight or eventually conical mandrels (Fig. 2). Winding is a manufacturing process that should keep the fibers continuous and aligned throughout entire part, offers a high degree of automation and a relatively high processing speeds (*Harry, 2012*). The process of winding fibers is known for a long time. However, until recently this technology was concerned especially to field of textile engineering (braiding of ropes, fluid – air hoses) and parts usually from some atypical sectors. Due to a big progress in using composite materials instead of conventional, we could met the winded composite parts in many industries.

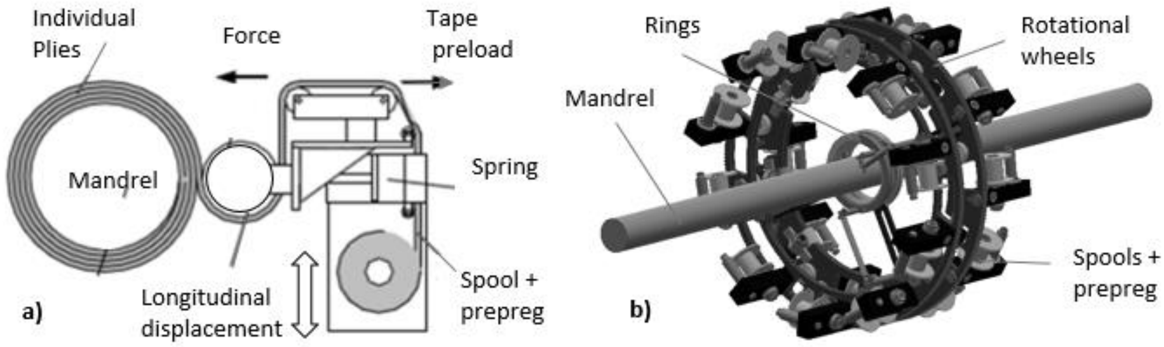

Fig. 1 The used manufacturing methods a) Wrapping b) Winding

The fundamental idea of this winding method is based on a registered patent (*Sevcik, 2013*), which was developed at the Technical University of Liberec. The head is formed by a base frame and two rotary wheels, which carry spools with material used for winding. During the process of prepregs winding the mandrel is pulled through the center of the rotational head. Compared to a conventional winding of dry fibers there is significantly bigger axial force caused by the dragging fibers over aluminum rings, some passive resistances and a braking moment in the spool mechanism. As mentioned (*Zhang, 2015*) for ensuring the best properties is necessary to preload the tape with a quite big and invariable force to improve alignment of individual fibers and to prevent warping and premature sticking of the winded tape.

Through the fibers, the force comes to the rotary wheel (*Kovar, 2016*). To assure the most optimal properties of the basic material (Tab. 1) should the semi-finished pre-impregnated fibers come from the manufacturers in frozen state with the individual plies protected by a foil of silicone paper. Tensile strength in the direction perpendicular to the direction of longitudinal fibers is for uni-directional materials even lower than the ultimate strength of the matrix itself, which is caused by the concentration of local stress on their interface (*Kherredine, 2012*).

Tab. 1 material properties of used UD prepreg materials

	E1 [MPa]	E2 [MPa]	ρ [g/cm^3]	μ [-]	Ductility [%]
Carbon	101 000	9 000	1,9	0,25	lim -> 0

The stiffness could be described by a set of five parameters: young-moduli ($E_{11}$and E_{22}), Poisson's ratios (ν_{12} and ν_{23}) and a shear-modulus (G_{12}). With using of homogenization techniques these five parameters describing the stiffness behavior of the composite can be derived. It is necessary to mention that this idea is valid only with an assumption of a really perfect alignment of fibres. Then the compliance matrix e.g. in (Kaw, 2006), can be rewritten in terms of the engineering constants.

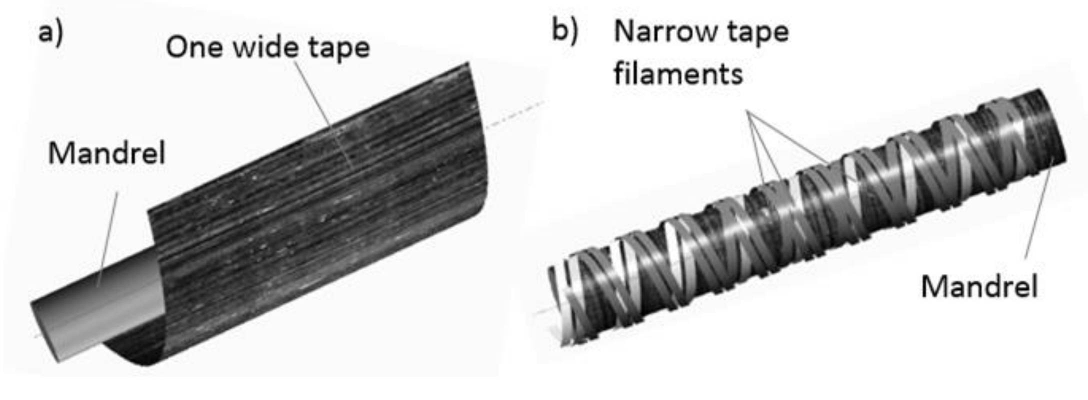

Fig. 2 The two principles how the fiber material is layered a) Wrapped b) Winded

With the optimal settings the resulting layer should have the same angle of the fibers, the thickness, the weight and theoretically almost identical mechanical properties. During the production of the sample, attention was paid to the aims that composition, number of layers, weight and curing parameters mutually correspond as much as possible, but as could be seen in the Fig. 3 it is possible to find fist visual differences immediately after the curing. In the winding process arising a lot of seemingly small unimportant defects in the fiber aligning and also sticking of the tape's edges.

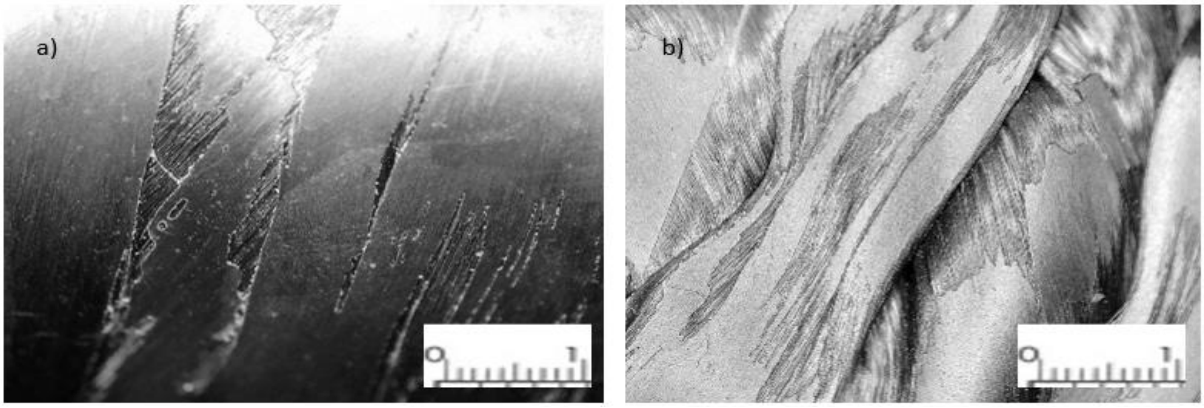

Fig. 3 The surface of the a) wrapped b) winded, parts from carbon prepreg (added scale 1 cm)

The prediction of composite mechanical behavior is a very complex problem, because the process induces whole spectrum of attributes like the fibres orientation, interface properties, cohesive forces and failure criteria. Advanced methods could describe the entire damage process from its initiation to a complete failure of a composite structure (*Ullah, 2012*). An unanswered question is, how accurate the simulation should be to be suitable: the mesh relevance, chosen formulations, failure criteria etc., when we consider the initial error caused by the material model and boundaries. Because the modeling of contact like in our case the between layered shell and solid element is very problematic. It is possible to find various simplifications, e.g. (*Gruber, 2013*) created and simplified static model of the part alone without using any contact.

In our case, the model was solved as a fully contact task, Fig. 4b. The tested part was laid on two fixed supports. For combination of solid and shell elements the pure penalty formulation with nodal-normal detection of integration points was used. The chosen basic normal stiffness 1e-002 could be additionally adjusted by program. The simplest way of handling an initially unconstrained model was to add weak springs. The spring constant can be made dependent on the load parameter, so that the spring has effect only in the beginning of the simulation (*Ansys, 2010*). Kirstein even described thesis that during the test could be the boundary of the plate considered to be free as the plate is supported at interior points, and no special treatment is required (*Kirstein, 1966*).

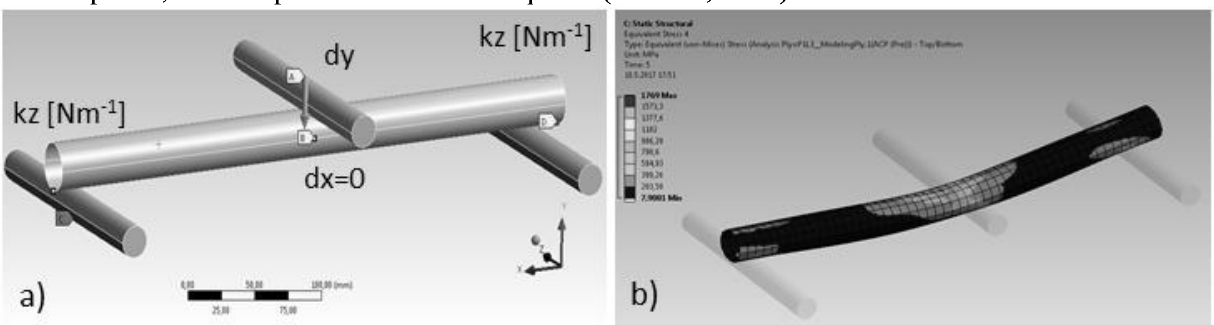

Fig. 4 The numerical model of shell composite bending test a) scheme with the boundary conditions b) An example of resulting stress in one ply

In our case the problem of numerical simulation of composite materials is an assumption of a homogeneous system with perfectly aligned fibers and their uniform distribution throughout the cross section. This idea is commonly applied to the simulation of laminated and wrapped parts. However, how much the results differ for the winding, (i.e. method with large randomness in the fiber alignment and even overlapping of filaments) is a question for comparing individual results in next chapter.

The flexural strength is the maximum stress that material subjected to bending load could resist before failure (*Chung, 2004*). In the conducted test the samples of almost identical wrapped and winded rods were tested and mutually compared. The distance *l* between the cylindrical supports was in our case equal to 380 mm. The applied quasi static loading had increased with step 0. 5 mm /s until caused the final displacement of used indenter 80 mm.

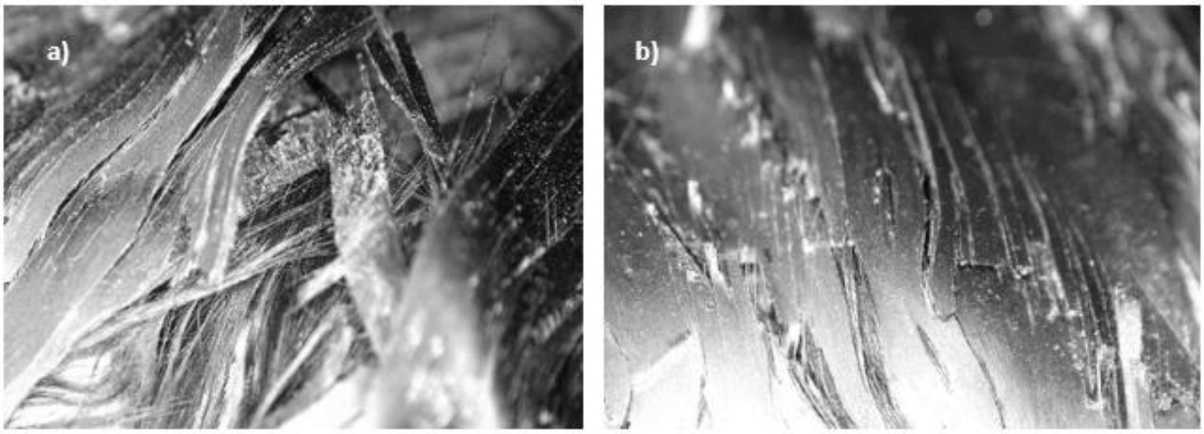

Fig. 5 The found typical failures of parts in bending test explored for the a) wrapped b) winded, parts

RESULTS AND DISCUSSION

The resulting flexural strength obtained for the two groups of tested parts were significantly different as could be seen in Table 2 and in Fig 6. There are differences not only in the maximum stress level, but also in the value of displacement and it is possible to see that the place of material ruptures looks differently (Fig. 5). In one case there were mainly delamination and the filament ruptures in the other. The carried model (Fig. 4) was in the beginning (i.e. until 25 mm of displacement) in a good agreement with the wrapped parts. Then, in the real part some first ruptures and delamination arose, while the force in the model still increased up to the deformation of 35 mm, where was not possible to reach the convergence of solution anymore.
When assessing the second test case, winded parts (not the one wide tape but 10 segments of relatively narrow filaments) the obtained values were significantly different.

Tab. 2 Resultant values from experiment compared with the numerical model

	Displacement	**F_{max}**	
	at Fmax	Experiment	Model
Wrapp	41 mm	840 N	~1600 N
Wind	16 mm	1300 N	360 N

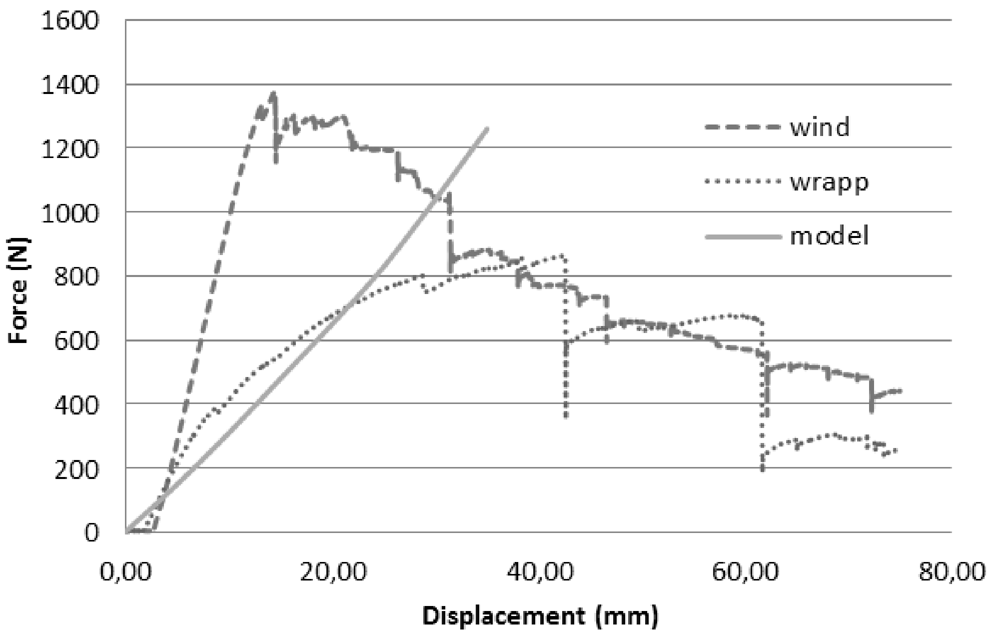

Fig. 6 The comparison of the tested parts (arithmetic mean of values for the tested sets)

CONCLUSIONS

Two sets of samples, one made by winding and second by wrapping of UD prepreg carbon material, were tested. Method one wrapping of a wide tape had a very good surface quality and homogeneity of material characteristics. In the second case we tried to use non-conventional method of winding combined with pre-impregnated materials. This method utilizes instead of one wide tape the segmentation, when each layer consists of 10 narrow strips. This method is suitable for straight shapes and with appropriate setting of the winding angle and can also create curved or closed shapes. A disadvantage is that the fibers are often not ideally aligned as in the case of one wide tape and there are many places of their mutual overlapping which cause the resulting structure forming characteristic warp defects. What could be important, is that the fibres are evidently more fastened. During the experiment we have obtained significantly different behavior of the two theoretically identical parts. There was not only different value of the maximal flexure strength, but also fundamentally different fracture mechanisms, delamination and the deformation of the entire test rods.

The found results have been evaluated also by using numerical model, created in ACP preprocessor. Good conformity with the wrapped part was obtained in the beginning of loading. Then it the composite materials arose some issues like delamination or fractures. With a standard material model it is not possible to consider all this phenomenas like it is usual for the conventional materials. In our next work will be necessary implement into the model also the cohesive interface layers and damage mechanisms that could describe the arising material failures. In the term of numerical simulation of the winded parts the entire approach to the model should be modified. In the first step is possible try to change the definition of input materials. It means do not use the verified material model of the ideal UD tape but homogenize the new tape by taking account the all occurring defects, pores and overlapping. However, it is also possible that the usual shell methods using stacked plies with different stiffness matrix will not be appropriate.

The main benefit of using prepreg instead of filaments is the simplification of consequent technologies like saturation and curing in form. As disadvantages are the considerably higher price of presaturated fibers and big, ideally constant preloading in the fibers throughout the entire process. The winding technology has also a big potential to replace the classical but for today using insufficient wrapping method. However, it will be necessary to spend a long time by optimizing the final structure and also find a way, how to correctly simulate the material model and mechanical behavior of this structure and also how to improve the technology to minimize all the imperfect places in the material structure.

ACKNOWLEDGMENT

This publication was written at the Technical University of Liberec as part of the project "Innovation of technical systems structures with the use of composite materials" with the support of the Specific University Research Grant, as provided by the Ministry of Education, Youth and Sports of the Czech Republic in the year 2017.

REFERENCES

1. Allen, A. K. (2004). A Method for Winding Advanced Composites of Unconventional Shapes using Continuous and Aligned Fibers, *Brigham Young University*.
2. ANSYS, Inc., (2010). Mechanical Structural Nonlinearities - Advanced Contact, *Training Material.*
3. Chung, S. M., Yap, A. U. J., Chandra, S. P. and Lim, C. T. (2004). Flexural strength of dental composite restoratives, Comparison of biaxial and three-point bending test, *Journal of Biomed. Material Research.*
4. Gruber, G., Wartzack, S., (2013). Three-point bending analyses of short fiber reinforced thermoplastic: Comparison between simulation and test results. *SAS Tech. Journal*.
5. Harry, N. E. (2012). Clean filament winding: process optimisation. United Kingdom, *University Of Birmingham*.
6. K. Kaw, (2006). Mechanics of Composite Materials, Second Edition, *Taylor and Francis Group*, United States of America,
7. Kherredine, L., Gouasmi, S., Laissaoui, R., Zeghib N. E., (2012). Evaluation and measurement of the damping properties of laminated CFRP composite plates. *Materiaux 2010*, IOP Publishing, 28.
8. Kirstein, A. F. (1966). Woolley RM. Symmetrical bending of thin circular elastic plates on equally spaced point supports. Washington DC: *National Bureau of Standards*, 1–9.
9. Kovar, R., Kulhavy, P., Lufinka, A. (2016). Stress analysis of the winding head frame for the production of the composites, *54th International conference on Experimental Stress Analysis,* University of West Bohemia.
10. Sevcík, L., Tuma, P., Petru, M., Martinec, T., Kovar, R., (2013). Composite reinforcement, *Patent Application no. 2013-1066*.
11. Suganuma, Y., Fukuda, H. (2007). Applicability of compression bending test to measure compressive failure strain, *16th conference on composite materials*, Kyoto, Japan.
12. Ullah, H., et al. (2012). Damage modelling in woven-fabric CFRP laminates under large-deflection bending, *Computational Materials Science*, Vol. 64.
13. Zhang, P., Sun, R., Zhao X., Hu L. *(*2015). Placement suitability criteria of composite tape for mould surface in automated tape placement. *Chinese Journal of Aeronautics*, 28(5): 1574-1581.

Corresponding author:
Ing. Petr Kulhavý, Technical University of Liberec, Faculty of Mechanical Engineering, Department of the Design of Machine Elements and Mechanisms, Studentská 2, 461 17 Liberec 1, Czech Republic, phone: +420 48 535 3321, e-mail: petr.kulhavy@tul.cz

DECISION MODEL OF AN OPERATION AND MAINTENANCE PROCESS OF CITY BUSES

Bogdan LANDOWSKI[1], Łukasz MUŚLEWSKI[2]

[1,2]*Faculty of Mechanical Engineering, University of Science and Technology*

Abstract
This paper presents an example of applying semi-Markov decision process to model and analyse the bus operation and maintenance process within an urban transport system and to forecast the influence of the operation and maintenance strategies realised for the technical objects on the transport system behaviour. Setting the values of the indices describing the process under the analysis is performed on the basis of a computerised simulation of the semi-Markov decision process, being a mathematical model of the technical objects operation and maintenance process. In order to simulate the operation and maintenance process and to evaluate the influence of the decisions being made on the course and effectiveness of the process being realised within the study object a simulation algorithm has been elaborated and a computer calculation program has been written.

Key words: *urban transport, operation and maintenance process, semi-Markov decision process.*

INTRODUCTION

The object of the investigations is generally defined operation and maintenance system of the technical objects. The controlled processes being the components of the operation and maintenance process are realized in this system.

As an example of the investigation object, serving to illustrate all the considerations, a real system of an urban bus operation and maintenance system within a large (approx. 400 thousand of residents) agglomeration has been chosen.

The subject of the investigations is a determined set of the operation and maintenance states of the means of transport and processes of their maintenance as well as the sets of possible decisions made in each of the w states affecting the flow of the operation and maintenance process, including relations occurring between the elements of the said sets and between them and effectiveness of the operation and maintenance process.

Supporting a decision maker in the decision making process regarding realization of the operation and maintenance process of the means of transport may be realized by forecasting the way the operation and maintenance is going to behave and by evaluating the influence of the chosen decision variants on the flow of the operation and maintenance process. The analysis of the results from investigations of the operation and maintenance process models may be helpful here (*Landowski, 1999; Landowski, Perczyński, Kolber & Muślewski 2016*). The investigations of such a type include determination of the value of the selected measures of the technical and economic efficiency of the process being realized for the assessed values of the model parameters corresponding to the analysed decision variants. A change of the model input parameters value may reflect a change of the way the internal and external factors affect the system behaviour. The analysis of the results of the investigations realized in such a manner makes it possible to evaluate operation of the system under investigation and of the process being realized in it as well as to determine the decision indices enabling reasonable control of the system (*Landowski, et al., 2016; Landowski, Woropay & Neubauer, 2004; Woropay, Knopik & Landowski, 2001*).

As examples of the of the criterion function, the following parameters may be considered: values of the transport system reliability features, values of the incomes discounted in a long range of time or an average value of the incomes for the determined ranges of time (*Landowski, 1999; 2013; Landowski, et al., 2016; Landowski, et al., 2004; Woropay, et al., 2001; Woropay, Landowski & Neubauer, 2004*).

This paper presents an example of using the semi-Markov decision process to model and analyse the urban bus transport operation and maintenance process. Determination of the values of the indices describing the process being analysed is performed on the basis of a computerized simulation of the

semi-Markov decision process, being a mathematical model of the technical objects operation and maintenance process.
In order to illustrate the investigations a calculation example and the chosen results of the simulation experiments have been presented herein.

MATERIALS AND METHODS

Mathematical model of the operation and maintenance process.
It has been assumed that the stochastic process $\{X_t, t \in T\}$ with finite number of the states from the space S={1,2,...n}, where the set T means non-negative real semiaxis $t \geq 0$ is a mathematical model of the bus operation and maintenance process. The changes of the process state occur at the moments $t=t_1,t_2,...t_n$. The states of the analysed stochastic process correspond to the identified bus operation and maintenance states.
A finite set A_i={1,2, ... $\overline{\overline{A_i}}$ } of decisions (actions, alternatives), which may be applied in the state $i \in S$ corresponds to each state $i \in S$. The power of the set A_i is denoted by $\overline{\overline{A_i}}$.
The space of possible decisions:

$$A = \bigcup_{i \in S} A_i \, .$$

The decisions are defined as determination of the proceeding way, for instance in relation to a technical object, at the moment of entering a particular state. In a real operation and maintenance system there may be various methods of servicing (repairs, inspections) or using the object (e.g. various routes, over which a bus is used), having an influence on the suffered costs and generated incomes as well as on the frequency and types of damages to the object (*Landowski, 1999; Landowski, et al., 2004; Woropay, et al., 2004*).
Let $p_i \geq 0$ denote a probability that the process will be in the state $i \in S$ at the moment t=0. Naturally $\sum_{i \in S} p_i = 1$.
The vector $p=[p_i]$, $i \in S$ is a stochastic vector of the initial process distribution $\{X_t, t \in T\}$.
If at the moment t_k, $k \in N$ the process is in the state i and the decision $a \in A_i$ was made when entering this state then p_{ij}^a, where $i,j \in S$ represents the probability that the process will be in the state j at the moment t_{k+1} (the next state of the process will be the state j).
It is assumed that $\sum_{j \in S} p_{ij}^a = 1$ and $p_{ij}^a \geq 0$ for all $i, j \in S$ i $a \in A_i$.
To simplify the considerations it has been assumed in the calculation example that:

$$p_{ij}^a = p_{ij}$$

Let r_i^a denote an income, when r_i^a >0 (a loss, when r_i^a <0) per a time unit generated by the system, when the process $\{X_t, t \in T\}$ is in the state $i \in S$ at the moment t and the decision $a \in A_i$ was made when entering the state i. It is assumed that the income r_i^a is limited for all $i \in S$ and $a \in A_i$.
The random variable denoting duration of the state $i \in S$ of the process, when $j \in S$ will be the next state and the decision $a \in A_i$ with the distribution determined by the distribution function $F_{ij}^a(t)$ was made when entering the state i has been identified with the symbol T_{ij}^a .
To simplify further investigations it has been assumed that

$$F_{ij}^a(t) = F_i^a(t) = F_{ia}(t), \; i,j \in S, \; a \in A_i \, .$$

The function $F_{ia}(t)$ is a distribution function of the distribution of the state $i \in S$ duration provided that the decision a was made when entering this state.

The random variable denoting the duration of the state $i \in S$, with the distribution determined by the distribution function $F_{ia}(t)$ has been identified with the symbol T_{ia}.

The stochastic process $\{X_t, t \in T\}$ determined this way is a special case of the semi-Markov decision process with incomes (*Baykal-Gürsoy & Gürsoy, 2007; Feinberg, 1994; Landowski, et al., 2004*).

Decision model of an operation and maintenance process

The investigations presented hereunder assume that from the point of view of the investigation aim, it is possible to identify n separable subsets of the homogenous objects in the set of the technical objects being operated and maintained in a transport system.

Various maintenance events requiring from the decision makers of the operation and maintenance system to make current decisions regarding the way of operating and maintaining the vehicles, the results of which affect the flow of the operation and maintenance process, including its economic effect occur when operating and maintaining the buses in an urban transport system. The bus operation and maintenance states are characterized by the distributions of these states durations and by unitary incomes (costs) generated by the system, when a vehicle stays in a specific state (*Landowski, 1999; Landowski, et al., 2004; Woropay, et al., 2001*).

The simplified model of operation and maintenance process of an urban bus transport system presented hereunder illustrates possibility to apply semi-Markov decision process and a computerized simulation to analyse and control the operation and maintenance process of the technical objects.

Three bus operation and maintenance states have been analysed. The state S_1 – using a technical object. A technical object including its operator carries out the transport tasks assigned to it. The state S_2 – servicing a technical object performed by so called technical service (TS) units. An unserviceable technical object staying in the environment of the operation and maintenance system is affected by the actions performed by mobile technical service units aimed at bringing back its serviceability. The state S_3 – servicing a technical object within the operation and maintenance system. An unserviceable technical object is affected by the actions aimed at bringing back its serviceability within a subsystem of assuring serviceability of the analysed vehicle operation and maintenance system or in another organizational unit (*Landowski, 1999; Landowski, et al., 2004; Woropay, et al., 2001*).

Such a state occurs in the investigated system at the moment when such a damage occurred that cannot be removed by the technical service units outside the service station or the vehicle was directed to the service station for other reasons.

The space of the states S of the process consists of three states S={i : i=1,2,3} in the investigated model. The states i of the analysed stochastic process correspond to the identified bus operation and maintenance states S_i.

On the basis of identification of a real urban bus transport operation and maintenance system the possible transitions between the identified bus operation and maintenance states have been determined. The changes of the operation and maintenance states are described with the stochastic process $\{X_t, t \in T\}$.

The transition matrix $P = [p_{ij}]$, $i,j \in S$ of the Markov chain inserted into the process $\{X_t, t \in T\}$ has been assessed on the basis of the investigations realized in a real system of the urban bus operation and maintenance system (Tab. 1).

Tab.1 Probability values p_{ij}, $i,j \in S$ of the process states changes $\{X_t, t \in T\}$

State	j		
I	1	2	3
1	0	0,81	0,19
2	0,9	0	0,1
3	1	0	0

When entering the state S_1 a decision may be made about the kind of the transport task (determined by the kind of so called communication route within the urban transport systems). Realization of the

transport tasks over a respective route may have an influence on the frequency and kind of the damages to the vehicles realizing the transport tasks. It is related to the condition of the roads, number of passengers, route length, number of bus stops etc. The income per a time unit related to being in this state is determined on the basis of so called buskilometre and average velocity of the travel over the respective route. The buskilometre price is settled on tender basis. Therefore, it is of significant importance for the transport companies to determine the technical and economic aspects of the task realization over the individual communication routes.
In the state S_2 a decision may be made to send a technical service unit of a special type (the technical service units used in the analysed operation and maintenance system differ from one another by their type and technical equipment which is crucial for the scope of the realized repairs).
In the state S_3 a decision may be made about performing the service within a subsystem of assuring serviceability of the analysed vehicle operation and maintenance system or to have one of the external companies realize such a service. The following factors are related to the type of the unit realizing the service process: scopes of the realized actions, diagnostic apparatuses in use, or service duration, number of people needed to realize the service, etc. which in an obvious way affect the costs of the services being realized.
In order to simplify the consideration, it has been assumed hereunder that a decision regarding selection of the respective communication route may be made only in the first state. Four communication routes have been analysed. The decision k made when entering the state i has been denoted by a_{ik}, $(i,k \in N)$. The decision space may be presented as $A=\{a_{11},a_{12},...,a_{14}\}$.

RESULTS AND DISCUSSION

In order to simulate the operation and maintenance process (semi-Markov decision process) and to evaluate the influence of the taken decisions on the flow and effectiveness of the process being realized within the investigation object a simulation algorithm has been elaborated and a computer calculation program has been developed (*Landowski, et al., 2004; Woropay, et al., 2004*).
The subject of the analysis in the considered example was transport realization effectiveness over the respective communication routes.
The simulation experiment has been carried out for all possible deterministic strategies for the considered example, assuming that there are 200 maintained and operated vehicles in the system and the duration of the simulation is equal to 31 days. The deterministic strategy is understood as a strategy to make the same decision in the respective state.
The chosen simulation results presented hereunder refer to four deterministic strategies and they are denoted respectively St-1, St-2, ..., St-4. The strategy denoted with the code St-k, k = 1. 2, ..., 4 means that the decision k (a_{1k}) was made when entering the state 1.
The data needed for the simulation regarding the probability of transition between the states and the times of staying in the states (for the strategy denoted with the code St-1) have been preliminary assessed on the basis of the fragmentary investigation results. The remaining data needed for the simulation are hypothetical ones and serve to illustrate the considerations.
The chosen simulation experiment results are presented in the Tab. 2 and 3. The results presented in the Tab. 2 include average values of the incomes generated by the system due to realization of the respective strategies by a single vehicle calculated per one day of realization of the transport tasks. However, the Tab. 3 includes number of entries to the respective states (jointly for all the vehicles) depending on the adopted strategies.

Tab.2 Chosen simulation results – incomes generated within 24 hours by a system due to operation and maintenance of a single vehicle depending on the adopted strategy

Strategy code	Average value	Standard deviation
St-1	238,61	39,93
St-2	301,24	30,03
St-3	329,24	30,68
St-4	468,29	38,24

Tab.3 Chosen simulation results – number of entries to the respective states depending on the adopted strategy

State	Strategy code			
	St-1	St-2	St-3	St-4
1	1569	4741	5242	6494
2	1338	4421	4901	4829
3	516	1481	1583	1585

CONCLUSIONS

The aim of the investigations was, among other things, to present possibility of applying chosen stochastic processes (that means semi-Markov decision processes) for mathematical modelling the system and vehicle operation and maintenance process.

The investigated example of the model of the urban bus transport operation and maintenance process is significantly simplified (due to the nature of the elaboration). However, the presented way of building and analysing such models shows that it is possible to apply them to provide preliminary prognosis for a system state, and to evaluate the co-operation results of the primary (using) and the auxiliary (servicing) processes and supporting the decision makers in the process of making decisions regarding the control of the operation and maintenance process and the system in which it is being realized.

The elaborated simulation program has been designed in such a way to assure possibility of using it in as extensive as possible class of problems related to the operation and maintenance of the technical objects. Realization of the simulation experiments enables determination of the parameter values (including momentary values) describing the vehicle operation and maintenance process that cannot be determined by means of an analytic method (for the most complex models).

It seems that the analysis of the investigation results of the presented model types, for different values of their parameters (decision variants) assessed on the basis of the results coming from the operation and maintenance investigations may facilitate making reasonable decisions regarding the control of the vehicle operation and maintenance process. Such an analysis enables, among other things, to evaluate preliminarily both the technical and organizational aspects of the vehicle operation and maintenance and the economic ones of the realized transports, which may be the basis for affecting a real operation and maintenance system in order to secure its rational operation.

Because of the nature of the affair the mathematical models of the operation and maintenance processes, realized within complex systems, constitute a simplification of the real processes. The consequence of the above is a necessity to formulate carefully the practical conclusions resulting from investigating these models. However, it does not limit the purposefulness of creating and analysing models of this type. The analysis of the results obtained by investigating these models, for the model parameter values, determined on the basis of the results from the operation and maintenance investigations realized in a real transport system, makes it possible to formulate conclusions and evaluations both in terms of quality and (in limited extent) quantity.

The presented method to model and analyse the operation and maintenance process, due to the complex degree of the description generality and the system-based approach to the problem may be used to analyse an operation and maintenance process being realized in other operation and maintenance systems than an urban bus transport system.

REFERENCES

1. Baykal-Gürsoy, M., & Gürsoy, K. (2007). Semi-Markov decision processes. *Probability in the Engineering and Informational Sciences, 21*(4), 635-657.
2. Feinberg, E. A. (1994). Constrained semi-Markov decision processes with average rewards. *Zeitschrift für Operations Research, 39*(3), 257-288.

3. Landowski, B. (2013). Example of applying Markov decision process to model vehicle maintenance process. *Journal of KONES, 20*(4), 209-218.
4. Landowski, B. (1999). *Method of determination values of the chosen decision variables to control rationally the operation and maintenance process in the transport system.* Doctoral thesis. Bydgoszcz: Academy of Technology and Agriculture.
5. Landowski, B., Perczyński, D., Kolber, P., & Muślewski, Ł. (2016). An example of Markov model of technical objects maintenance process. *Engineering Mechanics 2016, 22nd International Conference* (pp.346-349). Book of full texts: Institute of Thermomechanics Academy of Sciences of the Czech Republic.
6. Landowski, B., Woropay, M., & Neubauer, A. (2004). *Controlling reliability in the transport systems (Sterowanie niezawodnością w systemach transportowych).* Library of Maintenance Problems. Bydgoszcz-Radom: Maintenance Technology Institute.
7. Woropay, M., Knopik L., & Landowski, B. (2001). *Modeling processes of operation in transport system (Modelowanie procesów eksploatacji w systemie transportowym).* Library of Maintenance Problems. Bydgoszcz-Radom: Maintenance Technology Institute.
8. Woropay, M., Landowski, B., & Neubauer, A. (2004). Using of decision-making Semi-Markov processes for modelling and simulating of operation and maintenance process for buses. *Archiwum Motoryzacji (Archive of Automotive Engineering), 7*(1), 53-65.

Corresponding author:
Ing. Bogdan Landowski, Ph.D., Faculty of Mechanical Engineering, University of Science and Technology, Prof. S. Kaliskiego 7, 85-789 Bydgoszcz, Poland, phone: +48 523408208, e-mail: lbogdan@utp.edu.pl

ECONOMIC ASPECTS OF A CITY TRANSPORT MEANS PURCHASE

Bogdan LANDOWSKI[1], Daniel PERCZYŃSKI[2], Łukasz MUŚLEWSKI[3], Piotr KOLBER[4]

[1,2,3,4]*Faculty of Mechanical Engineering, University of Science and Technology*

Abstract
The research object is a technical system of city bus transport in a given agglomeration. The study deals with economic aspects involved in a purchasing a transport means. The subject of the study covers issues connected with decision making with incomplete information available. Constant striving for achieving high quality of transport services makes it important to match the transport means with the transport service it provides. The study includes basic assumptions of the method to be used for selection of a vehicle that would be suitable to perform transport services of a public transport system on the basis of economic criteria. The discussed implementation way of an economic method for investment assessment makes it possible to use it for technical systems other than the city transport systems.

Key words: *transport, city transport , maintenance costs, economic criteria.*

INTRODUCTION

In order to improve transport efficiency it is necessary to choose transport means that would effectively perform transport services.

Passenger transport is a very important branch of a city transport system. The notion of city transport, as compared to other forms of transport (automotive, railway, inland water, marine, air transport), was identified by means of horizontal classification, where the classification criterion is differentiation of territorial units, for which transport services are performed. The issue connected with passenger transport in a city has been identified not only according to its territorial operation range but first of all to its functional - economic specificity conditioned by the character of passenger transport services and the way they are provided. Therefore, the notion of passenger transport in a city is often narrowed and identified with the notion of city transport - regular transports of passengers by public transport means over assigned routes (*Landowski, Woropay & Neubauer, 2004; Woropay, Knopik & Landowski, 2001*).

The operation range of city transport is wider than one would expect, basing on its name, as it also covers suburban areas whose functions are similar to those of particular town districts. It needs to be noted that they are often situated at a significant distance from the administrative borders of the city (recreation areas, large industrial plants, etc.) (*Woropay, et al., 2001*).

Rapid development of urban agglomerations has been reported in Poland for the last several years. An increase in population migration, growing number of residents, increased mobility of the society have resulted in continuous extension of town borders. Thus, the city transport is characterized by the following factors:

- increase in the number of passengers,
- prolongation of the average journey distance,
- increase in the number of vehicles in the system of public transport.

Also the market offer of transport means used in public transport systems is observed to have become richer.

All these factors largely affect the search of more effective methods for selection of technical objects to be used in a given technical system.

The results of the economic model tests and computer programs for simulation of a vehicle operation and maintenance process can be used to support transport executives to make decisions about the selection of transport means to perform assigned transport services, under given operation and maintenance conditions and environmental factors. An example of the transport means operation model and other auxiliary tools for decision makers have been discussed in works such as (*Landowski, et al., 2004; Landowski, Perczyński, Kolber & Muślewski, 2016*; *Woropay, et al., 2001*).

MATERIALS AND METHODS

The research object is a real system of city bus transport in an urban agglomeration of app. 400 thousand inhabitants. This system is one of the basic subsystems of the whole city public transport system.

The research was carried out in one of city bus transport systems operating on the territory of mid-northen Poland.

The primary goal of a city bus transport operation is safe carrying of a given number of passengers over an assigned area. However, due to financial limitations, it is necessary to increase economic efficiency of the transport services, thus minimizing the outlays for public city transport.

Maintaining operability of the transport means is the responsibility of the system which ensures operability of vehicles and which cooperates with the diagnostic subsystem.

Damage to an technical object is a random event. During operation of buses there occur different events whose consequences affect the processes of bus operation and maintenance as well as the technical state and economic effect of the transport system. Vehicles used in the process of operation can enter different operational states. The costs of bus repairs and those connected with removal of damage effects as well as other costs involved in maintenance operability of the vehicles are of random character.

The research included the following buses:

- Mercedes-Benz O530 Citaro: 2 psc.,
- Mercedes-Benz O530G Citaro: 21 psc.,
- Mercedes-Benz O345 Conecto LF: 9 psc.,
- Mercedes-Benz O345G Conecto LF: 21 psc.,
- Mercedes-Benz O345G Conecto: 17 psc.,
- Solaris Urbino 12: 14 psc.,
- Solaris Urbino 18: 25 psc.,
- Solaris Urbino 8,6: 2 psc.,
- Mercedes Benz 628 B01 Conecto: 10 psc.,
- Mercedes Benz 628 B02 Conecto G: 1 psc..

A measure of a transport system performance in the analyzed bus transport system is the so called vehicle kilometer meaning coverage of one kilometer of a route by a bus with a definite number of seats (one-body, articulated) during operation. This measure of transport system performance is used in accountancy and tenders for providing city transport services.

The average number of kilometers covered by the buses used in the investigated company was above 13 million kilometers annually.

The most important categories of bus operation costs were determined on the basis of carried out investigations and the structure of costs in the analyzed company of city bus transport. Rational implementation of the bus operation processes involves respective costs including:

- propellants (29.42 % of total costs),
- tires (0.96 %),
- amortization (17.04 %),
- the so called current servicing (1.39 %),
- technical service (1,13 %),
- human related costs and their derivatives (36.22 %),
- repairs (13.21 %),
- installation, servicing and repairs, the so called ticket system (0.14 %),
- installation repairs and maintenance of the transport system 0.08 %),
- remaining (0.41 %).

Since alternative buses of public transport are supposed to perform the same transport tasks this work does not include technical aspects of the analyzed technical objects.

Investments in a transport system are capital consuming though being used in a relatively long time. Thus, there is a significant time span between the moment of a bus purchase and the time of expenses for its operation and maintenance and incomes from provided transport services In connection with this, the economic analyses need to include the time factor. This enables taking into account the change of money value in time. Hence, the used economic criteria take advantage of cost streams

during the accepted operation time for the assumed percentage rate. Further, in this work all the investment outlays, costs and incomes are given in PLN.
Stream of costs K z connected with operation of a city bus transport means can be expressed by the following dependence (*Drury, 2002; Samuelson & Nordhaus, 2012*):

$$K = \sum_{t=1}^{k} K_t \cdot (1+p)^{-t} , \tag{1}$$

where:
K_t – cost in year t, (or another accepted time interval t, e.g. quarter, month, etc.),
p – discount rate (capitalization ratio with reference to the accepted time interval),
t- successive years of the investment operation, (successive analyzed time intervals)
k – number of years for which an economic analysis is to be performed).
Commonly used method for assessment of an investment profitability is the method of net present value NPV described by the following dependence (*Drury, 2002; Samuelson & Nordhaus, 2012*):

$$NPV = \sum_{t=1}^{n} CF_t \cdot (1+p)^{-t} - K_A , \tag{2}$$

where:
NPV – net present value,
CF_t – cash flows net (Cash Flow) in period t (cash flow net expected in time t) not including investment outlays,
K_A – initial outlays connected with a purchase of a transport means.
n – number of years of income from an investment.
NPV method is based on an analysis of discounted cash flows with a given percentage rate. Net current value obtained using this method, represents the difference between flows of total incomes from implementation of this method, shows the difference between flows of total incomes from implementation of a new investment, and total outlays for a purchase of a bus and its operation.
In order to An analysis of the investment should include profitability which needs to be performed in order to guarantee safe and timely passenger transports includes different variants of implementation for an investment performing the same function. An investment should be understood as a purchase and next use of a given bus type and make. In the tested object the incomes from performance of transport services in the aspect of transport means operation type are dependent mainly on the number of a vehicle parts and subsequently with the number of seats. The operated are one part vehicles and two part ones , that is articulated.
Thus the incomes for transport services will be considered according to investment variants, for a given type of vehicle (one or two par vehicle), the same. Hence, in order to choose an optimal solution based on a modified method NPV, further only the sum of investment and operation cost values are taken into consideration with negligence of incomes for the performed transport service or other incomes connected with operating a vehicle of a given type.

RESULTS AND DISCUSSION

The categories and characteristics of bus operation costs to be presented in further part of this study result from the method of their recording in the research object. In this way particular kinds of costs can be linked with the vehicle. Acceptance of such a description method enables utilization of real data from the research object for analyses of bus makes and types used in the analyzed system. For vehicles of other makes and types, an estimation of the model parameter values should be made. A method of computer simulation of the transport means operation process, can among others, be used for this purpose.
The Tab. 1 shows a collective specification of the costs (referred to the first quarter of 2016) related to maintenance of buses of an urban transport system in the analysed urban transport enterprise

Tab. 1 Collective specification of the costs

Cost specification	Cost PLN
Propellants	5837733
Tyres	175932
Other materials	137806
Amortisation	3234071
Daily service	261208
Technical service	217112
Cost of repairs	2921655
Cost of repairs of ticket punchers	30076
Cost of repair and maintenance of communication system	10937
Personal costs and costs related to them	6380845

The total cost of the investment connected with a purchase of a bus can be expressed by the following dependence:

$$K_{IN} = K_z + K_d , \tag{3}$$

where:
K_z – bus purchase cost ,
K_d – additional costs connected with introduction of the investment.

If the analyzed variant of the investment economic efficiency assessment applies to an investment into a bus of make and type that has not yet been used in the system, additional costs should include the following components (Woropay & Perczyński, 2010):

- costs of providing service stations of a garage and technical emergency units with new diagnostic equipment and tools for servicing and repair of the analyzed variant,
- costs of service staff and drivers training,
- costs of introduction of a ticket system and transport management system,
- costs of bus color adjustment and necessary graphic information (identification number etc.).

Expenses involved in a purchase or creation of fixed assets are not considered to be tax deductible expenses at the moment they are borne but gradually throughout the period of their being used by depreciation deduction. However, only the estate components considered by law to be fixed assets or intangible and legal assets are subject to this rigor. The cost of bus amortization can be expressed by the following dependence:

$$K_{AM} = K_z \cdot r_{am} , \tag{4}$$

where:
K_{AM} –annual cost of bus amortization,
r_{am} – amortization cost ratio according to the law regulating annual amortization ratio.
Like other automotive vehicles, buses need to have motor insurance. Due to the fact that there are many insurance companies on the market and the prices of offered services are different, further analysis does not include this component of costs. Moreover, an economic entity owning a technical object can use an additional insurance (assistance, comprehensive cover). In consequence, this cost component would assume a similar value for all considered variants and would not affect the analysis result (Woropay & Perczyński, 2010).
Similarly, the analysis does not include indirect costs such as: department costs, company costs, management costs, etc. These cost components would not affect results of the analysis in the considered variants of the investment.
The costs connected with transport means operation and maintenance should involve a financial value of exhaust fumes emission, calculated according to the annex to legislation resolution of the European Parliament regarding promotion of ecological, clean and energy efficient vehicles in road transport. Since the buses analyzed in particular variants are supposed to perform the same transport tasks, that is, exhibit the same technical parameters, this component will be omitted in further analysis.

Outlays connected with ensuring operability, repair and maintenance of transport means, referred to as K_{OB}, make up an important component of the costs. The cost is expressed by the following dependence:

$$K_{OB} = K_{oc} + K_{ot} + K_{na} + K_{nk} + K_{ns}, \tag{5}$$

where:
K_{oc} - daily service costs,
K_{ot} - technical service costs,
K_{na}- costs of repairs performed in the service station and by technical emergency units,
K_{nk} - costs of bus cash machine repairs,
K_{ns} - repair and maintenance costs of the transport system.
Costs of operating materials K_{ME} are an important component of operation and maintenance costs. The most important ones can be expressed as follows (6).

$$K_{ME} = K_{mp} + K_{ol} + K_{sp} + K_{og}, \tag{6}$$

where:
K_{mp} - cost of propellants (fuel),
K_{ol} - cost of engine and gear box lubricant,
K_{sp} - cost of lubricants and operating fluids,
K_{og} - cost of tires.
It was assumed that human related costs including wages and other related expenses connected with accomplishment of transport services do not depend on the type of transport means and they do not affect the investment evaluation.
To build a model for economic evaluation of efficiency of investment connected with a purchase of a bus, a new modified net present value method (NPV) was used. The form of a criteria based functional is presented by dependence (7).

$$F_i = \sum_{t=1}^{n} K_{OBi} \cdot (1+p)^{-t} + \sum_{t=1}^{n} K_{MEi} \cdot (1+p)^{-t} + K_{INi} - \sum_{t=1}^{a} K_{AM_i} \cdot (1+p)^{-t}, \tag{7}$$

where:
i – i-th calculation variant,
a – number of bus amortization years.
Inclusion of amortization costs in the criteria based functional is connected with their influence on the tax costs involved in operation of the analyzed city bus transport company.
Having analyzed the value of criteria based functional for particular city transport buses it can be said that particular investment variants can be evaluated in the economic aspect I terms of the accepted assumptions. An optimal variant is a variant for which the value of functional F_i is the lowest, that is:

$$F_{opt} = \min(F_i), \tag{8}$$

where:
F_i - value of the functional for the i-th investment variant.
Presentation of source data sets and calculation variants is not a goal of this study.

CONCLUSIONS

The aim of this study is to present the substance and main assumptions of the developed method for selection of city transport buses to be used in a given company, according to the economic criterion. The considered model for selection of city transport buses is significantly simplified. However, the presented construction method of this type of model and its analyses make it possible to use it for an initial economic assessment of particular investment variants.
In this work only economic criteria for selection of a technical object to be used in a given transport system have been discussed, including technical and safety aspects of transport means. The proposed method should be used for selection of a technical object to perform efficiently transport services in a given transport system.
In practical applications there occurs a problem connected with estimation of values of the model parameters, especially for vehicles of other makes and types than those so far used. Also computer

simulation methods of the transport means operation and maintenance process can be used for estimation of values of the model parameters.

The presented way of description of the economic method for investment assessment allows to use it for technical systems other than a city transport system.

There is a need to conduct further research in order to evaluate properly the values of costs connected with operation and maintenance of buses of given types and makes.

REFERENCES

1. Drury, C. (2002). *Management and Cost Accounting*. Warszawa: PWN.
2. Samuelson, P., A., & Nordhaus, W., D. (2012). *Economy*. Poznań: REBIS.
3. Landowski, B., Perczyński, D., Kolber, P., & Muślewski, Ł. (2016). An example of Markov model of technical objects maintenance process. *Engineering Mechanics 2016, 22nd International Conference* (pp.346-349). Book of full texts: Institute of Thermomechanics Academy of Sciences of the Czech Republic.
4. Landowski, B., Woropay, M., & Neubauer, A. (2004). *Controlling reliability in the transport systems (Sterowanie niezawodnością w systemach transportowych)*. Library of Maintenance Problems. Bydgoszcz-Radom: Maintenance Technology Institute.
5. Woropay, M., Knopik L., & Landowski, B. (2001). *Modeling processes of operation in transport system (Modelowanie procesów eksploatacji w systemie transportowym)*. Library of Maintenance Problems. Bydgoszcz-Radom: Maintenance Technology Institute.
6. Woropay, M., & Perczyński, D. (2010). Economic aspects of selecting means of bus transport. *Journal of KONES*, *17*, 513-519.

Corresponding author:
Ing. Bogdan Landowski, Ph.D., Faculty of Mechanical Engineering, University of Science and Technology, Prof. S. Kaliskiego 7, 85-789 Bydgoszcz, Poland, phone: +48 523408208, e-mail: lbogdan@utp.edu.pl

DESIGN OPTIMIZATION OF COMPOSITE PARTS USING DOE METHOD

Petr LEPŠÍK[1], Petr KULHAVÝ[1]

[1]*Technical University of Liberec, Faculty of Mechanical Engineering, Liberec, Czech Republic*

Abstract
The paper is focused on design optimization of composite parts made of long fibers carbon composite material assembled into plies. Parameters as angles of particular plies and geometry of a part should be optimize according to specific loading of the part. The analytical approach to searching optimal parameters is difficult especially for complex parts. A task becoming more and more difficult with the number of optimized parameters. The way of searching of optimal parameters (angels of particular plies and geometrical parameters of a part) is using method DOE (Design Of Experiment) and SW Ansys which uses this method for optimization tasks. The paper introduces this optimization tasks for case of composite tube. This approach can be used for example for design optimization of composite tubes in innovated car seats etc.

Key words: *design optimization; composite parts; carbon fibers; prepreg; DOE; Ansys*

INTRODUCTION

In recent years using of composite materials is still exponentially growing, thanks to the excellent specific strength, possibilities of customize the properties and achievable weight savings. The use of modern advanced composite materials has gained wide acceptance in the last few decades. Compared to metallic structures, composite laminates offer some unique engineering properties while presenting interesting but challenging problems for analysts and designers (*Kherredine L., Gouasmi S., Laissaoui R., Zeghib N. E., 2012*).
In term of the project Innovation of Technical Systems Structures with the use of Composite Materials autors already dealed with the issues of bending properties of thin walled prepreg carbon fibers (*Kulhavý P.; Lepšík P., 2017a*), vibration response of composite structure (*Kulhavý P., Petřík J., Srb P., Lepšík P., 2016*), comparison of modal characteristic of wrapped and winded composite tubes from carbon prepreg (*Kulhavý P.; Lepšík P., 2017b*) etc. After these primary studies it is neccesary to find an effective way of optimization of part design and its parameters according to the specific loading. The method DOE (Design of Experiment) can be used for optimizing of variable input parameters according to the required output parameter. This method has been used with advantage for example for improving the production of composite pipes (*Srebrenkoska S., Kochov A., Minovski R., 2016*) or study of mechanical behaviour of matrix composites (*Deshmanya I., Purohit K., 2011*). The aim of this study is to find the optimal design of a loaded composite part with the use method DOE and SW Ansys.

MATERIALS AND METHODS

Materials

This study is focused on long fiber prepreg carbon composite materials assembled into particular plies (**Fig. 1**). Unidirectional prepreg tapes have been the standard material used within the aerospace industry for many years. Pre-saturated fibers are tape consist of fibers in a polymer (often impregnated with thermosetting resins) matrix and protected by a silicone paper. Usually, they are available in widths from 70 to 1300mm (*Srb P., Kulhavy P., Kovar R., Lepsik P., Syrovatkova M., 2016*). Depend on the constitution of the matrix (thermoset or thermoplastic) is the tape stored in a refrigerator. Then, the tape can be automatically or manually laied at various orientation to make the final composite structure. Then, follow the standard process of curing in vacuum, during pressure and temperature, may follow (*Kaw K., 2006*).
All prepreg materials have to be cured according to tightly controlled time, temperature and vacuum requirements. Quality assurance shall continuously record time, temperature and vacuum during the cure process (*Koushyar H, Alavi-Soltani S, Minaie B, Violette M., 2012*). Process of curing the final

product: Apply vacuum, Heat at 72-115°C, Hold on curing time 1-12 hours, then slowly cool at 48°C (*Srb P., Kulhavy P., Kovar R., Lepsik P., Syrovatkova M., 2016*).

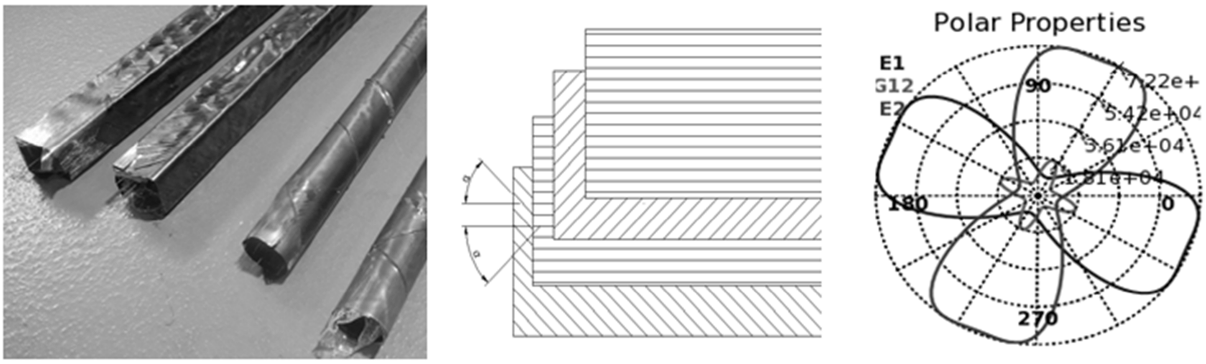

Fig. 1 Composite part a) Real tubes, b) A plies layout, c) The basic material properties

The design of curved tube of elliptical cross section made of 4 plies fixed at one end and loaded by force at opposite end was optimized in term of this study. Constant input parameters were lenghts and radius of the tube, angle of 1st and 2cd ply (45/-45), loading force (340N) and material properties. Optimized parameters were angles of 3rd and 4th ply and lenght of axes of elliptical cross section. The desired result was minimal deformation of the tube.

Methods

Method Design of Experiments (DOE) which is included in SW Ansys has been used for this task. First the computer model of the composite tube was created in SW Ansys then the algorithm of DOE was used.

The model of the curved tube of elliptical cross section is created of 4 plies with 2 constant angles (45/-45) and 2 parametrical angles with initial vaues (45/-45) Model (Fig. 2) is created as shell layered with the use of composite preprocessor ACP. The model contain mapped face mesh with quadrilaterals elements, 1124 nodes and 1107 elements. According to the geometry of draft profile with parametrical radius of the tube, edgewise defined rosettes were neccessary to use for accurate definition of directional vectors of particupar plies depending on the real curvature of the geometry. The numerical model was solved as a statical where one end of a tube was fixed and at the second one was the force.

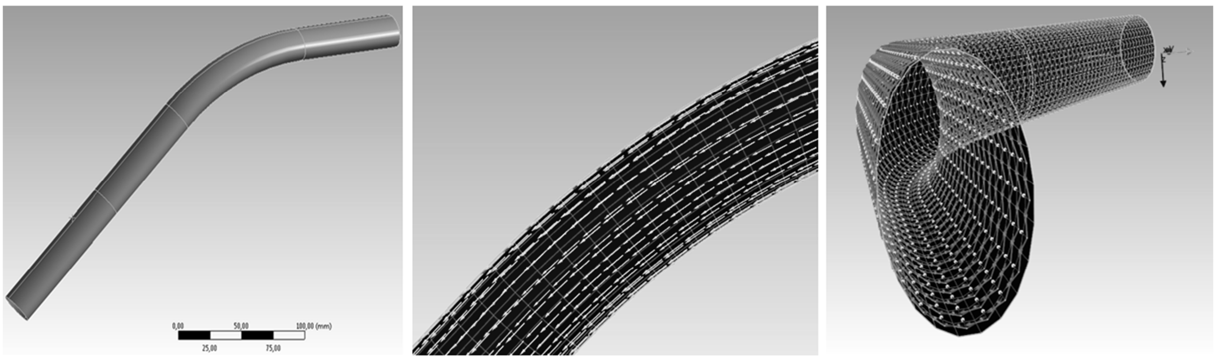

Fig. 2 Model of composite curved tube of elliptical cross section

Design of Experiments (DOE is a technique used to scientifically determine the location of sampling points and is included as part of the Response Surface, Goal Driven Optimization, and Analysis systems. There are a wide range of DOE algorithms or methods available in engineering literature. These techniques all have one common characteristic: they try to locate the sampling points such that the space of random input parameters is explored in the most efficient way, or obtain the required information with a minimum of sampling points. Sample points in efficient locations will not only reduce the required number of sampling points, but also increase the accuracy of the response surface

that is derived from the results of the sampling points. By default, the deterministic method uses a Central Composite Design, which combines one center point, points along the axis of the input parameters, and the points determined by a fractional factorial design.
We used DOE method for searching the most suitable value of the angles of 3rd and 4th ply and lenghts of axes of elliptical cross section of the tube (Fig. 3).

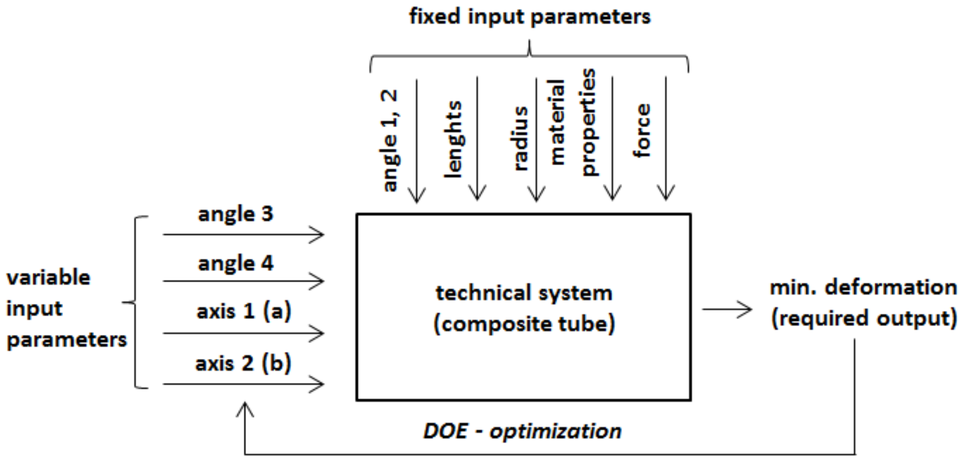

Fig. 3 System model of the optimization task

First part of the computation was searching of correlation dependencies between particular input parameters and output parameter. Total 100 design points were generated with the use of „function specimen“ also used in (Price K., Storn R., Lampinen J., 2005).

$$\text{Specimen} = \{(type^1; Lo^1; Hi^1); (type^2; Lo^2; Hi^2) \ldots (type^D; Lo^D; Hi^D)\} \quad (1)$$

$$Dp_j = Lo^j + rand(0,1)\left(Hi^j - Lo^j\right) \quad (2)$$

Where type mean the number character (real, integer, discrete set), Lo and Hi are the lowest and highest possible value (in our case the winding angle in actual ply) and j mean nr. Of the actual design point.
The limit values of angles 3 and 4 were chosen according to manufacturing technology which do not allowed to use angles close to 0 or 90 deg. Initial and limit values of variable parameters are in the Tab. 1.

Tab. 1 Initial and limit values of variable parameters

Variable parameter	Initial value	Lower limit value	Higher limit value
P1 – Longer axis - ellipse (mm)	35	30	40
P2 – Shorter axis - ellipse (mm)	20	15	25
P3 – Angle of ply 3 (deg)	45	20	80
P4 – Angle of ply 4 (deg)	-45	-20	-80

After finding correlation dependencies, it was necessary to find the optimal solution using the Response surface optimization algorithm. The solution consisted of new generations totaling 1000 design points.

RESULTS AND DISCUSSION

The correlation dependencies of input and output parameters are shown in Quadratic determination matrix (Fig. 4). The highest impact on the deformation (output parameter) has the lenght of longer axis of ellipse (absolut value of correlation coeficient lies in interval 0,4-0,6), lower impacts have angles of plies 3 and 4 (absolut value of correlation coeficient 0,2-0,4), the lowest impact has the lenght of shorter axis of ellipse (absolut value of correlation coeficient 0,1-0,2). Proportional impact of imput parameters to deformation is shown in pie chart Sensitivity of deformation on the input parameters (Fig. 4).

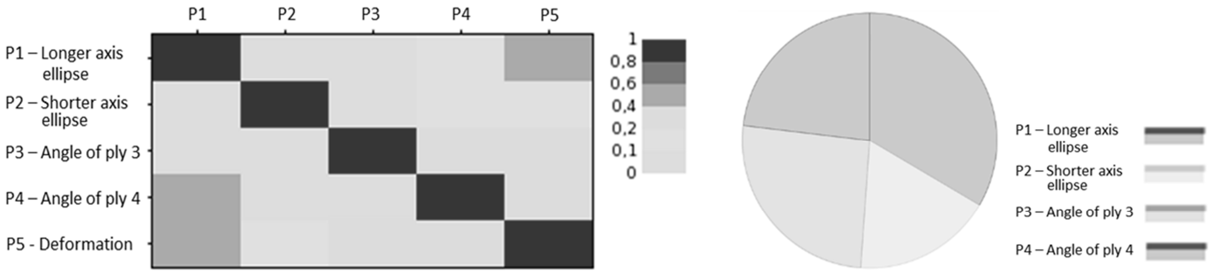

Fig. 4 The correlation dependencies a) Quadratic determination matrix b) Sensitivity of deformation on the input parameters

The dependence of maximal total deformation on length of longer axis of ellipse is shown in the Fig. 5. Between these two parameters (the most important input parameter and output parameter) is negative correlation.

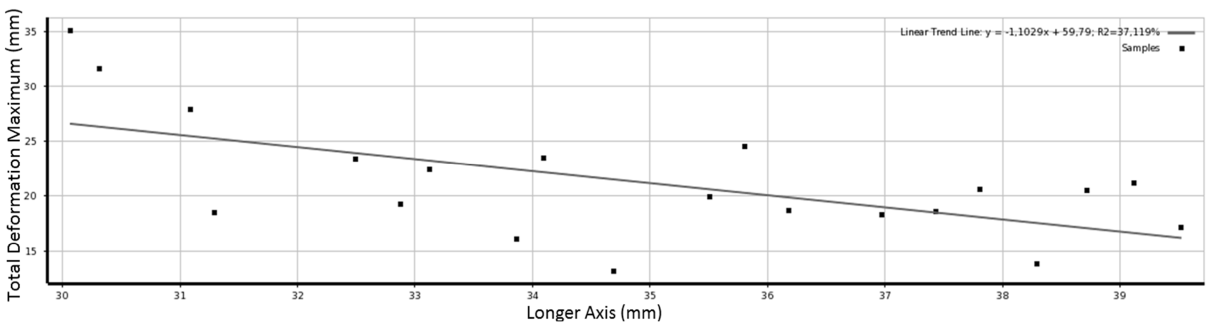

Fig. 5 The dependence of maximal total deformation on length of longer axis of ellipse

The dependences of maximal total deformation on two variable input parameters (agles of plies 3 and 4) or lenght of longer ellipse axis and angle of ply 3 are shown in the Fig. 6. The minimum deformation occurs when the fibers are oriented at 20 degrees (ply 3) and -20 degrees (ply 4).

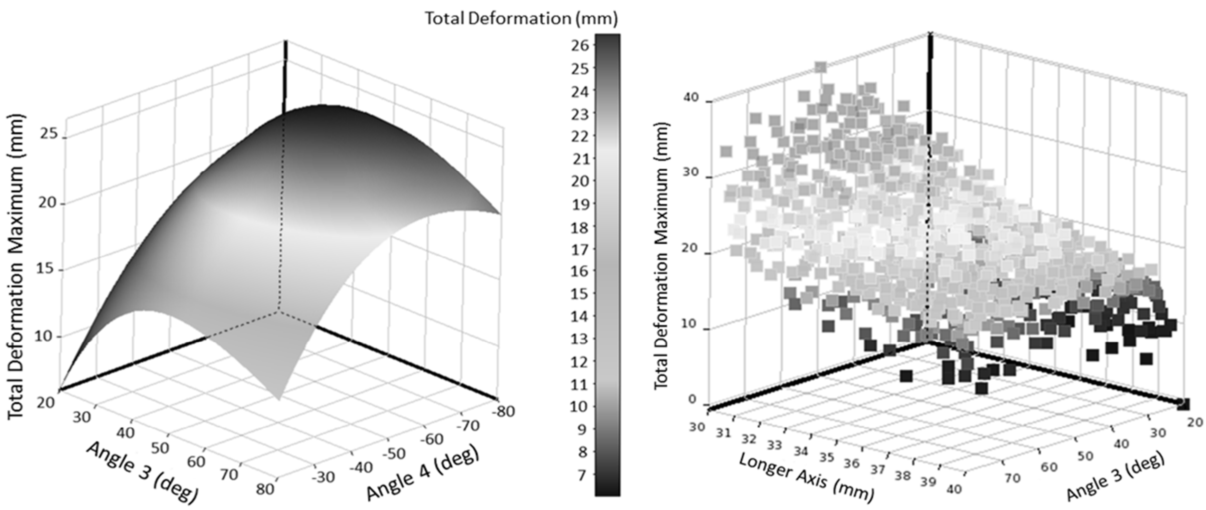

Fig. 6 The dependence of total deformation on two variable input paremeters a) Response surface b) Sampling points

After recognition of impact of particular variable input parameters to output parameter can be find optimal combination of parameters to achieve optimal value of output parameter (minimal total deformation). The best candidates has been chosen from generated 1000 points accorting to the fitness functions in our case represented by minimal total deformation. The parameters of the best candidate are introduced in Tab. 2. The results correspond with the theoretical expectation. The directions of fibers given by angles of the plies are in sum the closest possible to the tensile loading of the fibers. The cross section of the tube achives to maximal allowed value to minimize deformation of the tube.

Tab. 2 The best candidate of design point generation with the highest value of fitness function

Parameter	The Best Candidate Point (Optimized values)
P1 – Longer axis - ellipse (mm)	40
P2 – Shorter axis - ellipse (mm)	25
P3 – Angle of ply 3 (deg)	20
P4 – Angle of ply 4 (deg)	-20
P5 – Maximal Total Deformation (mm)	8,19

After receiving optimalized values of input paremeters the model was recalculated and results were compared (Fig. 7). Maximal total deformation of the tube was reduced from 14,8mm to 8,1mm using method DOE and Ansys for optimization of composite part design.

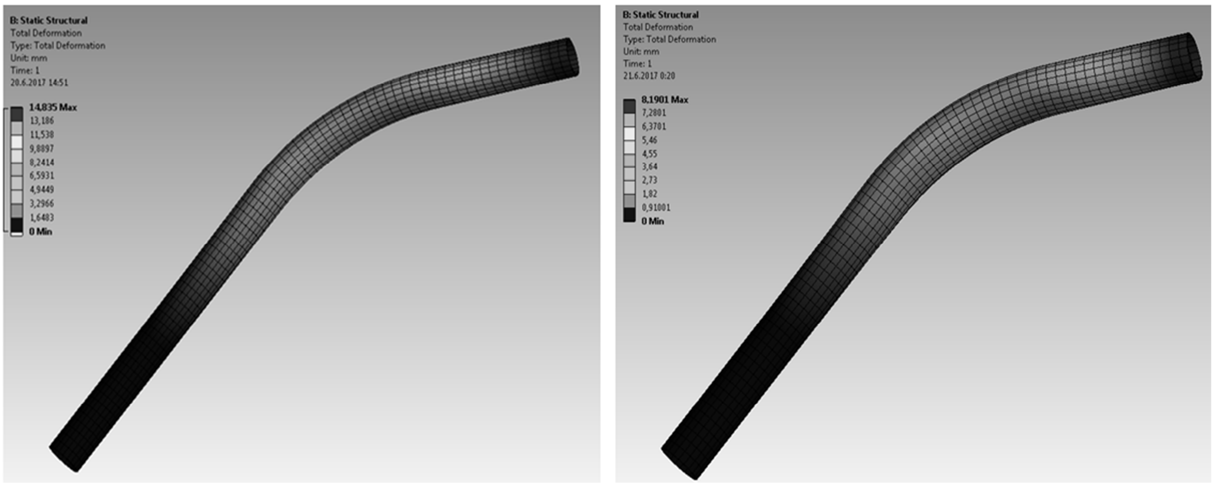

Fig. 7 The total deformation a) original b) optimized (angles of plies 3 and 4, lenghts of axes of elliptical cross section) design of the part

CONCLUSIONS

Designing advanced long fiber composites is not conceivable without the support of the latest computational CAD and FEM modellers today. Unlike the classical material, the parameters of the final composite part can be fundamentally influenced by the sequence and rotation of the plies from which the material is composed. Since the combination can exist theoretically countless, experimental testing is not practicaly possible. For this reason, the future is precisely the use of algorithms to search for the maximum of a given fitness function. Compared to conventional unimodal solvers, generic or evolutionary unimodal search algorithms should be used due to the complexity and amount of possible local maxima and minima of the function. Introduced study shown posibility of usage method DOE and Ansys for design optimization of long fiber carbon composite part. Optimization of parameters as orientation of particular plies and geometrical parameters of the part has led to improving of mechanical properties of the part. The benefit of this method will increase with the increasing complexity of a composite part.

ACKNOWLEDGMENT
This publication was written at the Technical University of Liberec as part of the project "Innovation of products and equipment in engineering practice" with the support of the Specific University Research Grant, as provided by the Ministry of Education, Youth and Sports of the Czech Republic in the year 2017.

REFERENCES

1. Deshmanya I., Purohit K., (2011). Study of Mechanical Behaviour of Metal Matrix Composites using Design of Experiments. Advances in Production Engineering & Management 6 (4), 303-309.
2. Kaw K. (2006). Mechanics of Composite Materials, Second Edition. United States of America: Taylor and Francis Group.
3. Kherredine L., Gouasmi S., Laissaoui R., Zeghib N. E. (2012). Evaluation and measurement of the damping properties of laminated CFRP composite plates. Materials Science and Engineering 28 (1). 1-9.
4. Koushyar H, Alavi-Soltani S, Minaie B, Violette M., (2012). Effects of variation in autoclave pressure, temperature, and vacuum-application time on porosity and mechanical properties of a carbon fiber/epoxy composite. Journal of Composite Materials 46(16), 1985-2004.
5. Kulhavý P., Petřík J., Srb P., Lepšík P. (2016). Vibration response of composite structures. 54th International Conference Experimental Stress Analysis.
6. Kulhavý P., Lepšík P. (2017a). Study of bending properties of thin walled carbon and flax composite rods winded of prepreg fibers. 55th International Conference Experimental Stress Analysis (pp. 316-321).
7. Kulhavý P., Lepšík P. (2017b). Comparison of modal characteristic of wrapped and winded composite tubes from carbon prepreg. Conference of Vibroengineering (pp. 91-96).
8. Price K., Storn R., Lampinen J., (2005). Differential Evolution. New York: Springer-Verlag.
9. Srb P., Kulhavy P., Kovar R., Lepsik P., Syrovatkova M. (2016). Winding of presaturated carbon fibres. 57th International Conference of Machine Design Departments (pp. 340-346).
10. Srebrenkoska S., Kochov A., Minovski R. (2016) Six sigma and DOE for improving the production of composite pipes. Journal for Technology of Plasticity 41 (2), 11-18

Corresponding author:
Ing. Petr Lepšík, Ph.D., Department of Machine Parts and Mechanisms, Faculty of Mechanical Engineering, Technical Univerzity of Liberec, Studentska 2, 461 17 Liberec 1, Czech Republic, phone: +420485353326, e-mail: petr.lepsik@tul.cz.

THE ASSEMBLY PROCEDURE OF THE TRACKER RAIL WEELDING SUPPORT FOR ATLAS ITK AT CERN – THE SIGNIFICANCE OF THE EXPERIMENT

František LOPOT[1,2,a], Martin JANDA[3,1,b], Marek RACHAČ[1], Daniel HADRABA[1,2], Pavel MALÝ[4,1],Václav VACEK[4]

[1]*Department of Designing and Machine Components, Faculty of Mechanical Engineering, Czech Technical University in Prague, Czech Republic*
[2]*Department of Anatomy and Biomechanics, Faculty of Physical Education and Sport, Charles University in Prague, Czech Republic*
[3]*Department of Engineering, Berkley Lab, California, USA*
[4]*Department of Physics, Faculty of Mechanical Engineering, Prague, Czech Republic*

[a]*Frantisek.Lopot@fs.cvut.cz;* [b]*Martin.Janda@fs.cvut.cz.*

Abstract
The article is focused on finding the correct assembly procedure of the welding support. The first step of finding the assembly procedure was based on the theoretical analysis - relationship between torque and axial force in the bolt - of the support which was then verified by the simple experiment in the second step. The support forces depending on the tightening torque were measured in the experiment. The experiment proved to be very important to understand the behavior of the welding support during the assembly procedure and the final assembly procedure is based on the experiment.

Key words: *experiment; assembly process; ATLAS ITk; CERN.*

INTRODUCTION

This year in February, we installed a welding tool (Tracker Rail Welding Support = TRWS) in CERN. The tool was developed and manufactured at our department, the information of this topic was provided last year. The tool is designed to lock the rails in defined position during their welding to the outer housing (Inner Warm Vessel = IWV) of the ATLAS inner detector. This modification of the mock-up is required so that its design will correspond to the intended design within the upgrade of the ATLAS detector and so that it could be trained and tested the assembly procedures for the individual components in detail. The visualization of the installation of the tool in the housing of the inner detector is presented in fig. 1.

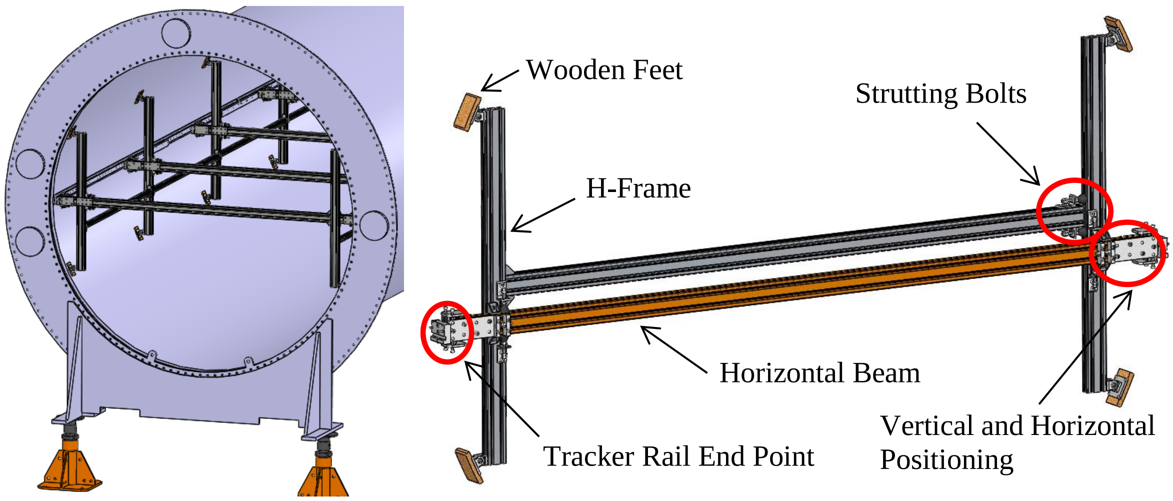

Fig. 1 Installation of the tool in the housing of the inner detector.

It is important to note that the tool consists of two parts. The H-frame is used to lock the tool position in the housing of the detector. The purpose of the horizontal beam is to carry the welded rails. While the position of the tool is secured, it is possible to change the position of the horizontal beam and thus set the required position of the rails very precisely. The reliable locking of the position of the H-frame in the housing of the detector is the essential condition, which is achieved by an adequate tightening of the H-frame strutting bolts, so that even when applied up to 1000 N in the direction of the longitudinal axis of the detector, the shifting of the tool will not be able. The aim of this article is to bring the readers closer to the problematics, which the authors encountered finding the correct assembly procedure.

MATERIALS AND METHODS

The assembly instruction was searched for by two approaches, where the first mentioned was also used as a basis to set up the conditions for the second one. The first approach was based on the classical relationship between torque and axial force in the bolt. The second one is based on the experimental finding of the actual torque relation with the measured supporting force. The first approach works with the scheme of Figure 2, which also describes the calculation of the required tightening torque.

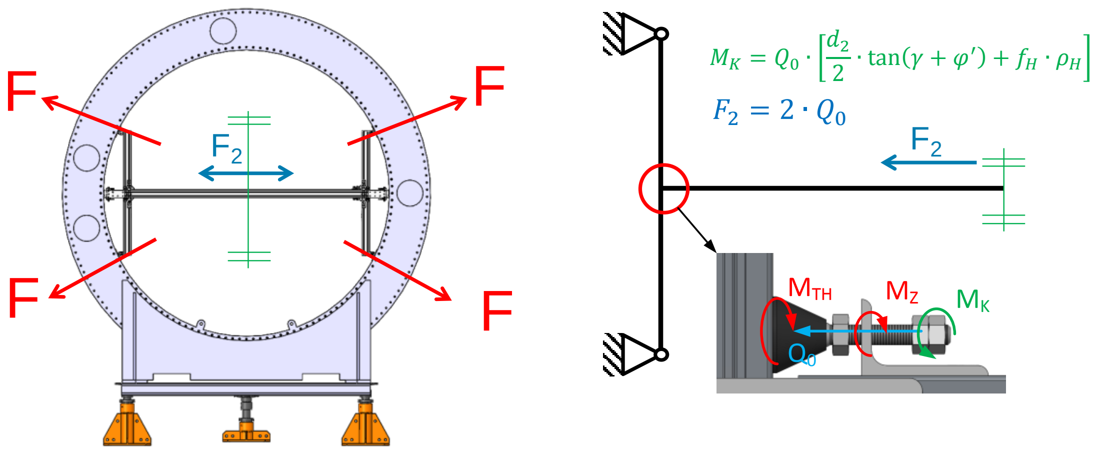

Fig. 2 Theoretical analysis of the welding support.

The diagram in Fig. 2 presents huge simplification in comparison to the reality where the considered force is not introduced by one but by two bolts positioned about the width of the horizontal beam apart and whereas the fact that the coefficients of friction are chosen values, the results of the calculation have to be taken with reserve and must be experimentally verified and specified. However used mathematical model provided us the value of tightening torque required to meet the structure conditions listed above. This value of the tightening torque (ca. 4.0Nm) was used as one of starting-points to set up the experiment.

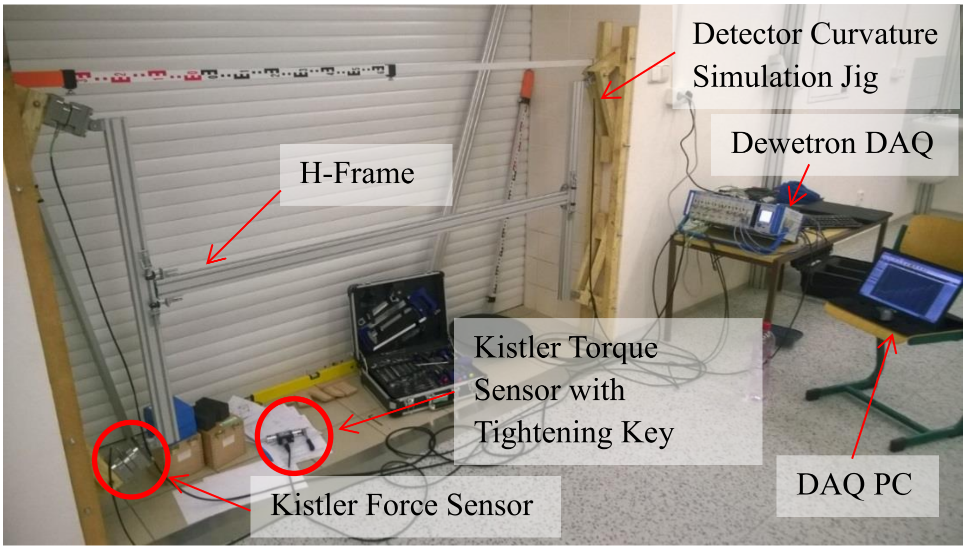

Fig. 3 Experimental measurement of the welding support the welding support in the Laboratory of Extreme Loading.

For the purpose of the experiment, a Kistler torque sensor with a sensitivity of 0.1 Nm was used. The sensor was connected directly on the head of the used tightening key. The tool was installed in the door of the Laboratory of Extreme Loading in special templates ensured a faithful simulation of the curvature of the detector housing (Fig. 3). The tightening process was acquired by the Dewetron apparatus and subsequently processed in the Matlab software. As the primary outputs of the data processing, courses over time of the tightening torque and of the contact forces in the end-plates of the tool are presented (Fig. 4).

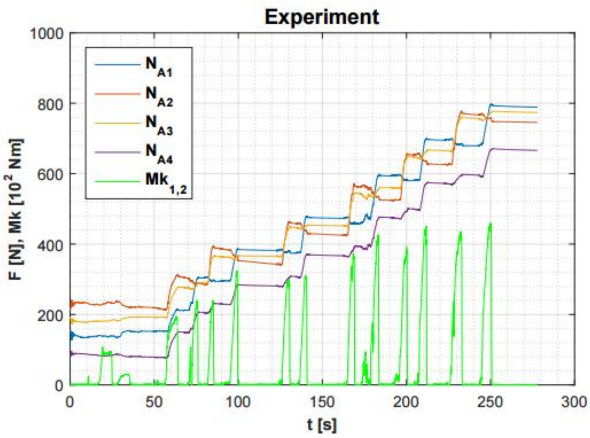

Fig. 4 The data (Forces and Tightening torque) measured over time.

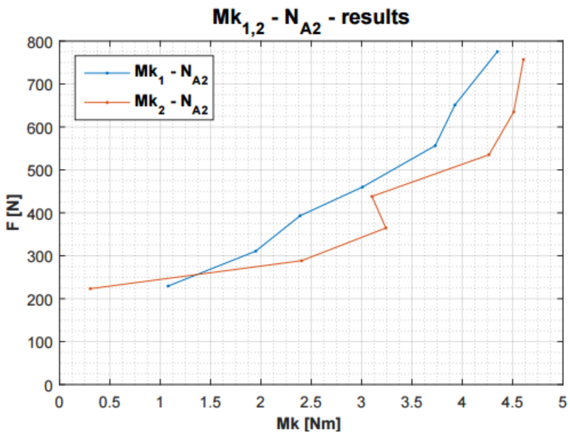

Fig. 5 The contact forces in dependence on tightening torque.

The measured data were also displayed in direct context – the contact forces in dependence on tightening torque (Fig. 5).

Based on presented courses, it will be appreciated that in order to achieve the necessary contact forces in the end-plates of the tool, the repeated tightening of the strutting bolts to the specified torque value is necessary. This fact is explained partly by the fact that there are two strutting bolts on the tool, i.e. there is not clearly defined junction between the horizontal and vertical beam of the H-structure in terms of loading distribution from both bolts, and partly by the fact that the total stiffness of the structure becomes to be changed during the tightening process. The principle of this change is schematically illustrated in Fig. 6, where the model works with partial stiffness k_1 and k_2).

$$F_2 = 2 \cdot Q_0 = 2 \cdot F_y \rightarrow F = \frac{M_K}{\left[\frac{d_2}{2} \cdot \tan(\gamma + \varphi') + f_H \cdot \rho_H\right] \cdot \cos\alpha}$$

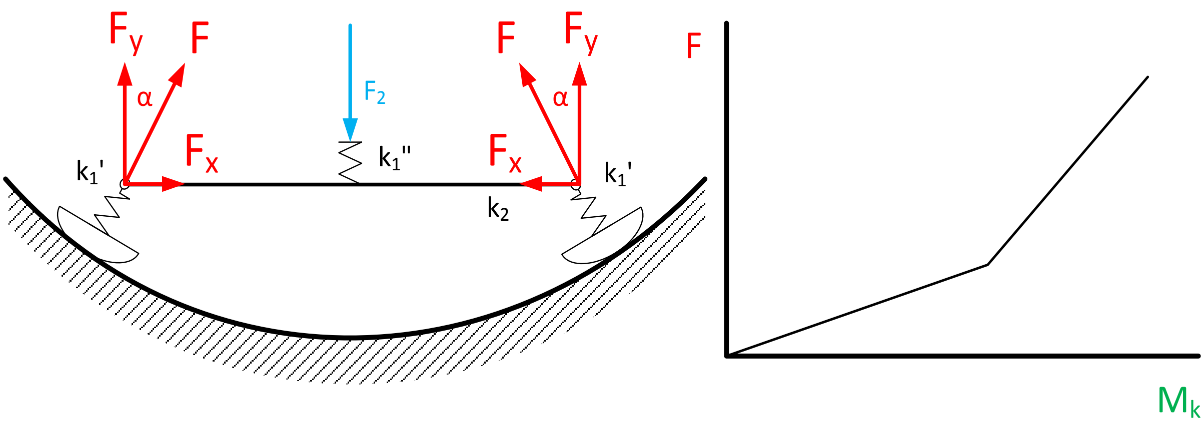

Fig. 6 Mathematical model of the structure stiffness changes

RESULTS AND DISCUSSION

Based on the above, it is obvious that used mathematical model was too simplified to provide us complete information on how to set up the tightening process. Nevertheless, the analysis provided us the value of tightening torque, which has proved to be usable in experimental measurement.
By linking both of these approaches, the essential information usable for design of the assembly process and adjusting the calculation model was obtained. The adjustment of the mathematical model was made despite the huge simplification by replacing of the two central supports with a central single one. The concept explains the stiffness changes due to the "contacting" of the articulating surfaces of the individual components more than sufficiently and offers also the possibility to consider the friction ratios in the tightening bolts.

CONCLUSIONS

The aim of the article was to highlight the problematics of strutting constructions and the danger of using simplified computational models without experimentally verification of their behavior. The experimental measurement shown the importance of an engineering experiment which was quite simple for the given case, but still provided crucial data for the correctness of the tool installation process. Based on this representative experience and on other similar experiences the recommendation of the application of experimental methods, also in cases where it may appear at the first glance that there is not any reasonable argument for can be concluded.

ACKNOWLEDGMENT

This study was supported by SGS16/069/OHK2/1T/12 - Konstrukční řešení podpůrného, manipulačního a servisního systému vnitřního detektoru ATLAS.

REFERENCES

1. Janda, M.; Malý, P.; Hadraba, D.; Dub, M.; Kamenický, J.; Lopot, F.; Dynybyl, V. (2016). Manipulator of the inner detector ITk of ATLAS experiment in CERN. In: *Book of proceedings of the 57th International Conference of Machine Design Departments*. Plzeň: Západočeská universita, 2016, ISBN 978-80-261-0609-8.
2. Rachač M.; Dub, M.; Janda, M.; Malý, P; Kamenický, J.; Berka, O.; Dynybyl, V.; Kubový, P.; Lopot, F. (2017). Experimental analysis of welding tooling for ITk ATLAS. In: *Book of proceedings of the 55th InternationalScientific Conference Experimental Stress Analysis*. Košice: Technical University of Košice, 2017, ISBN 978-80-553-3166-9.

Coressponding author: František Lopot, ČVUT, Fakulta strojní, Ústav konstruování a částí strojů, Technická 4, Praha 6, Česká republika, 16607, flopot@seznam.cz

CRASH TEST OF THE STUDENT RACING CAR IMPACT ATTENUATOR

Aleš LUFINKA[1]

[1]Department of the Design of Machine Elements and Mechanism, Technical university of Liberec, Studentská 2, 461 17 Liberec 1

Abstract
The student formula SAE [1] is the international competition for university student design teams. Each team must design and build its own racing car and then participates in international races. Strict rules are set for its design and great emphasis is placed on the safety of the driver. Therefore, every race car must be equipped with an impact attenuator in the front and it must meet the prescribed rules for the energy absorption in the crash event. Testing of the impact attenuator for a racing car that is built by the student team of the Technical University of Liberec is described in this article.

Key words: *crash test; impact attenuator; student racing car; testing device.*

INTRODUCTION

The student formula SAE organization was founded in 1981 in the United States and now brings together around 120 student design teams from universities all around the world. The team of the Technical University in Liberec joined this organization last year. Each team must demonstrate the ability to build a single-seat racing car of its own design, which will be well-handled, efficient, reliable, safe and environmentally friendly. Emphasis is also placed on aesthetic properties and the lowest production cost. Then each team can participate in competitive events all around the world. Races are divided into static and dynamic disciplines, from which the team gets a certain number of points. The winner will be the one who gets the most out of 1,000 possible points. In the first phase of static disciplines, each team presents the engineering design and maturity of the technical side of their design before a professional jury. The second part of the entrance presentation is the successful passing of safety tests, which is a necessary condition for participation in the following dynamic disciplines. The safety of the driver is most important, so every race car must be equipped with an impact attenuator in the front and it must meet the prescribed rules for energy absorption in the crash event. The used impact attenuator functionality has to be verified by a real crash test.

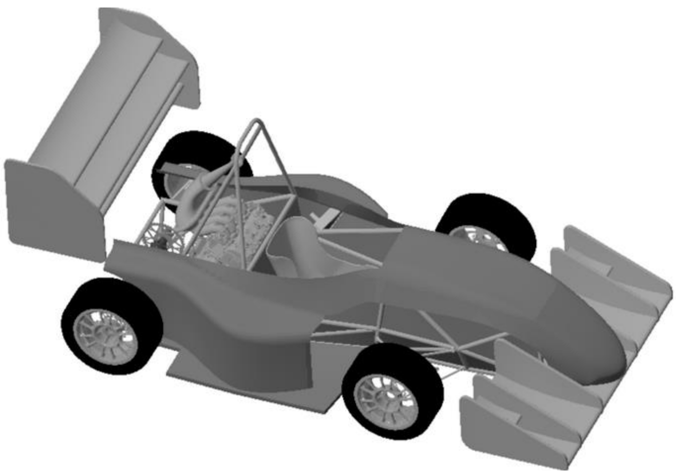

Fig. 1 Design of the Technical University of Liberec racing car

Crash tests are generally very expensive and this is in contrast to the requirement for a minimum price for a racing car. The student team did not first know where such a test could be done. It finally succeeded in Laboratory of Applied Mechanics at the Technical University of Liberec. It was big challenge for a laboratory staff and the student team to carry out this difficult test with minimal resources and moreover in a short term because the first race in Italy was approaching.

MATERIALS AND METHODS

Many parameters determine the impact attenuator dimensions, properties and location in the car. Of course, its dynamic properties are also prescribed and these are shown in the Table 1.

Tab. 1 Basic requirements for the impact attenuator crash test

Minimal impact attenuator absorbed energy	7350 J
Maximum value of the deceleration peak	40 g (392.4 ms^{-2})
Maximum average deceleration value	20 g (196.2 ms^{-2})
Maximum safety zone wall deflection	25 mm

After considering these test parameters and laboratory options, it was decided to carry out a crash test using the mass free fall. It was a very cheap and fast-realizable solution because a 4 m high portal crane is available in the lab. The real free fall height could be about 2.5 m because approximately 1.5 m was considered for the mass, its anchoring and the tested impact attenuator. The theoretical impact velocity v (if friction is neglected) for height h can be calculated using the classic Newtonian mechanics [2] by the next Equation 1.

$$v = \sqrt{2 * g * h} \ = \ \sqrt{2 * 9.81 * 2.5} \cong 7 \ [ms^{-1}] \qquad (1)$$

The weight of the mass was determined from this velocity and the required impact energy according to Equation 2.

$$m = \frac{2*E}{v^2} = \frac{2*7350}{7^2} = 300 \ [kg] \qquad (2)$$

Absolutely free fall of 300 kg mass from 2.5 m height would be very dangerous, because the mass movement after impact would be undefined. Therefore, a simple fall tower was built. The moving table was guided by four guide rods anchored to the base plate. Six 52 kg cast iron weights (which are available in the laboratory) were attached on this table, so the total weight (including the table) of the falling mass was 345 kg (see Fig. 2 left). For this weight the theoretical starting height was recalculated to 2.17 m (Eq. 2). The lower impact velocity due to friction at the guide bars was measured during first functional tests. In order to keep the impact speed, the starting height was gradually increased to 2.4 m. The rapid release of the moving table after its lifting by the crane was finally accomplished by burning the anchor rope with a small gas burner. Due to the small number of tests, it was again a very cheap and efficient solution, no trigger mechanism had to be proposed.

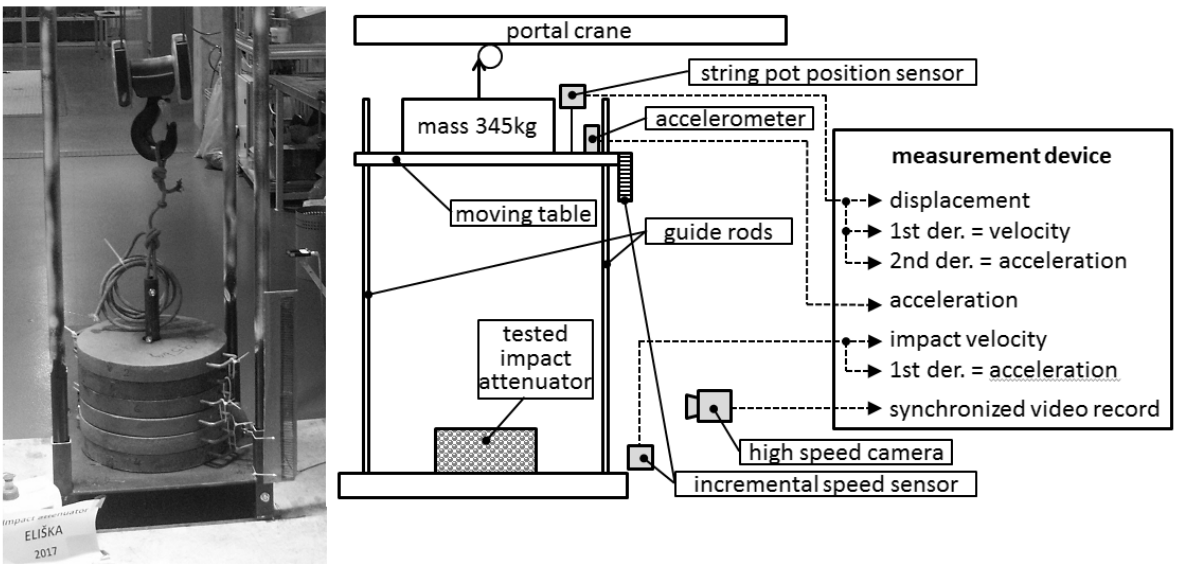

Fig. 2 The testing device real implementation (left) and its block scheme (right)

The moving table displacement was measured by the string pot position sensor, velocity and acceleration were calculated by the first and second derivations of this signal. Acceleration was further measured by a separate accelerometer and the final impact velocity by another incremental speed sensor. Acceleration was again calculated by deriving this signal. So the important signals measurement has been ensured several times. The crash test was also captured by the high speed camera. All sensor signals and the camera were connected to the Dewe5000 measurement device [3], which performed synchronic data and images recording. The sampling frequency was 5 kHz for the sensor signals and 600 Hz for the video.

RESULTS AND DISCUSSION

The impact attenuator is composed from two parts, the absorption and safety zones, their minimum dimensions are again given by the SAE. The absorption zone is deformed during the impact, absorbs the impact energy and reduces the deceleration peak. The safety zone must not be broken in the crash event (it protects the driver's legs), only its wall below the deformation zone may have a small deflection.

The student team designed the absorption zone from three layers of aluminium honeycomb panels [4] in two variants of their composition – cubic and pyramidal (see Fig. 3). They preferred the second solution because it was more convenient for installation to the car.

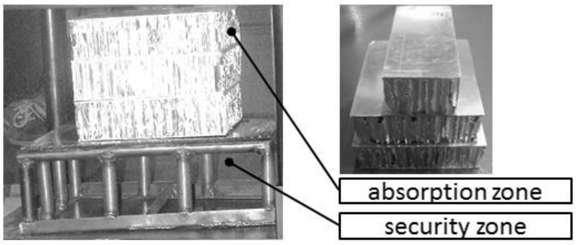

Fig. 3 The impact attenuator design, cubic composition left and pyramidal right

Because only one security zone part was made, two variations of the absorption zone without the security zone were first tested to verify their properties. So, security zone remained intact for the final test. These two measurement results are summarized in the Figure 4.

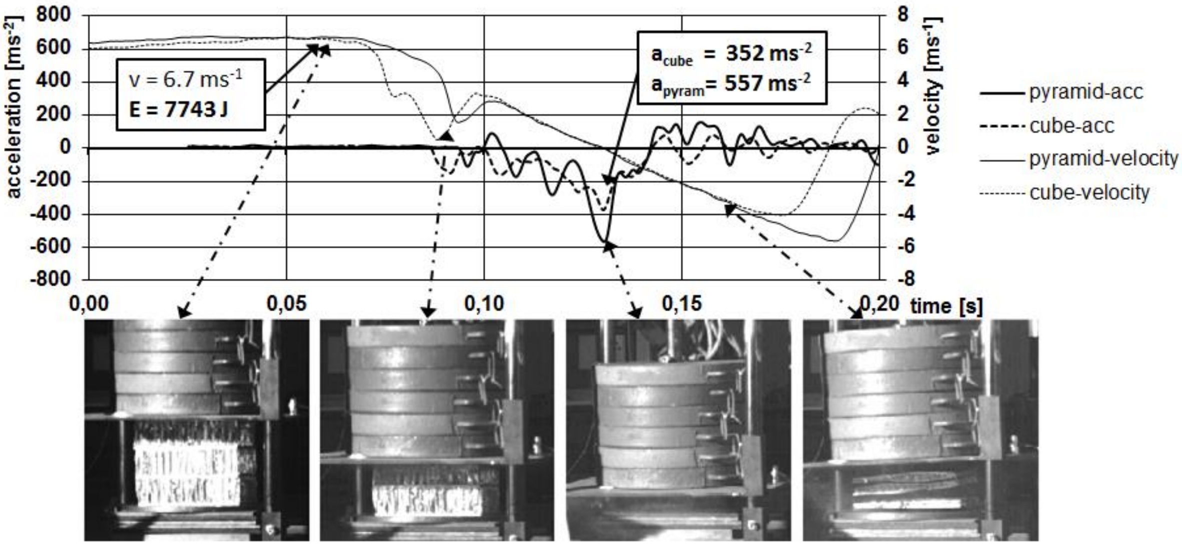

Fig. 4 Comparison of the cubic and pyramidal absorption zone

The impact velocity was 6.7 ms^{-1}, the impact energy 7743 J. The acceleration waveforms show that the pyramidal composition did not meet the requirement because its deceleration peak was 557 ms^{-2} (56.7 g). The area of the pyramid top part was too small. In contrast, the cubic composition meets the SAE requirement, the deceleration peak was less than 40 g.

So, the pyramidal solution was abandoned and the final impact attenuator was assembled with the cubic absorber. Its test is shown in the Figure 5. The impact velocity was 6.9 ms^{-1} and the impact energy 7743 J. The impact attenuator met all the requirements. The safety zone was not broken and its wall deflection measured after the test was only 15 mm. The maximal deceleration peak was 276 ms^{-2} and it is less than in the only deformation zone test because the peak size was reduced by the small deflection of the safety zone wall. All test results are summarized in the Table 2.

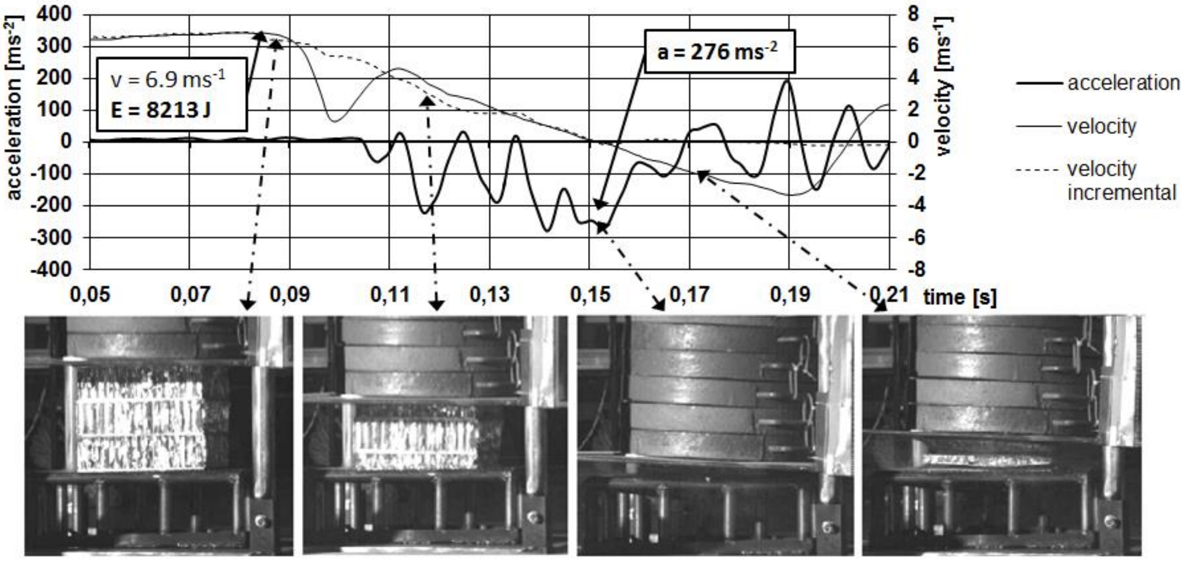

Fig. 5 The impact attenuator test

Tab. 2 The impact attenuator crash test results

Requirement	Criterion	Measured value	Status
Impact attenuator absorbed energy [J]	7350	8213	Passed
Value of the deceleration peak [ms^{-2}]	392.4	276	Passed
Average deceleration value [ms^{-2}]	196.2	115.8	Passed
Safety zone wall deflection [mm]	25	15	Passed

CONCLUSIONS

The team of students and laboratory staff of the Technical University of Liberec managed to design and manufacture test equipment and implement the required impact attenuator crash test in a very short time (only five days from the first idea to the final test). Also the price was minimal, only the material for the guide rods had to be bought. Everything else, including sensors and measuring device, was available in the lab.

The impact attenuator final version with the cubic absorber met all SAE requirements and it was built into the student racing car that was then entered into the race. So good luck!

ACKNOWLEDGMENT

This publication was written at the Technical University of Liberec as part of the project "Innovation of products and equipment in engineering practice" with the support of the Specific University Research Grant, as provided by the Ministry of Education, Youth and Sports of the Czech Republic in the year 2017.

REFERENCES

1. Formula SAE International. Information on *www.fsaeonline.com.*
2. Kleppner, D., Kolenkow, R. (2014). An Introduction to Mechanics. *Cambridge University Press, ISBN 978-0-521-19811-0.*
3. Measurement device Dewe 5000. Information on *www.dewetron.com/products/chassis/all-in-one-chassis/dewe-5000.*
4. Aluminium honeycomb. Information on *https://corex-honeycomb.co.uk/our-products/aluminium-honeycomb/*

Corresponding author:
Ing. Aleš Lufinka, Ph.D., Department of the Design of Machine Elements and Mechanism, Technical university of Liberec, Studentská 2, 461 17 Liberec 1, phone: +420 485 353 854, e-mail: ales.lufinka@tul.cz

TESTING MEASUREMENT DURING THE SHAFT ASSEMBLY OF THE OILSEED SCREW PRESS

Pavel MALÝ[1], František STARÝ[1], Pavel MOSSÓCZY[1], Jan HOIDEKR[1], Vojtěch DYNYBYL[1]

[1]*Department of Designing and Machine Components, Czech Technical University in Prague*

Abstract
The application of strain gauges experiment was used for analysis of a production inaccuracy during the assembly. The components (inserts and screws) were placed on the shaft and the deformation on specified places was measured so the influence of the geometrical accuracy was observed.

Key words: *experimental measurement; strain gauges; geometrical accuracy.*

INTRODUCTION

Oils are important components of different plants, nevertheless oilseed such as soyabean, rapeseed, sunflower, cottonseed and others are mainly utilized in commercial oil production. There are different oil extraction processes consisting of specific operations, oil pressing is one of them. The mechanical pressing with expeller utilize a rotating screw inside a horizontal cylinder that is capped at one end. The screw forces the seeds through the cylinder with gradually increasing pressure, reported by *www.attra.ncat.org*.

Measurements and experimental testing on machines are very important and are used firstly to obtain the information and parameters of the real components or processes. The measured data can be further utilized for the subsequent optimization of the specific parts, structural units or set up of the operational parameters. The measurements are also used for validation of computational simulations and analysis (*Berka et al. 2015, Dub et al. 2014*).

This article focuses on the experimental measurement on the shaft of the oil press using strain gauges to find out the dependence between the production accuracy of the parts geometry and the deformation of the shaft during the assembly.

MATERIALS AND METHODS

Investigated machine. The described measurement was carried out on the shaft of the oilseed screw press (figure 1) during the assembly in the premises of the producer. The final assembly of the shaft that is placed in the oilseed screw includes also the inserts and screws firmly fasten on the shaft by a special nut.

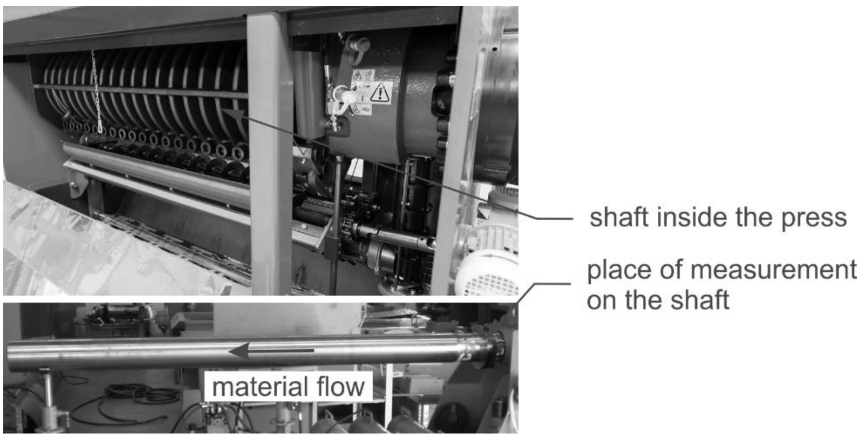

Fig. 1 Oilseed screw press FS 1010 and the measured shaft during the assembly, *www.farmet.cz*

Instrumentation and measurement protocol. The detailed scheme of the tested shaft with the measurement points can be seen in figure 2. Three strain gauges were placed in a groove at the end of the shaft. Regarding the flow of the material through the oil press, the measuring place was in the input end of the shaft. The strain gauges were used to obtain the uniaxial stress in three places in positions by 90° (see detail A and the cross-section B-B of the scheme in figure 2)

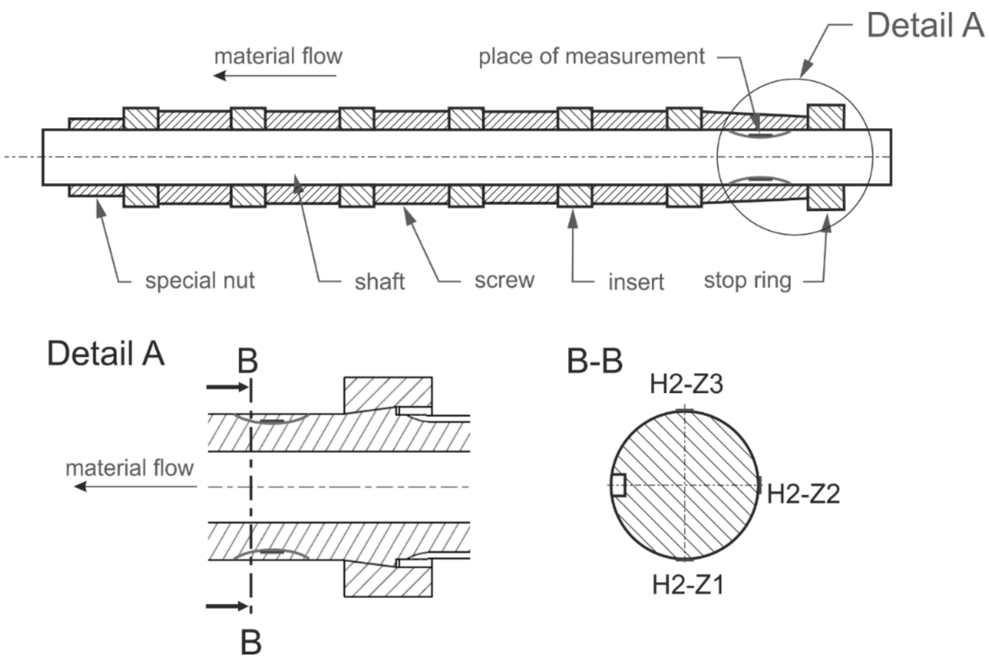

Fig. 2 Scheme of the tested shaft and detailed place of measurement with strain gauges

The set of three T rosette strain gauges with two measured grids HBM 1-XY11-6/120 in half-bridge configuration for axial strain measurement were used, *www.hbm.cz.*
The assembly of the shaft comprises of the insertion of the hubs (screws, spacers, inserts) on the shaft followed with the tightening by a special nut in precisely specified steps of the tightening moment (65 Nm, 130 Nm, 195 Nm, 250 Nm). The whole measuring cycle included also the loosening of the nut with the specified steps.

Data acquisition and processing. The National Instruments apparatus (Wi-Fi chassis cDAQ-9191, strain gauge measuring module NI-9237) and software LabView were used for the strain gauge measurement with the sampling frequency of 1000 Hz, see also *www.ni.com*. The data processing was performed in LabView software. Data were processed by Matlab and LabView software. The example of obtained time dependent filtered data from strain gauges in graphical form transformed to the uniaxial stress for the tightening is shown in figure 3.

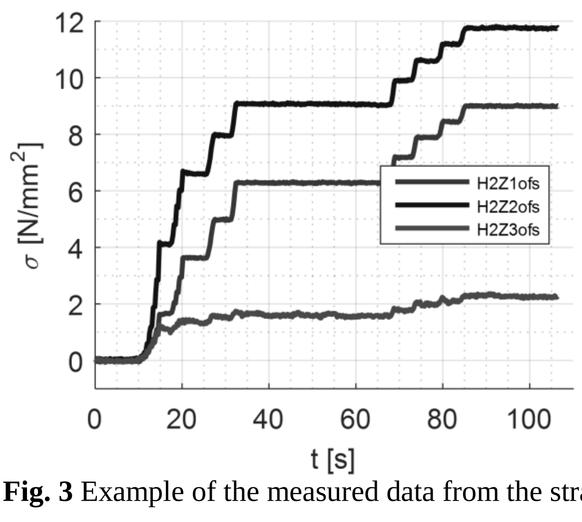

Fig. 3 Example of the measured data from the strain gauges

Experiment outcomes. The resultant stress components in the shaft were calculated from the stresses measured by the strain gauges. According the scheme in figure 4 the chosen stress components are tensile stress, bending stresses in the horizontal and vertical planes. The equations (1) are used for their determination from the measured data.

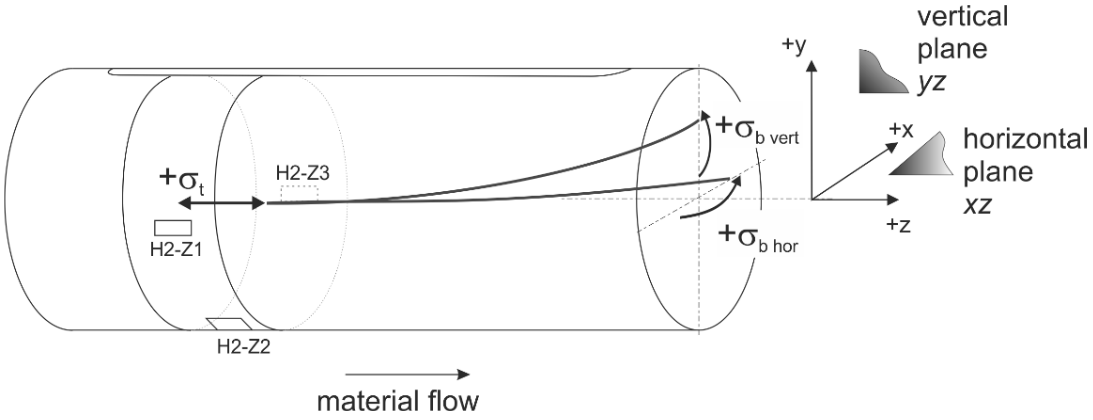

Fig. 4 Scheme of stress components in the shaft

$$\sigma_t = \frac{\sigma_{H2-Z1} + \sigma_{H2-Z3}}{2} \qquad \sigma_{b\,hor} = \frac{\sigma_{H2-Z1} - \sigma_{H2-Z3}}{2} \qquad \sigma_{b\,vert} = \sigma_{H2-Z2} - \sigma_t \qquad (1)$$

RESULTS AND DISCUSSION

Based on the measured data and determined stress components with help of equations (1) the final time dependent course of the stress components in the shaft is shown in figure 5 where the whole cycle comprising from tightening and loosening of the special nut is obvious.

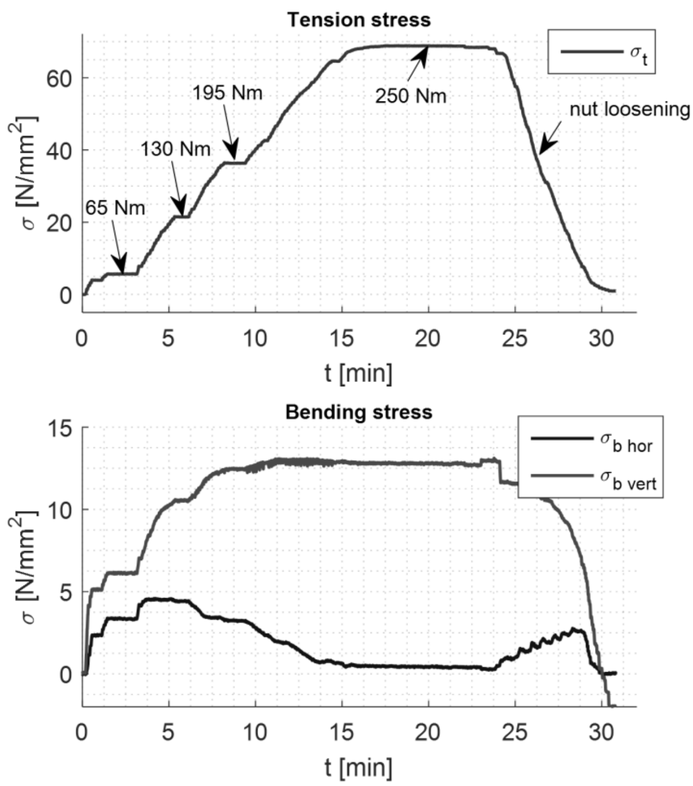

Fig. 5 Stress components dependent during the measuring cycle

The measured and processed data, i.e. the stress components in the shaft, were further analysed in comparison with the measured geometrical accuracy of the components (screws and inserts). The points of measurement in two planes on the components with the example of the accuracy analysis are shown in figure 6. The measured deviation in the points corresponds to the axis z, so the parallelism of the plane 1 and 2 can be determined.

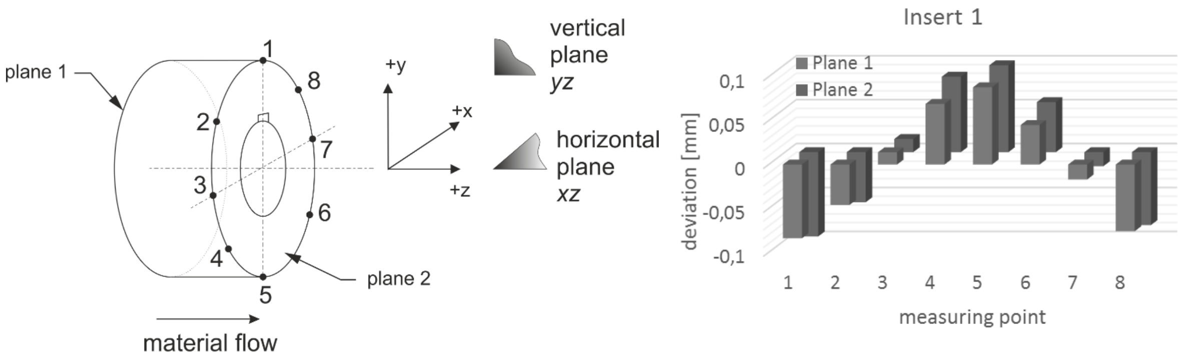

Fig. 6 Geometrical accuracy analysis of the components

The measured deviations in points1 and 5 fit the bending stress in the vertical plane, in points 3 and 7 fit the bending stress in the horizontal plane. The production inaccuracy of the first screw near the measured place has the significant influence on the bending stress in corresponding planes. The decrease of the bending stress in horizontal plane when the nut is fully tighten can be explained by the backlash elimination between the components.

CONCLUSIONS

The text describes the experimental method and its application where the strain gauge measurement and geometrical analysis are combined. First of all, the influence of the components production accuracy on the stress intensity of components in the real applications can be determined by this method. In the specific case the influence of the production accuracy on the stress distribution is evident.

ACKNOWLEDGMENT

This research has been realized using the support of Technological Agency, Czech Republic, project TA04010992, Research and development of technologies for obtaining vegetable oils and oil-cakes with an emphasis on quality of oil-cakes as feed and the appropriateness of used of the construction materials.. This support is gratefully acknowledged.

REFERENCES

1. Berka, O., Dub, M., Lopot, F., Dynybyl, V. (2015). Experimental analysis of stress state and motion of tram gearbox hinge. *EAN 2015 - 53rd Conference on Experimental Stress Analysis*.
2. Dub, M., Kolář, J., Lopot, F., Dynybyl, V., Berka, O. (2014). Experimental analysis of stress state and motion of tram gearbox hinge. *EAN 2014 - 52nd International Conference on Experimental Stress Analysis*.
3. Information on http://www.attra.ncat.org
4. Information on http:// www.farmet.cz
5. Information on http://www.hbm.cz
6. Information on http://www.ni.com

Corresponding author:
Ing. Pavel Malý, Department of Designing and Machine Components, Faculty of Mechanical Engineering, Czech Technical University in Prague, Technická 4, Praha 6, Prague, 16607, Czech Republic, phone: +420 224 352 418, email: pavel.maly@fs.cvut.cz

LOAD DISTRIBUTION ANALYSIS IN THE CONNECTION OF THREE CLINCHED JOINTS ARRAY IN THE ROW

Pavel MALÝ[1], František LOPOT[1], Jiří SOJKA[1]

[1]*Department of Designing and Machine Components, Czech Technical University in Prague*

Abstract
This article describes the experimental method with help of strain gauges used for testing of sheet-metal plates connection of three clinched joints in the row. The real behavior of the connection and the distribution of the total loading into each joint was observed.

Key words: *clinched joint; joints array; sheet-metal; experimental method; strain gauge*

INTRODUCTION
There are many production technologies that create structural components from sheet-metal plates. These methods are suitable and used in many industrial branches such as automotive, aerospace, or production of electric appliances and furniture. The crucial advantage is light weight with high strength at the same time. All final assemblies consist of many components, therefore suitable joining method is needed, clinching is one of those methods. This joining method is based on the plastic deformation of the base material and is characterized with many advantages. The creation of the round clinched joint is shown in figure 1. Connections of the sheet-metal parts are mainly composed of more joints so that the desired properties of the assemblies are achieved.
There are different methods how to obtain parameters of various machines elements and complex assemblies. Simulation methods represent one important group, the other one includes experimental methods. The applications of computational simulations, analysis and experimental measurement can be found in *Berka et al. 2015, Dub et al. 2014*.
This text is focused on the experimental testing of the specimen of sheet-metal plates connected by the row of three clinched joints. The experimental measurement with help of strain gauges was done to verify the analytical method, FE simulations (*Malý et al. 2015, Malý et al. 2016*) and theory of connections design described in (*Cvekl et al. 1976, Wittel et al. 2013*).

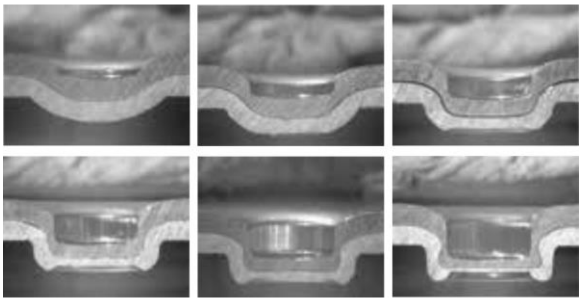

Fig. 1 Creation of the round clinched joint *(www.tox-de.com)*

MATERIALS AND METHODS
The used method was based on the experimental testing of the specimens by the unidirectional nondestructive test when the uniaxial stress near the joint is measured with help of the strain gauge, reported by *Malý 2017*.
Investigated set of specimens. The set of six specimens summarized in the table 1 was subjected to the experimental testing, Each specimen is the connection of two sheet-metal plates from low-carbon steel (1.0226) with the thickness of 3 mm and specific width (cross-section). The connection was created by the set of three equally spaced clinched joints in the row. The scheme with strain gauges notation and position with respect to the clinched joint can be seen in figure 2. Also the real sample with strain-gauges and wiring is shown in figure 2.

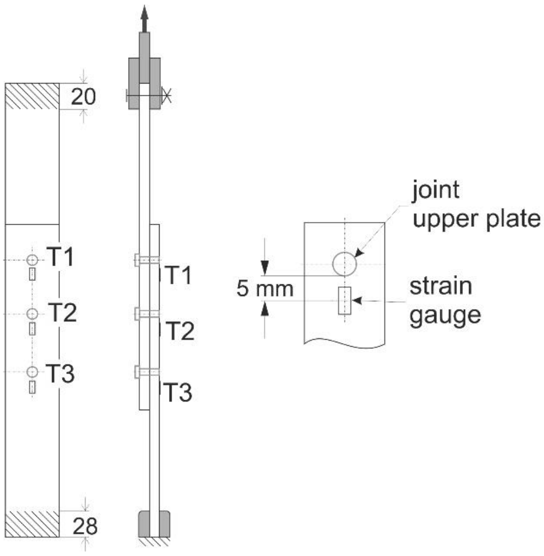

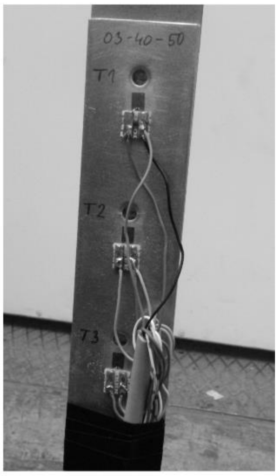

Fig. 2 Scheme and real sample of tested specimen

Tab. 1 Set of tested specimens

Specimen	Cross-section mm	Joints spacing mm
03-40-20	40×3	20
03-40-30	40×3	30
03-40-40	40×3	40
03-40-50	40×3	50
03-40-60	40×3	60
03-80-30	80×3	30

Instrumentation and measurement protocol. The detailed scheme of the testing stand that was designed and built for the realization of the testing can be seen in figure 3. The loading to the specimen was applied by a hydraulic cylinder (HM) with help of the loading system mechanism. Velocity of the hydraulic cylinder movement, i.e. velocity of the loading, was controlled by the proportional valve (PV). The actual loading force was the controlled variable and was measured by HBM force sensor (*www.hbm.cz*). The loading cycle consist of smoothly increases from 70 N to the maximum value and decreases back to the minimum value.

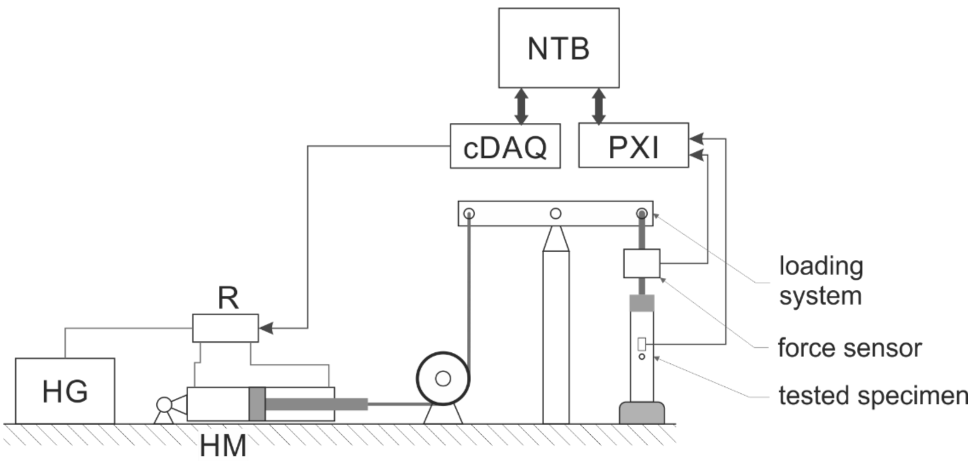

Fig. 3 Scheme of the testing stand

Data acquisition and processing. The testing equipment was controlled and the data were measured with National Instruments apparatus and LabView software (*www.ni.com*). Measured data were processed in Matlab software. Figure 4 represents the example of time dependent measured data, i.e. loading force and uniaxial stress outputs from the three strain gauges near the joints.

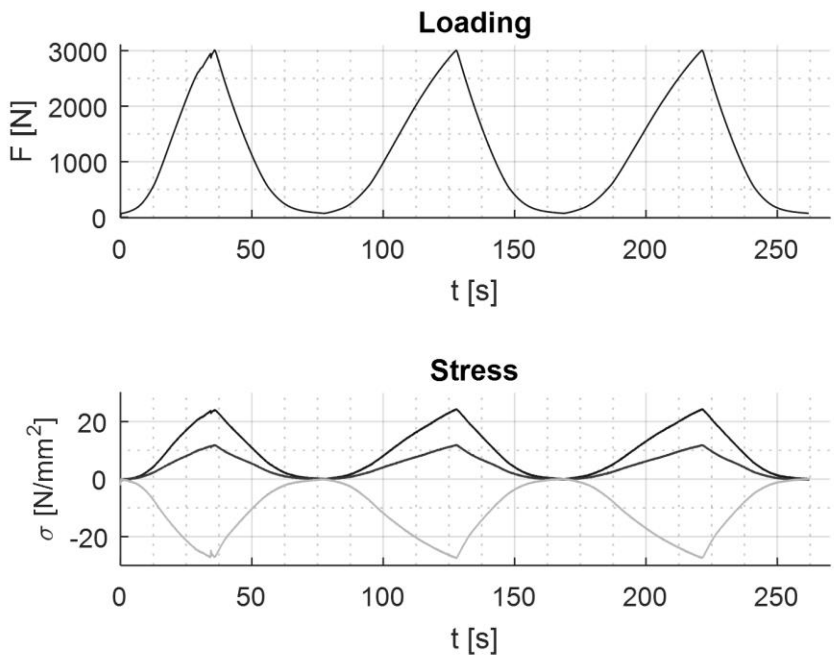

Fig. 4 Measured data

The graph in figure 5 shows the identification of dependency between loading force and measured stress for each strain gauge. It is visible the nonlinearity of the loading and unloading part of the cycle which can be explained by the influence of the testing stand properties.

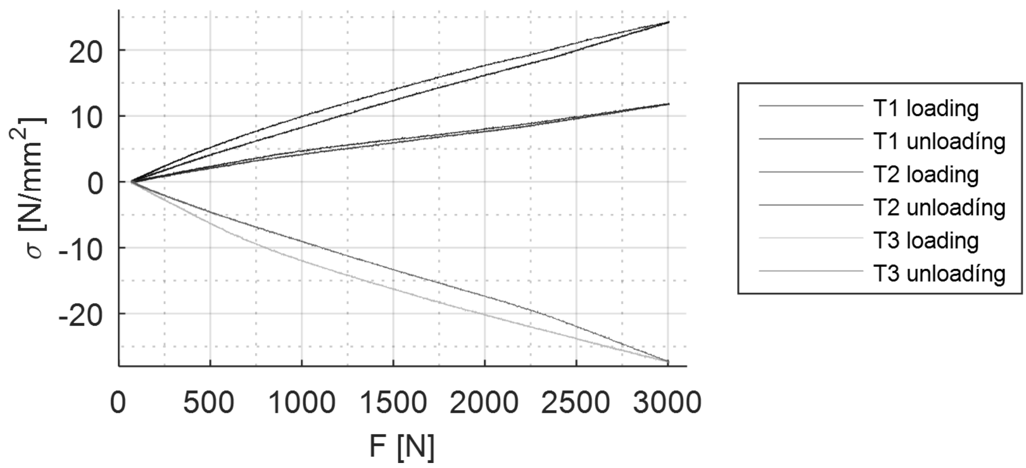

Fig. 5 Processed data

RESULTS AND DISCUSSION

The measured and processed data are summarized in table 2. The distribution of the total loading force between three joints was done assuming some simplifications and limitations of the used measurement method. The measured value from the strain gauge T3 is influenced by the additional bending of the specimen, so the assumption of the equal loading of joints T1 and T3 was used.

It is obvious from the results that the outside joints (T1 and T3) are loaded more than the inside joint (T2). This corresponds to the theoretical analytical calculations and FE simulations.

Tab. 2 Determined loading of each joint

Specimen	T1 %	T2 %	T3 %	Total loading %
03-40-20	40.13	19.75	(40.13)	100
03-40-30	39.75	20.49	(39.75)	100
03-40-40	36.72	26.56	(36.72)	100
03-40-50	36.58	26.85	(36.58)	100
03-40-60	33.97	32.05	(33.97)	100
03-80-30	38.21	24.94	(38.21)	100

CONCLUSIONS

This article describes the experimental method using strain gauges that can be used for nondestructive measurement of connections comprising from the array of single joints in the row. It is possible to obtain the load distribution between the joints in the connection with help of this method. The above described experimental method is subjected to the further verification, improvement and analysis using simulation methods.

ACKNOWLEDGMENT

This study was supported by the cooperation with the TOX®PRESSOTECHNIK (Weingarten, Germany).

REFERENCES

1. Berka, O., Dub, M., Lopot, F., Dynybyl, V. (2015). Experimental analysis of stress state and motion of tram gearbox hinge. *EAN 2015 - 53rd Conference on Experimental Stress Analysis*.
2. Cvekl, Z., Dražan. F. et al. (1976). *Theoretical basis of transportation equipment* (in Czech), Praha: SNTL.
3. Dub, M., Kolář, J., Lopot, F., Dynybyl, V., Berka, O. (2014). Experimental analysis of stress state and motion of tram gearbox hinge. *EAN 2014 - 52nd International Conference on Experimental Stress Analysis*.
4. Malý, P., Dynybyl, V., Sojka, J. (2015). Design and Verification of Connection Realized by the Array of Clinched Joints. *Book of Proceedings of 56th International Conference of Machine Design Departments*, 195-198.
5. Malý, P., Lopot, F., Sojka, J. (2016). Properties of The Clinched Joints Array in The Row. *57th International Conference of Machine Design Departments*.
6. Malý, P., Lopot, F., Sojka, J. (2017). FEM model and experimental measurement of clinched joint. *IOP Conference Series: Materials Science and Engineering, volume 179, number 1.*
7. Wittel, H., Muhs, D., Jannasch, D., Vossiek, J. (2013). *Roloff/Matek Machine Elements* (in German). Wiesbaden: Springer-Verlag
8. Information on http://www.hbm.cz
9. Information on http://www.ni.com
10. Information on http:// www.tox-de.com

Corresponding author:
Ing. Pavel Malý, Department of Designing and Machine Components, Faculty of Mechanical Engineering, Czech Technical University in Prague, Technická 4, Praha 6, Prague, 16607, Czech Republic, phone: +420 224 352 418, email: pavel.maly@fs.cvut.cz

COMPARISON OF CALORIFIC VALUES OF PETROLEUM-DERIVED FUELS WITH ALTERNATIVE FULES OF VEGETABLE ORIGIN

Marietta MARKIEWICZ-PATALON[1], Ewa KASZKOWIAK[2], Zbyszek ZBYTEK[3] , Marek SZYMCZAK[4]

[1] Faculty of Mechanical Engineering, UTP University of Science and Technology, Bydgoszcz, Poland.
[2]Faculty of Agriculture and Biotechnology UTP University of Science and Technology, Bydgoszcz, Poland
[3] Testing Laboratory for Agricultural Machines, Industrial Institute of Agricultural Engeneering Poznan, Poland
[4] Faculty of Mechanical Engineering, UTP University of Science and Technology, Bydgoszcz, Poland

Abstract: *Calorific value of fuels has an essential impact on the operation quality of engines with self-ignition. The laboratory studies during which measurements of heating value and heat of combustion showed, that only the content of bioester higher than 10% influences on the decrease of these values. The drop of the heating value and the heat of combustion showed, that at the content of bioester up to 10%, the changes of these both values are statistically unessential. No changes in the quantity of ash following combustion on which combustion of oxygen in the atmosphere could have impact on, have been observed.*

Key words: *diesel oil, bio component, calorific value, heating value, heat of combustion.*

INTRODUCTION

The limited resources of fossil fuels and legal requirements in force in different countries concerning the use of biofuels, to a large extent decide on the volume of production and possibilities of biodiesel's use. At present it is the European Union that is the bigger manufacturer of that type of fuel in the world. Oil taken from rapeseed is the basic raw material in EU for production of biodiesel, in small amounts however is used for bio components' manufacturing: sunflower seed oil, , animal fats, oils from recycling or imported soybean and palm oil (Oilseeds: World Markets and Trade. 2013).

In many union countries being big producers of rapeseed (Germany, France, Italy), or in the countries of the Eastern Europe (Belarus, Ukraine) for the last 15-months there has been observed a considerable increase of rapeseed crops' area occupying at present the third place in the world's production of oils and fats. The reasons of that raw materials' popularity increase is a very high nutrition efficiency of rapeseed oil, forage efficiency – middlings, and most of all the possibility to use seeds for bio components' production, being the additive to conventional fuels (Szkudlarski et al. 2014).

Relatively low prices of crude oil last year, together with high prices of vegetable oils prevailing for the last years, may reduce the increase of biodiesel production in the near future. Moreover, the requirement of reduction up to 50 % of GHG in sowing of rapeseed designed for biomass and biofuels production, as well as the decisions of the European Parliament reducing in many countries of up to 70% of the share of biofuels and generation in the total balance of fuels, may have a reducing impact on that production.

Producers of rapeseed pin in their highest hopes concerning reduction of costs of the ran cultivations and possibility of acquiring cheaper oil upon seeding big areas with newly registered hybrid varieties. These varieties are characterized by yielding higher than the population varieties (on average for 10%) and many positive agronomic features making it possible to simplify and to make the cultivation operations cheaper in the technologies of their cultivation (Wałkowski, 2012; Ogrodowczyk and Bartkowiak-Broda, 2013). For the purposes of improving of the energy balance at the time of rapeseed production, application of effective technologies of biomass' harvesting and processing into biofuels is recommended (Borowski, Zastempowski, Kaszkowiak, 2013).

In most of the union countries, fuels with additive of methyl esters of the fatty acids are allowed to be marketed and standardized with the EU Directive and with given countries' regulations. Legal acts obligate up to 5% of biodiesel's share in diesel fuels and determine the quality requirements concerning the fuels powering engines with self-ignition (Directive 2009/28/WE).

Most of the vegetable oils which are used in food industry, do not meet the criteria of the standard DIN 51605 (Standard for rapeseed oil fuels, 2010), in which the minimum and maximum quality parameters of bio components used as fuels or additives to fuels of compression-ignition engines (Tab. 1).

Tab.1. Quality parameters for vegetable biocomponents determined in the standard DIN 51605 (own study)

Parameter [unit]	**Limits**	**Unit**
Density	910-925	[kg*m^3]
Viscosity	>36	[mm^2*s]
Heating value	<36	[MJ*kg$^-$]
Acidity	>2	[mg]
Ignition point	<101	[°C]
Pollution	>24	[mg*kg^{-1}]
Content of sulphur	>10	[mg*kg^{-1}]
Content of water	>750	[mg*kg^{-1}]

One of the criteria of fuel's quality assessment are the following: calorific value (influencing among the others the engine's power and turning moment) and the ash's mass (polluting the filters of particulate solids).

In the own studies there has been conducted the analysis of the impact of different B 100 biocomponent's percentage share in the diesel fuel of fossil origin on the calorific value and the mass of ash following the fuel's burning.

MATERIALS AND METHODS

Setting of the calorific values of the base fuel (diesel fuel), methyl esters of the fatty acids received from the rapeseed oil and the mixture of the diesel fuel with methyl esters of the fatty acids were the subject matter of the studies. The research was conducted with the use of the calorimeter KL-12Mn, burning samples of fuels in the oxygen atmosphere. The scheme of the calorimeters used for the researches is shown in figure 1.

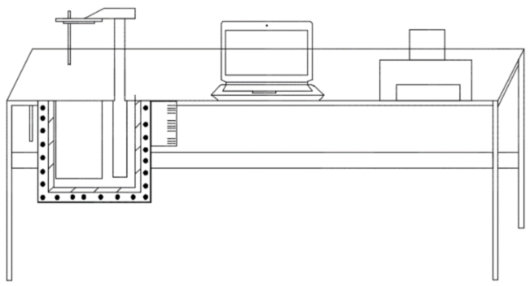

Fig.1. Scheme of the calorimeter KL-12Mn (own study)

The mixtures of the diesel fuel with biocomponent with reference to the diesel fuel and biocomponent in a clean form were tested. Proportions of samples are presented in table 2.

Tab. 2. Proportions of the tested samples (own study)

Sample I	100% Diesel fuel
Sample II	90% diesel fuel 10% methyl esters of the fatty acids
Sample III	70% diesel fuel 30% methyl esters of the fatty acids
Sample IV	50% diesel fuel 50% methyl esters of the fatty acids
Sample V	100% methyl esters of the fatty acids

Pursuant to the calorimeter's manual, tested were the samples of the weight of 1g. In order to set the mass of the ash, prior to the measurement there were tested clean and calcined melting pots for samples' burning. After each measurement, the melting pot with deposit was weighted. In the real terms, ash from the thermal process accompanies the processes of liquid fuels' combustion.

Examining of the heat of combustion, calorific value and measurement of the ash's mass was conducted in 5 repetitions for each sample. The obtained results were subject to statistical analysis with the use of the statistical software Analwar FR on the basis of Excel. The differences were verified with the Tukey's test of significance on the level of significance of 0,05. The mean values of the obtained results are presented in table 3.

RESULTS AND DISCUSSION

The volume of energy emitted at the time of thermal conversions during combustion of the mass of fuel, during complete combustion, considering condensation of water steam was determined. In table 3 there are presented the mean values of measurements of: heat of combustion, calorific value and the mass of ash for individual mixtures.

Table 3. Mean values of the heat of combustion, calorific value and mass of ash (own study)

Sample	Calorific value [MJ*kg^{-1}]	Heat of combustion [MJ*kg^{-1}]	Mass of deposit [g]
I	43,097^{a}	44,277^{a}	0,00397
II	42,199^{a}	43,779^{a}	0,00390
III	41,959^{b}	42,139^{b}	0,00113
IV	40,590^{c}	41,770^{c}	0,00140
V	37,906^{d}	39,097^{d}	0,00217
NIR	NIR (0,05)=1,006	NIR (0,05)=0,973	n. i. (nie istotne)

The obtained results were subject to the statistic analysis with the software ANALWAR FR on the basis of Excel. Both for the changes of the calorific value changes as well as for the heat of combustion, no essential changes between the fuel of 100% content of diesel fuel of fossil origin (sample I) and the mixture of the content of bio component 10% (sample II). In the remaining cases, between the sample I and V, there has been observed a statistically essential drop in calorific value for 12,1%. For the heat of combustion's parameter, the drop was also statistically essential and amounted to 11,7% between the samples I and V. However, no essential statistically differences have been disclosed for individual samples in the ash's mass.

The above dependencies are presented on the graphs 3 and 4.

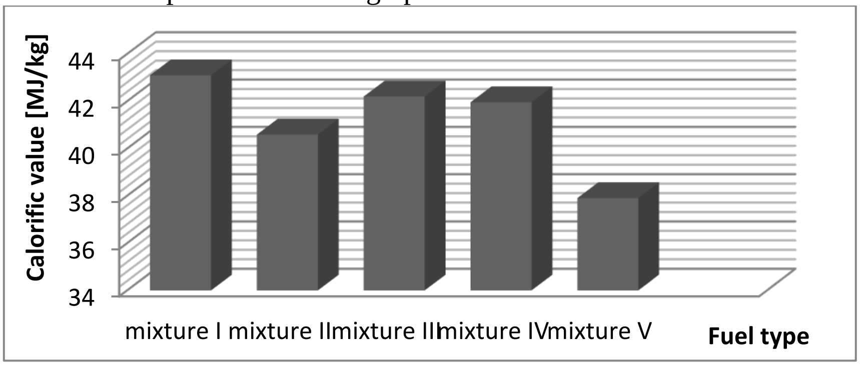

Fig.3. The set calorific value of individual samples (own study)

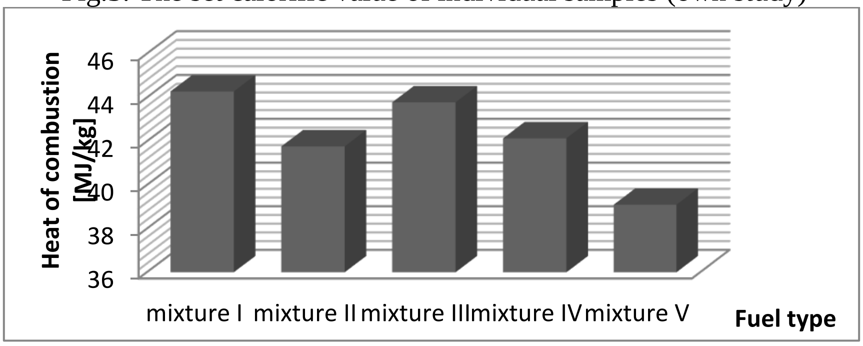

Fig.4. The set heat of combustion of individual samples (own study)

CONCLUSIONS

Addition of biocomponent B100 results in lowering of the fuel's calorific value and heat of combustion.

Essential statistical differences are visible only at the component's content in the diesel oil higher than 10%. Higher share of biocomponent results in the decrease of both the heat of combustion as well as the calorific value. The calorific value of the pure diesel oil amounts to 43,097 MJ*kg^{-1}, and of the methyl esters of the fatty acids to 37,906 MJ*kg^{-1}. The calorific value of fuel drops together with the increase of the biocomponent's content for the diesel oil and for mixtures III, IV and V and amounts respectively to 42,199 MJ*kg^{-1}, 41,959 MJ/kg and 40,590 MJ*kg. The differences are statistically essential. The heat of combustion of the diesel oil amounted to 44,277 MJ*kg^{-1}, however for the biggest proportion (sample V) it did not drop below 40 MJ*kg^{-1}, similar results were observed by other researchers [Jaworski, Kuszewski, Ustrzycki, 2011]. No statistically essential changes of the mass of ash remaining after all the samples' combustion were observed.

REFERENCES

1. BochańskiC., Bochańska A., 2008, Olej rzepakowy paliwem do silników Diesla, Czasopismo techniczne, PKrak, Kraków
2. DIN 51 605:2010-10 Rapeseed oil as fuel. ASG info letter
3. DYREKTYWA PARLAMENTU EUROPEJSKIEGO I RADY 2009/28/WE z dnia 23 kwietnia 2009 r. w sprawie promowania stosowania energii ze źródeł odnawialnych zmieniająca i w następstwie uchylająca dyrektywy 2001/77/WE oraz 2003/30/WE (Tekst mający znaczenie dla EOG)
4. Izdebski W., Skudlarski J., Zając St., 2014. Wykorzystanie surowców pochodzenia rolniczego do produkcji biopaliw w Polsce. Roczniki Nauk. *SERIA* XVI(2);93-97.
5. Jaworski A., Kuszewski H., Ustrzycki A., 2011, effect of biocomponents on the energetic parameters of fuels used by internal combustion engines of the means of transport
6. Jóźwiak D., Szlęk A., 2006, Ocena oleju rzepakowego jako paliwa, Energetyka i Ekologia, 2
7. Ogrodowczyk M., Bartkowiak-Broda., 2013. Ocena postępu biologicznego w hodowli rzepaku ozimego (*Brassica napus* L.). Rośliny Oleiste – Oilseed Crops 34 (2); 289-301.
8. Oilseeds: World Markets and Trade World Production, Markets, and Trade Reports. 2017.
9. Pasyniuk P., 2009, Olej roślinny jako alternatywne paliwo silnikowe, Problemy Inżynierii Rolniczej
10. Wałkowski T., 2012. Wýnos hybridnich odrud řepky ozimé v poregistračznich zkouškach v Polsku. Yield of winter oilseed rape hybryd varietes in post-registration trials in Poland. Prosperujici olejniny. Sbornik Konference s Mezinárodni Účasti, Česká Zemědělská Univerzita v Praze. 6-7.12. 2012.
11. www.fas.usda.gov/data/oilseeds-world-markets-and-trade [dostęp: 07.06.2017r., godz. 16:00]
12. Zastempowski M., Borowski S., Kaszkowiak J. 2013. New solution in harvesting plants for power purposes. Proceedings of 5th International Conference Trends in agricultural engineering, Prague 2013, p.673-676.

Corresponding author:

Marietta Markiewicz-Patalon, M. Sc.: Faculty of Mechanical Engineering, UTP University of Science and Technology, Poland, Al. Prof. Kaliskiego 7, 85-796 Bydgoszcz, e-mail: markiewicz-patalon@wp.pl

INNOVATION ENGINEERING METHODS FOR CONCEPTUAL ENGINEERING DESIGN – A REVIEW

Ivan MAŠÍN[1]

[1]*Department of the Design of Machine Elements and Mechanisms, Technical University of Liberec*

Abstract
This review deals with the description of innovation engineering methods that enable effective course of the initial steps of the innovation process, which aims to generate the best concept of innovated technical product.

Key words: *concept generation, methods, function analysis, creativity*

INTRODUCTION

Conceptual design differs from other phases of the design process (e.g. detailed design, design for assembly). The conceptual phase concerns the problem of coming up with new ideas or new solutions to problems. The goal of conceptual design theory is to understand the processes which lead to innovation and to create or describe techniques and engineering methods which generate proper changes in function in an systematic and repetitious basis (*Pahl, Beitz, Feldhusen & Grote, 2007; Pugh, 1991; Eversheim, 2009; Hubka & Eder, 1988; Eder & Hosnedl, 2010; Baxter, 1995*). Many of these sources, however, do not sufficiently described or underlined the importance of methods of so-called innovation science and systematic creativity, which has been dynamically developing over the last decade.

METODS OF INNOVATION ENGINEERING FOR INITIAL PHASES

Innovation engineering is one of the youngest engineering disciplines. This engineering field can be defined as an "interdisciplinary field, which deals with the effective process of the whole innovation process and the rapid transformation of the primary innovation idea into an innovative product applied in the market. For this purpose, he uses both specific industry methods as well as methods and knowledge from other engineering disciplines, from natural and social sciences, as well as knowledge from management theory. "

A very important role is played by methods for the initial phase of the innovation process. During this phase the concept of innovative products is generated and designers decide on the success of the product on the market, regardless of how well the subsequent engineering activities (modeling, prototyping, testing, etc.) are performed. Overview of these methods is given in the Table 1.

Tab. 1 Overview of methods for conceptual design phases

Innovation process phase	Innovation engineering methods
Innovation and technological forecasting	Technology Road Mapping Directed Evolution (DE) WOIS
Customer needs transformation	Thinking aloud protocol Quality Function Deployment (QFD) Innovation Situation Questionary (ISQ) Main Parameter Value analysis (MPV)
Problem decomposition and innovaton problem definition	Function analysis Trimming RCA, RCA+ Cause Effects Chain Analysis (CECA) Function Analysis System Technique (FAST)

Information search in cyberspace	Function Oriented Search (FOS) Function Behavior Oriented Search (FBOS)
Analysis of competing products	Reverse engineering
Creative concept generation	Morphological table 9 windows 40 inventive principles TRIZ Axiomatic design Bio-mimetics
Product architecture	Design Structure Matrix (DSM) Modular Function Deployment (MFD)
Concept evaluation and selection	Evaluation tables (Pugh) Analytical Hierarchy Process (AHP) Weighted Rating Method

FUNCTION ANALYSIS

Function is an action performed by one material object to change or maintain a parameter of another material object. Technical systems are created to perform functions, and those functions are realized through a set of specific components. Function analysis is an analytical tool that identifies functions, their characteristics, and the cost of the system and the super-system components. (*Litvin, 2010*) The main goals of function analysis are:

- To provide a functional representation of technical system.
- To identify functional disadvantages of the components of technical system.
- To rank the functions for further trimming.

The outcome of function analysis is the model of technical system in tabular or graphical forms. Function model is a model of the technical system that identifies and describes the functions performed by the components of the system and its super-system. Functions are characterized by category (useful or harmful), quality of performance (insufficient, normal and excessive), cost level (insignificant, acceptable and unacceptable) and cost of corresponding components. Function analysis is significantly powerful approach. It opens many new innovation possibilities by developing a function model of the system. This leads to multiple design options that significantly increase our ability to improve the system

CAUSE-EFFECT CHAIN ANALYSIS

There are a lot of methods for causal analysis. At traditional process improvement programs we can see many activities promoting one or another technique. For instance Lean Manufacturing and Industrial Engineering tend to process-oriented analysis, modern TRIZ toolkit contains function analysis where the problem is described as a chain of interactions or functions. Failure-analysis techniques promote fault tree, root-cause methods usually promote fishbone diagram and so on. Each of these forms of causal analysis has their place. They help to describe the problem and give us insights into what is causing it.

TRIMMING

Trimming is an analytical tool for reducing the number of components and simplifying the technical system. During trimming problem solvers or innovators remove certain components and redistribute their useful functions among the remaining system or super-system components. The outcome of trimming is a function model of the technical system as it would exist in the future after trimming. It also contains a set of trimming problems (questions) to solve. Trimming is driven by a set of rules defining how to redistribute useful functions of eliminated components. Maximum improvement of a technical system is achieved when a function is performed without any surplus components. This tool yields new, more effective problem statements and also points toward impactful solutions.

FUNCTION ORIENTED SEARCH

To dramatically improve a technical system, new solutions must be found. However, new solutions are not easy to implement, and many problems have to be solved before changes can be successfully implemented. Function-Oriented Search (FOS) or Function/Behaviour Search (FBOS) changes the paradigm by searching for existing solutions rather than inventing new ones (*Montecchi & Russo, 2015*). Once a solution is found in another industry, it becomes an adaptation problem, which is much easier to overcome than inventing new solutions. Adapting existing technologies is easier, more reliable, and requires fewer resources (manpower, capital, and time) than inventing new technologies and their applications. FOS or FBOS remove the industry-specific limitations of a potential solution, and uncovers possibilities, regardless of the source industry. It allows capitalizing on investments made in other industries. FOS also breaks psychological barriers for acceptance of new technologies, because there is already detected proof that the recommended solution will work. FOS is based on a generalization of functions, using a critical, two-prong approach: by action, and by object. This structured approach allows expanding the search for applicable technical solutions.

9 WINDOWS

Nine windows (or multi-screen diagram of thinking) is a creative tool originally introduced by G. S. Altshuller (*Altshuller, 1973*) for extracting opportunities in a systematic way by exploring changes which transformed the past generation of a system to its current generation. This tool specifies that any specific system (product, technology, organization, etc.) can be viewed at least from three layers: system, its subsystems and super-system. Nine windows help to analyze the system evolution deeper by taking into account relationships of the system with system environment and help with prediction of further evolution. According to G. S. Altshuller, this way of thinking is a feature of outstanding inventors who create new innovative ideas by seeing the whole world by system thinking.

TREND OF TECHNICAL SYSTEMS EVOLUTION

Trends of technical systems evolution are statistically proven directions of technical systems development. (*Zouaoua, 2015*) They describe the natural transition of technical systems from one state to another. These directions are statistically true for all categories of technical systems. Trends result from the general laws of technical systems evolution originally defined by G. S. Altshuller. According to Ikovenko we currently differentiate these trends:

- Trend of S-curve evolution
- Trend of increasing value
- Trend of transition to the super-system
- Trend of increasing completeness of system components
- Trend of increasing degree of trimming
- Trend of optimization of flows
- Trend of elimination of human involvement
- Trend of Increasing coordination
- Trend of uneven development of system components
- Trend of Increasing controllability
- Trend of increasing dynamicity.

INVENTIVE PRINCIPLES APPLICATION

Inventive principle is an abstract model that provides generalized recommendations for modifying a system to solve a problem formulated as a technical or physical contradiction. (*Rantanen & Domb, 2007*) A technical contradiction is a situation, in which an attempt to improve one parameter of an technical system leads to the worsening of another parameter. A physical contradiction is two justified opposite requirements placed upon a single physical parameter of an object. These requirements are caused by the conflicting requirements of a technical contradiction. G. S. Altshuller studied the engineering problems and their resolution by analyzing thousands of patent documents (*Altshuller, 1988*). He generalized 40 typical solutions to typical contradictions that work successfully in most situations and called them inventive principles. Those general recommendations must be translated into specific technical ideas that solve the initial technical contradiction.

CONCLUSIONS

Engineering methods were and are certainly an important factor in the development of human society. These methods have arisen either as a necessary response to the needs and pressure of the environment, or as a systematization or generalization of procedures used in successful technical solutions. The sophistication of engineering practices has grown and increased with the increasing pressure of the business environment, the growth of competition, and ultimately the complexity of engineering tasks or products. The application of innovation engineering methods during the conceptual phase of innovation process does not deny or diminish the quality, experience, specialization, and sometimes intuition of individuals or entire innovation teams. Conversely, innovative concepts will be generated through the synergy of individual skills, systematic teamwork and advanced creative skills.

REFERENCES

1. Pahl, G., Beitz, W., Feldhusen, J., & Grote, K. H. (2007) *Engineering Design. A Systematic Approach*. London: Springer-Verlag.
2. Pugh, S. (1991) *Total Design. Integrated Methods for Succesfull Engineering.* London: Prentice Hall.
3. Eversheim, W. (ed.) (2009) *Innovation Management for Technical Products. Systematic and Integrated Product Development and Production Planning*. Berlin: Springer-Verlag.
4. Hubka, V., & Eder, W. E. (1988) *Theory of Technical Systems: A Total Concept Theory for Engineering Design*. Berlin: Springer-Verlag.
5. Eder, W. E., & Hosnedl, S. (2010) *Introduction to Design Engineering. Systematic Creativity and Management*. Leiden: CRC Press/Balkema.
6. Baxter, M. (1995) *Product Design. Practical Methods for the Systematic Development of New Product*. London: Chapman and Hall.
7. Altshuller G. S. (1973) Algoritm izobretenija. Moscow: Moskovskij Rabotchij.
8. Altshuller, G. S. (1988) Creativity as an Exact Science. New York: Gordon and Breach.
9. Litvin, S. et al. (2010) O. Advanced function approach. *Proceedia Engineering*, 2010, Vol. 9, pp 92-102.
10. Montecchi, T. and Russo, D. (2015) FBOS: Function/Behavior Oriented Search. *Proceedia Engineering*, 2015, Vol. 131, pp 140-149.
11. Rantanen, K., & Domb, E. (2007) Simplified TRIZ: New Problem Solving Applications for Engineers and Manufacturing Professionals. Boca Raton: Auerbach Publications.
12. Zouaoua, D. et. al. (2015) Applicaton of Evolution Laws. *Proceedia Engineering*, 2015, Vol. 131, pp 922-932.

Corresponding author:
Doc. Dr. Ing. Ivan Mašín, Department of the Design of Machine Elements and Mechanisms, Faculty of Mechanical Engineering, Technical University of Liberec, Studentská 2, Liberec, 46117, Czech Republic, phone: +420 602 439 258, e-mail: ivan.masin@tul.cz.

TRANSFORMATION OF SURFACE LAYER AND SURFACE ISOTROPY CHANGES

Maciej MATUSZEWSKI

Faculty of Mechanical Engineering, University of Science and Technology

Abstract
The article presents possibilities of using the surface layer isotropy degree changes for a description of the surface structure operational transformation. Tribologic experimental tests were conducted for different external factors, and the occurring changes were described by the isotropy degree determined on the basis of the surface function of autocorrelation. The carried out analysis verified the usability of the surface layer isotropy degree change for a description of a surface operational transformation.

Key words: *tribological experimental tests, surface geometric structure, wear process, surface autocorrelation function.*

INTRODUCTION

Functional qualities of kinematic pairs, e.g. durability, reliability, motion resistance largely depend on the condition of the surface layer (SL). This has been confirmed by results of tests presented in numerous publications (*Horng, et al., 1995; Krawczyk, 2010; Krzyżak & Pawlus, 2006; Matuszewski, 2008; Nosal & Grześkowiak, 2004; Pawlus & Gałda, 2007; Zhu, et al., 2003*). The state of SL is determined by a set of characteristics which are described by parametric and nonparametric values. These characteristics can be external ones, usually connected with the surface structure geometry, (SSG) and internal ones which result from mechanical, physical and material properties.
Due to that fact that cooperation of components in a friction pair is accompanied with interaction of their surfaces, the surface structure has a significant influence on the functional qualities and tribological characteristics. Therefore, it is important to make a proper choice of methods and tools for evaluation of stereometric features of the surface. The metrological measurements of the topography should represent the actual texture of the structure in the best possible way which in turn will enable to provide an appropriate assessment of functional qualities of elements of friction pairs.
Roughness parameters are used in literature for a description of changes occurring during operational transformation of the surface layer, in particular the surface geometric structure, which largely determines functional qualities of the friction pair components (*Bernardos & Vosniakos, 2003; Lawrowski, 2008; Nosal & Grześkowiak, 2004; Ohlsson, et al., 2003*). These parameters are certainly an important element in the description of the process of wear and its intensity both for distributed and concentrated contact, though they do not characterize fully the SL and, therefore they do not account for all the changes in the contact area of two cooperating components. This drawback of tribological tests is indicated in many publications (*Trzos, 2011*).
Additionally, a big number of roughness parameters causes some problems in evaluation of the state of SSG (*Kedziora, et al., 2004; Panicz, 2000*). Creation of a universal set of parameters to be equally useful for assessment of a surface in terms of its functional qualities is not possible in practice. Even for similar values of basic amplitude parameters the remaining parameters can significantly differ (*Oczoś & Lubimow; Wieczorowski, et al., 2003*). Assessment of a surface can then be equivocal as they can have similar or the same values of roughness, and different functional qualities related to the stereometric shaping of SSG. However, attempting to evaluate the SSG by means of only one parameter, which unfortunately is still reported in industry, would be a big simplification. Selection of roughness parameters for determination of tribological characteristics is performed on the basis of scientific research statistical relations between them and availability of the equipment. There are no norms specifying when particular parameters should be used. The respective literature includes only recommendations which parameters of roughness provide the most adequate information for assessment of given functional qualities. Therefore, the selection of roughness parameters to be used for assessment of the SL condition will always be burdened with smaller or bigger subjectivism.

Internal features of a surface layer which largely affect its transformation, apart from roughness, include orientation of the surface structure, especially for the distributed contact which characterizes the surface structure in a specific way. Mutual orientation of irregularities of the cooperating surfaces – intersection angle between characteristic directions of their surfaces – affects the contact mechanics and the lubrication conditions. There are many measures of a surface direction assessment (*Dong, 2001; Thomas, 1999*). The most advanced and at the same time the most objective are methods for measurement using mathematical functions for a description of SSG. Direction of the structure is then referred to isotropy or its opposition – anisotropy. If a structure was entirely isotropic, it would mean that its geometric shape shows the same features in all possible directions – structure ideally symmetric in relation to all the symmetry axes. In practice, such a situation is not possible to achieve, therefore describing stereometrics shaping of a structure by isotropy whose degree is accepted for the description, which expressed, e.g. in percentage, is a measure of the structure direction.
In this paper, isotropy degree determined on the basis of frequency function of SSG, and more precisely, on the basis of surface autocorrelation function, was accepted to be used for a description of SSG changes. This function is a measure of the dependence of data values in one position on its values in the second position. Estimation of the surface function of autocorrelation is defined according to formula (*Oczoś & Lubimow, 2003)*:

$$R(\tau_i,\tau_j)=\frac{1}{(M-i)(N-j)}\sum_{l=1}^{N-j}\sum_{k=1}^{K-i}z(x_k,y_l)z(x_{k+i},y_{l+j}) \quad (1)$$

where:

M, N – areas of sampling ,
$z(x_k, y_l)$ – residual surface,
$z(x_{k+i}, y_{l+j})$ – bearing surface,
x, y – directions of sampling;
whereas: $i = 0, 1,..., m < M$; $j = 0, 1,...., n < N$; $\tau_i = i\Delta x$; $\tau_j = j\Delta y$.

For anisotropic surfaces the shape of the autocorrelation function diagram is asymmetrical, slender and prolonged in one direction, whereas for isotropic surfaces – round and symmetrical.
Experimental test were supposed to verify usability of surface isotropy degree for a description of transformation of the surface layer under the influence of external factors.

MATERIALS AND METHODS

The process of changes was observed for steel 102Cr6 specimens prepared for tests by grinding with 99A electrocorundum grinder with dimensions Ø 350 x 50 with the following parameters: circumferential velocity of grinder v_s = 26 m·s^{-1}; the table feed rate v_{ft} = 13.4 m·min^{-1}; grinding depth a_p = 0.04 mm, with conventional cooling and emulsion lubrication. So the machined surfaces were characterized by the following mean (eight measurements) values of SSG basic roughness parameters SSG: Ra = 1.37 μm; Rq = 1.73 μm; Rt = 7.39 μm. The values of isotropy degree of the test specimens were included in the interval 7.98÷8.04 %. In Fig. 1, there is an image of the obtained surface structure.

Fig. 1 Image of the tested surface structure (zoom x150)

Tribological tests were carried out on a specially designed test stand (*Matuszewski & Styp-Rekowski, 2008; 2004*). Variable operational forces were: force (*F*) and specimen hardness (*H*), whereas the constants were: velocity of relative motion (3 m·min^{-1}) and lubrication conditions (machine lubricant L – AN 68). The following values of variables have been accepted on the basis of literature: *F* = 300, 450 and 600 N (due to expected pushes); *H* = 30,.40 and 50 HRC. Taking into consideration the specimen surface contact with the counter-specimen – 300 mm^2, the accepted loading generated the following theoretical pressures: 1.0; 1.5 and 2.0 MPa. Fig. 2 shows the principle of the specimen and counter-specimen cooperation during tests. The tested object was a kinematic pair consisting of a specimen in the form of a cube with dimensions 10x10x10 mm and a counter-specimen prepared in the form of a flat ring shaped plate.

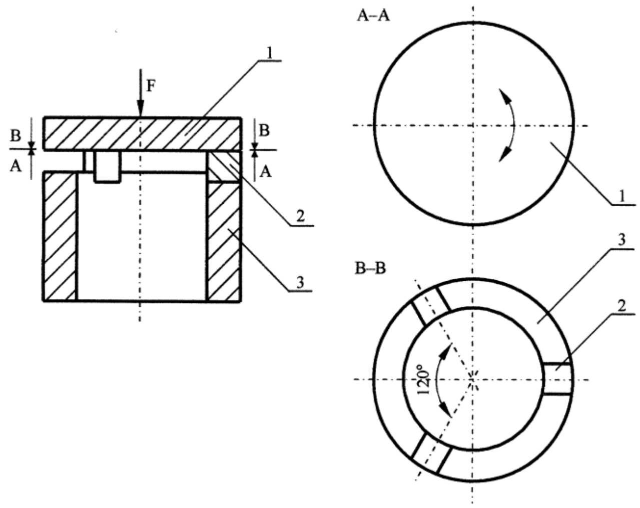

Fig. 2 Scheme of cooperation of sample – counter-sample of the tested friction pair: 1 – counter-sample, 2 – specimens, 3 – receiving sleeve samples

The tested samples (2) are immovably fixed to the head surface of the receiving sleeve sample (3) in three grooves, every 120°. Thus, a three surface, uniformly spread clamp of cooperating elements is obtained which is performed by the spring tension. Relative, oscillating motion is performed by the counter-sample (1), which is made of X210Cr12 steel hardened to 60±2 HRC. Hardness of the counter-sample definitely exceeded hardness of the samples to make transformation of the surface layer occur first of all on the samples.

The situation of machining traces in relation to each other was a very important factor – direction on the samples and on the counter-sample. The situation accepted for tests was chosen in such a way that the resultant cooperation angle was 90° due to the direction of the cooperation. It ensured theoretically optimal conditions for application of the lubricant.

As mentioned before, the surface isotropy degree and its changes were described as a surface autocorrelation function, by means of Talyscan 150 device of Taylor-Hobson company with the use of TalyMap Expert software. The measurements were taken along friction distance equal to 100 m, and observation of changes was being performed until it reached the length of 2000 m. However, stabilization of changes was recorded after 600 m – which is consistent with the assumed wear mechanism and, therefore the initial period of cooperation when the intensity of change is the highest, was accepted for analysis. The study was conducted for eight replicates.

RESULTS AND DISCUSSION

The results of experimental tests are presented in the form of diagrams. In Fig. 3 there are changes in isotropy degree (*Iz*) in the function of friction distance, for three different loadings, whereas for different values in Fig. 4.

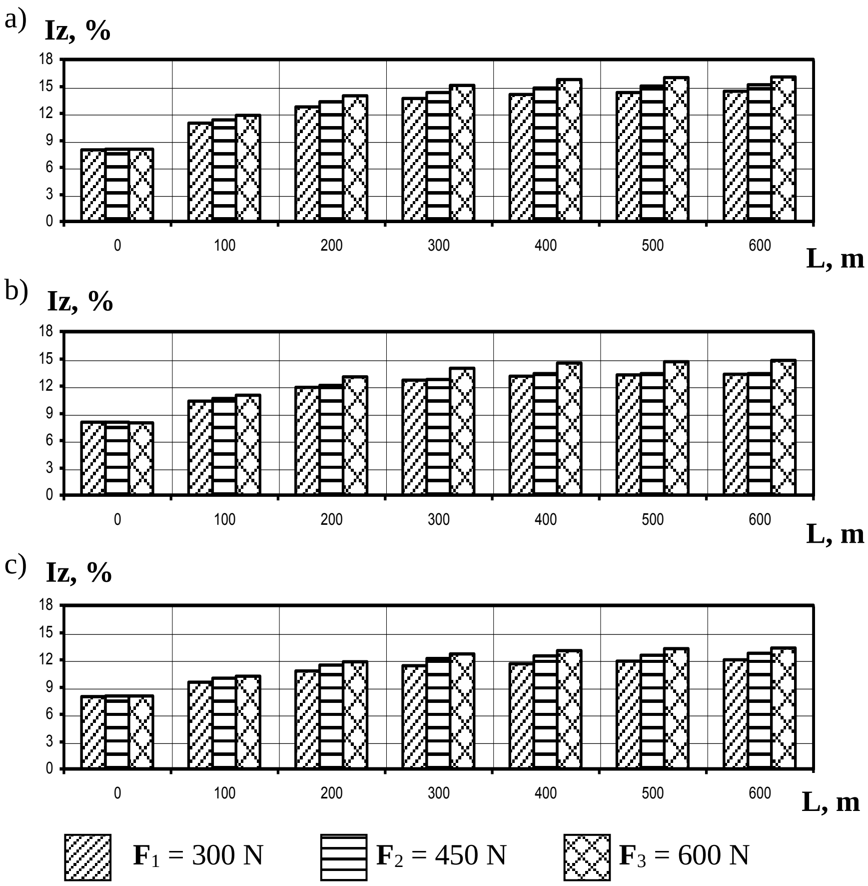

Fig. 3 Change of isotropy degree *Iz* in the function of friction distance for different loads *F* and for the following hardness: a) H_1 = 30 HRC, b) H_2 = 40 HRC, H_3 = 50 HRC

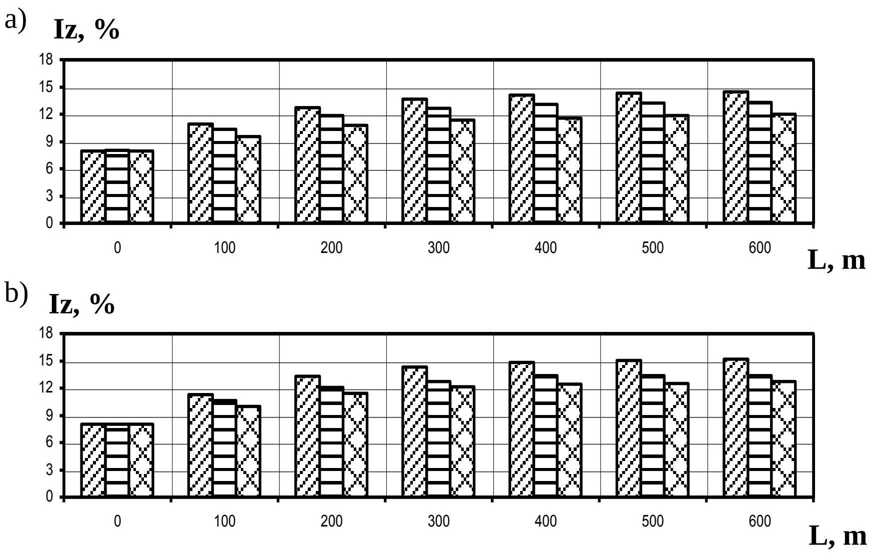

c)

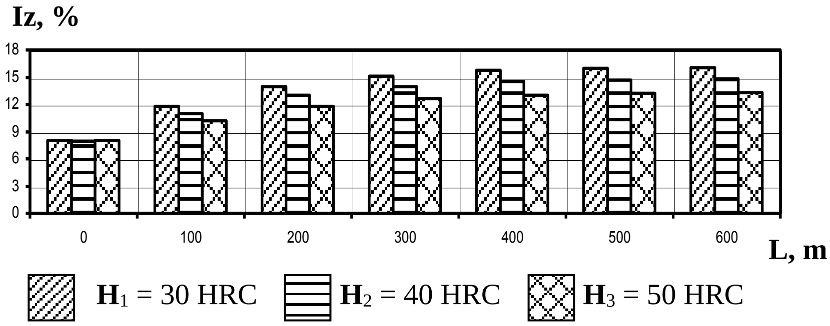

Fig. 4 Change of isotropy degree *Iz* in the function of friction distance for different hardness *H* and for the following loads: a) F_1 = 300 N, b) F_2 = 450 N, F_3 = 600 N

The scatter of results of SSG isotropy degree measurement did not exceed ±2.5% for all the analyzed cases.
It can be said, on the basis of the results presented in the diagrams, that the isotropy degree changes along with the friction distance increase. These changes reflect transformations of the surface structure during its operation. Generally, the value of isotropy degree increases which can be interpreted in such a way that stereometric formation undergoes ‘flattening’ and symmetry of this formation increases.
Particular peaks and ridges of micro-irregularities are partially or entirely cut off. Machining traces, which determine dominant directions of the surface formation, undergo deformation along with an increase in the isotropy degree, which can affect the conditions of lubrication and the motion resistance. The direction of machining traces is visible all the time, even for the maximum value of the isotropy degree obtained during the tests, whose value was app. 16 %.
Isotropy degree changes also depend on the acting forces. On the basis of analysis results of different loads (Fig. 3) it can be said that the lowest force – 300 N – generates the smallest changes, whereas the highest force – 600 N – generates the largest changes. Force equal to 450 N produces medium changes. This observation is rather obvious as elastic deformation is more likely to occur for a higher load, whereas after exceeding a certain level of stress, plastic strains are observed which lead to bigger changes in the controlled quantity. A similar dependence can be observed on the basis of analysis of the changes in terms of the sample hardness (Fig. 4). Stereometric structure of the surface of samples with the lowest hardness (30 HRC) is most susceptible to changes – easily deformed. Whereas, the smallest changes are observed for the highest hardness(50 HRC), when the structure is resistant to elastic and plastic deformation. Medium hardness– 40 HRC – produces changes as well.
Moreover, it can be observed, on the basis of the diagrams, that the changes in isotropy degree distribute more uniformly and proportionally throughout the accepted research range for hardness rather than for different force values. Moreover, it is particularly visible in Fig. 3b.
However, considering the research goal, it can be said that the changes in the surface isotropy degree recorded during tests, confirmed advisability of its application for a description of operational transformation of the surface layer.

CONCLUSIONS

The presented analytical and experimental verification has confirmed usability of a surface structure isotropy degree change for a description of operational transformation of the surface layer.
Due to the fact that the isotropy degree characterizes topographic formation of a surface it can be, apart from roughness parameters, an important element of characterization of the surface layer current condition.
In order to extend the possibilities of using SSG isotropy degree complex, experimental tests concerning the relations of isotropy changes with direct measurements of wear should be carried out.

REFERENCES

1. Bernardos, P.G., & Vosniakos, G.C. (2003). Predicting surface roughness in machining: a review. *International Journal Machine Tools Manufacture, 43*, 833-844.

2. Dong, W.P. (2001). Areal autocorrelation and spectral analysis of surface topography. In *Metrology and properties of engineering surfaces* (pp. 169-202). Kluwer Boston.

3. Horng, J.H., Lin, J.F., & Li, K.Y. (1995). Effect of surface roughness on steel roller scuffing. *Wear, 184,* 203-212.

4. Kedziora, H.J., Parsons, F., & Tabenkin, A. (2004). Industrial problems with proliferation and expansion of surface finish parameters. In *Proceedings 11th International Coll. on Surfaces* (pp. 93-100). Chemnitz.

5. Krawczyk, J. (2010). Tribological properties of selected structural steels. *Tribology*, 4, 223-233. (in Polish)

6. Krzyżak, Z., & Pawlus, P. (2006). „Zero-wear" of piston skit surface topography. *Wear, 260,* 554-561.

7. Lawrowski, Z. (2008). Tribology: friction, wear and lubrication. Wroclaw: Publishing House of Wroclaw University of Technology. (in Polish)

8. Matuszewski, M. (2008). Texture direction of a surface geometric structure as a distinctive functional quality. *Tribology, 3,* 105-114. (in Polish)

9. Matuszewski, M., & Styp-Rekowski, M. (2008). Kinematics of components and determination of the friction path in tribological research on a friction pair. *Tribology, 3,* 115-124. (in Polish)

10. Matuszewski, M., & Styp-Rekowski, M. (2004). Significance meaning of texture direction of surfaces' geometric structure for course of wear process. *International Journal of Applied Mechanics and Engineering, 9*, 111-115.

11. Nosal, S., & Grześkowiak, J. (2004). Influence of technological roughness on the course of lapping of cast iron sliding association. *Tribology, 4*, 71-77. (in Polish)

12. Oczoś, K.E., & Lubimow, W. (2003). Surface structure geometry. Rzeszow: Publishing House of Rzeszow University of Technology. (in Polish).

13. Ohlsson, R., Rosen, B.G., & Westberg, J. (2003). The interrelationship of 3D surface characterisation techniques with standarised 2D techniques. In *Advanced Techniques for Assessment Surface Topography*, (pp. 198-220). Kogan Page, London-Sterling.

14. Panicz, A. (2000). Surface roughness - what's new? *Measurement Automation Control, 5*, 39-47. (in Polish)

15. Pawlus, P., & Gałda, L. (2007). Tribological interaction of surface structure geometry. In *Proceedings 6th seminar* (pp. 9-23). Poznan. (in Polish)

16. Thomas, T.R. (1999). Rough surfaces. London: Imperial College Press.

17. Trzos, M. (2011). Influence of test equipment and friction process parameters on wear scatter. *Tribology, 2*, 169-179. (in Polish)

18. Trzos, M. (2011). Variability in the reproducibility and reproducibility of tribological characteristics. *Tribology, 6*, 227-239. (in Polish)

19. Wieczorowski, M., Cellary, A., & Chajda, J. (2003). Guide to measurement of surface roughness, ie roughness and not only. Poznan: Publishing House of Poznan University of Technology. (in Polish).

20. Zhu, H., Ge, S., Huang, X., Zhang, D., & Liu, J. (2003). Experimental study on the characterization of worn surface topography with characteristic roughness parameter. *Wear, 255*, 309-314.

Corresponding author:
Prof. Ph.D. Ing. Maciej Matuszewski, Department of Production Engineering, Faculty of Mechanical Engineering, University of Science and Technology, Prof. S.Kaliski Av. 7, 85-796 Bydgoszcz, Poland, phone: +48 52 340 86 23, e-mail: matus@utp.edu.pl

THE OPERATIONAL TEETH AND OIL TEMPERATURE DIFFERENCES

Martin MAZAC[1]

[1]*Department of Machinery Construction, Institute for Nanomaterials, Advanced Technology and Innovation, Technical University of Liberec*

Abstract
This short article describes the differences between teeth and oil temperature during the gearbox operation. The temperature is an operation parameter which can limit a lifetime of gearbox. The oil temperature impacts the friction parameters. The heat is naturally generated by the friction between tooth flanks during the gear operation. The temperatures of all gearbox parts by the generated heat are affected. The optimal temperature of oil and teeth for the failure-free gearbox operation is necessary. The goal of this article is temperature of teeth and oil temperature measurement research, temperature differences as an important parameters are emphasized.

Key words: *temperature; spur gear; pinion; teeth; final drive; automobile; gearbox; oil.*

INTRODUCTION

During the gearbox operation the heat is generated. For the trouble-free and economical operation of gearbox an optimal temperature is necessary. The optimal temperature about 90°C (194°F) is supposed. Temperature influence the condition of all gearbox parts, the mechanical wills can be changed too. Too high or low temperature can change viscosity and tribological parameters of oil, lubrication film can not be able to adequate lubricate a tooth flanks - damage is possible (f.e.(Davis, 2005)). The automobile gearbox is usually fixed to combustion engine and a heat is transferred to gearbox by the case (usually made from aluminium alloys with high thermal conductivity), the optimal oil temperature is easier to ensure.

Gears generate a heat during their operation, heat is transmitted by oil and other parts of gearbox to the surroundings. The oil parameters are depend on temperature. Tribological parameters during the gear operation on the current oil condition are depend too. The quantity of produced hest is on tribological parameters depend too (Elshourbagy, 2012).

The mathematical simulation for the behaviour and mechanical parameters (f.e (Skrivanek, 2012)) of mechanical system is possible to use. The simulation of all gearbox operation parameters is still almost impossible and ever passed simulation is useful to verify.

MATERIALS AND METHODS

This short paper describes a measurement of oil and teeth temperature inside a common automobile gearbox. The gearbox operation conditions are mostly similar as during the operation in car. For the measurements the gearbox MQ100 was used. MQ100 is a manual shifted gearbox used in small passenger car Skoda Citigo (or VW Up). The helical gears in MQ100 are used.

For the temperature measurements the special testing stand were used (Mazac, 2014). The stand is powered by the common Skoda 1,2HTP/44kW combustion engine. The loading by the electric dynamometer was realized. Maximal output torque of gearbox is about 1350Nm. The MQ100 gearbox similar as in car is fixed. The tested gearbox is isolated from the combustion engine by the shaft, the heat transfer is not possible. The electric fan for the cooling of tested gearbox was used. The air temperature around the tested gearbox was regulated by air conditioning and it was 20°C(68°F).

The temperatures of teeth were measured on a final drive pinion. The teeth temperatures by the thermistors were realized. The temperature data from the rotating shaft by the contactless equipment were transmitted (Mazac, 2015). The oil temperature were measured by the resistive thermometer Pt100 installed in the oil drain plug. The place of oil temperature measurement is near of final drive gear. The testing stand is on Fig.1., the measurement places are described here too.

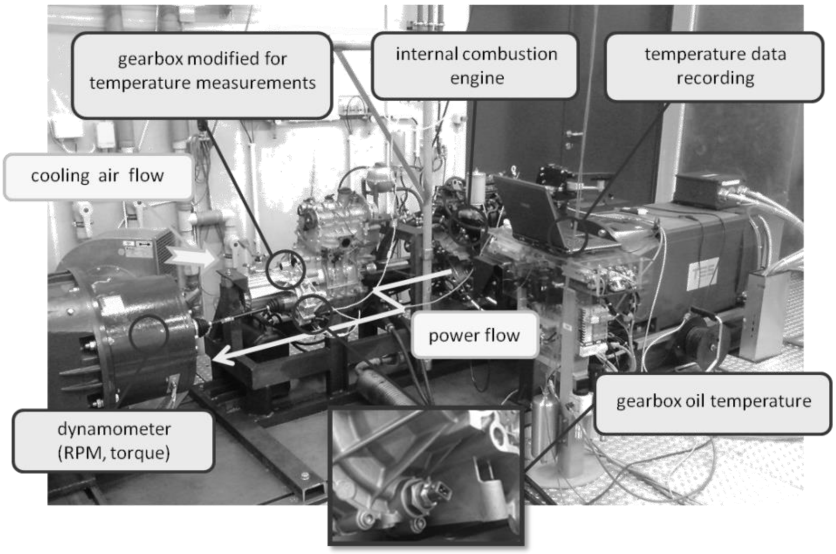

Fig. 1 The stand for gearbox loading and temperature measurement

The temperature measurements during a defined operation regimes were realized (Mazac, 2016). The temperature measurement during all five shifted speed operation were realized, our research were focused on 1st and 5th gear only. Engine velocity (input of gearbox) were 3000, 3650 and 4300RPM. Load of gearbox output was 25, 50, 75% of maximal torque, maximal input torque is 100Nm (73,8 lbf·ft). The loading parameters (output torque and RPM) for the 1st gear are in the Tab.1. The operation parameters during the 5th gear performance are in Tab.2.

Tab. 1 Operation and loading parameters - 1st gear (transmission ratio = 14,18)

Load [%]	3000[RPM] in		3650[RPM] in		4300[RPM] in	
	torque out [Nm]	RPM out [min^{-1}]	torque out [Nm]	RPM out [min^{-1}]	torque out [Nm]	RPM out [min^{-1}]
0%	0,00	211,45	0,00	257,26	0,00	303,07
25%	33,96	211,45	336,96	257,26	336,96	303,07
50%	673,93	211,45	673,93	257,26	673,93	303,07
75%	1010,89	211,45	1010,89	257,26	1010,89	303,07

Tab. 2 Operation and loading parameters - 5st gear (transmission ratio = 3,10)

Load [%]	3000[RPM] in		3650[RPM] in		4300[RPM] in	
	torque out [Nm]	RPM out [min^{-1}]	torque out [Nm]	RPM out [min^{-1}]	torque out [Nm]	RPM out [min^{-1}]
0%	0,00	967,32	0,00	1176,90	0,00	1386,49
25%	73,66	967,32	73,66	1176,90	73,66	1386,49
50%	147,31	967,32	147,31	1176,90	147,31	1386,49
75%	220,97	967,32	220,97	1176,90	220,97	1386,49

The gearbox ran for 15 minutes with a described mechanical parameters (Tab.1 and Tab.2). The final average tooth temperatures arise from last 60 temperature values mesured during the measurement interval (average of the last minute temperature values, temperature were measured every second).

RESULTS AND DISCUSSION

To verify the assumption that the temperature of the wheels is higher than the surroundings was the main aim of the study. When the wheel and teeth temperature is higher, the heat can be share to oil and other parts of gearbox. Can be that the dissipated energy during the tooth flank friction (natural process during the gear operation) is so low and the gears absorbing the heat from oil.

The graphs of teeth and oil temperature were create - Fig.2, Fig.3. The graphs contains the average teeth temperature and average oil temperature depends on input RPM and percent loading. The graph for the 1st gear is on Fig.2. The graph for the 5st gear is on Fig.3.

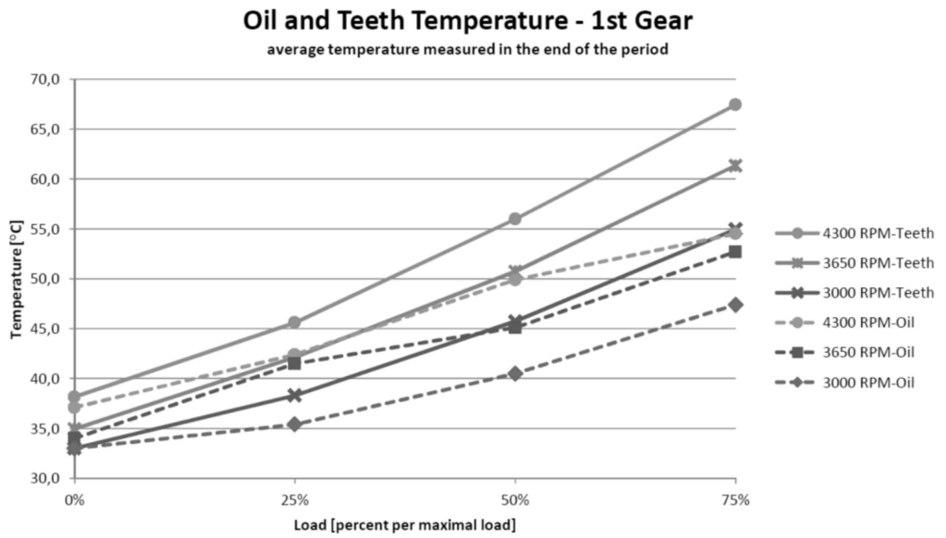

Fig. 2 Oil and teeth temperature graph - 1st gear

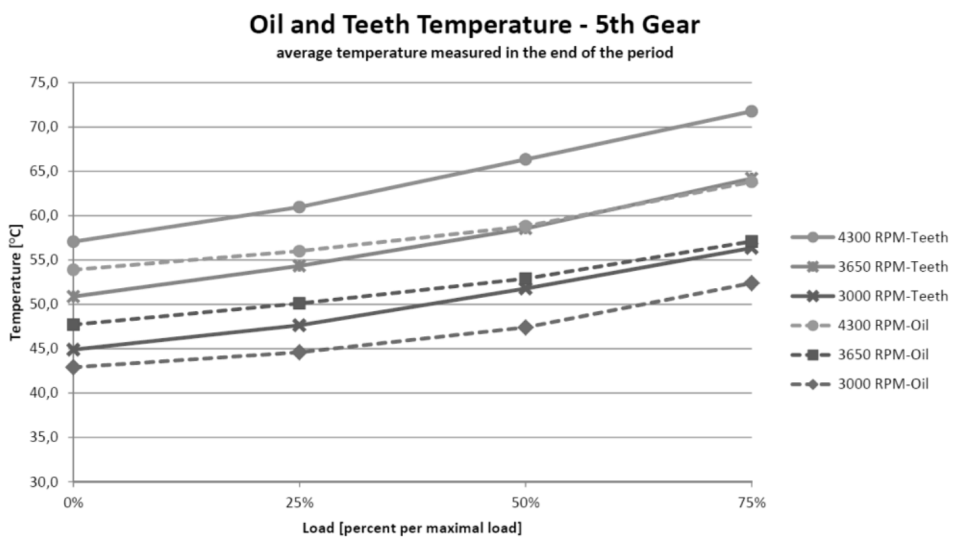

Fig. 3 Oil and teeth temperature graph - 5th gear

The average teeth temperature was higher than oil temperature in almost tested operation conditions. The assumption was confirmed and is possible to say that during the operation of MQ100 gearbox with chosen operation condition the teeth flank friction is the heat source.

The differences between temperatures of teeth and oil are contents in graphs Fig.4 and Fig.5.

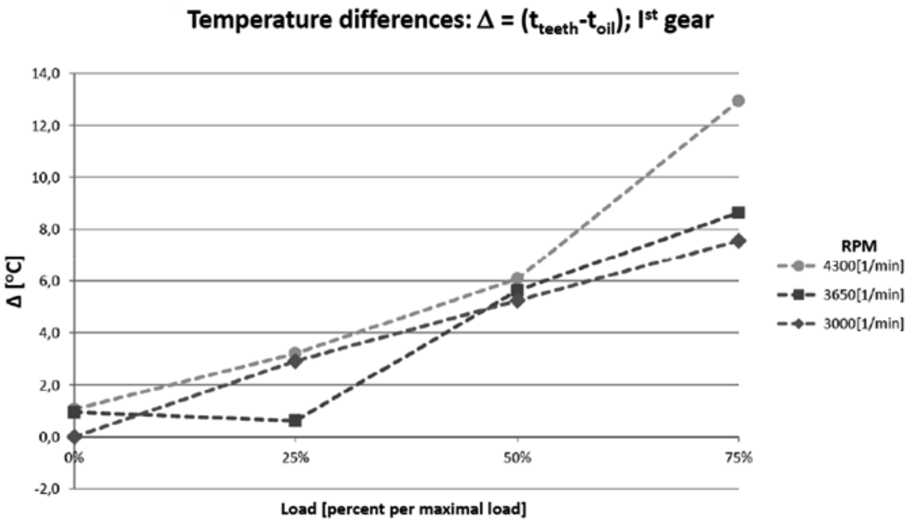

Fig. 4 Temperature differences graph - 1st gear

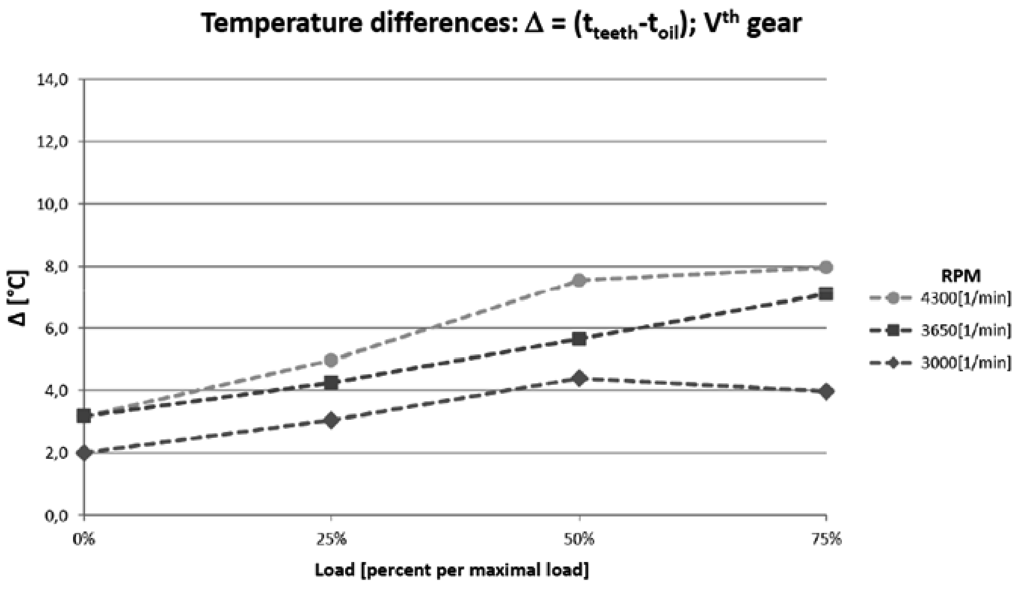

Fig. 5 Temperature differences graph - 5th gear

The graphs on Fig.4 and Fig.5 show that the highest differences of the teeth and oil temperature were measured during the 4300RPM, 75% load and 1st gear operation. The temperature difference was 13°C (23,4°F).

On the Fig.6 are plot the both temperature differences measured during the operation on a 1st and 5th gear. Is apparent that the temperature differences are lower during the low load operation and the temperature differences increasing trend depend on higher loading.

The gradients of the temperature connecting lines shows that the increasing rotation velocity of the gears cause the lower influence of the load on the temperature teeth and oil differences.

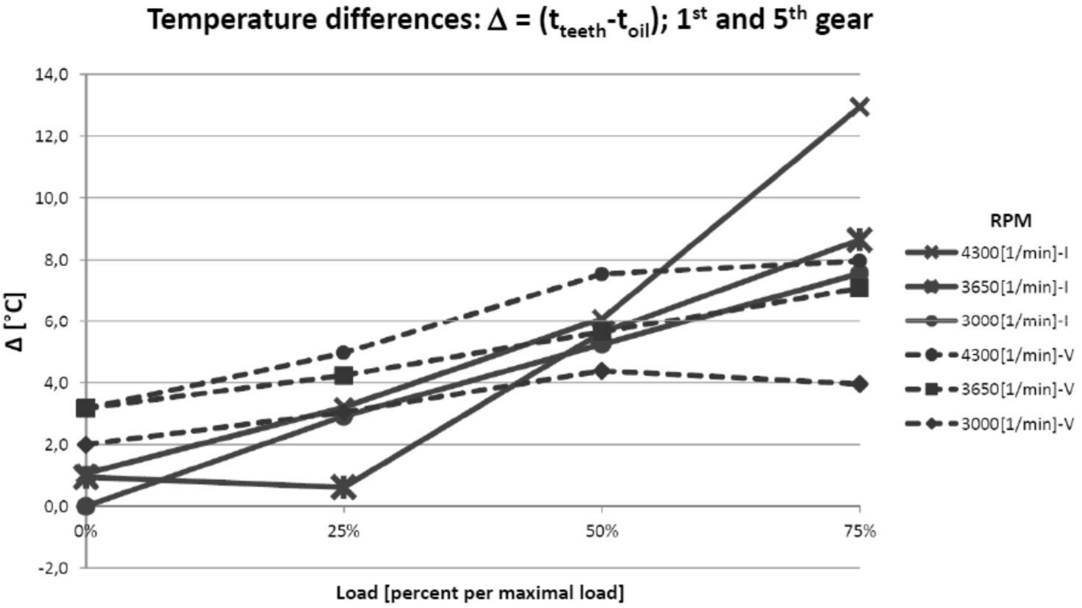

Fig. 6 Summary temperature differences graph - 1st and 5th gear

CONCLUSIONS

This short paper describes a measurement and evaluation the temperatures of average teeth and oil temperature during the mostly (without partial heating by the combustion engine) real operation of Škoda Auto a.s. MQ100 automobile gearbox. The research were focused on a 1st and 5th gear operation. The results show the teeth and oil temperature depended on the load. The temperature differences are higher during the higher load operation regimes. The differences are closer to constant during the operation with a higher RPM regimes. The differences of temperatures are compare in a summary graph.

ACKNOWLEDGMENT

The results of this Project LO1201 were obtained with co-funding from the Ministry of Education, Youth and Sports as part of targeted support from the "Národní Program Udržitelnosti I" program.

REFERENCES

1. Davis, J.R. & Associates (2005). Gear Materials, Properties, and Manufacture. *ASM International ® Materials Park, OH 44073-0002*, Ohio, USA. ISBN 0-87170-815-9.
2. Elshourbagy S. A. M. (2012). Effect of Lubrication on the Quantity of Heat Emission Of Two Spur Gears In Meshing In: *Proc. of the Int. Conf. ICAMAME*. Tokyo: WASET, 2012-05-27. Vol:6, pp. 1-26.
3. Skrivanek, J., Bilek, M. (2012). New structure of the drive of small-diameter knitting machines, AUTEX Research Journal, Vol. 12, No1, March 2012 © AUTEX, ISSN 1470-9589.
4. Mazac, M (2014). Stand for Measuring Temperatures of the Main Gears of Automobile Differential. In Modern Methods of Construction Design, Book Series: Lecture Notes in Mechanical Engineering, Edited by: Sevcik, L; Lepsik, P; Petru, M; Masin, I; Martonka, R. Germany: Springer Science + Busines Media. *DOI*:10*:*1007/978-3-319-05203-8-20, p.139-144.
5. Mazac, M., Herajn, P., Svoboda, M., (2015). The Equipment for Temperature Measurement Near a Gear Tooth Flank. In The Latest

Methods of Construction Design. Germany: Springer Science+Busines Media, 2015. *DOI* 10*:*1007/978-3-319-22762-7-69, ISBN 978-3-319-22761-0, p.457-463.
6. Mazac, M., Maly, M. (2016). The MQ100 Gearbox Final Drive Pinion Gearing Temperatures. In Proceedings příspěvků - 57th International Conference of Machine Design Departments (ICMD 2016). Železná Ruda: University of West Bohemia, 7.-9.9.2016. ISBN 978-80-261-0609-8.

Corresponding author:
Ing. Martin Mazač, Ph.D., Department of Machinery Construction, Institute for Nanomaterials, Advanced Technologies & Innovation, Technical University of Liberec, Studentska 1402/2, Liberec 1, Liberec, 461 17, Czech Republic, phone: +420 739 096 076, e-mail: martin.mazac@tul.cz

FEM-AIDED MATERIALS SELECTION USING TOPOLOGY OPTIMIZATION

Ivana MAZÍNOVÁ[1], Pavel FLORIAN[1], Filip HRDLIČKA[1], Martin KRATOCHVÍL[1]

[1]*Department of Machine Design, Faculty of Mechanical Engineering, UWB*

Abstract
This paper presents a method that combines material selection procedure with topology optimization using ANSYS. The method is applied on a suspension of a handbike.

Key words: *handbike; ANSYS; material indices, DOE.*

INTRODUCTION

Material selection and engineering design are usually performed sequentially, which means that firstly a candidate material can be selected and consequently product dimensions are calculated to meet for example stress criteria. However, with use of topology optimization and design-of-experiment methods both can be done simultaneously.

MATERIALS AND METHODS

The method of materials selection based on material indices described in (Ashby, 2003) is derived for simple textbook cases like strut subjected to tension and a cantilever beam loaded in bending. However, the real world problems are more complicated with combinations of loading and complicated shape of components. In our earlier work we developed a material index for buckling of a cylinder. This task was still limited with the shape of the part. In case that the shape of the part is arbitrary with certain constraints a more sophisticated tools such as topology optimization can be applied. The algorithm for material selection using topology optimization is developed as follows. Firstly design space is creating taking into account maximum dimensions, constraints and variable parameters. Then the topology optimization itself is performed for a number of design points. Consequently the geometry is validated and material index is derived using curve fitting. The overall workflow with its relation to standard material selection procedure is shown in Fig. 1.

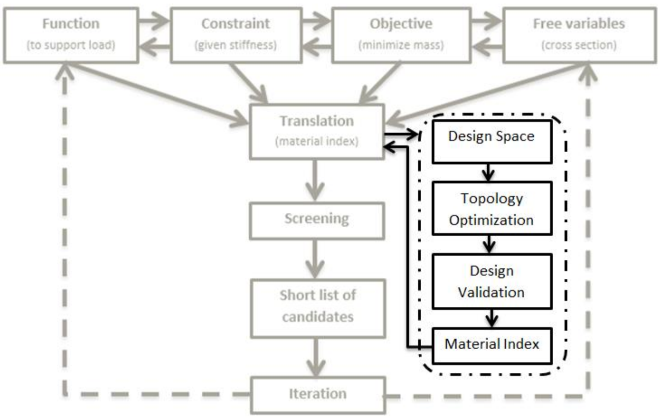

Fig. 1 FEM-aided Material Selection Algorithm

Topological optimalization

Topology optimization is a part of discipline called Structural Design Optimization. The goal of Structural Design Optimization is to find an optimal lay-out of material of a component. There are three different types of structural design optimization: size optimization, shape optimization and topology optimization. The size optimization determines optimal thickness of a part of a machine component. Structural optimization determines optimal profile or contour of a structure. Its goal is to find an opti-

mal shape of any element of machine component (circular or elliptical hole e.g.). Topology optimization is the most general and complex method. Topology deals with fundamental elements of geometry – number of holes or connections of a geometry of a component. Topology optimization works with topology, shape and size together. Can be used with isotropic, anisotropic or composite material, even fluids or gases. Topology optimization can solve structural, eigenvalue, thermal or fluid dynamics problems. (Bendsøe,& Sigmund, 2003)
Using one of mentioned method, a most of structural problems can be transformed to usual mathematic optimization scheme (to minimize an objective function) and solved using numerical method.
The characteristic input information for topology optimization is a design space (domain). The design space is a given volume of space, which is optimized (where optimized geometry is created) or initial design. The design space is divided to a subdomains due to discretization. Discretization is necessary for purpose of numerical solution. Another given information are applied forces, supports and material parameters of volume.
The next step is to create mathematical model of optimization. The objective function must indicate compliance of derived geometry. The goal is to minimize the objective function. The result must satisfy given constrains (maximal mass or stress).
The solution is an iterative process, consist of finite element analysis, sensitivity analysis, filtering and updating the design of structure in every step. Topology optimization can leads to very effective design, but a result strongly depends on proper settings of solver parameters. Theoretically is there many solutions can fulfill given mathematical requirements, but most of they isn't acceptable in technical scope.
Result is determined by size of elements, post processing (filtering, sensitivity), number of steps and solution options (penalty, gradient). To get smooth geometry, lowering size of element probably increases a number of connections. Another problem is creating complicated geometry with insufficient stiffness. Good post processing creates smooth geometry with required number of holes. The shape can be driven by method of filtering. A flowchart of topology optimization procedure is shown in Fig. 2.

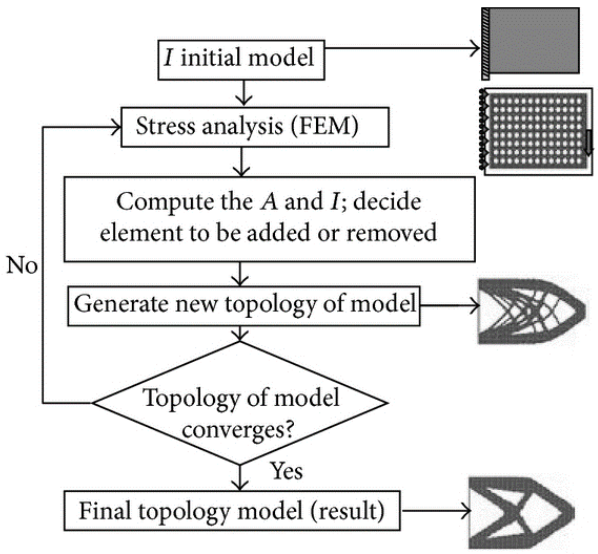

Fig. 2 FEM-aided Material Selection Algorithm (Rahman et. All, 2014)

Handbike

Handbike (also known as a handcycle) is a device enable cycling tourist for people with physical disabilities. Physical disability refers to the lower part body (amputation of the leg, spinal cord break). Because users cannot use their legs, they have to use for propulsion their hands.

Beside a classic bicycle is the handbike composed from frame with minimum 3 wheels (due to stability) and handlebars, where are placed all controls including propulsion. Because design of the handbike will be always more complex than a classic bicycle and users need to use their hands for propulsion, is very important to make the whole device as light as possible, because every extra gram unnecessarily exhausts the user.
In this case was selected a variant of the handbike with two front wheels with suspension. One of these parts is the front suspension fork which has been subjected to topological optimization.

RESULTS AND DISCUSSION

The described method was applied on suspension of a handbike in order to determine the relation between Young's modulus and density of an optimal material for given problem. In Fig. 2 the design space for topology optimization and resulting optimized shape is shown.

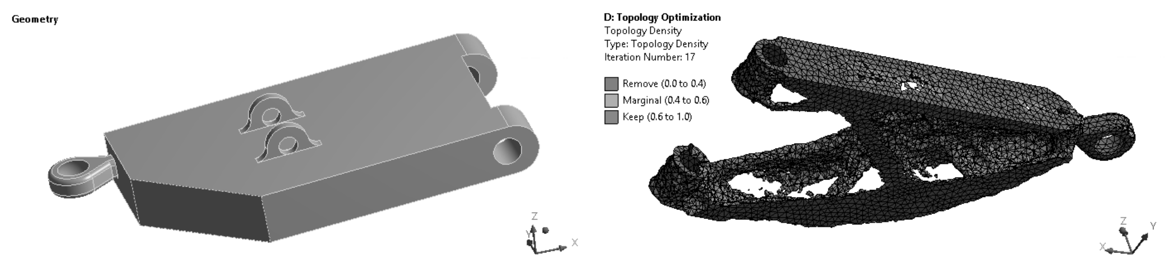

Fig. 3 Design Space for Topology Optimization and Optimized Shape

Preliminary results showing relation between Young's modulus and density for best performance of handbike suspension can be seen in Fig. 4. The output file resulting from topology optimization in ANSYS that contains the optimized shape results comes in .stl file format. This particular file format is used e.g. for 3D printing and the procedures of converting other CAD geometry file formats into .stl are well developed. However, in this case in order to perform design validation properly the .stl file needs to be converted back into solid geometry file format such as .stp. The back conversion is a rather complicated task and not all CAD systems are capable of such request. The processing time strongly depends on complexity of the input .stl file and therefore it conflicts with the requirements on mesh density. Therefore only preliminary results are given.

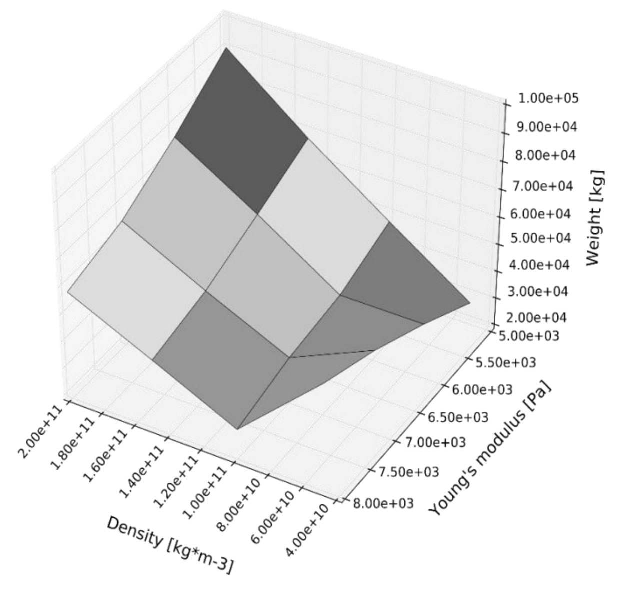

Fig. 4 Design Space for Topology Optimization and Optimized Shape

CONCLUSIONS

In this paper a method for material selection using topology optimization is described. The method can be utilized for material selection when the designed product is subjected to various sources of loading and the resulting shape is arbitrary with some constraints for neighboring parts in an assembly.

ACKNOWLEDGMENT

This study was supported by the internal project of University of West Bohemia SGS-2016-012.

REFERENCES

1. Ramani, A. (2011). Multi-material topology optimization with strength constraints. *Structural and Multidisciplinary Optimization*, *43*(5), 597-615.
2. Gao, T., Xu, P., & Zhang, W. (2016). Topology optimization of thermo-elastic structures with multiple materials under mass constraint. *Computers & Structures*, 173:150-160.
3. Ashby, M., F. (2011). *Material Selection in Mechanical Design*. Oxford: Butterworth-Heinemann
4. Mazínová, I., et al. (2016). Support of Material Selection Optimization using ANSYS. In *ICMD2016 International Conference of Machine Design Departments.*
5. Bendsøe, Martin P., and O Sigmund. *Topology Optimization: Theory, Methods, and Applications*. Berlin: Springer, 2003. ISBN 3-540-42992-1
6. Cardoso, E. L. and Fonseca, J. S. O.. Complexity control in the topology optimization of continuum structures. *J. Braz. Soc. Mech. Sci. & Eng.*2003, vol.25, n., pp.293-301. ISSN 1678-5878. DOI: 10.1590/S1678-58782003000300012
7. Rahman, K., Geni, M., Mamut, M., Yusup, N., & Yusup, M. (2014). Experimental observation of the skeletal adaptive repair mechanism and bionic topology optimization method. *Mathematical Problems in Engineering*, *2014*. DOI: 10.1155/2014/593867
8. Cazacu, R., & Grama, L. (2014). Overview of structural topology optimization methods for plane and solid structures. *Annals of the University of Oradea, Fascicle of Management and Technological Engineering*. ISSN 1583-0691. DOI: 10.15660/AUOFMTE.2014-3.3043

Corresponding author:
Ing. Ivana Mazínová, Ph.D., Department of Machine Design, Faculty of Mechanical Engineering, University of West Bohemia, Univerzitní 8, Plzeň, Pilsen, 30100, Czech Republic, phone: +420 37763 8271, e-mail: mazini@kks.zcu.cz

IMPACT OF DESIGN CONSTRAINTS ON THE SPUR GEAR PAIR PARAMETERS

Daniel MILER[1], Antonio LONČAR[2], Dragan ŽEŽELJ[1]

[1]*Chair of Machine Elements, Faculty of Mechanical Engineering and Naval Architecture, University of Zagreb, Ivana Lučića 5, 10002 Zagreb, Croatia.*
[2]*SedamIT Ltd, 10000 Zagreb, Koledovcina 2, Croatia.*

Abstract
During the gearbox design process, pinion and wheel parameters are selected so the transmission meets the client needs. The process is rather simple and often automated. However, when the special demands like the limited dimensions or weight are present, task becomes more complex, requiring systematic approach. In this paper we observe the impact of limited outer dimensions on the spur gear pair parameters. To find the optimal solution, we used the genetic algorithm optimization method and ISO standard for load capacity calculation. The gear module, the pinion number of teeth and the both profile shift coefficients were used as variables. The influence of constrained dimensions was examined on two different sets of input data; each consisting of outer gearbox dimensions, rotational speed and desired gear material, representing pairs for different uses.

Key words: *gear; design; constraints; genetic algorithm; optimization.*

INTRODUCTION

The gearbox design process is well known, mostly due to the numerous technical literature. Specialized manufacturers frequently use the automated software to adjust product design to the client needs, and are able to provide 3D models almost instantly. Problem arises when the special design constraints exist. If gearbox dimensions are limited or a maximum permissible weight is set, design changes accordingly and standard approaches are not applicable. Providing the best technical characteristics while meeting the additional constraints is a complex task, which requires a systematic approach. Even though experienced engineer can solve said task by using iterative methods and utilizing his experience, it is often a time consuming process. Since increased time-to-built frequently results in an inferior gearbox unit, optimized design process is required *(Almasi, 2014)*.

To shorten the design time, gear optimization problem is often solved using the genetic algorithm. Genetic algorithm (GA) is an optimization method inspired by the evolution theory, suitable for solving complex technical problems. Since proven to be applicable to the gear optimization problems *(Marcelin, 2001, 2005; Yokota, Taguchi, & Gen, 1998)*, it was regularly used for solving tasks ranging from the gear train weight optimization and preliminary gearbox design *(Gologlu & Zeyveli, 2009; Tudose, Buiga, Ştefanache, & Sóbester, 2010)* to altering the gear micro geometry *(Bonori, Barbieri, & Pellicanos, 2008)*.

In this article, we examined the impact of design constraints on the optimal spur gear parameters. Influence of the constraints restricted gearbox housing dimensions was investigated. After the initial considerations, the authors developed the approach which determines the optimal spur gear pair parameter values by means of GA. Loading capacity was calculated according to ISO 6336:2006 standard and both the tooth root strength and surface durability were calculated. Outer gearbox housing dimensions were used as input. The aim of this study is to enable the better space planning and management to product designers not versed in transmission design.

MATERIALS AND METHODS

Optimization process consists of the GA and ISO 6336:2006 standard for load capacity calculation. The set of constraints includes the user-provided housing dimensions. Gearbox housing shape is simplified; assumed to be a hollow square prism. Design guidelines (1) limit the housing wall thickness and gear tip to housing distance and are used to calculate the available volume to accommodate the gear pair (2). GA was then used to find the pair parameters enabling the highest operational torque, while meeting the

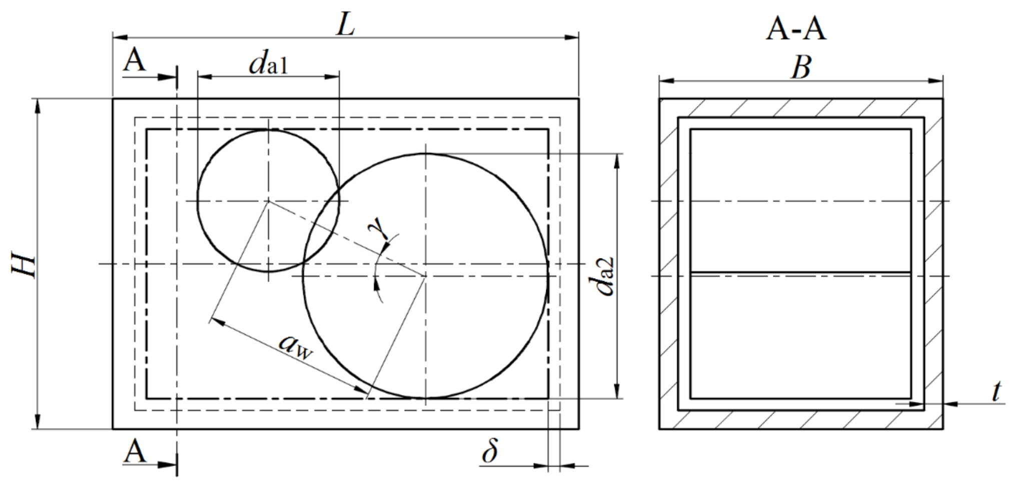

Fig. 1 Simplified gearbox

necessary dimension criteria. Input parameters comprise of the gear pair and shaft material properties, gear quality grade, rotational speed, transmission ratio, application factor and the largest acceptable housing dimensions. To avoid limiting the optimization space, centre distance a_w is taken as a non-standard value. Two shaft arrangements (Fig. 1) can be observed – with axes located in the horizontal ($\gamma = 0°$) or angled plane ($\gamma \neq 0°$). Largest plane angle value γ is limited by the available length l (2) and height h (2); occurring when the pinion addendum diameter tangents the upper or lower boundary plane, while the wheel tangents the opposite one (3). For a unit to be well-designed, gear pair has to satisfy the length condition (4). Pair width is equal to the available width b, but not larger then 25m to ensure the proper face load distribution.

$$\delta = t = 2 + 0.025 \cdot a_w; \qquad t, \delta \geq 8 \tag{1}$$

$$l \times h \times b = \begin{cases} b = B - 2(\delta + t) \\ l = L - 2(\delta + t) \\ h = H - 2(\delta + t) \end{cases} \tag{2}$$

$$\gamma_{max} = \arcsin\left(\frac{h}{a_w} - \frac{d_{a1} + d_{a2}}{2a_w}\right). \tag{3}$$

$$\frac{d_{a1} + d_{a2}}{2} + a_w \cos\gamma_{max} \leq l \tag{4}$$

Shafts are considered to be smooth and made of gear material to enable more compact design. Permissible shaft stress is found using to the expression $\sigma_P = \sigma_f / 4$ by *(Haberhauer & Bodenstein, 2014)*. To ensure viability of the solutions, necessary shaft diameters are calculated and compared against the pinion dedendum diameter (5):

$$d_{shaft1} = \sqrt[3]{\frac{32 M_{red}}{\pi \sigma_P}} \leq m \cdot \left[z_1 + 2 \cdot x_1 - 2 \cdot (1 + c)\right] \tag{5}$$

The optimization vector comprises of the four variables: gear module m, number of teeth (pinion) z_1 and profile shift coefficient of pinion x_1 and wheel x_2, with gear module values chosen from the standard. Furthermore, boundary conditions are set for each of the variables to ensure the industrially applicability of solutions. Initial population size was 300 and 1000 generations are calculated. Mutation rate of 0.55 is used with two elite chromosomes. Lastly, the objective for both types of constraints is to increase the operational torque T, which serves as the fitness function.

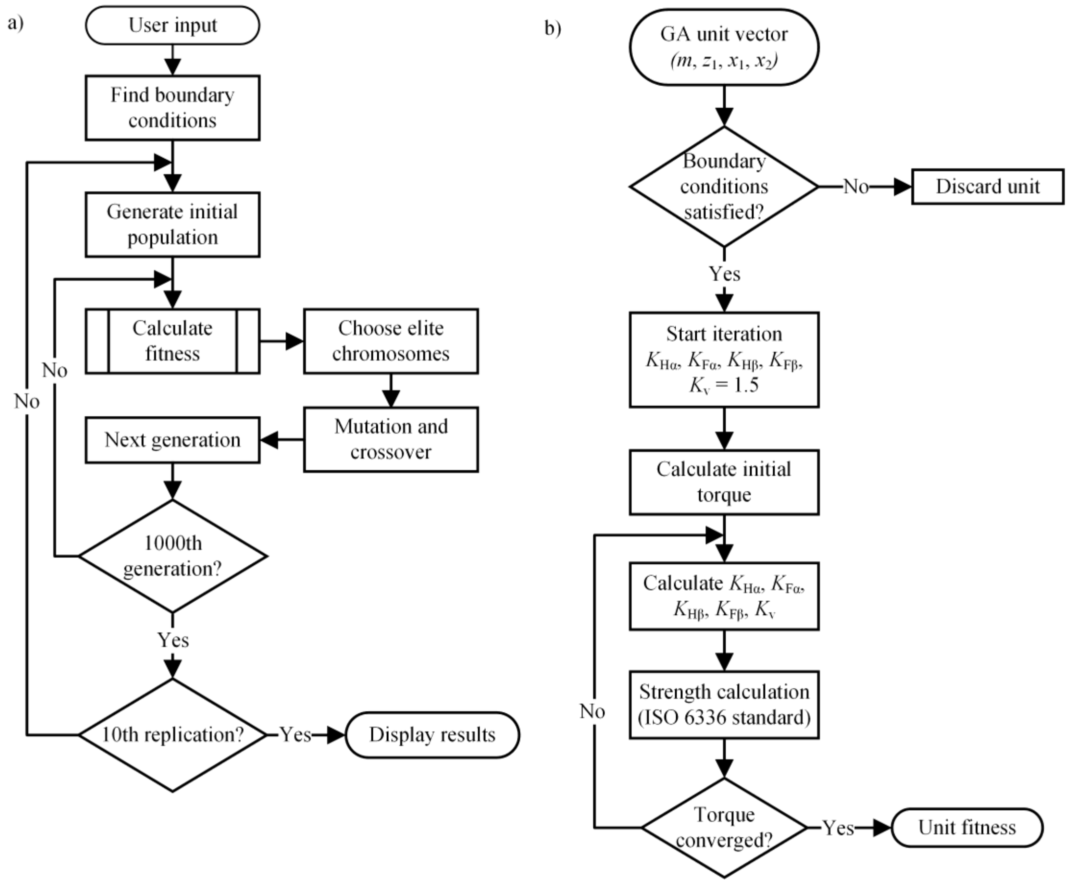

Fig. 1 Optimization process (a) and unit fitness calculation (b)

or calculated torques, the equations (6) and (7) derived from the ISO 6336:2006 standard ensure the necessary load capacity of both the tooth surface and root. Process algorithm is shown in the Fig. 2a and calculation of the unit fitness in the Fig. 2b. The approach was tested on two datasets (Tab. 2) made of 18CrNiMo7-6 and 34 CrMo 4 steel respectively. Permissible operational torque is calculated according to (6) and (7). Permissible contact pressure is responsible for the T_{maxH} and tooth root stress for the T_{maxF}. Lower one of the T_{maxH} and T_{maxF} is chosen as a unit fitness:

$$T_{\mathrm{maxH}} = \frac{m^2 z_1 z_2 b \sigma_{\mathrm{HP}}^{\;2}}{2 Z_{\mathrm{B}}^{\;2} Z_{\mathrm{E}}^{\;2} Z_{\mathrm{H}}^{\;2} Z_{\varepsilon}^{\;2} K_{\mathrm{A}} K_{\mathrm{H\alpha}} K_{\mathrm{H\beta}} K_{\mathrm{V}} (i+1)} \tag{6}$$

$$T_{\mathrm{maxF}} = \frac{m^2 z_1 b \sigma_{\mathrm{FP}}}{2 Y_{\mathrm{F}} Y_{\mathrm{S}} Y_{\mathrm{B}} Y_{\mathrm{DT}} K_{\mathrm{A}} K_{\mathrm{F\alpha}} K_{\mathrm{F\beta}} K_{\mathrm{V}}} \tag{7}$$

Tab. 1 Example input data and boundary conditions

		Set 1 (18CrNiMo7-6)	Set 2 (34 CrMo 4)
Rotational speed (input)	n_1, min^{-1}	970	1470
Transmission ratio	i	2.8	3.55
Allowable stress number (bending)	σ_{Flim}, N/mm^2	430	290
Allowable stress number (contact)	σ_{Hlim}, N/mm^2	1500	700
IT quality grade		7	8
Application factor	K_{A}	1.1	1.4
Boundary conditions			
Available housing dimensions, mm	L×H×B	300×230×140	500×360×210

Since the dynamic calculation factors $K_{H\alpha}$, $K_{F\alpha}$, $K_{H\beta}$, $K_{F\beta}$ and K_V are affected by the change of operating torque, calculation is iterative (Fig. 2b). To find the operating torque, initial values of the dynamic factors are assumed to be 1.5. Resulting torque is then used to calculate dynamic factor values. After the 5 iterations, results converged within the acceptable range. Tooth root stress factors Y_F, Y_S, Y_B, Y_{DT} and surface durability factors Z_E, Z_H, Z_ε, are unaffected by the operating torque variations. To account for influence of the single tooth contact, larger one of the factors Z_B and Z_D is included in the calculation. While determining the allowable stresses σ_{HP} and σ_{FP}, factors Y_{NT}, $Y_{\delta relT}$, Y_{RrelT}, Y_X, Z_{NT}, Z_L, Z_V, Z_R, Z_W and Z_X are assumed to be 1 and stress correction factor Y_{ST} is 2. Safety factor values are $S_{Hlim} = 1.2$ for surface durability and $S_{Flim} = 1.5$ for tooth root stress. Accuracy grade IT7 is chosen for set 1 and IT8 for set 2.
In order to rate the solutions provided by the genetic algorithm optimization, the use of provided dimensions is evaluated. Since the housing is assumed to be a hollow prism, it is not possible to achieve the full space utilization. Usage of all the three dimensions is assessed by comparing the resulting spur gear pair width, height and length with their available counterparts. Pair dimensions are measured as projections on the corresponding planes. Optimal set of parameter ratio value is 1, meaning that dimension is completely utilized. Furthermore, after determining the optimal parameters, algorithm can be used to suggest the possible reductions of input dimension. Unused length, width or height are found as a differences of available and calculated dimensions.

RESULTS AND DISCUSSION

Suggested approach was used to find the results. Optimization process was replicated 10 times for each of the datasets, with different initial populations to ensure that results do not represent the local, but a global maximum. 1000 generations were calculated for both sets and solutions converged after the 200 generations, while the changes between the 200th and 1000th generation were minor. Even though set 1 (Fig. 3a) displayed faster rate of convergence between the 1st and 70th generation, after the 100 generations, solutions were satisfying. Rate of convergence can be further increased by using Sobol quasi-random distribution of initial population *(Maaranen, Miettinen, & Penttinen, 2007)*. Mean operational torque value across the 10 replications was calculated and its convergence from generation to generation is shown in the Fig. 3. Logarithmic scale was used in order to better display the changes during the initial generations

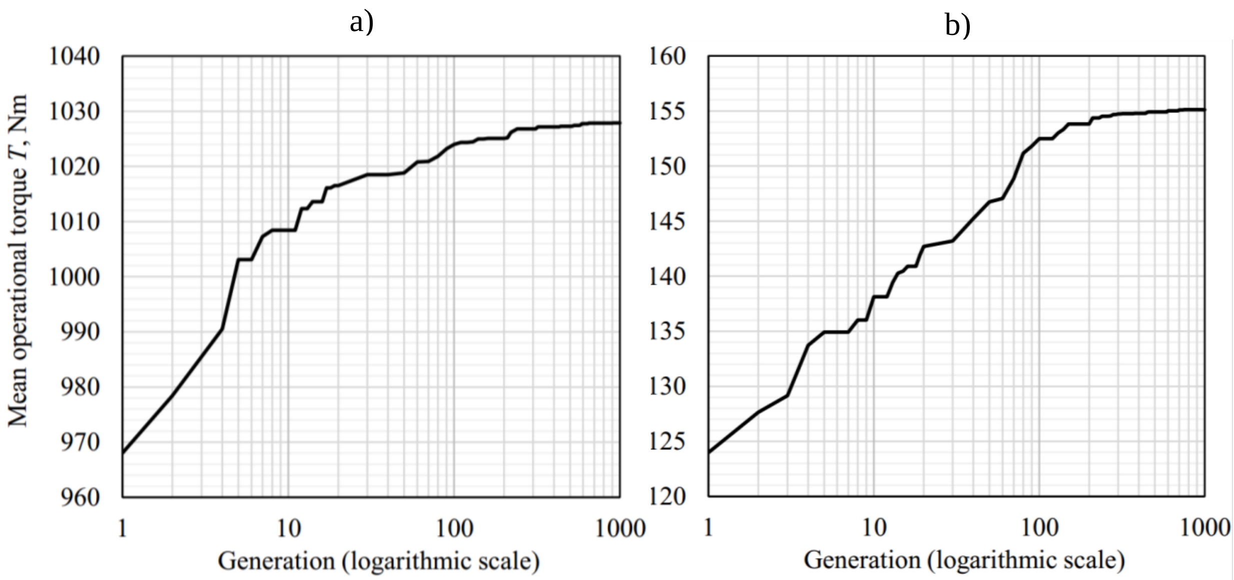

Fig. 3 Convergence diagrams for the both datasets – set 1 (a) and set 2 (b)

Tab. 2 Resulting spur gear pairs

	Set 1	Set 2
Transmissible operational torque, Nm	1029	155.6
Number of teeth (pinion)	18	15
Number of teeth (wheel)	50	53
Gear module, mm	3.75	6
Profile shift coefficient (pinion)	0.577	0.490
Profile shift coefficient (wheel)	-0.065	-0.216
Face width, mm	97.5	138
Pinion dedendum diameter, mm	62.45	80.88
Approximate pinion shaft diameter, mm	57.28	36.70

The spur gear pairs with the highest fitness are shown in the Tab 2. All the replications converged towards the same gear module and number of teeth. Differences were encountered among the profile shift coefficients, which were set as continuous instead of discrete variables. Among the replications, largest operational torque difference was 0.334% for data set 1, and 0.962% for set 2, with standard deviations of 1.189 Nm and 0.292 Nm respectively. Result dispersion could be further lowered by discretization of the profile shift coefficients.

Algorithm choses the gear module and pinion number of teeth that fit into the user-provided dimensions. To fill the rest of the available space, profile shift is used. Even though the larger wheel profile shift will result in the increased operational torque, it will also cause the wheel addendum diameter to exceed the available dimensions. Pinion profile shift coefficient was chosen as a largest allowable value considering the required tooth tip thickness. It should be noted that even though it is important for the gearing longevity, specific sliding is not considered in this paper.

Result evaluation was carried out by comparing the gear pair length, width and height against their available counterparts (Tab. 3). Height is utilized first and width second, so for the both pairs height ratio is equal to 1. However, pair length and width reductions are possible for the both sets. When analysing the set 2 results, unused length is mainly caused by the poor input data; wheel addendum circle diameter is equal to the available housing height. Fixed addendum diameter coupled with the constant transmission ratio results in a highly constrained pinion, and consequently, pair dimensions. The housing volume could be further lowered by changing its shape, which is currently a hollow prism. While optimizing the housing shape, finite element method (FEM) can be used for static and dynamic analysis *(Weis, Kučera, Pecháč, & Močilan, 2017)*.

Both datasets do not make use of available width. For set 1 cause is the negative shaft length influence on the bending moment. Beside the dimensional constraints, the shaft bending strength is an important condition. Required shaft diameter for set 1 is 5.17 mm lower than the pinion dedendum diameter, meaning that shaft and gear have to be made as a single part. Even though the gear teeth increase the shaft cross section moment of inertia, overlap of the shaft and tooth root bending stresses should be avoided not to cause local critical stresses. Furthermore, the sum of profile shift coefficients also influences the shaft bending moment; increased sum would result in a larger pressure angle at the pitch cylinder (α_w) responsible for the radial component of force. On the other hand, width of set 2 is limited by the empirical guideline; maximal recommended gear width should not exceed the 25 m. Since m is limited by addendum diameter equal to the available height, further increase in width is not possible even though input dimensions would allow it.

Tab. 3 Result evaluation

	Set 1			Set 2		
	Used	Available	Ratio	Used	Available	Ratio
Pair width, mm	97.5	108	0.903	150	178	0.843
Pair height, mm	198	198	1	328	328	1
Pair length, mm	250.9	268	0.936	391.1	468	0.836

CONCLUSIONS

The spur gear pair design process with special constraints was carried out. Our main goal was to develop the approach which will enable designer to achieve the necessary transmission characteristics in limited space. Proposed approach, which consisted of the genetic algorithm as optimization method and ISO 6336:2006 standard for gear load calculation, was tested using the two arbitrary data sets. Results for both sets were found, and calculation process was replicated 10 times to verify it.
The operational torque was used as the fitness function, which was maximized. Requirement to increase the torque, paired with the static geometrical constraints, directed the algorithm towards fitting the gears pair into the available volume. Limited dimensions coupled with the use of high-quality materials caused the shafts to become critical element in the chain for set 1.
Suggested approach could easily be adjusted to search optimal gear pair parameters for different types of constraints. For example, if the maximal gearbox weight is set as a limiting condition, replacing the dimensional constraints with the ones associated to weight will enable calculation of the corresponding optimal pair parameters.

REFERENCES

1. Almasi, A. (2014). Latest technologies and modern guidelines on gear units. *Australian Journal of Mechanical Engineering*, *12*(3). http://doi.org/10.7158/M12-085.2014.12.3
2. Bonori, G., Barbieri, M., & Pellicano, F. (2008). Optimum profile modifications of spur gears by means of genetic algorithms. *Journal of Sound and Vibration*, *313*(3–5), 603–616. http://doi.org/10.1016/j.jsv.2007.12.013
3. Gologlu, C., & Zeyveli, M. (2009). A genetic approach to automate preliminary design of gear drives. *Computers and Industrial Engineering*, *57*(3), 1043–1051. http://doi-.org/10.1016/j.cie.2009.04.006
4. Haberhauer, H., & Bodenstein, F. (2014). Machinenelemente - Gestaltung, Berechnung, Anwendung. Berlin: Springer-Verlag.
5. Maaranen, H., Miettinen, K., & Penttinen, A. (2007). On initial populations of a genetic algorithm for continuous optimization problems. *Journal of Global Optimization* (Vol. 37). http://doi.org/10.1007/s10898-006-9056-6
6. Marcelin, J.-L. (2001). Genetic optimisation of gears. *International Journal of Advanced Manufacturing Technology*, *17*(12), 910–915. http://doi.org/10.1007/s001700170101
7. Marcelin, J.-L. (2005). Using genetic algorithms for the optimization of mechanisms. *Int J Adv Manuf Technol*, *27*, 2–6. http://doi.org/10.1007/s00170-004-2162-z
8. Tudose, L., Buiga, O., Ştefanache, C., & Sóbester, A. (2010). Automated optimal design of a two-stage helical gear reducer. *Structural and Multidisciplinary Optimization*, *42*(3), 429–435. http://doi.org/10.1007-/s00158-010-0504-z
9. Weis, P., Kučera, Ľ., Pecháč, P., & Močilan, M. (2017). Modal Analysis of Gearbox Housing with Applied Load. *Procedia Engineering*, *192*, 953–958. http://doi.org-/10.1016/j.proeng.2017.06.164
10. Yokota, T., Taguchi, T., & Gen, M. (1998). A solution method for optimal weight design problem of the gear using genetic algorithms. *Computers & Industrial Engineering*, *35*(3–4), 523–526. http://doi-.org/10.1016/S0360-8352(98)00149-1

Corresponding author:
Daniel Miler, MSc., Chair of Machine Elements, Faculty of Mechanical Engineering and Naval Architecture, University of Zagreb, Ivana Lučića 5, Zagreb, 10002, Croatia, phone: +385 1 6168 175, e-mail: daniel.miler@fsb.hr

MECHANICAL CHARACTERIZATION OF WHOLE COCONUT SHELL

Čestmír MIZERA[1], Petr HRABĚ[2], David HERÁK[1]

[1]*Department of Mechanical Engineering, Faculty of Engineering, Czech University of Life Sciences Prague*
[2]*Department of Department of Material Science and Manufacturing Technology, Faculty of Engineering, Czech University of Life Sciences Prague*

Abstract
The article is focused on the description of whole coconut shell under compression loading. The coconuts (Cocos nucifera) were used for this experiment. The coconuts were measured and pressed in longitudinal and latitudinal direction. Compressive force and deformation energy were determined. The compressive force and deformation energy required for coconut extraction are significant smaller in the latitudinal direction.

Key words: *coconut husk; cracking of coconuts; agriculture product.*

INTRODUCTION
Being a nutritious and multi usable fruit, coconut is a popular drupe, of a tree with scientific name as “Cocos nucifera”, a member of the family “Arecaceae” (palm family) (*Moore & Howard., 1996*). Like the other fruits, it has three layers: exocarp, mesocarp, and endocarp. The exocarp is the botanical term for the outermost layer of the pericarp (or fruit). It forms the tough and waterproof outer skin of the coconut fruit weighing about 0.025–0.43 kg (*Gulve, Chakrabarty & Vyas, 2009*). The exocarp and the fibrous mesocarp make up the “husk” of the coconut. The mesocarp comprises of fibro vascular bundles of coir embedded in a nonfibrous connective tissue, usually referred as pith (*Khan, 2007*).
Inner stone or endocarp (outside shell), is the hardest part of the nut which has three germination pores that are clearly visible on the outside surface once the husk is removed. The radicle emerges through one of these germination pores when the embryo germinates. Adhering to the inside wall of the endocarp is the testa, with a thick albuminous endosperm (the coconut “meat”), the white and fleshy edible part of the fruit. The shell and husk becomes harder with maturity. The shell has three germination pores (stoma) or eyes that are clearly visible on its outside surface once the husk is removed (*Varghese, Francis & Jacob, 2017*). A thin brown layer (testa) separates the shell from the endosperm (kernel, flesh, meat), which is approximately 1–2 cm thick. A cavity within the kernel contains the coconut water (*Canapi, Augustin, Moro, et al., 2005*).
Only a few researchers studied the physical and mechanical properties of the different varieties of coconut. For example some authors (*Jarimopasa & Kusonb, 2007*) found some physical and mechanical properties of the young coconut for developing the young coconut opening machine. They investigated the size and the shape of the young coconut which include the diameter and the height and also found the mechanical properties which include the shell rupture force and husk moisture content.
For designing the coconut husking machine, it is very important to study the physical and mechanical properties of the coconut (*Varghese, Francis & Jacob, 2017*). The aim of this article is to determine the compressive force and deformation energy for cracking of whole coconut shell.

MATERIALS AND METHODS
Commercially available old coconuts, the fruits of the coconut tree (*Cocos nucifera*), were used for this experiment. All coconuts were initially centre-drilled to allow removal of coconut water. The dimensions of coconuts were determined using vernier calliper. All obtained results were expressed as mean of three replicates. For measuring of mass of each coconut an electronic balance (*Kern 440–35, Kern & Sohn GmbH, Balingen, Germany*) was used. The mass of nuts were determined without coconut water. To assess the mechanical properties and dimensions, the tests were performed on the both axis of the coconut, in directions analogous to lines of longitude and latitude on a globe (in the “equatorial” region), henceforth labelled “longitudinal” and “latitudinal” (Fig. 1). In total, 50 pieces of coconut, which were randomly divided into five groups (Set 1 – Set 5) were used for this experiment.

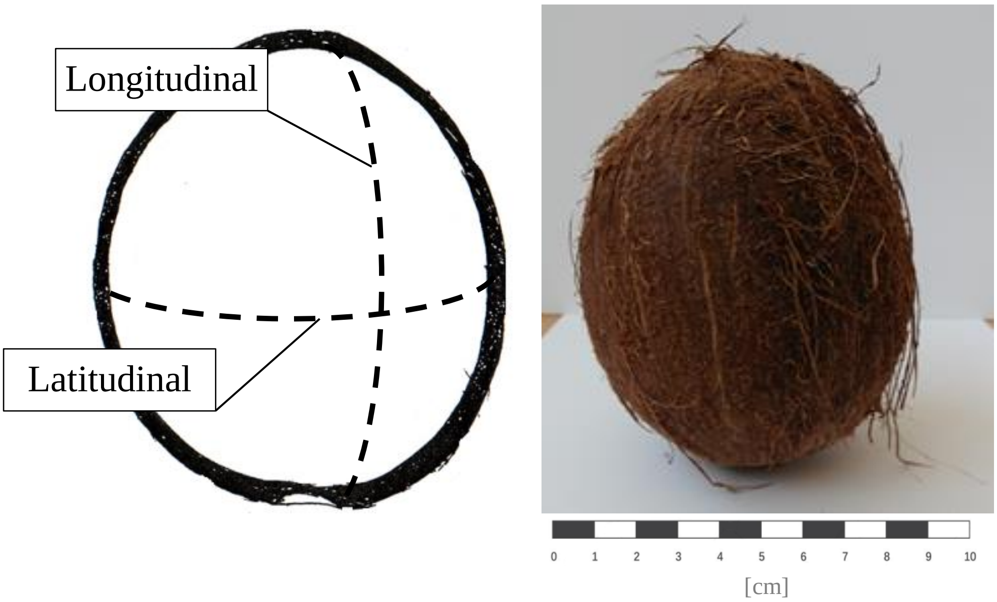

Fig. 1 Directions of measurement (a), overview of fruit of the coconut tree (Cocos nucifera) (b)

To determine the relationship between compression force and deformation, compression device (*ZDM, model 50, Germany*) was used to record the course of deformation function. The coconuts were measured and pressed in two directions (longitudinal and latitudinal) at the rate of 1 $mm.s^{-1}$ under the temperature of 20 °C. The experiment was repeated twenty-five times for each direction and individual measurements were digitally recorded.

RESULTS AND DISCUSSION

Individual coconuts were divided into 5 groups (Set 1 – Set 5). The dimensions and masses of each group are shown in Tab. 1. One of the most important tests for designing the coconuts extracting machines is compression test. The compression loading of whole coconuts is presented in Fig. 2. It is observed the compression load is higher in longitudinal direction than that registered in latitudinal direction by 35%. This is attributed to the structure and shape of coconut (*Kadam, Chattopadhyay, Bharimalla, et al., 2014*). The relationship between compression force and deformation of coconuts is presented in Fig. 3.

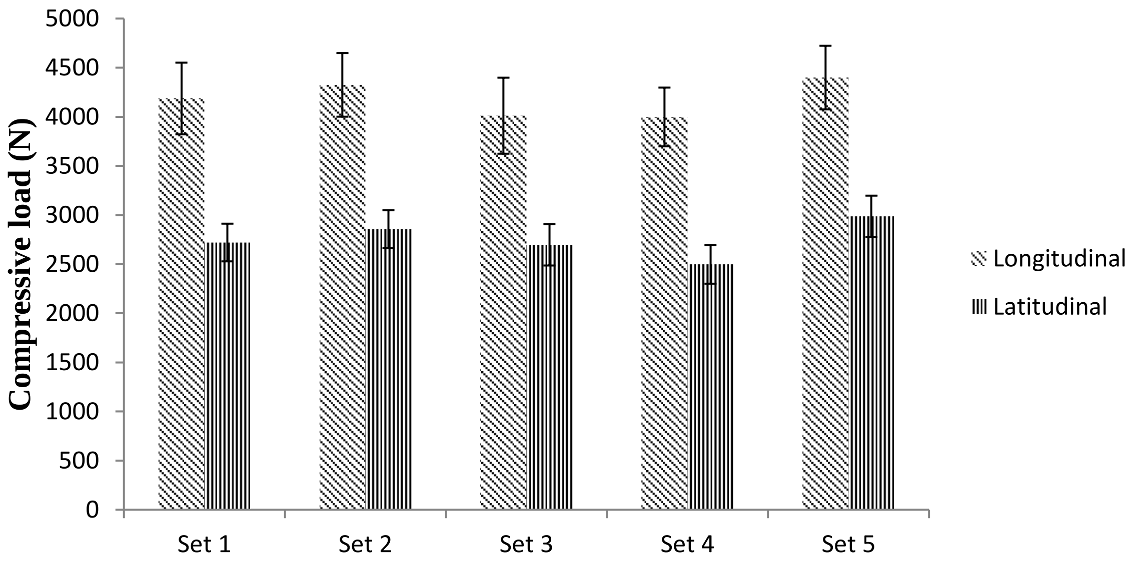

Fig. 2 Compressive load of coconuts (Cocos nucifera) in two different directions

As is also seen in Fig. 3, the coconuts which are loaded in longitudinal directions reach higher values of deformation energy, which is characterized as an area below a deformation curve.

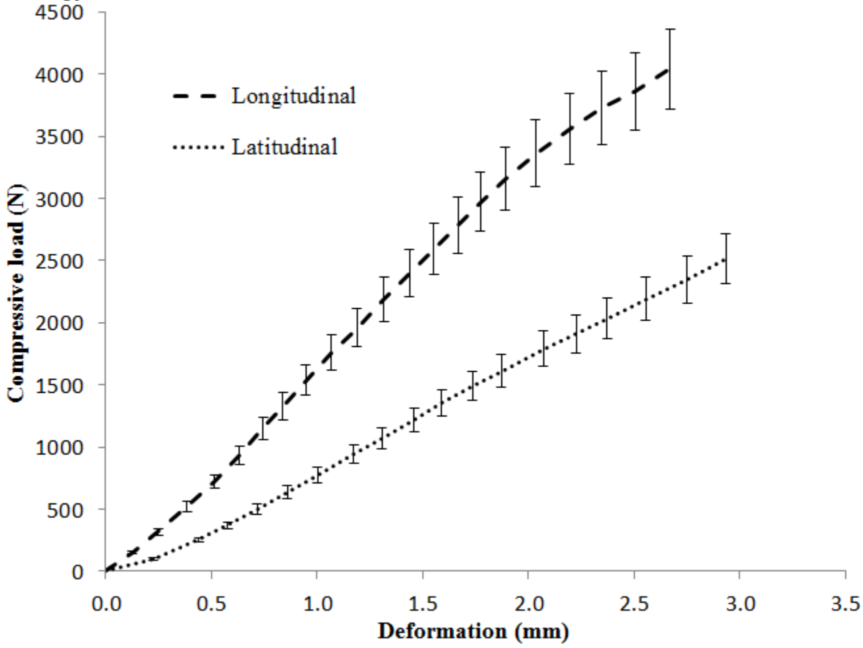

Fig. 3 Relationship between compression force and deformation of coconuts in two directions

The values of deformation energy of coconuts in two directions are shown in Tab. 1.

Tab. 1 Physical properties and deformation energy of coconuts (Cocos nucifera)

Sample	Mass	Longitudinal		Latitudinal	
	g	Dimension mm	Deformation energy J	Dimension mm	Deformation energy J
Set 1	335 ± 17	126 ± 4	15.86 ± 1.71	89 ± 4	10.14 ± 1.05
Set 2	349 ± 24	131 ± 6	16.34 ± 1.38	95 ± 3	10.78 ± 1.02
Set 3	310 ± 22	124 ± 5	15.55 ± 1.47	87 ± 3	9.47 ± 0.85
Set 4	307 ± 17	118 ± 7	14.47 ± 1.31	85 ± 5	8.62 ± 0.78
Set 5	378 ± 34	133 ± 4	17.33 ± 1.67	97 ± 3	10.98 ± 1.06

There is a significant difference in the compressive load of longitudinal and latitudinal direction. At first, a two-choice F – test was used for a statistical comparison of particular measured values for an analysis of an agreement of variance. After verifying the agreement of variance, T-test of a significance of differences of two chosen means was subsequently used. The parameters of T-test are shown in Tab. 2.

Tab. 2 T-test compressive force. Statistical comparison between longitudinal and latitudinal loading of coconuts

Sample	T_{stat} -	t_{crit} -	P_{value} -
Set 1	32.483	6.388	0.228
Set 2	37.141	6.388	0.228
Set 3	33.484	6.388	0.224
Set 4	25.987	6.388	0.245
Set 5	38.456	6.388	0.274

The mechanical behavior of coconut shell was also examined by other authors (*Gludovatz, Walsh, Zimmermann, et al., 2017*). Similar values of compressive force were also determined by other authors (*Kadam et al., 2014*).

CONCLUSIONS

In the present study, the mechanical properties of coconuts were observed. The deformation energy required for coconut extraction is significant smaller in the latitudinal direction. Therefore, it is recommended that feeding of the shell in the machine should be in the latitudinal direction for ease of coconut cracking.

ACKNOWLEDGMENT

This study was supported by Internal Grant Agency of Faculty of Engineering – Czech University of Life Sciences Prague – IGA 2017: 31130/1312/3111.

REFERENCES

1. Moore, D., & Howard, W., F. (1996). Coconuts. In E. E. lindquist, M. W. Sabelis, & J. Bruin (Eds.), Eriophyoid Mites: Their Biology, Natural Enemies and Control. New York, (pp. 561–570). Elsevier Science Publishers.
2. Gulve, A., S., Chakrabarty, & Vyas, S. (2009). Application of coir (coconut fiber) in geotextiles. Proceedings International. conference Emerging Trends Production Processing. Natural Fibers. Mumbai. (pp. 358–364).
3. Khan, B., A. (2007). Uses of coir fiber its products and implementation of geo coir in Bangladesh. Daffodil Intl. Univ. *Journal of Science and Technology*, 2, 33–38.
4. Varghese, A., Francis, K., & Jacob, J. (2017). A Study of Physical and Mechanical Properties of the Indian Coconut for Efficient Dehusking. *Journal of Natural Fibers*, 14, 390–399.
5. Canapi, E., C., Augustin, V., T., Y., Moro, A., E., Pedrosa, J., E., & Bendaño, L., M. (2005). Coconut oil. In Bailey's industrial oil products, ed. F. Shahidi, Vol. 1, 6th ed., Edible Oil and Fat Products: Chemistry, Properties, and Health Effects. London, UK: Wiley-Interscience.
6. Jarimopasa, B., & Kusonb, P. (2007). A young-coconut-fruit-opening machine. *Biosystems Engineering*, 98, 185–197.
7. Kadam, V., Chattopadhyay, S., K., Bharimalla, A., & Venugopal, B. (2014). Mechanical Characterization of Brown and Green Coconut Husk. Journal of Natural Fibers, 11, 322–332.
8. Gludovatz, B., Walsh, F., Zimmermann, E.,A., Naleway, S.,E., Ritchie, R.,O., & Kruzic, J.,J. (2017). Multiscale structure and damage tolerance of coconut shells. Journal of the *Mechanical Behavior of Biomedical Materials*, article in press.

Corresponding author:

Ing. Čestmír Mizera, Ph.D., Department of Mechanical Engineering, Faculty of Engineering, Czech University of Life Sciences Prague, Kamýcká 129, Praha 6, Prague, 16521, Czech Republic, phone: +420 22438 3374, e-mail: mizera@tf.czu.cz

AN APPARATUS FOR MEASUREMENT OF INCLINATION OF GEARS ON NEEDLE BEARINGS

Václav MOSLER[1], Jiří HAVLÍK[2], Jan PAVLÍK[3], Ivo KŘISTEK[4]

[1] *VŠB – Technical University of Ostrava, Czech Rebuplic*
[2] *VŠB – Technical University of Ostrava, Czech Rebuplic*
[3] *VŠB – Technical University of Ostrava, Czech Rebuplic*
[4] *VŠB – Technical University of Ostrava, Czech Rebuplic*

Abstract
The objective of the apparatus is to measure inclination of a gear on a needle bearing relative to the load and rotational speed. Furthermore, bearing clearance is to be optimised in terms of its noise and vibrations.

Key words: inclination of a gear, noise, vibration
.
INTRODUCTION

Transmission of personal vehicles with stepped changes of the gear ratio using the gears, transmissions are consist of drive shaft and driven shaft on witch are fitted gears in permanent contact. On one shaft is gear rigidly mounted, on the other is gear mounted on needle bearings, torque transmission between the gear and shaft is reached by synchronizer. Gears witch are not used for transfer torque, they are rotate freely on needle bearing. Currently are used on all forward speed gears, gears with witch helical cogs in transmission of personal vehicle. A diagram depicting a two-shaft transmission of a personal vehicle is provided in Figure 1.

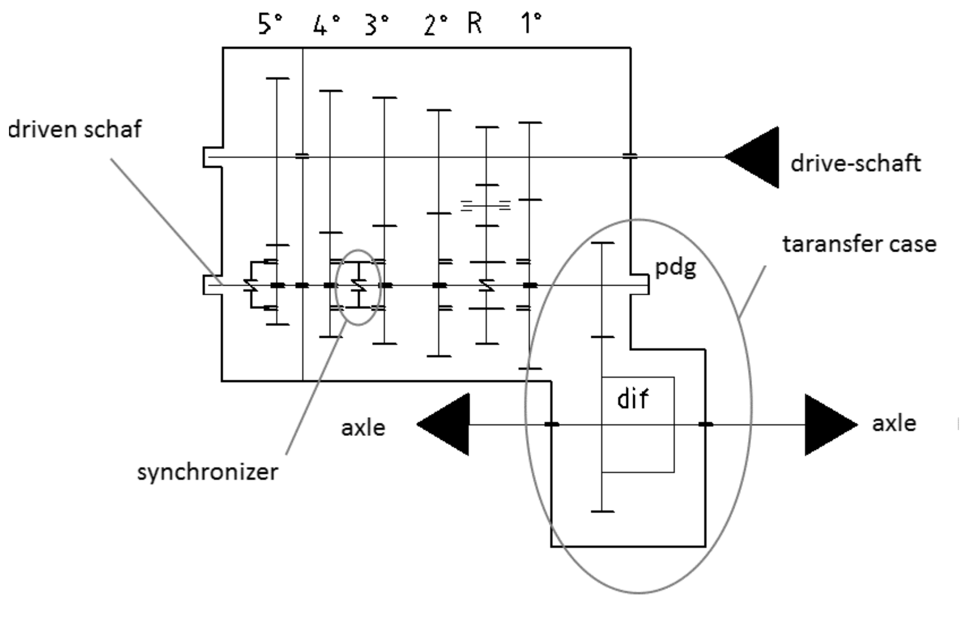

Fig. 1 A diagram of a two-shaft transmission

Transmission of torque between a gear and a shaft is realized by a synchronizer. Effects of force are transmitted from the gear to the shaft by a needle bearing. As an result of manufacturing of needle bearing, shafts and hubs arise radial clearance between the components. By using of helical cogs it can be assumed due to the effect of axial force from the gears, that the bearing is inclined towards the shaft because of the radial clearance, described in (Fujimura, Beppu, Hibi, Murakami, & Yokoi, 1987). Size of the inclination cannot be accurately computed, as it is affected by deformation of the needles as well, therefore it needs to establish experimental measurements. This phenomenon can be classified as a deviation of a gear transmission. It can be assumed, that the deviation will have an effect on vibrations and noise, described in (Jolivet, Mezghani, El Mansori, Vargiolu, & Zahouani, 2017; Moravec, Dejl, Němček, Folta, & Havlík, 2009). The objective of this work is design a test device to verify the above phenomenon

MATERIALS AND METHODS

Testing apparatus can be placed to an open or a closed trial circuit, described in (Moravec, et al., 2009). The differences between the circuits are considered to be widely-known, thus they will not be further analysed. From the above listed requirements it can be determined that a trial circuit with open energy flow (depicted in Fig. 2) is most suitable for application of the apparatus.

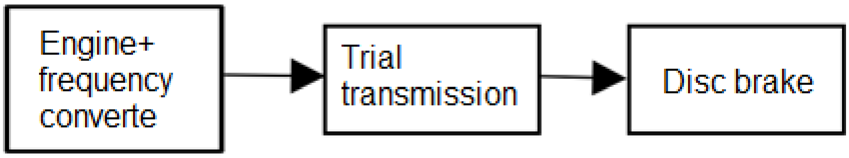

Fig. 2 Open circuit

RESULTS AND DISCUSSION

Fig. 3 depicts a trial stand used for placing of the testing apparatus. This stand is powered by a 30kW engine (1), which is connected to a frequency converter with ability of revolution control up to 3,000 RPM. The measuring apparatus (5) is bolted to the console (4), which is capable of axial shifting in the axis of the engine. The measuring apparatus and the engine are connected by a constant velocity shaft (4). Load of the circuit is delivered by the disc brake (7). This is placed on a tower, which is movable to a limited extent in translational fashion in the direction perpendicular to the engine's axis. Regulation of the braking moment is conducted by rotation of the handle of the braking cylinder (6). The measuring apparatus and the disc brake are connected by a constant velocity shaft. There are sensors of torque and rotational speed already placed on this shaft, therefore their selection is not considered in this work. A sensor of vibrations is to be placed magnetically, externally to the trial box of the transmission. Measuring of noise is to be conducted by an externally placed sound meter.

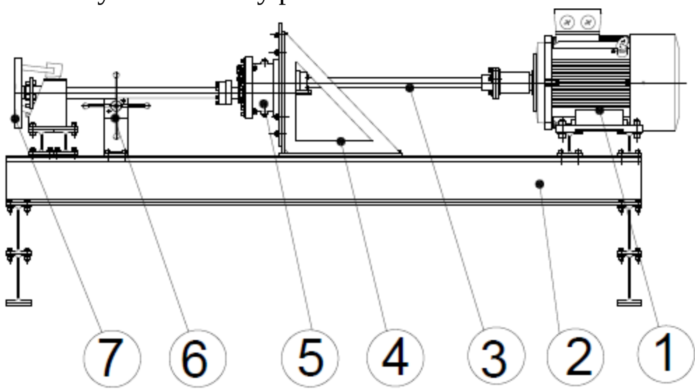

Fig. 3 Trial stand

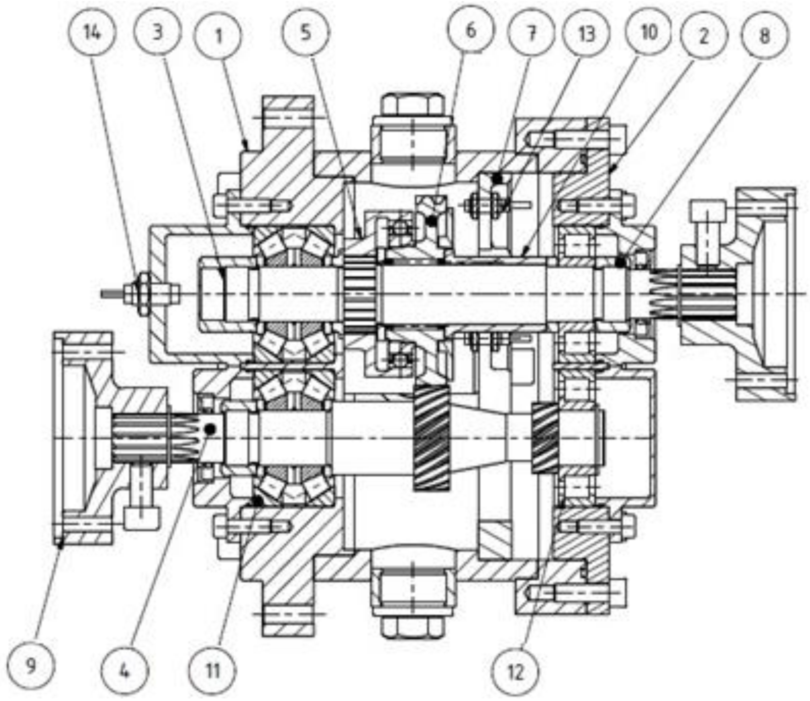

Fig. 4 Measuring apparatus

Fig. 4 depicts a trial testing apparatus. Box of the transmission (1) is welded to a thick-walled seamless pipe and sheet-metal rings of sufficient width. There are tapered roller bearings placed in the box (11). This bearings are axially conductive from both sides. There is a lid bolted to the box (2), in which axially-loose roller bearings ale placed (12). These bearings are fixed to the shaft by a nut. (8). The construction is created for simplifying of the assembly. The selected construction from thick-walled profile is significantly rigid, which ensures imperviousness of the result of the rigidity of the box. Arrangement in Fig.4 corresponds to measurement for A^{nd} gear ratio. The drive shaft is in this case a modified shaft from a transmission, which is due to the fact that the pinion of the A^{nd} gear_is manufactured on the shaft (4). For the rest of the gear ratios, there will be a separately manufactured shaft, onto which a corresponding gear is to be pressed. On the drive shaft (3), a body of a clutch with small spheres will be installed (5).This clutch serves as a substitute for a synchromesh for transmitting of torque from a gear (6) to the shaft. Synchromesh prevents the maximum possible tilt of the gear. This clutch type was developed for the specific case of use. The gear is to be changed together with carrier. Carrier is placed on the area of the gear, on which a synchronizer is attached. The tilt of the gear is to be recorded by three sensors based on eddy currents (13). Sensors are attached in the holder of sensors (7). In order to prevent influencing of the results of the measurements by axial oscillations of the drive shaft, a displacement transducer was attached to the face of the shaft (14). The sensor is bolted to the lid of the bearing. There are flanges (9) mounted on both the input and the output shaft by involute splines for connection with joint shafts of the stands. New clutch (Fig. 5) was developed for specific use in the measurement setting. The body of the clutch (1) is mounted on the involute splines of the drive shaft. There are grooves in the body, to which small spheres are placed. The same grooves are in carrier (2) as well, which is attached to the gear (4). The contact between the grooves and the spheres creates positive engagement. Thus, the spheres are free to rotate inside the grooves, which enables loose tilting of the gear. The annulus (5) serves as a sensing area for measurement of inclination.

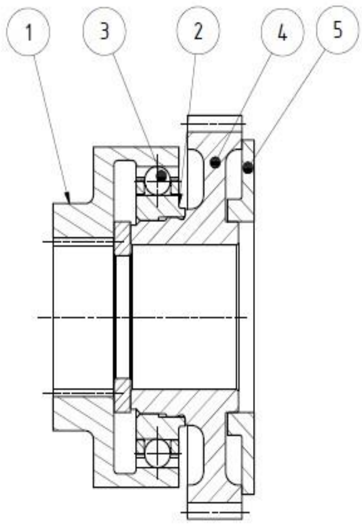

Fig. 5 Clutch with spheres

CONCLUSIONS

Currently, the apparatus is being manufactured and the measurement is being prepared. If it finds that incline of wheel is really happening. The possibility of optimization noise and vibration will research with help of adjustment radial clearance in needle bearing.

ACKNOWLEDGMENT

The trial apparatus was created with the help of the Technology Agency of the Czech Republic as a part of the "Competence Centre for Automotive Industry" project of Josef Božek and a project SP2017./39.

REFERENCES

1. Fujimura, N., Beppu, M., Hibi, K., Murakami, H., & Yokoi, M. (1987). Analysis of the behavior and resonant noise of needle roller bearings used for idler gears in transmission applications. *SAE Technical Papers,* doi:10.4271/871923
2. Jolivet, S., Mezghani, S., El Mansori, M., Vargiolu, R., & Zahouani, H. (2017). Experimental study of the contribution of gear tooth finishing processes to friction noise. *Tribology International, 115*, 70-77. doi:10.1016/j.triboint.2017.05.004
3. Moravec V., M., Dejl, Z., Němček, M., Folta, Z. & Havlík, J. (2014). Spur gearv in transmission car. *Ostrava: MONTANEX a.s, 2009*. ISBN 978-80-7225-304-3.

Corresponding author:
Ing. Václav Mosler, Department machine parts and mechanisms, Faculty of Engineering, Technical University of Ostrava, 17. Listopadu 15/2172, Ostrava – Poruba 708 33, Czech Republic, phone: +420 597 324 313, e-mail: vaclav.mosler@vsb.cz

THE INFLUENCE OF HARDNESS OF COOPERATING ELEMENTS ON PERFORMANCE PARAMETERS OF ROLLING KINEMATIC PAIRS

Janusz MUSIAŁ[1], Marek SZCZUTKOWSKI[1], Robert POLASIK[1], Tomasz KAŁACZYŃSKI[1]

[1] *Faculty of Mechanical Engineering, University of Science and Technology, Al. Prof. S. Kaliskiego 7, 85-796 Bydgoszcz, Poland*

Abstract
Hardness of an external surface is an important issue in a tribological approach. While the hardness of cooperating elements is a technological feature, it is directly connected with operating features. Two rolling kinematic pairs, with diversified hardness of elements, were accepted as a test object and underwent operating tests. In the article there was presented the analysis of external surface features (motion resistance as well as surface geometric structure) that influence its deformation affecting performance parameters of machines.

Key words: *surface geometric structure, moment of friction, roughness.*

INTRODUCTION

Knowledge on technological state and operational surface layer allows rational control of machine operational use. As a result, it is possible to increase life of machine and reduce the failure frequency.
Technological surface layer changes during the performance of individual treatments and operations provided in the manufacturing process and reaches a certain state upon its completion.
The next stage of the life cycle of a product after manufacture is the operation process characterized by the specific conditions determined by controllable factors and disturbances (uncontrollable ones). During machine operation the state of the surface layer (SL) constantly changes and it is a function of both the exploiting conditions and time (Kaczmarek & Wojciechowski, 1995, Grządziela, et al. 2015). As distinct from technological surface layer, for which relevant is the condition at the end of production state, for operation the current state of surface layer is essential, which is a consequence of the initial state.
Analysis of the extensive literature (Musiał, 2014, Blunt & Jiang, 2003, Dietrych, 1985, Oczoś & Liubimov, 2003, Frýza at al., 2015, Madej, at al., 2015) enabled to determine a set of the most important parameters that should characterize the surface layer ready for operation. According to the adopted order of importance with the diversification following the theory of machines three groups of technological features can be distinguished:

- material (MDF),
- geometrical (GDF),
- dynamical (DDF).

In tribological discussion the most important MDF is hardness of the surface layer. Hardness of cooperating elements is directly related with their performance parameters (Zwirlein & Schlicht, 1982, Łukasiewicz, at al., 2014, Czichos, at al., 1989, Hutchings, 2003, Kostek at al., 2015, Jin, at al., 2012, Kumar at al., 2000).
Characteristics of a kinematic pair are one of the factors of the relation algorithm between technological features and performance parameters of cooperating elements. The characteristics indicate differences in hardness occuring between cooperating surfaces. This feature has a big impact on the transformation of the surface layer which determines performance parameters of machines.
There are following performance parameters of cooperating kinematic pairs:

- wear (linear, volumetric, mass),
- friction (friction moment, resisting force),
- changes in the geometric surface structure.

Presented research results are a part of research related to the above functional characteristics of the surface layer. Below there is presented an analysis of kinematic pairs with diversified hardness of the surface layer regarding: movement resistance determined on the basis of changes of the value of friction moment and changes one of the parameters of the geometrical surface structure - *Ra*.

MATERIALS AND METHODS

Cylindrical roller bearings were the research object. Due to the nature of the load, kinematics of bearing components and the essence of operation of such kinematic pairs in real conditions, major changes appear on the inner ring and therefore during the studies there were observed changes taking place in those surfaces. Races of rolling bearings and rolling elements are made primarily from carbon-chromium steel which is normally subjected to heat treatment. As a result the material is hardened in the range of 55 to 65 HRC. Due to the widespread use of this type of steel in cylindrical rolling bearings specimens made of bearing steel with the designation 100Cr6 with a hardness of 55 HRC were accepted for tests while counter - specimens were made of the same steel but with hardness of 58 HRC - it was a one kinematic pair (with a small difference in hardness). The second kinematic pair (with a large difference in hardness) was the combination of the specimen of aluminum alloy EN AW-6082, and counter specimen the same as in the first combination. The chemical composition of materials used for tests was examined and shown in Tables 1 and 2. Testing of chemical composition were performed with a usage of the spectrometer made by SPECTRO, the SpectroMaxF model.

Tab. 1 The chemical composition of 100Cr6 steel (1.3505)

Si	Mg	Mn	Fe	Cr	Zn	Ti	Cu
investigated							
1,14	1,03	0,91	0,42	0,21	0,15	0,07	0,08
PN-EN 573-3							
0,7 – 1,3	0,6–1,2	0,4–1	≤ 0,5	≤ 0,25	≤ 0,2	≤ 0,1	≤ 0,1

Tab. 2 The chemical composition of EN AW-6082 aluminum alloy (3.2315)

Si	Mg	Mn	Fe	Cr	Zn	Ti	Cu
investigated							
1,14	1,03	0,91	0,42	0,21	0,15	0,07	0,08
PN-EN 573-3							
0,7 – 1,3	0,6–1,2	0,4–1	≤ 0,5	≤ 0,25	≤ 0,2	≤ 0,1	≤ 0,1

Operational tests were carried out with the use of the wear testing machine AMSLER 135. The rotational speed of the specimen was constant at 250 rev / min, the counter - specimen also rotated at a constant speed with a value causing slippage (sliding-rolling motion). In order to accelerate the process of wear, lubrication of combinations was made at the beginning of the test after precise cleaning of specimens and counter specimens using extraction naphtha. On such prepared surfaces there were applied and distributed 3 drops of paraffin. During research environmental conditions were controlled (temperature and relative humidity) in order not to influence the test results.

There were following variable parameters during the operational research:

– parameter describing the geometrical structure of the surface after turning: Ra_T [μm],
– load: P [N],
– time of test: τ [s].

In the experimental research there was used the Hartley PS/DS study plan (static, determined and multi-section one) – P: Ha 3(hK) (Górecka, 1995).

Central point of the plan had coordinates as follows:

– for combinations of aluminum-steel: Ra_T = 4,08 μm, P = 1128 N, τ = 18000 s,
– for combinations of steel-steel: Ra_T = 1,98 μm, P = 1128 N, τ = 18000 s.

The range and values of the load and the operating time of the combination were established on the basis of preliminary tests while the roughness was determined on the basis of the author's research results of the technological surface layer.

RESULTS AND DISCUSSION

Motion resistance expressed by the moment of friction is the main operating feature of rolling kinematic pairs. Dependance of the M_t moment on time τ, load P and roughness Ra_T of the tested tribological node of the combination aluminum- steel is shown in Fig. 1 and for steel- steel in Fig. 2.
On the base of on the figures it can be stated that in both cases the load influences friction the most in the examined nodes. Greater gradient of changes is characterized within a pair of steel - steel. Also, the analyzed values of moments of friction were twice bigger in that combination.

a) b)

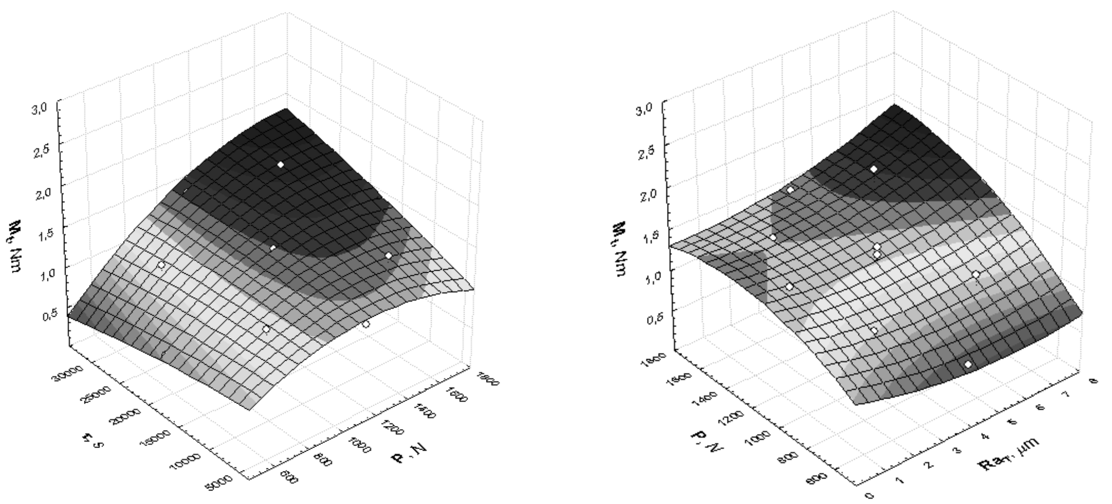

Fig. 1 Relationship chart of the friction moment M_t of the alloy aluminum-steel cooperating pair to: a) time τ and load P, b) load P and roughness Ra_T

a) b)

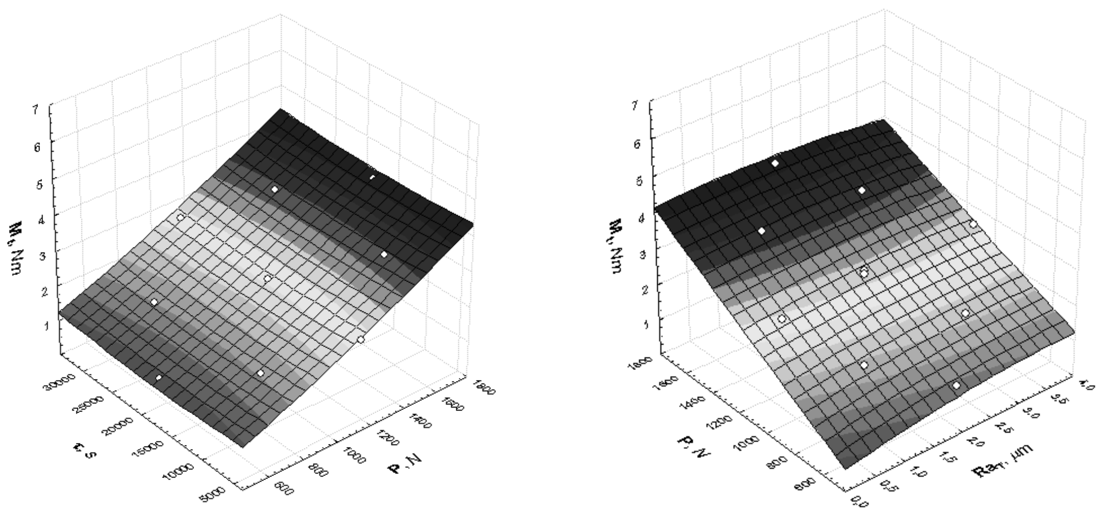

Fig. 2 Relationship chart of the friction moment M_t of the alloy steel-steel cooperating pair to: a) time τ and load P, b) load P and roughness Ra_T

The observed changes were described mathematically by the power function. Regression coefficients necessary in mathematical description of changes of the friction moment for the pair aluminium-steel are presented in Table 3. The rest of mathematical relationships were based on the observed regression coefficients.

Tab. 3 Regression coefficients and their statistical significance $M_t = f\ (Ra_T,\ P,\ \tau)$ for the kinematic pair aluminium-steel

	$\mathbf{b_0}$	$\mathbf{b_1}$ (Ra_T)	$\mathbf{b_2}$ (P)	$\mathbf{b_3}$ (τ)
$\mathbf{b_i}$	0,0164	0,0129	0,5492	0,0519
t-Stat	–4,1807	0,1807	5,1102	0,8285
p-value	0,0041	0,8617	0,0014	0,4347

Mathematical relationship taking into account data from Table 3 is defined as:

$$M_t = 0{,}0164 \cdot Ra_T^{0{,}0129} \cdot P^{0{,}5492} \cdot \tau^{0{,}0519} \tag{1}$$

Wheareas for the pair steel – steel is expressed by the formula:

$$M_t = 0{,}0029 \cdot Ra_T^{-0{,}0394} \cdot P^{0{,}9733} \cdot \tau^{-0{,}0056} \tag{2}$$

The surface roughness during operation Ra_E was the second of the analyzed parameters. Graph interpretation of variability of the factor for various combinations is shown in Figures 3 and 4.

a) b)

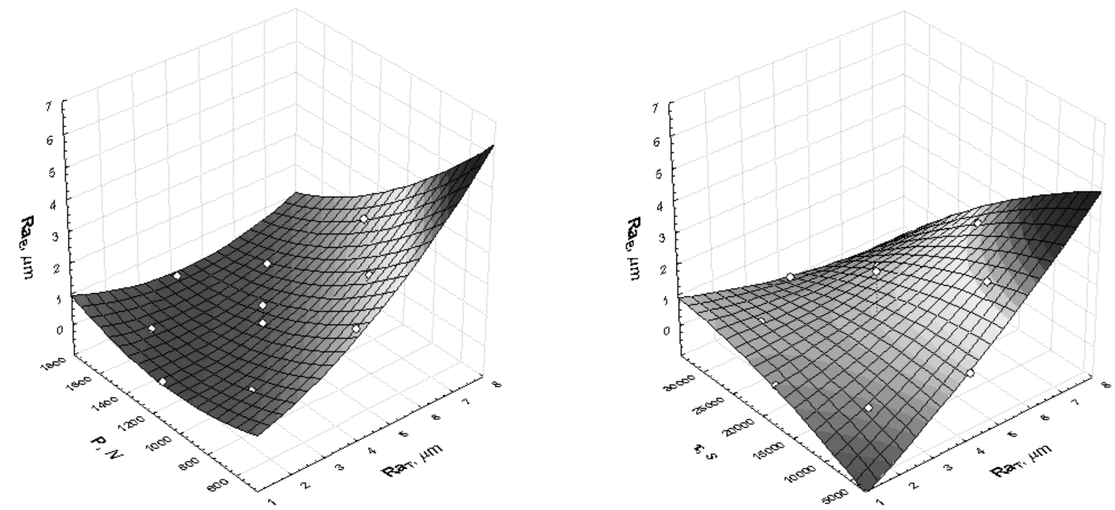

Fig. 3 Relationship chart of of roughness Ra_E of the alloy aluminum-steel cooperating pair to: a) time τ and load P, b) load P and roughness Ra_T

a) b)

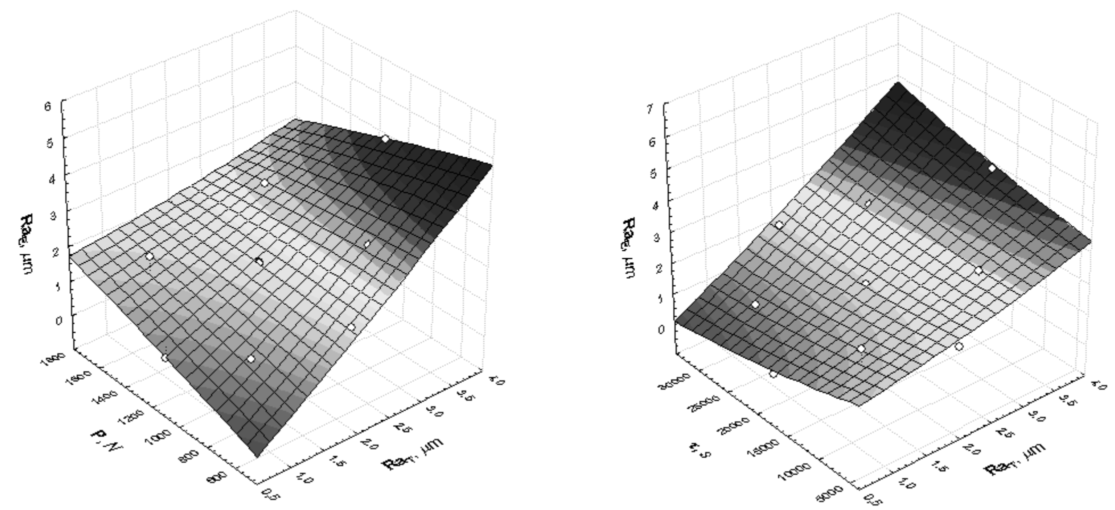

Fig. 4 Relationship chart of roughness Ra_E of the alloy steel-steel cooperating pair to: a) time τ and load P, b) load P and roughness Ra_T

On the basis of Figure 4 it should be noted that when the load was increasing the value of the parameter Ra_E was decreasing which is a result of flattening of surface vertices of the specimen made of aluminum alloy - Figure 5.

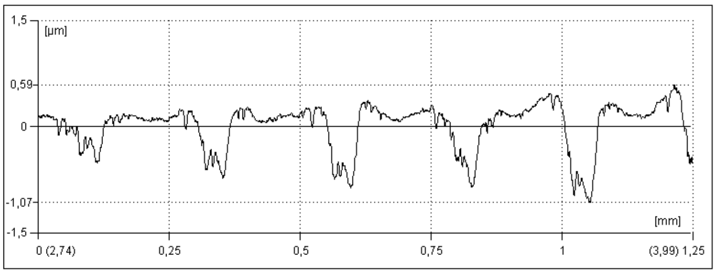

Fig. 5. Example of the surface roughness profile of the specimen EN AW-6082

The lower influence of the load was observed in the combination with similar hardness (steel-steel) where there was only a slight rounding of vertices of the tested surfaces – Figure 6.

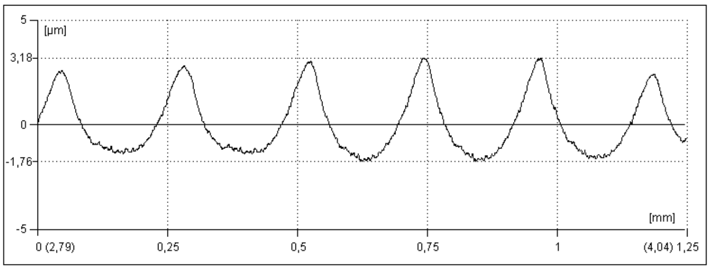

Fig. 6 Example of the surface roughness profile of the specimen 100Cr6

Mathematical description of surface roughness changes for the pair aluminium – steel is defined as (3):

$$Ra_E = 1473285 \cdot Ra_T^{1,0929} \cdot P^{-1,7509} \cdot \tau^{-0,3948} \tag{3}$$

The detailed form of equation of changes of the Ra_E parameters of the pair steel – steel is presented below (4):

$$Ra_E = 0,8931 \cdot Ra_T^{0,9052} \cdot P^{0,1525} \cdot \tau^{-0,0883} \tag{4}$$

CONCLUSIONS

The difference in hardness of cooperating elements has significant impact on performance parameters of kinematic pairs. Larger values of the moment of friction are present in the combination with similar hardness of elements which is mainly caused by the load. The load also determines changes in the combination with a large difference in surface hardness.

Comparing the surface roughness in the studied pairs the different nature of changes has to be noted. Along with the duration of tests the Ra_E value decreases for aluminum – steel specimens and increases for steel-steel specimens in the testing range.

Proper selection of the hardness of cooperating surfaces has impact on the lifespan and the failure rate of machines.

In order to verify research results, especially in order to apply them in practice, the authors consider to perform a set of tests in conditions of an accredited test laboratory on the base of their own experience (Szczutkowski, 2012, 2015)

REFERENCES

1. Kaczmarek J., Wojciechowski B. (1995). Changes of usage strategy of an external surface, *Tribologia 6*, 629-651.
2. Grządziela A., Musiał J., Muślewski Ł., Pająk M. (2015). A method for identification of non-coaxiality in engine shaft lines of a selected type of naval ships. *Polish Maritime Research 22(85),* 65-71.
3. Musiał J. (2014). Significance of surface topography in the surface layer transformation of the rolling kinematic pairs. Publishing House of University of Science and Technology in Bydgoszcz.
4. Blunt L., Jiang X. (2003). Advanced Techniques for Assessment of Surface Topography. Kogan Page London.
5. Dietrych J. (1985). Systems and Design. Wydawnictwo Naukowo - Techniczne Warszawa.
6. Oczoś K.E., Liubimov V. (2003). Surface geometrical structure. Publishing House of Rzeszów University of Technology.
7. Frýza J., Šperka P., Křupka I., Hartl M. (2015). Behaviour of EHL Films under Lateral Vibrations. In Book of Proceedings of 56th International Conference of Machine Design Departments, 349-352.
8. Madej M., Ozimina D., Kurzydłowski K., Płociński T., Wieciński P., Styp-Rekowski M., Matuszewski M. (2015). Properties of diamond-like carbon coatings deposited on cocrmo alloys. *TRANSACTIONS OF FAMENA XXXIX-1*, 79-88.
9. Zwirlein O., Schlicht H. (1982). Rolling contact fatigue mechanisms-accelerated testing versus field performance. Rolling contact fatigue testing of bearing steels. *ASTM STP 771*, 358-379.
10. Łukasiewicz M., Kałaczyński T., Musiał J., Shalapko J.I. (2014). Diagnostics of buggy vehicle transmission gearbox technical state based on modal vibrations. *Journal of Vibroengineering 16(6)*, 3137-3145.
11. Czichos H., Becker S., Lexow J. (1989). International multilaboratory sliding wear tests with ceramic and steel. *Wear 135,* 171-191.
12. Hutchings I. M. (2003). Friction and Wear of Engineering Materials. Tribology, University of Cambridge UK.
13. Kostek R., Landowski B., Muślewski Ł. (2015). Simulation of rolling bearing vibration in diagnostics. *Journal of Vibroengineering 17(8*), 4268-4278.
14. Jin Ch., Wu B., Hu Y. (2012). Heat generation modeling of ball bearing based on internal load distribution. *Tribology International 45*, 8-15.
15. Kumar R., Kumar S., Prakash B., Sethuramiah A. (2000). Assessment of engine liner wear from bearing area curves. *Wear 239(2),* 282-286.
16. Górecka R. (1995). Theory and techniques of an experiment, Publishing House of Cracov University of Technology.
17. Szczutkowski M. (2012). Computer aided accredited laboratory processes in public university environment. *Electronic International Interdisciplinary Conference EIIC, Z*ilina (Slovakia)
18. Szczutkowski M. (2015). Possibilities of cooperation with accredited testing laboratories from Polish higer education institutions from the point of view of reliability of research results. In Y. Shalapko (Ed.), *Study of problems in modern science: new technologies in engineering, advanced management, efficiency of social institutions,* Khmelnitsky: Khmelnitsky National University

Corresponding author:
Janusz Musiał, assoc. prof. Ing., Faculty of Mechanical Engineering, University of Science and Technology, Al. Prof. S. Kaliskiego 7, 85-796 Bydgoszcz, Poland, phone: +48 52 340 82 96, e-mail: janusz.musial@utp.edu.pl

GEOMETRIC AND MESHING PARAMETERS OF A PINION-RACK PAIR – A REVIEW

Miloš NĚMČEK

Department of Machine Parts and Mechanisms, VŠB-TU Ostrava

Abstract
This contribution deals with a relatively neglected area of meshing of a pinion-rack pair. Although it is in principle for a mesh between a pinion and a wheel with a very large number of teeth (infinitely one) so they can not apply all calculations of a pair pinion-wheel. This is mainly due the fact that they cannot work with neither central distances nor wheel diameters. Despite all relevant geometrical and meshing calculations are relatively easy ones.

Key words: *pinion; rack; geometry; mesh.*

INTRODUCTION
Pair pinion-rack is widespread in the area of gearing transmissions. As far as data for designers there is relatively well processed area of loading capacity calculations. But an area of geometric design is slightly neglected. Since a rack is a part of a wheel with infinitely big diameter, so there is this rack replaced by a wheel with a large number of teeth – for instance 1000 in geometric calculations. Results of such a mesh look like a lot to a mesh pinion-rack. But they are not fully exact. For achieving absolutely exact data it should be necessary to utilize equations which are commonly used for a design of a pair pinion-wheel. But they must be solved as limits for $z_2 \rightarrow\infty$. Some equations would be then unsolvable or they would became indeterminate expressions. This contribution shows some solving of these equations in the form right for toothed rack, otherwise $z_2 \rightarrow\infty$. Basic profile of the rack is on the fig. 1. On the fig. 2 is the basic profile of the tool for manufacturing of racks. It is a complex tool including for chamfering and for a protuberance undercutting of the rack.

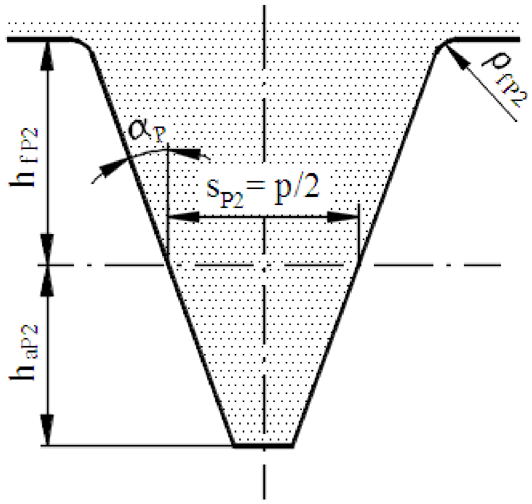

Fig. 1

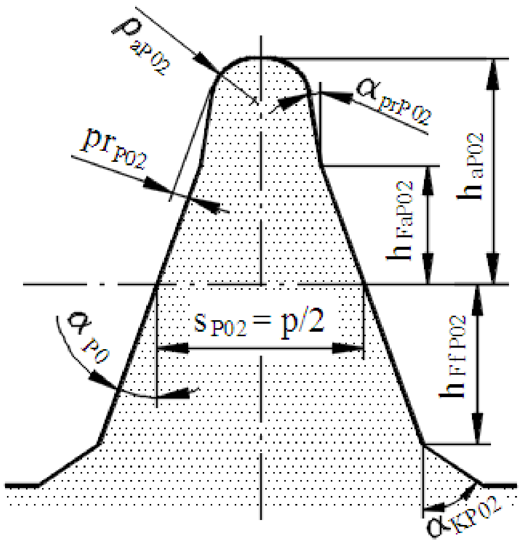

Fig. 2

MESH PINION – RACK
It is necessary to realize that a rack cannot be shifted (it is impossible to use other part of an involute with a different curvature). Due to it is always valid $x_2 = 0$. The next constant is working pressure angle which is independent on pinion addendum coefficient modification x_1. It applies $\alpha_{wt} = \alpha_t$. All detail are on the fig. 3.

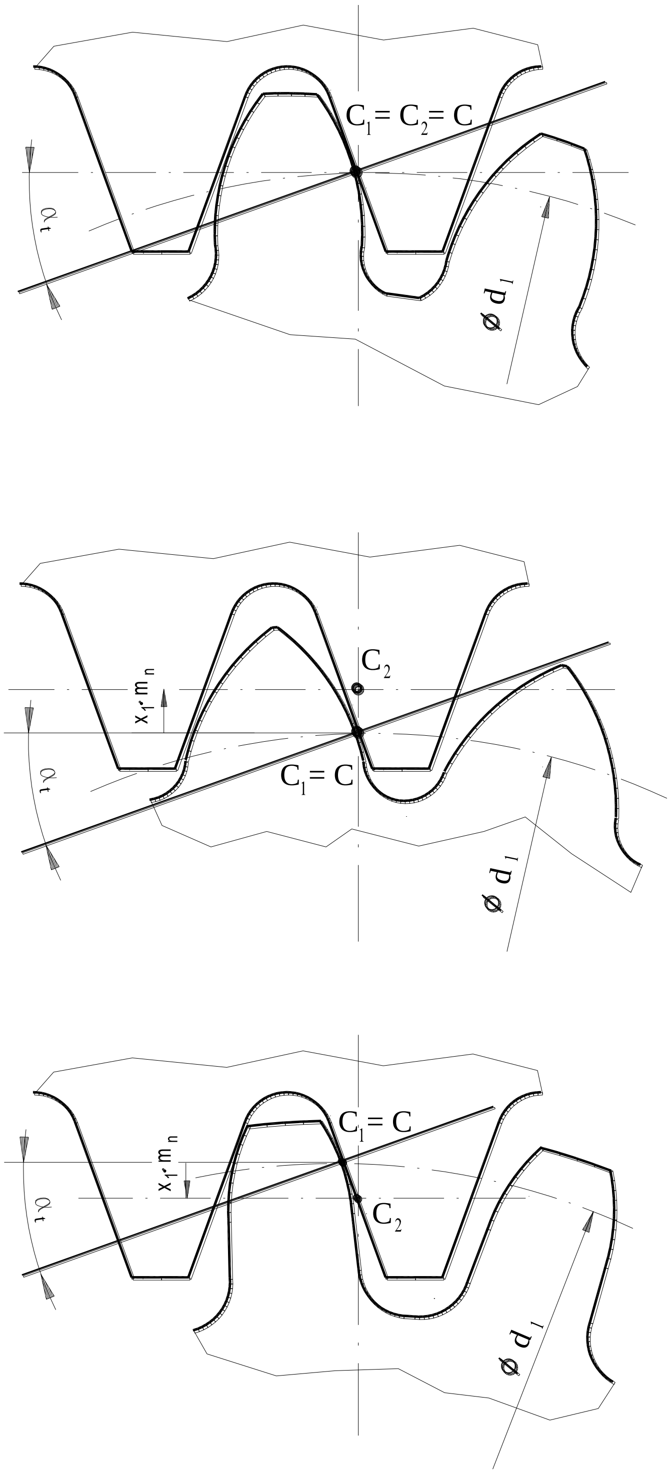

$x_1 = 0$
$O_1C = 0{,}5 \cdot d_1$
$O_1C_2 = 0{,}5 \cdot d_1$

$x_1 > 0$
$O_1C = 0{,}5 \cdot d_1$
$O_1C_2 = 0{,}5 \cdot d_1 + x_1 \cdot m_n$

$x_1 < 0$
$O_1C = 0{,}5 \cdot d_1$
$O_1C_2 = 0{,}5 \cdot d_1 + x_1 \cdot m_n$

Fig. 3

All important points at the rack tooth flank result from a mesh. They fully correspond with diameters of an ordinary wheel. Instead of diameters (infinitely big ones) heights parameters related to the reference line (point C_2) are used. There are basic dimensions on the fig. 4. Their nomenclature follows. Corresponding wheel nomenclature is in parentheses.

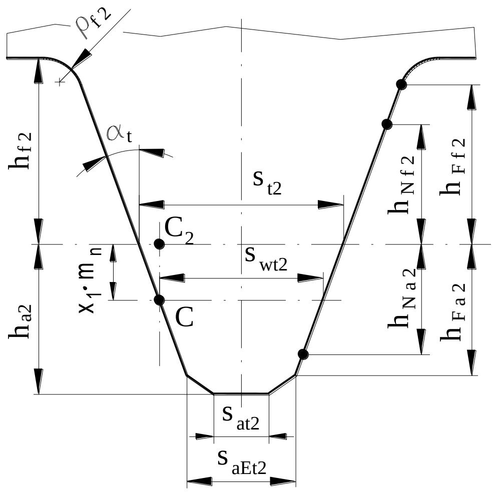

h_{f2} – root height (root diameter)
h_{Ff2} – root form height (root form diameter)
h_{Nf2} – usable root height (usable root diameter)
h_{Na2} – usable tip height (usable tip diameter)
h_{Fa2} – tip form height (tip form diameter)
h_{aE2} – generated height, usual the same as h_{Fa2} (generated tip diameter)
h_{a2} – tip height (tip diameter)
s_{t2} – transverse reference thickness
s_{wt2} – transverse pitch thickness
s_{aEt2} – transverse thickness at h_{aE2}
s_{at2} – transverse tip thickness

Fig. 4

INTERFERENCE

Interference also can occur during pinion – rack mesh. Either on the pinion's root or on rack's root. When a pinion is undercut one (or protuberantly undercut) the interference on pinion's root cannot occur. A rack cannot be undercut by common manufacturing. The undercutting of the rack appears only when it is protuberantly manufactured. And when the rack is protuberantly manufactured – interference cannot occur.

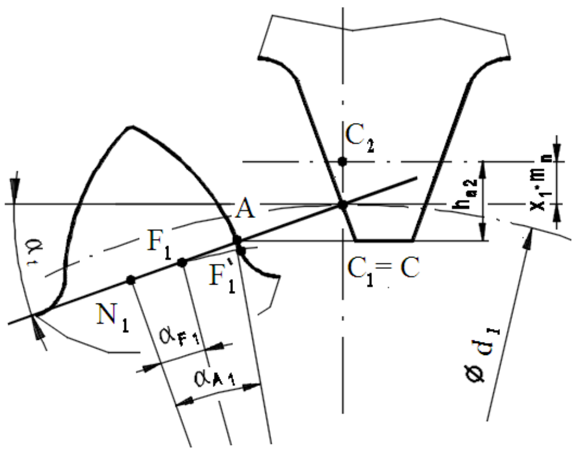

Interference on pinion's root

On the fig.5 relevant diameters goes through points -

F_1 (F'_1) – $\phi\ d_{F1}$ ($\phi\ d_{Ff1}$)
A_1 – $\phi\ d_{A1}$ ($\phi\ d_{Nf1}$)
C – $\phi\ d_1$
N_1 – $\phi\ d_{b1}$

Fig. 5

Interference on the pinion's root always occurs when it is valid for angles $\boldsymbol{\alpha_{A1} \leq \alpha_{F1}}$

Diameters d_1 , d_{b1} and d_{F1} which are defined by parameters of the pinion are easy to calculate. For diameter d_{A1} it applies –

$$AC = \frac{h_{a2} - x_1 \cdot m_n}{sin\alpha_t}$$

$$N_1A = 0{,}5 \cdot d_{b1} \cdot \tan \propto_t - AC \qquad (1)$$

$$d_{A1} = d_{Nf1} = 2 \cdot \sqrt{(0{,}5 \cdot d_{b1})^2 + (N_1A)^2} \qquad (2)$$

$$\alpha_{A1} = arccos\ \frac{d_{b1}}{d_{A1}} \tag{3}$$
$$\alpha_{F1} = arccos\ \frac{d_{b1}}{d_{F1}} \tag{4}$$

When chamfering of rack crests is used, instead of addendum height h_{a2} the height to do beginning of chamfering h_{aE2} (h_{Fa2}) is used. On the basis of equations 2,3 and 4 it is easy to enumerate the height h_{Na2} (point A joins with the point F_1 when a pinion is undercut).

Interference on rack's root

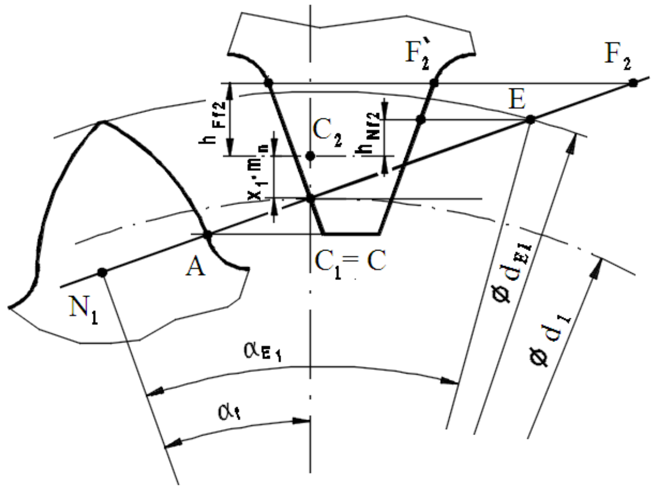

Fig. 6

Interference on the rack's root always occurs when it is valid $\mathbf{h_{Ff2} \leq h_{Nf2}}$

Diameters d_1, d_{b1} and d_{E1} which are defined by parameters of the pinion are easy to calculate. For height h_{Nf2} it applies –

$$N_1E = 0{,}5 \cdot d_{b1} \cdot \tan \alpha_{E1}$$

$$\alpha_{E1} = arccos\ \frac{d_{b1}}{d_{E1}} \tag{5}$$

$$CE = N_1E - N_1C = 0{,}5 \cdot d_{b1} \cdot (\tan \alpha_{E1} - \tan \alpha_t)$$

$$h_{Nf2} = CE \cdot \sin \alpha_t - x_1 \cdot m_n \tag{6}$$

When chamfering of pinion crests is used, instead of tip diameter d_{a1} for finding of diameter d_{E1} the diameter of beginning of chamfering d_{aE1} (d_{Fa1}) is used. It is also easy to enumerate diameter d_{a1max} at the interference limit. When rack is protuberantly undercut the interference cannot occur.

CONTACT RATIO

Transverse contact ratio ε_α is relation between length of a meshing line and transverse pitch on base diameter p_{bt}. Length of a meshing line is defined by points A and E as it is seen on the fig. 6. It applies that this length can be enumerate as $AE = N_1E - N_1A$. Where N_1A is in the equation (1).

$$N_1E = 0{,}5 \cdot d_{b1} \cdot \tan \alpha_{E1} = \sqrt{(0{,}5 \cdot d_{E1})^2 - (0{,}5 \cdot d_{b1})^2}$$

$$\varepsilon_\alpha = \frac{\mathrm{N_1E - N_1A}}{p_{bt}} = \frac{\mathrm{N_1E - N_1A}}{\pi \cdot m_n \cdot \cos \alpha_t} \cdot \cos\ \beta \tag{7}$$

Overlap ratio ε_β is enumerated consistently with ordinary helical gearings.

$$\varepsilon_\beta = \frac{\mathrm{b \cdot \sin \beta}}{\pi \cdot m_n} \tag{8}$$

RELATIVE SLIDINGS

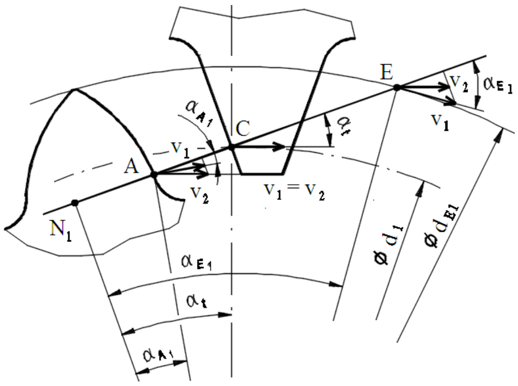

For rack applies that it has the same straight velocity v_2 in each point of the mesh. This figures out from a circumferential speed of the pinion at the reference circle. Both velocities are the same at the meshing point C and they have the same direction too

→ $v_1 = v_2$. See fig.7.

Fig. 7

For a relative sliding at pinion's root (point A) it applies for sliding velocities (perpendicular to the meshing line) –

$$\vartheta_{A1} = \frac{v_{1tA1} - v_{2t}}{v_{1tA1}} = \frac{v_1 \cdot \sin\alpha_{A1} - v_2 \cdot \sin\alpha_t}{v_1 \cdot \sin\alpha_{A1}} = \frac{r_{A1} \cdot \omega_1 \cdot \sin\alpha_{A1} - r_1 \cdot \omega_1 \cdot \sin\alpha_t}{r_{A1} \cdot \omega_1 \cdot \sin\alpha_{A1}}$$

After modifying –

$$\vartheta_{A1} = 1 - \frac{d_1}{d_{A1}} \cdot \frac{\sin\alpha_t}{\sin\alpha_{A1}}$$

Wheel's root (point E) –

$$\vartheta_{E2} = 1 - \frac{d_{E1}}{d_1} \cdot \frac{\sin\alpha_{E1}}{\sin\alpha_t}$$

Pinion's tip (point E) –

$$\vartheta_{E1} = 1 - \frac{d_1}{d_{E1}} \cdot \frac{\sin\alpha_t}{\sin\alpha_{E1}}$$

Wheel's tip (point A) –

$$\vartheta_{A2} = 1 - \frac{d_{A1}}{d_1} \cdot \frac{\sin\alpha_{A1}}{\sin\alpha_t}$$

Addendum modification coefficient for balanced specific slidings

To get the same relative slidings at pinion's and rack's roots (or tips) can apply by suitable choice of pinion's AMD (AMD for a rack is always zero). If relative slidings at roots are the same, relative slidings at tips are the same by themselves. Deriving is made for roots.

$$\vartheta_{A1} = \vartheta_{E2} \quad \rightarrow \quad 1 - \frac{d_1}{d_{A1}} \cdot \frac{\sin\alpha_t}{\sin\alpha_{A1}} = 1 - \frac{d_{E1}}{d_1} \cdot \frac{\sin\alpha_{E1}}{\sin\alpha_t}$$

$$(d_1 \cdot \sin\alpha_t)^2 - (d_{E1} \cdot \sin\alpha_{E1}) \cdot (d_{A1} \cdot \sin\alpha_{A1}) = 0$$

As far as gearing without undercutting, protuberance and chamfering think of, it is possible to use $d_{E1} = d_{a1}$. The diameter d_{A1} is derived from the rack's height h_{a2}, see fig 5 and equation (2).

$$d_{E1} = d_{a1} = d_1 + 2 \cdot (h^*_{a1} + x_1) \cdot m_n$$

$$d_{A1} = 2 \cdot \sqrt{\left(\frac{d_{b1}}{2}\right)^2 + \left(\frac{d_{b1}}{2} \cdot \tan\propto_t - \frac{h_{a2} - x_1 \cdot m_n}{sin\alpha_t}\right)^2}$$

After substitution –

$$(d_1 \cdot \sin\alpha_t)^2 - \left((d_1 + 2\cdot(h_{a1}^* + x_1)\cdot m_n)\cdot sin\left(arccos\,\frac{d_{b1}}{d_1 + 2\cdot(h_{a1}^* + x_1)\cdot m_n}\right)\right)\cdot$$
$$\cdot\left(2\cdot\sqrt{\left(\frac{d_{b1}}{2}\right)^2 + \left(\frac{d_{b1}}{2}\cdot\tan\propto_t - \frac{h_{a2} - x_1\cdot m_n}{sin\alpha_t}\right)^2}\right.$$
$$\left.\cdot\, sin\left(arccos\,\frac{d_{b1}}{2\cdot\sqrt{\left(\frac{d_{b1}}{2}\right)^2 + \left(\frac{d_{b1}}{2}\cdot\tan\propto_t - \frac{h_{a2} - x_1\cdot m_n}{sin\alpha_t}\right)^2}}\right)\right) = 0 \tag{9}$$

Although the resulting homogeneous nonlinear equation is extensive, its numerical solution is not difficult. For the sample solution is designed for a couple with a standard profile and with straight teeth, number of teeth of the pinion $z_1 = 20$.

For a pinion with no AMC the value of specific sliding at a root is extremely high –

f(x_1)

$x_1 = 0 \quad \rightarrow \quad \upsilon_{A1} = -5{,}890$

After calculation for balanced specific slidings (see fig. 8) –

$x_1 = 0{,}4429 \quad \rightarrow \quad \upsilon_{A1} = -0{,}909$

x_1

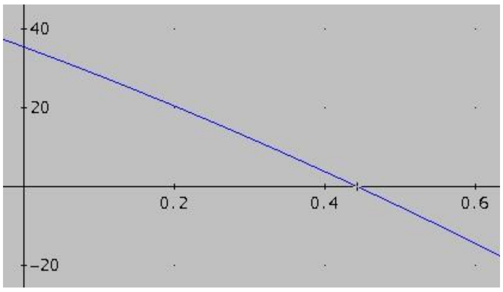

Fig. 8

CONCLUSIONS

Regard to the relatively widespread use of the racks in engineering it is helpful to use for the calculation of basic geometric and meshing parameters exact formulae. Substitution a rack along with a wheel with large number of teeth in the calculations is for many cases insufficient. In precision engineering (machine tools, measuring instr.), it is desirable to use precise calculations. This article presents them.

REFERENCES

1. Litvin, F., L., Fuentes, A.: *"Gear Geometry and Applied Theory."* Second Edition. CAMBRIDGE UNIVERSITY PRESS. ISBN 0-521-81517-7
2. Němček, M.: Návrhový výpočet pro ozubený hřeben. *Sborník mezinárodní XLIX. konference kateder částí a mechanismů strojů.* Str. 215-219. Srní 8. 9. – 10. 9. 2008. ISBN 978-80-7043-718-6.
3. Šalamoun, Č., Suchý, M.: "*Čelní a šroubová soukolí s evolventním ozubením.*" SNTL Praha 1990. ISBN 80-03-00532-9.

Corresponding author: Prof. Ing. Miloš Němček, Csc., Department of Machine Parts and Mechanisms, VŠB-TU Ostrava

THE CONCTACT ANALYSIS OF DESIGNING THE CAM MECHANISM BY USING ANSYS

Ha NGUYEN VAN[1], L. ŠEVČIK[2]

[1,2]Department of Design of Machine Element and Mechanism, Faculty of Engineering, Czech Technical University of Liberec, Studentska 1402/2, Liberec I, 461 17, Czech republic

Abstract
A cam mechanism is used to transmit rotary motion between two concentric shafts which was built by CATIA V5-R16 software. In this model, the cam mechanism is composed by rotary input cam shaft, a rotary output cam shaft, a middle part and two balls and a frame to mount all the parts. Due to the contact between the balls with their grooves on each part of the cam mechanism is very important, it could directly affect the lifespan and working ability of the structure. This paper mainly focuses on the determination of contact stress between the balls and straight grooves on output cam shaft, middle part as well as circular groove on the input camshaft by using fine element analysis. Through contact analysis, the changes could be shown in stress, strain, penetration, friction stress among the groove of the input, output, middle part and balls. Furthermore, the simulation results revealed that the computational values were consistent with theoretical values. It would provide a scientific basis for optimum design of the cam mechanism.

Key words: *cam mechanism, ball transmission, contact analysis, ANSYS.*

INTRODUCTION

Cam mechanisms are widely used in many types of modern machines because of their excellent property for operation speed, motion accuracy, structural rigidity and low production cost. Generally, cam mechanism used steel balls to transmit rotary motion between two concentric shafts, the main function of the balls is the transmission of forces and motion from the input cam shaft into the output cam shaft. So, when cam works each ball can be easily to move up and down with respect to their straight groove on the output cam shaft and middle part correspondingly. Moreover, these balls must move along with the circular groove on the input cam shaft. Therefore, the surface contact between the balls with their grooves is always changing when cam working. This contact phenomenon could be caused to make the balls can damage easily and result is failure of these balls [1, 5]. Therefore, in this work to study the stiffness, contact stress and deformation of the balls to optimize the cam mechanism.

Contact finite element analysis can show the information of the cam mechanisms under contact stress, strain, penetration and so on, which play a significant role in the optimum design of cam mechanism. Therefore, analysis of contact problem is a major concern in many engineering applications such as ball bearing, gears and pressure vessel attachment. The numerical modeling of practical contact problems requires special attention because the actual contact area between the contacting bodies is usually not known in advance. With the change of load, material, boundary condition or the other factors, touch or separation will take place between the surfaces. That is hard to predict, even is a abrupt change. Most frictional effects on the contact problems are needed to be considered. It may be disordered as well as nonlinear. So, ANSYS gives a good blue print for contact analysis which can take friction heat and electrical contact into account. It also has special contact guide which is conveniently for creating contact pairs. The internal expert system of contact analysis does not require any settings of related contact parameter in a general contact analysis. So, it can easily establish the contact analysis. This work is to study the contact between the balls and the grooves in the cam mechanism. Therefore, the mechanism has designed as an example and it discussed about the contact and built its finite element 3-D parameterized model by using Finite Element Analysis software ANSYS Workbench 18 and CATIA V5-R16. Based on these results, the nonlinear contact state was researched and analyzed.

MATERIAL AND METHODS

Assume that contact between the ball and circular groove is like contact of a sphere on a sphere and contact between the ball and straight groove is like contact of a sphere on a plat-plate. Hertz elastic contact theory has solved the calculation problems of contact stress and deformation of the balls and their grooves of the cam mechanism designed successfully. It used to make following assumptions to solve the contact shape and dimension and surface pressure distribution of elastic solids. The first, the objects contact with each other which only produce elastic deformation obey Hook's law. The second, the contact surface is smooth, which only have the effect of the normal force. The third, contact size is much smaller than the size of curvature radius of the contact bodies' surface. Contact problem of ball and groove basically corresponds with the Hertz assumption [2].
The basic steps in the cam mechanism's contact analysis are performed. In contact problem involved two boundaries, it is natural that take on boundary as target surface and take the other on as contact surface. Surface-surface contact is very suitable for those problems just as: interference fitting installation, or embedded contact, forging and deep-drawing. Surface-surface contact's analysis has many steps which include:

1) Build 3D geometry model and mesh;
2) Identify contact pairs;
3) Name target surface and contact surface;
4) Define target surface;
5) Define contact surface;
6) Set up element key options and real constants;
7) Define and control rigid goal's movement(only applicable in rigid-flexible contact);
8) Apply the necessary boundary condition;
9) Define solution options and load steps;
10) Solve contact problems, and look over and analyze results.

ANSYS software supports the surface contact element of rigid-flexible or flexible-flexible. The elements form contact pairs by using target and contact surface. For the rigid-flexible contact, it can be chosen as contact surface such as convex surface, dense meshing or little size surface, otherwise chosen as target surface. Under the condition that the model should be simplified as far as possible, so that the computational time could be reduced, simply and accurately reflects the mechanical property of the solid model. By use of CATIA the model is built (see Fig 1 a) [3, 4] and imported into ANSYS. In theory, it is feasible that model can be changed, such as material property, retrained displacement and applied load, and so on. Therefore, in this case the cam mechanism model which is created and imported into ANSYS without frame and bearings part. So, now the cam mechanism in ANSYS workbench is composed of the input cam shaft, output cam shaft, middle part and balls (see Fig 1b). The material of all parts made by steel, the elasticity model is 2 E5 MPa, the Poisson's ratio is 0.3. The meshing type is free, element size is set 0.5 mm for each contact pairs are shown in Fig 1 c.
In this work, the contact pairs are frictional between ball, groove and so on. Taking separately the groove surface of the input cam shaft, output cam shaft and middle part as target surface and taking correspondingly sphere surface of the balls as contact surface, two contact pairs can be built. It is necessary that to make sure the contact is rigid-flexible contact between balls and groove of each part, to set 0.15 as frictional factor value. Next step to set boundary condition and apply loads: Boundary condition restrained the all degrees of freedom(DOF) of the middle part (fix support), added frictionless support constraint to the input and output cam shaft, and applied moment load to the input cam shaft is given 1000 N.mm.

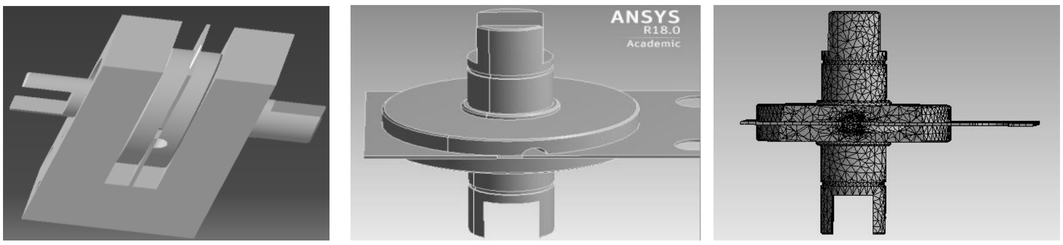

a b c

Fig. 1 (a) Cam mechanism assembly model, (b) the imported model in Ansys, c) meshed model

RESULTS AND DISCUSSION

According to the result was made by ANSYS, the phenomenon would be found that, the contact change status can be given, such as contact stress, strain, penetration, contact pressure among the input, output cam shaft and the balls, middle part.

Fig. 2 a, b shows von-Mises total strain. The biggest total displacement and strain of cam mechanism respectively is 0.03 mm, 0.01 mm. The bigger contact displacement mainly concentrated on the balls, and the straight groove of the output cam shaft.

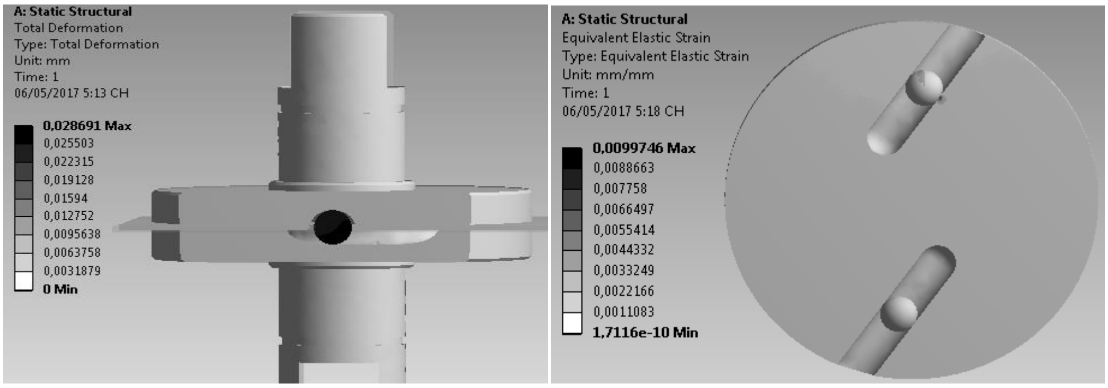

a b

Fig. (2a) Deformation cam mechanism, (2b) equivalent strain cam mechanism

From Fig 3, it is victimized that the contact area had an approximate ellipse shape in contact area of the balls and the grooves, which was consistent with the Hertzian contact theory.

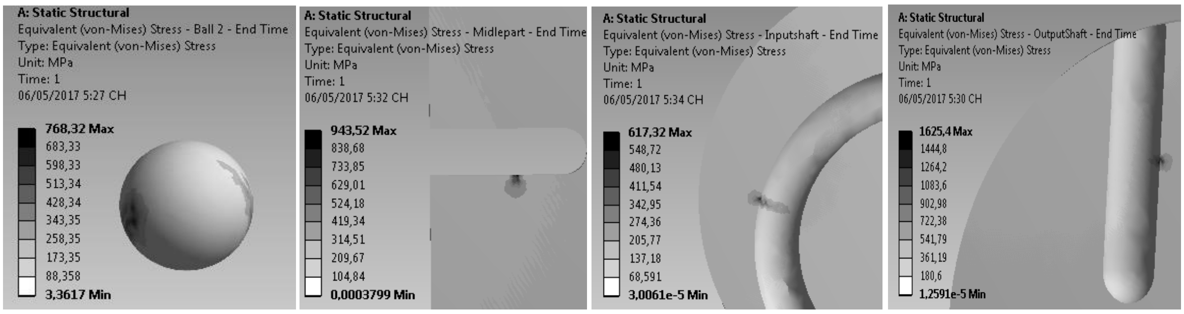

a b c d

Fig. 3 Equivalent stress of cam mechanism, (a) view on ball, (b) view on the groove of the middle part, (c) view on the circular groove of the input shaft, (d) view on the straight groove of the output shaft.

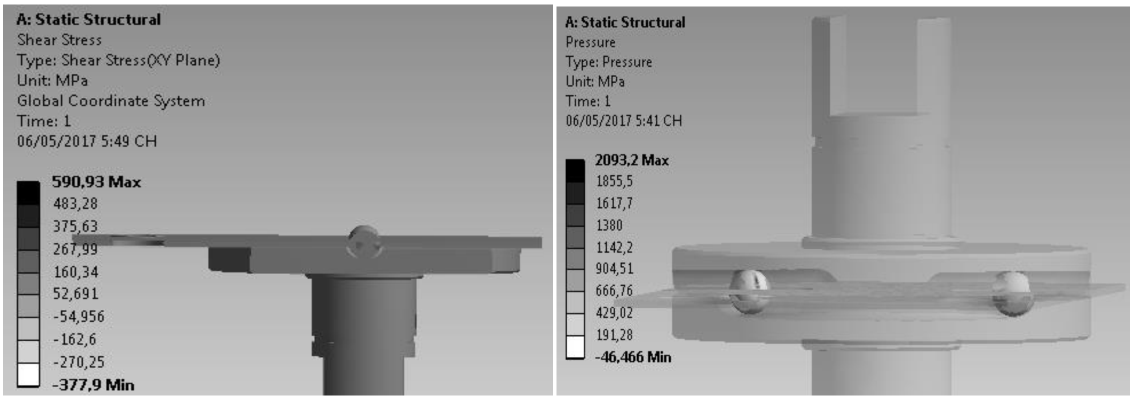

a b

Fig.4(a) Shear stress cam mechanism, (b) pressure stress cam mechanism.

Fig 4 shows the simulation of the calculation results of the maximal contact shear stress and contact pressure was 590 MPa, 2093 MPa respectively, while the Hertzian theory value was 651 MPa, 2100

MPa [3, 4]. The comparison revealed that there was good consistency between the Hertzian theory solution and finite element solution.

CONCLUSIONS

By using ANSYS 18 software to numerically simulate and analyze the stress and strain during cam mechanism contacts, the fine element solutions were shown the results, which had good consistency with the Hertzian theory. The contact analysis of finite element method can easily and intuitively get the stress and strain value as well as their cloud imagery, which can efficiently understand the parts running information, such as contact penetration, contact stress also. The results could provide a few of original ideas and would have a significant assistance for the life-design and structural optimum about cam mechanism.

ACKNOWLEDGMENT

In this occassion we would like to thank, Technical University of Liberec for providing the fund for this work under the project "Innovation of products and equipment in engineering practice" with the support of the specific University Research Grant, as provided by the Ministry of Education, Youth and Sports of the Czech Republic for the year of 2017.

REFERENCES

1. Gopalakrishnan, T., Ruban, M. (2015). Contact analysis of roller bearing using finite element method. Vels Journal of Mechnical Engineering,Vol-2, 30-33.
2. Norton, R. L.(2006). Machine Design an integrated approach, third edition. Pearson. ISBN 013-202012-2.
3. Nguyen Van, H., Sevcik, L. (2016). Designed calculation of the cam mechanism for transmission between two concentric shafts. In ICMD2017 57th International conference of Machine Design Departments (pp.137-140). ISBN 978-80-261-0609-8.
4. Nguyen Van, H., Sevcik, L. (2017). Apply steel balls for designing the Cam mechanism. Proceeding of 22 nd International Conference Mechanika (pp. 118-121). ISSN 1822-2951.
5. Tang Zhaoping, Sun Jianping. (2011). The contact analysis for deep groove ball bearing based on anasys. International Conference on Power Electronics and Engineering Application (pp. 423-428).

Corresponding author:
Ing. Ha Nguyen Van, Department of Design of Machine Elements and Mechanism, Faculty of Engineering, Czech Technical University of Liberec, Studentska 1402/2, Liberec I, 461 17, Czech republic, phone:+420485353318, e-mail: nguyenha.hut@gmail.com
Ing. Ladislav Sevcik, Prof. Department of Design of Machine Elements and Mechanism, Faculty of Engineering, Czech Technical University of Liberec, Studentska 1402/2, Liberec I, 461 17, Czech republic, phone:+420485353316, e-mail: ladislav.sevcik@tul.cz

58th ICMD 2017
6 - 8 September 2017, Prague, Czech Republic

KINEMATIC SIMILARITY OF ROLLING BEARINGS WITH PLANETARY GEARS – A REVIEW

Michael OELJEKLAUS[1], Lubomír PEŠÍK[2]

[1]Škoda Auto a. s. Mladá Boleslav & Faculty of Mechanical Engineering, Department of Machine Parts and Mechanisms, Technical University of Liberec, Czech Republic
[2]Faculty of Mechanical Engineering, Department of Machine Parts and Mechanisms, Technical University of Liberec, Czech Republic

Abstract
The knowledge of the bearing kinematics is very important for their diagnostics. There are more methods to determine the number of revolutions of all bearing components. It is necessary to know their values for the solving of diagnostic problems. The first method is based on the same tangent velocity of contact points of the bodies. The second one is much more transparent and is based on theory of planetary gears.

Key words: *bearing diagnostics, bearings kinematics, bearings damages, slowly running bearings.*

INTRODUCTION
The kinematics of rolling bearings (Fig. 1) falls into the area concerning simultaneous planar motions of bodies.

Fig. 1 Rolling bearings (ball and roller bearings)

They are described in elementary form by basic motion 21 and relative motion 32. The basic motion means the motion of carrier 2 relative to frame 1, and the relative motion means the motion of body 3 relative to carrier 2. In the plane, there are four combinations of elementary simultaneous motions of bodies 3 (translation-translation, translation-rotation, rotation-translation and rotation-rotation).
Kinematics of rolling bearings, in this sense, falls into the area of two simultaneous rotations.

KINEMATICS OF PLANETARY MECHANISM
In kinematics rolling, bearings represent a planetary gearing, in which the planet carrier is formed with a cage, and the rolling elements are planets (Fig. 2). This analogy allows the use of a variety of procedures well known from the theory of planetary gearing.
While carrier 2, wheels 4 and 5 with the central axis of rotation perform rotary motion, satellite 3 performs two simultaneous rotations around its axis and together with carrier 2 and rotation around the central axis of rotation.
For the description of kinematics of individual bodies bearing, it is possible to use methods that are used with kinematics of planetary gears. It is possible to use two methods, where with the character , there are described semi-diameters of several bearing components.
The first one is based on the conditions of rolling, and on equal peripheral velocity in respective contact points, which are the poles of relative motions.
The second method is based on substitution of planetary gear for countershaft gear. This substitution lies in conceptual stopping of the carrier. In such a case, an observer on the carrier can see how the gear rotates with relative velocity to the carrier. Then, the gear ratio can be expressed as the ratio of the relative angular velocity. Thus, the kinematic linkage of gearing is defined.

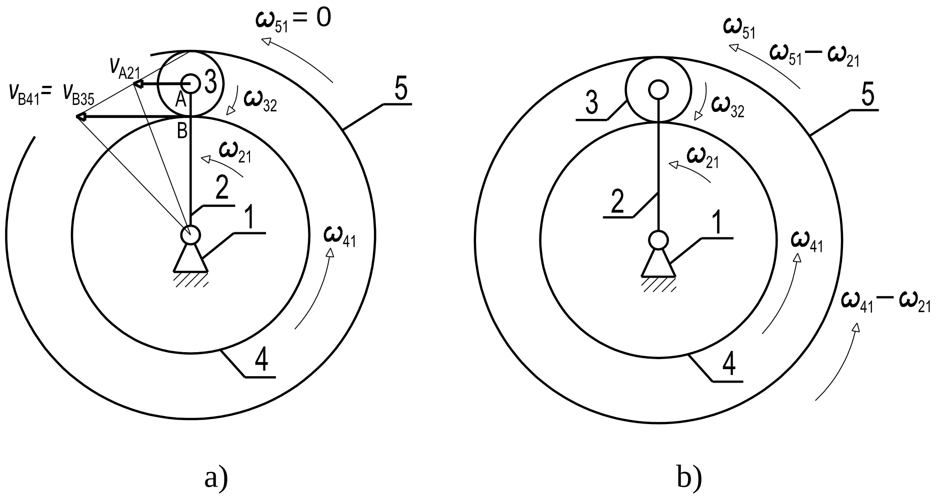

Fig. 2 Kinematics of planetary gearing with the help of rolling conditions

The angular velocity of any part of the gearing can be determined from such a linkage.
The first procedure is illustrated in Fig. 2a. When the gear 5 is not in motion and gear 4 is a driving gear, it applies that the tangential velocities

$$v_{B41} = v_{B35} \,. \tag{8}$$

Then

$$r_4\omega_{41} = 2r_3\omega_{35} \,. \tag{9}$$

Further

$$v_{A21} = \frac{v_{B41}}{2} \tag{10}$$

and from that

$$\omega_{21} = \frac{r_4}{2r_2}\omega_{41} = \frac{r_4}{r_4 + r_5}\omega_{41} \,. \tag{11}$$

To determine ω_{32}, basic decomposition can be used for velocity of point B

$$v_{B32} = v_{B35} + v_{B52} \tag{12}$$

And after substitution

$$r_3\omega_{32} = 2r_3\omega_{35} + (r_2 - r_3)\omega_{52} \,. \tag{13}$$

If we consider that

$$2r_3\omega_{35} = r_4\omega_{41} \tag{14}$$

And that ω_{52}, is

$$\omega_{52} = \omega_{51} - \omega_{21} \,. \tag{15}$$

We get

$$r_3\omega_{32} = r_4\omega_{41} - (r_2 - r_3)\omega_{21}. \tag{16}$$

And after the substitution of ω_{21}

$$r_3\omega_{32} = r_4\omega_{41} - (r_2 - r_3)\frac{r_4}{r_4 + r_5}\omega_{41}\,, \tag{17}$$

if

$$r_2 = r_4 + r_3 \tag{18}$$

we get for ω_{32}

$$\omega_{32} = \frac{r_5}{r_3}\frac{r_4}{r_4 + r_5}\omega_{41}\,, \tag{19}$$

which is the angular velocity of satellite 3 to carrier 2.
The method for calculating the angular velocity of planetary gear with the help of its substitution for countershaft gear is significantly shorter and the outcome more effective, especially in more complicated cases where the planetary gearing is combined. The essence of this method is shown again on an example of simple planetary gearing (Fig. 2b).
After definition of the positive senses of angular velocities of all parts of the gearing, which in this case is a differential (two degrees of freedom), we accede to the substitution of the planetary gearing for countershaft gearing, by imagining our position as an observer on the carrier. This way the carrier's motion towards us was stopped, although the kinematics of gears was not changed. The motion of the parts of the gearing is relative towards the carrier.
It is possible to compute the gear ratio of the relative angular velocity of any two parts of such defined countershaft mechanism. For example, the gear ratio of the relative angular velocity between gears 4 and 5 is

$$\frac{\omega_{41} - \omega_{21}}{\omega_{51} - \omega_{21}} = \frac{r_3}{r_4}\left(-\frac{r_5}{r_3}\right) = -\frac{r_5}{r_4}, \tag{20}$$

of which for $\omega_{51} = 0$ is

$$\omega_{21} = \frac{r_4}{r_4 + r_5}\,\omega_{41} \tag{21}$$

or similarly between gears 4 and 3 is,

$$\frac{\omega_{41} - \omega_{21}}{\omega_{32}} = \frac{r_3}{r_4} \tag{22}$$

and finally between gears 3 a 5 is

$$\frac{\omega_{32}}{\omega_{51} - \omega_{21}} = -\frac{r_5}{r_3}, \tag{23}$$

of which

$$\omega_{32} = \frac{r_5}{r_3}\frac{r_4}{r_4 + r_5}\omega_{41}\,. \tag{24}$$

It needs to be mentioned that angular velocity of planet 3, ω_{32}, is determined as relative to the carrier 2 considering that planet 3 has a different axis of rotation than the carrier and other parts of the planetary gearing.
If we use $\omega_{51} = 0$ in formulas (21) and (24) above, angular velocity ω_{21} of carrier 2 and angular velocity ω_{32} of planet 3 around the journal of the carrier 2 will be the same as in equations (11) and (19).
The planet gearing may be suitably combined to create gearing with the desired kinematic linkage. In some cases, double planets are used. However, in relation to the kinematics of the roller bearings it does not have adequate importance.

CONCLUSIONS

The kinematics of rolling bearing is necessary to be known for their diagnostics. The angular velocities determine frequencies in a frequency spectrum where damages of bearing parts can be monitored. The damage of the rolling body can be observed by the frequency dependent on angular velocity ω_{32}. The damage of the inner ring has its frequency which is given by number of rolling bodies and relative angular frequency $\omega_{41} - \omega_{21}$. The damage frequency of the outer ring is determined by number of rolling bodies and the angular velocity ω_{21}. The mentioned results are valid relative exact in the cases of slowly rolling bearings, but by fast running bearings, there it is necessary to calculate with slip between rolling bodies and inner or outer ring.

ACKNOWLEDGMENT

This publication was written at the Technical University of Liberec as a part of project "Innovation of Products and Equipment in Engineering Practice" with support of a Specific University Research Grant, provided by the Ministry of Education, Youth and Sports of the Czech Republic in 2017.

REFERENCES

1. Beneš,Š., Tomeh, E. (1991). *Metody diagnistiky valivých ložisek.*
2. Pešík, L. (2015). *Části strojů, 1. díl*. Technická univerzita v Liberci.
3. Pešík, L. (2015). *Části strojů, 2. díl*. Technická univerzita v Liberci.
4. Helebrant, F., Ziegler, J.: *Technická diagnostika a spolehlivost II – Vibrodiagnostika.* VŠB – TU Ostrava, Ostrava 2004, 1. vydání, 178 s., ISBN 80 – 248 – 0650 – 9.
5. Randall, R. B. (1987) *Frequency Analysis*, Denmark: Brüel&Kjær.
6. Němeček, P., Tomeh, E. (2010). *Vibrační diagnostika základních závad strojů*. Technická univerzita v Liberci.
7. Tomeh, E. (2007). *Diagnostic Methodology of Rolling Element and Journal Bearings.* Technická univerzita v Liberci.ISBN 978-80-7372-278-4.

Corresponding author:
Dipl.-Ing. Michael Oeljeklaus, Škoda Auto a. s. Mladá Boleslav & Technical University of Liberec, Faculty of Mechanical Engineering, Department of Machine Parts and Mechanisms, Czech Republic, Studentská 2, Liberec 1, Czech Republic, e-mail: michael.oeljeklaus@skoda-auto.cz

THE GROWTH OF CONTACT AREA OF THE TOOTH IN DEPENDING OF INCREASING THE LOADING

Jan PAVLÍK[1], Jiří ZAČAL[2], Jaroslav PROKOP[3], Zdeněk FOLTA[4]

[1]Department of Machine Parts and Mechanisms, VŠB-TU Ostrava
[2]Department of Machine Parts and Mechanisms, VŠB-TU Ostrava
[3]Department of Machine Parts and Mechanisms, VŠB-TU Ostrava
[4]Department of Machine Parts and Mechanisms, VŠB-TU Ostrava

Abstract
The article deals with measuring contact area of the tooth of helical gearing depending on increasing load. Overall contact area of the tooth has big influence on vibration and noise of gearing. The result is finding correlation between contact area of the tooth and the loading.

Key words: *helical gearing; footprints; involute gearing; gear wheels; vibration; noise.*

INTRODUCTION

The transmission of the torque in the gearbox is realized by meshing of helical gears. The teeth of the gear wheels fit together and thanks to attend they transfer the torque. However, in real operation it is very difficult to achieve that the contact of the tooth flanks is accurately through all surface. As the transmitted torque causes deformation on the individual components of the entire gearbox (shafts, tooth, gear case, etc.). All of these factors then causes that the contact of tooth flanks is not provide all his surface but only specific part of the tooth flanks. Therefore, the geometry of the tooth is modified in such a way that it will deliberately change its shape against the direction of all acting deformations so that the subsequent loading of the gearbox causes the deformations to be eliminated and the contact of the tooth flanks is higher than contact of the tooth flanks without modification *(Moravec, 2001; Mark, 2013).*These modifications go hand in hand with the level of radiated energy in the form of noise. Acoustic emission of gearbox is a very important factor, especially when designing gearboxes for the automotive industry *(Tůma, 2014)*. Gearbox noise reduction is antagonistic with weight reduction. This results in a number of negative factors. The main thing is that the gear case does not absorb radiant acoustic energy and so the noise more penetrates the surroundings. Therefore, a number of modifications are made to the tooth flanks to keep the contact area of tooth as large as possible while as little radiated acoustic energy as possible.

MATERIALS AND METHODS

The basic idea is that maximum tooth contact area radiates the least acoustic energy *(Tůma, 2014)*. For these studies, four pairs of toothed wheel sets were produced. On each of them were manufactured different modifications on tooth flanks. These modifications are intended to provide better growth of the tooth flanks contact area in the context of increasing the loading. Realization was performed on the test gearbox. In the gearbox was created hole for application identification layer on the tooth flanks and for photography of the results. Creation of identification layer was performed by special color. On the tooth flanks was applied by using a brush. Special color called: "Gear marking compound" is able created very thin layer of the color which don't change properties during the time. Layer of color is also very sensitive because is easy wipe it. The place on the tooth flank where is layer of color removed indicates real contact of teeth *(Pavlík, 2016)*. The gearbox with modified gears was placed in testing device. Testing device is able created different loading condition of torque. So on the tooth flanks was applied thin layer of color, on the testing device was set a torque and after that was turn on the testing device. Tested modified gear wheels created several of rotation and where tooth flanks in contact so identification layer was removed. After that was footprints on the tooth flanks photographed. This process was carried out on several load torque levels (0, 30, 50, 70, 100 Nm) and also for all four modified toothed wheel sets. At the same time this method verifies the correctness of created geometrical modifications on the toothed wheel sets. All created photography were in special software modified. The real places with contact of tooth flanks depending on different loading of torque are illustrated on figure (Fig. 1). For easier reading of footprints were photos redrawn.

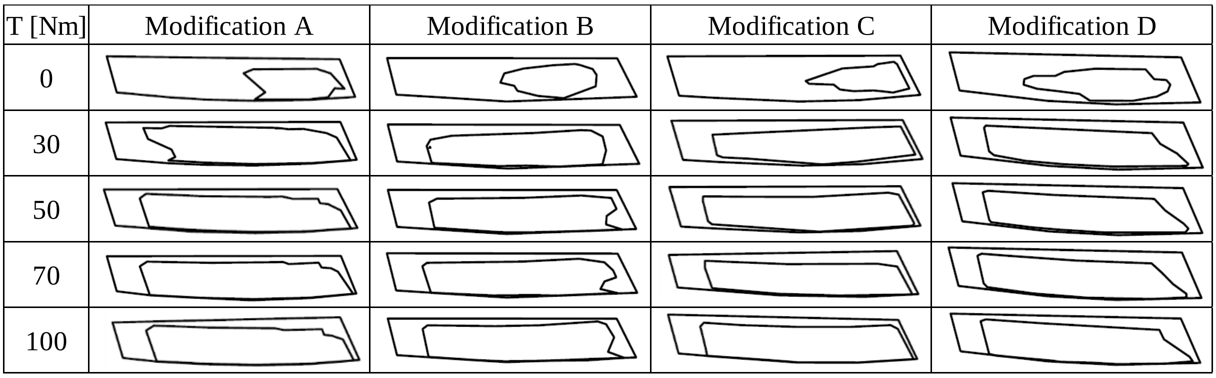

Fig. 1 Comparison of footprints created on gear wheels with different geometry modification

The redraw photographs give a clear view of the tooth modification and their dependence on the increasing loading of torque. Selected modifications which were used on four different toothed wheel sets are governed by generally known rules. Basically the modifications takes into account the initial position of footprints in the center of the tooth up to its edge. For these four different modifications were also measured average sound pressure. Results are shown in the next table (Tab. 1).

Tab. 1 Average sound pressure of different tooth modification

	Modification A	Modification B	Modification C	Modification D
Avg. sound pressure [dBA (20μPa)]	33,84	34,90	31,83	38,42

Measurement of acoustic pressure was for this case of study taken as supplementary information. The main point of these study is finding a correlation between the tooth contact area and increasing loading.

RESULTS AND DISCUSSION

In the special software were measured surfaces of created footprints from all four different toothed wheel set modifications. Results are shown in next table (Tab.2).

Tab. 2 Measured tooth flanks contact area

Torque [Nm]	Modification A [kpx]	Modification B [kpx]	Modification C [kpx]	Modification D [kpx]
0	780,39	772,96	631,24	1063,54
30	2030,54	1768,33	1929,63	1965,27
50	2170,13	1951,36	1955,43	2047,94
70	2214,99	1968,82	2070,19	2122,05
100	2323,28	2143,59	2339,72	2226,38

Showed values are in kilo-pixels because surfaces were evaluated from photos. So it was assessed how many pixels are located on the surface of the tooth flanks which are touching each other. This measurement method relatively simple and accurate. For clear view was created graph tooth contact area dependence on torque (Fig.2).

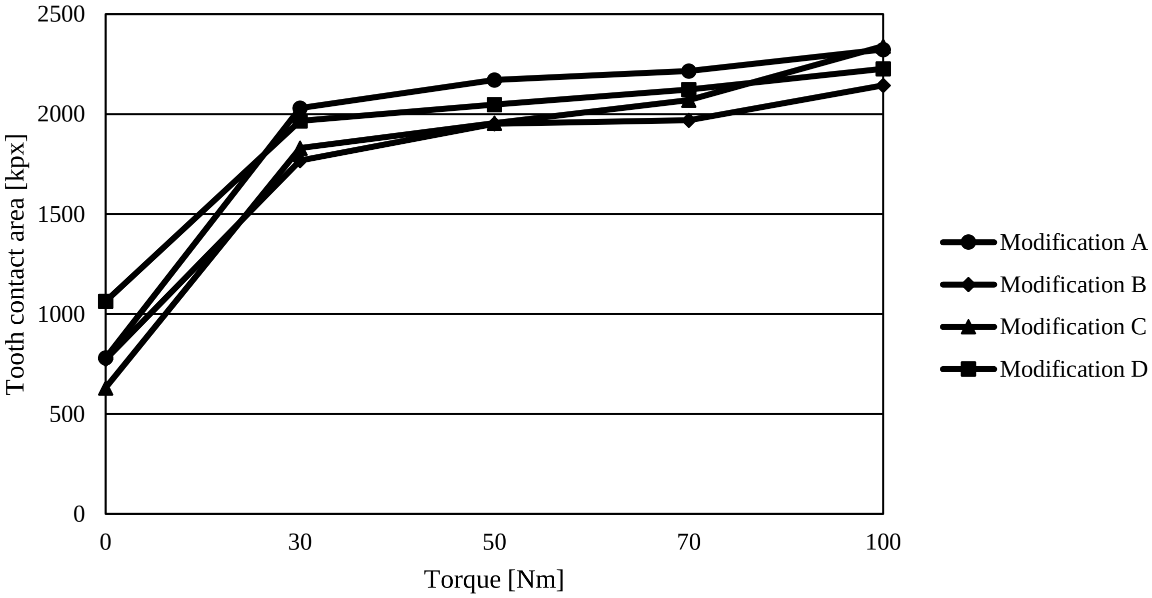

Fig. 2 Measured data of increasing tooth contact area depending on torque

The basic idea of this study was whether the growth contact surface of the tooth flanks is linear but graph (Fig. 2) clearly say that not. Is clear from the graph that course of surface growth is practically the same for all four modifications and also that the quietest toothed wheel set started from smallest surface area to largest surface area. More information is practically impossible to read. But when we compare the initial position of footprints and his appearance with average sound pressure, we see that in this test gearbox probably occurs a significant deflection of the shafts. Because the best result have Modification C with the initial position of footprints on the edge (only 31,83 dBA). This finding totally destroy all general recommendations regarding the appearance and position of contact surfaces on the tooth flanks. The general rule says that the footprint should extend evenly to all sides and that the edge touch is wrong *(Moravec, Deil, Němček, Folta, & Havlík, 2009)*. In this case is visible that edges contact can occur but only in low loading of torque. Of course that nevertheless immediately with increasing loading of torque must also increase contact area of teeth toward the opposite side. This assumption should be the subject for further investigation that would confirm the correlation between the growth of contact area and the deflection of the shafts.

CONCLUSIONS

The aim of this study was to find the growth of the contact area of the tooth in the depending of increasing the load. This study is basically experiment because is very difficult to find information in the literature and scientific articles that would serve as a good background. In the commonly available literature, problems are described very well, but only in general. For measuring contact surfaces was manufactured four toothed wheel sets. On their tooth flanks were made different geometrical modifications. This modification changes the initial position of the contact area and his overall size. On the testing device were created real contact area of tooth flanks at various values of loading torque. Created footprints were photographed and measured. Also for this four different toothed wheel sets were measured average sound pressure. All of these data were analysed and correlated. A simple general finding of the correlation between the tooth contact area and the loading has failed completely because from the graph (Fig. 2) is practically impossible anything to read. But comparison the initial position of footprints and his appearance with average sound pressure shown that the test gearbox probably have a significant deflection of the shafts. This idea shows fact that Modification C has initial position of contact on the edge with lowest overall average sound pressure. For future study of factors generating noises and vibration of the gearing, should be taken into account fact with the shafts deflection.

ACKNOWLEDGMENT

This research has been realized using the support of Technological Agency, Czech Republic, programme Centres of Competence, project # TE01020020 Josef Božek Competence Centre for Automotive Industry. This support is gratefully acknowledged.

REFERENCES

1. Mark, W. D. (2013). *Performance-Based Gear Metrology: Kinematic-Transmission-Error Computation and Diagnosis.* Pennsylvania : John Wiley & Sons, Ltd.
2. Moravec, V. (2001). *Construction of Machines and Equipment II: Spur Gears: Theory, Calculation, Design, Production, Inspection.* Ostrava: MONTANEX.
3. Moravec, V., Deil, Z., Němček, M., Folta, Z., & Havlík, J. (2009). *Spur gears in gearboxes of vehicles.* Ostrava: MONTANEX.
4. Pavlík, J. (2016). *Measurement of Gears Footprints.* Ostrava: VŠB - TU Ostrava.
5. Tůma, J. (2014). *Vehicle Gearbox Noise and Vibration: Measurement, Signal Analysis, Signal Processing and Noise Reduction Measures.* Chichester: John Wiley & Sons Ltd.

Corresponding author:
Ing. Jan Pavlík, Department of Machine Parts and Mechanisms, Faculty of Mechanical Engineering, VŠB – Technical University of Ostrava, 17. listopadu 15/2172, Ostrava - Poruba, 70833, Czech Republic, phone: +420 775698212, e-mail: jan.pavlik.st@vsb.cz

INDICATION OF FUNCTIONAL DIMENSION ACCORDING ISO GPS – HOW SHALL WE APPLICATE?

Karel PETR[1]

[1]*Department of Designing and Machine Components, Faculty of Mechanical Engineering, Czech Technical University in Prague.*

Abstract
The ISO GPS (Geometrical Product Specifications) define an internationally uniform description language, that allows expressing unambiguously and completely all requirements for the micro and macro geometry of a product with the corresponding requirements for the inspection process in technical drawings, taking into account current possibilities of measurement and testing technology. On the drawing are indicated many specifications (dimensions, geometrical tolerances …) on many features and not always correctly. Current practice in many companies – many function specification on drawing. Not all specifications in drawing are functional specification! For example are 250 specifications in the drawing, and 200 are functional specification. Here are questions to think about: How many functional specifications are needed? How shall we specification applicate?

Key words: *feature of size; GPS; standard; deviations; longitudinal specification; geometrical specification.*

INTRODUCTION

Engineering drawings without longitudinal tolerances, roughness, geometrical tolerances and datums or datum systems are in most cases incomplete, ambiguous, and therefore not unambiguously interpretable. The incomplete, ambiguous tolerancing of components in engineering drawings causes not only increased production and inspection costs but also makes impossible reasoned complaints of shortcomings and ultimately lead to an incalculable liability risk in the case of legal disputes. Therefore the designers and metrology engineers must have good knowledge on ISO GPS and verification methodology which ought to be given during studies or refreshed and supplemented by specialized training courses on the new standards.
ISO default specification operators and number of fundamental principles that apply to all GPS standards and technical product documentation are indicate in fundamental ISO GPS standards (ISO 8015, 2011). Each ISO GPS standard is placed in ISO GPS matrix model (see Fig. 1).

ISO 14638:2015 ISO GPS Standards matrix model	Chain links						
	A	B	C	D	E	F	G
	Symbols and indications	Feature requirements	Feature properties	Conformance and non-conformance	Measurement	Measurement equipment	Calibrations
Size	X	X	X	X	X	X	X
Distance	X	X	X	X	X	X	X
Form	X	X	X	X	X	X	X
Orientation	X	X	X	X	X	X	X
Location	X	X	X	X	X	X	X
Run-out	X	X	X	X	X	X	X
Profile surface texture	X	X	X	X	X	X	X
Areal surface texture	X	X	X	X	X	X	X
Surface imperfections	X	X	X	X	X	X	X

Fig. 1 Position in ISO GPS Standard matrix model for (ISO 8015, 2011).

MATERIALS AND METHODS

Feature Principle and Independency Principle - Base principles according (ISO 8015, 2011) which are necessary to keep are:

- Feature principle **-** a workpiece shall be considered as made up of a number of features limited by natural boundaries. By default, every ISO GPS specification for a feature or relation between features applies to the entire feature or features; and each ISO GPS specification applies only to one feature or one relation between features.

- Independency principle - by default, every ISO GPS specification for a feature or relation between features shall be fulfilled independent of other specifications except when it is stated in a standard or by special indication (e.g. (M) in circle; (L) in circle ; (E) in circle; (R) in circle; CT； CZ) as part of the actual specification.

For the indication of specifications on the drawing is very important keep up rules (principles) description in ISO 8015, especially feature principle and independency principle.

Longitudinal Specification – Linear and Angular Sizes – Application of Specification Modifier
Produced workpieces exhibit deviations from the ideal geometric form (Mazínová, 2015). The real value of the dimension of a feature of size is dependent on the form deviations and on the specific type of size applied. The type of size can be indicated on the drawing by a specification modifier (Fig 2) for controlling the feature definition.

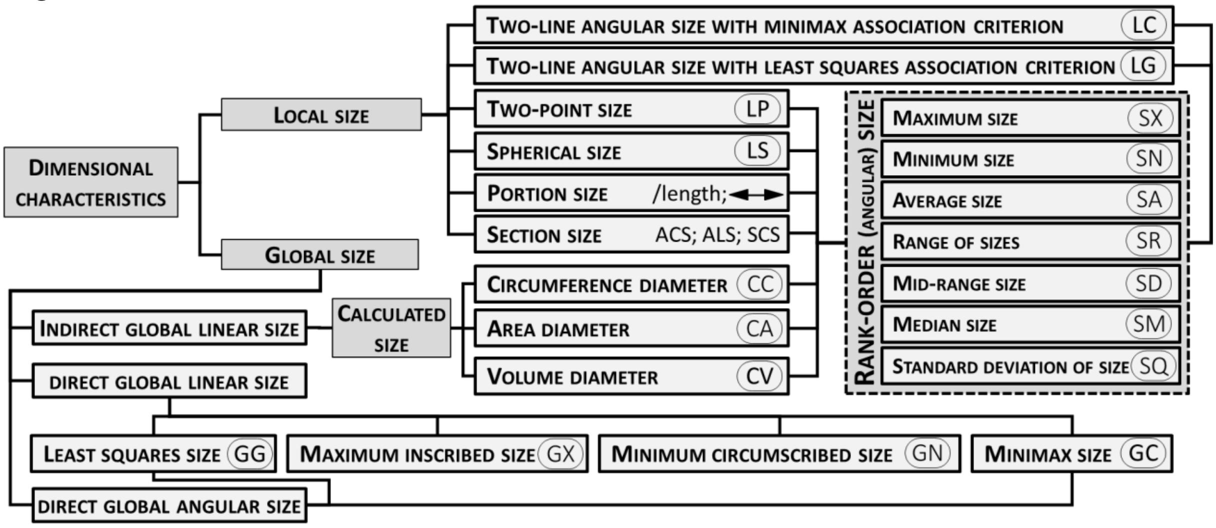

Fig. 2 Specification modifiers for linear (ISO 14405-1, 2016) and angular (ISO 14405-3, 2016) size.

When a drawing-specific default specification operator for size applies, it shall be indicated on the drawing in or near the title block in the following order:

- LINEAR SIZE ISO 14405 … Specification modifiers … - for linear size.
- ANGULAR SIZE ISO 14405 … Specification modifiers … - for angular size.

In basic principle is specification indicate on all feature of size, or only on restricted portion, if the specification applies to only one fixed restricted portion of the complete feature of size (see Fig. 3). Other choice is indicate specification in the section (SCS – specific cross section; ACS – any cross section; ALS – any longitudinal section) – see Fig. 6.
If the specification applies as an individual requirement for more than one feature of size (modifier Nx) or applies specification to a collection of more than one feature of size and this collection shall be considered as one feature of size (modifier Nx with modifier CT – common tolerance) – see Fig. 5.

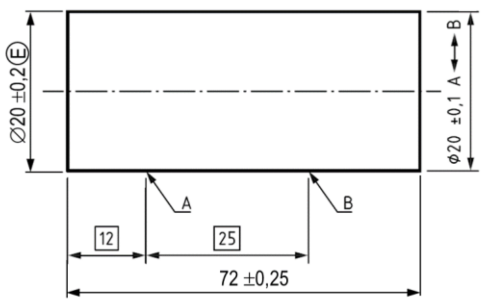

Fig. 3 Restricted portion (A↔B), length of feature of size 72±0.25.

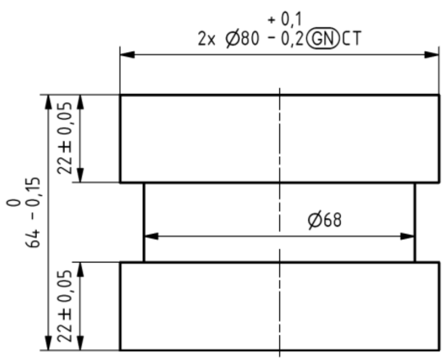

Fig. 4 Example of requirement for two features of size considered as one feature of size.

The specification applies by default to the complete toleranced feature of size. When the toleranced feature is the complete feature, no additional indication is necessary, see Fig. 4. When the specification applies to a united feature (UF) of size, see Fig. 6. An upper limit 0.004 applies to the range of the two-point size values defined in any cross section perpendicular to axis (Intersection plane indicator). An upper limit 0.006 applies to the range of the two-point size values defined in any longitudinal section symmetry to axis (Intersection plane indicator).

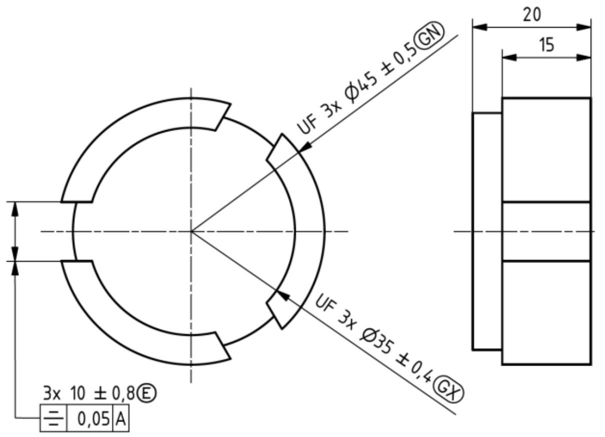

Fig. 5 Requirement for the complete united feature of size (UF).

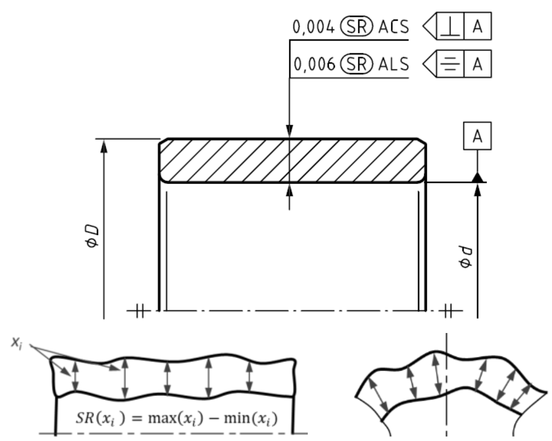

Fig. 6 Examples of the use of rank-order, section and plane specification modifier.

Geometrical Specification

A geometrical specification applies to a single complete feature (see Fig. 7), unless an appropriate modifier is indicated. When the toleranced feature is not a single complete feature, see Fig. 7 (R↔S).

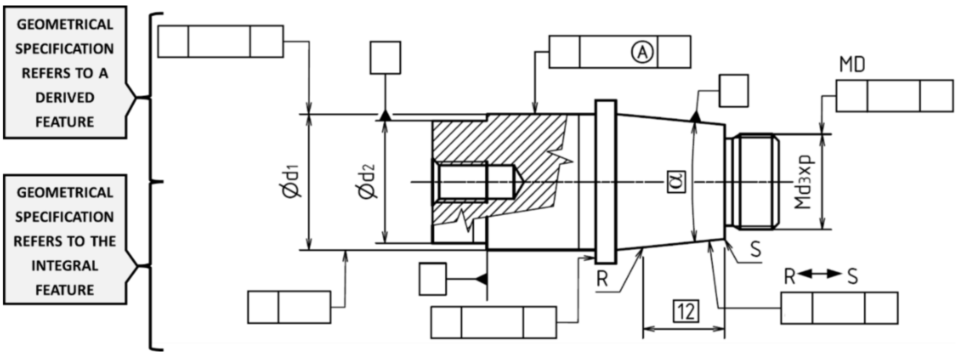

Fig. 7 Geometrical specification applies to drawing.

When the geometrical specification refers to the integral feature, the geometrical specification indication shall be connected to the toleranced feature by a reference line, and a leader line terminating according Fig. 7 (The bottom half of the figure). When the geometrical specification refers to a derived feature (a median point, a median line, or a median surface), it shall be indicated either by a reference line and a leader line terminated by an arrow on the extension of the dimension line of a feature of size or by modifier (A) in circle, see Fig. 7 (The upper half of the figure).

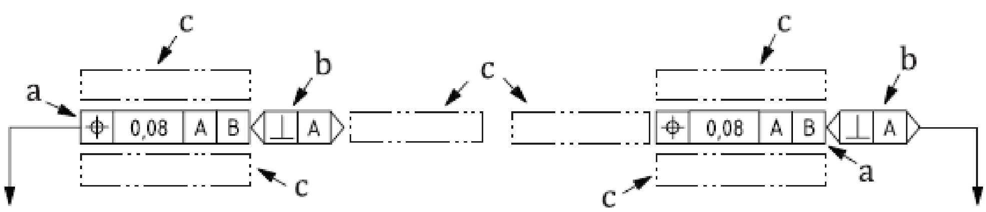

Fig. 8 Elements of a geometrical specification indication (ISO 1101, 2017). (a – tolerance indicator; b – plane and feature indicator; c – adjacent indications).

A geometrical specification indication consists of a tolerance indicator, optional plane and feature indications and optional adjacent indications (See Fig. 8).

Example of Application Geometrical Specification on Feature(s)
The drawing indications in Fig. 9 (2D drawing indication) shall be interpreted as follows: According to the feature principle, the specification applies to one complete feature, i.e. the feature identified by the leader line, which is a feature that forms a 90° section of a cylinder with a nominal radius of 15 (TED - Theoretically Exact Dimensions). In this case, the toleranced feature is defined as part of a cylinder with a radius of 15. The tolerance zone is limited by two equidistant surfaces enveloping spheres with a diameter equal to the tolerance value, the centres of which are situated on the TEF (Theoretically Exact Feature). This results in the tolerance zone limits being 90° sections of coaxial cylinders with radius 14.9 and 15.1, respectively (see Fig. 9 – tolerance zone) according (ISO 1660, 2016).

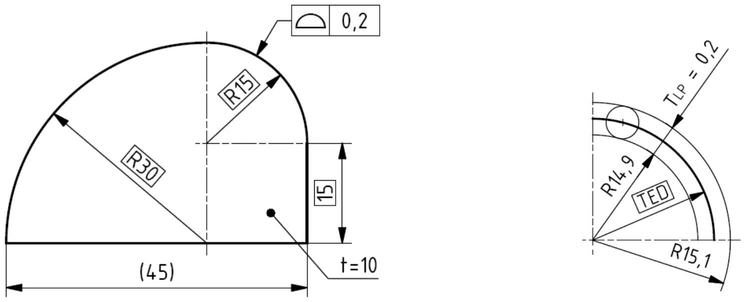

Fig. 9 Surface profile specification for a single feature 2D drawing indication – left; Tolerance zone – right).

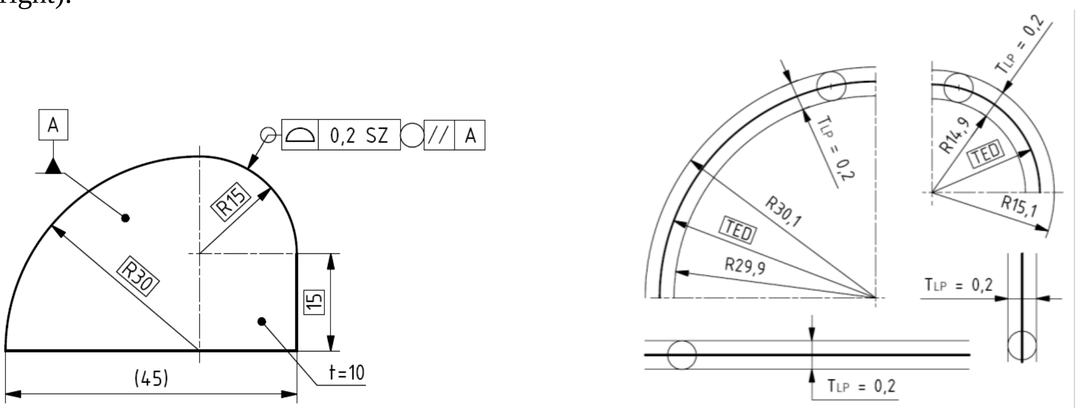

Fig. 10 Surface profile specification for a set of independent features (2D drawing indication – left; Tolerance zone – right).

The drawing indications in Fig. 10 (left) differ from the ones in Fig. 9 in that the “all around” modifier is used. The indication shall be interpreted as follows: The specification applies to a set of features that make up the periphery of the workpiece when seen in a plane parallel to datum A as indicated by the collection plane indicator.

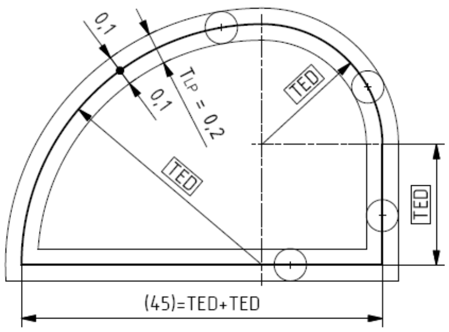

Fig. 11 Tolerance zone for a UF modifier.

The features are considered independent, i.e. the tolerance zones are not related to each other (see Fig. 10 – right). In this case, the toleranced features are defined as a part of a cylinder with a radius of 15, a part of a cylinder with a radius of 30, and two planar surfaces. If the UF (on top tolerance indicator) modifier is used instead of the SZ (separate zone), then the specification applies to a united feature built from the features that make up the periphery of the workpiece (see Fig. 11).

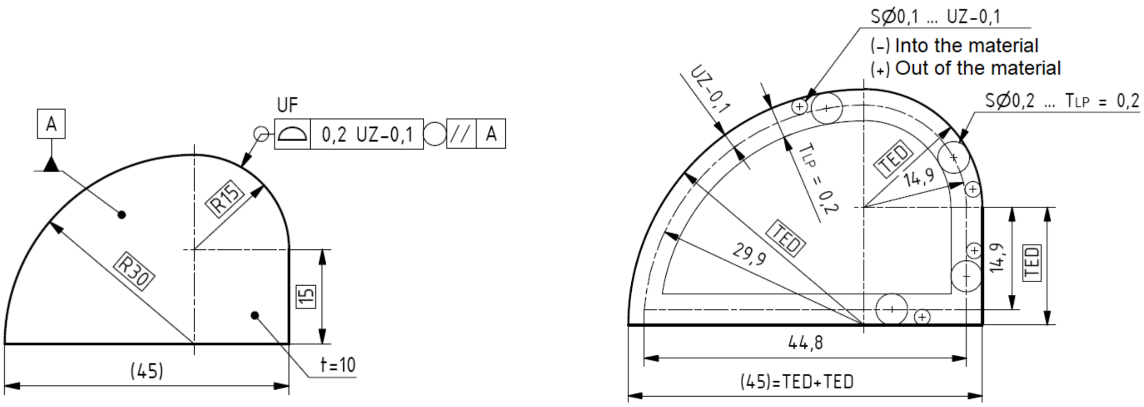

Fig. 12 Unequally disposed surface profile specification for a united feature (2D drawing indication – left; Tolerance zone – right).

The drawing indications in Fig. 12 (left) differ from the ones in Fig. 11 in that the UZ modifier is used to indicate that the tolerance zone is moved 0.1 into the material Fig. 12 (right). The indication shall be interpreted as follows: The specification applies to a united feature built from the features that make up the periphery of the workpiece when seen in a plane parallel to datum A, as indicated by the collection plane indicator. Because the UZ-0.1 modifier is used, the tolerance zone is unequally disposed around the TEF. An equidistant surface enveloping spheres with a diameter of 0.1 placed on the material side of the TEF, because the value is negative, defines the offset nominal geometry.

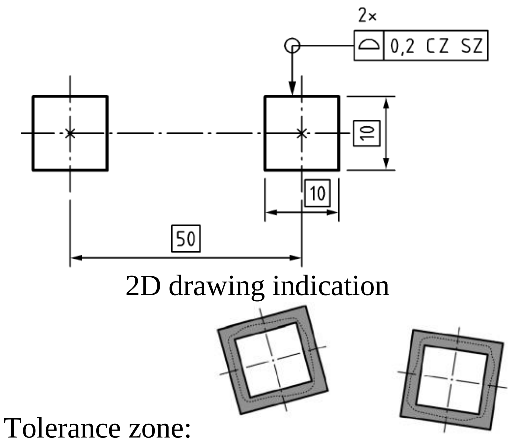

Fig. 13 Two independent patterns.

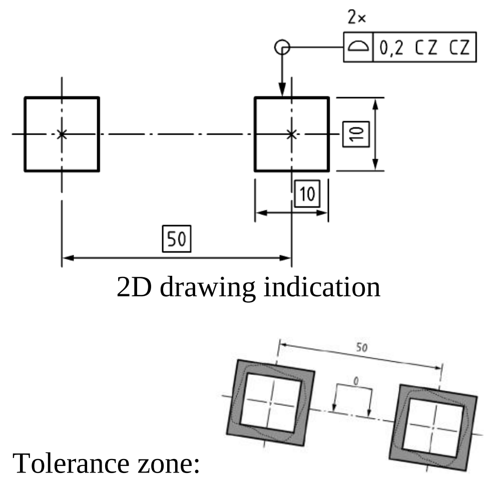

Fig. 14 Unequally disposed surface profile specification for a united feature (2D drawing indication – left; Tolerance zone – right).

RESULTS AND DISCUSSION

Example of Specification for Patterns according (ISO/DIS 5458, 2017). Pattern – compound feature, consisting of a set of more than one individual feature with defined nominal orientation and/or location to each other (without priority).

For indication on Fig. 13 it is possible to say – For each pattern, the tolerance zone is a pattern (a collected tolerance zone), constituted by four tolerances zones, constrained in location to be 10 mm (in a direction) and 10 mm (in another perpendicular direction) apart between them, with explicit TEDs, without external constraint coming from a datum (CZ). The tolerance zones of each pattern are independent (SZ).

For indication on Fig. 14 it is possible to say – The tolerance zone is a pattern (a collected tolerance zone), constituted by two tolerances zones, constrained in location to be 50 mm (in a direction) and 0 mm (in another perpendicular direction) apart between them, with an explicit TED and an implicit TED, without external constraint coming from a datum (CZ). The 1st CZ modifier creates a collected feature (collection in link with all around symbol – collection of four planes constraints between them in location and orientation). The second CZ modifier creates the collection of two collected features constrained in location between them.

CONCLUSIONS

What to say at the end? The ISO GPS (Geometrical Product Specifications) define an internationally uniform description language, that allows expressing unambiguously and completely all requirements.

On the drawing are indicated many specifications (dimensions, geometrical tolerances …), but do not forget, than each specification is only for one feature or for part of feature (if we used modifier). For applicate for more than one specification, we must used modifier. Not all specifications in drawing are functional specification!

REFERENCES

1. ISO 8015:2011. Geometrical product specifications (GPS) -- Fundamentals -- Concepts, principles and rules.
2. ISO 14405-1:2016. Geometrical product specifications (GPS) -- Dimensional tolerancing -- Part 1: Linear sizes.
3. ISO 14405-2:2011. Geometrical product specifications (GPS) -- Dimensional tolerancing -- Part 2: Dimensions other than linear sizes.
4. ISO 14405-3:2016. Geometrical product specifications (GPS) -- Dimensional tolerancing -- Part 3: Angular sizes.
5. ISO 1101:2017. Geometrical product specifications (GPS) -- Geometrical tolerancing -- Tolerances of form, orientation, location and run-out.
6. ISO 1660:2017. Geometrical product specifications (GPS) -- Geometrical tolerancing -- Profile tolerancing.
7. ISO/DIS 5458:2017. Geometrical product specifications (GPS) -- Geometrical tolerancing -- Positional and pattern tolerancing.
8. Mazínová I. Geometrical product specifications – Do We Know What We Prescribe?. 2015 ICMD2015

Corresponding author:

Ing. Karel PETR, Ph.D., Department of Designing and Machine Components, Faculty of Mechanical Engineering, Czech Technical University in Prague, Technicka 4, Prague 6, Prague, 16607, Czech Republic, phone: +420-224-352-415, e-mail: karel.petr@fs.cvut.cz.

DESIGN OF TEST RIG FOR BEVEL GEARS

Karel PETR[1], Jakub VOSYKA[1]

[1]*Department of Designing and Machine Components, Faculty of Mechanical Engineering, Czech Technical University in Prague.*

Abstract
The article describes the design of test rig for testing of bevel gears with different materials, parameters and way of lubrications. Further are described in detail elements of electrically closed loop and their properties.

Key words: *test rig; bevel gear; design; torque moment; gear-mash; gearbox; strain gauge.*

INTRODUCTION

Experimental testing of gearing (gears) can be done in several ways, e.g. by pulsating or operating (running) (*Petr & Dynybyl, 2014*). This article describes operating testing of bevel gears with perpendicular axis. Running tests on bevel gear set are cumulative test processes in which large number of manufacturing-dependent deviations are captured simultaneously. Pinions and wheels can be tested in pairs or compared to appropriate master gears. In most cases, bevel gears are pair-tested and the grading applies to the gear set.

Many running test methods have been developed in the past. Subjective methods include noise tests made by a tester and visual contact pattern testing. Objective methods are single-flank (*ISO 17485:2006, 2006*) and double-flank tests or the structure-borne noise test (*Klingelnberg, 2016*).

MATERIALS AND METHODS

Conceptual Scheme of Test Rig With Electrically Closed Loop

The article's goal is to give a detail description of each part of electrically closed loop that can be used for testing of gearboxes for rail vehicles. Electrically closed loop has been chosen as the best concept of the test rig for the testing of gearboxes (*Petr, Dynybyl &Češpíro, 2012*). The basic concepts are shown in the Fig. 1.

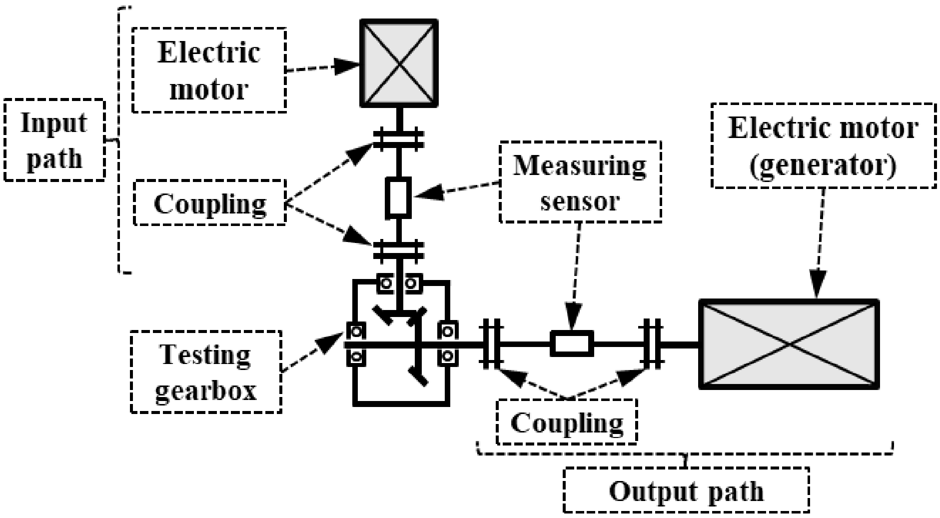

Fig. 1 Conceptual scheme of electrically close loop for testing of bevel gear.

Fig. 1 shows main components in the loop are two electro motors (on the input and on the output of gearbox), tested gearbox, servo insert coupling with collet clamp (KBE2) and designed measuring sensor for measuring of torque moments.

Design of Gearbox and Gear Parameters

Testing device (see Fig. 2) is designed for testing of bevel gears with module 3 or 3.5 mm, for maximum input torque moment 13.2 Nmm and for maximum speed 2 900 RPM.

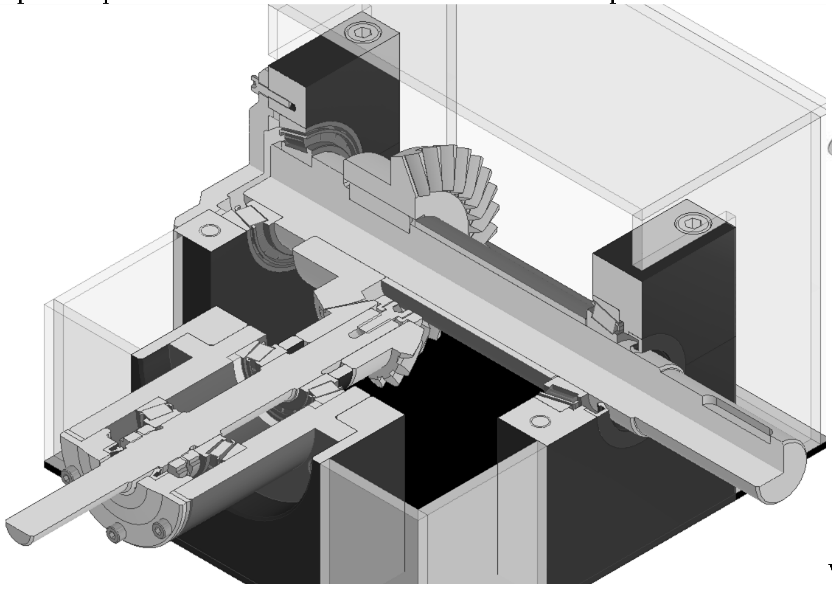

Fig. 2 3D model of gearbox for testing of bevel gears.

Fig. 3 3D model of gear set with shaft, bearings, selling and axial locking.

Fig. 3 shows gear set with shaft, bearings, selling and axial locking. For different gear ratio are necessary to used different distance tube, but position of bearings are still same.

Table 1 shows parameter of gear set for testing. Each gear set have been different gear ratio (1:2; 1:2.5; 1:3) or module (3 or 3.5).

Tab. 1 Parameter of gears for testing.

Parameters	Gear ratio			
	1:2	1:2	1:2,5	1:3
Module [mm]	3	3.5	3	3
Pitch diameter of the pinion [mm]	37.40	43.33	40.02	38.36
Pitch diameter of the gear (wheel) [mm]	74.79	86.66	100.04	115.08
Radial (Axial) force on the pinion [N]	229.33	197.92	222.49	237.14
Radial (Axial) force on the gear (wheel) [N]	114.67	98.96	89.00	79.05
Tangential force [N]	704.46	607.97	658.37	686.79

Measuring Sensor

For measure of torque moments was used frequency converter and has been designed measuring sensor (see Fig. 4). The sensor is composed of tube with two strain gauges (1-XY21-3/120), servo insert coupling with collet clamp (KBE2) for connection and rings for transmitting values on computer.

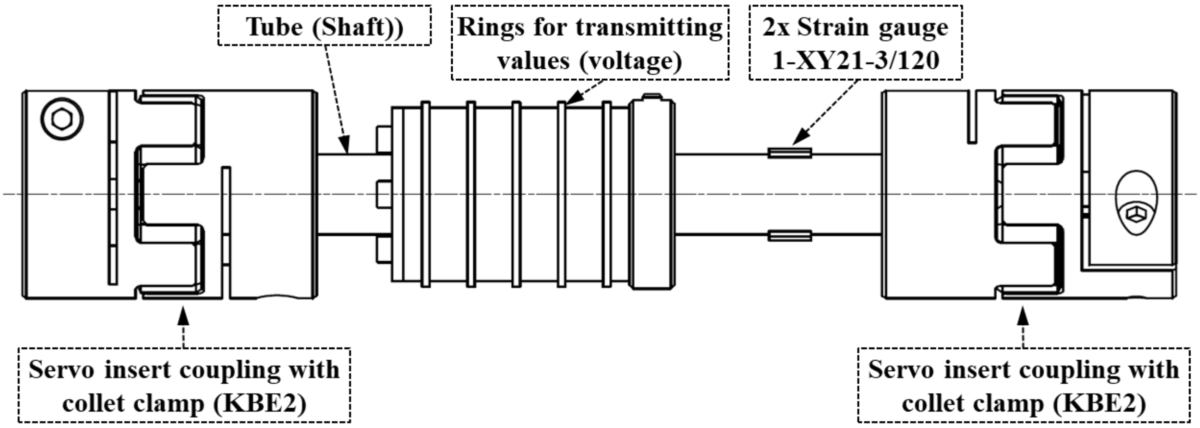

Fig. 4 3D model of measuring sensor with couplings.

Second type of measuring sensor will be designed with two semiconductor strain gauges.

RESULTS AND DISCUSSION

Design of Test Rig - Fig. 5 shows model of test rig for testing of bevel gears. The sensor is composed of welded frame from I-profiles, input motor (4 kW, 2 900 RPM), two measuring sensors (input and output run), output motor (7.5 kW, 1 490 RPM) and gearbox. Gearbox was see in Fig. 2, housing was designed as three separate bearing blocks and plates from glass or Plexiglas.

In the gearbox is possible tested different type of lubrication (lubrication by blurring, mist lubrication circulation lubrication, splash lubrication, directly sprayed into gear-mash) (*Petr & Boroš, 2016; Petr & Hanousek, 2015*).

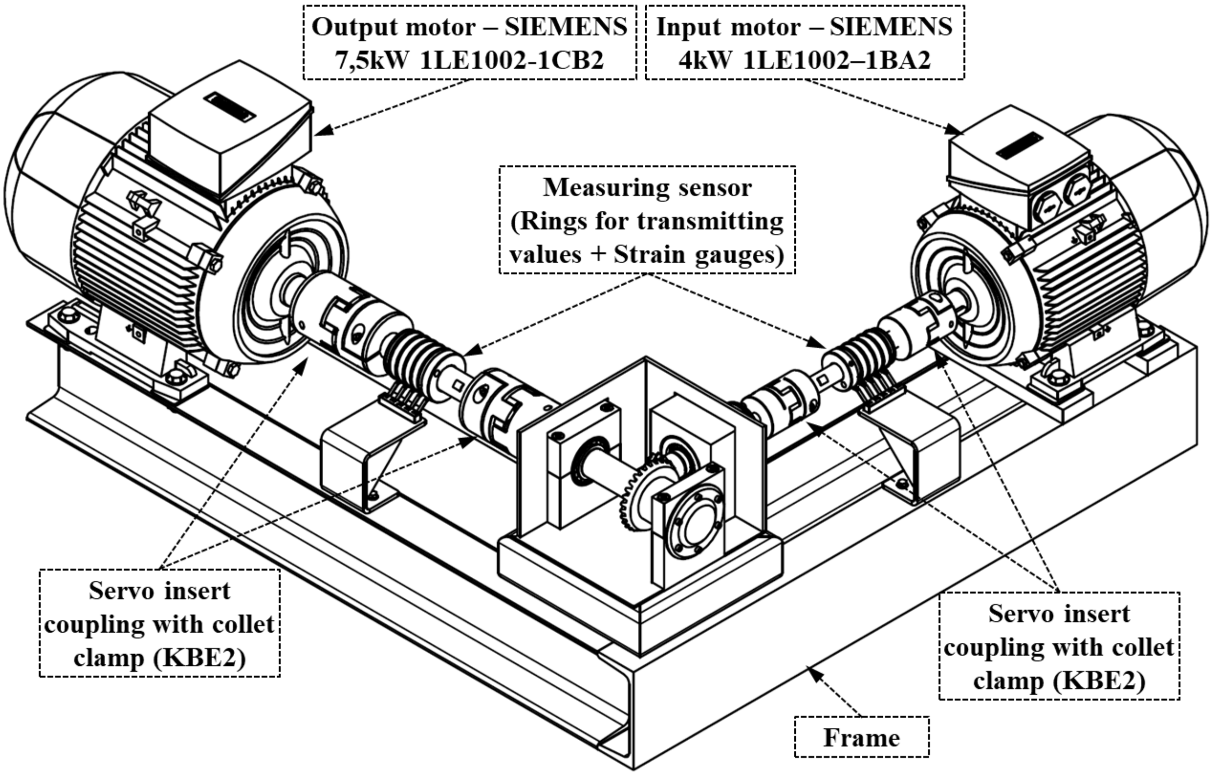

Fig. 5 3D model of test rig for testing of bevel gears.

CONCLUSIONS

The objective of this article was to design a test stand for testing of bevel gear set. All parts were designed for minimum durability 20 000 hours. Some parts were designed by FEM. It was created FEM model, which simulated gear-mash of bevel gears.

It was created FEM model, which can have simulated gear-mash of bevel gears. In the gearbox is possible tested different type of lubrication and different type of materials of bevel gear set. With measuring sensor will be possible measure torque moment and calculate efficiency (maybe).

ACKNOWLEDGMENT
This study was supported by SGS16/146/OHK2/2T/12.

REFERENCES

1. Petr, K.; Dynybyl, V. Methods of testing gearboxes of rail vehicles. In Applied Mechanics and Materials. Uetikon-Zurich: Trans Tech Publications, 2014, p. 277-282. ISSN 1660-9336. ISBN 978-3-03785-977-3.
2. ISO 17485:2006 Bevel gears -- ISO system of accuracy.
3. Klingelnberg, Jan. Bevel Gear: Fundamentals and Applications. Springer Vieweg. 2016. ISBN 978-3-662-43892-3.
4. K. Petr, V. Dynybyl, and Z. Češpíro. Development of the Driving Axle Transmissions for Trams and Suburban Trains. In: 53rd International Conference of Machine Design Departments. 53rd International Conference of Machine Design Departments. Mikulov, 12.09.2012 - 14.09.2012. Brno: Vysoké učení technické v Brně. 2012, pp. 57-62. ISBN 978-80-214-4533-8.
5. Petr, K.; Boroš, P. Conceptual Design of Gearbox for Kaplan Turbine. In: Book of proceedings of the 57th International Conference of Machine Design Departments. Plzeň: Západočeská universita, 2016, pp. 105-108. ISBN 978-80-261-0609-8.
6. Petr, K.; Hanousek, D. Design of Rear Drive Car Formula Student FSE.04. In: Book of Proceedings of 56th International Conference of Machine Design Departments. Bratislava: STU v Bratislave, SjF, 2015, pp. 219-222. ISBN 978-80-552-1377-4.
7. ISO 10300-1, 2, 3:2014 Calculation of load capacity of bevel gears -- Part 1: Introduction and general influence factors; Part 2: Calculation of surface durability (pitting); Part 3: Calculation of tooth root strength.

Corresponding author:
Ing. Karel PETR, Ph.D., Department of Designing and Machine Components, Faculty of Mechanical Engineering, Czech Technical University in Prague, Technicka 4, Prague 6, Prague, 16607, Czech Republic, phone: +420-224-352-415, e-mail: karel.petr@fs.cvut.cz.

MODELING OF MECHANICAL PROPERTIES OF COMPOSITE MATERIALS UNDER MECHANICAL VIBRATIONS

Michal PETRŮ[1], Ondřej NOVÁK[2]

[1]*Department of Machinery Construction, Institute for Nanomaterials, Advanced Technology and Innovation, Technical University of Liberec*
[2]*Department of nonwovens and nanofibrous materials, Faculty of Textile Engineering, Technical University of Liberec*

Abstract
This article focuses on numerical modeling of the mechanical properties of new nonlinear material structures with composite carbon fibers that would be applicable to industrial plants. These types of carbon composites will be applied especially for a construction of machines with high vibration during their operations. It was assembled composite sample numerical model with a given geometry including a bonded contact with a thin piezoelectric sensor for description and evaluation of mechanical properties. The results were compared with the measurements and statistically analyzed. It can be stated that the finite element method (FEM) can be used to describe the mechanical properties of the new type of composites.

Key words: *numerical modeling; composite materials; non-linear behavior; mechanical vibration.*

INTRODUCTION

Composite materials are increasingly used for various construction applications. The reasons are evident, because they have excellent mechanical properties, but they allow the structure to keep light weight. In the design of the final composite (fibers and matrix), due to the synergistic effect, it is possible to obtain high specific properties (a high strength, stiffness, toughness) that cannot be reached by either of the input components. The synergistic effect is characterized by a known "illogical rule 2 + 3 = 7", which describes that the sum of the properties of the individual input components (fibers + matrix) results in higher values of the specific properties of the newly prepared structure. Generally, the highest specific properties can be achieved when the fibers are loaded to acting ultimate tensile stress $\sigma_M^f\big|_{F^f \to \max}$ that is transferred by the matrix. The matrix provides not only a transfer of stress to fibers, but also the matrix creates final geometry of the composite, protects fibers against surface wear and damage, which would lead to a loss of the stability and strength of the resulting composite. A number of authors have been dealt with researches and studies of fiber-reinforced composite structures due to their potential and specific features (*Agarwal, Broutman & Chandrashekhara, 2006; Guedes, 2010; Mehar & Panda 2016; Martinec, Mlýnek & Petrů, 2015; Petrů, Martinec, & Mlýnek 2016, Teply & Reddy, 1990, Barthelot, 1999, Gibson, 1995)*. The authors agree that composite structures are unique materials whose mechanical properties cannot be generally described in an analytical or experimental manner. Theories also differ in mathematical relationships derived for unidirectional composite structures, and a creation of the comprehensive descriptions of mechanical properties for geometrically complicated structural members such as frames, springs, and beams with multi-directional fibrous is virtually impossible. This is because their properties differ significantly with the type of fiber and matrix (i.e., physical and mechanical properties, surface treatment, chemical composition, chemical bonds, density, thermal expansion, because only a slight change results in different combinations with completely different properties. This problem is further increased if mechanical properties for the application of composite materials to machines which are heavily loaded with vibrations. The properties of the composite will be determined on the basis of the modulus of elasticity by the indirect method based on the resonance properties of the composite. A comprehensive approach addressing this issue is very complex and poorly understood. However, some authors approach similar problems by measuring vibration and numerical modeling. *Panda & Singh, 2011* solve post-buckling of nonlinear shell under uniform thermal field. They developed a mathematical model for a curved panel by the help Green-Lagrange relations using higher order shear deformation theory (HSDT). They studied parameters laminate structure, geometry, dimensions, supporting and other were studied. Also influence of mesh size is studied. Obtained results are usable for nonlinear free vibration behaviour of single/doubly curved shell panel within the post-buckled state. Authors *Marjanović & Vuksanović, 2016* deals with FEM model for the free vibration analysis of laminated composite shells. In the shell a delamination is introduced. The authors use shells with different geometries like are cylinders with different height or conical cross-ply geometry. Orthotropic linearly elastic material models is applied. The solver is introduced in MATLAB. For pre/postprocessing GiD software is used. For model basic known material data are applied. The aim of models is to investigate the influence of delamination and its size on an own frequency and also mode shape. In this paper, a numerical model of a composite sample of given geometry with a thin piezoelectric sensor was established for describing and evaluating of mechanical properties.

MATERIALS AND METHODS

Experimental measurement

Measurements were performed on a square composite board with dimensions $l = 101{,}4\,mm$ and $h = 0.5\,mm$. One side was placed in the jaws so that the resulting sample had dimensions $l = 101{,}4x90\,mm$ (Fig.1 a). On the sample the piezoelectric ceramic thin plate was bonded. The piezoelectric sensors dimensions 40 x 20 x 0.3 mm^3 were placed in the middle of square. This type of measurements gives much better response because significantly higher magnitude of vibrations can be obtained. The problem consists in suitable excitation. On Fig. 1b a response on mechanical pulse excitation is seen. More sophisticated solution was done by the help of the electromagnetic hammer. The most usable solution was created using electromagnet and perm alloy target fixed on tested composite sample.

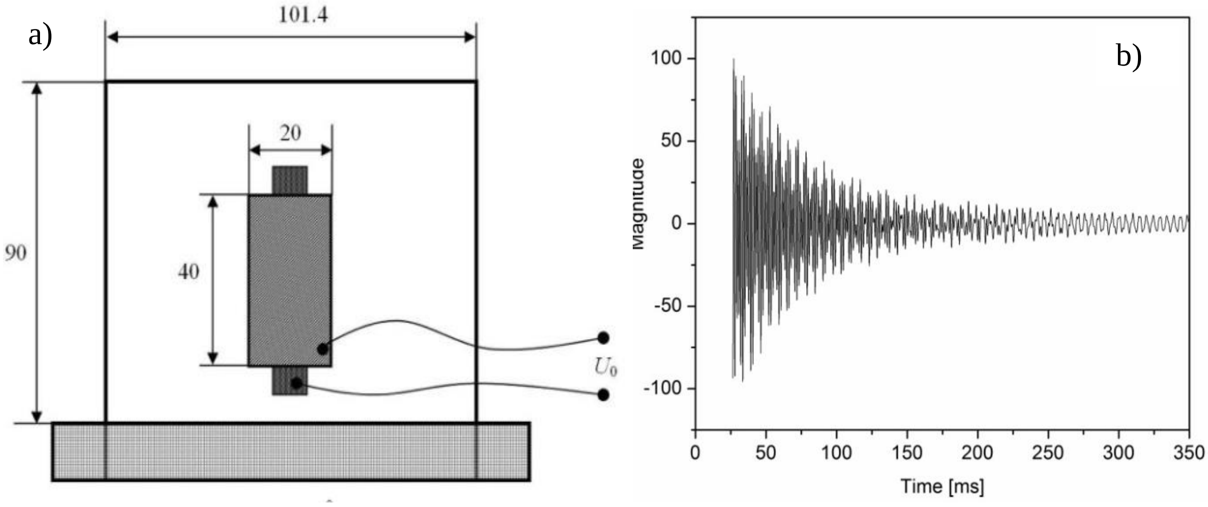

Fig. 1 Dimensions of vibrating plate from carbon composite with thin piezoelectric rectangular plate (left), An mechanical pulse excitation (right).

Numerical modelling

An accurate measurement and evaluation of the natural frequencies of composites for the purpose of a determination of mechanical characteristics such as elastic modulus, shear modulus, Poisson's ratio, and natural frequencies in composites is very difficult and complex problem. This problem consists in a suitable location and fixing of accelerometers and tensiometers. Also their weight, dimension and other properties can significantly influence measured values. Mathematical models are based on the mathematical description of the vibrating sample surface, which means you can build a matrix of elementary point sources. The displacements on the oscillating sensor surface ω in places fictitious point sources, diffuse field excited by a harmonic unit force can then be determined by equation (1).

$$w(x, y, \omega) = -\frac{F}{\rho h} \sum_{i=1}^{\infty} \sum_{j=1}^{\infty} \frac{\Theta_{i,j}(x_0, y_0)\Theta_{i,j}(x, y)}{\omega^2 - \omega^2_{i,j}} \tag{1}$$

where the function $\Theta_{i,j}(x, y)$ can be for harmonic excitation expressed as

$$\Theta_{i,j}(x, y) = \frac{2}{\sqrt{L_x L_y}} \sin\left(\frac{i\pi x}{L_x}\right) \sin\left(\frac{j\pi x}{L_y}\right) \tag{2}$$

where w is magnitude of sample deflection, F is amplitude harmonic exciting force moving sample, ρ is the density of vibrating sample, h is the thickness of vibrating sample, ω is angular frequency of harmonic exciting force F moving sample, $\omega_{i,j}$ are natural modal angular frequencies of vibrating plate, x_0, y_0 are x and y coordinates of exciting force moving sample, x , y are coordinates of fictive point source on the surface of the rectangular plate, L_x, L_y are dimensions of vibrating plate, i, j are natural modes of vibrating plate in the direction x , y . For expression of the shape modes (angular resonant frequencies) of vibrating plate using (*Zizka et al., 2006*) can be established by equation (3).

$$\omega_{i,j} = \pi^2 \sqrt{\frac{Eh^2}{12\rho(1-\nu)}} \left[\left(\frac{i}{L_x}\right) + \left(\frac{j}{L_y}\right)\right] \tag{4}$$

where E is modulus of flexibility (Young' modulus), ν is Poisson constant.

A development of simulation model of vibrating plate is a valuable tool for determining the distribution of stress and strain and other mechanical variables that cannot be obtained through analytical relations due to complicated shape and geometry of the real sample. The deformed shape of the surface of the sample can by analyze numerically through the finite element method (FEM - Finite element method) or the boundary element method (BEM - boundary element method). Numerical model can show founded variables as is stress, strain, deformation etc. and these values could be compared with experimentally determined values. Generally described by a system of constitutive law (5).

$$\boldsymbol{\sigma} = \mathbf{C} \cdot \boldsymbol{\varepsilon} = \begin{bmatrix} \sigma_{11} \\ \sigma_{22} \\ \sigma_{33} \\ \tau_{23} \\ \tau_{13} \\ \tau_{12} \\ D_1 \\ D_2 \\ D_3 \end{bmatrix} = \begin{bmatrix} C_{11} & C_{12} & C_{13} & \cdot & \cdot & \cdot & \cdot & \cdot & e_{31} \\ C_{21} & C_{22} & C_{23} & \cdot & \cdot & \cdot & \cdot & \cdot & e_{32} \\ C_{31} & C_{32} & C_{33} & \cdot & \cdot & \cdot & \cdot & \cdot & e_{33} \\ \cdot & \cdot & \cdot & C_{44} & \cdot & \cdot & \cdot & e_{24} & \cdot \\ \cdot & \cdot & \cdot & \cdot & C_{55} & \cdot & e_{15} & \cdot & \cdot \\ \cdot & \cdot & \cdot & \cdot & \cdot & C_{66} & \cdot & \cdot & \cdot \\ \cdot & \cdot & \cdot & \cdot & e_{15} & \cdot & \mu_1 & \cdot & \cdot \\ \cdot & \cdot & \cdot & e_{24} & \cdot & \cdot & \cdot & \mu_2 & \cdot \\ e_{31} & e_{32} & e_{33} & \cdot & \cdot & \cdot & \cdot & \cdot & \mu_3 \end{bmatrix} \begin{bmatrix} \varepsilon_{11} \\ \varepsilon_{22} \\ \varepsilon_{33} \\ \gamma_{23} \\ \gamma_{13} \\ \gamma_{12} \\ E_1 \\ E_2 \\ E_3 \end{bmatrix} \tag{5}$$

where $\boldsymbol{\sigma}$ is stress tensor, $\mathbf{C}$ is matrix of elastic coefficients, $\boldsymbol{\varepsilon}$ is strain tensor, e_{ij} is piezoelectric matrix for stress-charge form, E_i is electric field intensity vector, D_i is vector of electric displacements, e_i is dielectric matrix with coefficients of electric permittivity on a diagonal of the matrix.

Material parameters used in FEM model for piezoceramic sensor and carbon fibers composite are introduced in Tab.1 and Tab.2. Input values were verified by FEM model (Fig.2), because material list shows different values compare to experiment. Differences were found mainly in the case of piezoelectric ceramics, which exhibits anisotropic behavior.

Tab. 1 Initial and fitted material properties of carbon fiber composite

$\rho = 1540\ kg.\mathrm{m}^{-3}$, $C_{11} = 2900\,GPa$
$C_{22} = C_{33} = 9450\ MPa$, $C_{12} = C_{13} = 5500\,MPa$
$C_{13} = 3900\ MPa$
$\nu_{XY} = 0.27$, $\nu_{XZ} = 0.27$
$\nu_{YZ} = 0.4$

Tab. 2 Initial and fitted material properties of piezoceramic sensor

$\rho = 7800\ kg.\mathrm{m}^{-3}$, $C_{11} = C_{22} = 62500\,MPa$
$C_{33} = 52\,600\ MPa$, $C_{12} = 23\,500\,MPa$
$C_{13} = C_{23} = 23\,000\ MPa \rightarrow 23\,500\ MPa$
$\nu_{XY} = 0.289 \rightarrow 0.291$, $\nu_{XZ} = 0.512 \rightarrow 0.501$
$\nu_{YZ} = 0.408$, $\varepsilon_r = 1062$, $e_{31} = e_{32} = 5.6\,\mathrm{pCm}^{-2}$, $e_{33} = -12.8\,\mathrm{pCm}^{-2}$

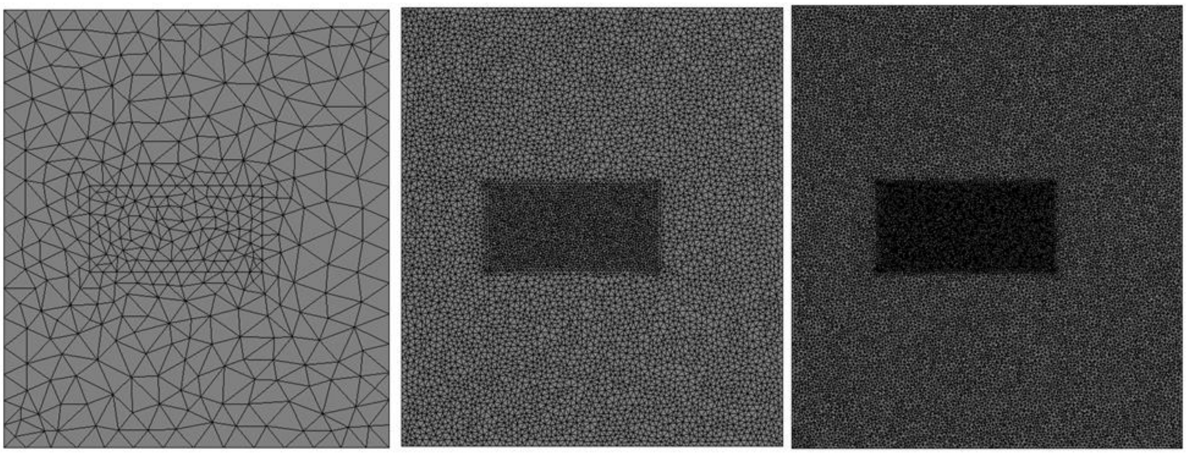

Fig. 2 FE meshing of the model in the calculation convergence: Adaptive meshing for the minimization of the residues in the solved area.

RESULTSAND DISCUSSION

For the measurement commercial impedance Analyzer HP 4192A working with 4 wire measuring system was used. The applied voltage was maximally 1.1 V. The frequency range was from 10 to 1000 Hz. The impedance method provides very low response on mechanical resonances of composite sample. This kind of measurement setup is not optimal for automatic measurement of natural frequencies of the samples. From these reasons it is not possible to use impedance measurement for evaluation of resonant frequencies by an automatic way. Therefore more suitable solution is application of an external mechanical excitation for carbon fiber composite. The problem of this type of test consists in a suitable way of the excitation. The mechanical vibration can be induced by applying a force that acts upon a negligibly short period i.e. from mathematical point of view it has character of function. It is a shock excitation, which is called the impulse excitation. The superposition principle implies that the Fourier transformation of the impulse response excitation contains wide frequency range. A FEM model of carbon fibers composite with glued piezoelectric senor plate was prepared. By FEM simulation algorithm with default values were optimized on natural frequencies 94 Hz, 240Hz and 548Hz that are in agreement with experimental measurements where piezoelectric plate is used as sensor. Both methods of measurements, direct impedance measurements using impedance analyzer, and indirect method that measures electrical response on mechanical excitation evaluated with FFT, show close values of natural frequencies. During the development and validation of methods and algorithms describing the natural frequency of composite structures is necessary to create a model that gives results close to experimental measurement and also it can describe a behavior of vibrating sample geometry of investigated composite. The model enables to compare the resulting shapes and sizes of vibration frequencies with the experimentally measured data. The model should be able to determine the spatial distribution of the displacement of the vibrating surface of the object, the stress distribution at different places and it allows the creation of graphical representation of results for comparison with the experiments (Fig.3 - Fig.5).

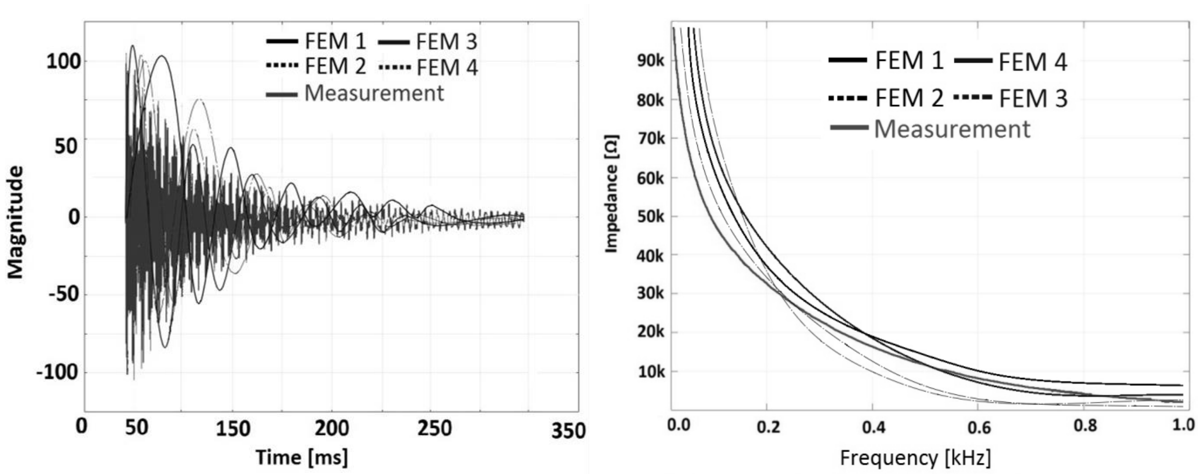

Fig. 3 Comparison of experimental input signal and FEM model for composite sample: Dependence of FEM model convergence on degree of adaptive network (left), Comparison of measurement and FEM model of impedance dependence on the frequency of alumina plate (right).

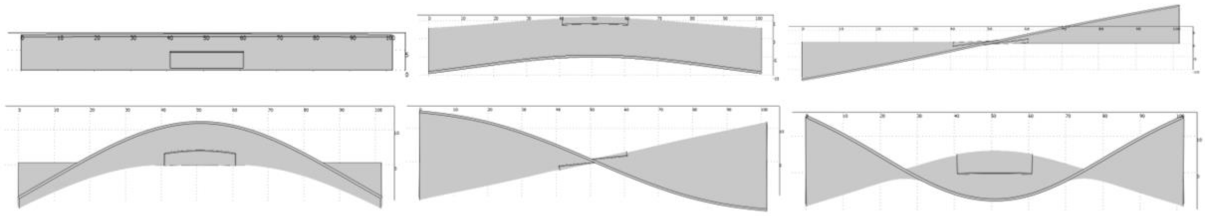

Fig.4 FEM shape mode of composite plate with piezoceramics sensor (1-6 mode).

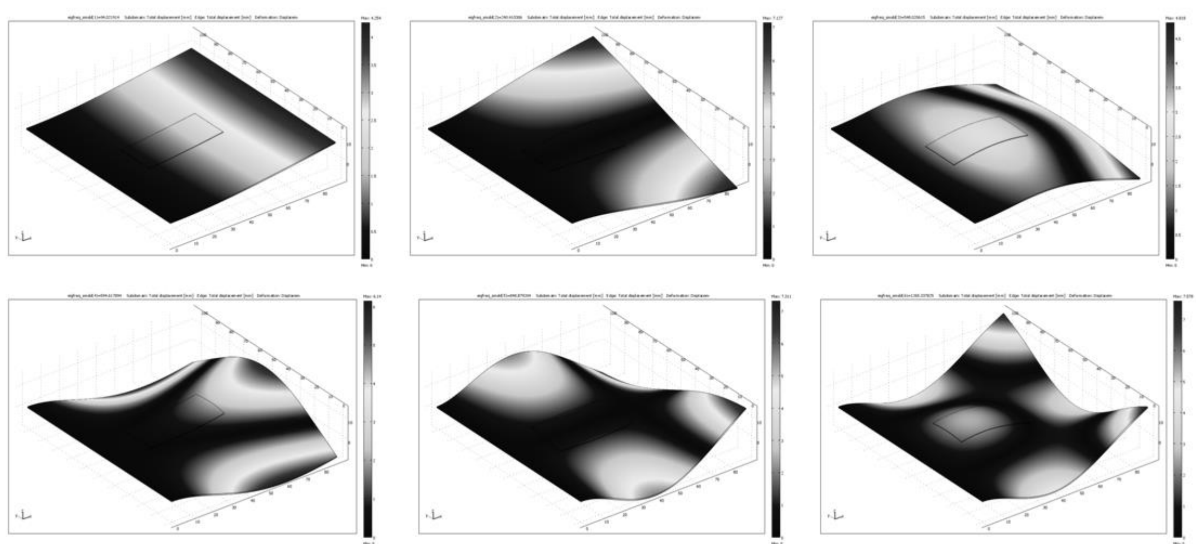

Fig.5 FEM distribution of total deformation for each mode of vibrations (1-6 mode of vibrations).

CONCLUSIONS

The main problem of measurement is small sensitivity of piezoelectric sensor at low frequencies caused probably by low energy of vibrations. Also optimal position of sensor plays an important role in sensitivity of measurements for vibration each mode. From experiments and simulations is recommended position of ceramic sensor in base (root) of vibrating strip. It is clear that electrical excitation is not strong enough especially at low frequencies. The reason is also very well visible on Fig. 5 where it is distribution of mechanical deformation on carbon fibers composite. For the second harmonic is stress very small around "vertical axes" of symmetry. It is caused by propeller like vibrating around the vertical axes. The results were compared statistically showed that the FEM model can be used for research of mechanical properties composites with carbon fibers structurally designed for industry. It turns out that these studies using FEM simulation model can contribute to the selection of an appropriate methodology for measuring mechanical properties composites are an important tool for obtaining valuable information for the design and optimization of parts construction.

ACKNOWLEDGMENT

The results of this project LO1201 were obtained with co-funding from the Ministry of Education, Youth and Sports as part of targeted support from the "Národní program udržitelnosti I" programme.

REFERENCES

1. Agarwal, B. D., Broutman, L. J., Chandrashekhara K. (2006). Analysis and Performance of Fiber Composites, 3rd Ed., pp. 576.
2. Guedes, R. M. (2010). Creep and Fatigue in Polymer Matrix Composites, Woodhead Publishing, pp. 600.
3. Mehar, K. & Panda, S. K., 2016. Geometrical nonlinear free vibration analysis of FG-CNT reinforced composite flat panel under uniform thermal field, Composite Structures, 143 (20), 336-346.
4. Teply, J.L. & Reddy, J.N. (1990). Unified formulation of micromechanics models of fiber-reinforced composites. In: Dvorak GJ, editor. Inelastic deformation of composite materials, New York: Springer, pp.341–370.
5. Berthelot, J.M. (1999). Composite materials: mechanical behavior and structural analysis, New York: Springer, pp. 158–81.
6. Gibson, R.F. (1994). Principles of composite material mechanics, McGraw-Hill, Inc., New York: Springer, pp.425.
7. Martinec, T.; Mlýnek, J. & Petrů, M. (2015). Calculation of the robot trajectory for the optimum directional orientation of fibre placement in the manufacture of composite profile frames, Robotics and Computer-Integrated Manufacturing, 35 (1), 42-54.
8. Petrů, M., Martinec, T. & Mlýnek, J., (2016). Numerical model description of fibres winding process for new technology of winding fibres on the frames, Manufacturing Technology, 16 (4), 778-785.
9. Panda, S.K., & Singh, B.N., (2011). Large amplitude free vibration analysis of thermally post-buckled composite doubly curved panel using nonlinear FEM, Finite Elements in Analysis and Design, 47 (4), 378-386.
10. Marjanović, M., & Vuksanović D., (2016). Free vibrations of laminated composite shells using the rotation-free plate elements based on Reddy'slayerwise discontinuous displacement model, Composite Structures, 156 (15), 320-332.
11. Zizka, J.; Hana, P.; Hamplova L.; Motyčka Z. (2006). Cutting Process Monitoring by Means of Acoustic Emission Method; Part I / New Approach of Acoustic Emission Sensor; Part II / Transformation of Acoustic Emission into Audible Sound, Advanced Materials Research, 13-14, 105-110.

Corresponding author:

Doc. Ing. Michal Petrů, Ph.D., Department of Machinery Construction, Institute for Nanomaterials, Advanced Technology and Innovation, Technical University of Liberec, Studentská 1402/2, Liberec, Czech Republic, phone: +420777996636, e-mail: michal.petru@tul.cz

EFFECT OF IMPELLER TUNING FOR PUMP USED IN TURBINE MODE

Martin POLÁK

Department of Mechanical Engineering, Faculty of Engineering, Czech University of Life Sciences in Prague, Kamýcká 129, 16521, Praha 6, Czech Republic

Abstract
This article presents results of experimental verification of construction modifications of radial centrifugal pump in reverse turbine mode. The measured characteristics indicated that a simple adjustment of the impeller by rounding the input edges, along with the reduction in roughness of the flow parts, resulted in an increase in efficiency of 2% and in performance, 1.5% while reducing the flow and gradient. The article also shows the correction of the conversion relationships needed when designing a pump for turbine mode, where it is necessary to take into account the varying efficiency of reversing pump operation. This correction results from real experience and has not yet been described in literature.

Key words: *pump as turbine (PAT), impeller trimming, efficiency.*

INTRODUCTION

In the field of small hydropower plants, hydrodynamic pumps as turbine (PAT) are often used as an alternative to conventional water turbines. This option is of particular interest because of its low investment cost and its applicability, especially for decentralized sources with outputs of up to 100 kW. When building small hydropower plants, the most expensive investment is the price of the turbocharger and hence the effort to find alternatives (*Alatore-Frenk*, *1994*). Given the wide range of pumps on the market, these relatively inexpensive and reliable units are often more advantageous in terms of maintenance than conventional custom-made turbines (*Bláha, Melichar & Mosler 2012*).

However, when selecting pumps for turbine operation, it is necessary to take into account the specificities associated with their reversibility. This concerns in particular the geometry of the flow cross sections, which are usually fixed and as such do not allow for regulation in changing operating conditions. Furthermore, it is necessary to consider that optimal parameters of pump and turbine operation differ (*Nautiyal*, *Varun & Kumar*, *2010*). The design process is based on the hydrotechnical parameters of the site where the machine is to be installed. These parameters are the gradient H (m) and the water flow Q ($m^3 \cdot s^{-1}$). Based on the theory of hydraulic machines, the parameters for selecting the corresponding pump are determined by the conversion, i.e. the water head H_P (m) and the flowrate Q_P ($m^3 \cdot s^{-1}$) (*Güllich, 2014, Munson, Zouny & Okiishi*, *2006*).

$$H_P = \frac{H}{{\eta_P}^x} \qquad [m] \tag{1}$$

$$Q_P = \frac{Q}{{\eta_P}^y} \qquad [m^3 \cdot s^{-1}] \tag{2}$$

where, η_P is the total pump efficiency. The values of the exponents x, y may vary in literature with authors. The most reported values are x = 2 and y = 1 (*Nautiyal, Varun & Kumar, 2010*).The most appropriate type and size in the pumps manufacturer's catalogue will be then selected according to the parameters H_P a Q_P. However, in some cases, the effectiveness of the machine is often a question. Here, it is assumed that it will not change by reversing the operation. Nevertheless, the efficiency of turbine and pump operations vary, with that of turbine operation being lower. This unfavourable state may be corrected through some design adjustments that lead to increased efficiency. The adjustments mainly concern flow geometry and require a thorough understanding of the hydraulic mechanisms of energy transfer (*Singh & Nestmann*, *2011*). These can be dealt with only by a combination of theory and experimental verification. Some of the modifications are described, for example, in (*Derakhshan & Nourbakhsh, 2008; Polák, 2013; Poláková & Polák, 2016; Raman, Hussein, Palanisamy & Foo, 2013*). This article focuses on experimental verification of impeller adjustments that may be performed on a finished pump and on verification of the above-mentioned conversion relationships, (1) and (2).

MATERIALS AND METHODS

The principle of additional optimization of the pump consists mainly in the reduction of hydraulic losses. There are basically two kinds of these - frictional and local losses. The proposed modifications are such as are easy to perform on the machine and do not further increase the purchase price. Most of the adjustments relate to the impeller and the areas directly connected, i.e. the zones of entry, passage and outlet of the fluid from the impeller (*Singh, 2005; Sedlář, Šoukal & Komárek, 2009*).

When the fluid passes through a pump in turbine mode, the output edges of the impeller blade become input edges. In these spots, the blades are usually ended with sharp edges which are not problematic in pump mode, but cause liquid shock in turbine mode, manifested by an increase in local hydraulic losses and a decrease in efficiency. The magnitude of the hydraulic loss depends on the wake region, i.e. the size of the fluid area affected by the immersed body. Such loss can be reduced by the appropriate shaping of the immersed body, in this case by rounding its edges. Fig. 1 schematically shows the size of wake region during fluid flow by unmodified input profile on the left, modified on the right. Both the edges of the blades and of the rear and front shroud of the impeller on its outer diameter, D_1 were rounded. This modification involves removing the impeller and rounding the edges, e.g. by grinding, which is a very simple process.

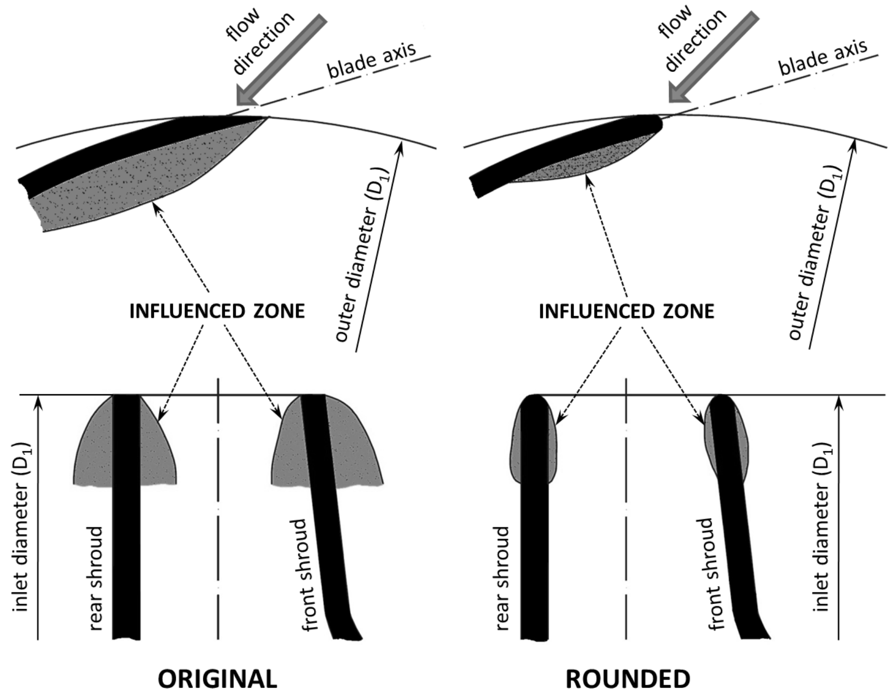

Fig. 1 Influence of rounding of input edges on fluid flow through the impeller

Further reduction of hydraulic losses in turbine operation is achieved by reducing the roughness of the surfaces which are in contact with the flowing fluid. This is achieved through additional machining (grinding, polishing, etc.) and eventually by applying suitable coatings of ceramics, plastic, etc. Such modifications are known for pumps used in special applications, e.g. in the chemical industry (*Güllich, 2003*). However, experience in verifying their effect on turbine pump operation is still lacking in literature.

Experimental verification of modifications

The META Plus 5 pump, manufactured by ISH Pumps Olomouc, was selected for experimental verification of the above mentioned optimization adjustments. From a design point of view, this is a one-stage centrifugal pump with a spiral box and impeller with outer diameter D_1 = 132 mm. The parameters of the original untreated pump at optimal efficiency, at 1450 rpm, are shown in Tab. 1. The diagram of the pump design is shown in Fig. 2.

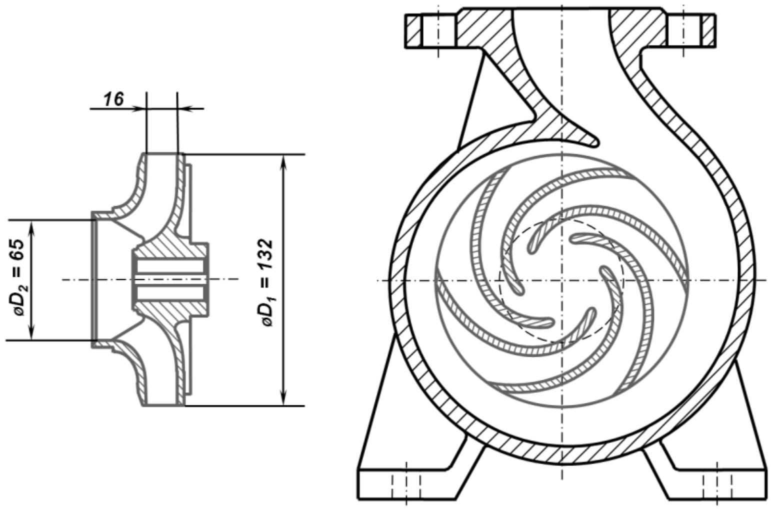

Fig. 2 Diagram of experimental radial centrifugal pump

On the pump above, the characteristics were measured on the hydraulic test circuit in pump and subsequently in turbine modes, on the original, untreated machine. The impeller was then dismantled and adjusted as shown in Fig. 1. The blade edges and both discs on the outer diameter, D_1 were rounded. The adjustment is evident from Fig. 3. In addition, a polymeric coating with a hydrophobic surface was applied to the inner flow parts of the impeller. Its purpose was to reduce the roughness of these surfaces which are wetted by the flowing fluid.

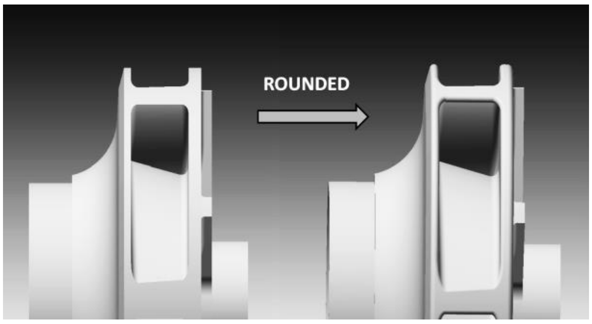

Fig. 3 Detail of the impeller rounding

After the assembly of the modified impeller, the effect of the modifications on operation in turbine mode was verified on the hydraulic circuit. The diagram of the hydraulic test circuit is shown in Fig. 4.

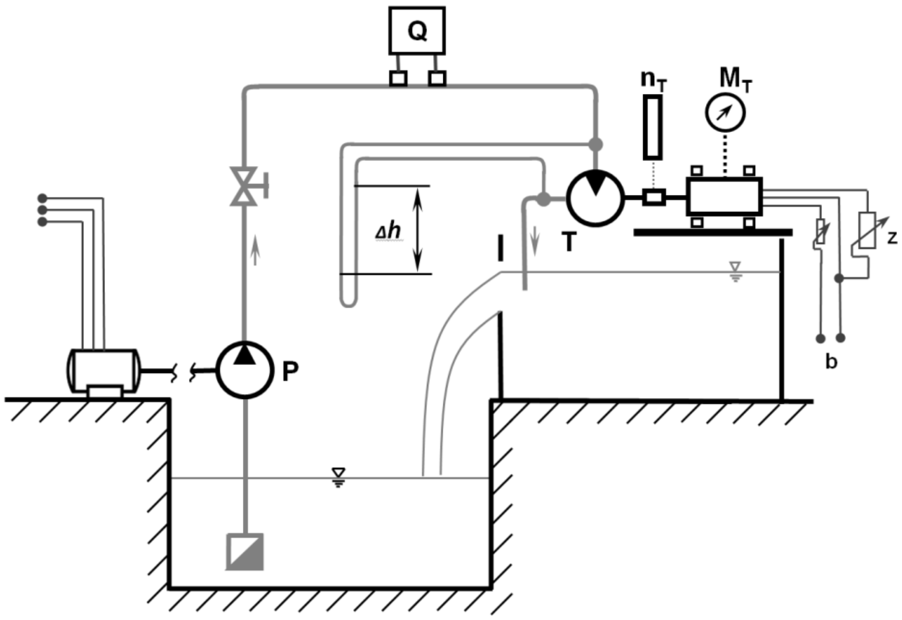

Fig. 4 Hydraulic circuit for testing pump as turbine (PAT)

The test circuit consists of two tanks and a pump (P) which produces hydrotechnical potential for the turbine (T) to be tested. The turbine is connected to a dynamometer (M_T) with continuously adjustable load. The mechanical output of the turbine is given by:

$$P_T = M_T \frac{\pi \cdot n_T}{30} \qquad [W] \tag{3}$$

where, M_T is the torque on the turbine shaft (N·m) and $n_{T,}$ the turbine speed (min^{-1}). The hydrotechnical potential (or hydraulic output delivered to the turbine) is determined by the flow Q and the differential pressure of the mercury manometer, Δh (m):

$$P_w = Q \cdot \rho_w \cdot \left(\frac{\rho_{Hg}}{\rho_w} \cdot \Delta h \cdot g + \frac{v_i^{\,2} - v_o^{\,2}}{g} + g \cdot y \right) \qquad [W] \tag{4}$$

where, ρ_{Hg} is the specific weight of mercury (kg·m^{-3}), ρ_w, the specific weight of water (kg·m^{-3}), v_i, v_o, the velocity of water in the inlet and outlet pipes, respectively (m·s^{-1}) and y, the vertical distance of zones generating pressure (m). The element in brackets of equation (4) expresses the specific energy of the turbine Y_T (J·kg^{-1}) (*ČSN EN ISO 9906, 2013*).
The overall efficiency of the turbine is:

$$\eta_T = \frac{P_T}{P_w} \qquad [-] \tag{5}$$

RESULTS AND DISCUSSION

The results of the experimental verification of pump optimization in turbine operation are in the form of the characteristics shown in Fig 5. The course of the main output quantities is shown here, i.e. the mechanical power P_T, the torque M_T, and the efficiency, η_P, in relation to the unit speeds n_{11}. Unit speeds of hydraulic machines are defined by:

$$n_{11} = \frac{n_T \cdot D_1}{\sqrt{Y_T}} \qquad \left[\min^{-1}\right] \tag{6}$$

Furthermore, the characteristic features the course of the gradients and unit flow rates, Q_{11} in relation to the unit speeds, n_{11}. Unit flow rate is defined as:

$$Q_{11} = \frac{Q}{D_1 \cdot \sqrt{Y_T}} \qquad \left[l \cdot s^{-1}\right] \tag{7}$$

Black curves correspond to the characteristics of the original untreated pump. Grey curves are the characteristics of the machine modified by the method described above.

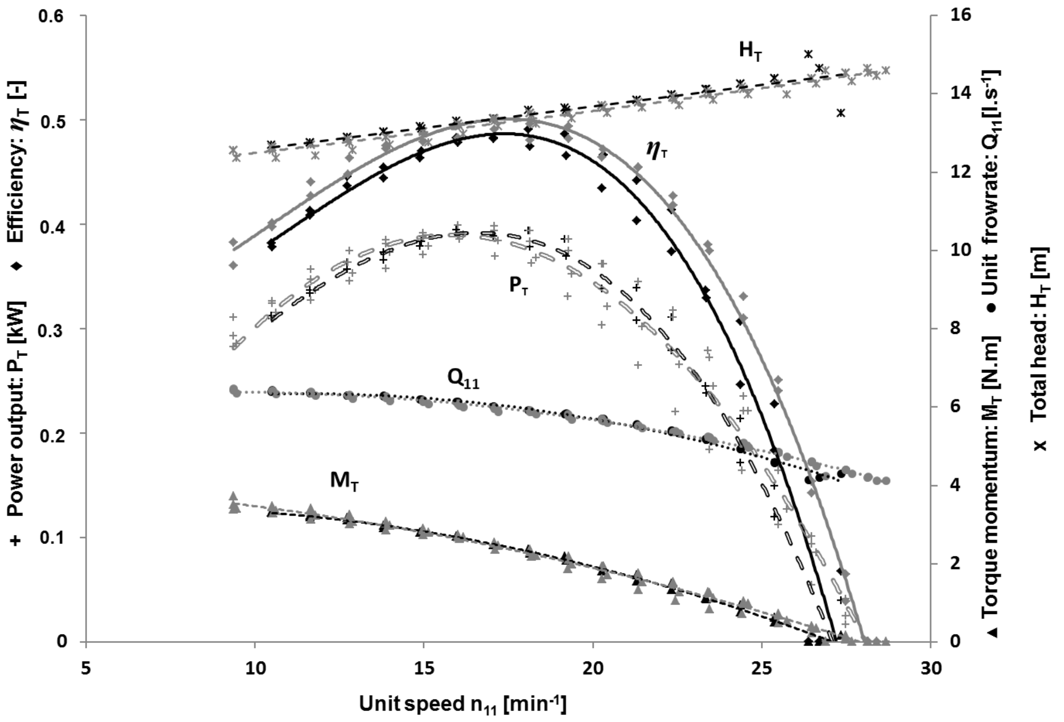

Fig. 5 Characteristics of turbine operation of radial centrifugal pump

Values corresponding to optimal operation at the highest efficiency of the machine (or Best Efficiency Point, BEP) are quantitatively summarized in Tab 1.

Tab. 1 Parameters of optimum pump operation and PAT

BEP		Pump	PAT original	PAT improved
Shaft speed	N [min^{-1}]	1450	1500	1500
Flowrate	Q [l.s^{-1}]	3.8	6.0	5.9
Total head	H [m]	5.8	13.4	13.3
Power input/output	P [W]	310	388	394
Total efficiency	η [%]	0.70	0.48	0.50

From the measured characteristics, there is another finding concerning the conversion relations (1) and (2). Recalculation assumes that the machine has the same speed in both pump and turbine modes. Only the direction of rotation of the shaft is the opposite. Maintaining the speed has its justification resulting from the requirement to use the set for electricity production. In this case, it is necessary to respect the frequency of the supply network and hence the generator, or the turbine, speed. However, the use of relations (1) and (2) also assumes unchanging efficiency in both pump modes. This condition may not apply in practice though, especially with smaller pumps, as it has been demonstrated experimentally in this case.

CONCLUSIONS

On the basis of the measured results it can be stated that the radial one-stage pump in turbine operation shows a 22% reduction in overall efficiency compared to the pump operation. Subsequent adjustment of the impeller by rounding the input edges on the outer diameter of the impeller, along with a reduc-

tion in roughness of the inter-blades flow channels resulted in an efficiency gain of 2%. At the same time, flow decreased by 1.7% and the gradient by 0.75%. Mechanical performance improved due to the modification by 1.5%. Overall, such a simple adjustment brings only a partial increase in performance parameters. Its benefits need to be seen as a further addition to the innovative adaptations of the connecting parts of the pump, such as the spiral case.
The measurement results further showed the necessity of correction of the conversion relationships when designing a pump for turbine mode. Based on the quantified parameters of the test pump, the exponents of equations (1) and (2) correspond to the values $x = 2.3$ and $y = 1.3$. It can be stated that the values of the exponents increased in a similar pattern as the efficiency of the pump in the reverse turbine operation decreased. This fact, including the change in the efficiency of the reverse operation of the machine is yet to be described in literature and it is necessary to examine it in further research.

ACKNOWLEDGMENT
This study was supported by ISH PUMPS OLOMOUC a. s., manufacturer of the pump technology.

REFERENCES

1. Alatore-Frenk, C. (1994) Cost minimization in microhydro systems using pumps-as-turbines, *Ph.D. Thesis*, University of Warwick.
2. Bláha, J., Melichar, J., & Mosler, P. (2012) Contribution to the use of hydrodynamic pumps as turbines. In: *Energetika 5/2012*. (in Czech)
3. ČSN EN ISO 9906 (2013) Hydrodynamic pumps - Acceptance tests of hydraulic performance parameters - Degrees accuracy of 1, 2 and 3, ČSNI 2013. (in Czech)
4. Derakhshan, S., & Nourbakhsh, A. (2008) Theoretical, numerical and experimental investigation of centrifugal pumps in reverse operation (2008) In: *Experimental Thermal and Fluid Science 32* 1620–1627, Elsevier.
5. Güllich, J. F. (2003) Effect of Reynolds Number and Surface Roughness on the Efficiency of Centrifugal Pumps. In: Journal of Fluids Engineering 125(4), 670-679.
6. Güllich, J. F. (2014) *Centrifugal pumps*. Berlin: Springer-Verlag
7. Munson, B. R, Zouny, D. F., & Okiishi, T., H. (2006) *Fundamentals of Fluid Mechanics – Fifth edition*, USA: John Wiley & Sons, Inc.
8. Nautiyal, H., Varun, & Kumar, A. (2010) Reverse running pumps analytical, experimental and computational study: A review. In: *Renewable and Sustainable Energy Reviews 14* (2010), 2059-2067.
9. Polák, M. (2013) The issue of energy utilization of low-potential water sources, *hab. thesis*, CULS Prague, (in Czech)
10. Poláková, Z., & Polák, M. (2016) Centrifugal pump in turbine mode for small hydropower. In: *Proceedings of 6th International Conference on TAE*, Prague, 500-505.
11. Raman, N., Hussein, I., Palanisamy, K., & Foo, B. (2013) An experimental investigation of pump as turbine for micro hydro application. In: *Proceedings of 4th International Conference on Energy and Environment 2013 (ICEE 2013)*, IOP Conf. Series: Earth and Environmental Science 16 012064
12. Sedlář, M., Šoukal, J., & Komárek, M. (2009) CFD analysis of middle stage of multistage pump opereting in turbine regime. In: *Engineering Mechanics*, Vol. 16, 2009, No. 6, 413–421.
13. Singh, P. (2005) Optimization of internal hydraulics system design for pumps as turbinek with Field Implementation and Evaluation, *PhD thesis*, Universität Fridericiana, Karlsruhe.
14. Singh, P., & Nestmann, F. (2011) Internal hydraulic analysis of impeller rounding in centrifugal pumps as turbines. In: *Experimental Thermal and Fluid Science 35*. 121–134.

Corresponding author:
doc. Ing. Martin Polák, Ph.D., Department of Mechanical Engineering, Faculty of Engineering, Czech University of Life Sciences Prague, Kamýcká 129, Praha 6, Prague, 16521, Czech Republic, phone: +420 224 383 183, e-mail: karel@tf.czu.cz

VERIFICATION OF CONSTRUCTION PROPERTIES MATERIALS FOR RAPID PROTOTYPING USING SLS TECHNOLOGY

Silvester POLJAK[1], Rudolf MADAJ [2], Pavol PODHORA[3]

[1]*University of Žilina, Faculty of mechanical engineering, Department of Construction and Mechanical Parts, Univerzitná 8215/1, 010 26 Žilina, silvester.poljak@fstroj.uniza.sk*
[2]*University of Žilina, Faculty of mechanical engineering, Department of Construction and Mechanical Parts, Univerzitná 8215/1, 010 26 Žilina, rudolf.madaj@fstroj.uniza.sk*
[3]*University of Žilina, Faculty of mechanical engineering, Department of Construction and Mechanical Parts, Univerzitná 8215/1, 010 26 Žilina, pavol.podhora@fstroj.uniza.sk*

Abstract
This article discusses the different mechanical properties of samples made using 3D printing, namely SLS-sampled specimens. This article describes 3D SLS printing technology, a selection of SLS 3D printing materials, and the influence of 3D print settings on samples. The article is mainly focused on storing samples in different directions of 3D printing, orientation in the direction of the x, y, z axes and then for the strength evaluation of these samples. The measured results are further evaluated at the end of the article.

Key words: *3D printing; SLS technology; stress strenght;*

INTRODUCTION

Nowadays, Rapid Prototyping technology is experiencing a lot of booming right Is proportionally related to the increase in materials usable by this technology. Although it exists Amount of usable materials, from metals and concrete to biocompatible materials, The most widely used are due to their versatility and price of plastics. This article will describe some of the most commonly used materials for Individual forms of production by Rapid Prototyping, in particular the SLS technologies. The mechanical properties of the samples in different directions of the individual samples will be examined. A brief description of the course of the material tests to be carried out in the practical part will be followed. From the data obtained, the material characteristics are calculated and compared with the values reported by the manufacturer in the material sheet. The results will be analyzed and the reasons for possible deviations between measured and reported values will be determined. The most common materials used in 3D printing today include plastics, metals, ceramics, paper, biomaterials, or even food. Each material is uniquely used and is therefore becoming an increasingly frequent combination of multiple materials to guarantee the best mechanical properties of the manufactured part. The most used material, however, is still plastic and mainly due to a wide range of usable types. Each type is characterized by different strength, flexibility, surface finish or color. Using SLS (Selective Laser Sintering) technology, we can achieve the creation of fully functional prototypes, the properties of which are comparable to prototypes created by injection. It is an ideal method for use in piece production thanks to a favorable price / performance ratio. The benefits of SLS include print speed, the creation of durable, functional and complex parts, while printing does not require the creation of a supporting structure, as well as the choice of a wide range of finishing operations. The drawbacks of printing using this technology are that the parts have different strengths in each direction of printing. This is due to the 3D printing technology itself.

SLS 3D Printing Technology

An additive manufacturing layer technology, SLS involves the use of a high power laser (for example, a carbon dioxide laser) to fuse small particles of plastic, metal, ceramic, or glass

powders into a mass that has a desired three-dimensional shape. The laser selectively fuses powdered material by scanning cross-sections generated from a 3-D digital description of the part (for example from a CAD file or scan data) on the surface of a powder bed. After each cross-section is scanned, the powder bed is lowered by one layer thickness, a new layer of material is applied on top, and the process is repeated until the part is completed.
Because finished part density depends on peak laser power, rather than laser duration, a SLS machine typically uses a pulsed laser. The method of creating a 3D model can be seen in Fig.1. The SLS machine preheats the bulk powder material in the powder bed somewhat below its melting point, to make it easier for the laser to raise the temperature of the selected regions the rest of the way to the melting point.

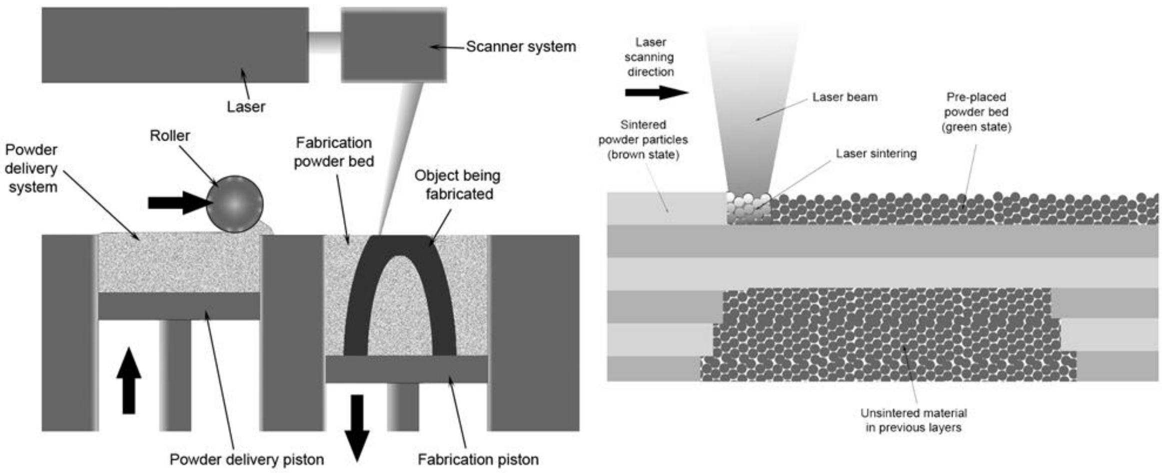

Fig.1 SLS 3D Printing Technology (*Anubis3d, 2017*)

MATERIALS AND METHODS

Materials used in sls technology and methods for testing

By using SLS (Selective Laser Sintering), we are able to create fully functional prototypes, the properties of which are comparable to prototypes created by injection. This is an ideal method for use in piece production thanks to a favorable price / performance ratio. The advantages of SLS include print speed, the creation of durable, functional and complex parts, while printing does not require the creation of a supporting structure, as well as the choice of a wide range of finishing operations.
Technical Specifications:
• Standard accuracy: ± 0.3% with a lower limit of ± 0.3mm
• Minimum wall thickness: 1mm
• Surface Structure: Displays have a typical grainy surface, but can be adjusted by any finishing method, e.g. They can be sanded, impregnated, coated etc .. (*Laser Sintering, 2017*)

PA (Polyamide)

The powder of this material is self-supporting, thus avoiding the generation of a supporting structure in the prototype process. Polyamide makes it possible to produce fully functional samples with high mechanical and thermal resistance and its particles are resistant to most chemicals. The material is also biocompatible due to its application in healthcare (*Laser Sintering, 2017*).

Testing materials used in 3d printing with sls technology

The tensile test is a basic test of the mechanical properties of the materials (*Rapid, 2017*). Testing is performed on standardized specimens clamped in jaws of the tearing machine, with the axis of the specimen being aligned with the force axis. A growing force develops on the sample until it breaks down. During the test the instrument measures the load force and the relative elongation of the rod. By evaluating the measured data we determine for the material to be tested the slope, the tensile strength, the relative elongation and the constriction. Test results are used to select the appropriate material for the required application, quality control, and prediction of material behavior under load. For extruded plastic samples, the test is performed according to STN EN ISO 527-1: Plastics. Determination of tensile properties. Part 1: General principles (ISO 527-1: 2012) and STN EN ISO 527-2: Plastics. Determination of tensile properties. Part 2: Test conditions for pressed and extruded plastics (ISO 527-2: 2012).

Test specimen for tensile strenght testing
The test sample has the most frequent cross-section of square, rectangular or circular shape. At the end of the sample, the so- Arms whose shape is adapted to the shape of the jaws of the jig machine into which the specimen clamps. The shape of the measured sample can be seen in Fig.2 and Fig.4. Among them, there is a calibration part of smaller cross-section that ensures initialization of the crack. Test rods are produced in long or short designs (*STN EN ISO 527-2: 2012, 2012*).

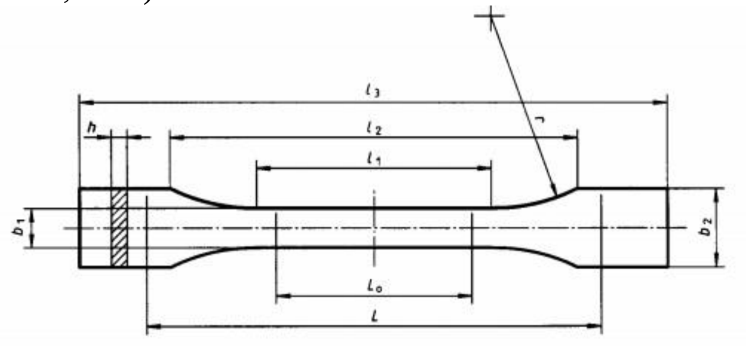

Fig.2 Test rod with rectangular cross section

Exam evaluation
The main result is the Hook diagram, which shows the dependence of the elongation of the bar on the voltage generated. From the graph, in addition to the voltage characteristics, such as the slope Re, the strength limit Rm, the elastic limit Rp, the deformation characteristics determining the plasticity of the material are deformed. Thus, it is possible to determine at what load the material occurs in the area of the elastic deformation, whether it comes into plastic deformation and therefore there is a breakage of the sample. The deformation curve can be seen in Fig.3. Criteria for assessing deformation characteristics are elongation and contraction (*Strojarstvo, 2017*).

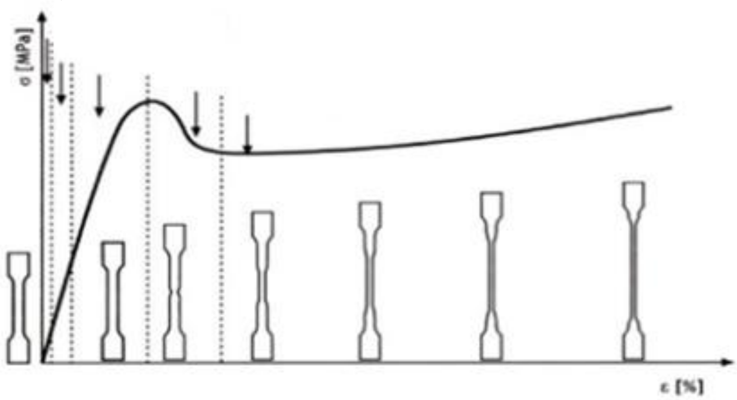

Fig.3 Deformation curve of thermoplastic materials rectangular cross section

Verification of materials properties by means of measuring instruments

The first step was to model the STD EN ISO 527 in the PTC Creo 3 CAD standardized sample for the tensile test. The sample model has been exported to STL, which is used to work with 3D models in modeling software and 3D printer control. Once the settings have been made in the software, samples were printed on the Formiga P 100 printer.

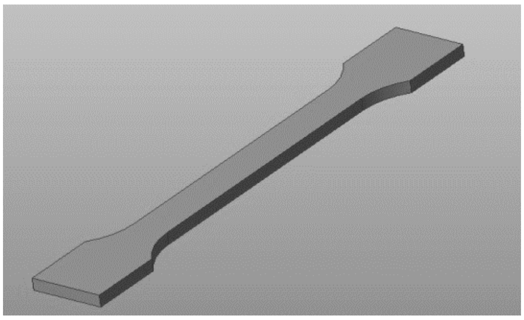

Fig.4 3D Model of specimen

The sample model has been exported to STL, which is used to work with 3D models in modeling software and 3D printer control. After performing the settings in the software, the samples were printed on the Formiga P 100 printer. 11 samples were printed out for the PA 2200 material, three pieces were printed on the X-axis and Y-axis, and five pieces were printed in the Z-axes. Due to such decomposition, it is possible to observe the influence of the printing direction on the mechanical properties of the sample. The orientation of the individually printed samples using a 3D printer is shown in Fig.5 and Fig.6

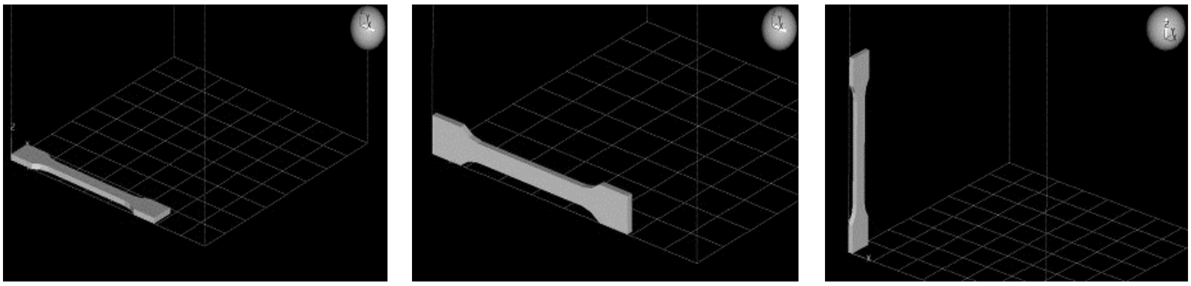

X axis Y axis Z axis

Fig.5 View samples in interface for 3D printer FORMIGA P100

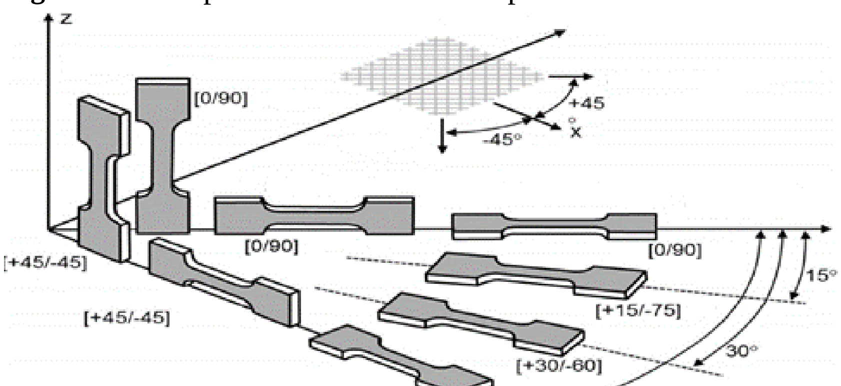

Fig.6 Sample of specimens in different angles

RESULTS AND DISCUSSION

From the measured values, the tensile stresses, elongations and Young's modules were calculated according to the respective relations. For printing in every direction. From these values, a graph and arithmetic mean were produced, the results of which were compared with the values reported by the manufacturer.

In this chapter there are tables and charts that compare the measured values in different axes. From the measured values for individual axes it can be stated that the measured values were almost the same for each measurement.

Evaluation of pa 2200 tensile strenght test

Tab.1 Resulting values for samples printed in X direction

	Specimen X_1	Specimen X_2	Specimen X_3
Duration of the test	97,48 s	95,1 s	98,50 s
Elongation	27,98 %	23,57 %	28,44 %
Tension stress	52,339 MPa	53, 025 MPa	53, 219 MPa
Young modulus	508,125 MPa	698,9 MPa	726,563 MPa

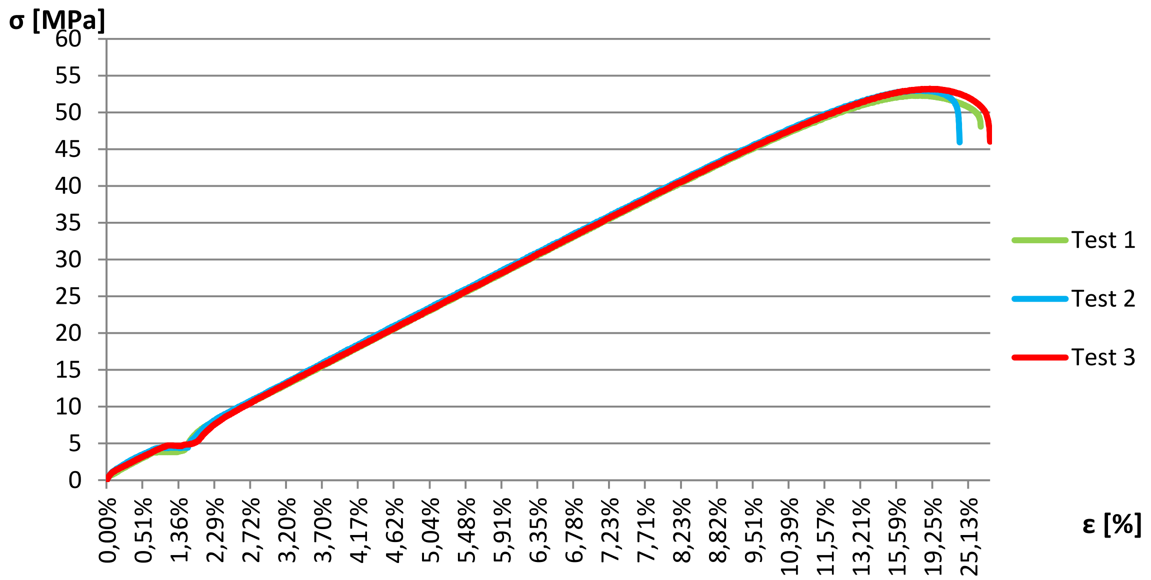

Fig.7 Dependence of the elongation from the stress on the sample pressed in the X-axis direction

Tab.2 Resulting values for samples printed in Y direction

	Specimen Y_1	Specimen Y_2	Specimen Y_3
Duration of the test	98,32 s	96,78 s	97,12 s
Elongation	26,73 %	25,58 %	28,97 %
Tension stress	53,579 MPa	53, 03 MPa	52,309 MPa
Young modulus	719,06 MPa	470,156 MPa	442,06 MPa

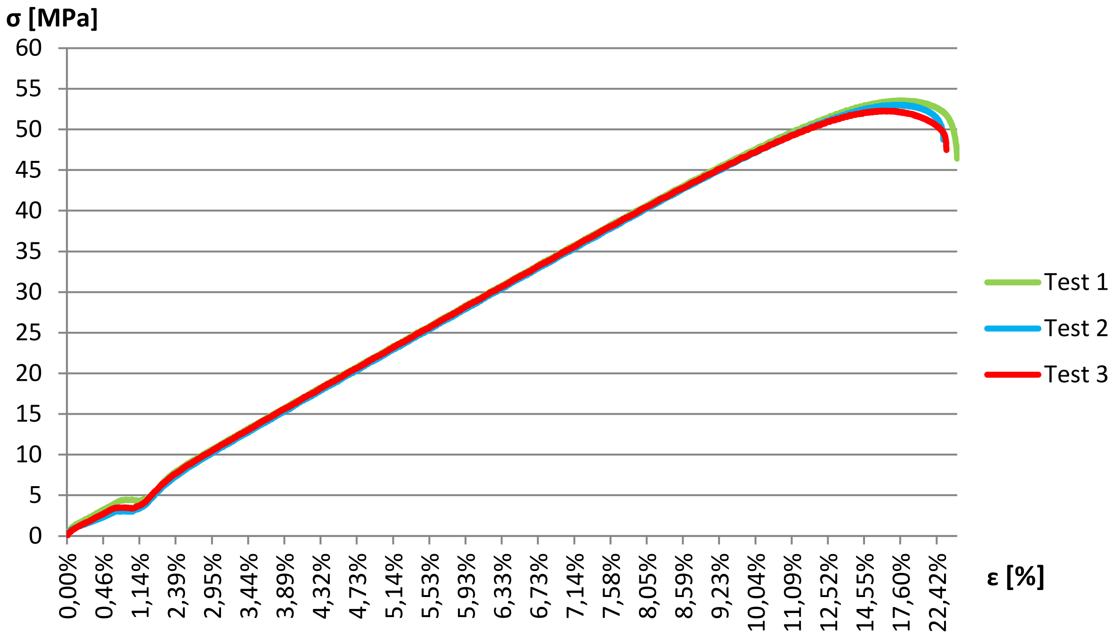

Fig.8 Dependence of the elongation from the stress on the sample pressed in the Y-axis direction

Tab.3 Resulting values for samples printed in Z direction

	Specimen Z_1	Specimen Z_2	Specimen Z_3	Specimen Z_4	Specimen Z_5
Duration of the test	65,3 s	73,38 s	67,92 s	70,02	67,88 s
Elongation	9,7 %	11,02 %	12,58 %	10,04%	10,24 %
Tension stress	41,241MPa	45,60 MPa	41,896 MPa	43,71MPa	42,31MPa
Young modulus	574,218 MPa	624,844 MPa	13,125 MPa	429,375 MPa	508,125 MPa

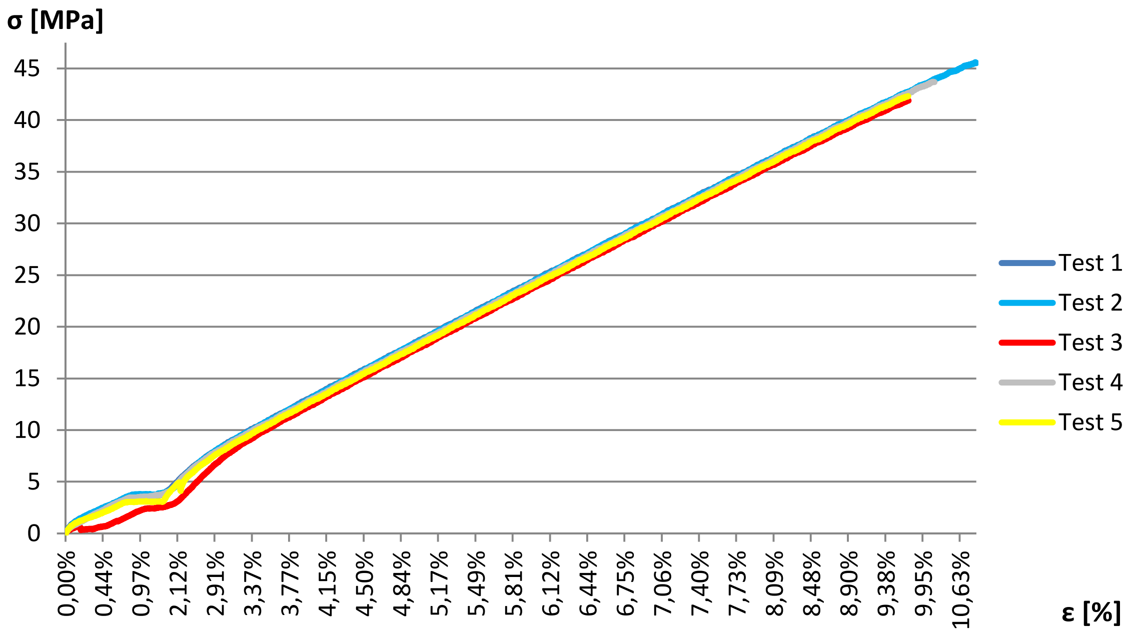

Fig.9 Dependence of the elongation from the stress on the sample pressed in the Z-axis direction

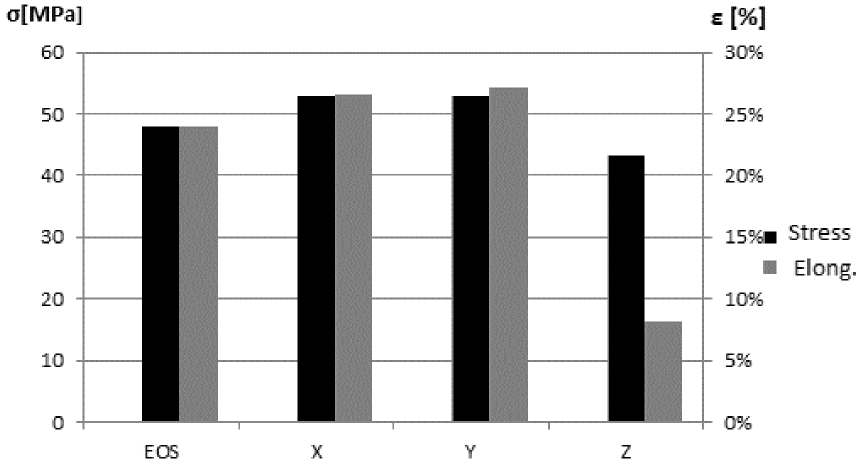

Fig.10 Comparison of declared and calculated values of stress and elongation

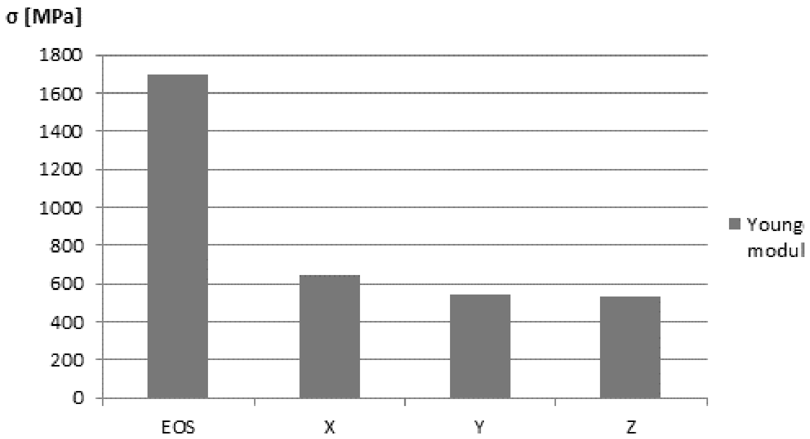

Fig.11 Comparison of the declared and calculated Young's module

Comparison of declared and calculated voltage and elongation values and comparison of the declared and calculated Young's modulus of elasticity can be seen in Fig.10 and Fig.11. Findings show that the printed material PA 2200 in the Y axis there is a marked difference in the allowable tensile stress, but when pushed in the axial direction from the tensile stress of the lower most bar 10 which is a difference of 19%. As far as the extension is concerned, it is again the worst Z axis, where the difference with respect to the axes X, Y is approximately 19 and thus 69.7%. The Young's module has the best X axis at 644.63 MPa followed by Y with 543.76 MPa and Z with 534.14 MPa. Compared to the manufacturer, the tensile stress values in the X and Y axes were higher and in the Z axis lower by approximately 5 MPa, representing a difference of 9.5%. On elongation, the X and Y axis measurements were greater than those reported by the manufacturer, approximately 11% in the Z axis, the elongation was measured by 66%. Younger modules, however, differ considerably from the values given by the manufacturer, since the average value of the manufacturer is 1700 MPa after the averaging is only 644.63 MPa, which is the difference of 62%.

CONCLUSIONS

From the measured values it is possible to find out that the declared values are different in different directions. When designing a 3D prototype, these contexts need to be considered. Different values are based on 3D printing technology, namely SLS. Differences between reported and measured values may be caused by multiple, technical or human factors. There are many

settings you can make on a 3D printer. Direction of bounce, angle rotation on the substrate, layer thickness, print speed, model fill method, quality and Material purity, sample placement on heated pad and method and speed of cooling has all the effect on the resulting properties. If we wanted to finish. The most likely actual mechanical properties of the investigated material, It would be necessary to do a few dozen samples at all Existing combinations of the above factors. The data would then be obtained Appropriate to achieve the most accurate results of the investigated properties. Next the effect of the job it plays during the print process is the temperature of the pad. Right print on a heated pad, there are other thermal passages than when printing a layer of material that affects the interconnection of the initial layers. Even in the middle the pads have a higher temperature than at their edges, measured at this temperature the values between the samples vary. In the static pull test, there are also factors that act on the data obtained. First, the quality of the device itself. As they appear in motion any inaccuracies and defects in the machine cause a deviation of the resulting data.
In the introduction, the article deals with the most frequently used materials for each of the Rapid Prototyping technologies, their properties and possibilities of use. Briefly, the pull test is described. That is, the material tests that are used to determine the mechanical properties of the materials. Also, the basic factors to be considered when determining the appropriate material for the desired application are described. The aim of the thesis was to verify the mechanical properties of the materials and thus to compare the values declared by the manufacturer with the measured and calculated values. The samples modeled in the PTC Creo3 CAD program were printed and then subjected to material testing. Samples were printed in X, Y and Z axes to determine the impact of the print axis on the mechanical properties of the material. After performing the measurements and calculating the values, the graphs and arithmetic means were compiled for comparison purposes.

ACKNOWLEDGMENT
This work was created by the implementation of the "Low-cost logistic system based on mobile robotic platforms for industrial use.", "ITMS: 26220220092" to support the Operational Programme Research and Development financed by the European Fund for Regional Development.

REFERENCES
1. https://www.anubis3d.com/technology/selective-laser-sintering/
2. Laser Sintering. [online]. [cit. 2016-11-25] web: http://www.materialise.com/en/manufacturing/3d-printing-technology/lasersintering
3. STN EN ISO 527-2: 2012 (64 0605), Plasty. Stanovenie ťahových vlastností Časť 2 Skúšobné podmienky pre lisované a vytláčané plasty (ISO 527-2: 2012)
4. Strojárstvo. [online]. [cit. 2017-1-7], web: http://www.engineering.sk/images/stories/pdf/stroj10_cb_kompl.pdf.
5. Rapid Prototyping Materials: Past, Present and Future, web: http://www.rapidprototyping-china.com/rapid-prototyping-materials-pastpresent-future

Corresponding author:
Ing. Silvester POLJAK, Ph.D., Department of Mechanical Parts, Faculty of Mechanical Engineering, University of Žilina, Univerzitná 8215/1, 010 08 Žilina, Slovak republic, phone: +421 41 5132901, e-mail: silvester.poljak@fstroj.uniza.sk

TRIBOLOGICAL PROPERTIES OF ELECTRO-SPARK DEPOSITED COATINGS AFTER LASER TREATMENT

Norbert RADEK [1], Jozef BRONČEK [2], Peter FABIAN [3], Jacek PIETRASZEK[4], Agata DUDEK[5]

[1]*Centre for Laser Technologies of Metals, Kielce University of Technology*
[2]*Department of Machine Elements and Design, University of Zilina*
[3]*Department of Technological Engineering, University of Zilina*
[4]*Institute of Applied Informatics, Cracow University of Technology*
[5]*Institute of Materials Engineering, Częstochowa University of Technology*

Abstract
The main objective of the present work was to determine the influence of laser treatment on microstructure, microhardness, surface geometric structure, porosity and tribological properties of coatings deposited on C45 carbon steel by the electro-spark deposition (ESD) process. The studies were conducted using WC-Cu electrodes produced by the powder metallurgy route.

Key words: *electro-spark deposition; laser treatment; coating; properties*

INTRODUCTION
The process of material growth resulting from electro-erosion is known as electro-spark alloying (ESA) or electro-spark deposition (ESD). The erosion of the anode and the spark discharges between the electrodes result in the formation of a surface layer with properties different from those of the base material (*Chang-bin, Dao-xin, Zhan, & Yang, 2011*; *Antoszewski, Evin, & Audy, 2008*; *Radek, Sladek, Broncek, Bilska, & Szczotok, 2014; Padgurskas, Kreivaitis, Rukuiza, Mihailov, Agafii, Kriukiene, & Baltusnikas, 2017*).
Electro-spark deposition is a cheap high-energy process. Developed in the post-war period, the technology has been frequently modified. Its main advantages are the ability to select precisely the area to be modified, the ability to select the coating thickness, which may range from several to several dozen micrometers, good adhesion of a coating to the substrate, and finally, inexpensive and simple equipment for coating deposition.
Electro-spark deposited coatings have some disadvantages but these can be easily eliminated. One of the methods is laser beam machining (LBM); a laser beam is used for surface polishing, surface geometry formation, surface sealing or for homogenizing the chemical composition of the deposited coatings (*Radek, Wajs & Luchka, 2008; Radek, Pietraszek, & Antoszewski, 2014*; *Pietraszek, Radek, & Bartkowiak, 2013; Radek & Konstanty, 2012; Scendo, Radek & Trela, 2013*).
Analysis of properties of coatings requires many methods (*Radziszewski, 2004; Szczotok, 2015; Korzekwa, Gadek-Moszczak, & Bara, 2016; Pietraszek, Gadek-Moszczak & Torunski, 2014*). There are many alternative technologies for producing coatings and material properties improvements in relation to ESD technology (*Dudek & Włodarczyk, 2010; Ulewicz, 2015*).
The work discusses the properties of electro-spark deposited WC-Cu coatings under applied laser treatment. The properties were established based on the results of a microstructure analysis, surface geometric structure, microhardness, porosity and tribological studies.

MATERIALS AND METHODS
The working electrode (a stationary) was made from C45 carbon steel. The elemental composition of the steel was as follows (wt.%): C: 0.42 – 0.50, Mn: 0.50 – 0.80, Si: 0.10 – 0.40, P: 0.04, S: 0.04.
In the experiment, the coatings were electro-spark deposited with using a WC-Cu (50% WC and 50% Cu) electrode with a cross-section of 4 x 6 mm (the anode) - onto samples made of carbon steel C45 (the cathode). The main characteristics of the powders used in this work are included in Table 1.
The powders were mixed for 30 minutes in the chaotic motion Turbula T2C mixer. The mixture was then poured into rectangular cavities of a graphite mould, each 6×40 mm in cross section, and consolidated by passing an electric current through the mould under uniaxial compressive load. A 3 minute

hold at 950°C and under a pressure of 40 MPa permitted obtaining electrodes of porosity <10% and strength sufficient to maintain integrity when installed in the electrode holder.

Tab. 1 Powders used to manufacture WC-Cu electrodes

Powder	Particle size µm	Producer
WC	~0.2*	OMG
Cu	~0.04*	NEOMAT

** measured using Fisher Sub-Sieve Sizer*

This method offers high efficiency in production of sintered parts, at elevated temperatures, assists in protecting metallic powders against oxidation. The protection is attributed to the formation of a CO/CO_2 reducing atmosphere inside the graphite mould which, in the old-type equipment shown in Figure 1, is exposed to air. The following parameters were assumed to be optimal for ESA (*Radek & Konstanty, 2012*). The samples with electro-spark deposited coatings were laser-modified using the following parameters (*Scendo, Radek & Trela, 2013*).

Fig. 1 Hot pressing operation carried out in air

RESULTS AND DISCUSSION

A microstructure analysis was conducted for WC-Cu coatings before and after laser treatment using a scanning electron microscope Joel JSM-5400.

Figure 2 shows the microstructure of an ESD WC-Cu coating. It is clear that the thickness of the obtained layer varied from 36 to 60 µm, whereas the heat affected zone (HAZ) ranged from 20 to 30 µm into the substrate. Figure 2 also reveals a clear boundary between the coating and the substrate and pores within the coating. The ESD WC-Cu coatings were modified by the laser treatment, which caused changes in their composition. The laser treatment homogenizes the coating chemical composition, causes structure refinement, and crystallization of non-equilibrium phases due to the occurrence of temperature gradients and high cooling rates.

The laser-modified outer layer does not possess microcracks or pores (Fig. 3). There is no discontinuity of the coating-substrate boundary. The thickness of the laser-treated WC-Cu coatings ranges from 40 to 62 µm. Moreover, the heat affected zone (HAZ) is in the range of 25 to 35 µm, and the content of carbon in the zone is higher.

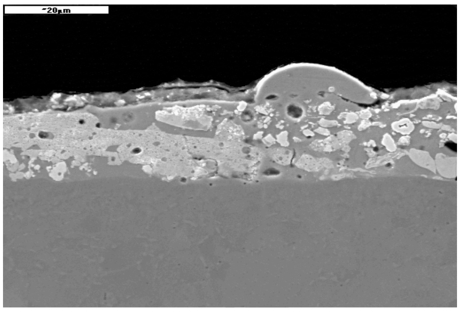

Fig. 2 WC-Cu coating microstructure after electro-spark alloying

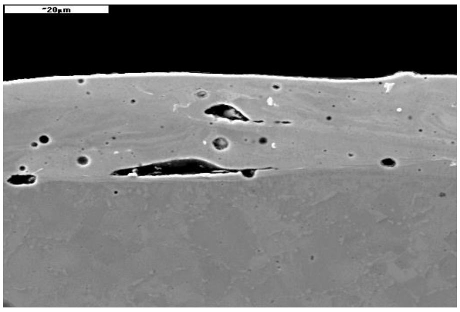

Fig. 3 Microstructure of the electro-spark alloying WC-Cu coating after treatment with an Nd:YAG laser

Microhardness testing was performed according to the Vickers method with a Microtech MX3 tester under the load of 40 G (0.4 N). Penetrator indentations were made on metallographic sections in three zones: in the coating (white layer), in the melted zone of coating (MZC), in the heat affected zone (HAZ), and in the base material (C45). Figure 4 summarizes the microhardness test results.
Laser treatment slightly decreased the microhardness of the ESD coatings. Laser irradiation reduced the microhardness of the WC-Cu coatings by 9% relative to the untreated coatings. The minor micro-hardness reduction after the laser treatment may improve the plastic properties of the coatings, which is important for the tools or machine elements operating under large loads, for example, drilling equipment in the mining industry or press elements used for ceramic building materialproduction. This effect may result from the dissolution of carbides.

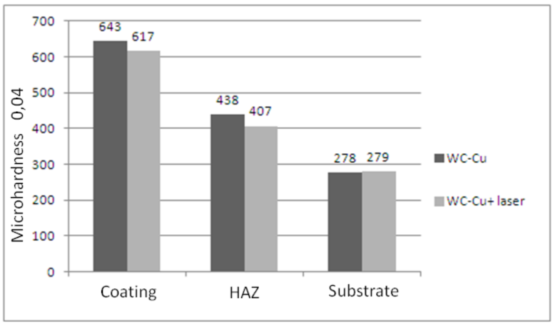

Fig. 4 Microhardness measurements for the WC-Cu coating before and after laser treatment

Surface geometric structure (SGS) substantially influences many processes that occur in the outer layer (*Miller, Adamczak, Świderski, Wieczorowski, Łętocha & Gapiński, 2017*).
Measurements of surface geometric structure (SGS) were carried out at the Laboratory of Computer Measurements of Geometric Quantities of the Kielce University of Technology. Those were performed using Talysurf CCI optical profiler that employs a coherence correlation algorithm patented by Taylor Hobson company. The algorithm makes it possible to take measurements with the resolution in the axis *z* below 0.8 nm. The result of measurements is recorded in 1024 x 1024 measurement point matrix, which for the x10 lens yields the 1.65 mm x 1.65 mm measured area and the horizontal resolution 1.65 μm x 1.65 μm.
Three-dimensional surfaces and their analysis with TalyMap Platinum software made it possible to precisely identify the geometric structure of the surfaces under consideration. Table 2 provides major parameters of the surface geometric structure of the examined specimens. Figure 5 present images of surface topography before and after laser treatment.
A greater value of the mean arithmetic deviation of surface roughness *Sa*, a basic amplitude parameter in the quantitative assessment of the state of the surface under analysis, was recorded for the specimen after the laser treatment, for the specimen before the laser treatment the value of this parameter was be almost 50% smaller.

A similar tendency is observed for the root mean square deviation of surface roughness *Sq*. Complementary information on how the surface of examined elements is shaped is provided by amplitude parameters, namely the coefficient of skewness (asymmetry) *Sku* and the coefficient of concentration (kurtosis) *Ssk*. Those parameters are sensitive to occurrence of local hills or valleys, and also defects on the surface. The parameter *Ssk* has a positive value for both specimens, the value is close to zero for the specimen before treatment, which indicates the symmetrical location of the distribution of ordinates with respect to the mean plane. The values of kurtosis that were obtained are close to *Sku* = 3, which indicates that the distribution of ordinates for both specimens is close to normal distribution.

Tab. 2 Parameters of the surface geometric structure

SGS parameters	Coating	
	WC-Cu	WC-Cu + laser
Sa [μm]	4.02	6.95
Sq [μm]	5.24	8.48
Ssk	0.15	0.02
Sku	3.89	2.77
Sp [μm]	26.44	34.03
Sv [μm]	21.21	66.76
Sz [μm]	47.65	100.80

Before laser treatment, the specimen had random isotropic structure (Iz = 88.52%), whereas after the treatment, that became a periodic structure, located in the transient area between isotropic and anisotropic structures (Iz = 55.32%). That is confirmed by the shape of the autocorrelation function of both surfaces, for the surface before treatment, the shape is circular and symmetrical, whereas for the surface after treatment, it is asymmetrical and elongated.

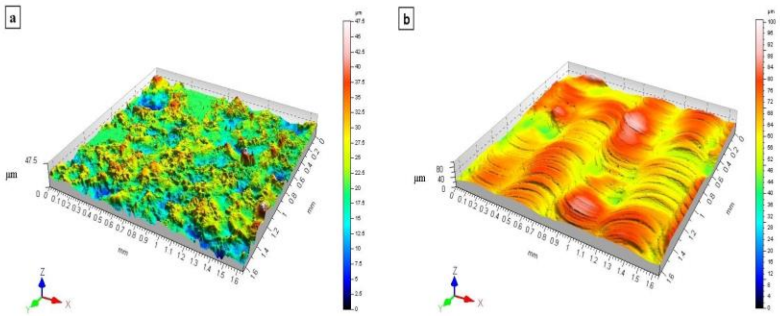

Fig. 5 Specimen surface topography: a) before laser treatment, b) after laser treatment

For assess the degree of porosity of the coatings tested WC-Cu before and after laser treatment, quantitative image analysis was performed using software supplied with the SIS which (SEM) Philips XL30 / LaB6. In the analysis guided by the principle of Cavalieri-Hacquerta according to which, a measure of the porosity can be shares of the pores:

- volume (the ratio of the total volume of voids to the total volume of the fragment of the coating),
- surface (the ratio of the total pore area to the total area analyzed grinding),
- the length of the control section (the ratio of the total length of the strings passing through the pores of the length of the analyzed section of the measurement plane grinding).

Tab. 3 Results of the surface porosity for the WC-Cu coating before and after laser treatment

Coating	Porosity % Number of measurement			Average value %
	1	2	3	
WC-Cu	5.7	6.3	3.5	5.2
WC-Cu +laser	0.4	0.2	0.1	0.2

Results of the surface porosity for the WC-Cu coating before and after laser treatment are shown in Table 3. Analyzing the table it can be seen that the applied coatings have a higher porosity with respect to the coating after laser treatment. Laser treatment reduced the porosity of the coatings more than 20 times. The porosity of the coatings WC-Cu was located in the range of 3.7 - 6.3%, and after laser treatment was 0.1 - 0.4%. Lower porosity of the WC-Cu coatings by positive influence on their performance characteristics, improving their corrosion resistance, adhesion and microhardness.

Seizure resistance tests were carried out using T-09 tribotester, in which the friction pair consisted of a cylinder and two prisms. Prisms with deposited WC-Cu coatings and C45 steel (laser treated and untreated) acted as specimens, whereas a roller of hardened carbon steel, ϕ6.3 mm in diameter, was used as a counter-specimen. In tests, three kinematic pairs were employed to investigate different material options, which made it possible to average experimental results. During the test, paraffin oil bath lubrication was used.

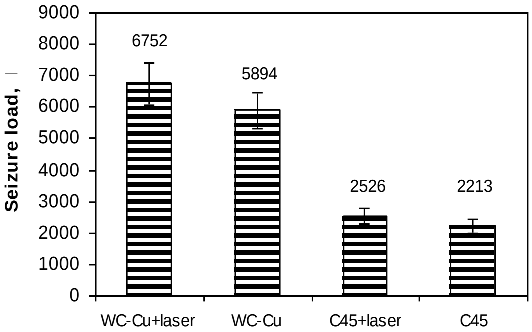

Fig. 6 Average values of seizure load

Figure 6 presents cumulative information on average values of seizure load for specimens before and after laser treatment. Those indicate that laser treatment resulted in an increase in the load that produced seizure both for electro-spark deposited coatings and for C45 steel.

CONCLUSIONS

1. A concentrated laser beam can be effective in modifying the state of the outer layer of electro-spark coatings and thus can modify their functional properties.
2. Laser irradiation of coatings resulted in the healing of micro-cracks and pores.
3. Parameters of surface geometric structure of electro-spark coatings have lower values when compared with SGS parameters of coatings after laser treatment.
4. Laser treatment caused an increase in the load at which seizure occurred for the tested materials. For laser-treated WC-Cu coatings, the value of the load is approx. 13% higher when compared to coated specimens without laser treatment.
5. Laser treatment caused a 9% decrease in the microhardness of the electro-spark alloying WC-Cu coatings.
6. Coatings after laser treatment are less porosity (more than 20 times).

ACKNOWLEDGMENT
This paper has been prepared in the framework of the international Slovak-Polish research project APVV SK-PL-2015-0008 on "Research of the Operational Properties of the Laser Treated Electro Spark Coatings".

REFERENCES

1. Chang-bin, T., Dao-xin, L., Zhan, W., & Yang, G. (2011). Electro-spark alloying using graphite electrode on titanium alloy surface for biomedical applications. *Applied Surface Science*, *257*, 6364-6371.
2. Antoszewski, B., Evin, E., & Audy, J. (2008). Study of the effect of electro-spark coatings on friction in pin-on-disc testing. *Journal of Tribology-Transactions of the ASME*, *3*, 253-262.
3. Radek, N., Sladek, A., Broncek, J., Bilska, I., & Szczotok, A. (2014). Electrospark alloying of carbon steel with WC-Co-Al_2O_3: deposition technique and coating properties. *Advanced Materials Research*, *874*, 101-106.
4. Padgurskas, J., Kreivaitis, R., Rukuiza R., Mihailov, V., Agafii, V., Kriukiene, R., & Baltusnikas, A. (2017). Tribological properties of coatings obtained by electro-spark alloying C45 steel surfaces. *Surface & Coatings Technology*, *311*, 90-97.
5. Radek, N., Wajs, E., & Luchka, M. (2008). The WC–Co electrospark alloying coatings modified by laser treatment. *Powder Metallurgy and Metal Ceramics*, *47*(3-4), 197-201.
6. Radek, N., Pietraszek, J., & Antoszewski, B. (2014). The Average Friction Coefficient of Laser Textured Surfaces of Silicon Carbide Identified by RSM Methodology. *Advanced Materials Research*, *874*, 29-34.
7. Pietraszek, J., Radek, N., & Bartkowiak, K. (2013). Advanced statistical refinement of surface layer's discretization in the case of electro-spark deposited carbide-ceramic coatings modified by a laser beam. *Solid State Phenomena*, *197*, 198-202.
8. Radek, N., & Konstanty, J. (2012). Cermet ESD coatings modified by laser treatment. *Archives of Metallurgy and Materials*, *57*, 665-670.
9. Scendo, M., Radek, N., & Trela, J. (2013). Influence of laser treatment on the corrosive resistance of WC-Cu electrospark coatings. *International Journal of Electrochemical Science*, *8*, 9264-9277.
10. Radziszewski, L. (2004).Intrusive effect of a contact transducer on testing results. *Metrology and Measurement Systems*, *11*(1), 31-43.
11. Szczotok, A. (2015). Study of casting from IN100 nickel-based superalloy using quantitative metallography and analytical electron miroscopy. *Materialwissenschaft und Werkstofftechnik*, *46*, 320-329.
12. Korzekwa, J., Gadek-Moszczak, A., & Bara, M. (2016). The Influence of Sample Preparation on SEM Measurements of Anodic Oxide Layers. *Praktische Metallographie-Practical Metallography*, *53*, 36-49.
13. Pietraszek, J., Gadek-Moszczak, A., & Torunski, T. (2014). Modeling of Errors Counting System for PCB Soldered in the Wave Soldering Technology. *Advanced Materials Research*, *874*, 139-143.
14. Dudek, A., & Włodarczyk, R. (2010). Structure and properties of bioceramics layers used for implant coatings. *Solid State Phenomena*, *165*, 31-36.
15. Ulewicz, R. (2015). Hardening of steel X155CrVMo12-1 surface layer. *Journal of the Balkan Tribological Association*, *21*(1), 166-172.
16. Konstanty, J. (2005). *Powder metallurgy diamond tools*. Oxford: Elsevier, 152.
17. Miller, T., Adamczak, S., Świderski, J., Wieczorowski, M., Łętocha, A., & Gapiński, B. (2017). Influence of temperature gradient on surface texture measurements with the use of profilometry. *Bulletin of the Polish Academy of Sciences*, *65*(1), 53-61.

Corresponding author:
dr hab. eng. Norbert Radek, univ. prof., Centre for Laser Technologies of Metals, Faculty of Mechatronics and Mechanical Engineering, Kielce University of Technology, Al. 1000-lecia P. P. 7, 25-314 Kielce, Poland, phone: 48 41 3424489, e-mail: norrad@tu.kielce.pl

58th ICMD 2017
6 - 8 September 2017, Prague, Czech Republic

IMPACT OF DOCKING METHOD ON LOADS IN ELEMENTS FLOATING DOCK – VESSEL UNIT

Przemysław RAJEWSKI[1], Oleh KLYUS[2]

[1,2] *Institute of Marine Propulsion Plants Operations, Maritime University of Szczecin, Poland*

Abstract
The paper concentrates on how a selected dock surfacing method affects the stresses formation in the structure of the dock and the vessel hull. Repairs and modernization of underwater hull parts are related mainly to placing the vessel on a working platform above the waterline. Docking operations are carried out using floating docks, hoists and slips or, less frequently due to high cost, by entry the vessel in a basin dry dock and draining the water. In each of the mentioned cases the method of supporting the bottom part of the hull changes from continuous support to multipoint support, which in extreme cases, may exceed the allowable loads and cause damage to the hull structure. The paper presents modern docking equipment and includes a discussion on the docking methods for vessels and technical aspects of the process affecting load variation in accordance with a selected dock surfacing method.

Key words: *vessel docking, floating dock, repairs, docking,*

INTRODUCTION
During the operation, a ship is subject to annual inspections proving that its technical condition meets the standards and requirements of a classification society supervising the ship. The preparation process for the inspection is usually preceded by conducting repairs. The scope of the inspection is specified in the classification rules and agreements made between the shipowner and the classification society. A ship must be a subject of the inspection of the underwater hull part twice in a five-year validity period of its class certificate (between the second and the third year and after five years of validity period). Inspections, repairs and modernization of underwater hull parts are related mainly to laying the ship on the working platform above the waterline. Activities related thereto are considered as a docking operation. Depending on the weight and dimensions of repaired vessels, shipyard equipment and acceptable costs, the operations are carried out using floating dry docks, hoists or slips or, less frequently due to high cost, by entry a vessel in a basin dry dock and draining the water. In each of the mentioned cases the method of supporting the bottom part of the hull changes from continuous support to multi point support, which in extreme cases, may exceed the allowable loads and cause damages to the hull structure *(Rules for classification floating docks, Chapter, 2 Steel hull structures, DNV.GL, Edition October 2015).* Upon having a docking date agreed, technical service of the shipowner provides a docking plan to the shipyard. Docking plan is a document developed by the shipyard constructing the vessel and includes essential information for the shipyard prior to docking the ship. Before the ship is docked it is necessary to carry out a number of preparatory activities related to the docking procedure, providing power and meeting the requirements for environment protection. In order to reduce the stresses of the vessel bottom where keel block it supports, it is required to remove cargo (load), petroleum waste, and to reduce the volume of ballast water to a minimum ensuring the stability of the ship entering the dock. The fuel amount should be also reduced to the least possible level. In order to facilitate docking the ship and grounding she on keels, it is aimed to keep the ship on a plate keel, without trimming of the ship. Upon the completion of the preparatory activities, a summary in a form of a table is developed. It shall include vessel weight, the arrangement of loads, the volume of fluids in tanks, draught. Figure 1 presents forces acting on the floating dry dock – vessel unit during emerging the ship above the waterline.

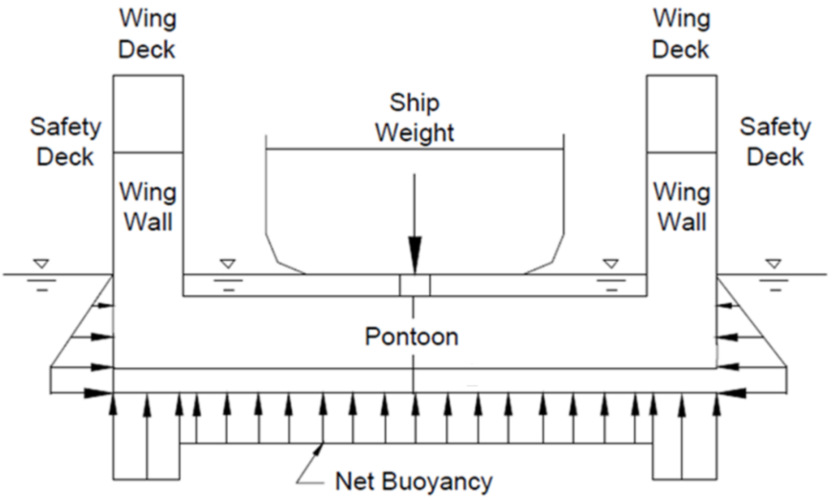

Fig. 1 Forces acting on a floating dry dock during surfacing a ship *Source: Author's elaboration based on* (2)

The paper aim is to present the factors affecting the changes of dock structure loads in reference to Dock No. 5 of repair yard "Gryfia" located in Szczecin, which occurred while docking two vessels namely m/s Narew and m/s Nogat. Different procedures for removing ballasts from the pontoon were applied.

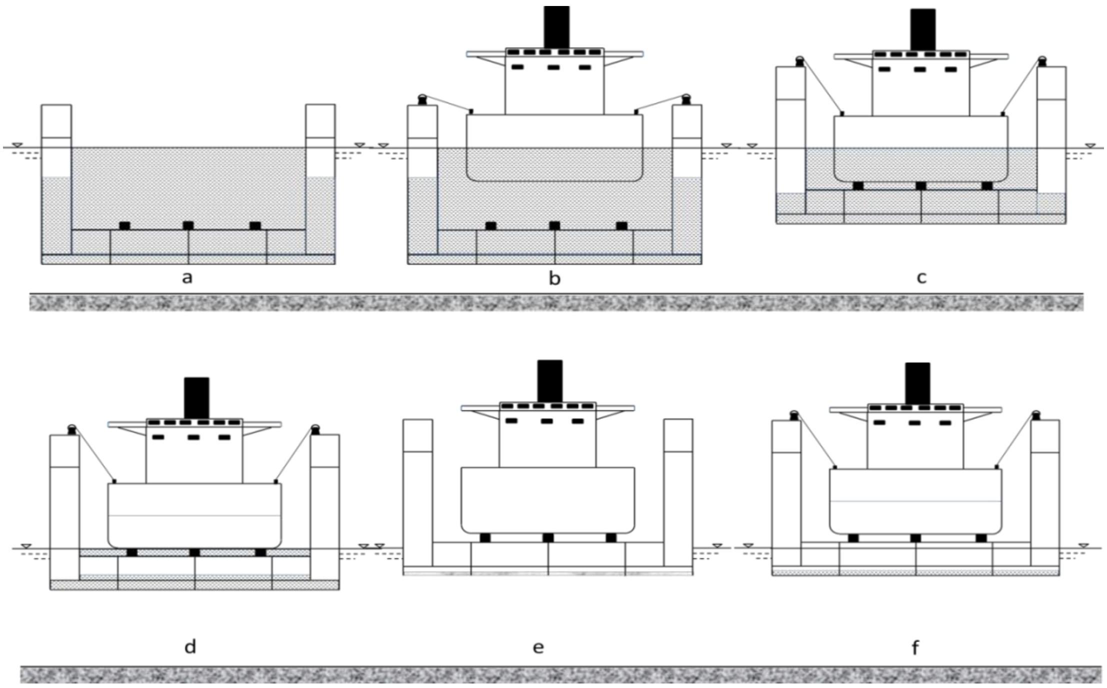

Fig. 2. Emerging phases for a dock-vessel unit (a – dock immersion, b – docking, c – grounding a ship on keel blocks, d – full load of keel blocks, e – pontoon just below water surface, f – dock emerged to the working position) *Source: Author's elaboration*

During the dock – vessel unit surfacing operation, there is a number of critical moments shown in Figure 2 namely Phase d and e. In Phase d water reaches the keel blocks' top, ballast tanks in the wing walls are drained and the water is pumped out from the ballast tanks in the pontoon. In Phase e the dock deck is just above the waterline and the water is still being drained from the pontoon's tanks.

The dock – vessel unit stability is the least in the said immersion phases. Even the slight tilt of the pontoon in Phase e may result in water overflowing to one sideboard and the dock stability is disturbed (6). Such a situation has occurred in April 2017 in a Polish shipyard.

MATERIALS AND METHODS

The complexity of activities related to preparing and docking a ship may result in the occurrence of threats and risks for safe docking operation. The main reason for this to happen is local exceedance of allowable stresses of dock structure or docked ship. The design values of bending moment and transverse strength related with loading the dock with the weight of docked ship, dock's weight along with water ballast and buoyant force should not be less than (1):

$$M = k_m g P_D\, L_D \quad (1)$$

$$Q = k_g g P_D \quad (2)$$

where M is bending moment (kNm), Q is the value of transverse strength in the dock (kN), k_m is a numerical factor of the values provided in Table 1, k_q is a numerical factor of the values provided in Table 1, g – gravitational acceleration (g = 9,81 m/s2), P_D – dock lifting capacity, [t]; the parameter the value of which is equal to the weight of the heaviest ship that may be docked in standard dock operational conditions; L_D – dock's length, [m]; it is a distance between the end walls (transverse bulkheads) of the pontoon (or pontoons), measured in the plane of the symmetry of the dock.

Tab. 1 k_m and k_q values (1)

Dock lifting capacity PD [t]	k_m	1 k_q
≤ 40 000	0,0333	0,13
≥ 70 000	0,0195	0,08

Linear interpolation should be applied to determine k_m and k_q for 40 000 t < P_D < 70 000 t. The formulas (1) and (2) should be applied if dock sagging and bending occurred. The above values M and Q are used to specify the required value of dock cross-section modulus and the cross-sectional area of vertical plates on the wing walls. The k_q value as a function of the dock cross-section is presented in Figure 3 and Figure 4.

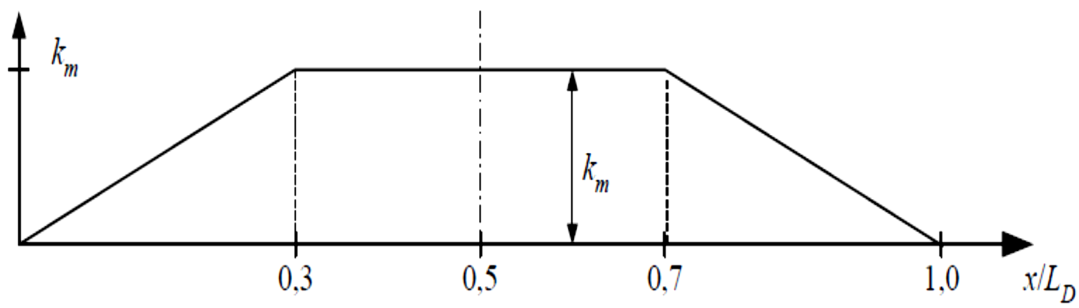

Fig.3. k_m value as a function of the dock cross-section (1)

The stresses in the dock's hull formed by general bending (or general bending including torsion) should not exceed the values provided in Table 2. The acceptable shear stress values, presented in the table, refer to mean stresses the values of which should be calculated by dividing transverse strength by the sum of cross-sectional areas of vertical plates on the wing walls.

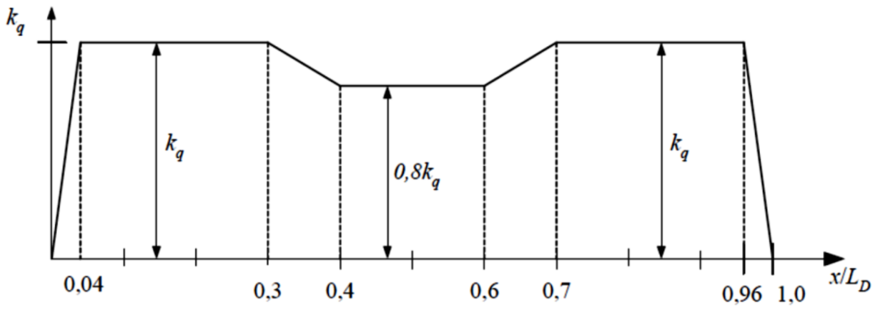

Fig.4. k_q value as a function of the dock cross section (1)

Tab. 2 Allowable stresses for dock's hull (1)

No	Load as per the equation	Normal stress σ_{dop} MPa	Shear stress τ_{dop} MPa
1	1	140k	100k
2	2	200k	120k

The value of strength modulus of dock's cross-section in any point along the dock should not equal less than the one determined as follows (3)(1)

$$W = \frac{M}{\sigma_{dop}} \cdot 10^3 \quad \text{cm}^3 \tag{3}$$

where
W is the value of the dock cross-section strength modulus (cm^3),
M is bending moment (kNm),
σ_{dop} is allowable stress (MPa)

The monitoring system of normal stresses formed by general bending and wing walls sagging enables to determine bending moments and stresses in a selected cross-section of the dock. In Dock No. 5 of repair yard "Gryfia", the measurements are read in the control room. Based on the above relation, an impact of dock ballast tanks draining method on bending moment value has been specified.

RESULTS AND DISCUSSION

Based on equations (1), (2) and (3), and by using the measurements of maximum deformations of the wing walls in Dock No. 5, the maximum bending moment values has been determined for two methods of draining water from the ballast tanks of the pontoon and the dock's wing walls. The results are presented graphically in Figure 5. In order to reach the maximum stability during emerging, it would be advisable to pump out the water firstly from the wing wall tanks and then from the ballast tanks of the pontoon. However, this draining procedure applied during the lifting process of a vessel the weight of which is almost equal to the dock lifting capacity causes that the transverse stresses of the dock structure are bigger than when the water is drained simultaneously from the pontoon and the wing walls are presented on Figure 5. In extreme cases, the stresses may cause damage to the dock structure. The dock deformations may be transfered onto the keel blocks and damage the shell plating. On the other hand, the operations of landing a ship on keel blocks and surfacing the dock with the grounded ship at extreme weather conditions or upon the failure to prepare the operation properly, or when the transverse stability of the dock – vessel unit is decreased while the water is pumped out simultaneously from the ballast tanks of both the wing walls and the pontoon, may result in the loss of stability of the unit, displacing docked ship (4) or, in extreme cases, overturning the dock together with the docked ship as presented on Figure 6.

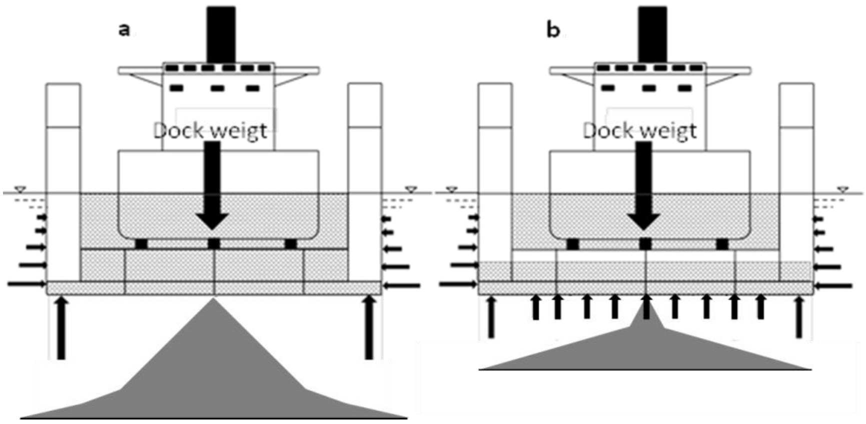

Fig. 5 Bending moments in cross section view for differnt draining methods during emerging a dock – vessel unit – Dock No. 5, a.- bending moment acting on dock's structure when water is drained from the wing wall tanks; b.- bending moment acting on dock's structure when water is being pumped out from the wing wall tanks and pontoon.*Source: Author's elaboration*

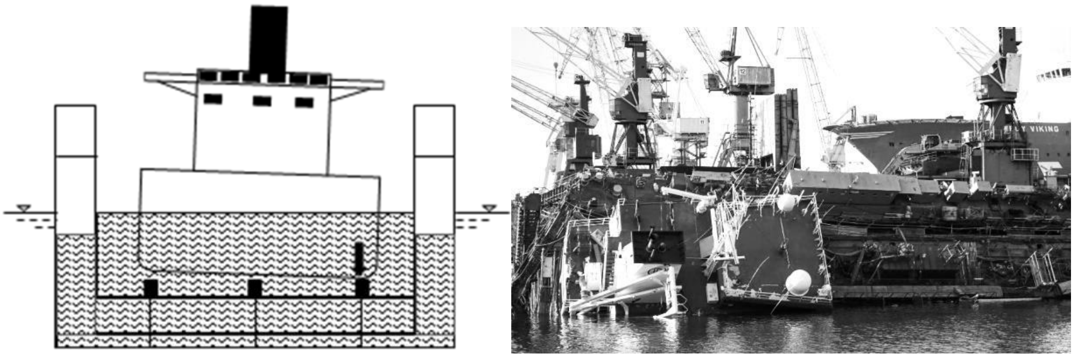

Fig. 6 Difference in hull pressure on keel blocks and change in the point of application of the resultant force when docking a ship with a tilt on the board *Source: Author's elaboration, photo Piotr Hukało*

If a ship has to be landed in the dock with a tilt on the sideboard due to certain technological reasons (eg. damage to the ship's hull, full double bottom tanks), the changes in pumping plan during surfacing the dock should be considered so as to compensate non-centered support during the firste phase of surfacing the ship (until she is layed down on keel blocks) and then return to draining the tanks symmetrically and align the initial tilt.

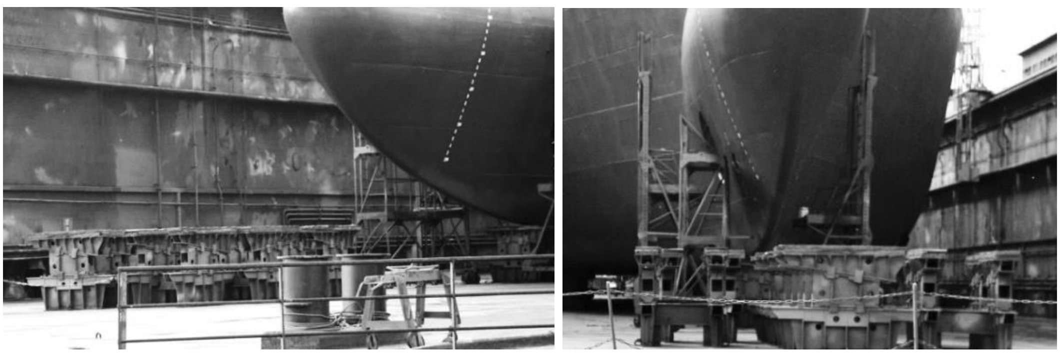

Fig. 7 Steel keel blocks on Dock No. 5 pontoon at SSR *Source: photo Przemysław Rajewski*

Damages of the ship bottom are mainly caused by using keel blocks of various structure, and thus with different deformation characteristics under load. The most commonly used keel blocks have a steel structure with a wooden coating of the top part interfacing with the ship bottom are presented on Figure 7. For the vessels of smaller dimensions and lower weight, supported on a keel, wooden supports are used

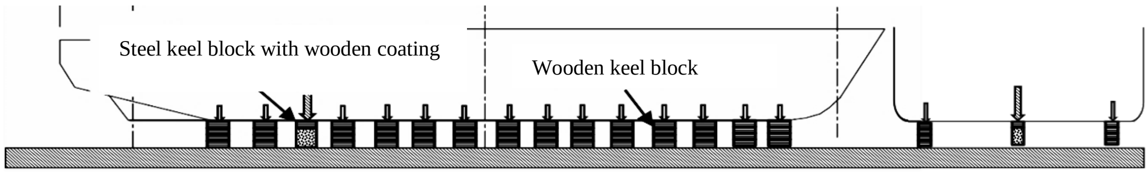

Fig. 8 Various hull pressure on keel blocks of different structure (2)

Using supports of different structure results in formation of stresses in supporting points as presented in **Figure 8** which may lead to dents in the shell plating, and even to permanent deformations of the bottom structure (2),(3).

CONCLUSIONS

Due to the safety of a floating dock structure and its stability, during the surfacing operation of a dock – vessel unit, it is advisable to develop a software or application to determine the landing method on keel blocks and to monitor on a current basis the process of draining the ballast tanks in the floating dock. The software or application should interface with signals collected on-line from dock structure stress controllers, tilt and trim sensors and should compute the unit stability updated in real time.

ACKNOWLEDGMENT

This research outcome has been achieved under the research project no. 1/S/IESO/2014 financed from a subsidy of the Polish Ministry of Science and Higher Educations for statutory activities of Maritime University of Szczecin.

REFERENCES

1. Polski Rejestr Statków (2007). Część II Kadłub i Wyposażenie kadłubowe. In *Przepisy Klasyfikacji I Budowy doków Pływających* (pp. 17 -39)
2. Heger Dray Dock, INC. June 2005, Block loading. In *Dockmaster training manual* (pp. 4 -5)
3. Rozenlit M.B.(1987) *Uniwersalnyje modeli dokowych opor*. In Sudostrojenie.No7, (pp..42-48).
4. Stasiak J.: *Flootability and stability dock-docked ship system.* (2005) In Polish Maritime Research, special issue. (pp. 46-50)
5. Marcinkowski P., Biernacka J., Olesiejuk-Kowalska M. (2005) *Management of liquid-wastes on floating docs in aspects of its impact on the environment*. In Polish Maritime Research, special issue 2005, (pp. 15-19).

Corresponding author:
Ing. Przemysław Rajewski, Ph.D., Instytute of Marine Propulsion Plants Operations, Faculty of Marine Engineering, Maritime University of Szczecin, Waly Chrobrego 1-2, 70-500 Szczecin, Poland, phone: +48 91 4809580, e-mail: p.rajewski@am.szczecin.pl
Prof. Oleh Klyus, Ph.D.hab. Ing., Instytute of Marine Propulsion Plants Operations, Faculty of Marine Engineering, Maritime University of Szczecin, Waly Chrobrego 1-2, 70-500 Szczecin, Poland, phone: +48 91 4809425, e-mail: o.klyus@am.szczecin.pl

DESIGN OF GAS BURNER FOR THE FIRE INTEGRITY TESTING OF SEGMENTAL DOORS

Ladislav ŠEVČÍK[1], Ha NGUYEN VAN[2], Michal PETRŮ[3]

[1,2,3]Department of Design of Machine Element and Mechanism, Faculty of Engineering, Czech Technical University of Liberec, Studentska 1402/2, Liberec I, 461 17, Czech Republic

Abstract
The article focuses on the design of a medium-efficient gas burner. The fuel is a mixture of air and propane-butane. The burner is used to test the fire resistance of a segmental door sample. The door sample is built and tested in a special chamber. The result is time dependence on heat transfer, flame resistance and high temperature.

Keywords: *fire, gas burner, resistance to flame, segment door.*

1. INTRODUCTION

The aim was to design a medium-efficient gas burner. The fuel is a mixture of air and propane-butane. Propane combustion heat 50 kJ / kg or 101 kJ / m3, flame temperature 1980 °C air, 2820 °C oxygen. Butane combustion heat 49 kJ / kg or 134kJ / m3, flame temperature 1970°C air, 2845°C oxygen. Propane volume of oxygen required for burning 1m^3 of fuel 5m^3, a volume of fuel in the combusted mixture 16.67%, a volume of air required for burning 1m^3 of fuel 5m^3 and butane the volume of oxygen required for burning 1m^3 of fuel 6.5m^3 (see Table 1, 2). The propane gas content varies depending on the gas content taken. Natural gas is mainly methane and other additives. From the above values, design the optimum burner design.

2. MATERIALS AND METHODS

Propane boils at -42.1 °C, butane -0.5 °C. This has several consequences. When using a mixture of pro-butane (for example purchased on a gasoline pump), the gas composition changes gradually. At a time when the bottle is full, the mixture contains more propane, leaving a butane to evaporate. The mutual ratio of the two gases in the mixture may also fluctuate according to the season or depend on what the particular mixture is intended for. For use in summer in cookers or for car drive (such as LPG), a mixture containing 60% butane and 40% propane is used. In the winter, the ratio may be the opposite. Therefore, the mixture will only be burned correctly in the burner, which has the ability to regulate the relative ratio of fuel and air (oxygen).

For boilers that do not have the option of setting the fuel ratio, it is preferable to use a clean propane, the combustion of which is usually customized at the factory. The use of propane itself is also advantageous when multiple bottles are attached to one bottle, where the cooling of the bottle is sometimes apparent due to the rapid evaporation of the liquefied gas, which may lead to a particularly slow evaporation of the gas (especially butane). The values in Table 1 and 2 were taken from [1].

Table .1

Fuel Comb [kJ/kg]	Heat Comb[kJ/kg]	Heat Flame [kJ/m³]	Temperature air flame (0 °C, 101,3 kPa) [°C]	Temperature Oxygen flame [°C]
Methane	55.760	39.888	1.957	2810
Ethane	51.690	69.250		
Propane	50.410	101.820	1980	2820
Butane	49.572	134.020	1970	2845
Hydrogen	142.443	12.790	3000	
Acetylene	50.367	58.990	2400	3200

With the increasing number of carbons in the fuel molecule, the amount of oxygen needed to burn the same volume of fuel increases. It is, therefore, necessary to vary the ratio of both gases. The values given in the Table 2 are calculated from the stoichiometric ratios of the respective reactions. In practice, they will vary slightly, inter alia depending on the flame mode used (oxidation /reduction).

Table. 2

Fuel comb	Volume of oxygen need to burn 1 m^3 of fuel [m^3]	Volume of fuel in combustion [%]	The volume of air needed [m^3]	The volume of fuel in combustion [%]
Methane	1.75	3.36	8.33	10.71
Ethane	3.50	22.22	16.67	5.66
Propane	5.00	16.67	23.81	4.03
Butane	6.50	13.33	30.95	3.13
Hydrogen	0.50	66.67	2.38	29.58
Acetylene	2.50	28.57	11.90	7.75

When working with the burner, only the flame temperature is not decisive. The amount of heat that the burner is able to pass to its surroundings, that is the burner's thermal output, is decisive. This is due to the amount of gas that the burner is capable of burning per unit of time, and this depends on the burner design and the burn rate. Since the rate of combustion with the increasing number of carbons in the fuel molecule decreases, it may be beneficial in certain circumstances to burn less heat fuel at a higher rate.

Analyzing the structure of the flame. If the carbon-containing gas is burned only by the air in the vicinity of the flame, oxygenation occurs only with the oxygen that comes into the flame from the vicinity of the diffusion. In that case, we are talking about a so-called luminous flame, which has a relatively large volume, a low temperature, and contains heated red particles of carbon originating from thermal decomposition of fuel. This flame is not suitable for glass processing.

For working with glass, a non-flammable flame occurs when combustion of a fuel/oxygen/air mixture.

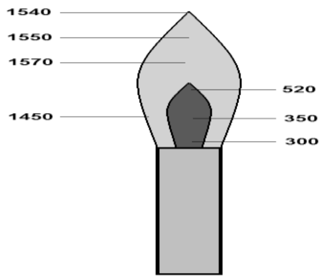

Fig.1 The phenomenological model of flame [2]

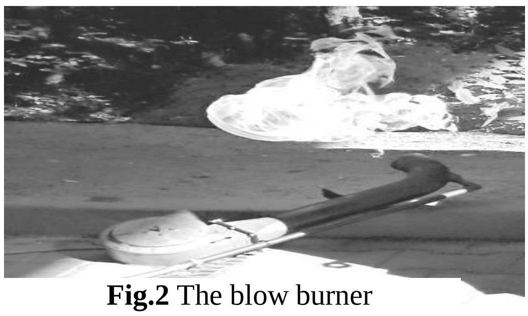

Fig.2 The blow burner

The gas is mixed with air or oxygen as soon as it enters the burner, and this mixture is gradually spawned. In doing so, it also pours more air from its surroundings. Before the flame mouth, an internal reduction cone and an outer bluish, non-luminous wrapper can be observed (Fig. 1) [2]. The internal cone contains a mixture of unburned gas and primary air (oxygen). This mixture is partially burned on the surface of the inner reduction cone and the combustion is completed in the outer shell by the secondary air which diffuses into the flame and is entrained by the flue gas stream.

Since there is incomplete combustion in the reduction zone of the flame, there is a lower temperature than in the outer package.

The dimensions of the inner reduction cone, as well as the outer package, diminish with the increasing amount of primary air (oxygen). For air-to-oxygen burners, the flame volume can also be changed by adjusting the relative air and oxygen ratios. By adding air, the flame volume increases with the influence of nitrogen, which practically does not enter into chemical reactions. Sometimes air can also be used to stabilize the flame. The structure of the flame depends to a certain extent on the design of the burner.

From the above analysises to achieve the required temperatures in the test chamber, a suitable burner must be used. The first experiments were built with a non-airborne burner, it was found that the flame was not sufficient to achieve similar temperature values as those used in testing at a test facility. The

blower burner (see Fig. 2) has met the temperature requirements, but which was originally designed for other purposes and does not allow automatic temperature control in the chamber**.**
Therefore, a new burner model was designed (see Fig. 3 a) that would better meet test requirements, and in the future enable automatic temperature control of the furnace according to a defined curve (according to the Fire Testing Standard). The principle of the burner lies in a controlled fuel and air supply. The amount of fuel is currently set on the propane-butane cylinder valve. The amount of air is adjusted by the size of the slot in the suction area of the fan. This design model is designed to optimally mix gas and air (see Fig. 3 b and Fig. 3c).

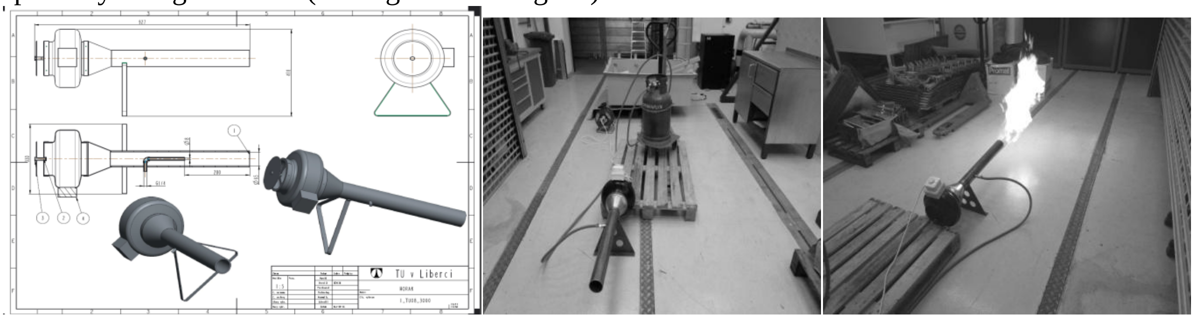

a **b** **c**

Fig.3 (a)The new shape of burner, (b) the new burner made, (c) the first tests of the new burner

4. RESULTS AND DISCUSSION

In this work, the test of reduced models of fire doors was established. Small models of fire doors were produced for chamber tests. The reality, many tests of the existing fire doors have been carried out. Firstly, the location of the fire door models in the chamber, including the location of sensors for temperature evaluation, flame supply, was approached so that we would approach test conditions in a certified laboratory. The chamber fitted with sensors before the start of the test is shown in Figure 4 a.

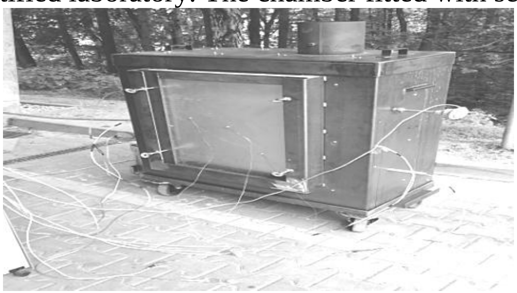

Fig. 4 a Chamber with thermocouples connected

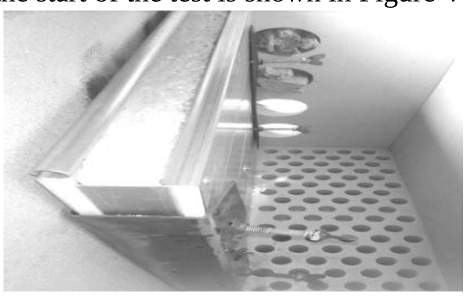

Fig. 4 b Fix the sample in the test chamber

Prior to the test, the specimen is fixed in the chamber so that the front vent hole of the chamber is sealed (see Fig 4 d). After the flame is ignited, the furnace temperature control is manually controlled by a valve on the gas cylinder. The air is fed through the blower and the amount of regulation is very difficult for the burner (see Fig 4 c and Fig 5).

Fig. 4 c Processing the flap door test and flame ignition

Fig. 4 d Test run of the door leaf model

Figure 5 shows the course of the test. The model of the segmental door after the test (see Fig 5 a) where apparent degradation of the material is due to extreme temperatures, Fig. 5 b a shows the image from the thermal camera, the temperature during the test refers Fig 5c.

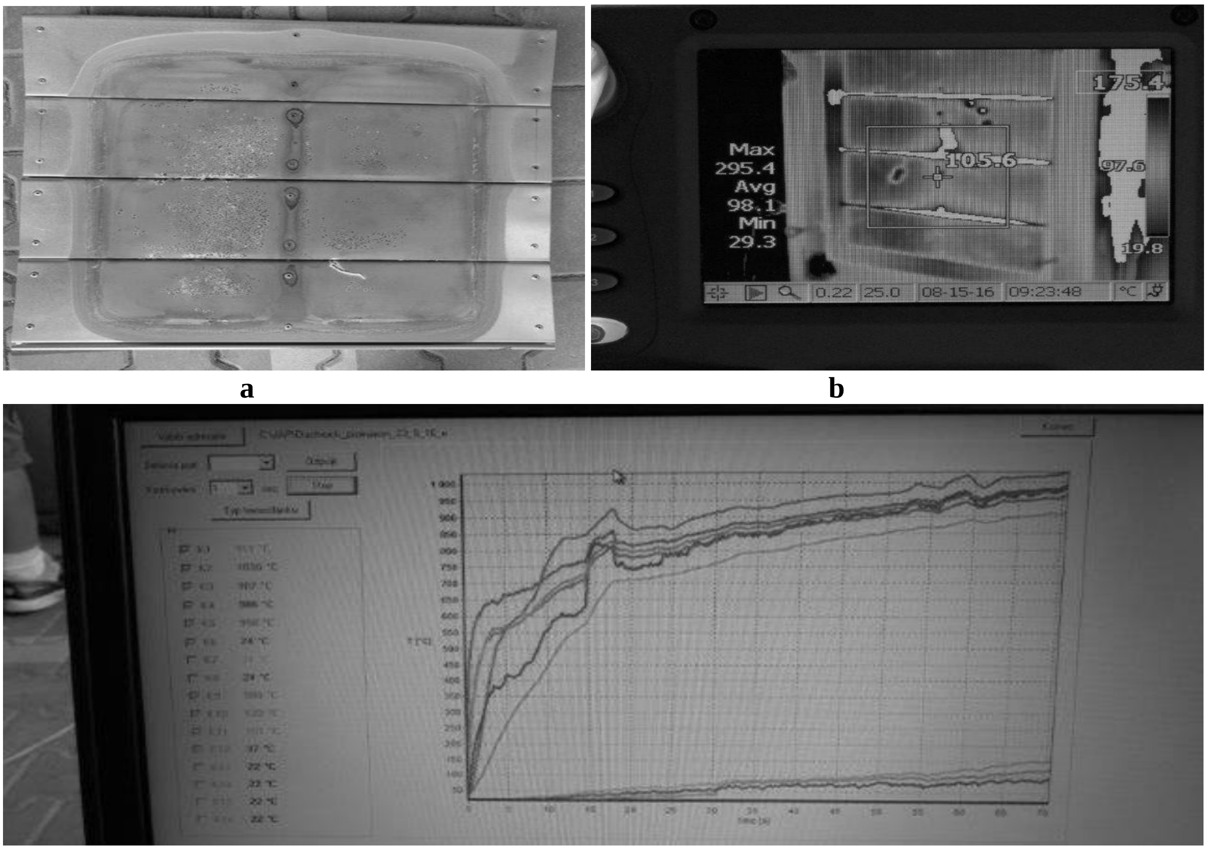

a b

c

Fig. 5 Sample of test models of fire doors in the test chamber

Also, Figure 5c is clearly shown that the temperature curve on the top, in the middle, the below represent of reduced door model, the temperature range of the sample, temperature course at different locations of the chamber respectively.

4. CONCLUSIONS

The gas burner for the fire integrity testing of segmental doors equipment which designed and manufactured is satisfying design specification, their operating is good and being able to utilize for fire integrity experiment. Also in the future which could be improved the design enables automatic temperature control.

ACKNOWLEDGMENT

The results of this project VI20152018046 were obtained with co-funding from the Ministry of the Interior of the Czech Republic as part of targeted support from the project " Use of modern modeling methods in the development and testing of the fire doors".

REFERENCES

1. Gas installation pipework and appliances for buildings. (c2013). Technical rules. ISBN 978-80-7328-291-2.
2. http://www.kacafurie.cz/kahany-horaky

Corresponding author:

Ing. Ladislav Sevcik, Prof. Department of the Design of the Machine Elements and Mechanism, Faculty of Engineering, Czech Technical University of Liberec, Studentska 1402/2, Liberec I, 461 17, Czech Republic, Phone:+420485353316, e-mail: ladislav.sevcik@tul.cz

PROCESSING OF ALUMINUM ALLOY EN AW 7075 USING SELECTIVE LASER MELTING: INITIAL STUDY

Petr SKALICKÝ[1], Daniel KOUTNÝ[1], Libor PANTĚLEJEV[2], David PALOUŠEK[1]

[1]Institute of Machine and Industrial Design, Brno University of Technology, Faculty of Mechanical Engineering, Technicka 2896/2, Brno 616 69, Czech Republic
[2]Department of Material Science, Brno University of Technology, Faculty of Mechanical Engineering, Technicka 2896/2, Brno 616 69, Czech Republic

Abstract
Selective Laser Melting (SLM) is an additive manufacturing process, that uses a fine metallic powder to produce complex parts. Unfortunately, the range of SLM processed materials is limited by available materials in powder form and for many materials process parameters have not been defined. Currently, about four aluminum alloys has been successfully processed. The aim of this paper was description the influence of the process parameters to the material processability of high strength aluminum alloy EW AW 7075 by SLM. Wide range of process parameters (100-400 W laser power and 300-1400 mm/s scanning speed) were examined to find the optimum processing parameters producing homogeneous material. In this study, maximum relative density of 96.2 % was achieved. However, typical hot cracks, which appears during welding process of aluminum alloy EN AW 7075, was observed in all parts. Cracks were reduced but were not eliminated.

Key words: *EN AW 7075, Selective Laser Melting (SLM), relative density, hot crack.*

INTRODUCTION

Selective Laser Melting (SLM) is one of the additive manufacturing technologies, which uses fine metal powder to produce high quality parts with complex shape. SLM is most commonly used in medicine, aerospace or automotive for manufacturing of components with complicated geometry which cannot be produced by conventional methods (Olakanmi, Cochrane, & Dalgarno, 2015). Parts are manufactured directly from 3D data, layer by layer. In each layer a laser beam is used to melt the powder into solid metal only in areas corresponding to cross section of the part.
SLM fabrication process and the also quality of the final product is controlled by many process parameters, which can be sorted as laser related, scanning related, powder related and temperature related.
In many current studies on the optimization of material homogeneity e.g. (Thijs, Verhaeghe, Craeghs, Humbeeck, & Kruth, 2010) (Prashanth, Scudino, Maity, Das, & Eckert, 2017) the authors used energy density E [J/mm3], defined in equation (1), to better compare the influence of dependent parameters on the porosity and final quality of the manufactured parts. It consider the main influence parameters such as laser power P_L (W), scanning speed v_s (mm/s), hatch distance h_d (mm), layer thickness l_t (mm). These process parameters mainly affect the formation of porosity in the manufactured components (Aboulkhair, Everitt, Ashcroft, & Tuck, 2014).

$$E = \frac{P_L}{v_s \cdot h_d \cdot l_t} \qquad (1)$$

The most used aluminum alloys for the production by SLM technology are Al-Si alloys. These alloys are used due to their good weldability. Aluminum alloys AlSi10Mg and AlSi12 were extensively studied, and the influence of process parameters to its behavior and mechanical properties were thoroughly described (Wei, et al., 2017), (Li, et al., 2016), (Zaretsky, Stern, & Frage, 2017), (Tang & Pistorius, 2017), (Siddique, Imran, Wycisk, Emmelmann, & Walther, 2015), (Vora, Mumtaz, Todd, & Hopkinson, 2015). These alloys in casted state have relatively poor mechanical properties compared to the 7-series (7xxx) high strength aluminum alloys. Aluminum alloy EN AW 7075 (AlZn5.5MgCu) is one of the aluminum alloys which achieves the best mechanical properties. In wrought state it has a high tensile strength of over 500 MPa and hardness of up to 160 HB. The main potential of this alloy is the high strength-weight ratio in combination with good corrosion resistance (Reschetnik, et al., 2016) (Michna

& Lukáč, 2005), however, up to now only several authors dealt with the processing of this alloy (Kaufmann, et al., 2016), (Montero Sistiaga, et al., 2016). Therefore the aim of this paper is to describe the influence of the process parameters to the material processability.

MATERIALS AND METHODS

Fabrication of samples

For this research was used SLM 280 HL (SLM Solutions, Germany) machine equipped with 400 W ytterbium fiber laser. All samples were manufactured with layer thickness 50 μm, hatch distance 0.10 mm, meander 79° as a scan strategy. Meander 79 ° means that each layer is scanned in both directions with a (n + 1) layer rotation of 79 °. The building chamber was filled up with argon and overpressured of 10-12 mbar with maximum oxygen level of 0.2 %. The range of laser power was 100-400 W, and range of scanning speed was 50-1500 mm/s. To optimize process parameters and to achieve the highest relative density, were used cube samples of dimensions (10 x 10 x 10 mm) fitted with a truncated pyramid on the underside and were built directly on the building platform. The truncated pyramid reduces the contact area of the cube sample with the building platform and thus reduces the cooling rate. The relative density was measured in the cube part of the sample.

Powder characterization

The metal powder EN AW 7075, produced by gas atomization, was supplied by LPW Technology. Tab. 1 shows the chemical composition provided by supplier LPW Technology. Particle size distribution was measured using Horiba LA-950 particle size analyzer. Results show (Fig. 1) that powder has Gaussian distribution while particle size below 26 μm represents 10 % and particles size below 64 μm represents 90 % of the total amount of particles. Particle median size is 41.5 μm, mean size is 43.9 μm and therefore layer thickness of 50 μm was used in all experiments.

Tab. 1 Chemical composition limits of standard material and powder material

Weight %	Al	Zn	Mg	Cu	Fe	Cr	Si	Mn	Ti	Other
DIN EN 573-3	Bal	5,1-6,1	2,1-2,9	1,2-2	≤0,5	0,18-0,28	≤0,4	≤0,3	≤0,2	≤0,15
SLM powder	Bal	5,9	2,4	1,5	0,07	0,27	0,4	0,26	0,01	

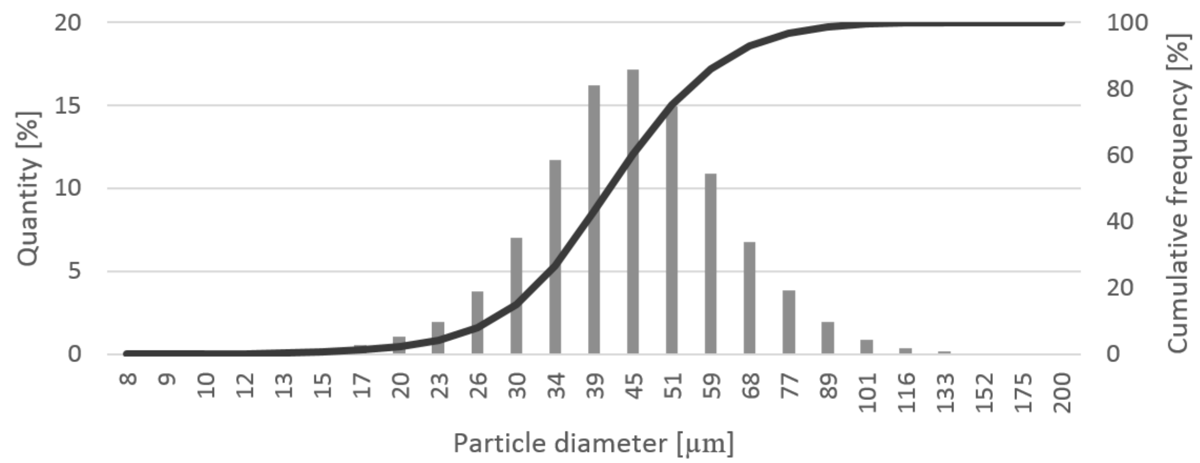

Fig. 1 Particle distribution of alloy EN AW 7075

Porosity analysis

To analyze the porosity, samples were grinded and polished, parallel to building direction, using metalografic grinder Leco GPX300 (LECO Instrumente, USA). To observe microstructure of material, samples were etched by FUSS etchant. Relative density was measured by image analysis in freeware software *Image J*, from images of samples taken on the OLYMPUS SZX7 microscope. The main investigated parameter was relative density, which includes both, pores and cracks. The selected region for the relative density analysis contained only the inner region of the sample (no contour).

RESULTS AND DISCUSSION

Cube samples were fabricated to describe the behavior of the material over a wide range of process parameter combinations and the influence of these process parameters on relative density.
The experiment was performed with hatch spacing 100 μm. Building platform was preheated to 200 °C. Fig. 2 shows polished sample images sorted by the combination of used laser power and scanning speed. Each samples image contains a relative density value and energy density value. If the energy density is less than 60 J/mm3, the samples contain a lot of keyhole pores (see dotted area in Fig. 2). Large metallurgical pores are visible on samples manufactured with laser power 300 W and 400 W and energy density higher than 100 J/mm3 (see dashed area in Fig. 2), but large metallurgical pores did not appear in samples with a laser output of 200 W. Cracks were visible throughout the range of process parameters. Lowering scanning speed reduces pores and cracks in samples with a laser power of 200 W, but cracks did not disappear completely. The best results of relative density 93.6 % was achieved using laser power of 300 W and a scanning speed 800 mm/s. However, results of relative density did not match with relative density values reported by (Kaufmann, et al., 2016). Fig. 3 shows, that (Kaufmann, et al., 2016) used only grinded samples in their research. This was verified on the sample with the same process parameters (laser power 400 W and scanning speed 1200 mm/s). Similar relative density was found in the grinded sample, but polishing revealed defects that were not seen after grinding. The difference in measured relative density was approximately 15 % (Fig. 3). This implies, that the cracks are most probably present in Kaufmann's study as well, however due to inapropriate technique it were not detected.

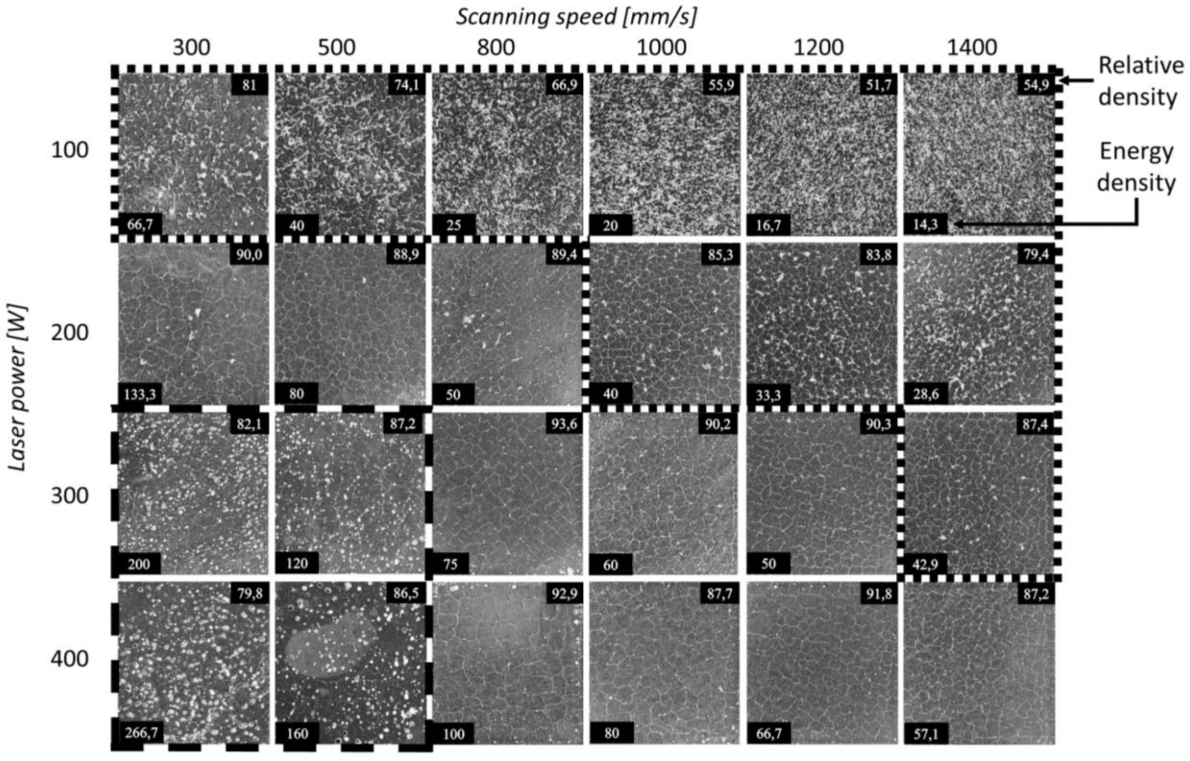

Fig. 2 Images of polished samples, relative density [%] (top right of images), energy density [J/mm^3] (bottom left of images)

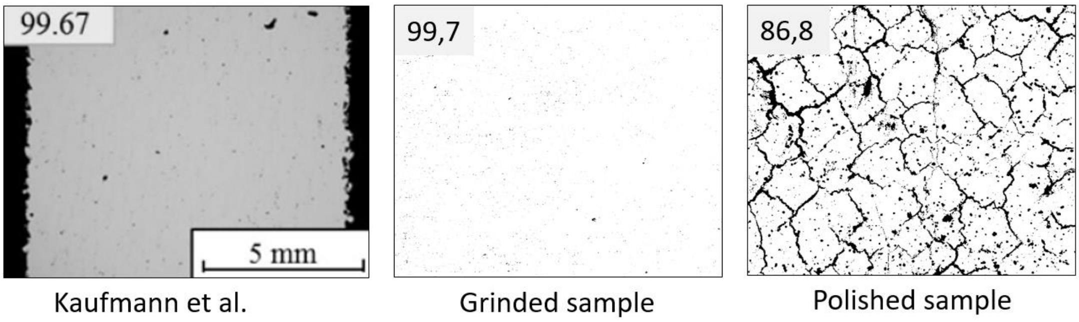

Fig. 3 Comparison of grinded sample and polished sample, relative density (top left of image)

Comparison of the relative density depending on the scanning speed for four values of laser power is shown in Fig. 4. In the case of the 300 W and 400 W laser power, the relative density increase with increasing scanning speed. If the scanning speed is higher than 800 mm/s, the relative density is stabilized around 90 %. Dependence of relative density and scanning speed for laser power 200 W shows that the relative density is not decreasing for scanning speeds below 600 mm/s as in case of 300W and 400 W *Lp*. Figure 4 also shows that use of 100 W laser power is inappropriate to reach higher relative density of material.

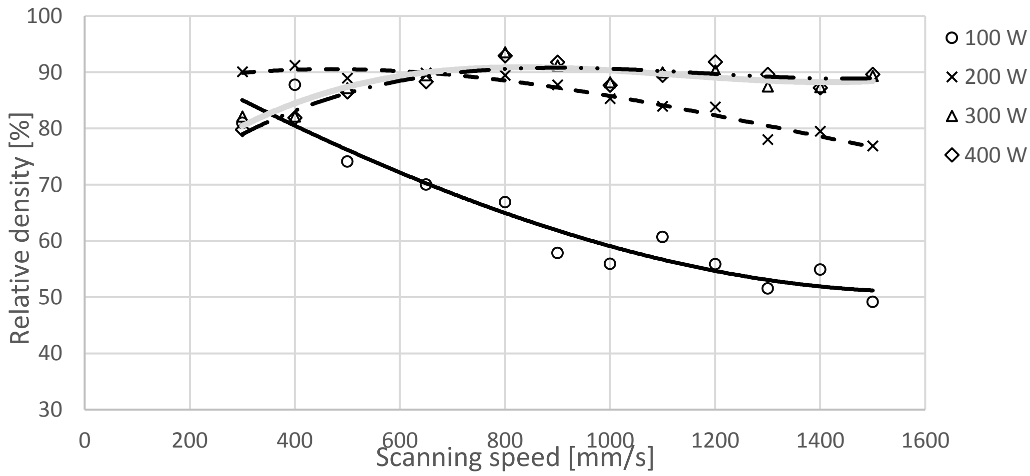

Fig. 4 Influence of scanning speed on relative density

Dependence of relative density and energy density in figure 6 show that between 50-80 J/mm3 energy density, the process for 200, 300 and 400 W laser power is stabilized with relative density about 90 %. Figures 3 and 5 shows that the cracks form a substantial part of the defective area, which is included to calculation of porosity. Thus the minimization of crack occurrence in future would improve the relative density values as well.

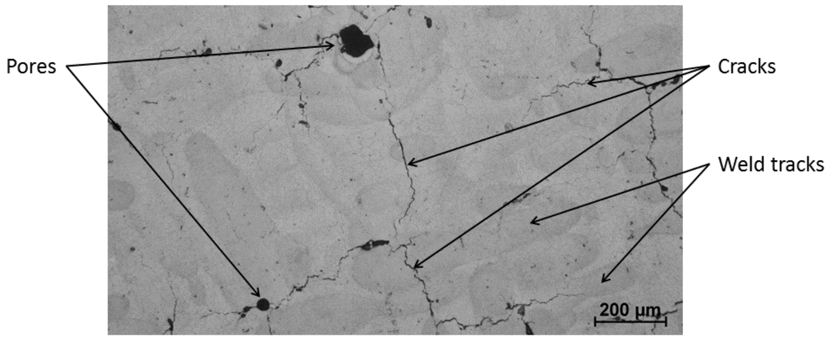

Fig. 5 Etched sample of SLM processed EN AW 7075 alloy showing microstructure with cracks

Microstructure in figure 5 show that cracks are preferentially oriented in scanning direction. During production of the next layer, cracks from both layers are interconnected and create a "net of cracks" (Fig. 3). This behavior is most probably due to high cooling rate of the SLM processing, because the semi-solid state of weld is present very short time and thus the high tension in material is induced as described by (Hu & Richardson, 2006).

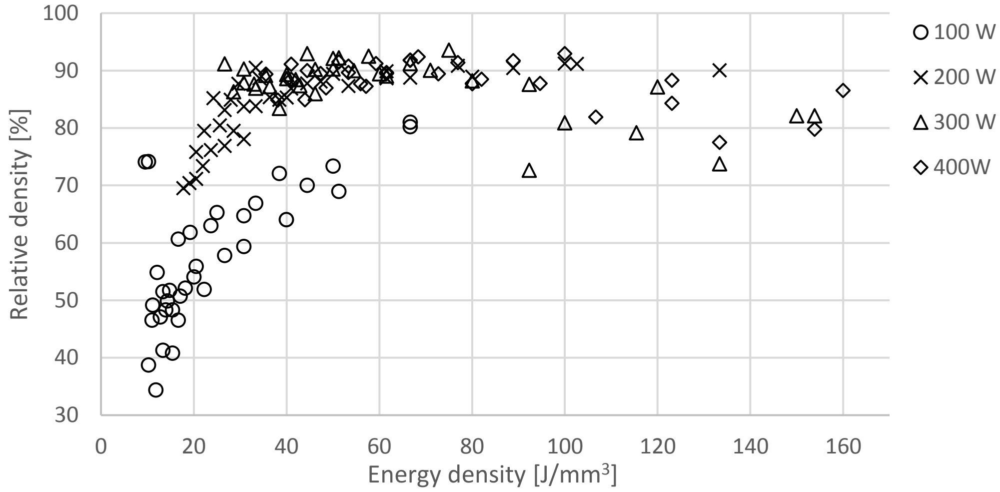

Fig. 6 Influence of energy density on relative density of samples

CONCLUSIONS

In this paper was found that the EN AW 7075 alloy is very difficult to process using SLM technology. Cracks were detected throughout the entire range of process parameters. A range of process parameters were found where the samples contained keyhole pores (low energy density) and the range of process parameters where the samples contained large metallurgical pores (too much energy density). Microstructural analysis showed that cracks are oriented in the direction of scanning. For reduction of hot cracking behavior, the lowering scanning speed and thus lowering temperature gradient during solidification seems to be perspective. Because, as the results show that the amount of cracks is slightly lower for the lower scanning speeds.

ACKNOWLEDGMENT

The research leading to these results has received funding from the Ministry of Education, Youth and Sports under the National Sustainability Programme I (Project No. LO1202). The presented work has been also supported by the Project No. FSI-S-14-2332.

REFERENCES

1. Aboulkhair, N., Everitt, N., Ashcroft, I., & Tuck, C. (2014). Reducing porosity in AlSi10Mg parts processed by selective laser melting. *Additive Manufacturing, 1-4*, 77-86. doi:10.1016/j.addma.2014.08.001
2. Hu, B., & Richardson, I. (2006). Mechanism and possible solution for transverse solidification cracking in laser welding of high strength aluminium alloys. *Materials Science and Engineering: A, vol. 429*(1-2), 287-294. doi:10.1016/j.msea.2006.05.040
3. Kaufmann, N., Imran, M., Wischeropp, T., Emmelmann, C., Siddique, S., & Walther, F. (2016). Influence of Process Parameters on the Quality of Aluminium Alloy EN AW 7075 Using Selective Laser Melting (SLM). *Physics Procedia, 83*, 918-926. doi:10.1016/j.phpro.2016.08.096
4. Li, W., Li, S., Liu, J., Zhang, A., Zhou, Y., Wei, Q., . . . Shi, Y. (2016). Effect of heat treatment on AlSi10Mg alloy fabricated by selective laser melting: Microstructure evolution, mechanical properties and fracture mechanism. *Materials Science and Engineering: A, 663*, 116-125. doi:10.1016/j.msea.2016.03.088

5. Michna, Š., & Lukáč, I. (2005). *Encyklopedie hliníku.* Děčín: Alcan Děčín Extrusions.
6. Montero Sistiaga, M., Mertens, R., Vrancken, B., Wang, X., Van Hooreweder, B., Kruth, J.-P., & Van Humbeeck, J. (2016). Changing the alloy composition of Al7075 for better processability by selective laser melting. *Journal of Materials Processing Technology, 238*, 437-445. doi:10.1016/j.jmatprotec.2016.08.003
7. Olakanmi, E., Cochrane, R., & Dalgarno, K. (2015). A review on selective laser sintering/melting (SLS/SLM) of aluminium alloy powders: Processing, microstructure, and properties. doi:10.1016/j.pmatsci.2015.03.002
8. Prashanth, K., Scudino, S., Maity, T., Das, J., & Eckert, J. (2017). Is the energy density a reliable parameter for materials synthesis by selective laser melting? *Materials Research Letters*, 1-5. doi:10.1080/21663831.2017.1299808
9. Reschetnik, W., Brüggemann, J.-P., Aydinöz, M., Grydin, O., Hoyer, K.-P., Kullmer, G., & Richard, H. (2016). Fatigue crack growth behavior and mechanical properties of additively processed EN AW-7075 aluminium alloy. *Procedia Structural Integrity*(2), 3040-3048. doi:10.1016/j.prostr.2016.06.380
10. Siddique, S., Imran, M., Wycisk, E., Emmelmann, C., & Walther, F. (2015). Influence of process-induced microstructure and imperfections on mechanical properties of AlSi12 processed by selective laser melting. *Journal of Materials Processing Technology*(221), 205-213. doi:10.1016/j.jmatprotec.2015.02.023
11. Tang, M., & Pistorius, P. (2017). Oxides, porosity and fatigue performance of AlSi10Mg parts produced by selective laser melting. *Journal of Fatigue*(94), 192-201. doi:10.1016/j.ijfatigue.2016.06.002
12. Thijs, L., Verhaeghe, F., Craeghs, T., Humbeeck, J., & Kruth, J.-P. (2010). A study of the microstructural evolution during selective laser melting of Ti–6Al–4V. *Acta Materialia, 58*(9). doi:10.1016/j.actamat.2010.02.004
13. Vora, P., Mumtaz, K., Todd, I., & Hopkinson, N. (2015). AlSi12 in-situ alloy formation and residual stress reduction using anchorless selective laser melting. *Additive Manufacturing,, 7*, 12-19. doi:10.1016/j.addma.2015.06.003
14. Wei, P., Wei, Z., Chen, Z., Du, J., He, Y., Li, J., & Zhou, Y. (2017). The AlSi10Mg samples produced by selective laser melting: single track, densification, microstructure and mechanical behavior. *Applied Surface Science, vol. 408*, 38-50. doi:10.1016/j.apsusc.2017.02.215
15. Zaretsky, E., Stern, A., & Frage, N. (2017). Dynamic response of AlSi10Mg alloy fabricated by selective laser melting. *Materials Science and Engineering A, 688*, 364-370. doi:10.1016/j.msea.2017.02.004

Corresponding author:
doc. Ing. Daniel Koutný, Ph.D., Institute of Machine and Industrial Design, Brno University of Technology, Faculty of Mechanical Engineering, Technicka 2896/2, Brno 616 69, Czech Republic, phone: +420 541 143 356, e-mail: Daniel.Koutny@vut.cz

PNEUMATIC WRENCH GEARBOX DEVELOPMENT FOR TIGHTENING TORQUE OF 6000 NM

Patrik SNIEHOTTA[1]

[1]*Department of Machine Parts and Mechanisms, Faculty of Mechanical Engineering, VŠB-TUO*

Abstract
Pneumatic wrenches are a common tool in many industries. With increasing demands on their tightening torque, increases their size and price. For the application of a pneumatic actuator is also required a large gear ratio to achieve large tightening torques. Based on the requirements of company KOEXPRO Ostrava a.s., a project was created to develop a modular gearbox for pneumatic wrench. In combination with the already used NKH torque multipliers, it could be possible, shifting several gearboxes in a row, achieve a tightening torque of 6000 Nm. At the same time, such pneumatic screwdriver should not weigh more than 20 kg. Only in such case, it would be a product, which would overcome his competitors. This article describes the development of this modular gearbox.

Key words: *pneumatic wrench, gearing, modularity, planetary gearbox.*

INTRODUCTION

Pneumatic wrenches are a common used tool, when you need to develop a high tightening torque. They are simple, easy to use and can be uses in explosive environment. But when you need high tightening torques, they become big, heavy and not easy to handle. The company KOEXPRO Ostrava had only these big and heavy wrenches. The goal was to develop a pneumatic wrench, which would have tightening torque 6000 Nm a weigh no more than 20kg.

Fig. 1 Similar tool from the company PD Profi

The only solution for such extreme claims was to use the torque multiplier MKH and a lamellar pneumotor, which is light and has enough power. The only problem with this type of motor is his high rpm. The solution for this problem was to use a series of planetary gearboxes, which can develop the gear ratio. The minimization of weight of planetary gearboxes is described if the article of Predki W., Jarchow F., Lamparski Ch. (2001). Based on this article it was chosen the classical type A, given its simplicity and effectiveness. The aim of was to design such planetary gearboxes and this articles describes this development.

MATERIALS AND METHODS

The requirement for the design was to use the already produced torque multiplayer NKH 65. This multiplayer can be use up to 6200 Nm, weight's 9 kg and has a gear ratio of i_{NKH}=21. That means that for the planetary gearboxes and lamellar engine was just 11 kg, to achieve the require weight of 20 kg.

The decision was to use the lamellar pneumotor for the company Deprag. Pneumotors form this company have 5250 rpm. Because such wrench is used just for tightening bolts/nuts (not for screwing), After a consultation with the company KOEXPRO, it was decided that the output revolutions would be 1 per minute. That means that the overall gear ratio i_c would be 5250 and therefore than ten overall required gear ratio of planetary gearboxes i_{pc} would be 250.

Fig. 2 Currently used torque multiplayer NKH 65

The best solution was to use 3 gearboxes. For cost reduction, all gearboxes would be the same. That means that it is necessary that only the last gear stage forcibly go out correctly. That means that each planetary gearbox needs to have a gear ration i_p=6,3. The gearbox would be with braked crown wheel, with 3 satellites and the numbers of teeth are

Tab. 1 Number of gear tooth

Gear wheel	Number of teeth
Central	15
Satellite	33
Crown	-81

The real gear ration of this gearbox is than i_p=6,4. For cost reduction it was decided to use standard gear profile and to use module m=1 mm, that the weight and dimension are low as possible. The resulting gearing parameter ware:

Tab. 2 Geometrical dimension of gears

Material	Central	Satellite	Crown
Number of teeth z (-)	15	33	-81
Normal module m (mm)		1	
Correction x (-)	0.328541	- 0.328541	0.328541
Working axial distance a_w (mm)		24 (-24)	
Pitch diameter d (mm)	15	33	-81
Head diameter d_a (mm)	17,6	34,3	-78,7
Heel diameter d_f (mm)	13,157	29,843	-82,8
Gearing width b(mm)		50	
Contact ratio coefficient ε_α (-]	1,487		1,875

For strength calculation it was of course necessary to know the output power of the lamellar engine. The suggestion was that the hole pneumatic wrench would have an overall efficiency of η_c=0,58 (efficiency of torque multiplayer η_{NKH}=0,8, planetary gearbox η_p=0,9). The wrench is designed so it stops when it achieves the required torque (the required torque is set up by changing the air pressure). That means that the lamellar engine does not have to be designed on the nominal torque, but it is enough that is designed on the starting (maximal) torque. That means, that for the tightening torque 6200 Nm, the engine has to have 1,95 Nm. To this condition the company Deprag has the lamellar engine

63X-001F07, with nominal output power P_M=900W, nominal speed n_M=5200 rpm, nominal torque M_{kn}=1,6 Nm and maximum torque M_{km}=2,4 Nm.

It is of course clear that the maximal torque is not always required. For the stress calculation The suggestion was that the maximum load is in 30% of time, in 40% of time the gearing is loaded with 85%, and 30% of time is the gearing loaded with 70%. The load is of course not equal on all satellites, so the load was increased by 20%. The final load between central-satellite and satellite-crown wheel ware:

Tab. 3 Calculated loads on each gearing

No.	Part of time (-)	central-satellite (N)	satellite-crown (N)
1.	30%	4240	4240
2.	40%	3600	3600
3.	30%	2970	2970

The material properties ware one of the biggest problems. Of course the best solution ware to have tooth with hardened tooth sides, but this would increase the final price. The decision was made to use nitrided gearing, which does not require a subsequent processing. The material properties ware

Tab. 4 Used materials for gear wheels

Gear wheel	Material	Processing
Central	15 230.6	Nitrided
Satellite	15 230.6	Nitrided
Crown	12 061.6	Refined

The question was, if central gearwheel and satellite should be on all stages made out of the same material, or to use on first two stages a lower grade material. With another material the wrench would be cheaper. On the other side this would negative affect the modularity and interchangeability of parts and increase the risk of compliment. In the end the indirect costs by using a cheaper material, would increase the final price, that it is no difference if you use a more expensive material on all gearboxes, or you give on some stages a cheaper material.

RESULTS AND DISCUSSION

The strength calculation was is always the last step in gearing design. The calculation was performed according to ČSN 01 4686. The problematic part of the calculation was the contact stress control for the gearing central/satellite. This problem was described by Predki W., Jarchow F., Lamparski Ch. (2001) and Savage M., Rubadeux K. L., Coe H. H. (1998) in their articles. The safety coefficient s_H came out just over 1. Such result is not ideal, but the gearing was calculated for the worst case (reversing operation, shocks ...). The load is also the maximal assumed and in normal condition the wrench will be not used so often for torques around 6000 Nm. Such torque is for example the maximal tightening torque for screws M48 with grade 8.8., and they are not so common.

Tab. 3 Calculated safety coefficients for each gearing

	central-satellite		satellite-crown	
Safety coefficient	central	satellite	satellite	crown
Bending safety coefficient s_F	2,286	2,156	1,731	1,609
Contact stress safety coefficient s_H	1,012	1,042	2,195	1,770

For satellite/crown gearing ware the safety confidents for bending s_F and contact stress s_H almost equal, between 1,6 and 2,2.

To minimize the weight and maximize, it came into consideration using High Contact Ratio (HCR) gearing. After the first calculations, there was an increase of bending and contact stress safety coefficients and a loss of weight (thanks to a smaller gearing width). However, the improvements ware not so radical, that they would justify the additional costs by using HCR gearing. In the following proposals the concentration was to increase the contact ration coefficient ε_α, that it would be greater than 2. This measure would ensure, that calculated load in the gearing would be lower, so the gearing would be than thinner. The idea was, that when the number of tooth increases the diameter of gearbox will also increase, but when the value 2 of contact ration coefficient ε_α is reached, the width will the degrease. The lower width would then compensate the bigger gearbox diameter and the overall gearbox weight would be then lower.

However the reality was different. To achieve that $\varepsilon_\alpha>2$ was not so difficult, but lower gearing width didn't compensate the bigger gearbox diameter as expected. Taking into account the higher cost of gearing tools and small number of wrenches pieces that would be produced, it was not cost-effective to use HCR gearing.

CONCLUSIONS

To design a planetary gearbox for a pneumatic wrench seems at the first glance as a not a hard task. But when you thing that the wrench should be for 6000Nm, powered by a pneumatic engine with 5250 rpm and weigh no more than 20 kg, then it is much more difficult task.

It was possible to design a planetary gearbox with standard gearing, which can withstand the expected loads. The calculated expected weight of each planetary gearbox is 3,45 kg, so the hole wrench should weigh 19,35, which is under the required weight of 20 kg. The problem with such proposal is to exactly specify the expected loads. If the gearbox would be calculated on full load for unlimited life the safety coefficients would then not come out. Also if the gearwheel should not be hardened, it is needed to use a high grade steel with corresponding surface finish.

ACKNOWLEDGMENT

This study was supported by SP2017/39.

REFERENCES

1. NĚMČEK, M. GEOMETRIE. Ostrava : VŠB-TU Ostrava, 2012. 3.2.
2. NĚMČEK, M. ČSNw. Ostrava : VŠB-TU Ostrava, 2012. 3.2.
3. HÖHN B.-R., STAHL K., GWINNER P. (2013). Light-Weight Design for Planetary Gear Transmissions. GEAR TECHNOLOGY, 9, 96-103
4. PREDKI W., JARCHOW F., LAMPARSKI Ch. (2001). Load Distribution in Planetary Gears. GEAR TECHNOLOGY, 4/5, 41-44
5. SAVAGE M., RUBADEUX K. L., COE H. H. (1998). Effects of Planetary Gear Ratio on Mean Service Life. GEAR TECHNOLOGY, 7/8, 24-29

Corresponding author:
Ing. Patrik Sniehotta, Ph.D., Department of Machine Parts and Mechanisms, Faculty of Mechanical Engineering, VŠB-TUO, 17. listopadu 15/2172, Ostrava – Poruba, 708 33, Czech Republic, phone: +420 597 324 313, e-mail: patrik.sniehotta@vsb.cz

DESIGN CONCEPT OF A DEVICE FOR ALIGNING RUBBER HOSES

Pavel SRB[1], Petr KULHAVÝ[1]

[1]Technical University of Liberec, Faculty of Mechanical Engineering, Department of the Design of Machine Elements and Mechanisms

Abstract
This article is focused on improving the production quality of reinforced rubber hoses used especially in the automotive industry. Some defects could occur during the hose production. One of the relatively frequently occurring problem is deviation of the perpendicularity and flatness of the end of the hose. This defect occurs during the vulcanization process when the hose is insufficiently pushed onto the shaped mandrel and leading to a refusing of the parts for subsequent processes. The way, how to correct this defect was sought in order to reduce the number of rejected hoses. Basic kinematic scheme and subsequently drafted design of a device based on orbital grinding have been created. This device grinds the unsatisfactory ends of the hoses so that the perpendicular tolerances could be easily met.

Key words: *Grinding, Manufacturing, Vulcanization.*

INTRODUCTION

The hoses are mainly used for the transport of liquids and gases. For low pressure transport it is possible to use simple hoses. The fiber reinforced hoses should be used for higher pressures of transported medium (*Brendan Rodgers, 2015*). The reinforced rubber hoses have wide variety of possible applications in automotive such as parts for the power steering, air conditioning systems, turbo charge, motor cooling circuit etc. Even though the most common used materials are the Nitrile and EPDM rubbers, the silicones and fluoroelastomers are more suitable to applications with high temperatures (*Anil K. Bhowmick, 1994*). Fig. 1 shows an example of reinforced rubber hose shape.

Fig. 1 Hose shape illustration.

The typical method of manufacturing reinforced hoses is shown in Fig. 2. The first step is to create a mixture of ingredients. Mixed ingredients fill an extruder where the mixture is pushed forward by the movement of the screw and heated by frictional heat. At the end of the screw there is a mixture with required properties that allows it to be pushed through the nozzle and according to the hole shape form a final profile of the created hose. After the extrusion the hoses passing through the cooling box where obtain dimensional stability. After cooling the adhesive backing layer is applied to the first layer of the hose. The next step is laying of the reinforcement layer. This layer can be made of some textile or metallic fibers and can be applied by various techniques such as winding, braiding, etc. The reinforcing fibers are impregnated with an adhesive rubber or latex prior to specific application. During application of the reinforcement it is necessary to keep the neutral angle of 54°44’. By keeping this angle the hose length does not change when the internal pressure is increased (*Demirkoparan, Pence, 2015*).

The outer layer of the hose is applied by a second extruder on the surface with the fibre reinforced layer. The number of reinforcement layers could be higher depending on the type of hose. Subsequently, the semifinished hose is cut to the required lengths. This way prepared semi-finished hoses are further pushed onto the complex shaped mandrels of the vulcanization device by operators.

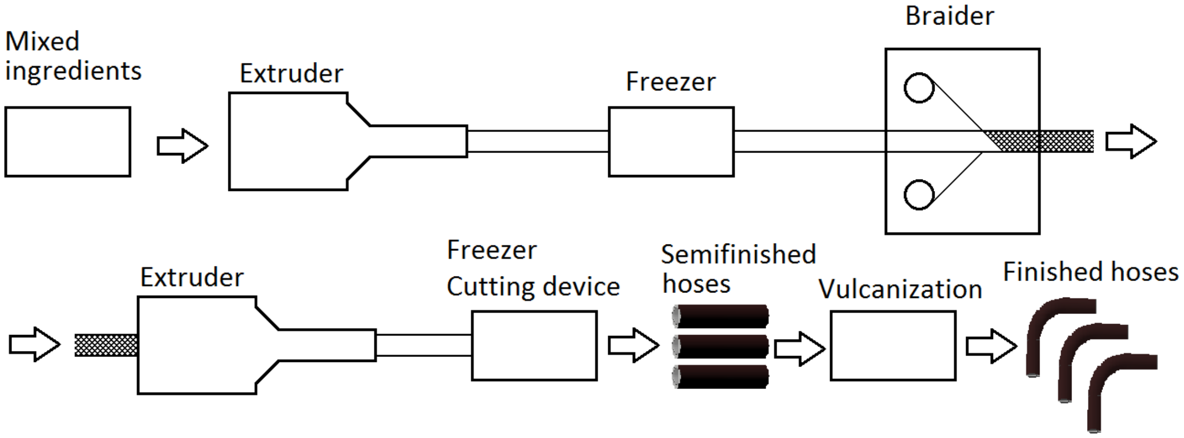

Fig. 2 Reinforced hose manufacturing line.

This is a very demanding physical work and also the place where the defects could occur. The blank hose of the exact length has to be evenly pushed on the mandrel. It is particularly important to properly tighten the ends of the hose to fit the mandrel ends. This correct placement depends mainly on the experiences and carefulness of the operator. Due to this fact occurs relatively large number of defects. When the operator does not press the hose on the mandrel properly, vulcanization can cause that the hose end deviate from the plane perpendicular to the actual axis in the end point as could be seen in the Fig.3. The maximum permissible deviation depends on the diameter of the hose. Usually for the standard diameters of hoses used in automotive is the tolerance about 1 mm in any of circumferential points. The aim of this article was to propose measures to prevent the occurrence of rejects parts or to design a device that the rejected hoses could simply repair.

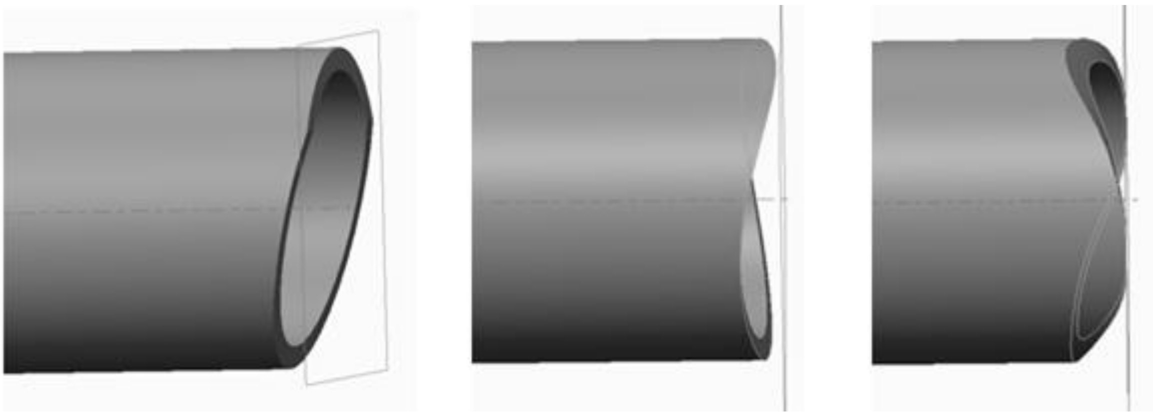

Fig. 3 Illustrations of the possible defects - oblique, concave, convex

MATERIALS AND METHODS

The first step in finding the corrective measures was to evaluate the current state. The problem is caused especially by the fact that unvulcanized rubber is very ductile. The mandrel is equipped at one end with a stop of a suitable shape (Fig. 4 left). Using of too high force can cause deformation in the stop area. On the other hand, with an insufficient force, the end of the hose will not be pushed to the stop. The other end of the mandrel is equipped with an undercut for the optical check of the sufficient hose push. First contact check was proposed, when several contact sensors were placed around the stop of the mandrel, and sufficient contact of the hose is checked with the entire front face of stop. Similarly, at the opposite end of the mandrel, the sensors are located in the radial direction to check the correct position of the hose, the design is shown in Fig. 4 right. Another option was using optical elements instead of contact in a similar configuration.

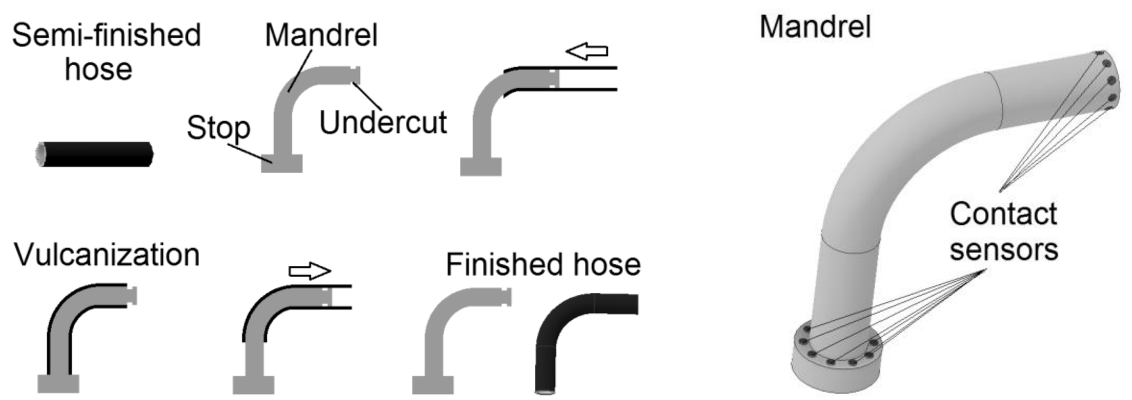

Fig. 4 Left - mandrel shape and hose placement, Right - locations of sensor on mandrel

Finally was decided that instead of preventing defects, faulty hoses will be repaired. Due to the relatively high complexity of the checking system and also because of the very variable range of hoses (lots of different mandrels shape and diameters). Each mandrel would have contain many active elements. In the vulcanization environment it is all burdened by high temperature and humidity, therefore it can be assumed that the electronic parts will lost their durability. The second considered option is to repair the already produced rejected parts. Usually the length of the hose has a considerably greater tolerance than the hose face from the plane. Here is the possibility to cut or grind the insufficient end of the hose to the required tolerance. Several experiments were performed with a grinding of hoses on conventional grinding machine Fig. 5. It has been proved that by grinding it is possible to achieve sufficient flatness of the end of the hose and also satisfactory surface quality.

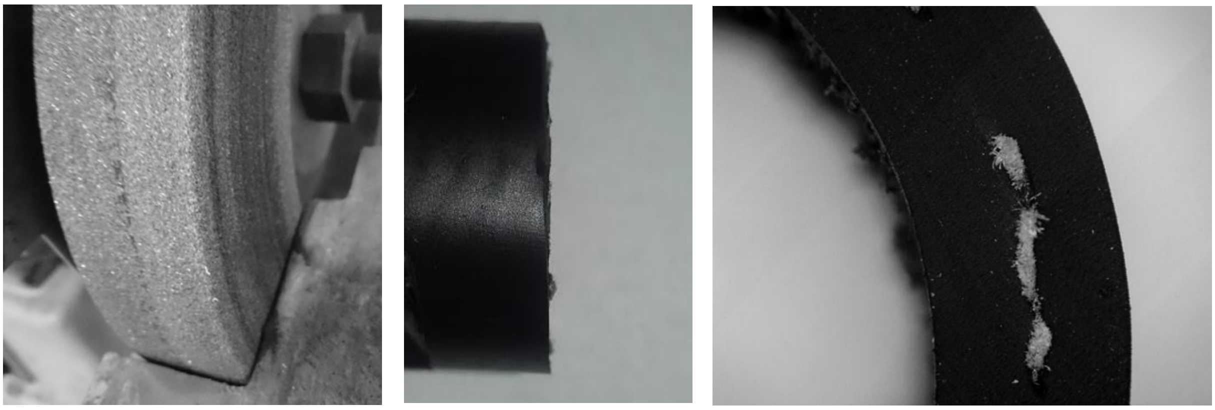

Fig. 5 Repairing of a rejected part: left – grinder, middle and right – the hose after grinding

RESULTS AND DISCUSSION

The conceptual design of a single purpose device for grinding the ends of hoses was developed (Fig. 6). The device consists of a rigid frame on which the hollow shaft is mounted by means of bearings. The fixed pin passings through the hollow shaft. The grinder is mounted on the hollow shaft slidably by means of grooving. The pneumatic drive enables the linear movement of the grinder. The stepper motor provides a rotary motion of the grinder around the pin. The principle of the device is that the hose is pushed onto pin and fixed. After that the grinder start rotation, the linear actuator sets the position of the grinder to the desired position and begins grind the hose face. The stepper motor performs a rotary movement of the grinder body around the circumference of the hose face. After circling the entire circumference, the grinder returns to the original position and the hose can be released and removed.

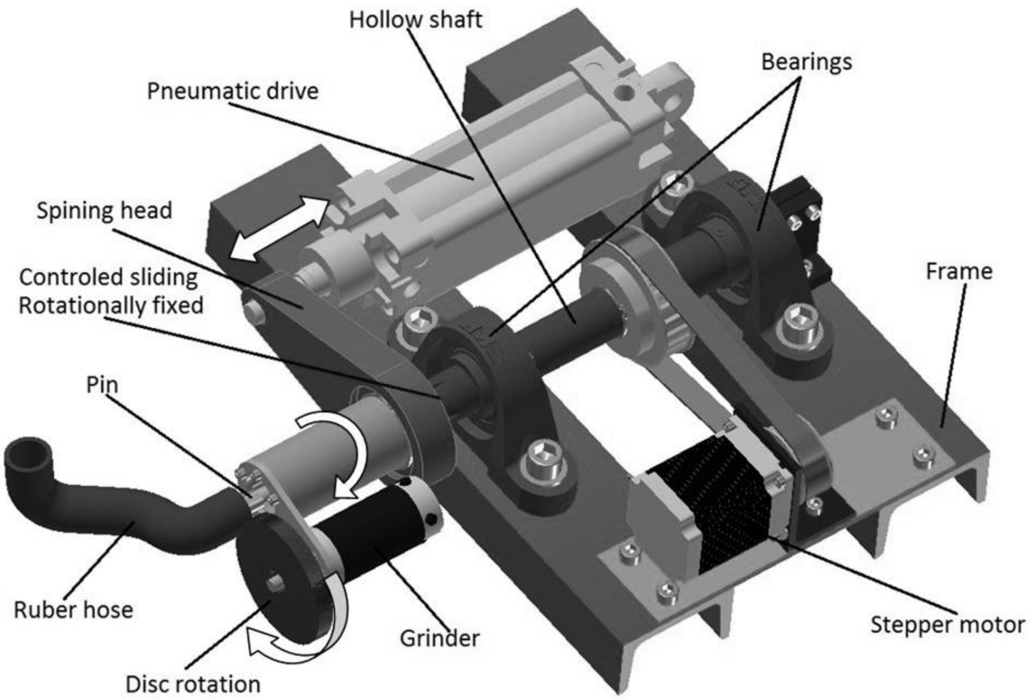

Fig.6 Design of device for aligning rubber hoses

CONCLUSIONS

The problem in the production of reinforced rubber hoses for automotive industry has been analyzed. At the beginning lot of efforts has been devoted to finding some possible mitigation measures. Later it was considered that the simplest way would be to repair the produced rejected parts subsequently after the manufacturing process. The concept of a one purpose device that could easily repair the refused parts with various diameters has been designed.

ACKNOWLEDGMENT

This publication was written at the Technical University of Liberec as part of the project "Innovation of products and equipment in engineering practice" with the support of the Specific University Research Grant, as provided by the Ministry of Education, Youth and Sports of the Czech Republic in the year 2017.

REFERENCES

1. Rodgers, B. (2015). Rubber Compounding, Chemistry and Applications, Second Edition, CRC Press 2015, ISBN: 978-1-4822-3549-4
2. Bhowmick, A. K. (1994). Rubber Products Manufacturing Technology, CRC Press, ISBN 9780824791124
3. Demirkoparan H., Pence T. J. (2015). Magic angles for fiber reinforcement in rubber-elastic tubes subject to pressure and swelling, International Journal of Non-Linear Mechanics, Volume 68, 87-95, ISSN 0020-7462.

Corresponding author:
Ing. Pavel Srb, Technical University of Liberec, Faculty of Mechanical Engineering, Department of Machine Elements and Mechanisms, Studentská 2, 461 17 Liberec 1, Czech Republic, phone: +420 48 535 3321, e-mail: pavel.srb@tul.cz

COMPARISON OF DIFFERENT CONSTRUCTION HOIST MASTS BY FEM ANALYSIS

František STARÝ[1], Karel PETR[1], Martin DUB[1], Vojtěch DYNYBYL[1]

[1]Department of Designing and Machine Components, Faculty of Mechanical Engineering, Czech Technical University in Prague.

Abstract
The article compares three variants of construction hoist masts. All three masts were calculated by FEM analysis and results discussed.

Key words: *construction hoist; FEM analysis; mast.*

INTRODUCTION

There is a demand on higher load capacity of construction hoists due to increasing productivity of construction work. Manufacturers of hoists want to satisfy this demand by innovation of masts, but they are limited by connection dimensions of nowadays used masts so the old and new masts could work together. Usage of construction hoists is shown on Fig. 1.

Fig. 1 Photos of construction hoists.

MATERIALS AND METHODS

The variant marked as A is original construction which started to lose its reliability due to increased load capacity of construction hoist. There is 3D model shown in Fig. 2. Detail of middle crossbeam is shown in Fig. 3. All three crossbeams are made from rolled L profiles.

The variant marked as B is based on variant A. Middle crossbeam shape was changed from half of its length to C profile and from half to L profile and it is made from bent sheet metal. Top and bottom crossbeam closed by a second L profile from bent sheet metal a welded to original rolled L profile. There is 3D model shown in Fig. 2. Detail of middle crossbeam is shown in Fig. 3.

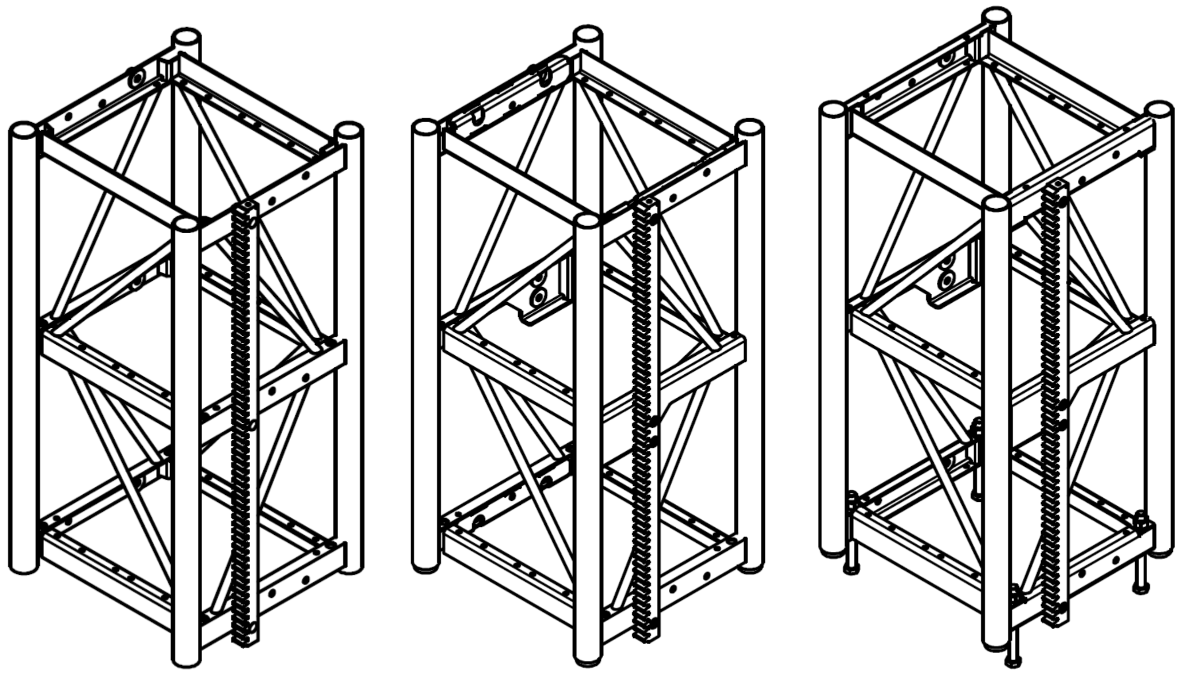

A B C

Fig. 2 3D model of mast variants (A – original, B – closed profile from two L – profiles, C – C profile).

The variant marked as C is based on variant B. Top and bottom crossbeam has been changed from closed shape to C profile from bent sheet metal. Middle crossbeam is same as in the variant B. There is 3D model shown in Fig 2. Detail of middle crossbeam is shown in Fig. 3.

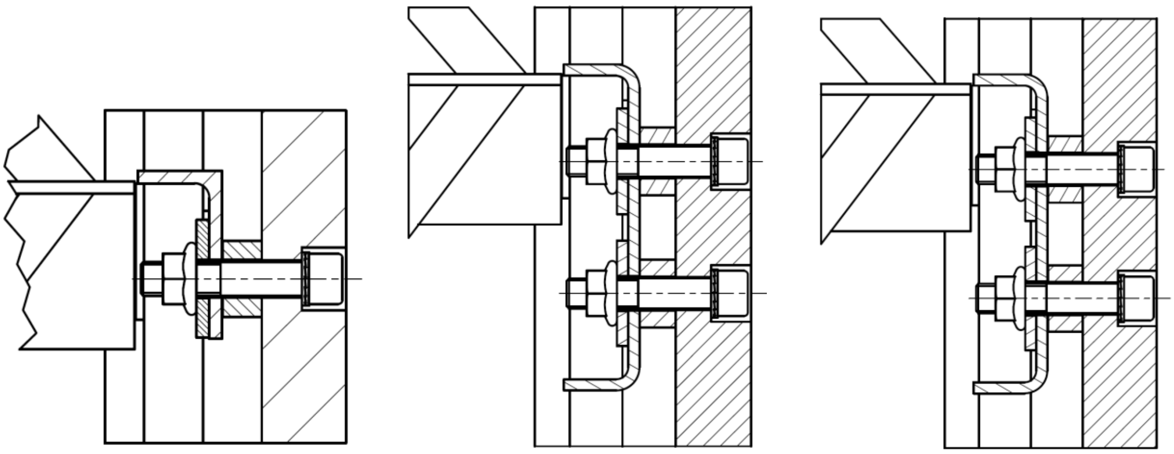

A B C

Fig. 3 Detail of middle crossbeam for variants A, B and C.

Maximal mast load capacity is 7 360 kg (cage + transported material in cage). Maximal speed of cage is up to 90 meters per minute. Cage is driven by three pinions distant 494 mm from each other. Cage is guided by vertical tubular profiles via side pulleys distant 2.1 meters from each other and three pulleys placed on the opposite side of rack (against pinions) with distance 123 mm from each other.

FEM analysis of mast was made in software RFEM from company Dlubal Software ltd. [1]. Calculations were made as 3D variant with 1D elements at whole part of mast and as 3D variant with 2D elements (shell elements) [2].
Model with 1D elements was created in two versions. First version was without rack (this version is not described in this article). Second version was with rack and it is shown in Fig. 4 for all three variants.

Model is created as a beam construction with assigned cross-sectional. Axes of beams are joint according to production drawings.

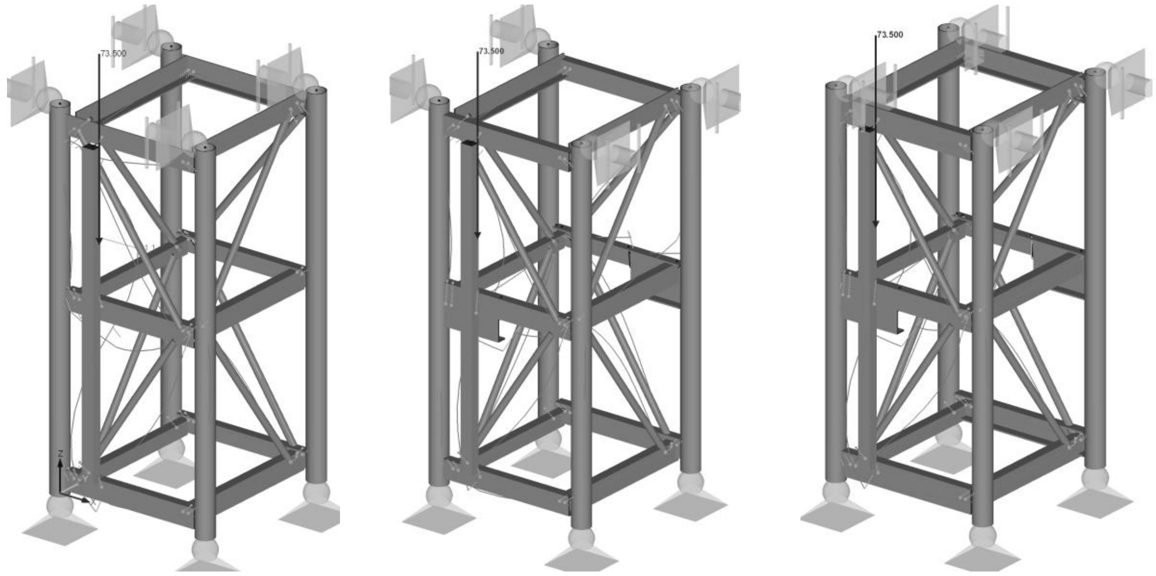

A B C

Fig. 4 1D model of masts with rack. From left to right variant A, B and C.

RESULTS AND DISCUSSION

In Fig. 5 there is shown comparison of von Mises stress at middle crossbeam for variants A, B and C, which are sorted from top to bottom and has the same color scale. Variants B a C has the same stress distribution and against variant A are crossbeams less stressed.

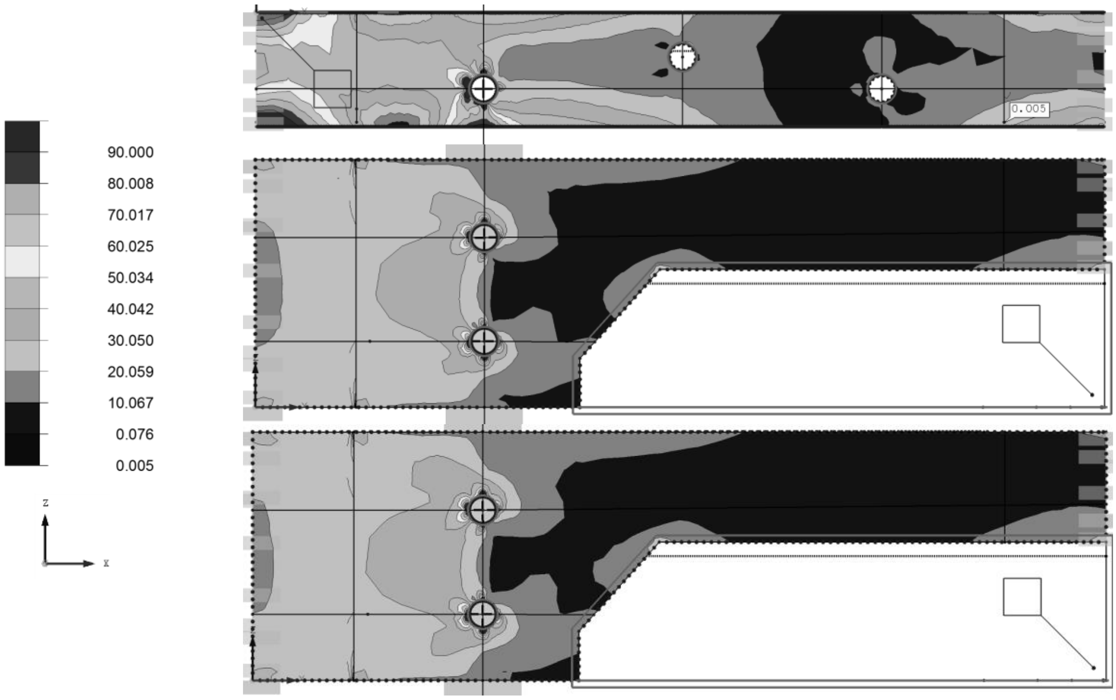

Fig. 5 Von Mises stress at middle crossbeam – variant A, B, C (from top to bottom) – color scale is united

In Fig. 6 there is made comparison of von Mises stress on top (bottom) crossbeam for variants A, B and C, which are sorted from top to bottom and has same color scale. The lowest values of stress is at variant B, where closed profile is used.

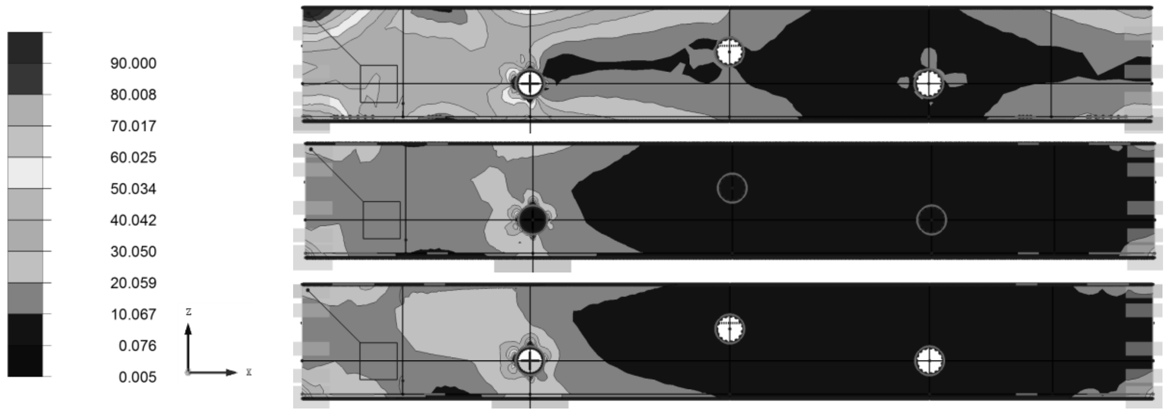

Fig. 6 Von Mises stress at top crossbeam – variant A, B, C (from top to bottom) – color scale is united

CONCLUSIONS

The results shows that closed profile is a best solution to lower maximal stress in construction. Thus the best solution for top and bottom crossbeam is to use shape of crossbeam from variant B. Variant B is however worse to productivity. Variant C has good productivity so closing this shape with another sheet of metal would significantly increase its toughness.

For middle crossbeam is suitable to use variant B (C). The von Mises stress was lowered by 15 Nmm^{-2} which is about 30% better than at variant A.

REFERENCES

1. Software RFEM - FEM Structural Analysis Software. 2016. www.dlubal.com
2. Petr, K.; Dynybyl, V.; Starý, F.; Mrázek, J. Applications of FEM to Optimizing of Machine Parts (Gear). In: WORKSHOP 2010. Praha: CTU in Prague, 2010, pp. 218-219. ISBN 978-80-01-04513-8.
3. STROS- Sedlčanské strojírny, a.s.. http://www.stros.cz/cz/

Corresponding author:
Ing. František Starý, Department of Designing and Machine Components, Faculty of Mechanical Engineering, Czech Technical University in Prague, Technicka 4, Prague 6, Prague, 16607, Czech Republic, phone: +420-224-352-415, e-mail: frantisek.stary@fs.cvut.cz.

SYNCHRONIZATION OF DIESEL-GENERATOR UNIT AND INLAND POWER NETWORK IN SHORE-TO-SHIP SYSTEMS

Marek Michał STAUDE[1]

[1]*Maritime University of Szczecin, Poland e-mail: m.staude@am.szczecin.pl*

Abstract
In the recent years, due to pollution emission by ships moored in ports, shore-to-ship power systems were introduced. Switch-over from ships' autonomous generator units to inland grid comes to carrying out automatic uninterrupted synchronization of both power sources. This task is burdened with several technological challenges, further complicated by lack of compatibility between electrical parameters of shore and marine power grids. These challenges, if not overcome, may disable the synchronization process or even lead to blackout on ship or emergency shutdown of shore-to-ship system. In this article, the author presents zero points synchronization method, which is usable in shore-to-ship systems based on power frequency converters. Proposed method leads to effective fail-free switch-over between ship and shore power sources.

Key words: *marine technology; zero crossing synchronization; power grid and generator synchronization; frequency converter.*

INTRODUCTION

Current environmental trends regarding pollution emission from marine vessels (*Directive 2005/33/EC of the European parliament and of the council, 2005*) made shore-to-ship (STS) systems increasingly popular solution installed in ports worldwide. In its premise STS system provides power, for moored ships, from inland power network, which allows ships' diesel-generator (DG) units to be shut down, thus reducing emitted pollution. Two problems must be solved in order to properly execute such process – first is matching electrical parameters of ship and inland power networks; second is synchronization of both networks and transfer of load to inland grid.

Mismatch of electrical parameters on ships and on the shore result from different voltage and frequency values in both systems. Inland grid structure forces installation of power transformers dedicated for STS systems, which makes problem of different voltage values negligible. Frequency incompatibility on the other hand is very common problem. Ship power systems use either 50 Hz (about 35% of ships) or 60 Hz (about 65% of ships) voltage (*Tarnapowicz, 2014*). High ratio of this values forces STS systems to provide voltages at both of these frequencies. In practice inland power grid of ports' country provides voltage at one of the frequencies and power frequency converters are installed to provide voltage of another, e.g. European continent utilises 50 Hz power grid, therefore to power 60 Hz ship frequency converter is required. Many ports (e.g. some of Swedish ferry terminals) have single high power frequency converter installed for all ships requiring frequency other than their regular inland grid provides. In cases like these synchronization of inland power grid to DG unit is done by modification of fuel rack settings on DG unit's diesel engine. Out voltages of both DG unit and frequency converter are used to control this process and determine moment of synchronization. Synchronization according to this procedure forces running DG network to match its' frequency with unloaded shore voltage source. This solution has following problems:

- Due to engine inertia loaded DG unit reacts to such change in nonlinear way (*Borkowski, 1990*). This increases the risk of triggering generator protection unit, which leads to blackout.
- Frequency change of running DG network affects every device connected to this network, this is especially important for electric motors powered by this network.
- STS systems with single frequency converter have another problem consequential to high sensitivity of converter protection units. While disconnecting from STS system ship's DG units must take on load. Frequency converter is however acts as ideal voltage source, so transfer of whole load from them to DG units is impossible. This forces automatic synchronization systems to disconnect ship from land while designated threshold of load is reached. Moment of disconnection is often interpreted, by converter protection unit, as occurrence of reverse pow-

er. This can lead to emergency shutdown of whole STS system, effectively creating blackout for all ships connected to it.

Solution to above problems is possible with different topology of STS system. Instead of single high power frequency converter multiple converters with smaller power output are used, one for each moored ship (*Borkowski & Tarnapowicz, 2014*). Implementation of this solution makes it possible to independently control output voltage of each converter, therefore inland network can be synchronized to ships' running network of DG units. While synchronized with ship's power network frequency converter will force its' parameters on DG units, because frequency converter behaves as ideal controlled voltage source. This predetermines use of synchronization method allowing fast correction of converter settings. Nowadays phase locked loop (PLL) method has been widely adopted for this purpose (*Tarnapowicz, 2013*). Method presented in this article, based on detection of DG unit's output voltage waveform crossing zeros, is an alternative to PLL method.

MATERIALS AND METHODS

Proposed method of synchronization relies on equalization of voltage waveform zero crossing time for both DG units and frequency converter being synchronized. Alternating current is a sine wave, therefore two zero crossings occur in one period, as presented in Fig. 1. Detection of these crossings comes to finding moments of sign change of voltage waveform. Time intervals between crossings are equal to length of half period of sine wave, thus voltage frequency can be calculated by equation (1)

$$f = \frac{1}{2t} \qquad (1)$$

where f is frequency (Hz) and t is time between transitions (s).

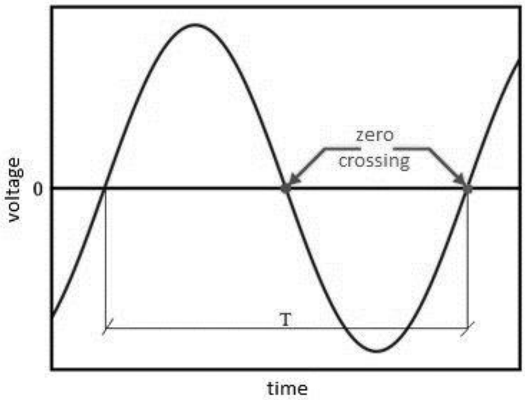

Fig. 1 One period of sine wave with marked zero crossings

Block for detection of zeros crossings is connected to STS system as presented in fig. 2.

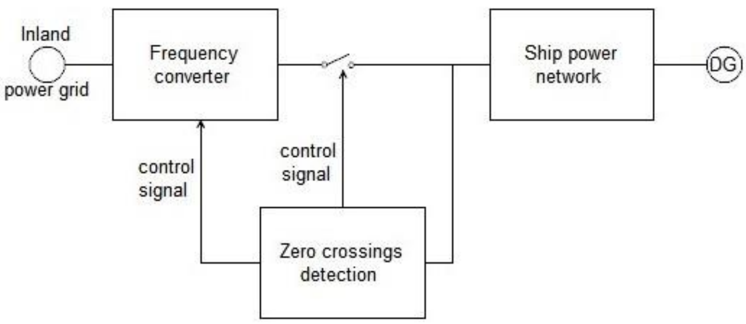

Fig. 2 STS system with block for detection of zero crossings

Detection block measures voltage in ship's power network and, when waveform's crossing of zero is detected, enables frequency converter in STS system and closes switch connecting both power networks. To prevent loss of synchronization, when DG unit's frequency fluctuations occur during load changes, zero crossings are measured constantly and adequate control signals for frequency converter are send. To increase precision of the method zero crossings are detected twice during each period – for both down and up slopes of sine wave.

RESULTS AND DISCUSSION

A simulation analysis of the synchronization of STS system's frequency converter and ship's DG units was performed with use of MATLAB-SIMULINK package. Following algorithm has been used for detection of waveforms crossing zeros:

- voltage signal is sampled at high frequency
- current sign is found by checking if value of the most recent sample is greater than zero
- current sign is compared with sign from the previous sample
- if signs differ crossing through zero occurred

In real-life cases digital signal processor would handle the high frequency sampling. To eliminate false data, coming from noises or lost samples, algorithm would test frame of samples (e.g. five most recent samples) and determine sign based on majority result.

Results of simulation are presented in fig. 3. Adjustment of frequency converter are seen at each zero crossing, with first synchronization occurring at 0,01 second.

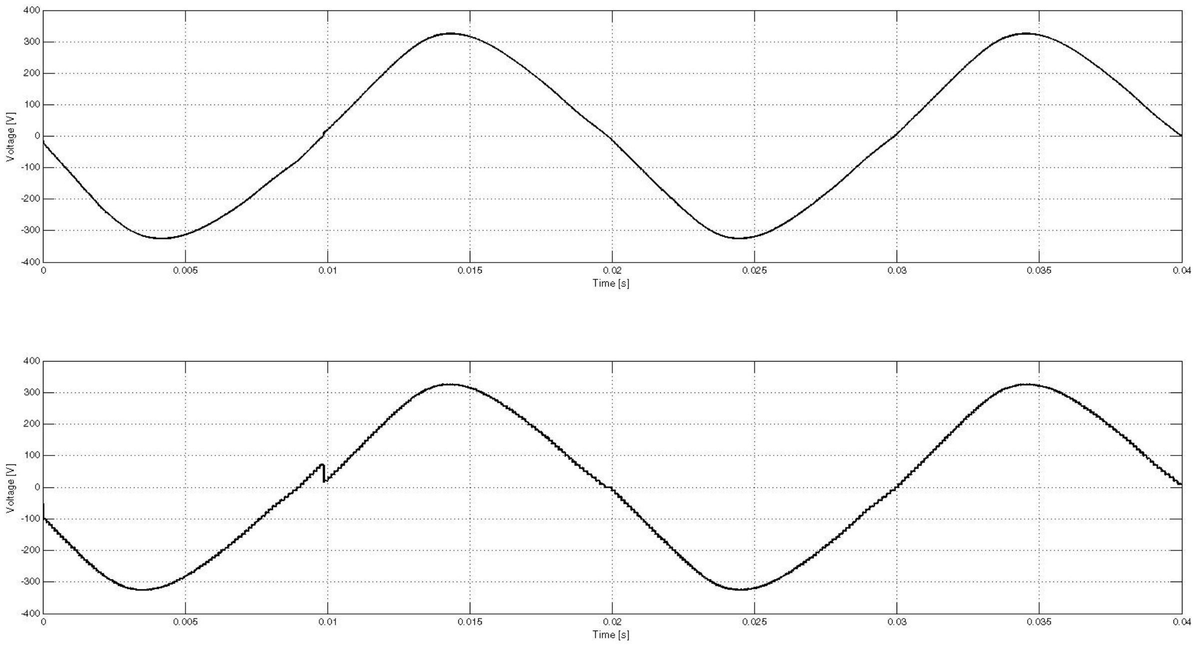

Fig. 3 Voltage outputs of ship's DG units (above) and STS frequency converter (below)

Difference between ship's DG voltage and STS voltage output is presented in fig. 4. After first synchronization measured differences mostly consist of the voltage distortions typical for frequency converter output. All distortions are in the same range as analogous measurements for PLL synchronization method, therefore distortion levels for both method are basically identical.

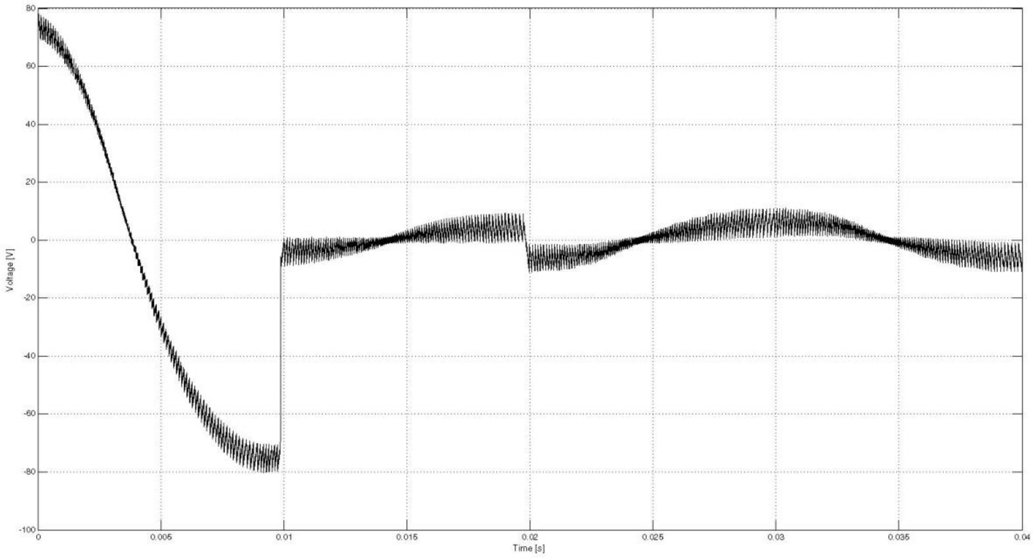

Fig. 4 Difference between voltage from ship's network and STS system

CONCLUSIONS

Method of voltage synchronization based on detection of DG unit's output voltage waveform zero crossings is good solution for STS systems. Detection of zero crossing with use of digital signal processor is simple, as is control over frequency converter's start signal. Proposed method requires STS system with independent frequency converters dedicated for each ship. This should not be a problem in the future, because this topology of STS systems is growing in popularity, due to fact that it solves other technological and quality of power problems. Most of future STS systems in European ports are supposed to have such topology.

ACKNOWLEDGMENT

This research outcome has been achieved under the research project: Nowoczesne technologie w systemach "Shore to Ship" No 2/S/IE-iAO/16 financed from a subsidy of the Ministry of Science and Higher Education for statutory activities

REFERENCES

1. *Directive 2005/33/EC of the European parliament and of the council*, amending Directive 1999/32/EC.
2. Tarnapowicz D. (2014). Quality guaranteed of electric power supply connecting of ships with shore systems while mooring in port. In *Management Systems in Production Engineering 2014* (pp. 179-183).
3. Borkowski T. (1990). *Hydrauliczne regulatory prędkości obrotowej „woodward“ w zastosowaniach okrętowych. Działania i regulacja.* WSM Szczecin
4. Borkowski T. Tarnapowicz D. (2014). Topology and elements of the STS system in *Shore to ship system – alternative power supply of ships in ports* (pp. 43-52). Szczecin. Scientific Publishing House of the Maritime University.
5. Tarnapowicz D. (2013). Synchronization of national grid with vessel electrical network in the „shore to ship“ system. In *Management Systems in Production Engineering 2013* (pp. 9-13).

Corresponding author:
Marek Staude, M.Eng., Faculty of Marine Engineering, Maritime University of Szczecin, Wały Chrobrego 1-2, 70-500 Szczecin, Poland, phone: +48 914 809 379, e-mail: m.staude@am.szczecin.pl

THE OPTIMIZATION PROCEDURE OF THE INNER GEOMETRY IN THE SPHERICAL ROLLER BEARINGS WITH REGARD TO THEIR DURABILITY

Ján ŠTEININGER[1], Slavomír HRČEK[2] , Tomáš GAJDOŠÍK[3], Marián STOPKA[4]

[1] *Department of design and mechanical elements,Univerzitná 1, Žilina 01008, Slovakia*
[2] *Department of design and mechanical elements,Univerzitná 1, Žilina 01008, Slovakia*
[3] *Department of design and mechanical elements,Univerzitná 1, Žilina 01008, Slovakia*
[4] *Department of design and mechanical elements,Univerzitná 1, Žilina 01008, Slovakia*

Abstract
This article deals with the optimization procedure of the inner geometry in the spherical roller bearings. The term optimization is in this case understood as the selection process of the most appropriate solution to the spherical roller bearing durability increase. It analyses the issue of current state of the spherical roller bearings, two-body line contact and the bearings durability. It describes the contact strain along the spherical roller in the spherical roller bearing using curves. It subsequently shows the optimization procedure of the contact strain curves and so the bearing itself. The article also describes the creation procedure of the 3D parametric model and the contact strain analysis using the finite element method.

Key words: *Spherical roller bearing; optimization; contact strain*

INTRODUCTION

Rolling bearings are an inseparable part of most machines and devices in which rotation movement and linear motion are performed. There are different requirements on rolling bearings. Production machines need bearings which are able to work in high revolution, in power engineering bearings have to carry heavy load, trains require bearings with high speed performance, etc.
Development or rather rolling bearing optimization is conditioned by the technical parameters increase in machines and devices. This fact refers especially to input parameters increase such as power and revolution, weight and volume reduction, noise level reduction, etc. However, the most important parameters requiring optimization are bearing lifetime and reliability. New technologies development introduces also new construction materials, new production techniques of semi-finished products and bearing components or new installation methods. It is important not to overlook the bearing construction. Here it is possible to perform geometry adjustment optimization. This adjustment applies especially to geometry adjustment of runways and rolling elements in the spherical roller bearings. (Kohár et al., 2016)

MATERIALS AND METHODS

The double row angular spherical roller bearing has a runway spherically ground on the outer ring. The bearing is able to accommodate very high radial loads, as well as heavy axial loads in both directions. High radial load capacity is caused by the great number of rolling elements, so-called spherical rollers and their close contact on the inner ring runways.
Rolling bearings durability depends on revolution number which the bearing is able to perform. Peeled material is a sign of a component fatigue. The fatigue is crucial and natural way of bearing damage. It is demonstrated by the presence of small cracks under the bearing runway surface. The depth of these cracks is usually about 0,05 – 0,3 millimetres depending on the surface curve radiuses of rolling elements and the bearing rings runways. The crack depth allows the material changes which are caused by slide pulsing strain. This process leads to the gradual crack formation under the surface. It can take quite a long time until it is visible on the surface in form of the material peeling off, so-called pitting.

It is possible to calculate the intensity of the contact pressure and the size of the contact surface - effective length l_{ef} and width 2b from the contact pressure distribution on the most strained point in the bearing inner ring. The picture (Fig. 1) shows the course projection (the curve) of the contact pressure along the contact surface l_{ef} of the contact ellipse on the bearing inner ring. The contact strain curve has been calculated using the finite element method. (Kohár et al., 2016)

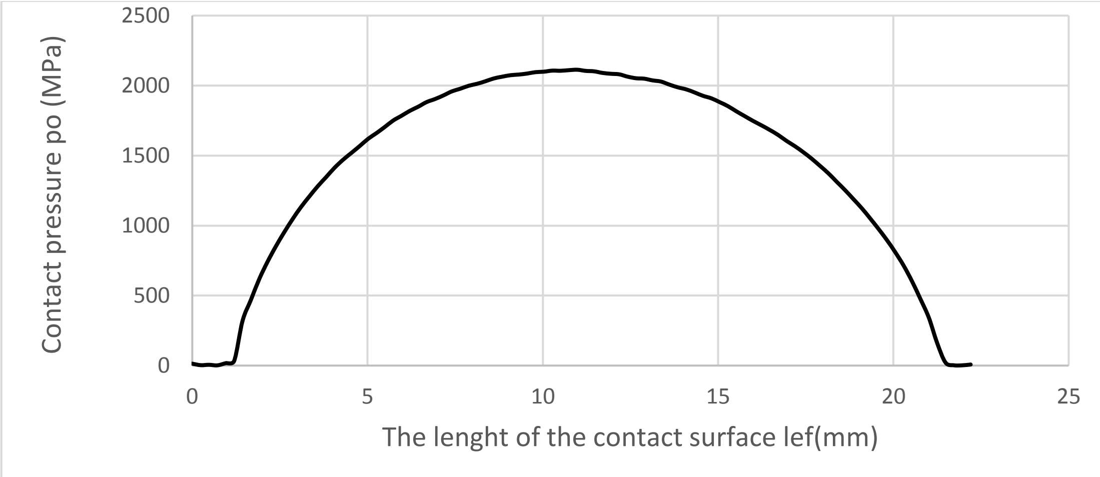

Fig. 1 The contact pressure course on the inner bearing ring runway

For under surface strain evaluation it is necessary to define a plane which crosses the maximum contact pressure point and it is orthogonal to the inner ring runway. It is possible to define the size of maximum orthogonal slide strain τ_{yz} in the defined plane for under surface strain evaluation. The coordinate system, in which the above mentioned slide strain will be evaluated, is oriented in the way that the axis x is in the tangent´s direction to the inner ring runway in the spherical roller bearing. This operation will be located in the maximum contact pressure point. (Lukáč, et al., 2016)

The preparation of the parametric 3d model and the contact analysis.
Double row spherical roller bearing model (Fig. 2) has been simplified to the maximum extent thanks to the even load distribution on both rows and individual roller elements. The model consists of the rolling element, the outer ring, the inner ring and the contact surfaces. These surfaces are important for more precise model meshing in FEM system ANSYS. The contact pressure will be measured in the above mentioned parts. (Tropp, et al., 2016)

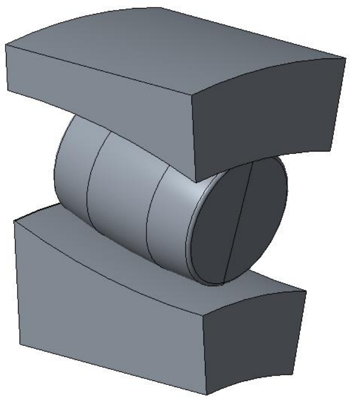

Fig. 2 The simplified model of the double row spherical roller bearing

RESULTS AND DISCUSSION

Spherical roller bearing will be optimized on the basis of the contact pressure decrease. This pressure exerts in the contact place of the rolling element and the outer and inner ring. The optimization relates to the rolling element profile. However, the calculation relates to the contact strain between rolling elements and bearing rings. The pictures Fig. 3 and Fig. 4 show the curve shape of the contact pressure in the spherical rollers depending on the length of the contact surface. The shape of this original curve is derived from the finite element analysis. The aim of optimization lies in the maximum contact pressure decrease in the contact place of the rolling element with the bearing rings runways. This is shown in the picture Fig. 3 (the inner ring), Fig. 4 (the outer ring) – so-called four-point contact. (Kohár 2016)

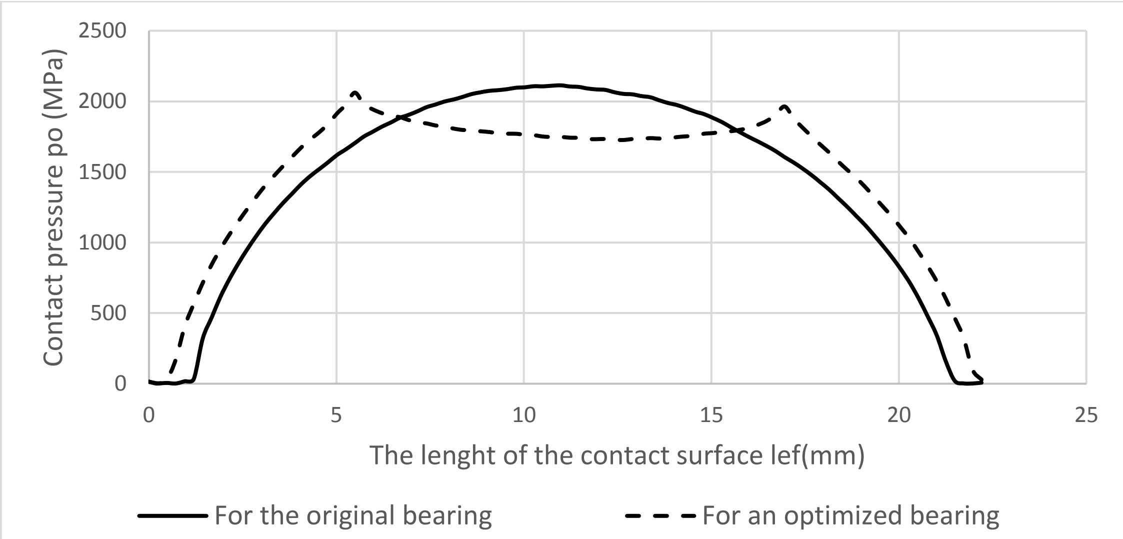

Fig. 3 The original and optimized contact pressure course projection on the inner bearing ring runway

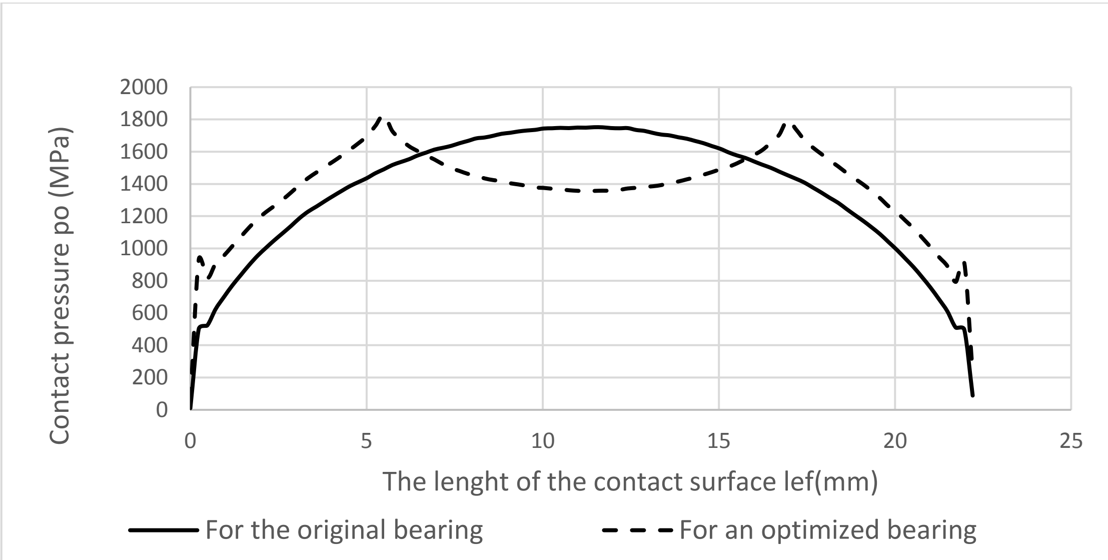

Fig. 4 The original and optimized contact pressure course projection on the outer bearing ring runway

CONCLUSIONS

Spherical roller bearings optimization can be performed using the geometry change in the rolling element – the spherical roller. The optimization involves the length change parameter of the adjusted spherical roller surface. Fig. 5 shows the contact pressure decrease of the inner and outer bearing ring using the lenght change parameter dsl increase.

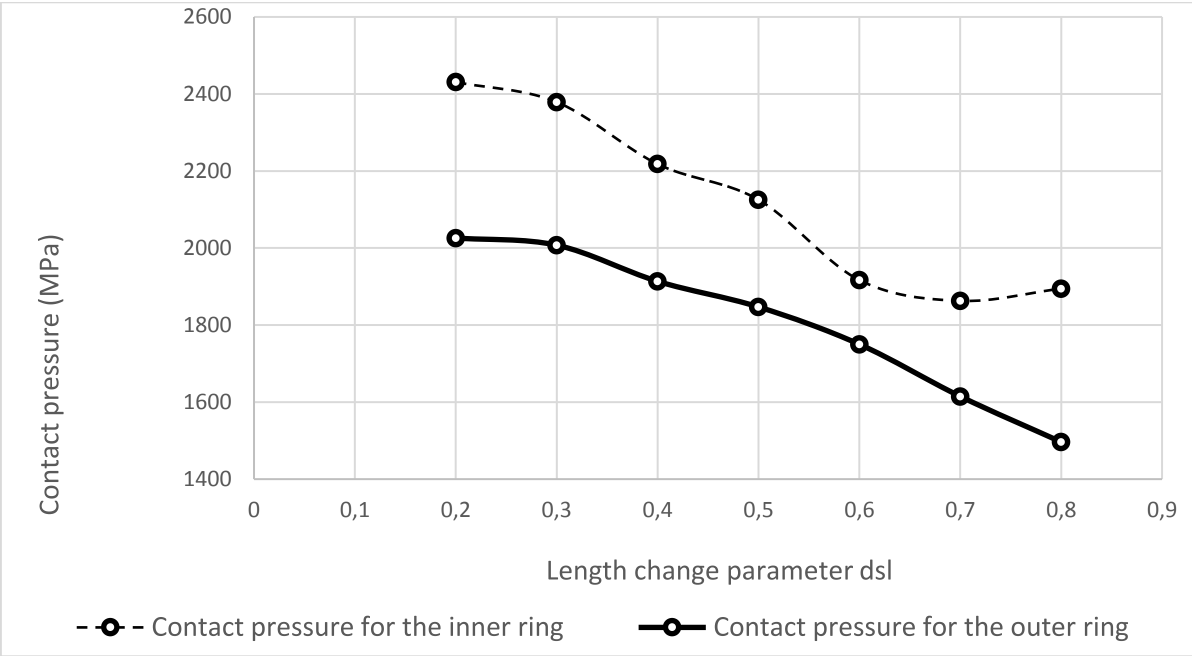

Fig. 5 The contact pressure decrease projection of the inner and the outer bearing ring using the length parameter dsl

ACKNOWLEDGMENT
This study was supported by Slovak Research and Development Agency under the contract no. APVV-14-0508 – Development of new methods for the design of special large-size slewing rings.

We support research activities in Slovakia / project financed from EU funds.
This article was created by the project "ProHiSpeB - prototype of telematics axle bearing for high speeds" on the basis Operational Programme Research and Development funded by the European Regional Development Fund.

REFERENCES

1. Kohár R., Brumerčík F., Lukáč M., Nieoczym A.: Numerical analysis of roller bearing. In: Applied computer science. - ISSN 1895-3735. - Vol. 12, no. 1 (2016), s. 5-16.
2. Kohár R.: Úvod do štrukturálnej optimalizácie. In: Wspomagane komputerovo modelowanie, analiza i projektowanie elementów maszyn i mechanizmów. - Lublin: Politechnika Lubelska, 2015. - ISBN 978-83-7947-135-5. - S. 95-103.
3. Lukáč M., Brumerčík F., Krzywonos L.: Driveability simulation of vehicle with variant tire properties. In: Communications : scientific letters of the University of Žilina. - ISSN 1335-4205. - Vol. 18, no. 2 (2016), s. 34-37.
4. Tropp M., Lukáč M., Nieoczym A., Brumerčík F.: Hydraulic circuits in transport and mechatronic systems. In: Logi : scientific journal on transport and logistics. - ISSN 1804-3216. - Vol. 7, no. 1 (2016), s. 143-149.

Corresponding author:
Ing. Ján Šteininger, Department of design and mechanical elements, Faculty of Mechanical Engineerig, University of Zilina, Univerzitná 1, Žilina 01008, Slovakia, e-mail: jan.steininger@fstroj.uniza.sk

WEIGHT OPTIMIZATION OF CHAMBER FOR VACUUM CASTING TECHNOLOGY

Marián STOPKA[1], Róbert KOHÁR[2], Peter SPIŠÁK[3], Ján ŠTEININGER[4]

[1] *University of Žilina , Slovak Republic, e-mail: marian.stopka@fstroj.uniza.sk*
[2] *University of Žilina , Slovak Republic, e-mail: robert.kohar@fstroj.uniza.sk*
[3] *University of Žilina , Slovak Republic, e-mail: peter.spisak@fstroj.uniza.sk*
[4] *University of Žilina , Slovak Republic, e-mail: jan.steininger@fstroj.uniza.sk*

Abstract
The purpose of this paper is optimization of real vacuum chamber. The goal is lowering the weight while geometry is kept. Methods of parametrical modelling and automated optimization in chosen FEM software will be used for executing the analysis. Results obtained during optimization can be used in the future realization of vacuum chamber for Rapid prototyping technology.
Key words: *vacuum chamber, stress analysis, welds shape.*

INTRODUCTION

Nowadays, there are high requirements on a manufacture. There is effort to make engineering process faster on one side, and to lower the cost on the other side. This is a reason why are more widely used technologies Rapid prototyping and also Vacuum casting. This method is highly effective for producing prototypes in limited amount. Increasing the number of pieces also increases the cost and complexity of whole process. It is useful to think about automation of manufacturing process in case of need producing tens or hundreds of pieces. This resulted to design an automated line for filling silicone moulds in vacuum.

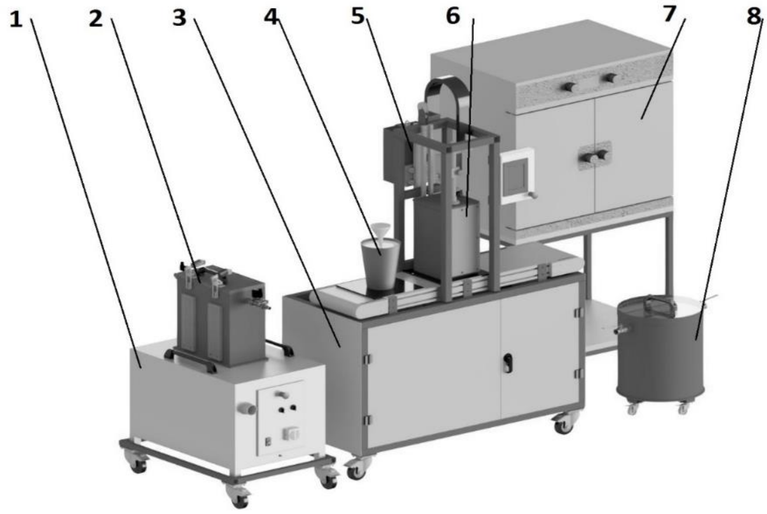

Fig. 1 Automatic vacuum casting technology device

Fig. 1 shows whole assembly for automated vacuum filling of silicone moulds. The mould (4) is placed on conveyor belt (3) and moved to a place of filling. Vacuum chamber (6) is moved down on a linear guide (5). The mould itself is filled there. Injected material is located in the buffer (2) and it is also connected to the source of vacuum. The material flows through gear pump – Dekumed (1). The chamber is lifted after the filling process is finished and it is able to place mould from belt to oven (7).
At this time the line is not fully completed, therefore the chamber has to be lifted manually. This chamber is relatively heavy according to dimensions and used materials. That’s why hand lifting is difficult. The dimensions of chamber are 200x200x400 mm (WxDxH) and it’s made of 5 mm thick steel plates welded

together. The front window is made of 20 mm thick polycarbonate. The original design counted with walls thickness 8 mm, but for verification process it was produced from 5 mm thick material.

MATERIALS AND METHODS

A static analysis was done to realize points of optimization. The model was cleared of unnecessary components (threads, etc.) and loaded by atmospheric pressure on outer surfaces. (Martikan, Brumercik, & Bastovansky, 2015)

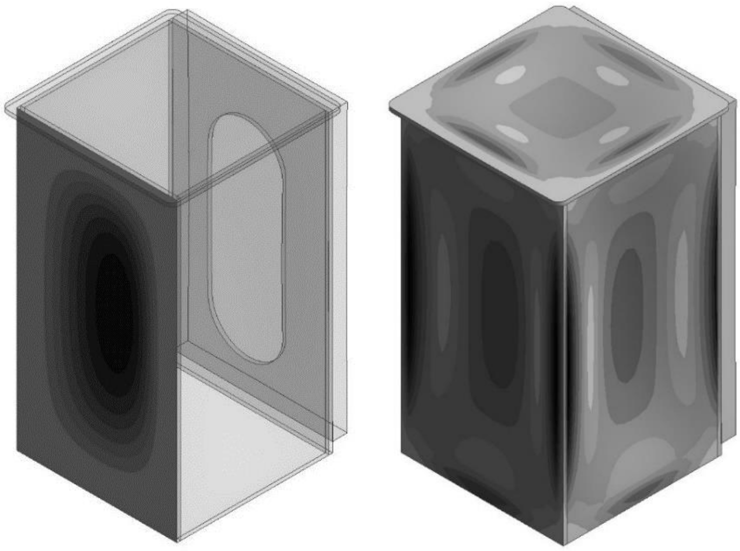

Fig. 2 Results of stress analysis, left - max. deformation, right - max. stress

Results showed that the construction is critical in two reasons. The first is deformation of walls and the second is stress in corners of the chamber. At this moment the optimization was divided into two steps:

- Find out the best shape of the weld according to maximal stress.
- Lower the thickness of walls with maximal deformation up to 0,5 mm.

All of the welds are corner type. We recognize three types of corner welds – flat, convex and concave. The goal of this chapter is to get know maximal stress in weld using the same welds height parameter. It's important to know also maximal allowed weld stress:

$$\sigma_{Dzv} = \beta . \alpha_{\perp} . \frac{R_e}{k} . c_{II} [MPa]$$

Where:

- Corner welds height parameter; β=1,3-0,03.t=1,15 (pre t<10mm)
- Welded connection conversion parameter; $\alpha_{\perp}$=0,75÷1, chosen 1
- Yeld point of steel 11 423; R_e=260 MPa
- Safety factor for non-hardened steels; k=1,7-2, chosen 1,7
- Pulsating load lowering parameter; c_{II}=0,85

After calculation:

$$\sigma_{Dzv} = 127\ MPa$$

Maximal stress can't exceed calculated value 127 MPa. (Málik, a iní, 2013)

Fig. 3 Differrent corner welds, left - convex, middle - flat, right – concave

The height of a weld is dependent on a thickness of welded material, according to standard STN 05 0025 (Čilík & Žarnay, 2001). The following condition must be satisfied:

$$a \leq 0{,}7\ .\ t$$

For thickness t=5 mm was height calculated to a_{max}=3,5 mm and this dimension was used for modelling. The analysis resulted, that the shape of weld does not affect magnitude of stress, but the distribution of it. The calculated stress didn't exceed 78 MPa for all 3 types of weld (concave – 68 MPa; flat – 78 MPa; convex – 73 MPa). The best stress distribution of stress provided convex shape, therefore was chosen for next computation and suggested for manufacture.

Parametric modelling in software Autodesk Inventor 2017 was connected with optimization algorithms of Ansys Workbench v17.5 for optimizing vacuum chambers walls. (Lawrence, 2013) Thickness of wall was used as an input parameter and the range was set from 3 mm to 8 mm. Output parameter was deformation and it couldn't exceed more than 0,5 mm. Dependence between walls thickness and deformation shows **Fig. 4**.

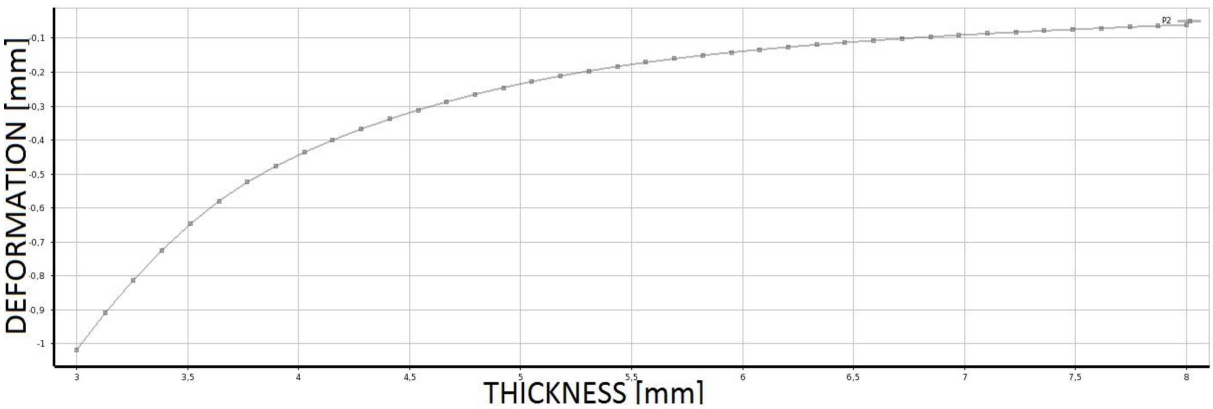

Fig. 4 Dependence of deformation on thicknes

The simulation resulted that minimal thickness with deformation to 0,5 mm is 3,84 mm. (Faturik, Trsko, Hrcek, & Bokuvka, 2014) According this results was model modified, calculated its weight and statically loaded once again.

RESULTS AND DISCUSSION

Using optimization process was calculated minimal thickness of sheet metal to 3,84 mm. The height of weld a=2,7 mm matches to this thickness. The chamber was modelled using these parameters to be used for control calculation. Chamber manufactured by this method doesn't exceed maximal allowed stress or deformation. Maximal stress was calculated to 111 MPa and the deformation to 0,499 mm. Comparison of weight-loss of the chamber shows **Tab. 1**

Tab. 1 Comparison of weight-loss

Variant	Weight [kg]	Saving [%]	Saving [kg]
Design – 8 mm	24,84	0	0
Reality – 5 mm	16,36	34,1	8,48
Calculated minimum – 3,84 mm	13,09	47,3	11,75

CONCLUSIONS

It's able to lower the weight significantly by using optimization processes. The weight of chamber was lowered by 3,27 kg (20%) against real piece and by 11,75 kg (47,3%) against the first design. It's needed to remember that sheet metals are produced in standardised thicknesses with tolerances (±0,3 mm in this case). The calculated thickness was rounded up to 4,5 mm which resulted into weight-loss only 1,4 kg (8,6%) against real weldment.

ACKNOWLEDGMENT

The research is supported by the following institutions with project Cultural and Educational Grant Agency of the Ministry of Education, Science, Research and Sport of the Slovak Republic under the contract no. 040ŽU-4/2016 - Modernization of teaching with Rapid Prototyping Technology.

REFERENCES

Čilík, L., & Žarnay, M. (2001). *Metodika konštruovania.* EDIS.

Faturik, L., Trsko, L., Hrcek, S., & Bokuvka, O. (2014). Comparison of structural design in high and ultra-high cycle fatigue regions. *Transactions of FAMENA, 34*(4), s. 1-12.

Lawrence, L. (2013). *ANSYS Workbench Tutorial Release 14.0.* University of Texas at Arlincton.

Málik, L., Medvecký, Š., Brumerčík, F., Hrček, S., Chrzová, J., Kohár, R., & Lukáč, M. (2013). *Konštruovanie II.* Žilina: EDIS.

Martikan, M., Brumercik, F., & Bastovansky, R. (2015). Development of mechatronic deformation system. *Applied mechanics and materials*, s. 173-178.

Corresponding author:

Ing. Marián Stopka, Department of Design and Mechanical Elements, Faculty of Mechanical Engineering, University of Zilina. Univerzitná 1, Žilina, 01026, Slovak Republic, phone: 00421949233117, e-mail: marian.stopka@fstroj.uniza.sk

TWO-MASS LINEAR VIBRATORY CONVEYOR

Martin STURM[1], Lubomír PEŠÍK[2]

[1]Faculty of Mechanical Engineering, University of Applied Sciences Zittau/Görlitz, Germany
[2]Faculty of Mechanical Engineering, Department of Machines Parts and Mechanisms, Technical University of Liberec, Czech Republic

Abstract
Linear vibratory conveyors are a common equipment for conveying goods in different industries such as for example building, mining, food industry. These systems are used for the supply of mainly bulk goods into further processing operations. The goods to be conveyed typically requesting a heavy duty design of the conveyor and eccentric excitation drives with relatively high torque, supplying strong vibrations to the floor of the installation location. The target of this article is to determine a dynamic model, based on a two-mass absorber system, for the effective avoidance of the transfer of vibrations to the ground by enabling an optimum supply of goods by the same time.

Key words: *Vibratory conveyor, dynamic absorber, resonance frequencies, dynamic model.*

INTRODUCTION

Linear vibratory conveyors are mainly built to forward bulk material for the mining, building and food industry, such as rock, grit and flour. The assembly of these vibratory conveyors consists of two principal parts, the conveying element build as a conveying trough and a supporting element, build of steel elements and fixed to the ground by heavy-duty screws (Harris, 2005), (Buja, 2007). This type of conveyors representing a one-mass system with the disadvantage to have only very limited possibilities to optimize the efficiency regarding the conveying of the goods and even more, the reduction of vibrations transmitted to the floor.
A two-mass conveyor as shown in Fig. 1 represents an alternative solution to the one-mass linear vibrating conveyor, which is not so common.

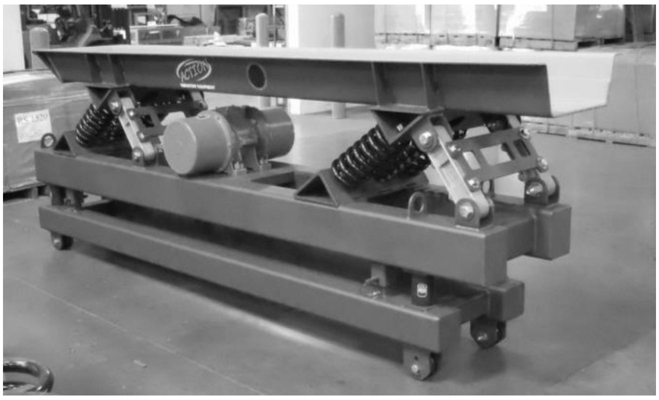

Fig. 1 Vibratory conveyor with two masses (*Action Equipment Company*, Inc., 2017)

MATERIALS AND METHODS

The theoretical solution is done in two steps. At first, a dynamic model is deigned and then the dynamic parameters are determined.

Determination of the conveyors dynamic model

The assembly of the following two-mass vibratory conveyor consists of three principal parts, the conveying element build as a conveying trough, represented by character m_2, the excited mass with the drive, represented by character m_1 and a supporting element, fixed to the ground. Both masses are connected by springs. In this case, helical springs are installed. The excitation of m_1 is done by an eccentric drive, installed to excite the mass 90° to the lever (Dresig, Holzweißig, 2008). The stiffness and the springs are defined as k_1 and k_{21}. The damping of the system is neglected. Mass $m_1$is connected to the ground by levers under an angle of β_1, mass $m_2$is connected to mass $m_1$by levers under an angle of β_2. The levers enabling a better definition of the masses motion. Fig. 2 shows the mechanical model of the two-mass conveyor.

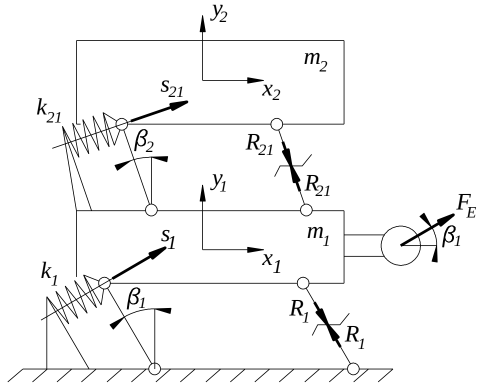

Fig. 2 Mechanical model of the vibratory conveyor

Calculation of dynamic parameters

Based on the mechanical model shown in Fig. 2, the following equations are formed (Knaebel, Jäger, Roland, 2009):

$$m_1\ddot{x}_1 + k_1x_1 - k_{21}x_{21} - F_{R1}\sin\beta_1 + F_{R21}\sin\beta_2 = F_E\cos\beta_1\,, \tag{1}$$

$$m_1\ddot{y}_1 + k_1y_1 - k_{21}y_{21} - F_{R1}\cos\beta_1 + F_{R21}\cos\beta_2 = F_E\sin\beta_1\,, \tag{2}$$

$$m_2\ddot{x}_2 + k_{21}x_{21} - F_{R21}\sin\beta_2 = 0\,, \tag{3}$$

$$m_2\ddot{y}_2 + k_{21}y_{21} - F_{R21}\cos\beta_2 = 0\,, \tag{4}$$

Summing up the equations (1) and (3), (2) and (4) as well as (3) and (4), the following equations can be formed:

$$m_1\ddot{x}_1 + k_1x_1 - F_{R1}\sin\beta_1 + m_2\ddot{x}_2 = F_E\cos\beta_1\,, \tag{5}$$

$$m_1\ddot{y}_1 + m_2\ddot{y}_2 + k_1y_1 - F_{R1}\cos\beta_1 = F_E\sin\beta_1\,, \tag{6}$$

$$(m_2\ddot{x}_2 + k_{21}x_{21})cos\beta_2 + (m_2\ddot{y}_2 + k_{21}y_{21})sin\beta_2 = 0\,. \tag{7}$$

Merging equation (5) and (6), the equation can be formed as

$$\frac{m_1\ddot{x}_1+k_1x_1+m_2\ddot{x}_2}{sin\beta_1} + \frac{m_1\ddot{y}_1+k_1y+m_2\ddot{y}_2}{cos\beta_1} = F_E\,\frac{\cos\beta_1}{\sin\beta_1} + F_E\,\frac{\sin\beta_1}{\cos\beta_1}, \tag{8}$$

and after converting equation (8)

$$(m_1\ddot{x}_1 + m_2\ddot{x}_2 + k_1x_1)\cos\beta_1 - (m_1\ddot{y}_1 + m_2\ddot{y}_2 + k_1y_1)\sin\beta_1 = F_E\,, \tag{9}$$

Splitting up the motion of x_2 and $y_2$into the components, the following form can be written

$$(m_1\ddot{x}_1 + m_2\ddot{x}_1 + m_2\ddot{x}_{21} + k_1x_1)\cos\beta_1 - (m_1\ddot{y}_1 + m_2\ddot{y}_2 + m_2\ddot{y}_{21} + k_1y_1)\sin\beta_1 = F_E\,, \tag{10}$$

$$(m_2\ddot{x}_1 + m_2\ddot{x}_{21} + k_{21}x_{21})cos\beta_2 + (m_2\ddot{y}_1 + m_2\ddot{y}_{21} + k_{21}y_{21})sin\beta_2 = 0\,. \tag{11}$$

The levers guide the motion of each of the two masses between floor and mass m_1 and between mass $m_1$and mass m_2. Therefore the coordinate vectors with the characters x and y can be merged and replaced by character s. Then the equations (10) and (11) can be formed as

$$m_1\ddot{s}_1\cos^2\beta_1 + m_2\ddot{s}_1\cos^2\beta_1 + m_2\ddot{s}_{21}\cos\beta_2\cos\beta_1 + k_1s_1\cos^2\beta_1 + m_1\ddot{s}_1\sin^2\beta_1 + m_2\ddot{s}_1\sin^2\beta_1 + \\ + m_2\ddot{s}_{21}\sin\beta_2\sin\beta_1 + k_1s_1\sin^2\beta_1 = F_E\,, \tag{12}$$

$$m_2\ddot{s}_1\cos\beta_1\cos\beta_2 + m_2\ddot{s}_{21}\cos^2\beta_2 + k_{21}s_{21}\cos^2\beta_2 + m_1\ddot{s}_1\sin\beta_1\sin\beta_2 + m_2\ddot{s}_{21}\sin^2\beta_2 + \\ +k_{21}s_{21}\sin^2\beta_2 = 0\,. \tag{13}$$

with

$$s_{21} = s_2 - s_1 \tag{14}$$

After simplifying the equations (12) and (13), the final equations of motion for the analyzed conveyor model are

$$(m_1 + m_2)\ddot{s}_1 + m_2\ddot{s}_{21}(\cos\beta_2\cos\beta_1 + \sin\beta_2\sin\beta_1) + k_1s_1 = F_E\,, \tag{15}$$

$$m_1\ddot{s}_1(\cos\beta_2\cos\beta_1 + \sin\beta_2\sin\beta_1) + m_2\ddot{s}_{21} + k_{21}s_{21} = 0\,. \tag{16}$$

RESULTS AND DISCUSSIONS

The results of the above equations can be used for the optimisation of dynamic parameters.

Variation of the angles of the dynamic model

For the further analysis of the dynamic model, three cases of particular interest have to be observed, i.e. case one with $\beta_1 = \beta_2$, case two with $\beta_1 = 0$ and case three with $\beta_2 = 0$.

For case one with $\beta_1 = \beta_2$, equation (15) can be converted step by step

$$(m_1 + m_2)\ddot{s}_1 + m_2\ddot{s}_{21} + k_1s_1 = F_E\,, \tag{17}$$

$$m_1\ddot{s}_1 + m_2\ddot{s}_1 + m_2\ddot{s}_2 - m_2\ddot{s}_1 + k_1s_1 = F_E\,, \tag{18}$$

$$m_1\ddot{s}_1 + m_2\ddot{s}_2 + k_1s_1 = F_E\,, \tag{19}$$

to the final form

$$m_1\ddot{s}_1 + k_1s_1 - k_{21}(s_2 - s_1) = F_E\,. \tag{20}$$

Equation (16) is transformed by the same way into the final form

$$m_2\ddot{s}_2 + k_{21}(s_2 - s_1) = 0. \tag{21}$$

For case two with $\beta_1 = 0$, the equations are

$$(m_1 + m_2)\ddot{s}_1 + m_2\ddot{s}_{21}cos\beta_2 + k_1s_1 = F_E\,, \tag{22}$$

$$m_2\ddot{s}_1cos\beta_2 + m_2\ddot{s}_{21} + k_{21}s_{21} = 0. \tag{23}$$

For case three with $\beta_2 = 0$, the following equations can be formed

$$(m_1 + m_2)\ddot{s}_1 + m_2\ddot{s}_{21}cos\beta_1 + k_1s_1 = F_E\,, \tag{24}$$

$$m_2\ddot{s}_1cos\beta_1 + m_2\ddot{s}_{21} + k_{21}s_{21} = 0. \tag{25}$$

Calculation of the displacements

The corresponding equations for case one, i.e. $\beta_1 = \beta_2$ to find the zero displacement s_{10} and the maximum displacement s_{20} of mass m_1 can be formed as

$$s_{10} = \frac{(k_{21} - m_1\omega^2)F_{E0}}{(k_1 - m_1\omega^2)(k_{21} - m_2\omega^2) - k_{21}m_2\omega^2}\,, \tag{26}$$

$$s_{20} = \frac{k_{21}F_{E0}}{(k_1 - m_1\omega^2)(k_{21} - m_2\omega^2) - k_{21}m_2\omega^2}\,. \tag{27}$$

Equation (26) can be adjusted in a way that s_{10} will become zero. For that case, the minimum transmission of forces to the floor is achieved (Nendel, 2008), (Risch, 2008).

Based on this dynamical model, the optimum parameters for an efficient conveying of goods by a minimum transmission of vibration and forces into the floor can be found.

The optimum conveying of goods and the minimum transmission of vibration by the same time is given for the case that mass m_1 during the excitation remains stationary, while the full excitation is passed over to the absorber mass m_2 (Pešík, 2013).

CONCLUSION

The paper deals with the determination of dynamic model parameters of a two-mass linear vibratory conveyor conducted with the calculation of kinematic parameters for the model. The result of the elaboration is a mechanical model, which can be used as base for the modification of the conveyors motion and simultaneous the elimination of vibration forces to the floor of a building. The excitation of the system is connected to an absorber mass which supplies the full effect to the motion of the goods to be conveyed, without the transfer of vibrations to the ground.
General equations for the model are developed and the equations for the calcuation of minimum and maximum displacements of the excited mass are shown.
Based on the results of the paper, parameters for the design of two-mass linear vibratory conveyors can be defined and simultated.

AKNOWLEDGEMENTS

This publication was written at the Technical University of Liberec as part of the project "Innovation of products and equipment in engineering practice" with the support of the Specific University Research Grant, as provided by the Ministry of Education, Youth and Sports of the Czech Republic in the year 2017.

REFERENCES

1. Harris C.M. (2005), *Shock and Vibration Handbook,* Fifth edition, McGraw-Hill, New York.
2. Buja, H.O. (2007): *Praxishandbuch Ramm- und Vibrationstechnik*. Bauwerk Verlag Berlin.
3. *Action Equipment Company*, Inc.. [online].[Cit. 17.06.2017]. Available on WWW: http:// http://actionconveyors.com/products/vibratory-feeders/
4. Dresig H., Holzweißig F. (2008), *Maschinendynamik 8*, Auflage, Springer Verlag, Berlin.
5. Knaebel, M., Jäger, H., Roland Mastel (2009), R., *Technische Schwingungslehre*, 7.Auflage, Vieweg+Teubner Verlag, Wiesbaden.
6. Nendel, K. (2008), *Zweidimensionale Bewegungsformen bei Vibrationsförderern* [online].. Available on WWW: http://www.vibrationsfoerdertechnik.de/ Download/ 2D-Bewegungsformen_WGTL_Tagungsband08.pdf.
7. Risch, T. (2008), *2D-Vibrationsformen bei Vibrationsförderern*. [online].. Available on WWW: http://www.vibrationsfoerdertechnik.de/Download/2D-Bewegungsformen_WGTL_Poster08.pdf
8. Pešík, M. (2013), *Function and Performance Optimization of Vibration Conveyors*. Liberec: Technical University of Liberec.

Corresponding author:
M.A. Dipl.-Ing. Martin Sturm, HS Zittau/Görlitz Faculty of Mechanical Engineering, Germany, e-mail: m.sturm@hszg.de

MODELING AND MEASURING MECHANICAL DAMAGE FOR ADJUSTABLE LUMINAIRE

Josef VOSÁHLO[1], Martina SYROVÁTKOVÁ[2]

[1]The Institute for Nanomaterials, Advanced Technology and Innovation; Technical University of Liberec, Studentská 2, 46117 Liberec, Czech Republic,[1]josef.vosahlo@tul.cz,[2]martina.syrovatkova@tul.cz

Abstract
The article describes one of the tests that were performed on the street light fittings. Simultaneously with the test a mathematical model was developed with the parameters of the test part – angularly positional flange and the modelling result was compared with the results of the experiment. On the basis of the data obtained, a new model of the tested component of the luminaire with optimized toothing was created in order to simplify the production of the aluminium casting of the luminaire.

Key words: *adjustable luminaries, optimization, toothed couplings, flange, FEM model*

INTRODUCTION

Part of the public lighting luminaires being tested is a flange that can be adjusted to allow for an illumination angle from -30 to + 90 °; The flange can be seen in Fig.1. The flange principally comes from the front toothed coupling, also known as the Hirt's coupling (*Pešík, Části strojů, 2015, Budynas, Shigley's mechanical engineering design,2011*). The teeth in the form of an equilateral triangle are located at the periphery of the coupling faces. Working surfaces of the teeth are subjected to the pressure and bending. The coupling is preferably used where the small dimensions are required. Easy to assemble and disassemble. Its disadvantage is very precise production.

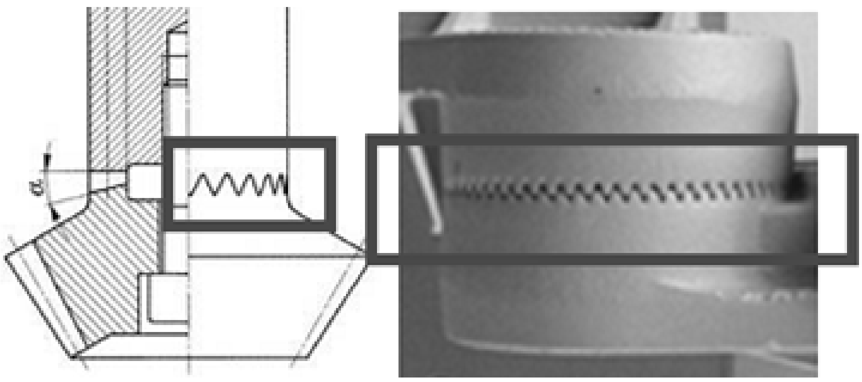

Fig.1 a) Coupling with front teeth, b) Positional flange

MATERIALS AND METHODS

Luminaire with an integrated adjustable flange which is mounted on a mast or boom, was the object of the testing . The luminaire body is adjustable in the range of -30° to + 90° thanks to the toothed joint (flange). The flange is in Fig.2. The luminaire can be divided into two parts; body of luminaire - an aluminum casting and an electrical part that provides primary lighting function. The luminaire including the flange was loaded with force acting in one direction at a distance of 0,33m from the center of the flange in the first phase of the test. The test was performed using a hydraulic motor, and the rod (Fig.3). The force was captured using a force cell GTM with a range of up to 50kN. The aim of the test was to identify the weakest spot on the luminaire, the load value and the condition and mode of damage (Fig.4).

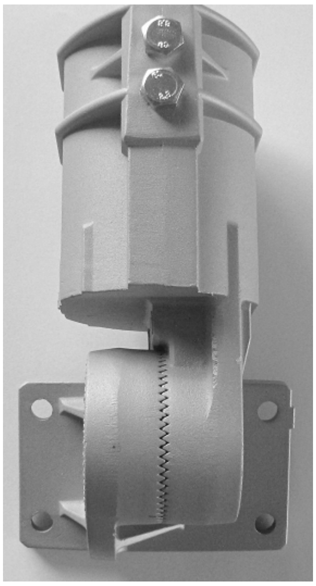

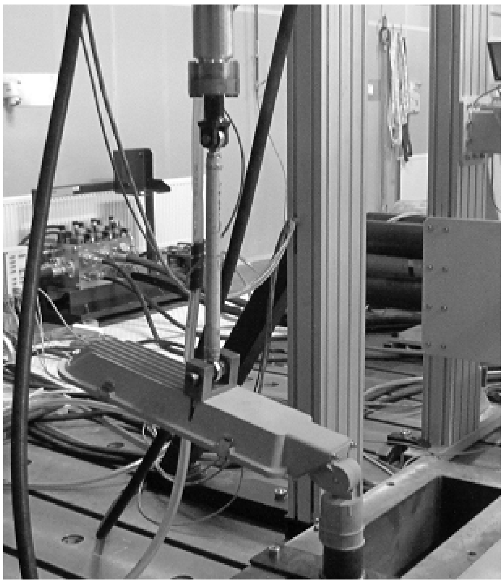

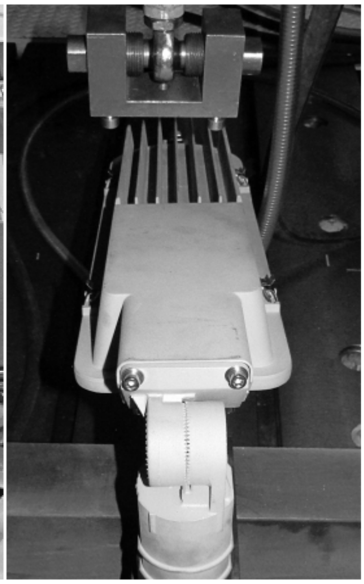

Fig.2 Detail of flange **Fig.3** Loading of the luminaire **Fig.4 F**lange after test

During the experiment, a maximum force F = 1700N was measured; the graph in Fig. 5 indicates the value by a dashed line. With this force, the teeth of the flange were damaged, as can be seen in Fig.6.

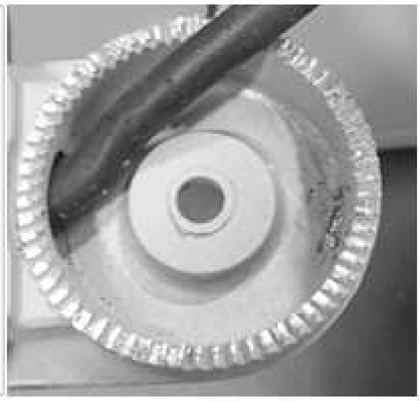

Fig.5 Result of measurement **Fig.6** Teeth damage of flange

Moment of force M [Nm] was calculated according to formula (1) at 561Nm at the point of force action. Force F[N] and radius r [mm] was measured.

$$M_K = F \cdot r \tag{1}$$

Samples were taken from the body of the luminaire for image analysis and a determination of the weight of impurities in the aluminium alloy from which the luminaire is made. A mathematical model was also created and a simulation of the experiment was performed.Based on the measurement of the maximum force that damaged the flange, an attempt was made change the flange tooth geometry. The formula (2), (3) and (4) were used for the calculation.

$$M_k = F \cdot r = F_1 \cdot r \cdot z \tag{2}$$

z – number of teeth, F1 – force acting of one tooth, r – radius of flange

$$\sigma_O \geq \frac{a \cdot F_1}{W_O} \qquad W_o = \frac{b \cdot h^3}{12} \tag{3}$$

a, b, h – parameters of one tooth, σ_o – bending stress

$$\tau_s \geq \frac{F_1}{S} \tag{4}$$

S – working tooth content, τ_s – shear stress

The results of the calculations are summarized in Table 1. The results were used to model the new teeth of the adjustable flange so as to make it easier to produce while maintaining the same load characteristics.

Tab. 1 Parameters of toothed couplings

	z	F1 [N]	σ_o [MPa]	τ_s [MPa]
real flange	62	292,2	52,2	27,2
optimized model	36	500,9	22,4	23,3

NUMERICAL MODEL

Numerical model for the description and study of the mechanical properties of the samples of aluminium is based on analytical models. For homogeneous isotropic materials simple relations exist between elastic constants Young's modulus E, shear modulus G, bulk modulus K, and Poisson's ratio ν that allow calculating them all as long as two are known (5 – 8):

$$E = 2G(1+v) = 3K(1-2v) \tag{5}$$

$$G = \frac{E}{2(1+v)} \tag{6}$$

$$K = \frac{E}{3(1-2r)} \tag{7}$$

$$v = -\frac{d\varepsilon_{trans}}{d\varepsilon_{axial}} = -\frac{d\varepsilon_y}{d\varepsilon_x} = -\frac{d\varepsilon_z}{d\varepsilon_x} \tag{8}$$

Where: $d\varepsilon_{trans}$ is transverse strain (negative for axial tension (stretching), positive for axial compression);
$d\varepsilon_{axial}$ is axial strain (positive for axial tension, negative for axial compression).

Simplified lamp lighting models were created in Solidworks software. One model was designed with original tooth dimensions. The optimized model has twice teeth dimensions. Lamp models were imported into the Ansys program, where the topology of the model was modified. The aluminium alloy parameters were inserted into the model. Friction contacts with a friction coefficient of 0.3 were inserted between the parts of the teeth. Fixed boundary condition was inserted into the bottom of the model, the model was deprived of all movements and rotation. As a second boundary condition, a vertical force of 1700 [N] is applied to the upper part of the model (Fig.7). The output of the simulation was the maximum von-Mieses tension between the teeth.

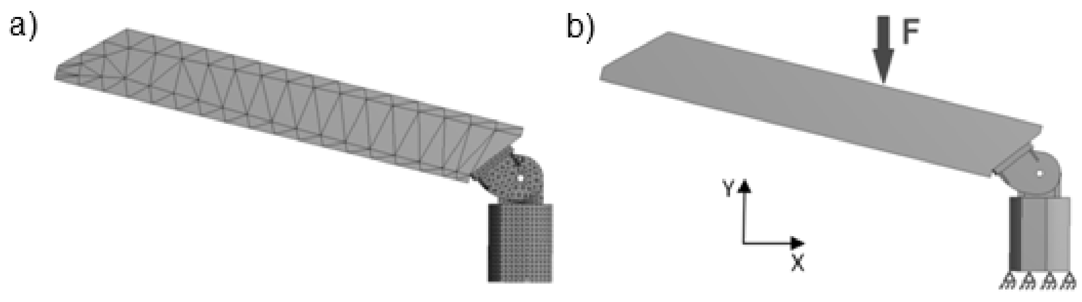

Fig.7 a) Mash of model, b) Inserting boundary conditions into the model.

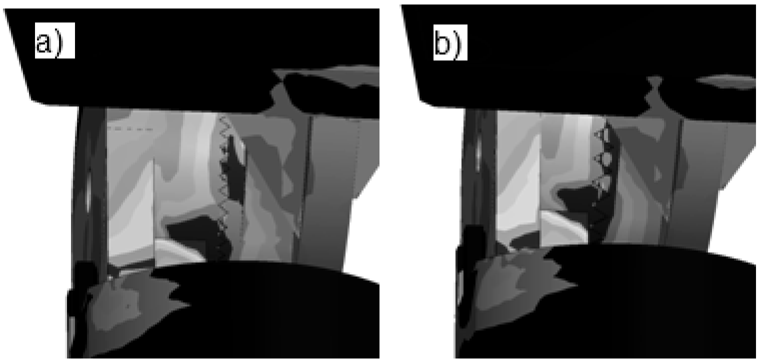

Fig.8 Detail of the von-Mises maximum tension a) for the flange, b) for the optimized model

RESULTS AND DISCUSSION

Calculations according to formulas 1-4 showed that a change in the geometry of the teeth did not significantly change the mechanical parameters of the flange. The safety of the adjustable flange when using a public light bulb under real conditions is not significantly affected.

The value of stress 316.8 [MPa] was measured when simulating real conditions. During optimization, a maximum stress of 286.5 [MPa] was measured. Changing the teeth geometry has affected the mechanical properties of the flange positively.

CONCLUSIONS

The measurement showed a high degree of security of the adjustable flange. Using the calculation and the proposed mathematical simulation, we pointed out the following possibilities: Tooth enlargement will simplify the production of aluminum casting, the positioning will be maintained at 10 ° and the safety of the light is not significantly affected.

ACKNOWLEDGEMENT

The results of this project LO1201 were obtained with co-funding from the Ministry of Education, Youth and Sports as part of targeted support from the "Národní program udržitelnosti I" program.

REFERENCES

1. Budynas, R.G., Nisbett, J.K., (2011). Shigley’s mechanical engineering design, McGraw-Hil, New York, ISBN 978-0-07-352928-8
2. Michna, Š., Lukáč, I., Louda, P., Očenášek, V., Schneider, H., Drápala, J., Kořený, R., Miškufová, A., et al, (2007). Aluminium materials and technologies from A to Z. Adin s.r.o., Prešov, ISBN 978-80-89244-18-8.
3. Pešík, L. (2015). TechnickáUniverzita v Liberci. Částistrojů, pp.39, ISBN 978_80- 7494-184-9
4. Wang, H.R., Wang, W., Gao, J.O.,(2010). Materials Letters 64, pp. 219-221.
5. ČSN EN 60598-1 ed.5, (2009). Svítidla – Část 1: Všeobecnépožadavky a zkoušky; Úřad pro technickounormalizaci, metrologii a státnízkušebnictví.
6. Katalogový list svítidla, dostupnýna: http://www.modus.cz/productoo/getfile.php?fileID=Mjk0MA%3D%3D&forceDownload=false

Corresponding author:

Ing.Martina Syrovátková, Ing. Josef Vosáhlo. he Institute for Nanomaterials, Advanced Technology and Innovation; Technical University of Liberec, Studentská 2, 46117 Liberec, Czech Republic; phone +420485353872, e-mail: martina.syrovatkova@tul.cz, josef.vosahlo@tul.cz .

DEMAND FOR ELECTRICITY FOR HYDRAULIC POWER SYSTEMS AT FISHING CUTTERS

Marcin SZCZEPANEK[1]

[1] *Maritime University of Szczecin, Faculty of Mechanical Engineering, Institute of Ship Power Plant Operation, 70-500 Szczecin Poland*

Abstract
The paper is focused on the presentation of operational research regarding the demand for electricity for hydraulic power systems based on an example of two typical solutions applied at fishing cutters belonging to the Polish fishing fleet. The selection of the particular cutters was determined by taking into consideration the economic and statistical aspects. This type of cutters is the most commonly used in the Polish fishing fleet. On the grounds of gathered operational data, two hydraulic power systems, installed on two real vessels, have been compared with each other. The obtained results prove that it is possible to reduce and limit the demand for electricity necessary to supply hydraulic power systems.

Key words: *hydraulic power systems, fuel consumption, operational state*

INTRODUCTION
The automation supporting crews of small fishing cutters and fishing boats used to be based on the solutions including the use of mechanical energy provided by the main diesel engine. Main reduction gear installed in the propulsion system not only transferred the power generated by the main diesel engine onto the propeller but also provided the power to auxiliary devices by additional power take-off shafts. Additional chain drive or belt drive drove rope winches, net winches and trawl winches. The complex structure of mechanical gears, low efficiency of energy transfer and low flexibility to select work parameters, problems with maintenance and poor safety of service were the main causes for changing the solution. Nowadays, on modern fishing cutters hydraulic power systems are used, rarely electric power systems (*Rajewski&Behrendt,2013*).

The older cutters, depending on the investment made on the modernization, were equipped with simple hydraulic power systems. They were used for driving the already existing net winches. The devices at cutters were also complemented with trawl winches and rope winches. The newer cutters, as well as the older ones, are subjected to thorough modernization and are equipped with hydraulic power systems of complex configurations. The hydraulic system at fishing cutters may be used to drive (*Behrendt,2014):*
- steering gear,
- trawl winches,
- net winches,
- rope winches,
- anchor winches,
- pumps for fish selection from the net,
- the remaining equipment with hydraulic power system e.g. deck cranes, power generators.

MATERIALS AND METHODS

Hydraulic pumps used at fishing cutters are driven directly by the main diesel engine or main reduction gear. It is presented in Figure 1 and Figure 2.

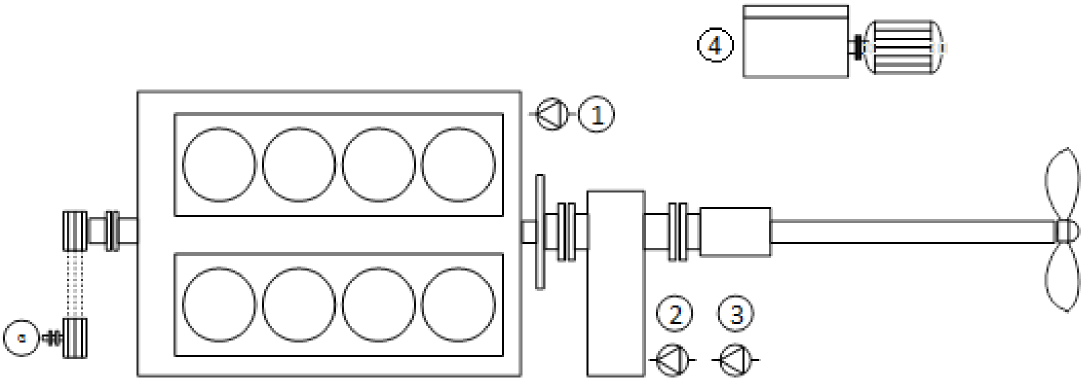

Fig 1. Propulsion system with hydraulic pumps driven by main reduction gear (*Borkowski&Myśków, 2015)*.
1.hydraulic pump for deck equipment and devices; 2. hydraulic pump for deck equipment and devices; 3. steering gear hydraulic pump, G – shaft power generator 4. power generator unit.

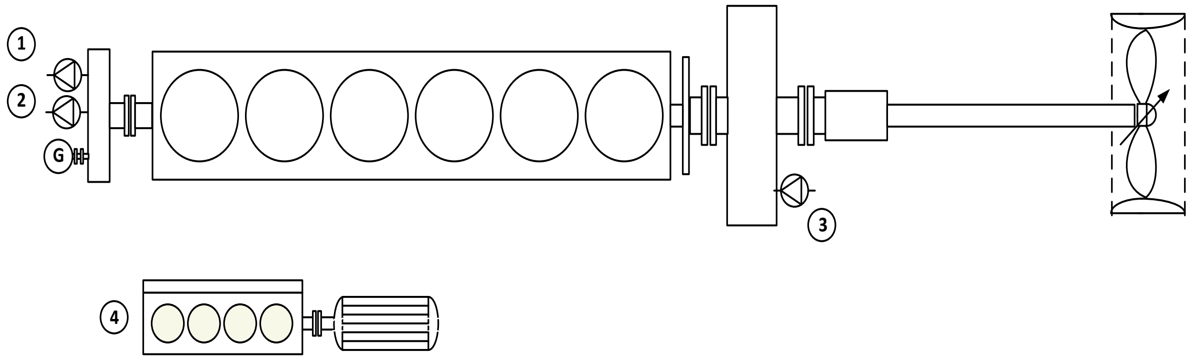

Fig 2. Propulsion system with hydraulic pumps driven by main diesel engine (*Borkowski&Myśków, 2015)*.
1. hydraulic pump for deck equipment and devices; 2. hydraulic pump for deck equipment and devices; 3. gear lubrication pump; G - shaft power generator; 4. power generator unit.

At fishing cutters, the hydraulic pumps are driven by the main diesel engine (Fig. 1) using mechanical or belt drive. In the case of the drive from the main reduction gear (Fig. 2) it is necessary to use a drive with an additional stage and power take-off shafts. An advantage of this solution is a high operational certainty. However, a disadvantage is that the pump is continuously working when the engine is activated. The only possible method to unload the hydraulic power system when it is not used to drive power devices (trawl winches, net winches, and auxiliary devices) is to change the working liquid circulation into the tank-tank flow, bypassing the remaining system part. However, even when the solution is applied, it is necessary to provide mechanical energy to drive the hydraulic pump. As the research showed, the demand for power is within 4% and even with unheated oil in the system, it equals up to 10% of the power consumed by the pumps at full working load *(Szczepanek&Kamiński, 2013)*.

RESULTS AND DISCUSSION

When using hydraulic driven devices and equipment, the energy is converted into mechanical work performed by a hydraulic engine. The research has been carried out at two fishing cutters of the same type, equipped with winches with various hydraulic drives, in three operational states of hydraulic power systems which are specific for catching fish process:

1. throwing trawl net – the work of net winch at throwing the trawl net, and then of two trawl winches (around 40 min.)
2. retrieving trawl– the work of two trawl winches (around 30 min.)
3. retrieving trawl net - the work of net winch (30 min., depending on the weight of fish caught).

The measurement and calculation results are presented in Table 1.

Table 1. Basic measured and calculated load values for winches with hydraulic drive during catching fish process at cutters subject to research

	Measured and calculated parameters	Unit	Catching fish process stages					
			Vessel 1			Vessel 2		
			Retrieving trawl	Retrieving trawl net	Throwing trawl net and a trawl	Retrieving trawl	Retrieving trawl net	Throw-ing trawl net and trawl
1	Input power of hydraulic pump PB	kW	26.0	21.0	16.0	29.0	28.0	18.0
2	Input power of hydraulic pump LB	kW	26.0	21.0	16.0	29.0	26,0	18.0
3	Trawl winch power PB	kW	11.6		7.2	13.0		8.1
4	Trawl winch power LB	kW	11.6		7.2	13.0		8.1
5	Net winch power PB	kW		9.4	7.2		12.5	8.1
6	Net winch power LB	kW		9.4	7.2			
7	Torque of trawl winch PB	kNm	6.2		3.8	6.9		4.3
8	Torque of trawl winch LB	kNm	6.2		3.8	6.9		4.3
9	Torque of net winch PB	kNm		9.8	7.5		13.0	8.4
10	Torque of net winch LB	kNm		9.8	7.5			
11	Pull force of trawl winch PB	kN	30.9		19.0	34.4		21.4
12	Pull force of trawl winch LB	kN	30.9		19.0	34.4		21.4
13	Pull force of net winch PB	kN		16.3	12.4		21.7	14.0
14	Fuel consumption	kg/h	6.5	5.3	4.0	7.3	3.5	4,5

The data included in Table 1 allowed for drawing charts presenting the demand for power and fuel consumption required to provide power by the main diesel engine to the hydraulic pumps' drive (Fig. 3-6)

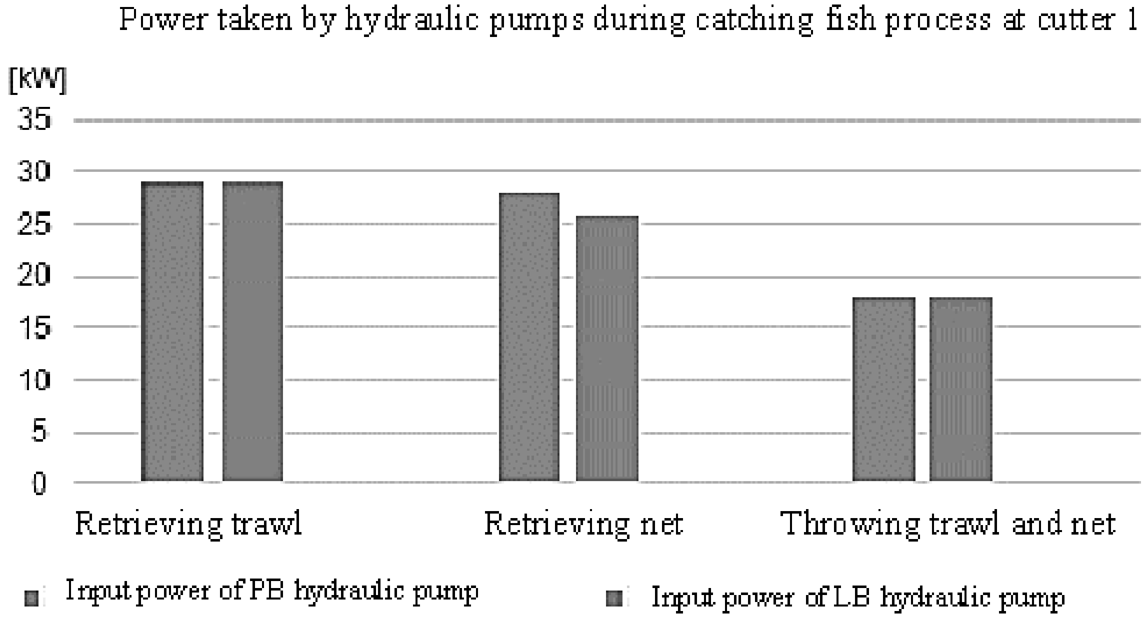

Fig 3. Power taken by PB hydraulic pumps at cutter 1

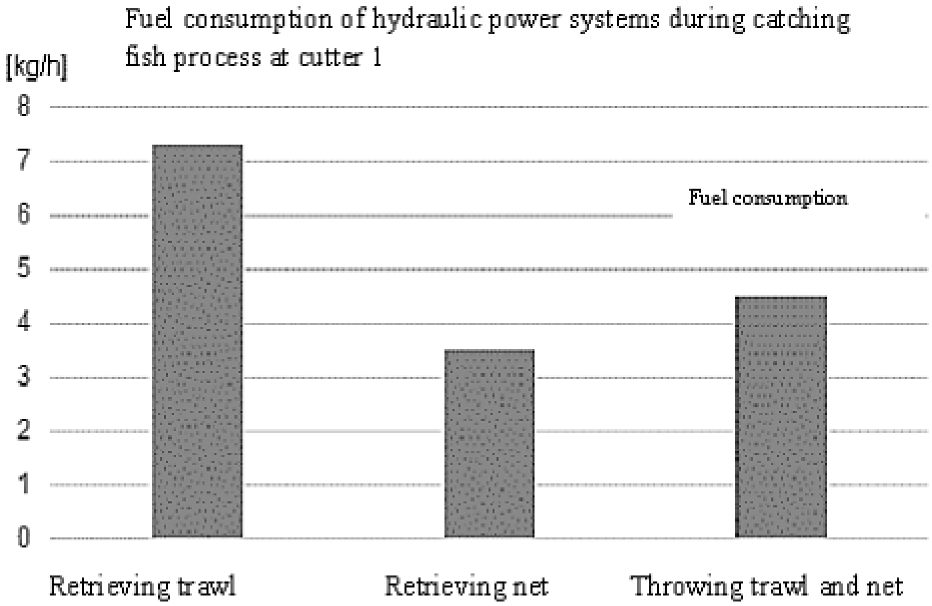

Fig 4. Fuel consumption of hydraulic power systems during catching fish process at cutter 1

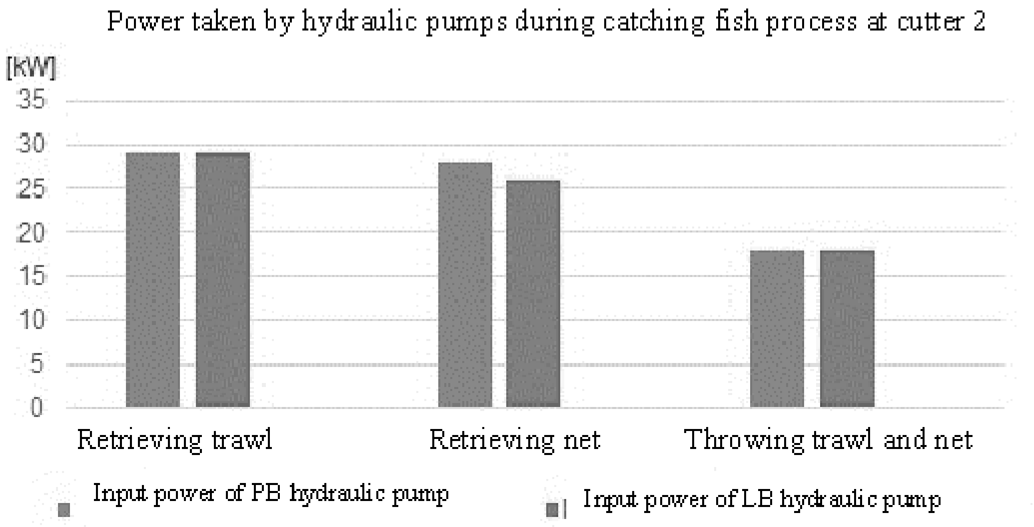

Fig 5. Power taken by hydraulic pumps at cutter 2

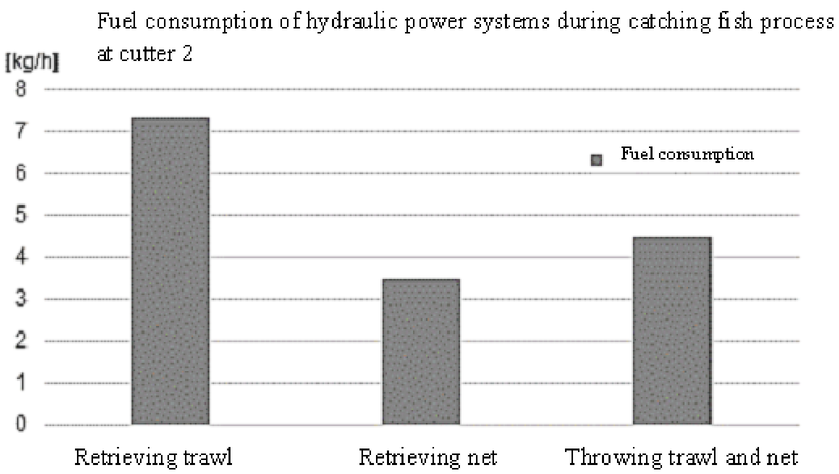

Fig 6. Fuel consumption of hydraulic power systems during catching fish process at cutter 2

The research results presented in the paper refer to the hydraulic systems. They are the outcome of the energy efficiency audits carried out at the vessels belonging to the Polish fishing fleet. The research has been performed for the very first time and therefore the results should be useful in order to reduce the energy consumption at the vessels. However, comparable methods aimed at the limitation of fuel consumption have been presented by Rajewski, P., Behrendt, C., and Szczepanek, M., Kamiński, W. and Szczepanek, M., Skarbek-Żabkin, A. in terms of the engine as a system, Erwin M. Schau.,Harald Ellingsen, Anders Endal, Sevin Aa. Aanondsen in reference to the Norway fleet, Mikkel Thrane in reference to the Dutch fleet and Muir James F in global overview the utilization of fuel energy by the global fisheries industry .
Based on the data included in the paper, it is justified to state the operational condition of a vessel may significantly affect the power consumption. Raising the crew members technical awareness may impact on the reduction of same.

CONCLUSIONS

Summing up, the hydraulic power systems used at fishing cutters are significant elements of the cutter equipment. The analysis of the obtained results proves that the demand for electricity at the selected cutters vary insignificantly, regardless of the catching fish process. However, given that the main propulsion systems, auxiliary unit and the drives of hydraulic power systems at the cutters were comparable, the differences in fuel consumption should be noted. It should be assumed that this is a result of various technical conditions of the cutters, knowledge, financial situation of shipowners and the fact that these systems are in a different state of wear. Various demand for electricity depending on the operational state (maneuvers, trawling) may also be the effect of the above. Turning the systems on leads to extreme changes of the load of ship electrical power system, and in the case of power generators driven by the main diesel engine, it may result in changes of load. The observations made on real objects showed that the power of devices used in the hydraulic power systems at the cutters is larger than needed to perform the cutter tasks and they do not operate at minimum load at any operational condition, which affects in an economically unjustified increase of operational cost by the increased fuel consumption. Properly selected and adjusted devices and equipment for hydraulic power system might result in the reduced demand for electricity.

ACKNOWLEDGMENT

This research outcome has been achieved under the research project no. 2/S/IESO/2014 financed from a subsidy of the Polish Ministry of Science and Higher Educations for statutory activities of Maritime University of Szczecin.

REFERENCES

1. Behrendt, C. (2014). Energy saving technologies for fishing cutters. *39 Scientific Journals Maritime University of Szczecin*, No. 39 (111), 2014, pp.11-15.
2. Borkowski, T., Myśków, J. (2015). Przeprowadzenie badań zużycia i rejestracji, jakości energii jednostek typu B-25s, w eksploatacji. Raport z realizacji projektu Przeprowadzenie audytów energetycznych dla grup statków rybackich celem przygotowania systemu zarządzania eksploatacją w sposób przyjazny środowisku realizowanego w Akademii Morskiej w Szczecinie finansowanego z Programu Operacyjnego RYBY 2007-2013 działanie 3.1
3. Muir James F. (2015). Fuel and energy use in the fisheries sector, Approaches, inventories and strategic implications. *FAO Fisheries and Aquaculture Circular No.C1080 FIRO/C1080* (En) 2015.
4. Schau Erwin M., Ellingsen H, Endal A, Aanondsen Sevin Aa. (2009). Energy consumption in the Norwegian fisheries. *Journal of Cleaner Production,Volume 17, Issue 3, February 2009*, pp. 325-334.
5. Szczepanek, M., Kamiński, W. (2013). Test methodology assumptions for energy test of fishing fleet cutters. *Materials Conference DEMaT'13, Rostock, Germany 2013*, pp. 263-270,
6. Szczepanek, M., Skarbek-Żabkin, A. (2015). Analysis of Energy Loss in the Propulsion System in Terms of Identification of Energy Saving Potential. *Transcom Proceeedings 2015*, pp.153-156.
7. Rajewski, P., Behrendt, C. (2013). Possibilities of increasing energy efficiency of small fishing cutters. *Materials Conference DEMaT'13, Rostock, Germany 2013*, pp.297-304.
8. Thrane M,. (2004). Environmental impacts from Danish fish products. *Publisher's PDF, Materials Aalborg University*, Denmark 2004.

Corresponding author:
Marcin Szczepanek, Ph.D. Ing, Maritime University of Szczecin, Faculty of Mechanical Engineering, Institute of Ship Power Plant Operation, 70-500 Szczecin Poland, phone: +48 91 480 9376, e-mail: m.szczepanek@am.szczecin.pl

THE PYROLYSIS OIL AS AN ALTERNATIVE MARINE FUEL

Magdalena SZMUKAŁA[1], Robert JASIEWICZ[1]

[1]*Martime University of Szczecin, Poland*

Abstract

The paper analyses physicochemical properties of oil obtained as a result of waste tyre pyrolysis and assesses their usefulness as alternative marine fuel for diesel engines. The results of the analysis of oil parameters and marine distillate fuel were compared with ISO 8217 requirements. The analysed fuels were, moreover, subjected to the examination of number, size, and shape of solid particles which was conducted in the Fuel Research, Hydraulic Fluids and Environmental Protection Centre of the Maritime University of Szczecin. Based on the tests it has been found out that the oil obtained by pyrolysis of waste vehicle tyres has not met some of the requirements in the standards for marine distillate fuel and must not be used as independent fuel. However, the pyrolysis oil may be applied as an additive to conventional fuels or in fuels mixture for marine vessels propelling.

Key words: *alternative marine fuel, pyrolysis oil, marine distillate fuel, morphology, physical and chemical properties.*

INTRODUCTION

With dwindling oil resources and their restricted accessibility as well as a rising environmental awareness, the need for alternative fuel research has increased. The MARPOL convention has imposed on ship owners a duty of sulphur reduction (since 2015) from 1% to 0,1% in fuels used within the Emission Control Area (ECA).

One of the ways to do that would be to use alternative fuels for marine vessels propelling. Such fuels may be obtained from a variety of sources and by means of technology which is under constant development. The alternative fuels can be used independently or as components in conventional fuels mixtures. The alternative fuels currently in use include methanol, ethanol, biodiesel (FAME), Dimethyl ether (DME), also known as methoxymethane as liquid fuels or LNG, LPG and hydrogen as gas fuels (Deniz, Zincir, 2016). Attempts have also been made to apply recycled fuels for diesel engines. Recycled fuels comprise oils from polyethylene and polypropylene waste (Mani at el. 2011) and oils recycled from used lubricant oils (Gabina at el.2016)

As another alternative fuel a liquid fraction obtained from pyrolysis of waste vehicle tyres is also used. The oil resulting from a high temperature pyrolysis (300-900 ^{0}C) is a mixture of over 100 different organic compounds (aliphatic, aromatic compounds and their derivatives) (Williams, 2013).

The physicochemical properties of the oil obtained from waste tyre recycling show some similarity to the diesel oil properties , which makes it possible to use it as fuel (Quek, Balasubramanian, 2013). The article aims at examining the properties of the oil obtained from the waste vehicle tyres pyrolysis as well as marine distillate fuel and comparing the with the standards and requirements of ISO 8217.

MATERIALS AND METHODS

The testing material were samples of marine distillate fuel and waste tyres pyrolysis oil. The samples were analysed in the context of viscosity, density, sulphur content, flash point, acid number, carbon residue and lubricity. The presence of vanadium, aluminium and silicon was tested by means of a rotating disc electrode.

Moreover, the oil samples were filtered through membrane filterand morphologically singled out. With the aid of Morphologi G3 (Malvern) shape and size particle analyser, the number of solid particles was stated and they were classified according to their diameter.

All the research was carried out in the Fuel Research, Hydraulic Fluids and Environmental Protection Centre of the Maritime University of Szczecin.

RESULTS AND DISCUSSION

Table 1 shows the results of the physicochemical properties of the analysed fuels.

Tab. 1 Main properties of Pyrolysis Oil, Marine Distillate Fuel, and requirements according to the standard ISO 8217

Property	Unit	Pyrolysis Oil	MDF	Limits by ISO 8217
Viscosity at. 40°C	mm^2/s	4,17	3,69	2,00 – 6,00
Density at. 15°C	kg/m^3	906	882	max. 890
Cetane index	–	40,5	45,8	min. 40
Sulphur	mass %	1,09	0,1	max.1,5
Flash point	°C	50	90	min. 60
Acid number	mg KOH/g	0,3	0,1	max. 0,5
Carbon residue (10%V/V distillation bottoms)	mass %	0,74	0,11	max. 0,3
Vanadium	mg/kg	0	0	–
Aluminum i Silicon	mg/kg	26	2,5	–
Lubricity, corrected wear trace diameter wsd 1,4 at 60 ° C	µm	458	319	max. 520

Based on the examination it was shown that the viscosity of pyrolysis oil (4,17 mm^2/s) is bigger than of the distillate fuel (3,69mm^2/s). But in both cases the results are still within the norms of ISO 8217. The density for pyrolysis oil was 906 kg/m^3 and went above the allowed norm for this parameter. The obtained results of the cetane index referring to the flash point quality of the compressed fuels mixture in both tested fuels were in accordance with the required norms.

The sulphur content in the marine distilled fuel was 0,1% and met the norms of both ISO and ECA. However, while the sulphur content in the pyrolysis oil was 1,09 % and was still within the ISO norm, it definitely did not meet the MARPOL directive. What imposes limitations on pyrolysis oil as fuel for marine vessels is – first - the flash point temperature – the parameter essential for fire safety during the fuel application, which is highly combustible. The pyrolysis oil sample was ignited at 50°C and did not fulfill the requirements, while the distilled fuel at 90°C, which met the norms.

The second parameter restricting the use of pyrolysis oil as independent fuel is the high carbon residue (0,74%) over twice as much as the allowed amount. Such a high value is due to the chemical composition of pyrolysis oil which contains unsaturated hydrocarbons, organic acids and sulphur compounds (Williams, 2013) facilitating the fuel to create residue in the combustion chamber, on valves, piston rings, and injection elements.

The acid number of pyrolysis oil was 0,3mg KOH/g, while the distillate fuel 0,1 mg KOH/g. Both values were below the allowed level. The content of vanadium, aluminium, and silicon was defined by means of a rotating disc electrode spectrometer. In both samples there was no trace of vanadium responsible for high temperature corrosion (Chaala, Roy, 1996). The acceptable amount of aluminium and silicon equals 25ppm. If it exceeds the norm, both metals may contribute to an excessive wear of the fuel feed system. In the case of pyrolysis oil the altogether content of the metals was just slightly above the norm – 26ppm.

Next, the lubricity of the sampled fuels was examined, i.e. the wear scar diameter corrected to the value of the normal water vapour pressure conditions of 1.4 kPa. The results showed that both samples met the required norms. Yet, the wear scar diameter in pyrolysis oil was significantly greater than in the distilled fuel.

In order to determine differences in the structure of petroleum product samples, a morphological analysis was conducted to identify solid contaminants, using a microscopic image analysis by a G3 particle MALVERN size and shape analyzer. Example images of contaminant particles contained in the samples of Pyrolysis Oil and Marine Distillate Fuel (MDF) are depicted in Fig. 1.

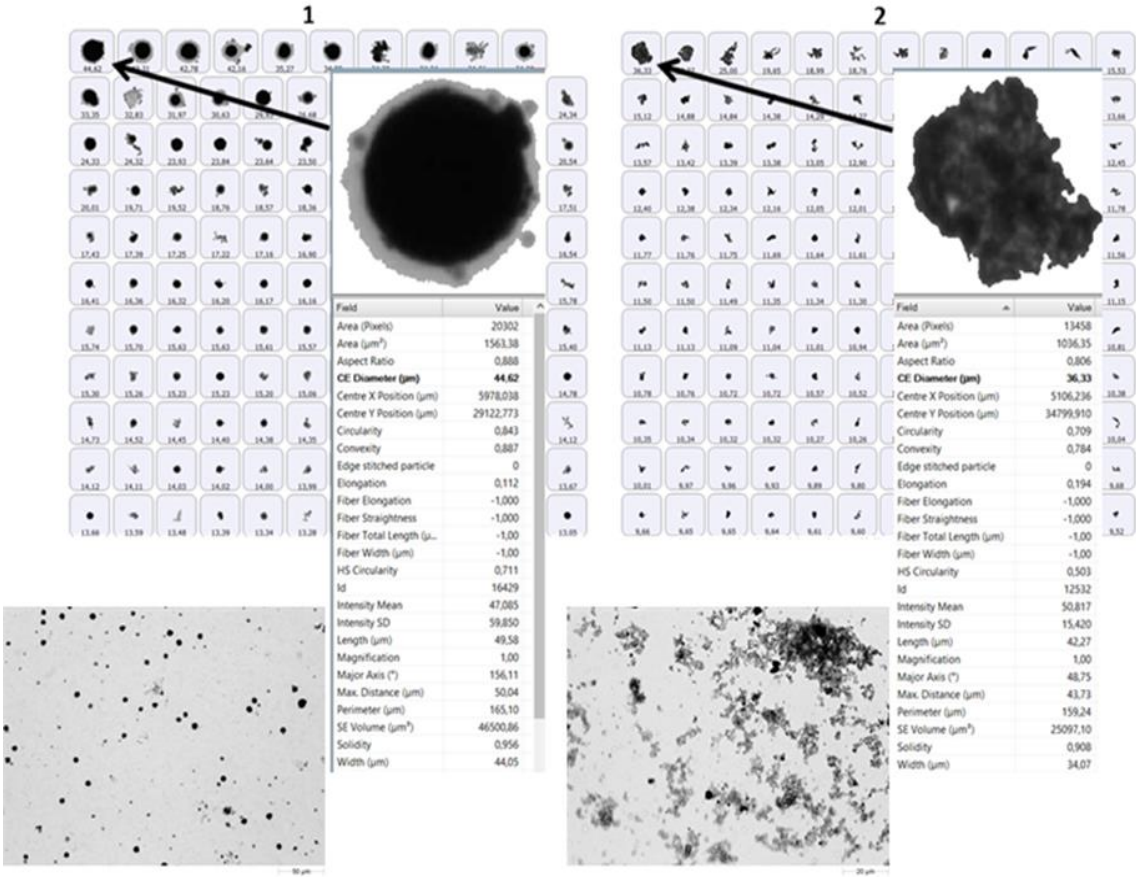

Fig.1 Examples of Particle window and detailed information on single particles
1- Pyrolysis Oil, 2 - Marine Distillate Fuel

Having analyzed the morphology of the samples, it has been found out that the contaminants in pyrolysis oil and marine distilled fuel differ in size and shape. One of the most important morphological parameters of the shape is the circularity. Circularity is the ratio of the circumference of a circle equal to the object's projected area to the perimeter of the object. Figure 2 displays the HS (HS for High Sensitivity) Circularity distribution of particles for Pyrolysis Oil and Marine Distillate Fuel. HS Circularity has a squared term in the numerator and denominator to sensitise the parameter to very subtle variations in the area and perimeter relationship (Malvern Instruments Ltd., 2008).

Circularity has values in the range 0 - 1. A perfect circle has a circularity of 1, irregular or spiked particles has a circularity value closer to 0. For Pyrolysis Oil HS Circularity maximum of particles is 1,00, minimum equals 0,092, HS Circularity D [n, 0.5] is 0,952, D [n, 0.1] is 0,763, D [n, 0.9] is 0,989 and HS Circularity Mean: 0,9114. D [n, 0.5], D [n, 0.1] and D [n, 0.9] are standard percentile readings from the analysis when :D [n, 0.5] is the size at which 50% of the sample is smaller and 50% is larger. This value is also known as the Mass Median Diameter (MMD) or the median of the volume distribution. D[n, 0.1] is the size of particle below which 10% of the sample lies. D [n, 0.9] is the size of particle below which 90% of the sample lies (Malvern Instruments Ltd., 2008).

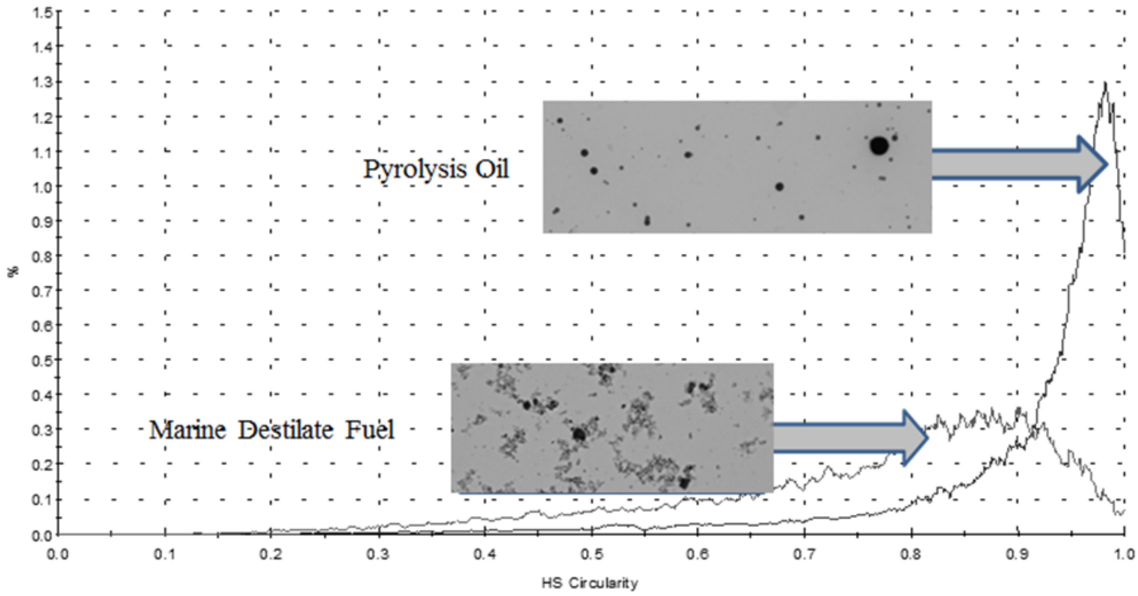

Fig.2. HS Circularity number distribution for Pyrolysis Oil and Marine Distillate Fuel

For Marine Distillate Fuel HS Circularity maximum of particles is also 1,00 minimum equals 0,071, HS Circularity but D [n, 0.5] is 0,807, D [n, 0.1] is 0,503, D [n, 0.9] is 0,935 and HS Circularity Mean equals 0,764.

The particles in pyrolysis oil are characterized by a greater circularity than in MDF, thus the MDF contaminants have a higher tendency to accumulate asphaltene-resinous conglomerates than pyrolysis oil.

In each sample the particles were counted and subsequently grouped by the following particle diameter size: 1 – 5 µm, 5-10 µm, 10-15 µm, 15-25 µm, 25-50 µm, and above 50 µm.

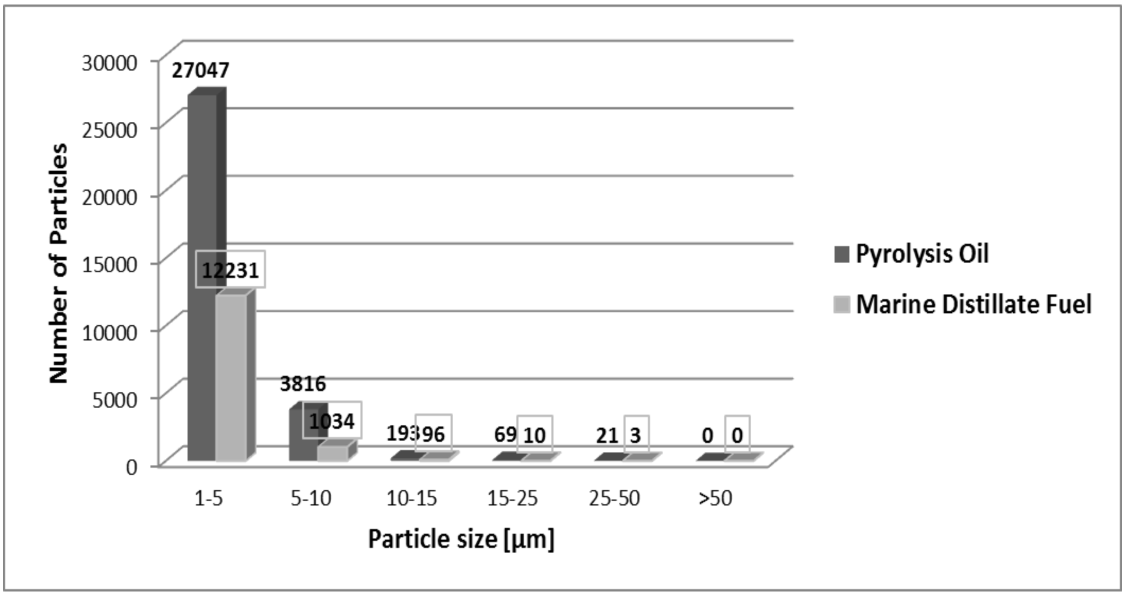

Fig.3. Number of particles in the tested liquids

The morphological analysis of the tested samples (Fig. 3) shows that within the size range of 1- 50 μm Pyrolysis Oil contains the biggest number of particles insoluble in Pentane. Above 50 μm for all samples there were no particles visible for the selected sample preparation method for analysis.

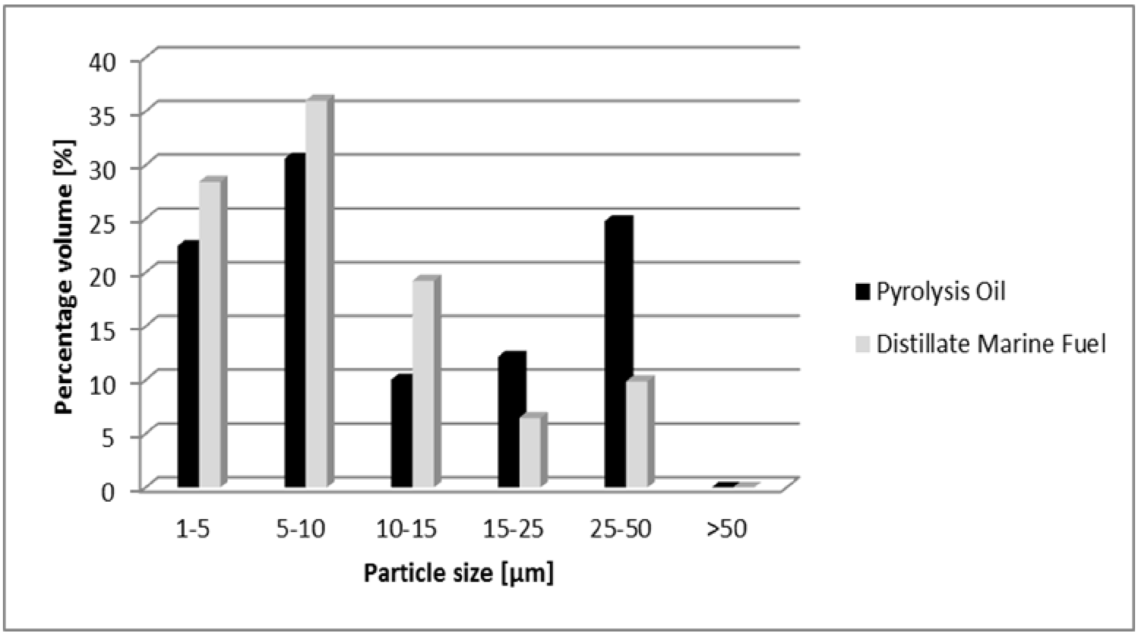

Fig.4. Percentage volume of particle groups distinguished in the tested liquids

Figure 4 shows the percentage volume of particles' groups distinguished in the tested liquids. The carried out analysis proved that for Marine Distillate Fuel the biggest percentage volume is seen in 1-10 μm, 5-10 μm, 10 – 15 μm and equals 28,43%, 35,98% and 19,24% respectively. Pyrolysis Oil can be characterized by a bigger percentage volume within size range of 15 - 25 μm (circa 12,16%) and 25- 50 μm equals 24,75% (above 50 μm for all samples there were no particles visible for the selected sample preparation method for analysis).

Having analysed the samples, it has been proved that Pyrolysis Oil contains the biggest number of insoluble particles, while the biggest percentage volume of particles is seen in Marine Distillate Fuel within the size range of 15 - 25 μm and 25- 50 μm.

The particle contamination analysis proved that in order to use Pyrolysis Oil as engine fuel, the gravitational sedimentation, filtering process and/or the centrifugal separation process are highly inevitable.

CONCLUSIONS

1. The oil obtained by high temperature waste tyres pyrolysis does not fulfill all standard requirements for marine distilled fuel ISO 8217.
2. The tested pyrolysis oil had higher values of density, sulphur content, and carbon residue.
3. The disqualifying factor as an independent fuel was the too low flash point.
4. The morphology of the tested fractions requires the processes of their gravitational sedimentation, filtration and separation due to heavy contamination (big number of particles present) within the wide diameter range.
5. Due to the positive results of the remaining physicochemical indicators meeting the norms of Marine Distillate Fuel MDF, pyrolysis oil may be used as one of the components of fuel mixtures for marine diesel engines

ACKNOWLEDGMENT

This research outcome has been achieved under the research project No 2/S/IESO/ 2014 financed from a subsidy of the Polish Ministry of Science and Higher Education for statutory activities of the Maritime University of Szczecin

REFERENCES

1. Chaala A., Roy C. (1996). Production of coke frome scrap tire vacuum pyrolysis oil. *Fuel Processing Technology, 46(3),* 227-239.
2. Deniz C., Zincir B. (2016). Environmental and ceonomical assessment of alternative marine fuels. *Journal of Cleaaner Production, 113,* 438-449.
3. Gabina G., Martin L., Basurko O., Clemente M., Aldekoa S., Urindo Z. (2016). Waste oil-based alternative fuels for marine diesel engines. *Fuel Processing Technology, 153,* 28-36.
4. ISO 8217:2012 (E) Petroleum Products – Fuels (class F) Specification of marine fuels.
5. Mani M., Nagarajan G., Sampath S. (2011). Characterisation and effect of using waste plastic oil and diesel fuel blends in compression ignition engine. *Energy, 36*, 212-219.
6. Morphologi G3 User Manual (2008).Malvern Instruments Ltd.
7. Quek A., Balasubramanian R. (2013). Liquefaction of waste tires by pyrolysis for oil and chemicals – A review. *Journal of Analytical and Applied Pyrolysis, 101*, 1-16.
8. Williams P.T. (2013). Pyrolysis of waste tyres: A review. *Waste Management, 33(8),* 1714-1728.

Corresponding author: Magdalena SZMUKAŁA, Martime University of Szczecin, Poland, m.szmukala@am.szczecin.pl

METHOD OF DETERMINING OPTIMAL CONTROL STRATEGY

Mirosław SZUBARTOWSKI[1], Klaudiusz MIGAWA[2], Andrzej NEUBAUER[3], Leszek KNOPIK[4]

[1]Management Business and Service, Bydgoszcz, Poland
[2]Department of Mechanical Engineering, UTP University of Science and Technology, Bydgoszcz, Poland
[3]Department of Economic and Management, Nicolaus Copernicus University, Toruń, Poland
[4]Department of Management, UTP University of Science and Technology, Bydgoszcz, Poland

Abstract
The paper presents a description of the method of determining the optimal (quasi-optimal) strategy of technical objects operation and maintenance process with the implementation of decisive semi-Markov processes as well as multicriteria genetic algorithm in which the result constitutes the set of optimal solutions according to Pareto (the so-called Pareto frontier). The method discussed in the paper allows for determining the quasi-optimal strategy of technical objects control process from the point of view of the values of selected criteria functions: technical objects availability as well as unit income generated during the carrying out of the analyzed operation and maintenance process. This is connected with selection from possible decisive variants of such strategy of process operation control for which the functions constituting evaluation criteria reach values from the set of Pareto optimal solutions.

Key words: *multicriteria optimization; genetic algorithm; decision processes; Pareto front.*

INTRODUCTION

The paper discusses the issues connected with the process of operation of technical objects. In complex technical objects operation systems, the selection of rational control decisions from possible decisive variants is should be carried out with the implementation of appropriate methods and mathematical tools rather than "intuitively" based solely on the knowledge and experience of the deciders of the systems. Introducing appropriate mathematical methods of operation process control facilitates selecting rational control decisions in a way which provides correct and effective carrying out of tasks assigned to the system. Depending on the kind of analyzed research problems, appropriate methods of delineating optimal and quasi-optimal solutions were implemented (e.g.: *Grabski, 2010; Knopik, Migawa & Wdzięczny, 2016; Kulkarni, 1995; Lee, 2000; Zastempowski & Bochat, 2014*). Genetic algorithm belongs to the group of nondeterministic methods of defining optimal solution in which consecutive solutions are random modifications of previous ones and significantly depend on them. The basic assumption while using genetic algorithm to search for optimal solution is the fact originating in the theory of evolution claiming that the smallest probability of modification is connected with solutions of the highest degree of adaptability defined as the value of adaptability function (function of the goal of optimizing task). The single criterion concept of genetic algorithm was developed by Holland in the 1960s, whereas the first practical methods were created at the turn of the 1960s and 1970s (*Holland, 1975*). The first genetic algorithm used in solving the questions of multiple criteria optimization of presented by Schaffer in 1985 and was called Vector Evaluated Genetic Algorithm (VEGA) (*Schaffer, 1985*). The following years saw an intense development of nondeterministic methods created on the basis of evolutionary algorithms. Using these methods made it possible to arrive at solutions in complicated issues of multi criteria optimization in a simple and fast way. The most important methods include (*Konak, Coit & Smith, 2006*): Multi-objective Genetic Algorithm (MOGA), Niched Pareto Genetic Algorithm (NPGA), Weight-Based Genetic Algorithm (WBGA), Random Weighted Genetic Algorithm (RWGA), Nondominated Sorting Genetic Algorithm (NSGA), Strength Pareto Evolutionary Algorithm (SPEA), Pareto-Archived Evolution Strategy (PAES), Pareto Envelope-based Selection Algorithm (PESA), Region-based Selection in Evolutionary Multiobjective Optimization (PESA-II), Fast Nondominated Sorting Genetic Algorithm (NSGA-II), Multi-objective Evolutionary Algorithm (MEA), Rank-Density Based Genetic Algorithm (RDGA) and Dynamic Multi-objective Evolutionary Algorithm (DMOEA). The objective of the paper is development of a method of determining technical objects operation process control strategy with the implementation of stochastic decisive models as well as nondeterministic methods of multi criteria optimization. The paper discusses the example of determining optimal control strategy in the case when criteria functions constitute the availability of technical objects (means of transport) as well as unit income (cost) generated while carrying out the analyzed operation process.

MATERIALS AND METHODS

Due to the random nature of the factors influencing the running of the technical objects (transport means) operation process introduced in a complex system, most often in the process mathematical modelling of the operation process, stochastic processes are used (Markov and semi-Markov processes as well as decision-making Markov and semi-Markov processes).

Assuming that the analyzed model of technical object operation process is a random process $\{X(t)\colon t \geq 0\}$ of finite number of process states $i \in S = \{1,2,\ldots,m\}$, then

$$D_i = \left\{d_i^{(1)}(t_n), d_i^{(2)}(t_n), \ldots, d_i^{(k)}(t_n)\right\} \tag{1}$$

means a set of all possible control decisions which can be implemented in i-state of the process at the moment of t_n, where $d_i^{(k)}(t_n)$ means k-control decision made in i-state of the process, at the moment of t_n.

In the case of optimization task involving the choice of optimal strategy of technical object operation process control from among the acceptable strategies, then as the strategy we understand the δ sequence, where the words are the vectors, comprising of the decision $d_i^{(k)}(t_n)$ made in the following moments of the t_n changes of the state of the process $X(t)$

$$\delta = \left\{\left[d_1^{(k)}(t_n), d_2^{(k)}(t_n), \ldots, d_m^{(k)}(t_n)\right]\colon \ n = 0,1,2,\ldots\right\} \tag{2}$$

In order to determine the optimal control strategy (decision sequence) it is possible to implement decision-making semi-Markov processes. The decisive semi-Markov process is a stochastic process $\{X(t)\colon t \geq 0\}$, the implementation of which depends on the decisions made at the beginning of the process t_0 and at the moments of changing the process t_1, t_2, …, t_n, …. At work it is assumed that the analyzed semi-Markov process possess a limited number of states $i = 1,2,\ldots,m$. In case of implementation of the decisive semi-Markov processes making the decision at the moment of t_n, k-controlling decision in i- state of the process means a choice of i-verse of the core of the matrix from the following set

$$\left\{Q_{ij}^{(k)}(t)\colon t \geq 0, \ \ d_i^{(k)}(t_n) \in D_i\,, \ \ i, j \in S\right\} \tag{3}$$

where

$$Q_{ij}^{(k)}(t) = p_{ij}^{(k)} \cdot F_{ij}^{(k)}(t) \tag{4}$$

The choice of the i-verse of the core of the process specifies the probabilistic mechanism of evolution of the process in the period of time $<t_n, t_{n+1})$. This means that for the semi-Markov process, in case of the change of the state of the process from one into i-one (entry to the i-state of the process) at the moment t_n, the decision is made $d_i^{(k)}(t_n) \in D_i$ and according to the schedule $\left(p_{ij}^{(k)} \colon j \in S\right)$ j-state of the process is generated, which is entered at the moment of t_{n+1}. At the same time, in accordance with the schedule specified by the distributor $F_{ij}^{(k)}(t)$, the length of the period of time is generated $<t_n, t_{n+1})$ to leave the i-state of the process, when the next state is the j-state. The choice of appropriate control strategy δ called the optimal strategy δ, concerns the situation, when the function (functions) representing the selection criterion of the optimal strategy takes an extrene value (minumum or maximum)

$$f_C\left(\delta^*\right) = \min_{\delta}\left[f_C(\delta)\right] \ \ or \ \ f_C\left(\delta^*\right) = \max_{\delta}\left[f_C(\delta)\right] \tag{5}$$

In the paper, the criteria functions are the availability of individual technical object $A^{OT}(\delta)$ and the unit income generated in the states of the modeled operation and maintenance process $C^{OT}(\delta)$:

$$f_{C_1}(\delta)=A^{OT}(\delta)=\sum_{i\in S_A}p_i^*(\delta)=\frac{\sum_{i\in S_A}\pi_i\cdot\Theta_i(\delta)}{\sum_{i\in S}\pi_i\cdot\Theta_i(\delta)} \tag{6}$$

$$f_{C_2}(\delta)=C^{OT}(\delta)=\sum_{i\in S}c_i(\delta)\cdot p_i^*(\delta)=\frac{\sum_{i\in S}c_i(\delta)\cdot\pi_i\cdot\Theta_i(\delta)}{\sum_{i\in S}\pi_i\cdot\Theta_i(\delta)} \tag{7}$$

where:

$S_A \subset S$ – set of availability states of modeled operation and maintenance process,
$c_i(\delta)$ – unit incomes generated in the states of process $X(t)$,
$p_i^*(\delta)$ – limit probabilities of remaining in states of the analyzed process $X(t)$ were determined based on limit theorem for semi-Markov processes (*Grabski, 2014*)

$$p_i^*(\delta)=\frac{\pi_i\cdot\Theta_i(\delta)}{\sum_{i\in S}\pi_i\cdot\Theta_i(\delta)} \tag{8}$$

where:

$\Theta_i(\delta)$ – average values of unconditional duration of the states of process,
π_i – probabilities of stationary distribution of the complex Markov chain fulfilling the system of linear equations

$$\sum_{i\in S}\pi_i\cdot p_{ij}=\pi_j,\quad j\in S,\quad \sum_{i\in S}\pi_i=1 \tag{9}$$

p_{ij} – conditional probability of passing from state i to state j:

$$p_{ij}=\lim_{t\to\infty}p_{ij}(t) \tag{10}$$

$$p_{ij}(t)=P\{X(t)=j|X(0)=i\} \tag{11}$$

The choice of the optimal strategy δ^* is made on the basis of the following criterions:

$$A^{OT}(\delta^*)=\max_{\delta}\left[A^{OT}(\delta)\right],\ C^{OT}(\delta^*)=\max_{\delta}\left[C^{OT}(\delta)\right] \tag{12}$$

The genetic algorithm constitutes the convenient tool for selection the optimal strategy δ^* process control operation of technical objects on the base of developed semi-Markov model of the process. In case of the implementation of the genetic algorithm to determine the optima strategy of controlling the operation processes for technical objects, the following guidelines should be considered:

– the examined stochastic process is the m-state decisive semi-Markov process,
– in each state it is possible to implement one of the two decision $D = \{0,1\}$,
– if the decisions are marked as 0 and 1 then the number of control strategies to be implemented for the m-state model of the operation process of the means of transport amounts to 2^m,
– the set of control strategies is the set of functions $\delta : S \rightarrow D$.

On the basis of the following guidelines each possible control strategy can be presented as m-positioning sequence consisting of 0 and 1. Therefore, an exemplary control strategy for the model of the operation process consisting of m = 9 states can be determined in the following way: $\delta=[1,0,1,1,0,1,0,0,1]$. For 9th state semi-Markov model of the means of transport operation and maintenance process presented in the paper (*Migawa, Knopik & Wawrzyniak, 2016*) as well as data obtained from tests of the existing operation and maintenance system, calculations were made with the help of developed computer software, implemented multicriteria genetic algorithm.

RESULTS AND DISCUSSION

The presented example was prepared on the basis of operational data obtained from tests of the existing means of transport operation system (municipal transport buses). In the tested system 182 municipal buses are in use, while the service and repair processes are carried out at technical infrastructure posts as well as technical emergency units. Operation process control is possible as a result of correct decision making at decisive states of the process (Tab. 1). The analyzed model of the operation and maintenance

process distinguishes the following states of the technical object: 1 – awaiting at the bus depot parking space, 2 – preparation at the bus depot parking space during the stanby time, 3 – carrying out of the transport task, 4 – refuelling between of the transport task, 5 – diagnosing and repair by the technical support unit without losing a ride, 6 – diagnosing and repair by technical support unit with losing a ride, 7 – awaiting the start of task realization after repair by technical support unit, 8 – emergency exit, 9 – realization of maintenance process at the posts of serviceability assurance subsystem (refuelling, check on the operation day, realization of periodical servicing, diagnosing, repair).
For the analyzed model of the operation and maintenance process of means of transport values of input parameters of genetic algorithm were determined, while, on the basis of operation data, the values of the elements of probability transfer matrix (13) were determined, as well as possible decisions made at decisive states of the process (Tab. 1) and mean values of time periods as well as unit incomes generated at the states of the process were established (Tab. 2).

$$P = \begin{bmatrix} 0 & 0.02831 & 0.97169 & 0 & 0 & 0 & 0 & 0 & 0 \\ 0 & 0 & 1 & 0 & 0 & 0 & 0 & 0 & 0 \\ 0 & 0 & 0 & 0.14377 & 0.08818 & 0.03520 & 0 & 0.03753 & 0.69532 \\ 1 & 0 & 0 & 0 & 0 & 0 & 0 & 0 & 0 \\ 0 & 0 & 1 & 0 & 0 & 0 & 0 & 0 & 0 \\ 0 & 0 & 0.10224 & 0 & 0 & 0 & 0.89776 & 0 & 0 \\ 0 & 0 & 1 & 0 & 0 & 0 & 0 & 0 & 0 \\ 0 & 0 & 0 & 0 & 0 & 0 & 0 & 0 & 1 \\ 1 & 0 & 0 & 0 & 0 & 0 & 0 & 0 & 0 \end{bmatrix} \tag{13}$$

Tab. 1 Decisions at states of analyzed process $X(t)$

Process state	Decision „0” - $d_i^{(0)}$	Decision „1” - $d_i^{(1)}$
1	Not decision-making process state	
2	Preparation type N (normal)	Preparation type I (intensive)
3	The route marked code L („light” conditions of the delivery task)	The route marked code D („difficult” conditions of the delivery task)
4	Not decision-making process state	
5	Repair type B (basic range)	Repair type E (extended range)
6	Repair type B (basic range)	Repair type E (extended range)
7	Not decision-making process state	
4	Not decision-making process state	
9	Maintenance process type N (normal)	Maintenance process type I (intensive)

Tab. 2 Mean time periods and unit incomes generated at states of process $X(t)$

Process state	$\Theta_i^{(0)}$ [h]	$\Theta_i^{(1)}$ [h]	$c_i^{(0)}$ [PLN/h]	$c_i^{(1)}$ [PLN/h]
1	5.659	5.659	-6.77	-6.77
2	0.280	0.224	-68.08	-87.21
3	8.852	7.967	28.44	33.56
4	0.743	0.743	-8.88	-8.88
5	0.336	0.318	-53.28	-68.86
6	0.811	0.691	-101.87	-132.43
7	0.442	0.442	-24.66	-24.66
8	0.712	0.712	-231.70	-231.70
9	2.064	1.880	-48.02	-55.01

Genetic algorithm input parameter values: length of chromosome m = 9, size of population n = 100, number of iterations I = 100, probability of chromosome selection via elitism principle η = 0.2, probability of hybridization occurrence κ = 1, probability of mutation occurrence μ = 0.05.
In the presented model the states of the availability of technical objects are: 1, 2, 3, 7.
Then, calculations were performed with the help of the developed computer program implementing the multicriteria genetic algorithm. On the basis of the calculations performed, for the criteria adopted, optimal (quasi-optimal) control strategies were determined for the operation and maintenance process carried out at the tested transport system. Calculation results were presented in Fig. 1 as well as Tab. 3.

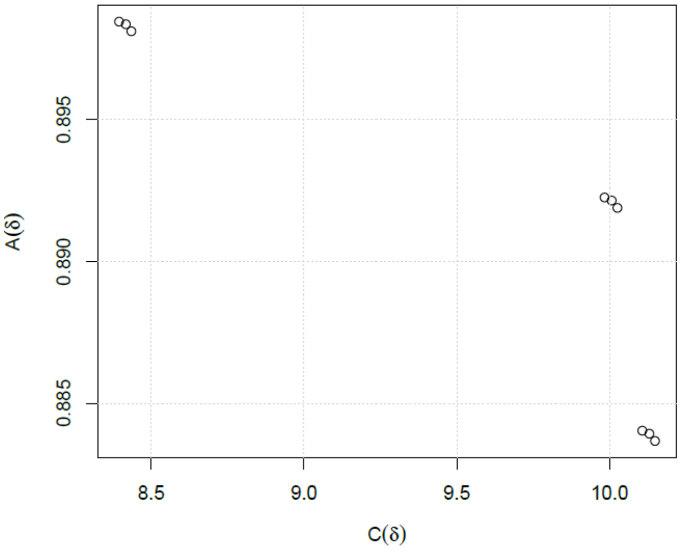

Fig. 1 Pareto frontier for optimal solutions determined on the basis of multicriteria genetic algorithm

Tab. 3 Optimal control strategies δ^* as well as value of criteria functions determined on the basis of multicriteria genetic algorithm

Strategy δ^*	$A^{OT}(\delta^*)$	$C^{OT}(\delta^*)$ [PLN/h]
[1,0,0,0,1,1,0,0,1]	0.8984	8.39
[0,0,0,1,0,1,0,0,1]	0.8983	8.42
[1,0,0,1,0,0,1,0,1]	0.8981	8.44
[0,0,1,0,1,1,0,0,1]	0.8922	9.98
[1,1,1,1,0,1,1,1,1]	0.8921	10.01
[1,1,1,1,0,0,0,1,1]	0.8919	10.02
[0,0,1,1,1,1,1,0,0]	0.8840	10.11
[0,1,1,0,0,1,0,0,0]	0.8839	10.13
[1,1,1,0,0,0,1,0,0]	0.8837	10.15

Articles (*Migawa, Knopik & Wawrzyniak, 2016*) and (*Migawa, Knopik, Neubauer & Perczyński, 2017*) discuss 9-state models of the means of transport use process (semi-Markov and simulation process, respectively) the implementation of which facilitates determining a control strategy taking into consideration a single criterion (availability of technical objects). The method presented in the article, on the other hand, applies to multi-criteria analysis (e.g. when two criteria of evaluation are applied, such as availability and unit income). On the basis of the results obtained it is noticeable that an increase in means of transport availability is connected to lowering of unit income. This stems mainly from the need to bear additional costs connected to maintaining the roadworthiness of technical objects. This is carried out by an increase of intensity of services and repairs performed, e.g. involving more efficient tools and devices as well as a bigger number of workers. In the example given, one may notice that the increase in availability from the level of ca. 0.884 to 0.892 is possible with little additional expenses (a decrease of income from ca. 10.13 to 10.00 [PLN/h]). However, a further increase in availability of technical objects above the value of 0.898 requires a significant increase of expenses on services and repairs of technical objects, thus resulting in a decrease of unit income below the level of 8.45 [PLN/h].

CONCLUSIONS

On the basis of the results of operation tests at the existing system of means of transport operation, input data were determined for the developed genetic algorithm and calculations were performed. As a result, the values of criteria functions as well as a corresponding set of control strategies constituting a set of optimal solutions according to Pareto were determined. The optimal set according to Pareto is a set of non-dominated solutions of the whole acceptable search space. Optimal solutions according to Pareto form the so-called Pareto frontier. On the basis of the results obtained, a selection of a single solution from the determined set of optimal solutions (located on the so-called Pareto frontier) may be made. Such selection is usually made by the decider (a group of deciders) on the basis of additional circumstances connected to particular decisive situation as well as current conditions in which the operation and maintenance system functions. Depending on the requirements, the developed genetic algorithm, including the decisive model of operation and maintenance process, may be used for mathematically formulating and solving a wide range of problems connected with control of complex technical systems. This is mainly connected to economical analysis, risk and safety managements as well as availability and reliability of the utilized technical objects.

REFERENCES

1. Grabski, F. (2014). Semi-Markov processes: Applications in system reliability and maintenance. *Elsevier, Amsterdam.*
2. Grabski, F. (2010). Risk analysis in decisive semi-Markov models of operation process. *The 38th Winter Reliability School, Szczyrk*, 43-52, (in Poland).
3. Holland, JH. (1975). Adaptation in natural and artificial systems. *Ann Arbor: University of Michigan Press*.
4. Knopik, L., Migawa, K., & Wdzięczny, A. (2016). Profit optimalization in operation systems. *Polish Maritime Research, vol. 23, no. 1(89),* 93-98.
5. Konak, A., Coit, DW., & Smith AE. (2006). Multi-objective optimization using genetic algorithms: A tutorial. *Reliability Engineering and System Safety 91, Elsevier,* 992-1007.
6. Kulkarni, V. G. (1995). Modeling and analysis of stochastic systems. *Chapman & Hall, New York*.
7. Lee, K. W. (2000). Stochastic models for random-request availability. *IEEE Trans. Reliability 49,* 80-84.
8. Migawa, K., Knopik, L., & Wawrzyniak, S. (2016). Application of genetic algorithm to control the availability of technical systems. *Engineering Mechanics, Institute of Thermomechanics Academy of Sciences of the Czech Republic*, 386-389.
9. Migawa, K., Knopik, L., Neubauer, A., & Perczyński, D. (2017). Simulation of the model of technical object availability control. *Engineering Mechanics, Institute of Thermomechanics Academy of Sciences of the Czech Republic*. 654-657.
10. Schaffer, JD. (1985). Multiple objective optimization with vector evaluated genetic algorithms. *In: Proceedings of the international conference on genetic algorithm and their applications*.
11. Zastempowski, M., & Bochat, A. (2014). Modeling of cutting process by the shear-finger cutting block. *ASABE Applied Engineering in Agriculture, vol. 30, no. 3,* 347-353.

Corresponding author:
RNDr. Mirosław Szubartowski, DSc., Management Business and Service, Fordońska 40, 85-719 Bydgoszcz, Poland, phone: +48 340 84 24, e-mail: analityk@karor.com.pl

SIMULATION MODEL OF RISK EVALUATION IN TRANSPORT SYSTEM

Mirosław SZUBARTOWSKI[1], Klaudiusz MIGAWA[2], Leszek KNOPIK[3], Maciej GNIOT[2]

[1]*Management Business and Service, Bydgoszcz, Poland*
[2]*Department of Mechanical Engineering, UTP University of Science and Technology, Bydgoszcz, Poland*
[3]*Department of Management, UTP University of Science and Technology, Bydgoszcz, Poland*

Abstract
The article presents the description of the developed simulation model of technical objects operation and maintenance process carried out in transport system. The simulation model of operation and maintenance process discussed in the paper allows for the evaluation of quality of technical system performance from the point of view of selected evaluation criteria: the risk of the occurrence of undesired events as well as availability of technical objects. The simulation model of the operation and maintenance process of technical objects was developed on the basis of the mathematical model of this process (semi-Markov model). On the basis of the results of tests performed in an existing means of transport operation system, input data of the model were established and simulation experiments performed. As a result, typical values for the analyzed characteristics of technical system operation quality.

Key words: *risk; availability; simulation model; operation and maintenance process.*

INTRODUCTION

One of the methods enabling effective assessment of operation quality of complex systems of technical objects is application of mathematical models for a description and analysis of the operation and maintenance processes of technical objects. Due to a significant complexity of processes carried out in existing systems of technical objects operation, there appears the need to implement appropriate methods and tools, including stochastic models (*Lee, 2000; Kulkarni, 1995*), matrix calculus (*Grabski, 2014; Zastempowski & Bochat, 2015*) as well as computer simulation programs providing effective carrying out of the tests of the models of analyzed operation processes as well as an analysis of results obtained (*Marbach & Tsitsiklis, 2001; Migawa, Knopik, Neubauer & Perczyński, 2017; Muślewski, Migawa & Knopik, 2016*). These models provide the possibility of assessment and control of operation quality of complex technical systems according to selected criteria such as costs, reliability, availability and also risk connected with the technical objects functioning. Depending on the kind of analyzed research problems, appropriate methods of delineating optimal and quasi-optimal solutions were implemented. Semi-Markov decisive model of availability control in which the selection of optimal strategy was carried out with the help of genetic algorithm was presented in the paper (*Migawa, Knopik & Wawrzyniak, 2016*). However, the issues connected to the evaluation of safety and risk were presented in the paper (*Grabski, 2010*) which contains the model of safety control developed with the use of decisive semi-Markov processes and Howard's algorithm. In the paper (*Migawa, Knopik, Sołtysiak & Kolber, 2017*) the semi-Markov model of risk evaluation in transport system is discussed as well.
In the case of risk connected with operation of technical systems, numerous methods are used for threat or safety level evaluation and analysis, including qualitative methods, analytical and graphic methods as well as quantitative methods. Although these methods make it possible to evaluate, control and reduce the value of risk to acceptable levels, they do not take into consideration, or do it only to a limited degree, the influence of important parameters of technical objects operation process. There is no connection between the evaluation of risk and fulfilling the criteria pertaining to providing the possibility to correctly carry out assigned tasks, e.g. taking into consideration the required level of availability, reliability as well as the values of economic indexes in the system of technical objects operation. Such an approach requires not only taking into consideration risk, but also an additional criterion of the evaluation of technical system. The objective of the paper is to develop and present the results of the tests of the simulation model of operation process the use of which makes it possible to evaluate the risk of the occurrence of undesired events, at the same time taking into consideration the requirements facing the operation systems regarding the level of availability of technical objects for carrying out the assigned transportation task.

MATERIALS AND METHODS

The presented approach involves determination of the risk connected with functioning of one technical object (transport mean). The risk associated with functioning of a single transport mean has been determined on the basis of a simulation model of the operation and maintenance process. The simulation model was built on the basis of an event model and a mathematical model (semi-Markov model) of this process. The event model of the operation and maintenance process was created on the basis of the analysis of the space of operation and maintenance states and events connected with technical objects (transport means) operating in the analysed real transport system. Applying semi-Markov processes in the mathematical operation and maintenance process, the following assumptions were made:

– the modelled process has a finite number of states $i = 1, 2, \ldots, m$,
– if the technological object at moment t is in state i, then $X(t) = i$,
– random process $X(t)$ being a mathematical model of the operation and maintenance process is homogenous,
– at moment $t = 0$ the process is in state i, i.e. $P\{X(0) = i\} = 1$.

Limit probabilities p_i^* of remaining in states of the analyzed process $X(t)$ were determined based on limit theorem for semi-Markov processes (*Grabski*, *2014*), then:

– value of the unit risk of functioning disruption of transport means is described with the formula (1)

$$r(\delta) = \sum_{i \in S_U} p_i^* \cdot c_i = \frac{\sum_{i \in S_U} \pi_i \cdot \overline{\Theta_i} \cdot c_i}{\sum_{i \in S} \pi_i \cdot \overline{\Theta_i}} \tag{1}$$

– value of the technical object availability function is described with the formula (2)

$$A(\delta) = \sum_{i \in S_A} p_i^* = \frac{\sum_{i \in S_A} \pi_i \cdot \overline{\Theta_i}}{\sum_{i \in S} \pi_i \cdot \overline{\Theta_i}} \tag{2}$$

where:

c_i – values of unit cost generated in the states of process $X(t)$,
$\overline{\Theta_i}$ – average values of unconditional duration of the states of process $X(t)$,
π_i – values of probabilities of stationary distribution of the complex Markov chain,
p_i^* – values of limit probabilities of remaining in states of semi-Markov model process $X(t)$,
$S_U \subset S = \{1,2,\ldots,m\}$ – the set of unwelcome states of semi-Markov model process $X(t)$,
$S_A \subset S = \{1,2,\ldots,m\}$ – the set of availability states of semi-Markov model process $X(t)$.

The results of the tests of the semi-Markov model of operation and maintenance process used in the evaluation of risk in the transport system was discussed in the paper (*Migawa, Knopik, Sołtysiak & Kolber, 2017*).

In order to provide the possibility of considering different computational variants, e.g. through changing the parameters of the modeled process or a number of analyzed technical objects, a program has been created for simulation of a model of technical objects operation process. The program developed for simulation of the operation process makes it possible to perform simulation experiments for different numbers of operational events (changes in the process states), intervals of simulation time both for an individual technical object and a group of technical objects. In the simulation program, successive duration times of the operation process states are determined by generating pseudorandom numbers yielding values form exponential, gamma, normal, logarithmic-normal and Weibull distributions. The structure of the simulation program was created so that the simulation experiment will be able to reflect a set of the analyzed technical objects and the sequence of events happening to each technical object in the analyzed real system. In Fig. 1 there is a block scheme depicting operation of the program for the model of technical objects operation process.

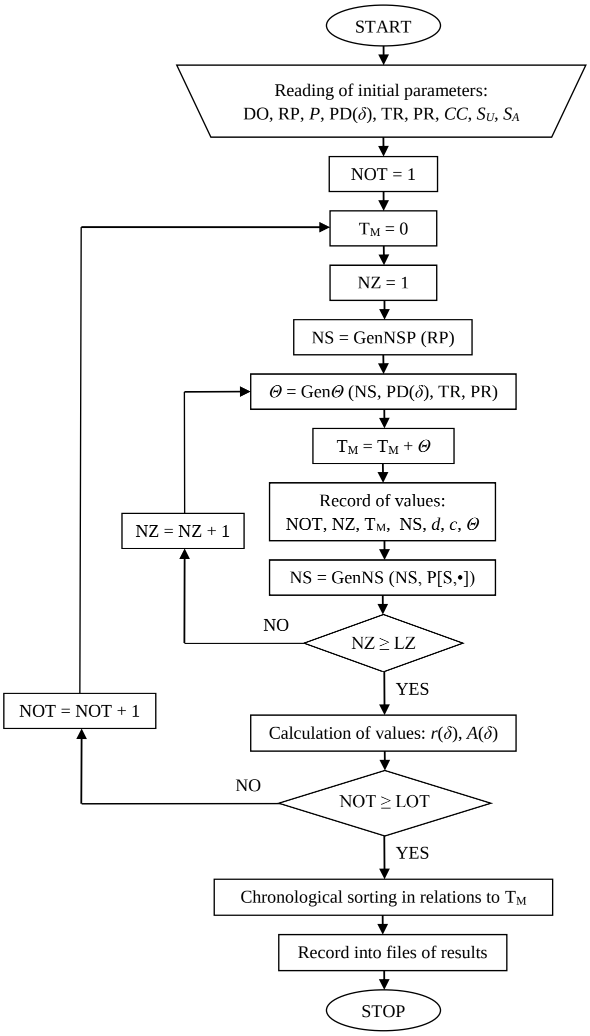

DO (general data characterizing the simulation experiment):
LOT – number of technical objects used in the simulation experiment,
LZ – number of a technical object events in the simulation experiment,
m – number of the process states, defined on the basis of a set of the modeled operation process states,
LD – number of decisions possible to be made in particular states of the modeled operation process,
Lδ – number of strategies δ possible to be used in the simulation experiment;

RP (the process initial distribution);
P (matrix of probabilities of the process states changes);
PD (matrix of probability of decision choice in the process states);
TR, PR (types and parameters of time distributions of being in particular states of the process);
CC (matrix of unit costs in the process states);
S_U (set of the process unwelcome states);
S_A (set of the process availability states);
GenNSP – generation of the model initial state number;
GenNS – generation of the model current state;
GenΘ – generation of the time value of being in the model state.

Fig. 1 Block scheme depicting operation of the program for technical objects operation process simulation model

In each moment of the simulation experiment in which the modeled operation process undergoes change (for the analyzed technical object) the following data is being entered into the file of results: number of the technical object NOT, number of the current event NZ, time of the current event (current time of model T_M), number of the model current state NS, current decision *d*, value of unit cost *c* related to the object's being in the process current state, generated value of the object's being in a current state Θ. Next, values of functions applied in the simulation program are determined for the set of data generated during the simulation experiment:

– value of the unit risk of functioning disruption of transport means while carrying out the operation and maintenance process is described with the formula (3)

$$r(\delta)=\frac{\sum_{k=1}^{Z}\Theta_k(S_U)\cdot c_k(S_U)}{\sum_{k=1}^{Z}\Theta_k} \tag{3}$$

– value of the technical object availability function is described with the formula (4)

$$A(\delta)=\frac{\sum_{k=1}^{Z}\Theta_k(S_A)}{\sum_{k=1}^{Z}\Theta_k} \qquad (4)$$

where:

Θ_k – k-th time of the object's being in the modeled operation process states $S=\{1,2,\ldots,m\}$,

$\Theta_k(S_U)$ – k-th time of the object's being in the modeled operation process states belonging to unwelcome states $S_U \subset S=\{1,2,\ldots,m\}$,

$c_k(S_U)$ – k-th performance of a unit cost connected with being in the unwelcome states of the modeled operation process $S_U \subset S=\{1,2,\ldots,m\}$,

$\Theta_k(S_A)$ – k-th time of the object's being in the modeled operation process states belonging to availability states $S_A \subset S=\{1,2,\ldots,m\}$,

Z = LOT · LZ – number of events (changes of the model states) for a specified number of technical objects.

RESULTS AND DISCUSSION

Fig. 2 depicts a directed graph of imaging of the considered process of technical objects operation and maintenance. The analyzed model of the process of operation and maintenance distinguishes the following states: 1 – stopover at depot parking space, 2 – carrying out of transport task, 3 – downtime caused by damage (unwelcome event), 4 – downtime caused by an accident or collision (unwelcome event), 5 – intervention and rescue action after accident or collision (unwelcome event), 6 – repair after an unwelcome event, 7 – preventive diagnosis, 8 – preventive repair, 9 – supply, 10 – servicing (operation day, periodical, seasonal).

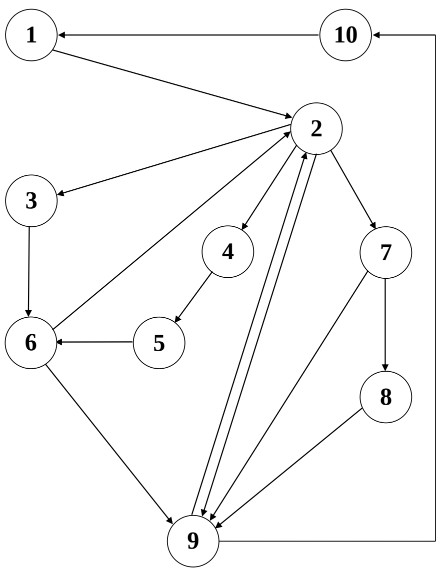

Fig. 2 A directed graph depicting operation and maintenance process of transport means

In the presented model the following unwelcome states of technical object have been distinguished: 3, 4, 5, 6; and the following availability states of technical object have been distinguished: 1, 2.

For the analyzed model of the operation and maintenance process of transport means, basing on the functioning data, values were estimated for the elements of matrix of passage probabilities:

$$P = \begin{vmatrix} 0 & 1 & 0 & 0 & 0 & 0 & 0 & 0 & 0 & 0 \\ 0 & 0 & 0.2320 & 0.0030 & 0 & 0 & 0.4988 & 0 & 0.2661 & 0 \\ 0 & 0 & 0 & 0 & 0 & 1 & 0 & 0 & 0 & 0 \\ 0 & 0 & 0 & 0 & 1 & 0 & 0 & 0 & 0 & 0 \\ 0 & 0 & 0 & 0 & 0 & 1 & 0 & 0 & 0 & 0 \\ 0 & 0.4702 & 0 & 0 & 0 & 0 & 0 & 0 & 0.5298 & 0 \\ 0 & 0 & 0 & 0 & 0 & 0 & 0 & 0.0799 & 0.9201 & 0 \\ 0 & 0 & 0 & 0 & 0 & 0 & 0 & 0 & 1 & 0 \\ 0 & 0.2242 & 0 & 0 & 0 & 0 & 0 & 0 & 0 & 0.7758 \\ 1 & 0 & 0 & 0 & 0 & 0 & 0 & 0 & 0 & 0 \end{vmatrix}$$

Below in Fig. 3 and in Tab. 1 sample tests results for the operation process model obtained from input data processed after being provided from a real system of technical objects operation have been shown.

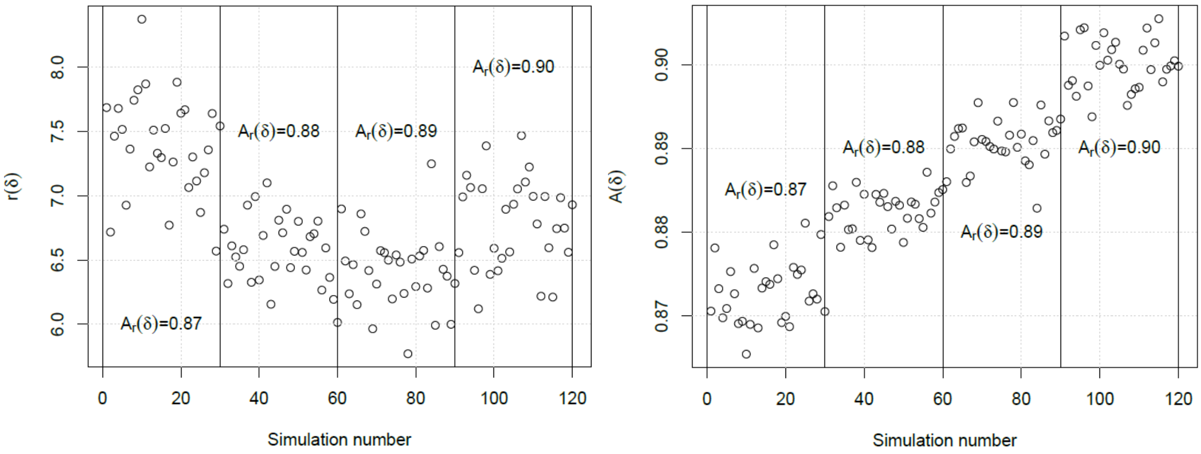

Fig. 3 Values of unit risk $r(\delta)$ [PLN/h] as well as availability of technical object $A(\delta)$ on the basis of simulation experiments for individual control strategies

Tab. 1 Values of statistics determined for unit risk and availability of a technical object

	$A_r(\delta)$=0.87		$A_r(\delta)$=0.88		$A_r(\delta)$=0.89		$A_r(\delta)$=0.90	
Statistic	$r(\delta)$ PLN/h	$A(\delta)$	$r(\delta)$ PLN/h	$A(\delta)$	$r(\delta)$ PLN/h	$A(\delta)$	$r(\delta)$ PLN/h	$A(\delta)$
Mean	7.398	0.8728	6.567	0.8825	6.417	0.8907	6.789	0.9001
Standard deviation	0.394	0.0037	0.260	0.0024	0.299	0.0029	0.349	0.0030
Minimum	6.569	0.8655	6.013	0.8782	5.769	0.8829	6.120	0.8938
1 Quartile	7.190	0.8698	6.378	0.8805	6.249	0.8896	6.558	0.8976
Median	7.414	0.8727	6.573	0.8831	6.446	0.8909	6.837	0.8999
3 Quartile	7.663	0.8752	6.732	0.8843	6.552	0.8923	7.039	0.9025
Maximum	8.375	0.8811	7.100	0.8872	7.249	0.8955	7.469	0.9055

The performed experiments involved 30 simulations of the operation process for four selected strategies δ, so that the designated availability of technical objects $A(\delta)$ was at least equal to required availability $A_r(\delta)$ for appropriate realization of transport tasks (for $A_r(\delta)$ = 0.87, 0.88, 0.89, 0.90). As a result of the realization of simulation experiments, sets of 30 values of unit risk $r(\delta)$ as well as 30 values of technical object availability $A(\delta)$ were obtained. Tab. 1 shows the results of simulation experiments: mean values, values of standard deviation and values of positional statistics (minimum, 1 quartile, median, 3 quartile, maximum), determined for the considered characteristics of the technical objects operation process quality and selected strategies δ. On the basis of obtained results, it is noticeable that in terms of required availability $A_r(\delta)$ from 0.87 to 0.89, the increase of availability is accompanied by a decrease of mean risk value $r(\delta)$ from 7.398 to 6.417 [PLN/h] respectively. However, obtaining a higher level of availability of technical objects (for $A_r(\delta) > 0.90$) is connected with an increase of risk value up to the level $r(\delta) = 6.789$ [PLN/h]. This results from the need to provide additional operations and means connected with treatment of technical objects (both due to higher unit costs as well as treatment period).

CONCLUSIONS

On the basis of results obtained, it is possible to conclude that ensuring a higher level of technical object availability does not have to cause a decrease in risk of occurrence of undesired events in operation system. This may result from the fact that the increase of the level of availability of technical objects does not influence the decrease of probability of occurrence of undesired events, as it only necessitates additional costs to be incurred in connection with removing the effects of such events. On the basis of a detailed analysis of the results of tests it was concluded that it had been caused by an increase in time of remaining at states of maintaining worthiness of technical objects.

REFERENCES

1. Grabski, F. (2014). Semi-Markov processes: Applications in system reliability and maintenance. *Elsevier, Amsterdam*.
2. Grabski, F. (2010). Risk analysis in decisive semi-Markov models of operation process. *The 38th Winter Reliability School, Szczyrk*, 43-52, (in Poland).
3. Kulkarni, V. G. (1995). Modeling and analysis of stochastic systems. *Chapman & Hall, New York*.
4. Lee, K. W. (2000). Stochastic models for random-request availability. *IEEE Trans. Reliability 49*, 80-84.
5. Marbach, P., & Tsitsiklis, T. N. (2001). Simulation based optimization of Markov reward process. *IEEE Trans. Automat. Contr. 46*, 191-209.
6. Migawa, K., Knopik, L., & Wawrzyniak, S. (2016). Application of genetic algorithm to control the availability of technical systems. *Engineering Mechanics, Institute of Thermomechanics Academy of Sciences of the Czech Republic*, 386-389.
7. Migawa, K., Knopik, L., Neubauer, A., & Perczyński, D. (2017). Simulation of the model of technical object availability control. *Engineering Mechanics, Institute of Thermomechanics Academy of Sciences of the Czech Republic*, 654-657.
8. Migawa, K., Knopik, L., Sołtysiak, A., & Kolber, P. (2017). The method of risk assessment in transport system. *Engineering Mechanics, Institute of Thermomechanics Academy of Sciences of the Czech Republic*, 658-661.
9. Muślewski, Ł., Migawa, K., & Knopik, L. (2016). Control of technical objects operation quality with the use of simulation modeling PE. *Risk, Reliability and Safety: Innovating Theory and Practice: Proceedings of ESREL*, 1388-1395.
10. Zastempowski, M., & Bochat, A. (2015). Mathematical modelling of elastic deflection of a tubular cross-section. *Polish Maritime Research, vol. 22, no. 2(86)*, 93-100.

Corresponding author:
RNDr. Mirosław Szubartowski, DSc., Management Business and Service, Fordońska 40, 85-719 Bydgoszcz, Poland, phone: +48 340 84 24, e-mail: analityk@karor.com.pl

REQUIRED AVAILABILITY OF THE SERVICEABILITY ASSURANCE SYSTEM

Mirosław SZUBARTOWSKI[1], Andrzej NEUBAUER[2], Klaudiusz MIGAWA[3], Sylwester BOROWSKI[3]

[1]*Management Business and Service, Bydgoszcz, Poland*
[2]*Department of Economic and Management, Nicolaus Copernicus University, Toruń, Poland*
[3]*Department of Mechanical Engineering, UTP University of Science and Technology, Bydgoszcz, Poland*

Abstract
In complex operation systems, the processes of rendering technical objects roadworthy are carried out at specifically designed technical infrastructure posts. The possibility of carrying out the assigned service and repair tasks depends on the availability and the number of such posts. The article presents the method of defining the operational availability of technical infrastructure posts required for appropriate functioning of assigned service and repair task. Then typical calculation results are presented in charts prepared on the basis of data obtained from tests at existing transport means operation system.

Key words: *technical infrastructure posts; operational availability; posts productivity.*

INTRODUCTION

In systems of means of transport operation in order to achieve appropriate completion of assigned transportation tasks it is necessary to maintain a required number of means of transport in the state of availability for carrying out of transportation task (roadworthy and stocked). In general, the processes of rendering vehicles roadworthy are connected to supplying them with fuel and operational materials, carrying out services and repairs, condition diagnostics. In the analyzed system of transport means operation, the processes are carried out in serviceability assurance subsystem SAS. The subsystem of the type may function properly only when appropriate availability of service and repair posts is granted. The problem of control of the processes carried out at serviceability assurance subsystems from the point of view of evaluation criteria such as reliability and availability is discussed in numerous scientific publications (*Knopik & Migawa, 2017; Landowski, Perczyński, Kolber & Muślewski, 2016; Chen & Trivedi, 2002*). It reflects issues connected to selection of optimal strategy (policy) of servicing and repair as well as evaluation of the operation of serviceability assurance subsystems (service and repair posts). Papers (*Kosten, 1973; Piasecki, 1996*) discuss issues connected with modeling and organization of technical objects service systems. The authors of paper (*Woropay, Żurek & Migawa, 2003*) suggested that the methods of shaping the availability of technical backup area posts, whereas papers (*Szubartowski, 2012; Woropay, Migawa & Bojar, 2010*) discuss the methods of the evaluation of the effectiveness and productivity of processes carried out at service and repair posts. Among the many methods supporting the evaluation and control process, the semi-Markov decisive processes have been implemented (*Chen & Trivedi, 2005*), non-deterministic methods of defining optimal solutions (genetic algorithms, evolutionary algorithms, Monte Carlo method) (*Migawa, Knopik & Wawrzyniak, 2016; Marseguerra & Zio, 2000*), as well as methods and models of mass service theory (*Vaurio, 1997*). The objective of this paper is to work out a method of determining serviceability assurance subsystem post availability at such a level that would ensure appropriate carrying out of service and repair tasks assigned for to be carried out at such posts.

MATERIALS AND METHODS

Presented below are formulas defining availability of individual post of a serviceability assurance subsystem. If

$$V_{ij}(t) = P(X_{ij}<t),\ i=1,2,...,p,\ j=1,2,\ldots,q_i \quad (1)$$

is the distribution function of serviceability time X_{ij}, $i=1,2,...,p$, $j=1,2,\ldots,q_i$ of a single post s_{ij}, $i=1,2,...,p$, $j=1,2,\ldots,q_i$ at serviceability assurance subsystem, while

$$W_{ij}(t) = P(Y_{ij}<t),\ i=1,2,...,p,\ j=1,2,\ldots,q_i \quad (2)$$

is the distribution function of renovation time Y_{ij}, i=1,2,...,p, j=1,2,…,q_i of a single post s_{ij}, i=1,2,...,p, j=1,2,…,q_i at serviceability assurance subsystem, then the availability $A_{ij}(t)$ of a single post s_{ij} determined at point t as probability that at point t the post s_{ij} is serviced and provided for, is defined by the formula

$$A_{ij}(t) = R_{ij}(t) + \int_0^t R_{ij}(t-x)\ dH_{ij}(x) \tag{3}$$

as well as

availability $A_{O_{ij}}(t,\tau)$ of a single post s_{ij} of serviceability subsystem, determined over time interval $<t,t+\tau)$ as probability that over time interval $<t,t+\tau)$ the post s_{ij} is available and provided for, is defined by the formula

$$A_{O_{ij}}(t,\tau) = R_{ij}(t+\tau) + \int_0^t R_{ij}(t+\tau-x)\ dH_{ij}(x) \tag{4}$$

where:

$R_{ij}(t)$ – is the function of reliability of a single post s_{ij} of the serviceability assurance subsystem,

$H_{ij}(t)$ – is the function of renovation of a single post s_{ij} of the serviceability assurance subsystem.

In the case, in which $t\to\infty$, the functions defined by formulas (3) and (4) have limit values called limit availability coefficients:

$$A_{ij} = \lim_{t\to\infty} A_{ij}(t) = \frac{E(X_{ij})}{E(X_{ij}) + E(Y_{ij})} \tag{5}$$

$$A_{O_{ij}}(\tau) = \lim_{t\to\infty} A_{O_{ij}}(t,\tau) = \frac{1}{E(X_{ij}) + E(Y_{ij})} \cdot \int_\tau^\infty R_{ij}(x)\ dx \tag{6}$$

where:

$E(X_{ij})$ – is the expected value of the time of serviceability of a single post s_{ij} of the serviceability assurance subsystem,

$E(Y_{ij})$ – is the expected value of the time of renovation of a single post s_{ij} of the serviceability assurance subsystem.

Availability of serviceability assurance subsystem depends on the structure which couples individual posts as well as groups of such posts. Presented below are formulas defining availability of individual post group s_i, i=1,2,...,p of a serviceability assurance subsystem in the case of the posts of the analyzed system are coupled via a threshold structure.

Availability of group s_i, i=1,2,...,p consisting of j=1,2,...,q_i homogenous posts of serviceability assurance subsystem coupled by threshold structure „k_i with q_i”:

– determined at moment t defined by formula

$$A_i(t) = \sum_{c=k_i}^{q_i} \binom{q_i}{c} \cdot \left[\overline{A_{ij}(t)}\right]^c \cdot \left[1 - \overline{A_{ij}(t)}\right]^{q_i - c} \tag{7}$$

– determined over time interval $<t,t+\tau)$ defined by formula

$$A_{O_i}(t,\tau) = \sum_{c=k_i}^{q_i} \binom{q_i}{c} \cdot \left[\overline{A_{O_{ij}}(t,\tau)}\right]^c \cdot \left[1 - \overline{A_{O_{ij}}(t,\tau)}\right]^{q_i - c} \tag{8}$$

When $t\to\infty$, functions described by formulas (7) as well as (8) reach the following border values:

$$A_i = \sum_{c=k_i}^{q_i} \binom{q_i}{c} \cdot \left[\frac{E\left(\overline{X_{ij}}\right)}{E\left(\overline{X_{ij}}\right) + E\left(\overline{Y_{ij}}\right)}\right]^c \cdot \left[\frac{E\left(\overline{Y_{ij}}\right)}{E\left(\overline{X_{ij}}\right) + E\left(\overline{Y_{ij}}\right)}\right]^{q_i - c} \tag{9}$$

$$A_{O_i}(\tau) = \sum_{c=k_i}^{q_i} \binom{q_i}{c} \cdot \left[\frac{1}{\left[E\left(\overline{X_{ij}}\right) + E\left(\overline{Y_{ij}}\right)\right]} \cdot \int_\tau^\infty \overline{R_{ij}(x)}\ dx\right]^c \cdot \left[1 - \frac{1}{\left[E\left(\overline{X_{ij}}\right) + E\left(\overline{Y_{ij}}\right)\right]} \cdot \int_\tau^\infty \overline{R_{ij}(x)}\ dx\right]^{q_i - c} \tag{10}$$

Complexity of the existing structure coupling the individual post groups depends primarily on the equipment of posts, worker qualification as well as the type of tasks to be carried out at individual post groups. The general instance is connected to the situation involving individual serviceability assurance subsystem groups, due to specialist equipment as well as worker qualifications may not replace each other and are supposed to carry out tasks of various type and range. Thus, the post groups of serviceability assurance subsystem s_i, i=1,2,...,p are coupled by threshold structure. Then, availability of serviceability assurance subsystem is determined as product of the availability of its individual groups:

– at moment t

$$A(t)=\prod_{i=1}^{p} A_i\,(t) \tag{11}$$

– over time interval τ

$$A_O(t,\tau)=\prod_{i=1}^{p} A_{O_i}(t,\tau) \tag{12}$$

Availability of the SAS serviceability assurance subsystem is understood as capability to carry out the assigned service and repair task. Each task assigned to SAS is determined by the length of the time interval τ devoted to the completion of the task, the size of the task (how many technical objects should be rendered roadworthy and/or stocked) as well as the scope of the task (what should be done). The measure of operational availability of SAS posts in carrying out of the assigned task is the product of the probabilities of two events taking place:

– the event of SAS posts being available at any point (roadworthy and stocked) to undertake the assigned task and will remain in this condition for the time interval τ of the task duration; this probability is expressed through the operational availability value of analyzed subsystem $A_O(\tau)$,
– the event of the task assigned at the posts of the subsystem in question will be carried out, i.e. in the time interval τ the number of objects rendered technically roadworthy will be higher than k; this probability is expressed through the value of the productivity index $Z^{(k)}(\tau)$ of SAS posts – the way of defining the productivity index is presented in paper (*Woropay, Migawa & Bojar, 2010*).

Taking the above discussion into consideration, the operational availability of the serviceability assurance subsystem in carrying out the assigned service and repair task in the time interval τ, is defined as follows

$$A_{OZ}^{(k)}(\tau)=A_O(\tau)\cdot Z^{(k)}(\tau) \tag{13}$$

where:

$A_O(\tau)$ – operational availability of the posts of serviceability assurance subsystem defined as the probability of this subsystem being available at any point t and remaining in this condition over a required time interval τ,

$Z^{(k)}(\tau)$ – probability of the number of technical objects rendered roadworthy at serviceability assurance subsystem posts in the time interval τ being bigger than k.

Required operational availability of the serviceability assurance subsystem for carrying out of service and repair task (rendering k number of technical objects roadworthy in the time interval of τ length), determined as product of required availability $A_{O_{req}}^{(k)}(\tau)$ as well as the required value of productivity index $Z_{req}^{(k)}(\tau)$ for analyzed posts in the time interval of τ length is realized in the formula

$$A_{OZ_{req}}^{(k)}(\tau)=A_{O_{req}}^{(k)}(\tau)\cdot Z_{req}^{(k)}(\tau) \tag{14}$$

Service and repair task assigned to the serviceability assurance subsystem is determined by the required number k of technical objects which should be rendered roadworthy and/or stocked in the given time interval of τ length, at posts for this subsystem. Whereas the required availability $A_{O_{req}}^{(k)}(\tau)$ of serviceability assurance subsystem determined for number k of technical objects rendered roadworthy in the time interval of τ length is described as follows

$$A_{O_{req}}^{(k)}(\tau)=\frac{T_{req}^{(k)}(\tau)}{T_{req}^{(k)}(\tau)+U_{req}^{(k)}(\tau)} \tag{15}$$

where:

$T_{req}^{(k)}(\tau)$ – required availability time for SAS posts for given *k* and *τ*,

$U_{req}^{(k)}(\tau)$ – required unavailability time for SAS posts for given *k* and *τ*.

Assuming that for any time interval of *τ* length the sum of required availability and unavailability times for serviceability assurance subsystem equals the time interval of *τ* length, i.e. $T_{req}^{(k)}(\tau)+U_{req}^{(k)}(\tau)=\tau$, then formula (15) may be written as follows

$$A_{O_{req}}^{(k)}(\tau)=\frac{T_{req}^{(k)}(\tau)}{\tau} \tag{16}$$

Required availability time $T_{req}^{(k)}(\tau)$ for SAS posts depends on the anticipated total time of rendering *k* number of technical objects (transport means) roadworthy in the time interval of *τ* length as well as the *q* number of uniform posts of the analyzed subsystem and is described by the condition

$$T_{req}^{(k)}(\tau)=\frac{k\cdot\overline{U^{OT}}(\tau)}{q}\leq\tau \tag{17}$$

where

$\overline{U^{OT}}(\tau)$ – mean time of technological object remaining at serviceability assurance subsystem (mean time of rendering technical objects roadworthy).

When $T_{req}^{(k)}(\tau)>\tau$, then in the time interval for the posts of the analyzed subsystem (SAS) the rendering of the required *k* number of technical objects roadworthy is not possible.

Evaluation of operational availability of serviceability assurance subsystem SAS for carrying out the assigned task consists of determining the value of actual availability of the subsystem (for the required time interval of *τ* length as well as required *k* number of technical objects which should be rendered roadworthy and/or stocked) and then comparing to the value of required availability the SAS should has in order for the assigned task to be carried out according to the relation

$$A_{OZ}^{(k)}(\tau)=A_O(\tau)\cdot Z^{(k)}(\tau)\geq A_{OZ_{req}}^{(k)}(\tau),\quad for\quad k=N_{U_{req}}(\tau) \tag{18}$$

where

$$Z^{(k)}(\tau)=P\left(k\geq N_{U_{req}}(\tau)\right) \tag{19}$$

means the probability of the number of technical objects rendered roadworthy at posts of SAS in the time interval of *τ* length is not lower than the required number $N_{U_{req}}(\tau)$ of technical objects which should be rendered roadworthy in this time interval. If the value of operational availability of the SAS posts for carrying out the assigned task is lower than required, e.g. $A_{OZ}^{(k)}(\tau)<A_{OZ_{req}}^{(k)}(\tau)$, the assigned task at SAS posts may not be carried out properly (in the time interval of *τ* length it is not possible to render the required number $N_{U_{req}}(\tau)$ of technical objects roadworthy).

In the case of the serviceability assurance subsystem comprise $i=1,2,\ldots,p$ of groups containing $j=1,2,\ldots,q_i$ of posts linked to a given structure, it is possible to determine the required availability of posts $A_{ij_{req}}$ at individual groups. Assuming that the *i*-th group comprises uniform posts, the required availability of posts $A_{ij_{req}}$ is assigned (when posts are liked by threshold structure)

$$A_{ij}=A_{ij_{req}}\Leftrightarrow A_{O_i}(\tau)=\sum_{c=k_i}^{q_i}\binom{q_i}{c}\cdot\left[A_{ij}\right]^{c}\cdot\left[1-A_{ij}\right]^{q_i-c}\geq A_{O\,i_{req}}(\tau) \tag{20}$$

RESULTS AND DISCUSSION

The sample results presented below were prepared for serviceability assurance subsystem posts in an existing system of municipal bus transport in which 182 municipal buses are in use.

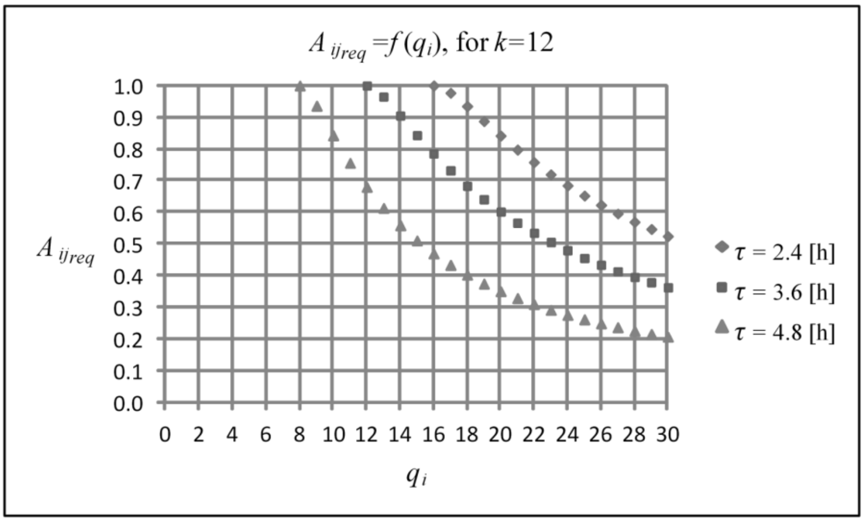

Fig. 1 Required availability of individual post $A_{ij_{req}}$ of functions of the number posts of the *i*-th group q_i, for given values of roadworthiness time period τ and the number of objects rendered roadworthy k

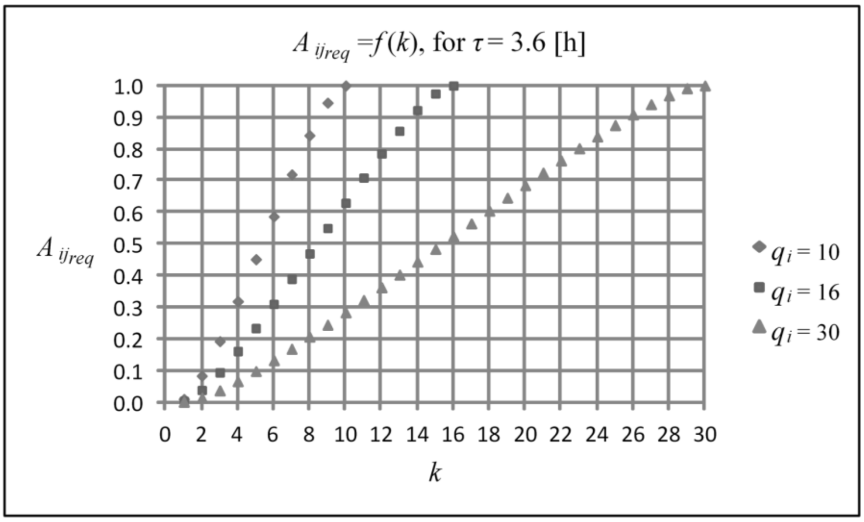

Fig. 2 Required availability of individual post $A_{ij_{req}}$ of functions of the number of objects rendered roadworthy k, for given number of q_i posts of the *i*-th group as well as roadworthiness time period τ

Fig. 1 and Fig. 2 present values of required availability $A_{ij_{req}}$ of posts at *i*-th group of serviceability assurance subsystem, determined in relation with number of posts of the *i*-th group q_i as well as the value of parameters determining the assigned service and repair task (number of objects as well as the time of rendering them roadworthy). For example, for the number of objects rendered roadworthy $k = 12$, the time of rendering $\tau = 2.4$ [h] and the number of posts $q_i = 18$, the required availability of a single post $A_{ij_{req}} = 0.935$(Fig. 1) as well as rendering period $\tau = 3.6$ [h], number of posts $q_i = 10$ and the number of objects rendered roadworthy $k = 8$, the required availability of a single post $A_{ij_{req}} = 0.853$(Fig. 2).

CONCLUSIONS

On the basis of the method presented in the paper, it is possible to select (determine) the minimum required availability of posts at *i*-th group of serviceability assurance subsystem so that the assigned service and repair tasks are carried out properly. It is completed on the basis of the selected criteria for evaluation when actual availability of *i*-th group of serviceability assurance subsystem equals at least the required availability.

The presented method may be utilized in order to evaluate operational availability of an individual post as well as a group of posts of a given type coupled with an appropriate structure or a serviceability assurance subsystem consisting of various types of posts. Providing the required availability of serviceability assurance subsystem is possible due to:

– adjusting the number and structure of service and repair posts,
– adjusting the equipment at posts in order to, when necessary, facilitate carrying out of particular tasks at posts in various groups,
– implementation of posts (devices and tools) of higher reliability, durability, and productivity.

REFERENCES

1. Chen, D-Y., & Trivedi, KS. (2002). Closed-form analytical results for condition-based maintenance. *Reliability Engineering and System Safety, Elsevier, 76*, 43-51.
2. Chen, D-Y., & Trivedi, KS. (2005). Optimization for condition-based maintenance with semi-Markov decision process. *Reliability Engineering and System Safety, Elsevier, 90*, 25-29.
3. Knopik, L., & Migawa, K. (2017). Optimal age-replacement policy for non-repairable technical objects with warranty. *Eksploatacja i Niezawodnosc – Maintenance and Reliability, Vol. 19, No. 2*, 172-178.
4. Kosten, L. (1973). Stochastic theory of service systems. *Pergamon Press, London*.
5. Landowski, B., Perczyński, D., Kolber, P., & Muślewski, Ł. (2016). An example of Markov model of technical objects maintenance process. *Engineering Mechanics, Institute of Thermomechanics Academy of Sciences of the Czech Republic*, 346-349.
6. Marseguerra, M., & Zio, E. (2000). Optimizing maintenance and repair policies via a combination of genetic algorithms and Monte Carlo simulation. *Reliability Engineering and System Safety, Elsevier, 68*, 69-83.
7. Migawa, K., Knopik, L., & Wawrzyniak, S. (2016). Application of genetic algorithm to control the availability of technical systems. *Engineering Mechanics, Institute of Thermomechanics Academy of Sciences of the Czech Republic*, 386-389.
8. Piasecki, S. (1996). Problems of technical organization of machines and means of transport. *Technical Society of Lublin, Warsaw-Lublin*, (in Poland).
9. Szubartowski, M. (2012). Efficiency of repairs performed within the emergency repair subsystem of municipal bus transportation system. *Journal of KONES Powertrain and Transport, 19(2)*, 507-514.
10. Woropay, M., Migawa, K., & Bojar, P. (2010). The model of defining the efficiency of logistics subsystem posts in the transport system. *Journal of KONES Powertrain and Transport, 17(4)*, 607-614.
11. Woropay, M., Żurek, J., & Migawa, K. (2003). Models of evaluation and shaping of operational availability of transport system traffic maintenance subsystem. *ITE Institute for Sustainable Technologies, Radom*, (in Poland).
12. Vaurio, JK. (1997). On time-dependent availability and maintenance optimization of stanby units under various maintenance policies. *Reliability Engineering and System Safety, Elsevier, 56*, 79-89.

Corresponding author:
RNDr. Mirosław Szubartowski, DSc., Management Business and Service, Fordońska 40, 85-719 Bydgoszcz, Poland, phone: +48 340 84 24, e-mail: analityk@karor.com.pl

IMPACT OF THE SHIP GENERATING SETS' POWER FACTOR ON THE DETERMINATION OF THE LOAD FACTOR IN AUXILIARY ENGINE

Dariusz TARNAPOWICZ[1], Zbigniew MATUSZAK[2]

[1] *Maritime University of Szczecin, Poland, e-mail: d.tarnapowicz@am.szczecin.pl*
[2] *Maritime University of Szczecin, Poland, e-mail: z.matuszak@am.szczecin.*

Abstract
In order to evaluate the work of marine power plants, it is necessary, among other things, to determine the load factor in auxiliary engines. The load factor's value is usually used in analyzes of economical exploitation of the power plant, and also in the ecological aspect – limitation of exhaust emissions by auxiliary engines. In many scientific reports and publications, the load factor is determined directly from measurements of loads in generators (active power). The efficiency of the generator is not taken into account. In this article, the authors present the impact of the nature of the generator's load on its efficiency, and hence on the determination of the load factor in auxiliary engines.

Key words: *load factor of auxiliary engines; power factor; efficiency of synchronous generator*.

INTRODUCTION

Statistically, the most commonly used in shipbuilding industry methods of generating electricity on ships are autonomous generating sets consisting of combustion auxiliary engines (AE) and self-excited synchronous generators (G).

For the assessment of the operation of marine power plants, for example in terms of environmental protection or optimization of fuel consumption, it is crucial to determine the load factor for auxiliary engines (LF_{AE}). In the majority of studies, the load factor of auxiliary engines is a direct correlation with active power of the generator's load read on meters or recorders e.g.:(U.S. EPA, 2009). In this case, the excess power of auxiliary engines with respect to generators and the generator's efficiency are not taken into account. The importance of the AE load factor in terms of economy, but also ecology, is perfectly presented by the characteristics of the specific fuel consumption (SFC) depending on the load factor (LF_{AE}) (Tarnapowicz, Borkowski, 2016).

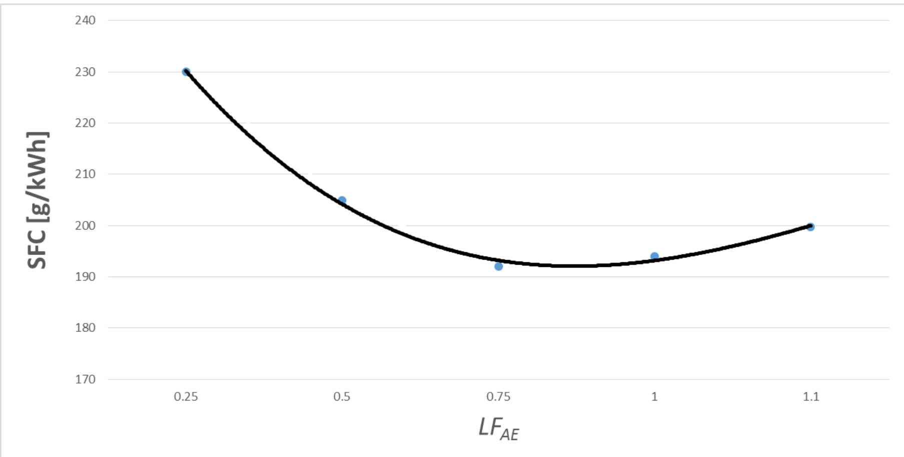

Fig. 1. Dependence of SFC in the function of LF_{AE} load factor (Tarnapowicz, Borkowski, 2016)

Based on the presented characteristics (Figure 1), it is possible to optimize the auxiliary engine's operation – achieving a minimum SFC. This optimization is carried out especially during the parallel operation of generating sets in the so-called asymmetrical work. The parallel work is performed on the ship in order to provide power reserve. Then we can deal with symmetrical work (symmetrical load of generating sets with minimum SFC). The second reason for parallel work of generating sets is to ensure power supply reliability. In this case, low load factor of auxiliary engines *(LF_{AE})* would cause a high

SFC. In order to optimize the work of generating sets, an asymmetric operation is possible (asymmetric load of generating sets).

MATERIALS AND METHODS

Load factor of generating sets.
The load factor of auxiliary engines LF_{AE} that takes into account the excess power of the engine and the efficiency of generators demonstrates the following relation (Nicewicz, Sosiński, Tarnapowicz, 2014):

$$\boldsymbol{LF_{AE}} = \frac{\boldsymbol{LF_{GS}}}{\boldsymbol{\eta_G \cdot \alpha_{NM}}} \tag{1}$$

where:
LF_{GS} – marine generating set (generator) load factor,
η_G – generator‘s efficiency,
α_{NM} – excess power factor of the auxiliary engine to the generator.

Factors of the excess power of the main engine in relation to the generator α_{NM} vary depending to the type of ship and the year of construction. On the basis of researches conducted by the authors, it can be concluded that the smallest values of factors were recorded on ships built after 2000. This leads to the conclusion that the significance of the factor α_{NM} for determination of LF_{AE} is smaller for newly built vessels. A summary of α_{NM} values on selected ships is shown in Table 1(Nicewicz, Tarnapowicz, 2012).

Tab. 1 excess power factor of the auxiliary engine to the generator on the test ships

Type of ship	Year of construction	α_{NM}
container ship	2005	1,05
container ship	1999	1,40
container ship	2001	1,05
container ship	2003	1,06
container ship	1982	1,21
semi-container ship	1986	1,62
bulk carrier	1993	1,60
bulk carrier	2003	1,10
bulk carrier	2000	1,09

The second feature taken into account in the formula (1) is the generator’s efficiency. The efficiency of generator depends on several factors. The specification of synchronous generators includes dependences between the efficiency and the generator’s load (ABB, 2012). At low loads of generators, the efficiency decreases. The second characteristic that affects the efficiency is the power of generators. Based on the analysis of the above-mentioned specification for various powers of generators, it can be stated that the efficiency of generators increases along with the increase of power (Tarnapowicz, Borkowski, 2016). The impact of the load on the generator’s efficiency is very rarely analyzed. As already mentioned, the load of marine generators has a resistive-inductive nature. The power factor (cosϕ) can range from 0 to 1.Figure 2 presents the dependence of the generator’s efficiency taking into account the nature of the load (generator with a power of 2545 kVA). Characteristics are prepared on the basis of specification for the selected generator. This feature shows a high dependence between the generator and the power factor (power factor - cosϕ). For small power factors, the generator’s efficiency decreases by a few percent.

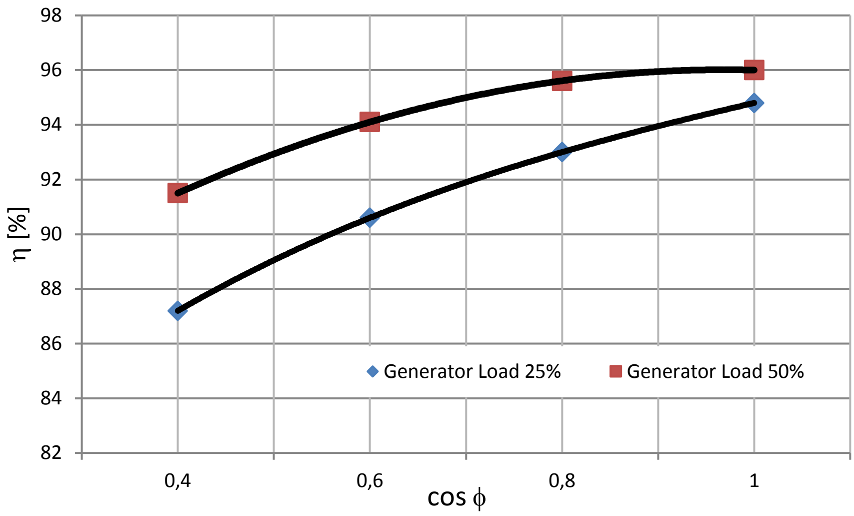

Fig. 2. The efficiency of the generator, depending on the power factor

An electrical ship network is a "soft" network. Powers of individual receivers are comparable to the power of the generating set. The main receivers are electric squirrel-cage motors. Their power changes along with the motor's load (cosϕ). These motors are often underpowered (with a low power factor). Then the efficiency of the generator is lower.

The greatest differences in the nature of generating sets' load can be observed in the parallel operation. According to the rules of qualifying societies, the distribution of active and passive powers between working in parallel generating sets must be uniform (with the same nominal powers of sets). In practice, this situation does not always occur. Controllers of the auxiliary engines' rotations are responsible for the distribution of active powers. On the other hand, the distribution of passive powers (the nature of the generators' load) is controlled by voltage regulators for generators – their static characteristics (U=f (Q) where U – generator's load voltage, Q – Load of the generator with passive power). The vector diagram of synchronous generators (working in parallel in case of equal loads with active powers and different loads with passive power) is presented in Figure 3. It was made on the basis of equations (2):

$$\begin{aligned} \underline{E_1} &= \underline{U_1} + \underline{I_1} \cdot R + j \cdot \underline{I_1} \cdot X_r = \underline{U_1} + \underline{\Delta U_{I \cdot R}} + \underline{\Delta U_{I \cdot x}} \\ \underline{E_2} &= \underline{U_2} + \underline{I_2} \cdot R + j \cdot \underline{I_2} \cdot X_r = \underline{U_2} + \underline{\Delta U_{I \cdot R}} + \underline{\Delta U_{I \cdot x}} \end{aligned} \tag{2}$$

where:

E_1, E_2 - SEM induced in the winding of an armature during the generators' loading
U_1, U_2 – voltage during the load of generators
I_1, I_2 – generator load currents,
R – resistance of the armature's winding
X_r – reactance for the diffusion of the armature's winding

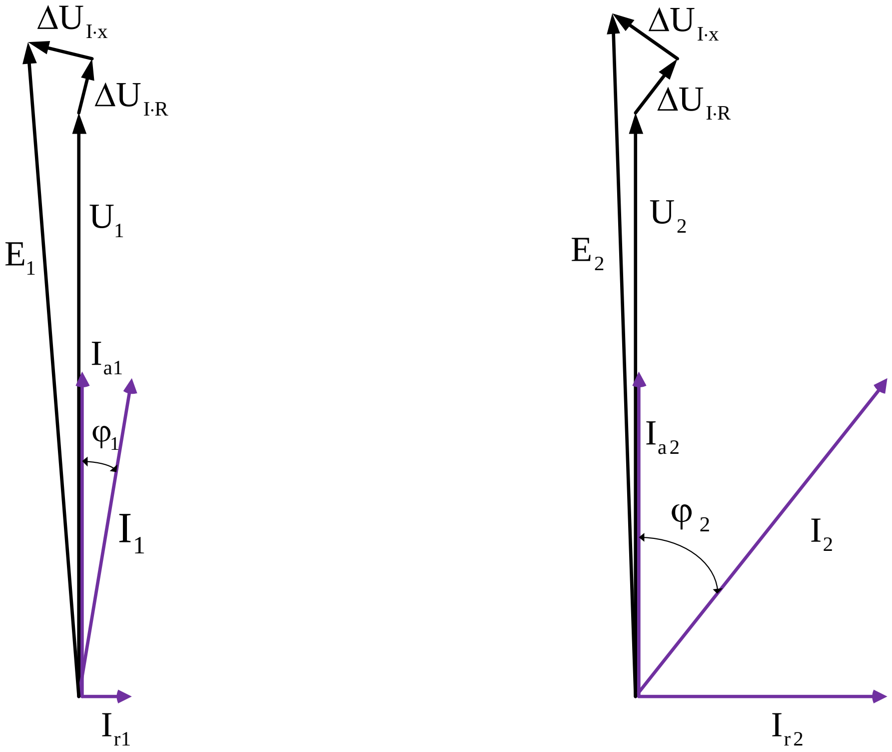

Fig. 3. Phasors for generators in parallel operation at different load of generators with passive power (different cos ϕ of generators).

RESULTS AND DISCUSSION

Figure 4 shows an example of changes in a power factor of a generator in the generating set for a modern container ship during one day. The vessel with a total length of 286.45 m was built in 2009. The researches were conducted during a sea voyage at the operation of an independent generating set. The measurement system enabled the record of data at intervals of one second. The measurements started on 3 February 2013 at 8 a.m. (traditional start of the machine watch on the ship) and ended at 8 a.m. on the following day (the end of machine watch). The time axis was formatted in such a way that subsequent values in seconds correspond to full hours.

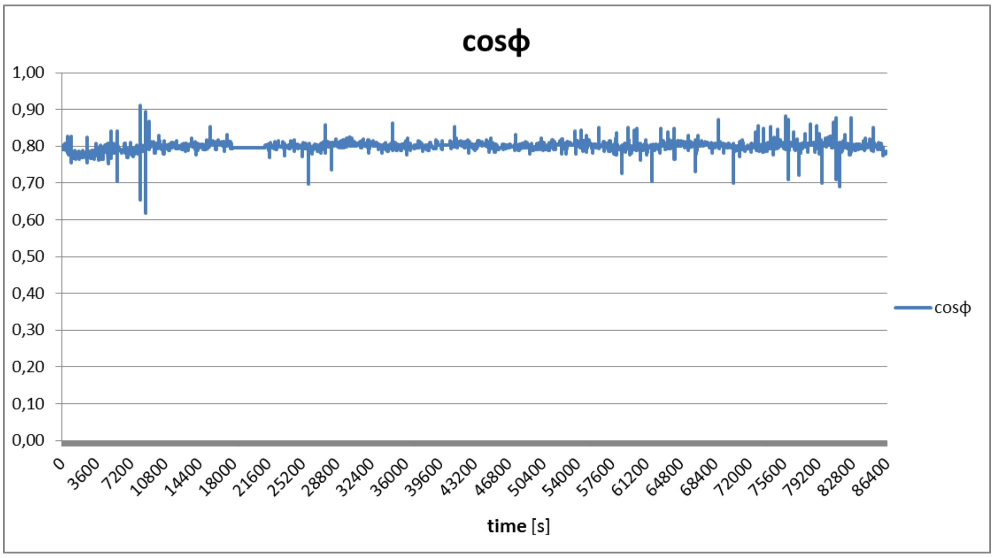

Fig. 4. Change in the nature of the load (cos ϕ) during the operation of a generating set within one day (sea voyage).

During the operation of a single generating set on the selected vessel, the power factor (cos ϕ) changed in the range from 0.62 to 0.92. In other cases, changes (cos ϕ) may be even greater.
Figure 5 shows the course of changes in power factor of parallel working diesel - generators on a modern bulk carrier. The vessel with a total length of 228 m was built in the year of 2013. The study was conducted during ship maneuvers at a port. The measurement system recorded data in 15 minute intervals.

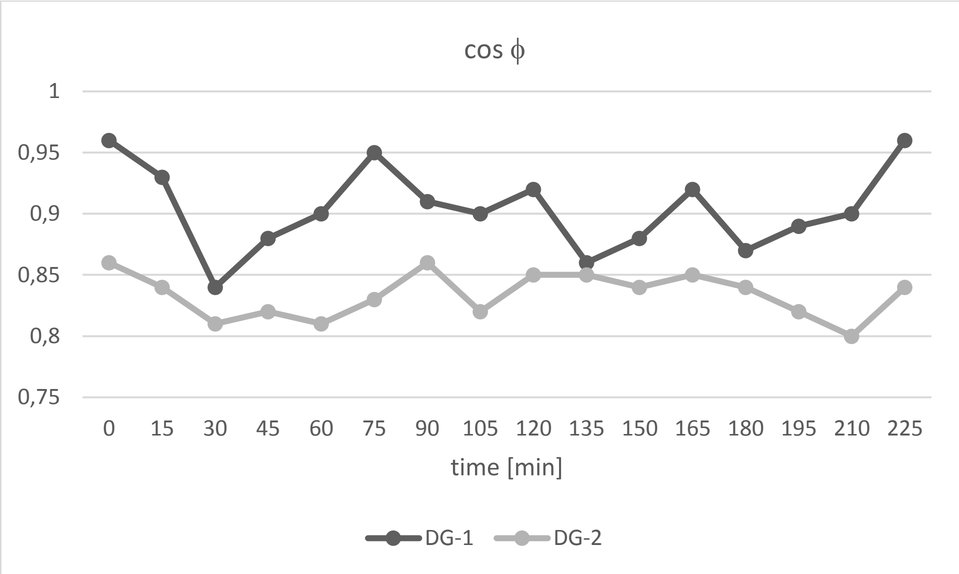

Fig. 5. Change in the nature of the load (through cos ϕ) during the parallel operation of two generator sets (maneuvers)

During parallel operation of two identical generator sets, the ratio of power factor oscillated between 0.8 and 0.96.
The results of both autonomous and parallel work of the generator sets have confirmed some changes in the nature of generator's load (through cos ϕ). This leads to a change in the efficiency of the generators, and thus affects the determination of the generator load factor.
The calculation of the load factor without taking into account cos ϕ is burdened with a large error caused by the wrong calculation of efficiency.

CONCLUSIONS

The load factor of marine auxiliary engines must be determine taking into account the factor of excess power of the engine in relations to the generator and the generator's efficiency (above all). One of the important factors affecting the efficiency is the nature of the generator's load (cos ϕ). The operation of a single generating set (cos ϕ) is determined by the load – usually the asynchronous engine is not always burdened with power rating. During the parallel operation of generating sets, there may be an uneven distribution of passive powers, and hence – a different cos ϕ of generators.

ACKNOWLEDGMENT

This research outcome has been achieved under the research project: Nowoczesne technologie w systemach "Shore to Ship" No 2/S/IEiAO/16 financed from a subsidy of the Ministry of Science and Higher Education for statutory activities

REFERENCES

1. U.S. EPA (2009) Environmental Protection Agency: Current Methodologies in Preparing Mobile Source Port-Related Emission Inventories. Final Report. *IFC INTERNATIONAL*. April 2009.
2. Tarnapowicz, D., Borkowski, T. (2016). Analysis of main ship propulsion operation

with shaft generator. *57th International Conference of Machine Design Departments (ICMD),* 2016 p 287-292
3. Nicewicz, G., Sosinski, M., Tarnapowicz, D. (2014) Identification of power factor in marine electrical grid. *Geoconference on energy and clean technologies, vol II.Book Series: International Multidisciplinary Scientific GeoConference-SGEM,* 2014 (pp. 391-398).
4. Nicewicz, G., Tarnapowicz D. (2012) Assessment of marine auxiliary engines load factor in ports. *Management Systems in Production Engineering* . No 3(7), 2012 p 12-17
5. ABB. (2012): Low Voltage Synchronous Generators for Industrial Applications, Technical Specfcations AMG2 2012, http://www.abb.com/product/2012.

Corresponding author:
Dariusz Tarnapowicz, Ph.D.Eng, Faculty of Marine Engineering, Institute of Marine Electrical Engineering and Vessel Automation, Maritime University in Szczecin, 70-500 Szczecin, Poland, and phone: 091-4809460, e-mail: d.tarnapowicz@am.szczecin.pl
Zbigniew Matuszak Prof. Eng, Faculty of Marine Engineering, Institute of Marine Propulsion Plants Operation, Maritime University in Szczecin, 70-500 Szczecin, Poland, phone: 091-4809414, e-mail: z.matuszak@am.szczecin.pl

QUALITY OF GEAR MESH AND ITS EFFECTS ON TRANSMISSION ERROR

Miroslav TROCHTA[1], Zdeněk FOLTA[2], Jan PAVLÍK[3]

[1] *Department of Machine Parts and Mechanisms, VŠB-TU Ostrava*
[2] *Department of Machine Parts and Mechanisms, VŠB-TU Ostrava*
[3] *Department of Machine Parts and Mechanisms, VŠB-TU Ostrava*

Abstract
This contribution shows the measuring results on the several involute gears. On every gear pair, actual gear mesh was assets based on its footprint and then transmission error was measured. Results of this measurements shows quality of contact, of involute gears and its effects on the transmission error of gears.

Key words: *transmission error; gear; gear mesh; footprint*

INTRODUCTION

The transmission error is generally considered to be indicator of overall gear quality. It's also closely related to the gear noise. Because its relation with gear quality it's also related with real contact conditions between tooths of gears. Contact condition between gears can be evaluated with knowledge of real total contact ratio. This can be determinate with footprint method. As you can see on Fig. 1 (Moravec, et al., 2009) contact ratio have quite good impact on gear noise and because of this it should also have impact on transmission error. Real contact ratio can differ from calculated one due to the manufacturing inaccuracies of gears and shafts, shaft bends, etc. This article will show how transmission error change with real total contact ratio of gears.

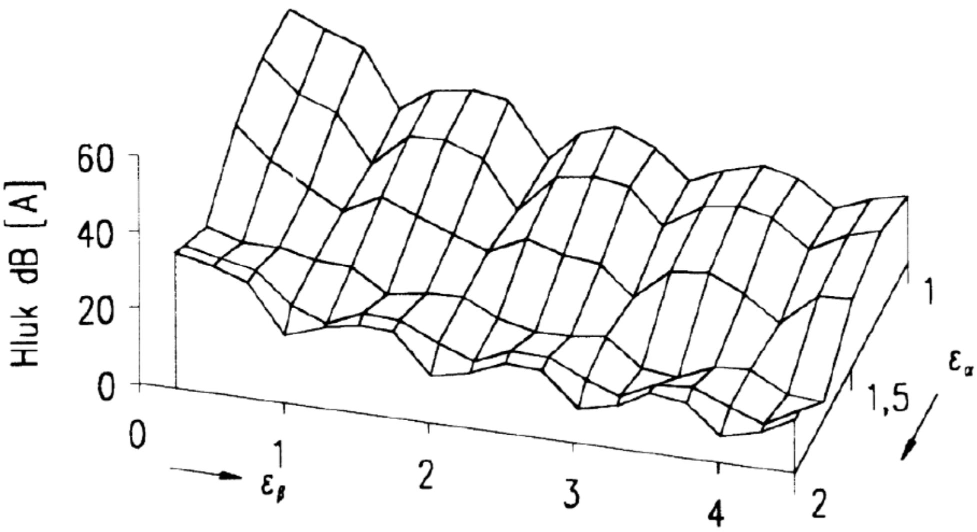

Fig. 1 Measured data

MATERIAL AND METHODS

Quality of gear mesh is evaluated with use of footprint method (*Pavlík, 2016*). This method is based on putting paint on gear and then under defined torque load made one spin of gear and take a look on the foot print that is made during contact of painted gears with other gear teeth. Example of these footprints can be seen on Fig. 2. Footprints are from same gear pair only different is in direction of load this mean in side of tooth's which are in contact together. On Fig.2 we can see that on one side is contact almost perfect bellow picture on Fig. 2 on the other side not so much top picture on Fig. 2. To make this footprints load of 50 N.m where applied on pinion gear.

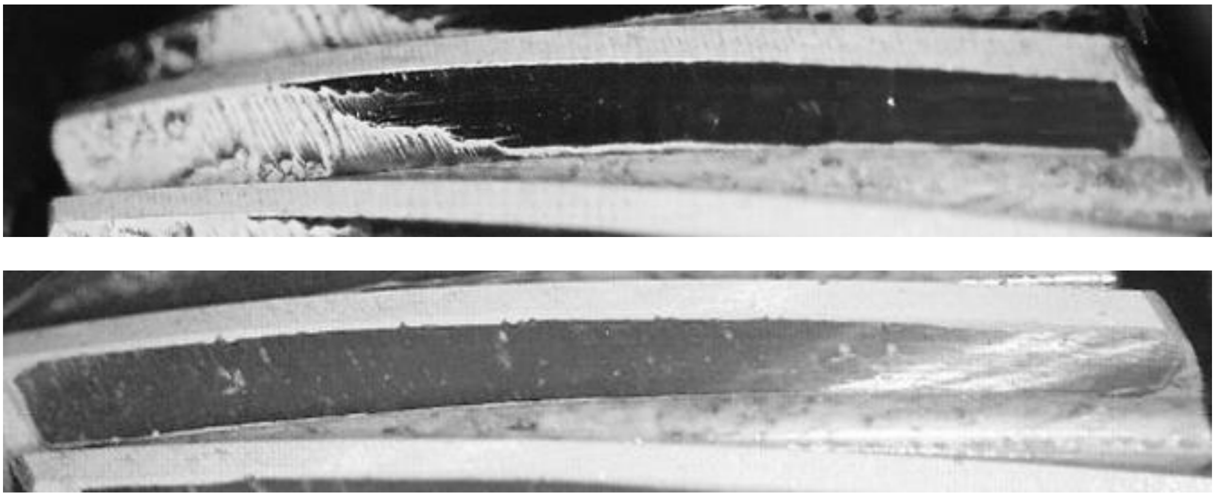

Fig. 2 Footprint of the gear pair 1

Real contact ratio was determinate by comparing areas of real contact and area of theoretical contact of gear using Autodesk AutoCAD software Fig.3. For gear pair on Fig.2 theoretical contact ratio is 4,48 this correspond with real ratio of contact on button picture on fig. 2. If we analyse real contact ration for contact on the top picture of Fig.2 than we get contact ratio 3,14.

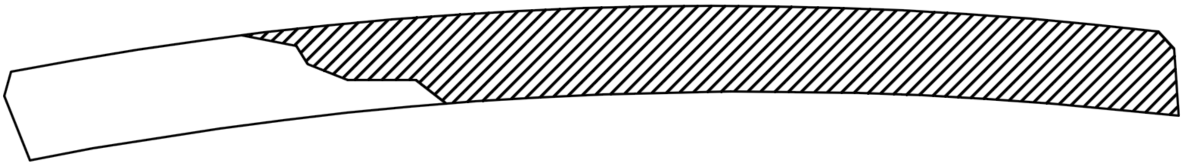

Fig. 3 Footprint area analysis

We recognize two types of transmission error, dynamic transmission error and static one (*Houser, Blankenship, 1989*). For the purposes of this article if transmission error is mentioned it mean dynamic transmission error. Difference between these two are in the condition of measurement. Static transmission error is measured with zero or very small RPM of shafts, dynamic TE its measured at relatively height speeds, basically as close to the real device as can be. As for the values of transmission error is evaluated with peak to peak method as shown on Fig.4.

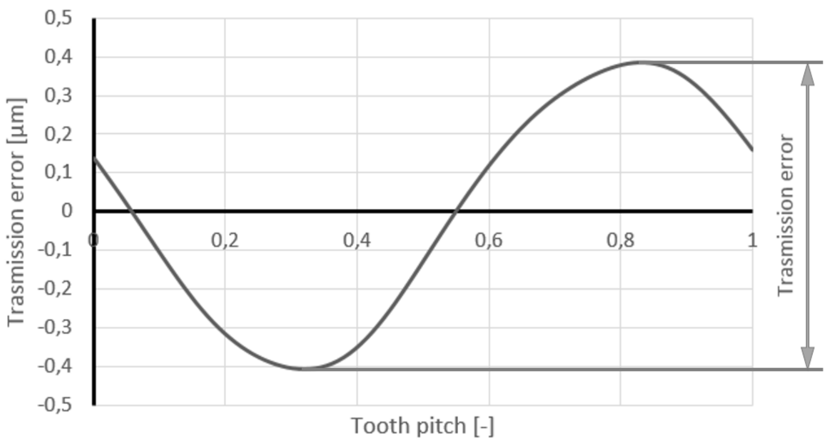

Fig. 4 Peak to peak transmission error

Transmission error measurement is performed by measuring angular position of each gear on not-loaded end of the shafts (*Mark, 2013; Tůma, 2014*) at testing device specially made for such measurement. Because transmission error is value that depends on a lot of parameters during measurements we must be sure to have same starting condition for measurement. To evaluate transmission error methodology was changed according to the latest finding. Change mainly consist of measurement setup and stabilization of measurement conditions and in the evaluation part of measurement the averaging of transmission error signals that is mention in (*Tůma, 2014*) is not used. But every contact of each tooth pair is evaluated individually and then these results are averaged to get the average transmission error.

RESULTS AND DISCUSSION

After measurement on 4 gear pairs (two pairs with CSN geometry and two with HCR) Fig.5. We got data in table 1 these shows total contact ration and measured transmission error.

Fig. 5 Pair of tested gears

Tab. 1 Measured data

Total contact ratio -	Transmission error μm	Total contact ratio -	Transmission error μm
4,48	1,113	5,37	0,682
4,48	1,091	5,37	0,552
3,34	1,452	3,38	1,159
3,34	1,211	3,38	1,279
5,37	0,616	4,48	0,906
5,37	0,544	4,48	0,954
3,29	1,167	3,45	1,421
3,29	1,539	3,45	1,220

Values from table 1 can be seen in graph on Fig.6. Here can be clearly seen that theory and measurement are alight. With increasing of the total contact ratio, transmission error is decreasing.

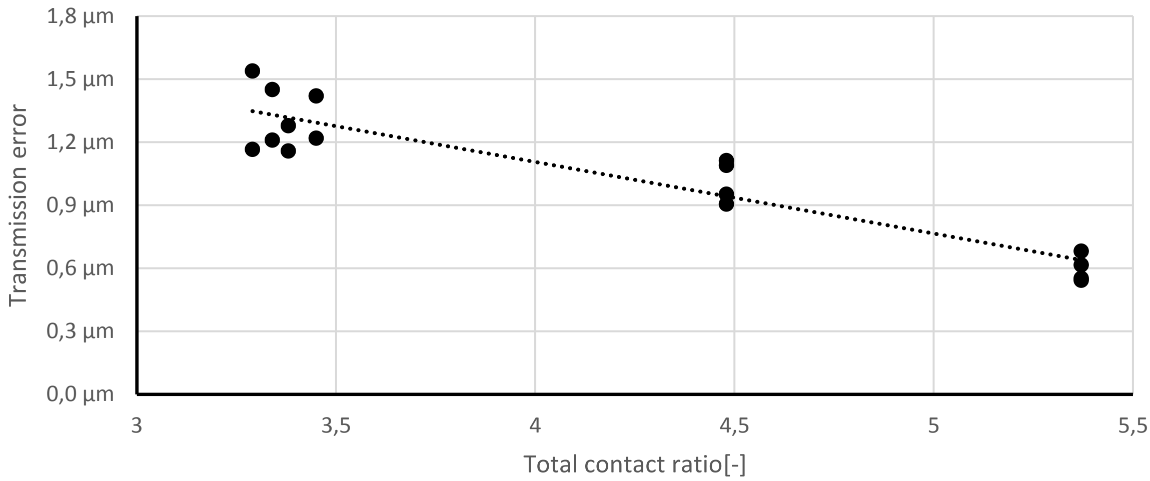

Fig. 6 Graph of Transmission error to total contact ratio

On Fig. 6 we can see that real contact ratio must be measured, because if we do not do this measurement we cannot be sure how good real contact between pairs of gears is. Contact ratios 4,48 and 5,37 corresponds with perfect contact of gears and its equal to design total contact ratio. Other values are calculated according to the area of real contact.

CONCLUSIONS

The noise and vibrations generated by gears, its topic that companies from automotive industry deals with on daily basis. Transmission error is indicator of overall gear quality and it seems that it is closely related to the many process that can occur during gear contact. In article, its shown how total contact ratio influence transmission error. From results of measurement we can say that at least for transmission error value bigger total contact ration its always better.

ACKNOWLEDGMENT
This research has been realized using the support of Technological Agency, Czech Republic, programme Centres of Competence, project # TE01020020 Josef Božek Competence Centre for Automotive Industry. This support is gratefully acknowledged.

REFERENCES

1. Moravec, V., Dejl, Z., Němček, M., Folta, Z. Havlík, J. (2009). *Spur gears in vehicle gearboxis.* Ostrava: VŠB - TU Ostrava
2. Mark, W. D. (2013). *Performance-based gear metrology kinematic-transmission-error computation and diagnosis.* Chichester: Wiley.
3. Houser, D. R., & Blankenship, G. W. (1989). *Methods for Measuring Gear Transmission Error Under Load and at Operating Speeds*. SAE Technical Paper Series. doi:10.4271/891869.
4. Tůma, J. (2014). *Vehicle gearbox noise and vibration: measurement, signal analysis, signal processing and noise reduction measures*. Chichester: Wiley.
5. Pavlík, J. (2016). *Measurement of Gears Footprints.* Ostrava: VŠB - TU Ostrava.

Corresponding author:
Ing. Miroslav Trochta., Department of Machine Parts and Mechanisms, Faculty of Mechanical Engineering, VŠB-TU Ostrava, 17.listopadu 15, Ostrava, 708 33, Czech Republic, phone: +420 597 323 393, e-mail: miroslav.trochta@vsb.cz

TRANSIENT THERMAL SIMULATION OF WORKING COMPONENTS OF MECHATRONIC SYSTEM FOR DEEP DRAWING OF MOLYBDENUM SHEETS

Michal TROPP*[1], Mária TOMÁŠIKOVÁ[1], Ronald BAŠŤOVANSKÝ[1], Leszek KRZYWONOS[2], František BRUMERČÍK[1], Zbigniew KRZYSIAK[3]

[1]Department of Design and Mechanical, Faculty of Mechanical Engineering, University of Žilina Elements, Univerzitná 1, Žilina 010 26, Slovakia
[2]Lublin University of Technology, Faculty of Mechanical Engineering, 36 Nadbystrzycka Street, 20-618 Lublin, Poland
[3]University of Life Science in Lublin, Faculty of Production Engineering, 28 Głęboka Street, 20-612 Lublin, Poland

Abstract
The subject of this article is an optimization of the concept of a device for deep drawing in extreme conditions. In this case, extreme conditions represents drawing process in vacuum by high temperatures required by molybdenum sheets forming. The first part of the paper deals with the design of working components. The paper describes also boundary conditions of transient thermal simulations of working components with their results.

Key words: *deep drawing; molybdenum; thermal simulation, reinforced shell components*

INTRODUCTION

The subject of this article is an introduction of the concept of a device for deep drawing in extreme conditions. In this case, extreme conditions represents drawing process in vacuum by high temperatures required by molybdenum sheets forming. Article deals with description of possible variants of the mechanism structure and their functional changes. The paper describes also with the results of the thermal simulations by evaluating the variants.
Deep drawing is a process in which the sheet is formed into a deep container free from cracks. The design and control of deep drawing is apart of the choice of material and also on the links between forming tools, mechanisms of plastic deformation, and the device used to control the flow of material during the process. Pressure, shape and height of stamper, forming speed, lubrication, blank holder force, blank holder gap and material have the biggest influence on working process.

MATERIALS AND METHODS

Boundary conditions and design of working components

For correct process of deep drawing of molybdenum sheet, higher temperature of formed material is required, due the bad ductility of molybdenum in temperatures near the 20°C. During our process the formed material needs to be warmed in temperature range from 200°C to 300°C.
On the Fig. 1 is visible, why are required so high forming temperatures. At room temperature, strength of molybdenum is 1035MPa, while by 200°C is approx. 880MPa and by 300°C is strength of molybdenum only 800MPa. Also ductility of material raised from 3% to 12% by 300°C.
This part of paper deals with design of chosen part of device. On Fig. 2 is structure of working part of device is shown. Transparent part on picture is a vacuum chamber, which is required due the poor oxidation resistance of molybdenum by temperatures highest than 300°C. Next components are:

- a – pistons
- b – stamper
- c – punch
- d – blank holder

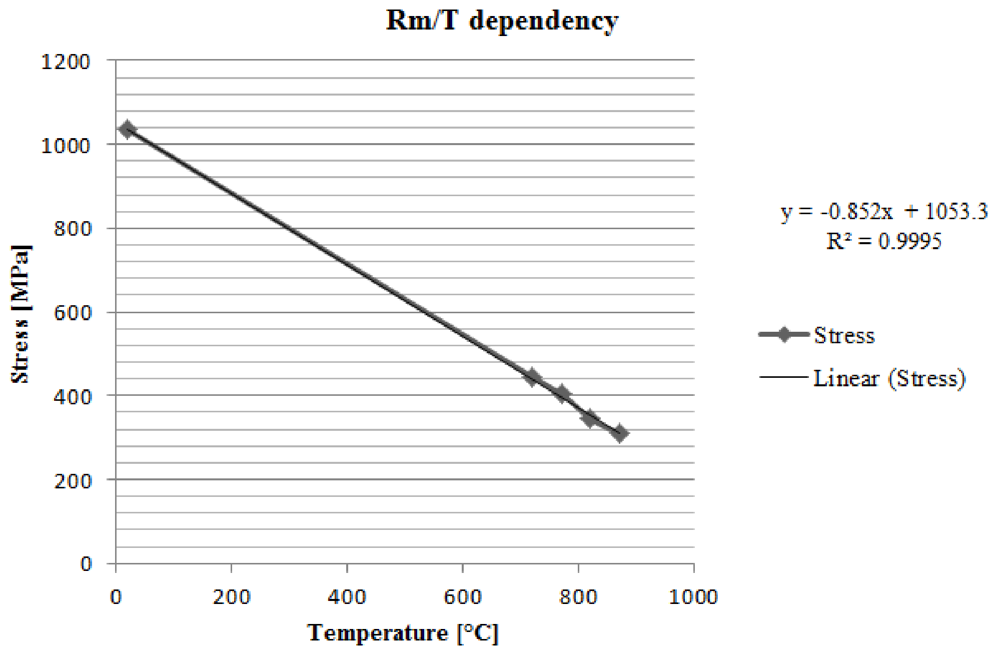

Fig. 1 Graph of Rm/T dependency of molybdenum

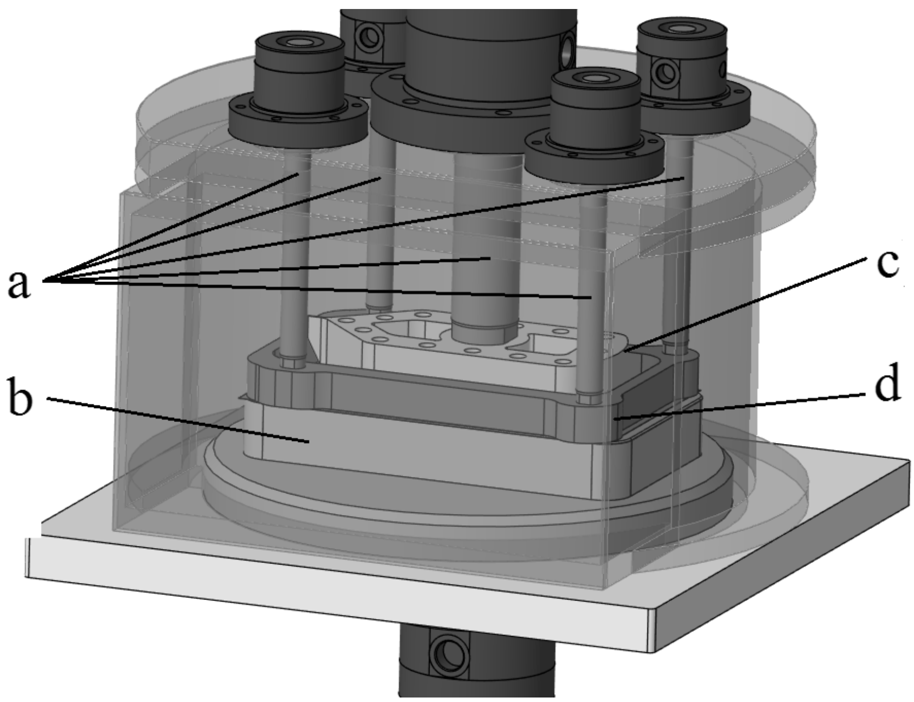

Fig. 2 Structure of working part of mechatronic system

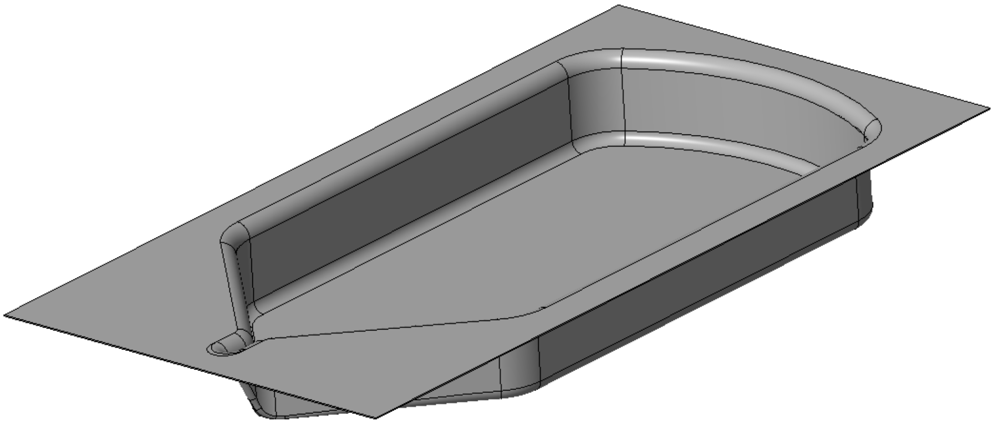

Fig. 3 3D CAD model of molybdenum sheet shaped into the finally form

Picture number 3 shows finally shape of the product. Next very necessary step in design on this mechatronic system is thermal simulation of components which are the part of working process. The most thermally stressed parts of device are punch and stamper. Simulation starts with basic models of components. Whole evolution of components shapes is possible to see on next picture.

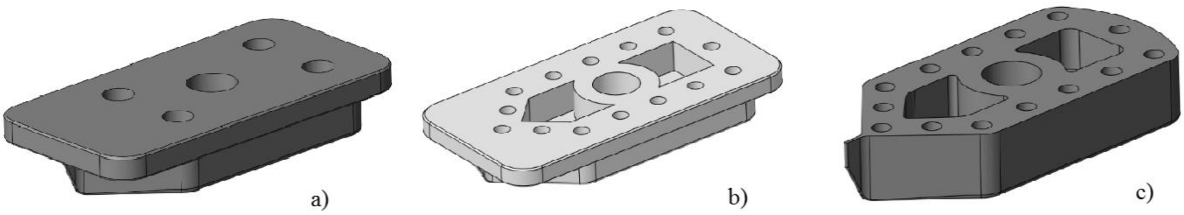

Fig. 4 Changes of shape and mass of punch

Process of optimization of punch and stamper was based on lightening of component (Fig. 4). The very first model of punch (a) was made only with drilled holes for piston and four heaters. The second model (b) has drilled more holes and also milled two more holes near the central area of unloaded part of component and at the end third model of punch was milled and drilled such like second one, but edges of punch was also removed.

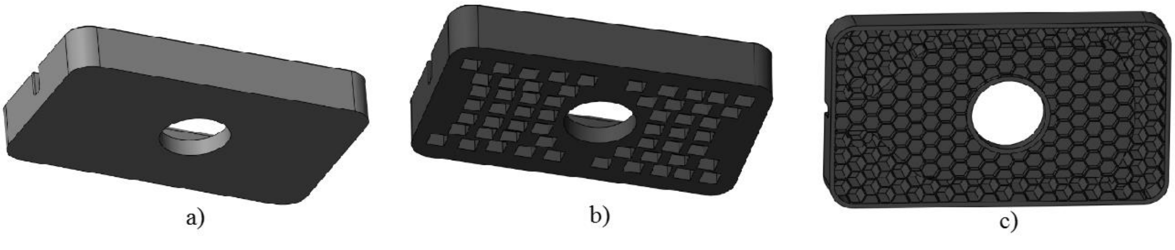

Fig. 5 Changes of structure of stamper

By lighten of stamper, other principle was used (Fig. 5). First model (a) was only a solid geometry without some structure. The second model (b) was lightening by using a simply pattern of square shaped holes. The last model (c) of stamper was made as a shell which is reinforced by honeycomb structure. This structure is light and sufficiently strong in one axis of strain.

RESULTS AND DISCUSSION

Process and results of simulations

This part of paper describes transient thermal simulations. In this case was there a four simulations in which every fall had a different configuration of stamper and punch. The aim of those calculations was an influence of mass loss of working component of the pre-process temperature of molybdenum sheet. All components was during the simulation in heating position, which means that blank holder, stamper and punch was in the contact with an undistorted plate of molybdenum sheet. Heating power was specified on 6000W.s^{-1} and duration of simulation was 1800s.
Of course all components near the source of heat was influenced by high temperatures, but for deep drawing process more is important the temperature of forming material. That is, why in the following results, temperatures of components are ignored.
On the Fig.6 we can see a result of simulations. Each simulation had the same heating power and duration. On Y-axis represents the temperature of material and on X-axis time of simulation. For the first simulation were used punch and stamper the both in the a) variants. Maximal temperature of molybdenum sheet on the end of the simulation was 322.59°C. This temperature was then set as the reference temperature. The gradient of temperature is shown on upper left side of Fig. 6.
Second simulation was made with punch of b) type, with a) stamper. Result of simulation – upper left side of the same picture, 272,54°C. Althought the mass of the working components was lower then in first simulation, finally temperature was lower then before. That was caused by different pattern of sources of heat, which ca be considered as a mistake in simulation process.
Third simulation represents b) type punch and b) type stamper. Pattern of heating devices was returned to the first layout. That causes better comparative ability of results. The results of simulation, shows on the left bottom side of Fig.6, that the highest temperature of foming material before process is 358,74°C. Now is visible, that a mass loss brings a positive outcome.
In the last simulation was used c) model of punch with c) model of reinforced shell model of stamper.

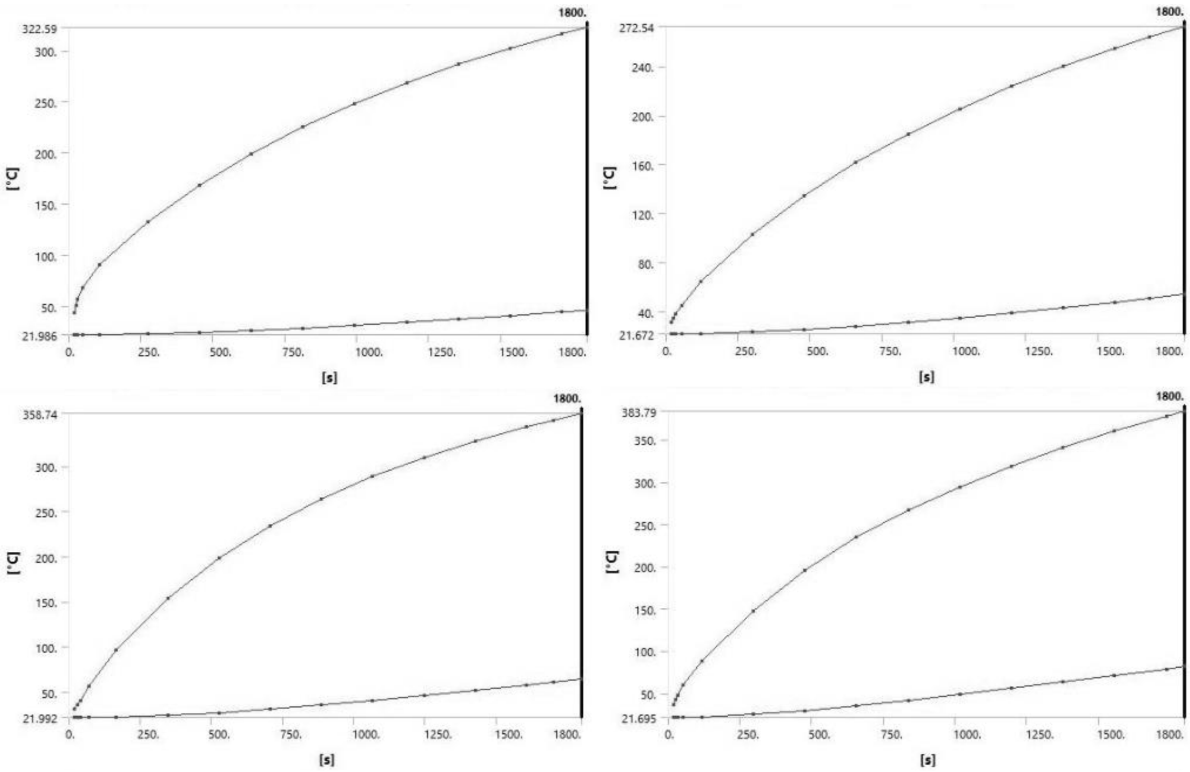

Fig. 6 Gradients of temperature in simulations

CONCLUSIONS

Universal method for transient thermal simulation of mechatronic system for deed drawing in extreme conditions was determined. The estimation can be based only on dimensions and type of working material. This procedure can be useful when the temperature of working material is specified and temperatures of working component are required.

ACKNOWLEDGMENT

This paper presents results of work supported by the Slovak Scientific Grant Agency of the Slovak Republic under the project No. VEGA 1/0077/15.

REFERENCES

1. Arab. N., Nazaryan E. A., Arakelyan M.: Investigation to production molybdenum container to growth single crystals by deep drawing process. International Journal of Mechanical and Materials Engineering (IJMME), Vol. 5 (2010), No. 1, 116-122.
2. Brumercik F., Brumercikova E., Bukova B.: Mechatronic and Transport System Simulation. Applied mechanics and materials, Vol. 803 (2015), pp. 201-206.
3. Faturik L., Trsko L., Hrcek S., Bokuvka O.: Comparison of structural design in high and ultra-high cycle fatigue regions. Transactions of FAMENA, Vol. 38, No. 4 (2014), pp. 1-12.
4. Cheng J., Nemat-Nasser S., Guo W.: A unified constitutive model for strain-rate and temperature dependent behavior of molybdenum. Mechanics of materials 33 (2001) 603-616.
5. Kołtunowicz T. N., Zukowski P., Sidorenko J., Bayev V., Fedotova J. A., Opielak M., Marczuk A.: Ferromagnetic resonance spectroscopy of CoFeZr-Al2O3 granular films containing “FeCo core – oxide shell” nanoparticles. Journal of Magnetism and Magnetic Materials, 421 (2017) 98–102.
6. Krolczyk G. M., Nieslony P., Krolczyk J. B., Samardzic I., legutko S., Hloch S., Barrans S., Maruda R. W.: Influence of argon pollution on the weld surface morphology. Measurement 70 (2015) 203-213.
7. Krolczyk J. B., Gapinski B., Krolczyk G. M., Samardzic I., Maruda R. W., Soucek K., Legutko S., Nieslony P., Javadi Y., Stas L.: Topographic inspection as a method of weld joint diagnostic. Technical Gazette 23, 1(2016), 301-306.
8. Martikan, M., Brumercik F., Bastovansky R.: Development of Mechatronic Deformation System. Applied mechanics and materials, Vol. 803 (2015), pp. 173-178.
9. Meng B., Wan M., Wu X., Zhou Y, Chang Ch.: Constitutive modeling for high-temperature tensile deformation behavior of pure molybdenum considering strain effects. journal of refractory metals and hard materials 45 (2014) 41-47.
10. Meng B., Wan M., Wu X., Zhou Y.: Development of thermal deep drawing system with vacuum environment for difficult-to-deformation materials. Trans. Nonferrous Met. Soc. China. 22 (2012), pp. 254−260.
11. Meng B., Fu W. M., Wan M.: Drawability and frictional behavior of pure molybdenum sheet in deep-drawing process at elevated temperature. Journal of advanced manufacturing technology, 78 (2015) 1005-1014.
12. Rudawska A.: Influence of the thickness of joined elements on lap length of aluminium alloy sheet bonded joints. Advances in Science and Technology Research Journal, Volume 9, No. 27, 2015, 35–44.
13. Sawicki B., Miaskowski A.: Nonlinear higher-order transient solver for magnetic fluid hyperthermia. Journal of Computational and Applied Mathematics, 270 (2014) 143–151.
14. Swić, A., Draczew, A., Gola, A.: Technology of heat treating-straightening of long shafts with low rigidity. Advances in science and technology-research journal 2016, Vol. 10 Is. 31 pp. 207-214
15. Swić, A., Draczew, A., Gola, A.: Method of achieving accuracy of thermo-mechanical treatment of low-rigidity shafts. Advances in science and technology-research journal, 2016 Vol. 10 Is. 29 pp. 62-70.
16. Walczak M., Pieniak D., Zwierzchowski M. The tribological characteristics of SiC particle reinforced aluminium composites. Archives of Civil and Mechanical Engineering, 15(1), 2015, 116–123.
17. Walczak M., Zwierzchowski M., Bieniaś J., Caban J.: The tribological characteristics of

Al-Si/graphite composite. Tribologia 1/2017, pp. 97–104.
18. Zmindak, M., Donic, T., Jurik, P.: Numerical simulation of rectangular deep draw containers made from thin molybdenum sheet. IOP conference series: Materials science and engineering. 159 (2016) [8] pp.

Corresponding author:
Ing. Michal Tropp, Univerzity of Žilina, Faculty of Mechanical Engineering, Department of Design and Mechanical Elements, Univerzitná 1,Žilina 010 26, Slovakia, e-mail: michal.tropp@fstroj.uniza.sk

GEOMETRIC SPECIFICATION OF COMPLEX SPATIALLY-ORIENTED AND COMPLIANT COMPONENTS I.

Václav VANĚK[1], Roman POLÁK[2]

[1,2]Department of Machine Design, University of West Bohemia in Pilsen, Czech Republic

Abstract
The article is focused on geometric specification of complex spatially-oriented and compliant components. Manufacturers of complicated and flexible machine parts, particularly in the automotive industry, are finding themselves in almost insoluble problems when designing TS and preparing their technical documentation. These problems arise mainly in describing the geometrical properties of technical products in order to ensure their errorless production and control in subsuppliers. Unfortunately, GPS standards are not flexible enough to meet these specific requirements, and from this reason manufacturers or their consortiums respond to this situation by defining their own procedures and regulations that allow them to solve these problems. However, the negative consequence of this state is that there is no general agreement and consistency in the description between the individual internal rules of the firms and this creates considerable problems for the subcontractors, who cannot properly read the technical documentation and correctly set up production and control procedures, which in some cases can lead to a fatal consequences. The aim of this paper is to identify these inconsistencies and propose ways to solve the above-mentioned problems.

Key words: *reference points system; RPS; local coordinate system, global coordinate, CMM.*

INTRODUCTION

Correct localization and orientation of machine parts and their design parameters on the drawing, confusion in defining coordinate systems and their description, removal of degrees of system freedom and related fixation of movement of tolerance fields of geometric tolerances, determination of exact position of datums and directions of measurement for complex parts, definition of pressure and free states of flexible parts, uncertainty of parameter specification in dimensioning and resulting uncertainty for control and measurement, and a number of other uncertainties are the impetus for introducing a certain system and establishing clarity in the specifications of individual GPS parameters.

MATERIALS AND METHODS

If we take into account the needs of the automotive industry, which is very widespread in the Czech Republic, we have to introduce two coordinate systems. Global Coordinate System, which is a system of the whole car and is used for determining the localization of concrete machine part of in the whole system and a local coordinate system, which is used for specification of the geometric parameters of a particular part, for their control and measurement. The relationship between these coordinate systems is defined by reference points (RPS) of technical system (TS). Figure 1 illustrates the use of three methods of designating coordinate system axes. In the table showing the removal of the degrees of freedom, the directions of the axes according to the orientation of the car body (Fore/Aft; Up/Down; Cross/Cross) are given. There is also a similar system where O.L. (object location) is followed by the identification of the direction. The last direction is marked ℄, which is mistakenly taken over with the ISO drawing of piping systems, where it indicates the axis direction, the definition of which is completely absent and would be needed it for hose drawings in the automotive industry. Other directions can be indicated by a coordinate grid where the individual lines represent Water Line (WL), Buttock Line (BL), and Traverse Line (TL). In Figure 1, the coordinates of the reference points of the technical system (RPS) are designated X, Y, Z. In the drawing of Figure 1, it is very difficult to compare individual coordinate systems according to axes directions, which are however differently labeled. The solution is to introduce the unambiguous and usual designation of the coordinate axes and rotations [x, y, z, r_x, r_y, r_z]. The designer will determine the location and orientation of the global GCS coordinate system on the model of a complex technical system GCS [0,0,0,0,0,0]. In the production drawings, local coordinate systems (LCS) are localized. The position of origin and rotation of the LCS is given to the GCS in the so-called absolute coordinates and is given in the table for RPS points LCS [ACx, ACy, ACz, r_x^{GCS}, r_y^{GCS}, r_z^{GCS}] in the production drawing. The relevant specifications given in the drawing are then given in relative coordinates related to LCS. It is then possible to specify other target coordinate systems (TCS) in the drawing. In this system, it is necessary to define the origin with the RPS point and its rotation to the LCS, either by angles of coordinate rotation or more simply by coupling properties such as axial $TCS_{P1(XA,Y,Z,\ rx^{LCS})}$. The designation indicates that x is in the direction of the axis of the element passing through the RPS by the point P1 and the TCS_{P1} is rotated about the X LCS by r_x^{LCS}. The origin of TCS_{P1} lies in the RPS point marked P1. TCS are suitable, for example, for determining the degrees of freedom of the end sections of flexible systems.

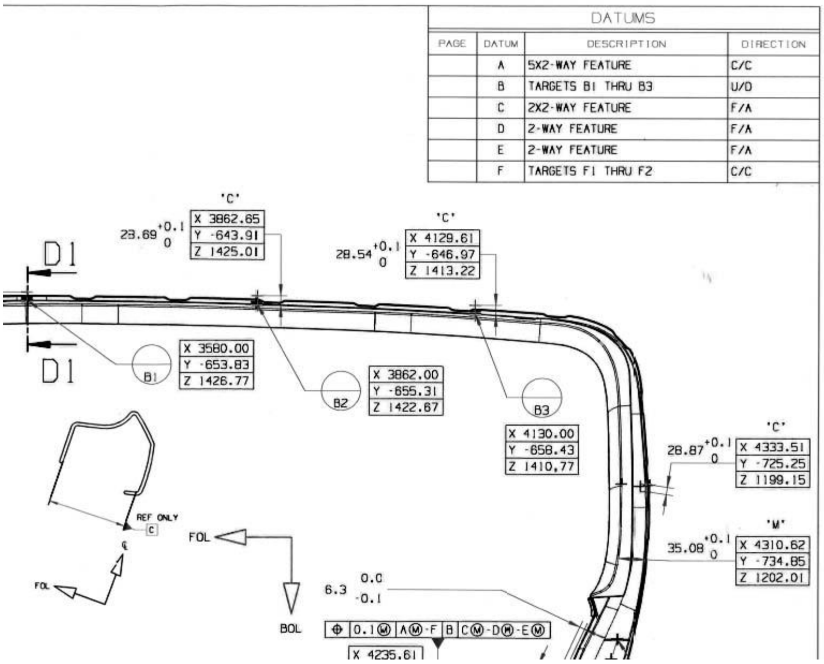

Fig. 1 Technical drawing (coordinate systems, table of degrees of freedom, RPS references)

RESULTS AND DISCUSSION

Similarly to reference datums elements, reference points can be used to set, ensure the correct position and orientation of a component. The establishment of the RPS should be based on a functional approach again, depending primarily on the purpose of the RPS:

1) RPS used for linking 3D models in CAD systems.
These RPS used to provide a link between the models defined in the GCS and the machine parts defined in the LCS. This makes it easy to fit individual parts into the overall TS (TS) model and to easily assess the smooth surface continuity, collision solutions, and so on. These points must be marked as follows in the drawing: ${}_{D}P_n$ $[x_{GCS}, y_{GCS}, z_{GCS}, x_{LCS}, y_{LCS}, z_{LCS}]$ or to specify the RPS drawing in the table. Coordinates of RPS are considered theoretically accurate. Note: The CATIA module supports the creation of RPS points according to the corporate standard VW 01055.

2) RPS used for the positioning of coordinate systems and references defined in the drawings.
The meaning of this RPS results from the context of the drawing, and therefore it is not necessary to specify it in the lower left index of the point designation. At the base line, two RPS points are needed to specify the exact specification. In some special cases (a line parallel to the reference element and tangent to the structural element), it is sufficient to specify only one RPS. Similarly, this applies to moving targeted datum only by the fact that it is necessary to define the origin of the RPS vector in the so-called reference position and the direction of the vector (lines) is given by the start and the next RPS. For

targeted bases with a defined contact surface, the RPS point lies within the geometric center of the specified area. Point coordinates are again considered theoretically accurate.

3) RPS for specifying directional vectors.
The significance of this RPS point again arises from the context of the drawing. In Fig. 1 we can observe the confusing definition of the directional vector. The beginning of the vector is given by, for example, a targeted base B_2, Whose position is given by unlabeled RPS, and the direction is again given by an unlabeled RPS point [3862.65, -643.91, 1425.01]. In the direction of the vector, the size measurement is performed and is specified by the dimension $28.69_{0}^{+0.1}$. For a clear definition in the drawing, we suggest that the specification be done according to Fig. 2, where coordinates of labeled RPS points are listed in the RPS drawing table. Coordinates can of course be placed directly in the RPS point information field. The direction vector is then marked as follows: $\overrightarrow{DV}[P_{na}, P_{nb}]$. Coordinates of points are again considered theoretically accurate.

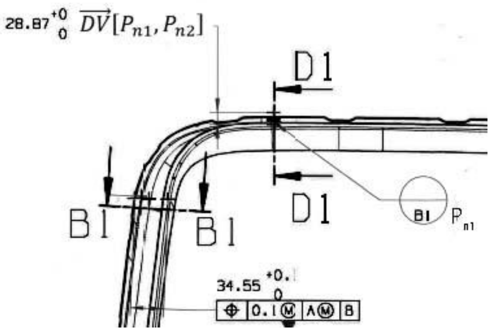

Fig. 2 Coordinates of points are again considered theoretically accurate.

4) RPS for control on metering machines (CMM).
We suggest the following way to mark such a point
${}^{Y(St)}_{CMM}P_n u_x, u_y, u_z / C(NC)^{SR\ x\ (F\ \phi D\ (a\ x\ b))}_{PF\ x/da[\%]} [x_{LCS}, y_{LCS}, z_{LCS}][ST_x, ST_y, ST_z]$, where
P = point mark, n = serial number, Y = yielding and St = stiff part, u_x , … = determines the directions in which CMM approaching the measurement, C/NC = contact / non-contact method of measurement, SR x = ball measuring contact with radius x, Fϕ D (a x b) = Measuring contact with a circular surface ϕ D or with an area of dimensions a x b, PF x = pressure force of the x-size [N], where $da[\%]$ allowable deviation from the nominal force, $[x_{LCS}, y_{LCS}, z_{LCS}]$ = measured LCS-related coordinates (if not specified, not measured), $[ST_x, ST_y, ST_z]$ = coordinate tolerance specification can be given by ES/ EI deviations, zero if it is theoretically accurate dimensions (used for reference elements), or not specified and then general tolerances. Fig. 3 shows the RPS points on the drawing in practice. The marking of point $P_5 u_x$ means that measuring contact track in direction of coordinate of LCS. Other required point parameters are specified in the RPS table.

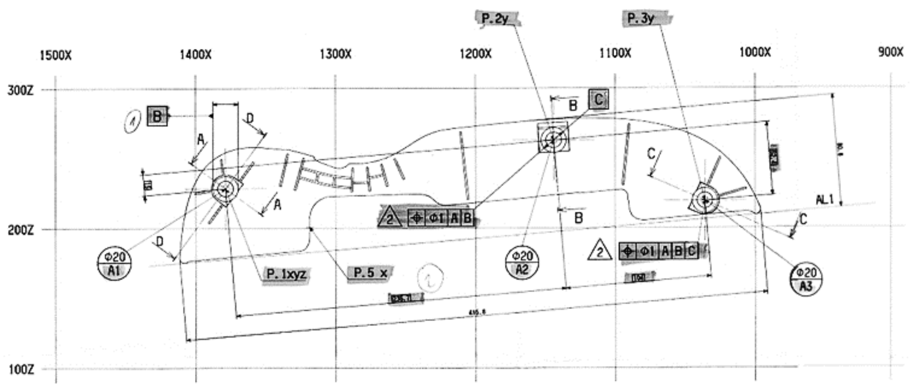

Fig. 3 RPS points on a technical drawing

5) RPS for specifying reference curves for tool making and control of machine parts shapes.
In Fig. 4 we can see the definition of the hose centerline in the automotive production drawing using RPS points. The centerline is seen here as the reference base of the curve type and therefore the coordinates of the individual RPS are theoretically exact dimensions. At the points of the transverse arcs, points are defined at the intersection of the tangent lines, which must be supplemented by the radius of the transition arc in the RPS point table. In Fig. 1, the coordinates of the RPS points in both GCS and LCS are given in the tables. We propose the following point designation:

${}_{RefC}P_n\ [x_{GCS}, y_{GCS}, z_{GCS}, x_{LCS}, y_{LCS}, z_{LCS}][R_T^{P_i,P_s}]$ kde

P = point mark, n = serial number, RefC = reference curve, $[x_{GCS}, y_{GCS}, z_{GCS}, x_{LCS}, y_{LCS}, z_{LCS}]$ = theoretically accurate coordinates (unnecessary coordinates are not required), $[R_T^{P_i,P_s}]$ = The radius of the tangent arc to the point connecting line $\overline{P_i\ P_n} and\ \overline{P_n\ P_s}$.

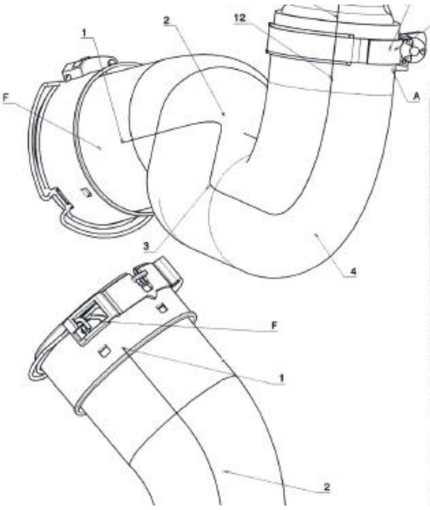

PART COORDINATE AXIS

REF.	X	Y	Z	Radius
1	-454,06	356,31	-170,79	
2	-403,51	295,22	-167,71	R75
3	-411,52	127,26	-192,62	R80
4	-358,37	-26,97	-216,56	R70
5	-347,26	-34,93	-109,78	
6	-8,74	-7,3	11,73	
7	-34,24	-28,61	45,92	R50
8	-86,81	-40,62	48,83	R50
9	-112,2	-39,92	36,45	R45
10	-118,57	-38,78	31,31	R45
11	-153,99	-38,78	17,14	
12	-350,36	-32,71	-139,53	
13	-341,87	-38,78	-57,99	
14	-124,28	-38,78	29,03	
A	-320,12	43,5	-135,79	
B	-321,57	43,5	-125,49	
C	-318,67	43,5	-125,49	
D	-156,92	21,33	-29,12	
E	-149,71	17,87	-29,12	
F	-464,95	369,48	-173,61	
G	0	0	0	

VEHICLE COORDINATE AXIS

REF.	U	V	W	Radius
1	-363,14	102,31	258,65	
2	-312,6	41,22	271,73	R75
3	-320,61	-126,74	236,82	R80

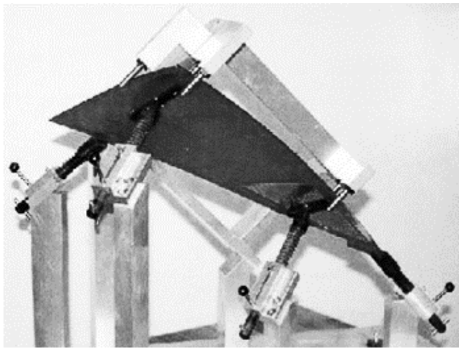

Fig. 4 RPS for specifying reference curves

Fig. 5 RPS for clamping in measuring devices

The definition of reference centerlines finds application, for example, in the design of hose shaping pins. The production of the hoses takes place by means of a non-vulcanized straight rubber hose, followed by vulcanization. After shaping it is necessary to remove the hose from the mandrel, which can cause problems. It is advisable for the reference center line of the hose to be composed of a line and tangent arcs whose spatial position and orientation is given by RPS points. It is not recommended to create a centerline in the CAD system using a spline curve => Problematic hose production. It is also not recommended to connect two tangent arcs. It's not a bug, but it's difficult for programmers to bend the thorns. Table for entering RPS points is good to supplement by the total length of the hose centerline. This information serves as a check number in case any error occurs when entering the 3D coordinate of the hose. Tolerances of the shape of the outer surface of the shaping hub of the hose are specified in the drawing by means of the geometric tolerance of the shape relative to the reference axis of the mandrel. The reference center can also serve to specify the geometrical tolerances of the surface of the hose and to design special control means to control the shape of the hose.

6) RPS for clamping in measuring devices and their designing (Fig. 5.)
For defining these RPS points, RPSs are used to locate the references defined in the drawings according to 2). Most often, they are targeted datums and hence the coordinates of the point are understood to be theoretically accurate.

${}_{MI}P_n\ [x_{GCS}, y_{GCS}, z_{GCS}, x_{LCS}, y_{LCS}, z_{LCS}]$

Targeted bases may have prescribed force-specified depressions. In this case, it is within the competence If it is necessary to define precise positioning pressures with RPS points, then the following point is necessary:

${}^{Y(St)}_{MI}P_n u_x, u_y, u_z{}^{SR\ x\ (F\ \phi D\ (a\ x\ b))}_{PF\ x/da[\%]}[x_{LCS}, y_{LCS}, z_{LCS}]$, where
Individual indicators are already explained in 4) with the difference that u_x, u_y, u_z Indicates the direction take the contact to job and the load on the contact. Unless specified, the load direction in the normal direction to the tangent face is the area of the measured surface at the RPS site. The contact may be again at a point or in the area.$[x_{LCS}, y_{LCS}, z_{LCS}]$ = coordinates of the RPS point of reference in which pressure is to occur, and therefore these coordinates can be considered theoretically accurate. Deviations from the exact position of the pushing point are compensated by the pre-tensioning springs.

7) RPS for the construction of the contact measuring templates – 'LER' (Fig. 6)
In practice, LER is used very often, mainly because of its ease of use and providing a quick and inexpensive measurement of the measured parameters. It is mostly about checking the accuracy of achieving the shape parameters of the surfaces. The CMM performs a part-time measurement that is determined by an internal company policy. This procedure are investigated, using the SPC, trends in the magnitude of deviations from the reference shape of the component, which leads to the timely adjustment of the LER and thus to the reduction of the risk of a defective part => achieve low PPM (parts per million).
For defining these RPS points, RPS are used again to locate the references defined in the drawings according to 2).
${}_{LER}P_n\ [x_{GCS}, y_{GCS}, z_{GCS}, x_{LCS}, y_{LCS}, z_{LCS}]$
If it is meaningful, it is possible to define additional points and mark them as follows>
${}^{Y(St)}_{MI}P_n{}^{SR\ x\ (F\ \phi D\ (a\ x\ b))}_{PF\ x/da[\%]}[x_{LCS}, y_{LCS}, z_{LCS}]$,
If necessary, it is possible to define the pressure at the point of the measuring contact $F\ x/da[\%]$. In most cases, however, in technical practice this force is not defined, which leads to the simplification and acceleration of the measurement process. Whether this is a flat or spot control element is differentiated by using $SR\ x\ (F\ \phi D\ (a\ x\ b)$. Since it is again a point of reference between the part structure and the LER construction, the coordinates $[x_{LCS}, y_{LCS}, z_{LCS}]$ theoretically accurate. Permissible deviations of contact faces/points of clamping contacts from reference position and shape are specified using geometric tolerances on the LER technical drawings.

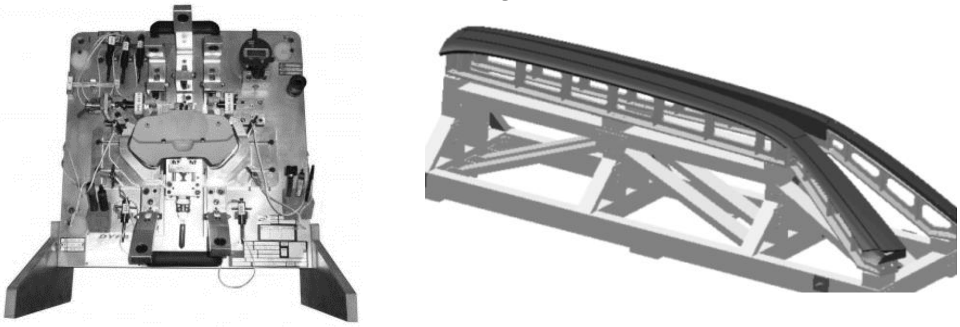

Fig. 6 'LER' for measure shape and dimensions [3]

8) RPS for the designing of cubings – CBG (obr. 7)
For the construction of complex cubing, the RPS is most often used to locate the references defined in the drawings according to 2). Most often, these are targeted reference datums, through which the parts are connected to the surroundings (generally the frame) and to one another. Therefore, when defining target bases, the designer must respect the interdependence of parts and the overall structure of the proposed TS.
${}_{CBG}P_n\ [x_{GCS}, y_{GCS}, z_{GCS}, x_{LCS}, y_{LCS}, z_{LCS}]$
When designing partial cubings, the situation is somewhat more complicated, since some bonds may be removed and thus the self-sustainability of the part under consideration may be impaired. In this case, another RPS needs to be defined. Points so that all the necessary design freedom points are taken and an adequate substitution for the omitted part of the total TS is ensured.
${}^{Y(St)}_{MI}P_n{}^{SR\ x\ (F\ \phi D\ (a\ x\ b))}_{PF\ x/da[\%]}[x_{LCS}, y_{LCS}, z_{LCS}][TC/PC/FC/FIX]$

Since it is again a point of reference, the coordinates are considered theoretically accurate. TC = indicator of two surfaces in contact with each other (since the contact is solid, it is possible to loosen the surfaces due to inaccuracies, deformations and vibrations during operation), PC = indicator of pre-tensioned contact (eg with a pre-tensioned screw connection), FC = indicator flexible contact free (combining the indicators it is possible to define a flexible contact pre-fed FC / PC). It is used, for example, to dampen the mutual transfer of vibrations between the parts. FIX = fixed contact secured eg with snap pins or teeth.

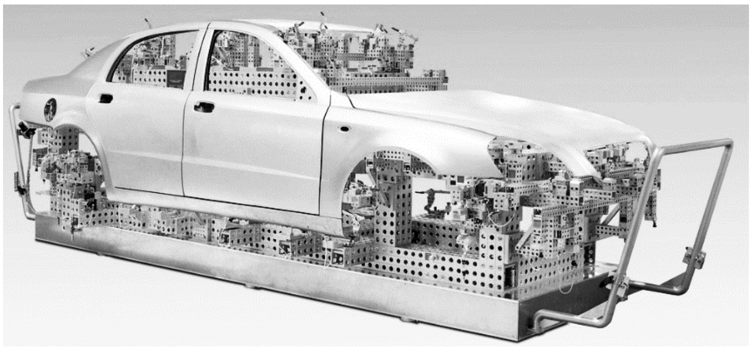

Fig. 7 Complex car cubing

CONCLUSIONS

The paper deals with the issue of the full specification of RPS points. Since there is no standard for RPS points, individual firms are creating their own internal regulations that are not in line with the regulations of other companies. This confusion leads to problems with the correct reading of the technical documentation, which is reflected in the serious problems arising from reading drawings and understanding the individual specifications. The above presents considerable problems for the production, measurement and control of machine parts. The authors' suggestion is to establish order in the RPS specification and to perform their breakdown by function and purpose of use. Since RPS points are particularly widespread in the automotive industry and essential for specifying geometric parameters of technical systems, it is necessary to create an impetus for RPS points to become part of official normative documents, thus achieving the unification of RPS point definitions and hence higher clarity and understanding of this problem by people in technical practice.

REFERENCES

1. Hosnedl, S., Krátký, J. (2000). Příručka strojního inženýra 1, 2. Praha: Computer Press.
2. Hosnedl, S., Vaněk, V. and Borusíková, I. (2001). Design Science for Engineering Design Practice, *Proceedings of the ICED 01, Vol. 3, Eds. Culley S. et al.,* Glasgow, (pp. 363- 370). IMechE, London.
3. Neuhäusl, E. (2010/4). Vady výstřiků – 2. díl: Vady tvaru a rozměrové vady. MM Spectrum: kód článku: 100406, rubrika: Výroba / Plasty, (s. 64)

Corresponding author:
Doc. Ing. Václav Vaněk, Ph.D., Department of Machine Design, Faculty of Mechanical Engineering, University of West Bohemia in Pilsen, Univerzitni 22, Pilsen, 30614, Czech Republic, e-mail: vanek@kks.zcu.cz

THE TRIAL STUDY ABOUT THE MICRO POWER GENERATION BY USE OF VORTEX INDUCED VIBRATION

Yoshifumi YOKOI[1]

[1]*Department of Mechanical Engineering, Faculty of Engineering, National Defense Academy of Japan*

Abstract
In order to construct a micro power generation system using a piezo-electric element, power generation was tried using excitation oscillation of the bluff cylinder by the vortex shedding from the bluff cylinder. The bluff cylinder consists of a board spring section in which the piezo-electric element was attached, and a body section. The bluff cylinder was inserted into the water flow, the shape and the submersion depth of the bluff cylinder, and the flow velocity were varied, and the power generation characteristic was investigated. As a result, it was found that it can generate electricity by vortex excitation. It was found that the length and the submersion depth of the body section influence power generation. It was shown that the power generation characteristic changes with cross-sectional shape of the bluff cylinder.

Key words: *vortex; flow induced vibration; cylinder: piezo-electric element.*

INTRODUCTION

Considering an energy problem in recent years, it is interesting to exploit effectively the hydraulic power energy of the small scale and medium scale which is not yet used. As the example, the development and utilization in a river, an irrigation canal, etc. of low drop micro hydropower generation are performed actively. Those trends were reported by Turbomachinery Society of Japan (Turbomachinery Society of Japan ed. 2002a, 2002b). In realization of the plan, there are many matters which cannot be suitable by extension of the technique developed in the large-scale water-power generation of the concentration of all aspect of a society in one place. Therefore, development of new power generation technique or some method is needed. In response to such background, the power generation method using the self oscillation (vortex excitation) by the vortex shedding from the bluff cylinder placed into the flow is proposed by Bemitsas et al. (2008), Uno & Kawashima (2010), Koide et al. (2011) and Hiejima et al. (2013). In order not to have a rotation mechanism the merit of vortex excitation type power generation is a maintenance-free. And the assembly and installation are also easy. Furthermore, since there is no impeller, power generation is possible, without damaging the living thing which lives in water by rotation of the impeller.

In this study, the piezo-electric element was used for the power generation element, and power generation was tried using excitation oscillation of the bluff cylinder by the vortex shedding from the bluff cylinder. Design manufacture of the power generation bluff cylinder was performed. And some tests were performed by the power generation bluff cylinder which was inserted into the water flow. In such tests, the shape and the submersion depth of the submersion section, and the flow velocity were varied, and the power generation characteristic was investigated.

EXPERIMENTAL APPARATUS AND METHOD

Experimental apparatus consists of a closed circuit water channel, a test bluff cylinder-traverse apparatus, and an oscillating frequency measuring device. The closed circuit water channel is the apparatus (water capacity 4 m^3) used by the previous report (Yokoi, 2016). The sizes of the test section were 2 m in length, 800 mm in width, and 430 mm in depth, the flow velocity range was 0 - 1.2 m/s, and the turbulence to the average flow velocity was less than ±1.5 %. The test bluff cylinder-traverse apparatus is 2 axis dial slight movement type, and those moving ranges are 72 mm and 64 mm, respectively. Those directions of moving are the depth direction and the width direction. As for the oscillation frequency measuring device, the storage oscilloscope (KENWOOD, DCS-7020) was used.

The schematic drawing of the test bluff cylinder (oscillating pendulum) is shown in Fig.1. The test bluff cylinder consists of a spring section (upper part) and a body section (lower part). The spring is a board with a length of 70 mm, a width of 16 mm, and a thickness of 2 mm made from vinyl chloride.

As for the body, the circular cylinder, the triangular cylinder, and the square cylinder were prepared. Figure 2 shows the shape of those cylinders. The length of circular cylinder is two kinds, 250 mm and 500 mm, and the diameter is 16 mm. The length of a triangular cylinder and a square cylinder is 250 mm, and those side lengths are 15 mm.
The power generation object was set in the section of the board spring. The used power generation objects were shown in Fig. 3. One of which is a piezo-electric sensor (Tokyo sensor company, DT1-028 K/L) and the other is a piezo-electric buzzer (SPL company, PT08-Z185). These two kinds of power generation objects are made by different material and the manufacture method.
Experiment parameters are the length of bluff cylinder, the submersion depth of the body (draft), its setting posture, and water flow velocity. The submersion depth of the body is three kinds (70, 140 and 210 mm). The posture of a triangular cylinder and a square cylinder is in the state where the angle was directed to the flow, and the state which directed the plane. The water flow velocity was varied to 44 steps in the range of 0 - 1.2 m/s.
The experiment procedure is the following. The power generation object is set in the board spring section of the test bluff cylinder, and the test bluff cylinder is attached in the traverse apparatus. The direction is decided to oscillate right-angled to the flow in the case of the attachment. The body is sunk in the target submersion depth. An aspect that it was set based on the procedure is shown in Fig. 4. The target flow velocity is caused by inverter operation of the pump of the closed circuit water channel. The voltage variation waveform from the power generation object sensor is observed with the storage oscilloscope, and output voltage and frequency are measured. Here, the frequency measured the signal of voltage waveform, observed the time jitter with the storage oscilloscope, and determined for fluctuation frequency.

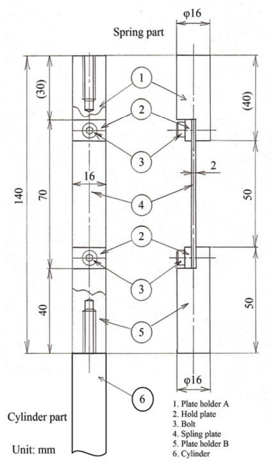

Fig. 1 The schematic drawing of a test cylinder spring section

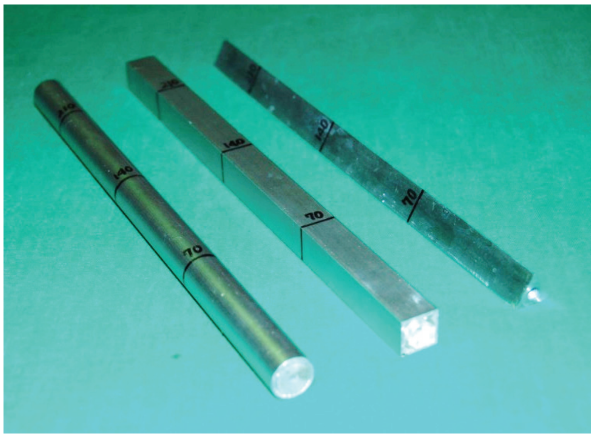

Fig. 2 Body section shape of the test cylinder (circular cylinder, square cylinder, and triangular cylinder)

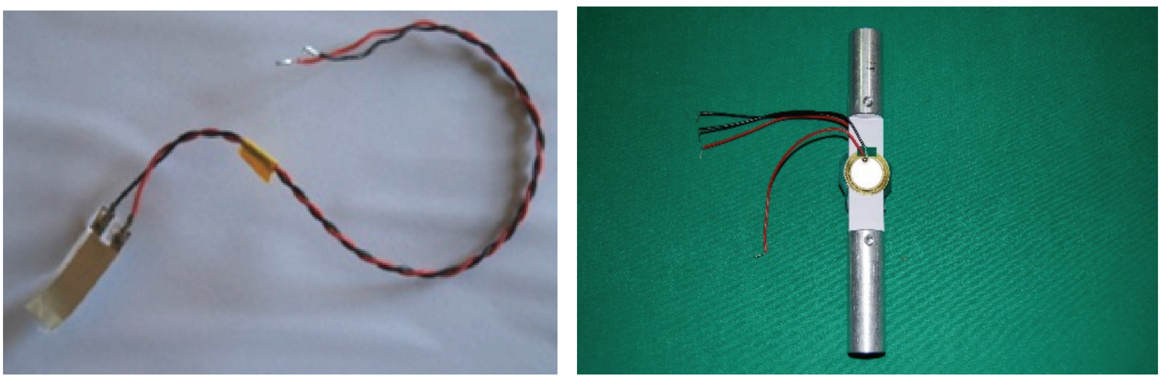

(a) (b)

Fig. 3 The aspect of the power generation object, (a) piezo-electric sensor, (b) piezo-electric buzzer

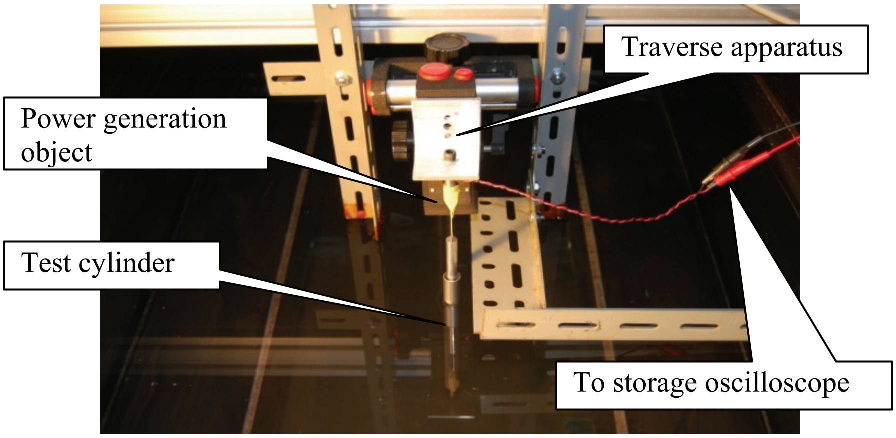

Fig. 4 The photograph of the situation where the test cylinder was set in the traverse apparatus

Tab. 1 Synthetic character frequency of the test cylinder

Situation (mm)		Cylinder shape (Hz)				
span	draft	C.C.	S.S.	F.S.	S.T.	F.T.
	70	2.5	2.0	1.9	2	2.2
250	140	2.2	1.7	1.7	1.9	2
	210	2.1	1.6	1.6	1.9	
500	205	0.9				
	380	0.8				

EXPERIMENTAL RESULTS AND DISCUSSION

The result of having measured the characteristic vibration of the overall system of the test bluff cylinder with a board spring is shown in Tab. 1. The meaning of the symbols used in the table are the following. The symbol "C.C." is a circular cylinder, the symbol "S.S." is the square cylinder which directed the angle to the flow, the symbol "F.S." is the square cylinder which directed the plane to the flow, the symbol "S.T." is the triangular cylinder which directed the angle to the flow, and the symbol "F.T." is the triangular cylinder which directed the plane to the flow. When the submersion depth of the body (draft) became shallow, it was confirmed that the character frequency as the overall system tends to become high.

Since the piezo-electric element reacts to unsteady stress, it can generate electricity by the lift alternately produced by the Karman vortex. An example of the power generation voltage waveform is shown in Fig. 5. In the beam which generally has a uniform section, if amplitude becomes large near critical oscillation frequency and it passes over it, it is known that amplitude will become small. If the vortex excitation based on the Karman vortex shedding also makes the flow velocity increase from a halt condition, vortex shedding frequency also increases, and the bluff cylinder begins to oscillate based on critical oscillation frequency, and obtains a soon large amplitude point. Moreover, amplitude will become small if it passes over this point, and it is predicted that oscillation ceases. Figure 6 shows the relationship between the flow velocity and the produced voltage. An abscissa is the average flow velocity in the test section of the closed circuit water channel, and the ordinate is the average value of the peak-to-peak voltage observed by the oscilloscope waveform. In the case of the circular cylinder (C.C.) and the sharp square cylinder (S.S.), the number of peaks is one and after the peak with the increase in the flow velocity, the voltage shows a gently-sloping reduction. On the other hand, in the case of a flat triangular cylinder (F.T.) and a flat square cylinder (F.S.), there is no particular peak and the tendency which the voltage produced to the increase in the flow velocity is increasing is seen. In the case of a sharp triangular cylinder (S.T.), there was no response to the increase in the flow velocity. In the case of a circular cylinder and a sharp square cylinder, one peak with wide width can see. Since voltage is obtained even if the flow velocity changes, the peak with wide width is a thing desirable in use. Since the voltage of 500mV or more is obtained in the range of the flow velocity 0.22 - 0.38 m/s, considering this matter, as for the circular cylinder body and the sharp square body, it turns out that it is in the setting situation of having been most suitable for the use. The Karman vortex is not generated behind the flat triangular cylinder and the flat square cylinder. The motion of body is carrying out large oscillation to the flow and the perpendicular direction very slowly. The difference of water level occurred in the body upstream and body down stream side, and a cavity was made behind the body. The aspect of the motion and cavernous generation are shown in Fig. 7. The experimental result when using a piezo-electric buzzer as the power generation object is shown in Fig. 8. In this experiment, using the circular cylinder with length of 250 mm, the submersion depth of the body was set to 70, 140, 210 mm, and water flow velocity was varied to 44 steps in the range of 0 - 1.2 m/s. Even when it changes into the piezo-electric buzzer, the power generation characteristic does not change, but since a case with a submersion depth of 140 mm of the body has wide peak width, it is thought that it is most suitable for the use. Figure 9 shows and compares the power generation voltage characteristic of two kinds of power generation objects (piezo-electric sensor and piezo-electric buzzer). Here, the circular cylinder of 250 mm length with submersion depth of 140 mm is used. In any case, the peak of power generation voltage is shown at the flow velocity range of 0.22 - 0.38 m/s. However, the clear difference is shown among both. It is shown that the voltage which a piezo-electric buzzer produces is about 4 times the voltage which a piezo-electric sensor produces. Since there is a difference on manufacture in the used product of two piezo-electric elements, it is guessed that such a result was obtained. It was found that it is important to choose the piezo-electric element corresponding to the purpose.

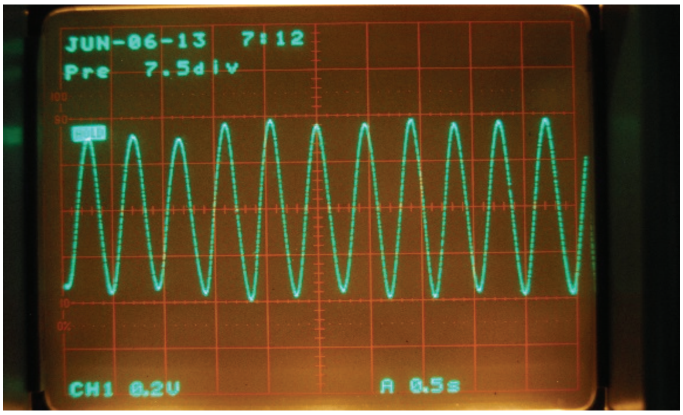

Fig. 5 An example of the output waveform from the power generation object

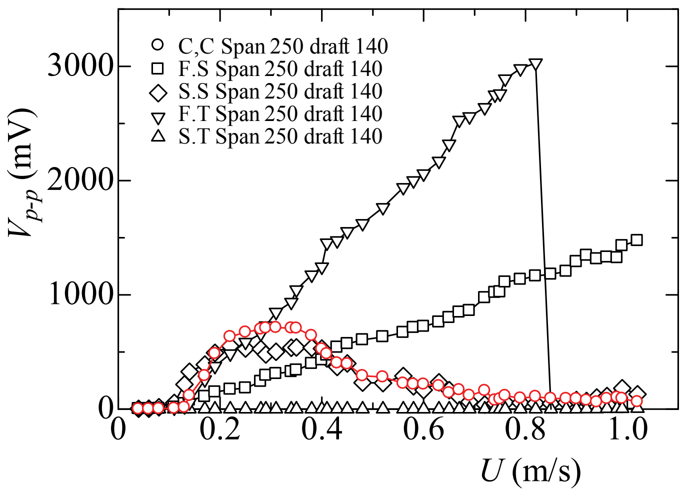

Fig. 6 Relationship between flow velocity and output voltage, in the case of circular cylinder

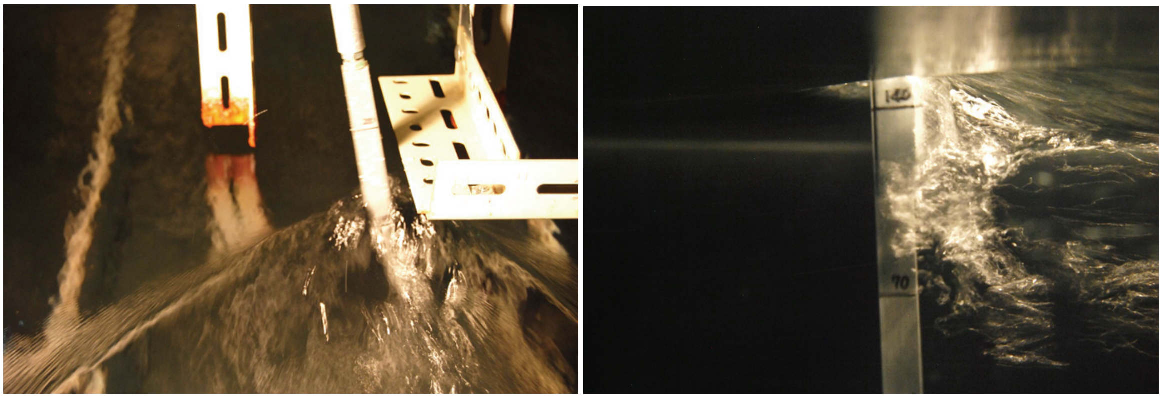

Fig. 7 The behavior of the plane square cylinder, and the aspect of flow; the span of the square cylinder was 250 mm, and the submersion depth was 150 mm, (a) the photograph seen from the down stream side, (b) the underwater photograph seen from the width side

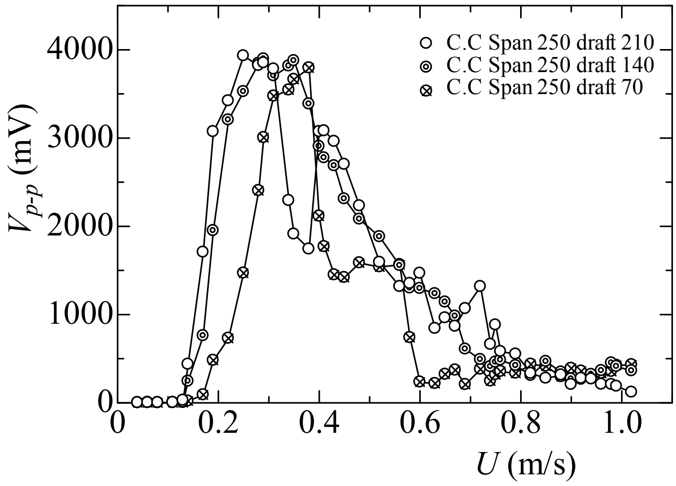

Fig. 8 Relationship between flow velocity and output voltage, in the case of sharp square cylinder

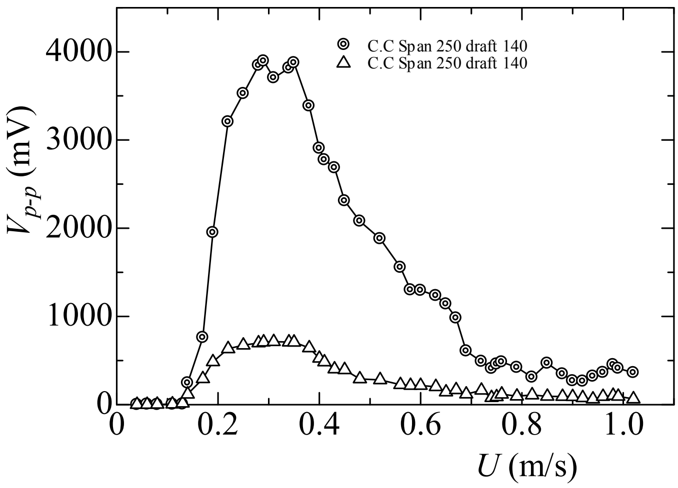

Fig. 9 Relationship between flow velocity and output voltage, in the case of flat square cylinder

CONCLUSIONS

The following conclusions were obtained as a result of performing the characteristic test of the bluff cylinder pendulum aiming at generating electricity by vortex excitation.
(1) Generating of voltage was accepted by vortex excitation through the piezo-electric element.
(2) The length and the submersion depth of bluff cylinder influence the movement of the oscillating pendulum.
(3) The magnitude and its peak width of the voltage produced by vortex excitation corresponding to the flow velocity are changed by cross-sectional shape of the body section.
(4) It is important to choose the power generation object which suited the use purpose.

ACKNOWLEDGMENT

Author is thankful to Mr. Jalernsk Kamon, Mr. Srisuntornsiri Rungsak and Mr. Kouichirou Ooue who helped this work and who are the student staff of my laboratory.

REFERENCES

1. Bemitsas, M. M., Raghavan, K., Ben-Simon, Y., & Garcia, E. M. H. (2008). VIVACE (Vortex Induced Vibration Aquatic Clean Energy): A New Concept in Generation of Clean and Renewable Energy From Fluid Flow. *Journal of Offshore Mechanics and Arctic Engineering*, 130, 041101.
2. Hiejima, S., Oka, K., Hayashi, K., & Inoue, H. (2013). Fundamental Experiment for Energy Harvesting from Flow-Induced Vibration of Inverted Pendulum. *Annual Journal of Civil Engineering in the Ocean*, 69(1), 12-21. (in Japanese)
3. Koide, M., Sekizaki, T., Yamada, S., Takahashi, T., & Shirakashi, M. (2011). Prospect of Micro Power Generation Utilizing VIV in Small Stream Based on Verification Experiments of Power Generation in Water Tunnel. *Transactions of the Japan Society of Mechanical Engineers*, 77(775), 702-714. (in Japanese)
4. Turbomachinery Society of Japan ed. (2002a). Special Issue: Application Technology of Micr-Hydropower 1. *Turbomachinery*, 30(3), 129-160. (in Japanese)
5. Turbomachinery Society of Japan ed. (2002b). Special Issue: Application Technology of Micr-Hydropower 2. *Turbomachinery*, 30(4), 193-253. (in Japanese)
6. Uno, M. & Kawashima, R. (2010), The New Micro Water Power Generation by Use of the Oscillating Bluff Body. *Turbomachinery*, 38(2), 121-125. (in Japanese)
7. Yokoi, Y. (2016). A Study about the Design and Development of the Water Flow Experimental Facilities for the Study of Flow Induced Vibration Phenomenon, In 57th International Conference of Machine Design Departments (ICMD2016)(pp.175-180).

Corresponding author:
Prof. Yoshifumi Yokoi, Department of Mechanical Engineering, Faculty of Engineering, National Defense Academy of Japan, 1-10-20 Hashirimizu, Yokosuka, Kanagawa, Japan 239-8686, phone: +81468413810, e-mail: yokoi@nda.ac.jp

DESIGN OF A SENSOR FOR MEASUREMENT OF BOLT PRETENSION

Jiří ZAČAL[1], Zdeněk FOLTA[2], Lukáš JANČAR[3]

[1]Department of Machine Parts and Mechanism, VŠB-TU Ostrava.
[2]Department of Machine Parts and Mechanism, VŠB-TU Ostrava.
[3]Department of Machine Parts and Mechanism, VŠB-TU Ostrava.

Abstract
The article discusses the issue of strain gauges sensors for measuring bolt pretension. The aim of the research is to determine negative effect of both low rigidity of joint contact surface and uneven layout of contact force on the accuracy of measurements. In the conclusion, design alterations of the sensor and a new principle of measurement for elimination of these negative effects are proposed.

Key words: *strain gauges; bolt pretension; sensor; screw.*

INTRODUCTION

Bolt connections are arguably the most commonly used type of mechanical connection. However, in some fields of technical practice these connections must meet particularly high technical requirements. These are the so called critical connections *(Zhu, et al., 2017)*, where these connections are subject to great pressure and temperature load, or alternating temperature in the operation exerted by external forces *(Začal, 2016)*. Furthermore, the specific tightness given by standard *(ČSN EN 1591-1, 2015)* must be met. In addition, these connections might pose a threat to both lives and the environment. In order to satisfy all these requirements, a number of experimental measurements needs to be conducted, so as to determine the actual magnitudes of bolt pretensions. This needs to be done at various combinations of tightening torque, lubricant, types of screw washers, material of the bolts, technology of manufacturing of the thread etc. When a suitable method is applied, the friction factor under the screw and in the thread, can be found from the bolt pretension as well. A tensometric sensor was developer for this purpose. After calibration of the first design, the sensor appeared to be fully operational, despite the low credibility of the measured data when compared to the practice.

In the article, the design and operation of the sensor are described, as well as the analysis of the measurements, identification of the error and its eliminations. The results are supported by graphs and figures.

MATERIALS AND METHODS

Firstly, a sensor of a simple cylindrical geometry was proposed. On the outer side of the cylinder, four foil resistance strain gauges for measuring of stress-strain were attached, which were subsequently plugged into a measuring bridge according to Wheatston *(Hoffmann, 1989)*. The calibration was conducted on a tear machine, where ten levels of compression force in the interval of 40 to 400 (kN) were exerted on the sensor. The maximum measurement deviation *(Bernard, 1999)* was 8.7 (%) and corresponded to the lowest level of compression (Fig. 3, A). In greater strain, the magnitude of the measurement devitation can be considered tolerable, given the anticipated strain in the practice, where the expected magnitude of measured pretension in a bolt is greater than 100 (kN). The proposed sensor, therefore, satisfied all the requirements. However, the sensor was designed only as a part of a testing device (stand). In reality, the sensor was placed between two steel plates, that were then drawn to each other using bolts. After a series of measurements of the magnitudes of pretension in bolts, the resulting values appeared to be lower than expected. Thus, it was apparent, that the stand significantly influences the results. This was concluded on the assumption that as a result of uneven contact areas of the sensor and in the connected parts, a change of strain flow can be observed (Fig. 1). In the left-hand and right-hand side of the picture, there is an example of symmetric strain and of the strain on uneven contact area respectively.

Subsequently, the sensor was again calibrated, this time together with the testing device. The error of the sensor's measurement was as high as 16.7 (%) (Fig. 3, B), and it did not fall below 10 (%) (Fig. 3, B) in any of the levels of compression. The effect on the results was also due to a slight rotation of the sensor (Fig. 3, C). Therefore, a control of the sensor's geometry was conducted using three-dimensional measuring mechanism, in which values of planarity, perpendicularity and parallelism were ensured. Nevertheless, the functional areas of the sensor did not show any malfunction. After a further analysis of the tightening, a slight rotation of the contact area was exhibited, as a result of incorrect construction of the testing device. Furthermore, a significant and uneven compression damage was of contact areas of the steel plates occurring, as they had been manufactured from a steel of low rigidity. The impact of the rotation of the parts of the testing device can at least partially be eliminated by a suitable modification the shape of the sensor. By means of symmetrical narrowing of the casing, such point is created in which tension, arising as a result of added bending from uneven contact of the contacting areas.

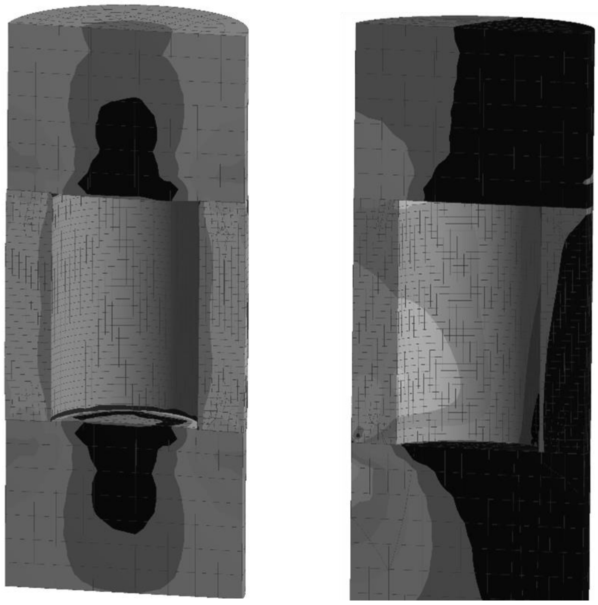

Fig. 1 *The change in the strain flow on the sensor of a cylindrical shape.*

Using the FEM calculation (in ANSYS Workbench R18.0 Academic), several different geometries of the sensor were tried. It was shown that symmetrical reduction of the casing from outer and inner side is the the optimal modification of the shape (Fig. 2).

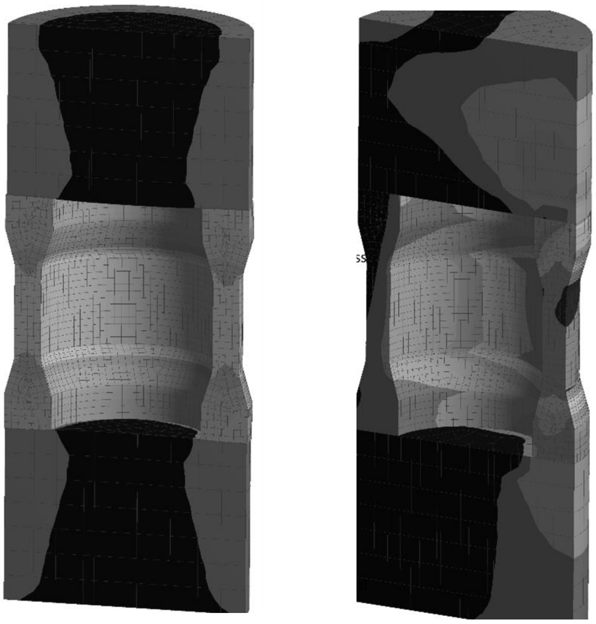

Fig. 2 *The change in the strain flow on the sensor with shape modification.*

However, even here a complete elimination of the uneven contact surface was not achieved. For better elimination of these impacts, the sensor would need to be longer, which would in this case not be possible. The given size of the unevenness of the contact areas in the FME calculation was 0.5 to 1 (mm).

Subsequently, the sensor was manufactured according to the new construction (Fig. 2). This time, four strain gauges of the XY type T/Rosette were used. Two of them were attached to the outer side of the casing on the opposite sides. Remaining two strain gauges were attached opposite to them from the inner side. Foil resistance strain gauges were again plugged in the Wheatston bridge. Owing to this configuration, both the bending of the coating and the effect of the temperature can be compensated. Moreover, amplification of the signal from strain gauges increased measurement sensitivity were also achieved. Calibration of the new sensor exhibited significant improvements of the results, even in case of it’s inserting into the stand. However, the measurement devitation was still found around 3.5 (%) (Fig. 3, D) and was substantially determined by the change of the position of the sensor. It was, therefore, necessary to verify the impact of the compression damage of soft contact surface of the stand. Areas with damaged surface due to compression were removed by machining and then hardened washers were inserted into them.

RESULTS AND DISCUSSION

The final modification of the shape of the sensor led to further reduction of the measuring devitation (Fig. 3, E). Due to the modification of the contacting areas, manipulation of the sensor is enabled without causing indefinite change of measurement properties of the sensor. However, the precision of the sensor strongly depends on following certain conditions. Its dimensions limit the range of use in terms of size of the used bolts, and by that the magnitude of the measured pretension in the bolts. Reliable results can only be guaranteed only for clamping force exceeding 80 (kN). Furthermore, either sufficiently hard contacting areas or elimination of any source of uneven strain need to be ensured.

Considering these limits. it can be concluded that the use of resistance gauge strains for sensors of pressure force is not suitable. Modification of the contacting areas to a spherical shape can be considered, however precise manufacture would be demanding and expensive. Thus, it is proper to consider a completely different principle of the measurement. The principle of magnetostrictive sensors might be a possibility. As a result of deformation arising as a result of acting external forces, a change of permeability of the ferromagnetic is observed. Thus, the inductivity changes, which can be evaluated using methods of the measuring bridge *(Hoffmann, 1989)*. However, the design of such sensor needs to be subjected to thorough experiment. Further method of measurement is utilisation of hydraulic or pneumatic mechanism. Measured parameters would be shifting or change of pressure, and would then by converted to the magnitude of the bolt pretension.

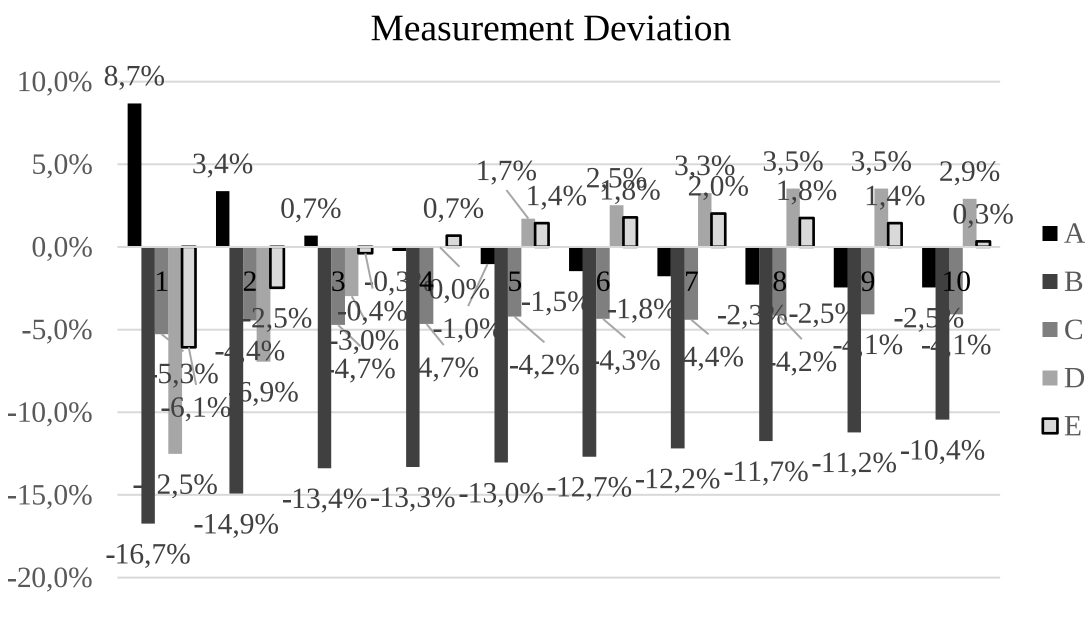

Fig. 3 *Graph of measurement deviation*

Fig. 3 shows the results of all measurements. In Tab. 1 is a detailed description of the groups in which the measurements were divided.

Tab. 1 Detailed description of measurement groups.

Measuring group	Measurement process
A	Measurement with a cylindrical sensor situated in the tear machine.
B	Measurement with a cylindrical sensor situated in the testing device (stand).
C	Measurement with a cylindrical sensor situated in the stand, after a change of the position of the sensor.
D	Measurement with shape modification sensor without hardened contact surfaces.
E	Measurement with shape modification sensor but with hardened contact surfaces.

CONCLUSION

It was shown that the design of the strain-gauge resistance sensor for measurement of the pretension in bolts is largely complex. This is, in particular, if the relative high precision of its measurement (up to 3 %) is required in a large strain interval. Based on the measured data and empirically observed phenomena, a modification of the original sensor with a simple cylindrical geometry was introduced in a way, that enables improvement of the measurement precision. It was proven that unmodified cylindrical shape is unable to satisfy the requirements of the sensor. The resulting evaluation of the data (Fig. 3) was proceeded by a series of experimental measurements on a universal tear machine, where various combinations of strain, sensor area and pressure-force distribution were tested. Subsequently, the causes of the experimental error were determined. These were then at least partially eliminated.

Nevertheless, the conditions under which the resistance strain-gauge sensor is able to produce precise measurements are too limiting. Considering these limits, new and more suitable principles of measurements were introduced, The most suitable principle seems to be the one of magnetostrictive sensor. However, it is necessary to verify everything by experiment.

1. ČSN EN 1591-1 (2015). *Flanges and their joints - Design rules for gasketed circular flange connections - Part 1: Calculation method.* Praha: , © Czech Standards Institute.
2. Hoffmann, K. (1989). *An Introduction to Measurements using Strain Gauges.* Darmstadt: Hottinger Baldwin Messtechnik GmbH.
3. Zhu, L. B.-H. (2017). Numerical and experimental study of elastic interaction in bolted flange joints. Journal of Pressure Vessel Technology, Transactions of the ASME, 139(2) doi:10.1115/1.4035316.
4. Začal, J. (2016). *Problem solving of Bolted Connection of a Pressure Vessel.* Ostrava: VŠB-TUO (e.g. in Czech).
5. Bernard, J. (1999). *Technical Experiment.* Praha: Vydavatelství ČVUT (e.g. in Czech).

Corresponding author:
Ing. Jiří Začal, Department of Machine Parts and Mechanism, Faculty of Mechanical Engineering, VŠB-Technical University of Ostrava, 17. listopadu 15/2172, Ostrava-Poruba, 708 33, Czech Republic, phone: +420 605 913 871 (597 324 203), e-mail: jiri.zacal@vsb.cz.

58th ICMD 2017
6 - 8 September 2017, Prague, Czech Republic

DYNAMICS OF THE MOVEMENT OF THE CUTTING ASSEMBLY'S CUTTER BAR

Marcin ZASTEMPOWSKI[1], Andrzej BOCHAT[2]

[1,2] *Faculty of Mechanical Engineering, UTP University of Science and Technology, Poland.*

Abstract
This article presents the dynamics of the cutting assembly's cutter bar movement. The derived mathematical dependencies describing the dynamics' loading of the cutter bar may be used at the stage of designing that type of cutting assemblies and their power transmission systems. The simulation calculations conducted on the derived mathematical dependencies, made it possible for the authors to develop a computational tool for quick identification of demand for power and forces operating in the shear cutting assembly under the influence of changes in the characteristic input values.

Key words: *shear-finger cutting assembly, dynamics of movement, cutter bar, simulation calculations.*

INTRODUCTION

The shear-finger cutting assembly is the basic working assembly occurring in many agrarian machines. It is used in machines like mowing machines, chaff cutters and combine harvesters, the purpose of which is cutting of plant material for the fodder, consumption and energy purposes (Gach, Kuczewski & Waszkiewicz, 1991; Bochat, 2010; Bochat & Zastempowski, 2013)
It results from the generally available literature's analysis, that the subject matter of kinematics and dynamics of cutting units‘ of the machines‘ working assemblies was raised only by Bochat and Zastempowski (2013). Other authors, within the frames of machines' construction, have mainly raised the subject area relating to the rules of designing and the analysis of a construction's resistance (Strzelecki et al., 2016; Tomaszewski et al., 2014), with the rules of use of MES and numerical analysis (Szala, 2014; Knopik et al., 2016) with mathematical modelling and the construction's optimization (Knopik et al., 2016; Knopik & Migawa, 2017; Ligaj & Szala, 2010; Zastempowski and Bochat, 2014, 2015; Keska & Gierz, 2011) as well as the influence of technical devices on the environment (Karwowska et al., 2013, 2014) as well as processing of the harvested plant material (Dulcet et al., 2006).
Fig. 1 presents the shear-finger cutting assembly's construction.
The essence of its construction lies in that it is made of a movable cutter bar making a reciprocating movement and an immovable finger bar. Knives riveted to the cutter bar are of a trapezoid shape. Fingers fastened to the finger bar are used to divide the harvested material into batches.
The principles of the shear-finger cutting assembly's operation constists in that the fingers enter between the harvested plants and divide them into batches. Then, individual knives squash the stalks or plants‘ stems to the side fingers‘ edges and make the plants‘ cut. The shear-finger cutting assemblies are split into: the ones of standard cut with single knives‘ stroke (classical), the ones of standard cut with double knives‘ stroke, of medium cut and of low cut (Bochat, 2010).

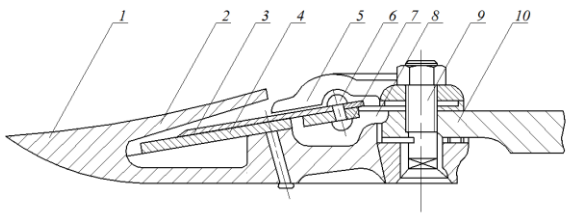

Fig. 1 Shear-finger cutting assembly (Bochat, 2010): 1 – finger, 2 – finger's blade, 3 – knife, 4 – liner, 5 – button, 6 – rivet, 7 – movable cutter bar, 8 – guide, 9 – screw, 10 – immovable finger bar

The purpose of the study is to analyse functioning of the shear-finger cutting assembly in the aspect of dynamic loads of its cutter bar. The knowledge of mathematical dependencies describing the cutter bar's dynamic load is necessary for its correctly designing of power transmission system.

MATERIALS AND METHODS

Conducting of an appropriate analysis of the shear cutting unit's operation in the aspects of dynamic loads of the cutter bar is embarassing, because of the system's complexity and imperfection of dynamic dependences describing it.
However, the experimental surveys of the cutting assembly are insufficient due to the fact, that they concern summary loads having an effect on individual construction elements and do not isolate unequivocally the reasons of their arising.
In literature it is most often assumed, that the force P_1 counteracting the cutter bar's movement (constituting the resistance of its movement) is equal to the sum of forces having an effect on it (fig.2) and is described with a formula:

$$P_1 = P_s + P_B + T_c, \tag{1}$$

where P_S is the average value of cutting resisting forces, P_B is the inertial force of the cutter bar and T_C is the friction force of the cutter bar against guide elements.

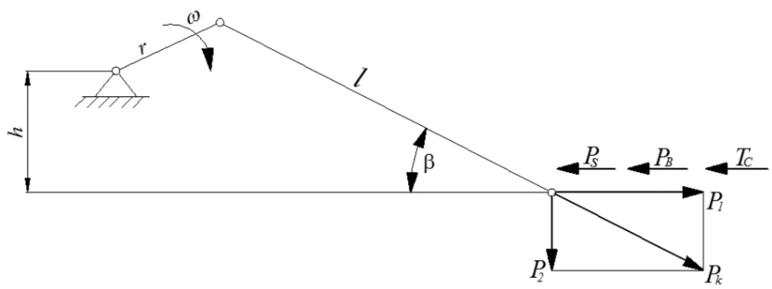

Fig. 2 Forces having an effect on the cutter bar powered with the asymetrical crank mechanism (own study): P_k – force having an effect along the connecting rod, P_1 and P_2 – vertical and horizontal constituent of force P_k, P_S – mean value of cutting resisting force, P_B – inertial force of the cutter bar, T_C – friction force of the cutter bar against guide elements, r – length of crank, l – length of connecting rod (pitman), h – distance of the rotating disc's shaft with the crank from the bar movement's plane, β - the angle of the connecting rod's inclination.

Cutting resistances are theoretically hard to determine, as they depend on many factors just like: species and variation of cut material, stiffness and humidity of individual blades, weediness, intensity of the cutting assembly's feeding, cutting speed, technical condition of the cutting assembly and other ones.
In practice the mean value of the cutting resisting forces is calculated from the dependence:

$$P_s = \frac{L_j\, F_0\, i}{x_c}, \tag{2}$$

where L_j is the value of work necessary to cut the plants from the area of 1cm^2, F_0 is the fiels of the cutting assembly's loading, i is the number of knives of the cutter bar, and x_C is the knife's way from the beginning till the end of cutting.
The number of plants falling on 1cm^2 of cultivation, shall for the cereals assumed to be equal to z = 0,2 – 0,8 $\text{szt.}\cdot \text{cm}^{-2}$, while for forage grasses z = 1,2 – 2,0 $\text{szt.}\cdot \text{cm}^{-2}$.
It has been experimentally established, that if the value of work needed for cutting plants from 1 cm^2 amounts more or less for cereals, then L_j = 0,01 - 0,02 $\text{J} \cdot \text{cm}^{-2}$, and for forage grasses, L_j = 0,02 – 0,03 $\text{J} \cdot \text{cm}^{-2}$ (Bochat, 2010; Gach, Kuczewski & Waszkiewicz, 1991).

At the time of the analysis of operation of different types of cutting assemblies there stands out the so-called feeding field and load field. The field from which plants are cut during one stroke of knives is called the feeding field *F*, while the field from which plants are cut at the time of one knife's stroke with the use of one finger is called the load field F_0 (according to the formula (2)) as described by Bochat (2010).
For a normal cut assembly with a single stroke of knives we have: $F = F_0$.
Figure 3 presents the load field for a normal cutting assembly with a single stroke of knives.

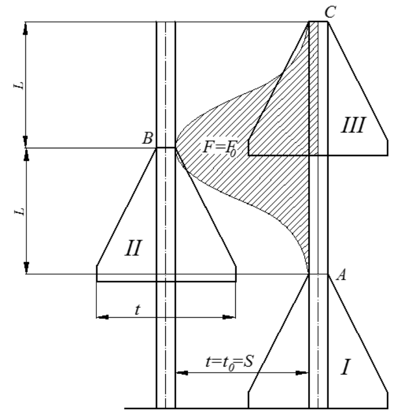

Fig. 3 The load field for a normal cutting assembly with a single stroke of knives (Bochat, 2010)

In the normal cutting assembly with a single stroke of knives, the top of a given knife's cutting edge at the time of a single revolution of a rotating disc with a crank circles the ABC (movement trajectory). The filed limited with that curve and the line *AC* is the feeding field *F* equal to, as earlier mentioned, the load field F_0 . So, taking into consideration the fact, that any point of a knife's edge makes a complex movement (according to the mechanisms' theory) it covers the relative motion and „transportation". In this case, the relative motion is described by the formula of the cutter bar's dislocation (3):

$$x = r(1 - cos\ \omega t). \tag{3}$$

Dependency (3) is received on the basis of the cutter bar's kinematics of movement analysis.
The formula (3) constitutes an equation of a harmonic movement describing translocation of projection of crankpin on the line of the cutter bar's movement. The „transportation" is described with the equation:

$$y = L\frac{\omega t}{\pi} = L\frac{\varphi}{\pi}. \tag{4}$$

The load field F_0 may be expressed with the formula:

$$F_0 = \int_0^{2\pi} x\ dy. \tag{5}$$

Taking into consideration, that:

$$dy = L\frac{d\varphi}{\pi}, \tag{6}$$

we shall receive:

$$F_0 = \int_0^{2\pi} \frac{L\ r}{\pi}(1 - cos\varphi)d\varphi, \tag{7}$$

Having solved the equation (7) finally we shall receive:

$$F_0 = S\ L. \tag{8}$$

So, the load field F_0 in the cutting assemblly of a normal cutting with a single stroke of knives equals to the product of the cutter bar's stroke S and the feeding way L.
According to calculations of the study's authors, for the low cut cutting assembly, the load field amounts to:

$$F_0 = 0{,}32\, S\, L. \tag{9}$$

However, for the normal cut cutting assembly with double stroke of knife, the load field amounts to:

$$F_0 = 0{,}18\, S\, L. \tag{10}$$

Concluding it may be said, that the load fields of cutting assemblies on the stage of their theoretical calculations may be determined based on the derived dependencies: (8), (9) and (10) or for the analysed, special construction of the cutting assembly they should be determined independently.
The inertial force P_B of the cutter bar's mass is the product of the cutter bar's mass m together with the part of the connecting rod's mass making the to-and-fro motions and its acceleration a.
Taking into consideration the fact, that:

$$m = (m_1 + m_2), \tag{11}$$

and

$$a = \omega^2\, r\, cos\omega t = \omega^2\, r\, \left(1 - \frac{x}{r}\right), \tag{12}$$

we have received:

$$P_B = (m_1 + m_2)\, \omega^2\, r\, \left(1 - \frac{x}{r}\right). \tag{13}$$

where m_1 is the cutter bar's mass , m_2 is the part of the connecting rod's mass making to-and-fro motions, r is the length of the crank, ω is the crank's angular speed, $x_{nż}$ is the cutter bar's displacement.
Mass m_1 of the cutter bar is calculated assuming that the mass falling per 1m of its lendth amounts to: 2,20-2,35 $\mathrm{kg \cdot m^{-1}}$ (Zastempowski & Bochat, 2014).
However, m_2 is calculated from dependences:

$$m_2 = m_k \frac{l_0}{l}, \tag{14}$$

where m_k is the mass of a connecting rod, l_0 is the distance of the centre of the connecting rod's mass from the crankpin, l is the total length of the connecting rod.
From the analysis of the selected crank drives' design solutions it results, that the connecting rod's mass most often amounts to: 2,30–3,25 kg, and in extreme cases it assumes the value equal to 5 kg (Bochat, 2010).
The friction force T_C of the cutter bar against the cutter assembly's guide elements is the sum of the friction force T_1, coming from the weight of the cutter bar and the friction force T_2, coming from the connecting rod's operation.
So:

$$T_c = T_1 + T_2. \tag{15}$$

The friction force T_1 is determined from the dependence:

$$T_1 = \mu\, m_1 g, \tag{16}$$

where μ is the sliding friction co-efficient and assumes the values within the range 0,25-0,30 [2, 3], m_1 is the mass of the cutter bar, and g is the gravitational acceleration.
However, the friction force T_2 is determined on the basis of the depenedence:

$$T_2 = \mu\, P_2, \tag{17}$$

whereas

$$P_2 = P_1\, tg\beta, \tag{18}$$

where P_2 is the normal constituent of the connecting rod's having an effect on the cutting assembly (fig. 2), and β is the temporaty inclination angle of a pitman (connecting rod) to the cutting plane. Taking into consideration that:

$$P_2 = (P_s + P_B + \mu\, m_1 g + \mu\, P_2)\, tg\beta. \tag{19}$$

Following conversion we have received:

$$P_2 = \frac{(P_s + P_B + \mu\, m_1 g) tg\beta}{1 - \mu\, tg\beta}. \tag{20}$$

From the analysis of the formula (20) it results, that the temporaty inclination angle of a pitman (connecting rod) β to the level, has an important impact on the T_2 force value, which changes its value within a closely determined scope.
The scope of changes determines the value of eccentricity ε of the crank mechanism:

$$\varepsilon = \frac{h}{l}, \tag{21}$$

where h is the distance of the crank shaft from the cutter bar movement's plane, and l is the length of the pitman.

RESULTS AND DISCUSSION

Within the frames of the task's realization, on the basis of the derived mathematical dependences, an own software has been developed for quick simulation calculations, within the frames of which there have been identified demands for power and forces operating within the frames of shear-finger cutting assemblies under the influence of characteristic input values such as: μ- friction co-efficient, m_1 – mass of the cutter bar, m_2 – mass of the connecting rod, h_k – distance of the symmertry axis of the crank shaft's distance from the cutter bar movement's plane, l – length of the connecting rod (pitman) and n – the shaft's rotational speed. At the stage of the simulation surveys' realization, there have been calculated in order: $v_{snż}$ – mean speed of knives, P_S – mean value of cutting resistances, P_B -maximum inertial force, T_1 – friction force from the cutter bar's weight, T_2 – frinction force on the connecting rod's operation, P_{max} – maximum value of the total force, N – demand for power.
In table 1 there are presented the exemplary results of simulation calculations of the movement dynamics of the cutter bar's movement of the shear finger cutting assembly.

Tab. 1 Results of the exemplary simulation calculations of the shearfinger cutting assembly (own study)

	Fixed input data		
	h_k = 75 mm	*l = 230 mm*	*n = 1020 rev min^{-1}*
	Variable input data		
	μ=0,3 m_1 = 4 kg m_2 = 1,4 kg		*μ=0,19 m_1 = 2 kg m_2 =1,4 kg*
	Results of calculations		
$v_{snż}$ [m s^{-1}]	2,59		2,59
P_S [N]	952,5		952,5
P_B [N]	2347,34		1477,95
T_1 [N]	11,77		3,72
T_2 [N]	2186,62		1498,43
P_{max} [N]	4112,01		3059,80
N [kW]	15,81		11,76

The tool developed for simulation calculations makes allows for quick identification of demand for power and the values of the operating forces, also in other working assemblies of the shear-finger cutting assemblies following implementation of changes in their construction.

CONCLUSIONS

Within the frames of the study's realization, functioning of the shear-finger cutting assembly in the aspect of dynamic loads of its cutter bar has been analysed. According to the assumed purpose of the study, there have been drawn up mathematical dependencies describing the cutter bar's dynamic loads. For the purposes of quick designing of the power transmission systems of the cutter bar and the shear-finger cutting assembly, there have been conducted the simulation calculations as well as the own software for quick identification of the demand for power and forces operating within the shear cutting units under the influence of the characteristic input data's changes has been developed.

REFERENCES

1. Bochat, A. (2010). *Theory and design of cutting units for agricultural machines*. Publishing house - UTP University of Sciences and Technology Bydgoszcz.
2. Bochat, A. and Zastempowski, M. (2013). Modeling the Dynamics of the Vegetable Material Detachment Process from Undisturbed Areas to Improve the Design of Selected Agricultural Machines. *Transactions of the ASABE*, vol. 56(4), 1309-1314.
3. Dulcet, E., Kaszkowiak, J., & Borowski, S. (2006). Effects of microbiological additive on baled wet hay. *Biosystems engineering*, 95 (3), 379-384.
4. Gach, S., Kuczewski, J. & Waszkiewicz, Cz. (1991) *Maszyny rolnicze. Elementy teorii i obliczeń.* Wyd. SGGW w Warszawie.
5. Karwowska, M., Mikolajczak, J., Dolatowski, Z., & Borowski, S. (2013). The effect of varying distances from the wind turbine on meat quality of growing finishing pigs. *Annals of Animal Science*, 15, 4, 1043-1054.
6. Karwowska, M., Mikolajczak, J., Borowski, S., Dolatowski, Z., Marc-Pienkowska, J., & Budzinski, W. (2014). Effect of noise generated by the wind turbine on the quality of goose muscles and abdominal fat. *Annals of Animal Science*, 14, 2, 441-451
7. Keska, W., & Gierz, L. (2011). Mathematical modeling and computer simulation of sowing. *69th International Conference on Agricultural Engineering LAND TECHNIK AgEng. Hannover, GERMANY*, 459-464.
8. Knopik, L., Migawa, K. & Kolber, P. (2016). Statistical analysis of parameters of rail vehicles. *22nd International Conference on Engineering Mechanics Location: Svratka, CZECH REPUBLIC*, 286-289.
9. Knopik, L., Migawa, K. & Wdzieczny, A., (2016). Profit optimalization in operation systems. *Polish Maritime Research*, 23, 1, 93-98.
10. Knopik, L., & Migawa K. (2017). Optimal age-replacement policy for non-repairable technical objects with warranty. *Eksploatacja i Niezawodnosc – Maintenance and Reliability*, Vol. 19, No. 2, 172 -178.
11. Ligaj, B., & Szala, G. (2010). Experimental verification of two-parametic models of fatigue characteristics by using the tests of S55J0 steel as an example . *Polish Maritime Research*, 17, 1, 39-50
12. Strzelecki, P., Tomaszewski, T., & Sempruch, J. (2016). A method for determining a complete S-N curve using maximum likelihood. *22nd International Conference on Engineering Mechanics Location: Svratka, CZECH REPUBLIC*, 530-533.
13. Szala, G. (2014). Comments on linear summation hypothesis of fatigue failures. *Polish Maritime Research*. 21, 3, 77-85
14. Tomaszewski, T., Sempruch, J., & Piatkowski, T. (2014). Verification of selected models of the size effect based on high-cycle fatigue testing on mini specimens made of EN AW-6063 aluminum alloy. *Theor. App. Mech*., 52, 883–894.
15. Zastempowski, M., & Bochat, A. (2014). Modeling of cutting process by the shear-finger cutting block. *ASABE Applied Engineering in Agriculture*. Vol. 30, No. 3, 347-353.
16. Zastempowski, M., & Bochat, A. (2015). Mathematical model ling of elastic deflection of a tubular cross-section. *Polish Maritime Research* No.2 (86), Vol. 22, 93-100.

Corresponding author:
Marcin Zastempowski, PhD.: Faculty of Mechanical Engineering, UTP University of Science and Technology, Poland., Al. Prof. Kaliskiego 7, 85-796 Bydgoszcz, e-mail: zastemp@utp.edu.pl

58th ICMD 2017
6 - 8 September 2017, Prague, Czech Republic

DESIGN CONCEPTS AND FUNCTIONAL PARTICULARITIES OF WEARABLE WALKING ASSIST DEVICES AND POWER-ASSIST SUITS – A REVIEW

Yang ZHANG[1], Vigen ARAKELIAN[1,2], Jean-Paul LE BARON[1]

[1]*Department of Mechanical and Control Systems Engineering, INSA, 20 avenue des Buttes de Coësmes, CS 70839, 35708 Rennes Cedex 7, France*
[2]*LS2N / ECN, 1 rue de la Noë, BP 92101, 44321 Nantes Cedex 03, France*

Abstract
In all likelihood, robotics will lead to a revolution in our lifestyle similar to internet or mobile phone. In this context, the assistive robotics is currently one of the most invested fields which leads to the design of new products with large diversity. Among of these products may be well distinguished the walking assist robotic systems which improve daily life. Therefore, it is not accidental that during the last few years a tendency to develop the robotic systems for different applications of walking and handling assistance emerged. This paper provides a design overview of wearable assist devices. We attempt to cover all of the major developments in these areas, focusing particularly on the development of the different concepts and their functional characteristics.

Key words: *assistive robotics; wearable walking device; power-assist suit; exoskeleton*

INTRODUCTION

Assistive robots have application in industrial field as well as for patients and the elderly with mobility impairments. They free people from much labor and the burdens of many kinds of manual work. There have been many approaches to the reduction of labor that do not only fully assist but also partly aid workers, such as in the use of extremely heavy payload-oriented construction equipment, which are manipulated by humans. Manual or semi-automatic machine tools are mostly used in contemporary industries. In particular, without manpower, especially without the manipulability and mobility of human limbs, full automation will be incompatible with today's technologies. The assistive robotized devices have strong advantages given their unique features such as their outstanding physical performance, exceeding that of humans, and their agility. As a result, attempts to adopt these devices in the industrial field, especially at construction sites, indicate the use of feasible approaches to factory automation (*Okamura, et al., 1999; WRITING, et al., 2010*).
Locomotor disability is the most commonly reported type of disability. It is defined as a person's inability to execute distinctive activities associated with moving both himself and objects, from place to place and such inability resulting from affliction of musculoskeletal and/or nervous system. All over the world, several dozen million people suffer from the effects of post-polio, multiple sclerosis, spinal cord injury, cerebral palsy, paraplegia, quadriplegia, muscular dystrophy etc. and could benefit from the advances in robotic devices for rehabilitation. The temporary or permanent loss of human motor functions can be compensated by means of various rehabilitation and assistive devices. Robotic systems for rehabilitation or for assistance in daily living offer real advantages. In the last decade, the interest in this field has raised mainly due to the growing demand caused by increasing number of stroke patients. Stroke is the third most frequent cause of death worldwide and the leading cause of permanent disability in the USA and Europe. One-third of surviving patients from stroke do not regain independent walking ability and those ambulatory, walk in a typical asymmetric manner.
Worldwide statistics about locomotor disability show that in Australia: 6.8% of the population had a disability related to diseases of the musculoskeletal system, which is 34% of the persons with any kind of disability; in USA: there are more than 700.000 Americans who suffer a stroke each year, making it the third most frequent cause of death and the leading cause of permanent disability in the country. 10.000 suffer from traumatic spinal cord injury, and over 250.000 are disabled by multiple sclerosis per year; in Italy: 1.200.000 people have declared the locomotor disabilities (*Williams, et al., 1999*). The number of people with locomotor disabilities is growing permanently as a result of several factors, such as: accidents, population growth, ageing and medical advances that preserve and prolong life. Besides, it is necessary to take into account that the world population is rapidly ageing. This problem

is quite serious also in France. In 2005, one Frenchman by five was aged 60 years or older. In 2050, this ratio will be one by three. It is therefore most likely that the research in the development of wearable walking assist devices will be intensified because undoubtedly today there is a great demand for such robotic systems.

WEARABLE WALKING ASSIST DEVICES

The given wearable walking assist devices are described via innovation and technical achievements. It is also disclosed the particularities of some kinds of modern electroactive polymer actuators and McKibben type fluidic actuators which can be served for development efficient walking assist devices.
Hybrid Assistive Limb (HAL) (CYBERDYNE Inc, Japan) is an exoskeleton that is targeted for both performance-augmenting: heavy works, physical training support and rehabilitative purposes (*Hayashi, et al., 2005; Suzuki, et al., 2007*). HAL employs controller, computer, harmonic drive motors at the hip, knee, and ankle joints. Power for the motors is supplied by a battery pack mounted on the backpack. HAL system utilizes a number of sensors for control: skin-surface EMG electrodes (Electromyographic electrodes for measuring the activation level of the muscles), potentiometers for joint angle measurement, ground reaction force sensors, a gyroscope and accelerometer mounted on the backpack for torso posture estimation.
These sensing modalities are used in two control systems that together determine user intent and operate the suit. It requires AC100V electricity and can operate continuously approximately 2 hours 40 minutes. The total weight of the device is 21kg. HAL supports activities like standing up from a chair, walking, climbing up and down stairs, holding and lifting heavy objects up to 70kg. However, to date was not reported the effectiveness of the exoskeleton's lower-limb components for the improvement of locomotory function. Reportedly, it takes two months to optimally calibrate the exoskeleton for a specific user. It requires much patience to wear and difficult to maintain the quality of EMG signal for every wearing.

Fig. 1. Hybrid Assistive Limb.

BLEEX system provides a versatile load transport platform for mission-critical equipment, so it has several applications without the strain associated with demanding labor such as that of soldiers, disaster relief workers, fire-fighters, industrial and construction workers and so on.
The Berkeley Lower Extremity Exoskeleton (BLEEX) is powered by an internal combustion engine which is located in the backpack (*Chu, et al., 2005; Kazerooni & Steger, 2006*). The hybrid engine delivers hydraulic power for locomotion and electrical power for the electronics. The exoskeleton is actuated via bidirectional linear hydraulic cylinders. BLEEX consumes an average of 1143 Watts of hydraulic power during level-ground walking, as well as 200 Watts of electrical power for the electronics and control. In contrast, a similarly sized, 75 kg human consumes approximately 165 W of metabolic power during level-ground walking. The control system utilizes the information from eight encoders and sixteen linear accelerometers to determine angle, angular velocity, and angular acceleration of each of the eight actuated joints, a foot switch, and load distribution sensor per foot to determine ground contact and force distribution between the feet during double stance, eight single-axis force sensors for use in force control of each of the actuators, and an inclinometer to determine the orientation of the backpack with respect to gravity. This control algorithm essentially minimizes the interaction forces between the human and the exoskeleton and instead, utilizes mainly sensory information from the exoskeleton. BLEEX can support a load of up to 75 kg while walking at 0.9 m/s, and can walk at speeds of up to 1.3 m/s without the load. This development continues with the HULC prototype, under Lockeed Martin license.
Sarcos is a full-body exoskeleton designed for load-bearing, that results in decreasing the wearer's metabolic cost (*Huang, 2004*). Sarcos has a portable internal combustion engine to deliver the hydraulic power necessary for locomotion. The exoskeleton comprises hydraulic actuators located at the hip and knee and a linear hydraulic actuator for the ankle. The onboard computer processes data delivered from twenty sensors on each leg. Sarcos control algorithm is similar to BLEEX's where the exoskele-

ton senses what the user's intent is and assists in performing the task. The Sarcos exoskeleton is able to carry a 90 kg load.

A drawback for both the BLEEX and Sarcos exoskeletons is that an internal combustion engine may be undesirable for military applications, since the noise from the engine may give away the position of soldiers in a covert operation. Even though they can be utilized in industrial field, where the noise from the engine is not crucial, or the service personnel who is wearing the exoskeleton can be located close to the immobile power source.

Hercule (figure 2) is an exoskeleton designed for accompanying persons and providing assistance to carry and manipulate heavy loads, developed by the French company RB3D and CEA LIST Interactive Robotics Laboratory (*Garrec, et al., 2013*). It uses highly efficient electric actuators allowing the current prototype to carry a 40 kg load at 4 km/h speed with an electric autonomy of 4 hours. Only the flexion /extension joints of knee and hip are actuated.

Fig. 2. Hercule (LIST, CEA)

The controller principle is that actuated joints are providing torques to counteract the load weight. The high back-drivability of the actuators (CEA patents) is a key feature to have machine following the user smoothly. The back of the exoskeleton can transmit the load carried by the arms to the exoskeleton legs.

ReWalk (figure 3, ARGO Medical Technologies Ltd.) is a wearable, motorized quasi-robotic exoskeleton that can be used for therapeutic activities (*Goffer, 2006*). ReWalk comprises light wearable brace support suit, which integrates DC motors at the joints, rechargeable batteries, an array of sensors, and a computer-based control system. Upper-body movements of the user are detected and used to initiate and maintain walking processes. ReWalk allows paraplegic patient to walk, sit and stand-up, climb up and down the stairs. It lacks of body weight support and stability, hence for that reason there is a need to utilize crutches, to maintain upright position and balance. It might be insecure for paralyzed patient wearing ReWalk exoskeleton; in case of losing balance he/she will just fall on the ground. Similar to ReWalk by application and actuators technology is the EKSO exoskeleton, developed on Kazerooni laboratory (*Strausser & Kazerooni, 2011*).

Fig. 3. ReWalk

Walking Assist Device with Bodyweight Support Assist (Figure 4, Honda Motor) helps support bodyweight to reduce the load on the user's legs while walking. This could lead to reduced fatigue and less physical exertion (*Koshiishi, 2010*). The device comprises of 2 motors and gears, rechargeable lithium ion batteries, control computer, shoes with foot force sensors and a seat. It weighs 6.5 kg. Honda's device lightens the load on the user's legs and helps maintain a center of gravity via special mechanisms developed by the company. Walking, crouching, climbing stairs all become easier with the help of this device.

There is plenty of use cases for this product, not the least of which would be helping industrial workers, people afflicted with mobility issues or leg problems. It can also be used for rehabilitation. Despite its' advantages, still it will be uncomfortable, limiting and aesthetic for everyday life.

Walking Assistive Device with Stride Management (Figure 5, Honda Motor) is developed for patients with weakened leg muscles who are still able to walk (*Hirata & Koyama, 2012*). It is comprised with 2 brushless DC motors, rechargeable lithium ion battery, angle sensors, control computer and operates about 2 hours. A motor helps lift each leg at the thigh as it moves forward and backward. This helps lengthen the user's stride, making it easier to cover longer distances at a greater speed. Its lightweight and simple design with a belt worn around the hips and thighs reduces the wearer's load and fits different body shapes. The device weights 2.8kg with batteries.

Fig. 4. Walking Assist Device with Bodyweight Support Assist.

Fig. 5. WADSM

POWER-ASSIST SUITS

Another type of wearable devices which is similar with the walking assist devices, however, the main purpose of this kind of devices is to enhance the physical competence of human instead of walking assistance. This so-called "power-assist suit" can be used for heavy load carriage, enhancement of stamina or operating heavy tools.

In some factories, workers need to operate hand tools like driller and welding gun and using these tools for long time can not only be physically exhausting but also lead to muscle fatigue and injure. An exoskeleton recently designed by Lockheed Martin named FORTIS (Fig.6) allows its operators to support heavy tools and enhancing their strength and endurance (*Lockheed Martin Corporation, 2016*). FORTIS weighs less than 12.3kg and it transfers the weight of tools to the ground through a series of joints at hips, knees and ankles. One of the great advantage of FORTIS is that it does not need any actuators (i.e. unpowered) and it can be used in different environments from factory to field work because it is a wearable device and it moves along with the operator's natural movement while standing, bending, leaning or kneeling.

Fig.6. FORTIS

Dexterous Robotics Lab (DRL) at the NASA Johnson Space Centre in Houston developed an exoskeleton named X1 (Fig.7) in cooperation with the Florida Institute for Human and Machine Cognition (IHMC) in Pensacola (*Rea, et al., 2013*). Initially designed as a mobility device for people with paraplegia, X1 had been tailored as an in-space countermeasures device and a dynamometry device to measure muscle strength. The X1 exoskeleton currently has four active degrees of freedom (DOF) at the hips and the knees, with powered movement constrained to the sagittal plane which can assist or resist human movement. It also has six passive degrees of freedom for abduction and adduction; internal and external rotation; and dorsiflexion and plantarflexion. Any of these passive DOFs may be left free to move or locked out to intentionally constrain movement.

Fig.7. X1

These previous mentioned exoskeletons are all fabricated by rigid frames and linkages, connected with wearers at certain position on their body via pads, straps or other linking mechanisms. Therefore, these rigid links will add considerable inertia while users move their biological joints, and this impedance must be compensated by motors or by users themselves. Furthermore, during the movement, the misalignment between user's body and exoskeleton can be up to ±10cm, even if the exoskeleton was well aligned at the start of movement, and this misalignment will cause pain or even injury to the user (*Schiele & van der Helm, 2013*).

To solve this problem, a new way of design exoskeleton is to use soft materials to fabricate a cloth-like "Exosuit" and add actuated moments to the joints which need to be assisted. Because of using soft materials like fabrics and cables, the exosuits much lighter than the exoskeletons, therefore, only a little inertia is added to the wearer's movement. Additionally, since there is no rigid joints or frames exist in exosuits, so there is no problem relating to the joint misalignment. Unlike conventional exo-skeleton, Exosuit does not contain any rigid elements which can transfer loads to the ground, hence the wearers must sustain all the compressive forces by their own bones.

Fig.8. Soft exosuit actuated by pneumatic actuator.

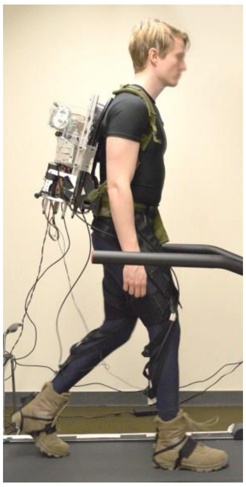

Fig.9. A cable-driven exosuit.

Recently, two prototypes of exosuit have been designed by several researchers from the Wyss Institute for Biologically Inspired Engineering at Harvard University. The first one is a lower-extremity exosuit actu-ated by custom Mckibben style pneumatic actuators (Fig.8) which can assist the hip, knee and ankle (*Wehner, et al., 2013*). The actuators attach to the exosuit through a network of soft, inextensible webbing tri-angulated to attachment points. Because of the use of soft material, this exosuit itself (human interface) weighs only 3.5kg, and experiment shows that it can comfortably transmit joint torques to the user while not restricting mobility. However, it also has some drawbacks like the air supplier is not portable which can limit its mobility.

The second one is a soft cable-driven exosuit (Fig.9) that can apply forces to the body to assist walk-ing (*Asbeck, et al., 2013*). The exosuit is fixed on the body by straps and actuated cables can generate moments at the ankle and hip with magnitudes of 18% and 30% of those naturally generated by the body during walking, respectively. The geared motors are used to pull on Bowden cables connected to the suit near the ankle. Like the first design, the worn part of the suit is extremely light, hence the suit's unintentional interference with the body's natural biomechanics is negligible.

CONCLUSIONS

The review showed that there are some limitations related to the development of wearable walking assist devices. One of the largest problems facing designers of these devices is the power supply. There are currently few power sources of sufficient energy density to sustain a full-body via a weara-ble device for more than a few hours. Initial wearable walking assist devices experiments are com-monly done using inexpensive and easy to mold materials such as steel and aluminium. However steel is heavy and the device must work harder to overcome its own weight in order to assist the wearer, reducing efficiency. The aluminium alloys used are lightweight, but fail through fatigue quickly. As the design moves past the initial exploratory steps, the engineers move to progressively more expen-sive and strong but lightweight materials such as titanium, and use more complex component con-struction methods, such as molded carbon-fiber plates. Carbon nano tubes are light weight, 10 times stronger, and more heat resistant than titanium. The powerful but lightweight design issues are also true for joint actuators. Standard hydraulic cylinders are powerful and capable of being precise, but they are also heavy due to the fluid-filled hoses and actuator cylinders, and the fluid has the potential to leak onto the user. Pneumatics is generally too unpredictable for precise movement since the com-pressed gas is springy, and the length of travel will vary with the gas compression and the reactive forces pushing against the actuator. Generally electronic servomotors are more efficient and power-dense, utilizing high-gauss permanent magnets and step-down gearing to provide high torque and re-sponsive movement in a small package. There are several muscles that flex the leg at the knee joint. Thus, the flexibility is another design issue, and which also affects the design of shell space suits. It is important that the walking assist device does not interfere with the movement of a leg during walking and designed joints will be flexible enough.

Thus, several challenging topics exist with regard to the development of wearable walking assist de-vices

REFERENCES

1. Asbeck, A. T., Dyer, R. J., Larusson, A. F., & Walsh, C. J. (2013). Biologically-inspired soft exosuit. In *Rehabilitation robotics (ICORR), 2013 IEEE international conference on* (pp. 1-8). IEEE.
2. Chu, A., Kazerooni, H., & Zoss, A. (2005). On the biomimetic design of the berkeley lower extremity exoskeleton (BLEEX). *In Robotics and Automation, 2005. ICRA 2005* (pp. 4345-4352).
3. Garrec Ph., Coste F., Grygorowicz S., Perrot Y., Ponsort D., & Riglet A. (2013) Lower Exoskeleton. *FR2981266 / WO2013057057*. Pub. Date: 19/04/2013, Bulletin 13/16.
4. Goffer, A. (2006). *U.S. Patent No. 7,153,242.* Washington, DC: U.S. Patent and Trademark Office.
5. Hayashi, T., Kawamoto, H., & Sankai, Y. (2005). Control method of robot suit HAL working as operator's muscle using biological and dynamical information. *In Intelligent Robots and Systems, 2005. (IROS 2005)* (pp. 3063-3068).
6. Hirata, T., & Koyama, T. (2012). *U.S. Patent No. 8,221,339*. Washington, DC: U.S. Patent and Trademark Office.
7. Huang G. (2004) Demo: Wearable Robots. *Technology Review*, July/August.
8. Kazerooni, H., & Steger, R. (2006). The Berkeley lower extremity exoskeleton. *Journal of dynamic systems, measurement, and control*, 128(1), 14-25.
9. Koshiishi, T. (2010). *U.S. Patent No. D614,394*. Washington, DC: U.S. Patent and Trademark Office.
10. Lockheed Martin Corporation (2016). URL:http://www.lockheedmartin.com/content/dam/lockheed/data/mfc/pc/fortis/mfc-fortis-pc.pdf, *Online resources*, Accessed on: 06 April 2017
11. Okamura, J., Tanaka, H., and Sankai, Y. (1999) EMG-based Prototype-powered Assistive System for Walking Aid, Bangkok, Thailand. *In Proc. of the Asian Symposium on Industrial Automation and Robotics (ASIAR'99)* (pp. 229-234).
12. Rea, R., Beck, C., Rovekamp, R., Neuhaus, P., &Diftler, M. (2013). X1: A robotic exoskeleton for in-space countermeasures and dynamometry. In *AIAA SPACE 2013 Conference and Exposition* (p. 5510).
13. Schiele, A., & van der Helm, F. C. (2009). Influence of attachment pressure and kinematic configuration on pHRI with wearable robots. *Applied Bionics and Biomechanics*, 6(2), 157-173.
14. Strausser, K. A., & Kazerooni, H. (2011). The development and testing of a human machine interface for a mobile medical exoskeleton. In *Intelligent Robots and Systems (IROS), 2011 IEEE/RSJ International Conference on* (pp. 4911-4916). IEEE.
15. Suzuki, K., Mito, G., Kawamoto, H., Hasegawa, Y., & Sankai, Y. (2007). Intention-based walking support for paraplegia patients with Robot Suit HAL. *Advanced Robotics*, 21(12), 1441-1469.
16. Wehner, M., Quinlivan, B., Aubin, P. M., Martinez-Villalpando, E., Baumann, M., Stirling, L., ... & Walsh, C. (2013). A lightweight soft exosuit for gait assistance. In *Robotics and Automation (ICRA), 2013 IEEE International Conference on* (pp. 3362-3369). IEEE.
17. Williams, G. R., Jiang, J. G., Matchar, D. B., & Samsa, G. P. (1999). Incidence and occurrence of total (first-ever and recurrent) stroke. *Stroke*, 30(12), 2523-2528.
18. WRITING, G. M., Lloyd-Jones, D., Adams, R. J., Brown, T. M., Carnethon, M., Dai, S., ... & Gillespie, C. (2010). Heart disease and stroke statistics--2010 update: a report from the American Heart Association. *Circulation*, 121(7), e46.

Corresponding author:
VigenArakelian, Ph.D., Full Professor, Department of Mechanical and Control Systems Engineering, INSA, 20 avenue des Buttes de Coësmes, CS 70839, 35708 Rennes Cedex 7, France, phone: +33(0)223238492, e-mail: vigen.arakelyan@insa-rennes.fr

58th ICMD 2017
6 - 8 September 2017, Prague, Czech Republic

SPEED CHANGES ON THE SECTION OF A ROAD AND THEIR IMPACT ON THE GEARBOX OPERATION

Tadeusz ŻUREK[1]

[1]*Faculty of Mechanical Engineering, UTP University of Science and Technology*

Abstract
The network of roads on the territory of a specific area is subject to different divisions. There are speeds assigned to sections occurring at different areas. Justification for the level of their assignment is different, and very often is unconnected from the conditions which are to be observed in correct exploitation of vehicles. So, the divergences in exploitational arrangements for a road and vehicles are contradictory. The consequences of these divergences emerge in speeding up of the wear and tear of many vehicle's assemblies, including a gearbox.

Key words: *speeds on roads, limitation in the vehicles' traffic, wear and tear of a gearbox.*

INTRODUCTION

The networks of roads allowing the movement of vehicles, constitute the element of the state's assets managed by its administrative units, both the centralized ones as well as the regional ones. This management covers, among the others, ensuring of the required exploitational conditions including determination of possible speeds for individual roads. Undoubtedly, the following elements constitute the grounds for making arrangements within that scope:

- state of the road,
- its location,
- surroundings of the road,
- construction of the road/ width, profile /.

The issue of speed on the roads in Poland is covered by the regulation of the Minister of Transport and Maritime Economy of March 3, 1999 on the technical conditions that public roads and their use should correspond to. In that regulation, it has been specified in particular the design speed, as the technical and economical parameters that the boundary value of the road elements, proportions among them and the scope of a road's fittings are assigned to *(Regulation, 1999*). So, the design speeds established for individual road classes are presented in the table 1 (*Regulation, 1999*).

Tab. 1 Designed speeds for individual classes of roads in Poland

Class of road		A	S	GP	G	Z	L	D
The design speed of road (km/h)	Outside city limits	120 100 80	120 100 80	100 80 70 60	70 60 50	60 50 40	50 40	40 30
	Inside city limits	80 70 60	70 60	60 50	60 50	60 50 40	40 30	30

A road, due to most often common accessibility, adopts the character of an universal infrastructure. So, the arrangements for these roads do not take into consideration the diversity of vehicles travelling on them, and in particular, of their performance parameters specified by producers/ designers/ and the terms of their use. The situation in transport takes notes of adjustment of the means of transport to the characteristics of a road in principle in one case, that is, with reference to ships/ vessels/ inland shipping, where adjustment of the means of transport to the waterway's parameters takes place. The occurring discrepancies between the road infrastructure /motor transport / and the conditions of correct exploitation of the means of transport – vehicles, have a negative impact on the process of their use. The objective situation was verified on the basis of the selected section of the road and a vehicle. However, the purpose of this article is, in particular, presentation of the obtained results and through them – presenting of paradoxical and inconsistent operational solutions anticipated and realized for roads and vehicles. The made findings point at absurdity in roads administrators proceeding with reference to the implemented speed limits.

MATERIALS AND METHODS

The route of the national road no 80, connects among the others the cities Bydgoszcz – Toruń and remains in its part in the network of municipal streets of both the cities. The course of the road comprises the places: Pawłówek – Bydgoszcz – Fordon – Toruń – Lubicz Dolny and amounts to 66,0 km. For the findings, within the frames of the conducted studies, there was taken into consideration the section connecting both the cities between the central points determined to be the head offices of the Polish Post. So, the subject study was started by the head office of Polish Post at Jagiellońska 6 st. in Bydgoszcz. For the studies – findings, there was used the vehicle make Skoda model Octavia version Elegance. The vehicle is characterised by the following data:

- year of production – 2010,
- cylinder capacity 1798 cm3
- power 160 KM/118 kW
- odometer reading 27553 km
- volume of fuel in the tank – full.

Selection of the vehicle for the studies results from the fact, that both the brand names as well as the model, dominate among the vehicles exploited on Polish roads.
That vehicle had a valid periodical vehicle technical inspection conducted at the Motor Vehicle Diagnostic Station /PSKP/, lately conducted on May 17, 2017 / according to the provisions in force valid for the period of one year /. That vehicle has also undergone the inspection and servicing activities that should be performed every two years were conducted by the authorised service station on June 28, 2016. Pressure in the vehicle's wheels was controlled on the day preceding the inspection, and according to the producer's recommendations it was written down on the filler's cover.
The test was conducted on May 26, 2017. It was a sunny day, no precipitations, dry surface. At the moment of the test's commencement, that is at 6.07 the temperature was 12 °C and was determined on the basis of the indications of the sensor presented at the display. In order to determine the total distance as well as the distance of individual sections of the road, there was used the correctly functioning daily vehicle's odometer.
The test was started at 6.07 by the head office of Polish Post at Jagiellońska 6 st. in Bydgoszcz. The time for the findings was to allow for easy vehicle's drive in the conditions of average traffic.
Carrying out of the findings was completed at 7.03 by the head office of Polish Post in Toruń at Piekary 26 st. Along the whole route there were no disruptions and the weather conditions remained unchanged. The outside temperature at the moment of the tests' completion amounted to 13,5 °C. The odometer reading confirmed travelling the distance of 46,8 km. Because of the traffic limitation on the Staromiejski market, the test was completed at Piekary street. The passage was realized as the drive in easy traffic in accordance with the road safety procedures and occurring limitations. The course of the tests at the time of passage, that also means that the made findings were documented on a current basis in the prepared reports. At the time of the tests certain inconsistencies in determining speed for the subject section of the road by that road's administrator were found. However, it had no impact on the made findings.

RESULTS AND DISCUSSION

At the time of the values' testing – parts of the section together with speeds assigned to them, describing thereby the changes in the vehicle's driving are presented in the table 2. In the table below, the division of the whole road's section into the municipal and rural areas is presented.

Tab. 2 List of the results of the test divided by areas

No.	Areas covered by findings	Kilometer of road from – to	Speed limit (km/h)	Distance of limitation (m)
1	2	3	4	5
1		0,0 – 1,0	50	1000

2		1,0 – 1,1	40	100
3		1,1 – 3,9	50	2800
4		3,9 – 4,8	30	900
5		4,8 – 6,6	50	1800
6		6,6 – 9,2	70	2600
7		9,2 – 9,5	50	300
8		9,5 – 10,1	70	600
9		10,1 – 10,2	50	100
10		10,2 – 10,3	30	100
11		10,3 – 10,8	50	500
12		10,8 – 11,7	40	900
	Total municipal in Bydgoszcz			11700
13		11,7 – 13,8	70	2100
14		13,8 – 14,4	90	600
15		14,4 – 14,6	70	200
16		14,6 – 18,4	90	3800
17		18,4 – 18,9	70	500
18		18,9 – 20,2	50	1300
19		20,2 – 24,6	90	4400
20		24,6 – 24,9	70	300
21		24,9 – 26,0	50	1100
22		26,0 – 32,1	90	6100
23		32,1 – 32,8	70	700
24		32,8 – 32,9	50	100
25		32,9 – 36,8	70	3900
26		36,8 – 37,7	50	900
27		37,7 – 38,1	90	400
28		38,1 – 38,9	70	800
29		38,9 – 39,0	50	100
30		39,0 – 39,1	70	100
31		39,1 – 39,8	90	700
	Total rural			28100
32		39,8 – 40,9	50	1100
33		40,9 – 43,6	70	2700
34		43,6 – 46,6	50	3000
35		46,6 – 46,8	30	200
	Total municipal in Torun			7000
36	Total	46,8	x	46800

The layout of the occurring speeds falling on individual sections occurring in the measurement order is presented on the graph 1. In particular also the presentation of “jumps” in speeds has also been taken into consideration in it. The average speed of the vehicle classified to be technical and reached at the time of the test amounted to below 50 km/h.

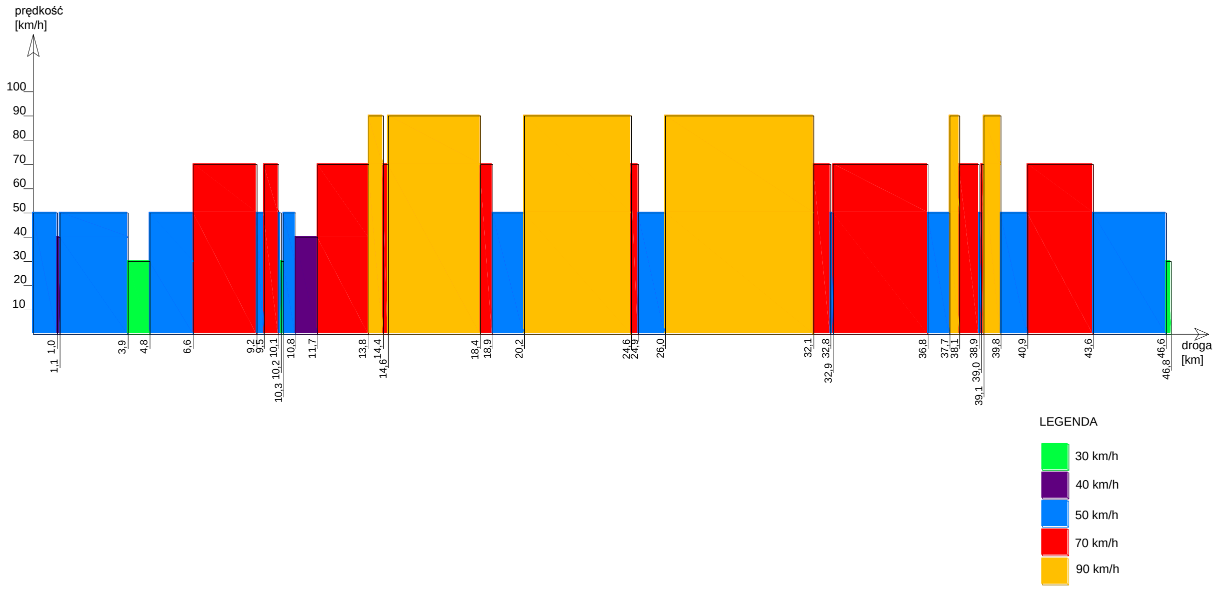

Fig. 1 Speeds falling on individual sections of a road

It results from the above graph, to what extend the gearbox is used for performance of brakings and speedings. Easy driving also does not occur outside the built-up area, on the section of which there are speed limits covering only 100 running meters of the road.

From the presented by the producer graphical information, in the factory's manual concerning economical change of gears it results, that their transmission should cover the ranges: (Manual 2010)

- on gear II from 15 to 50 km/h
- on gear III from 30 to 62 km/h
- on gear IV from 45 to 80 km/h
- on gear V from 50 to 102 km/h
- on gear IV from 58 to 110 km/h.

The maximum speed has been determined to amount to 223 km/h (Schwarz, 2010).
Higher gear should be switched on at the engine speed of about 2000 to 2500 revolutions per minute. "Early" switching on a higher gear is an effective manner of fuel's saving. Reaching the top of the engine speed's range on gear results in unnecessary fuel consumption. The highest consumption of fuel is on the first gear, the lowest one on the fifth or the sixth gear. The farsighted and economical mode of driving makes it possible to reduce easily the fuel consumption for 10 – 15 %. (Manual 2010)
Optimizing the manufacturer's instructions included in the manual and concerning the use of the gearbox's transmissions, increase of the output speed for each of them was made by half of the areas of the ranges determined for them. Taking the above into account it may be assumed, that the gears should have been changed having reached the speeds and respectively:

- from II to III at 32,5 km/h,
- from III to IV at 46.0 km/h,
- from IV to V at 62,5 km/h,
- from V to VI at 84,0 km/h.

Gearbox transmissions, according to the Extract from the homologation certificate are the following: (Extract from the homologation, 2010)

- I gear – 3,778	- III gear – 1,455	- V gear – 0,875
- II gear – 2,063	- IV gear – 1,107	- VI gear – 0,725.

It results from the above, that the speeds determined with limits may be reached respectively:

- 30 km/h – on the second gear,
- 40 km/h – on the third gear,
- 50 km/h – on the fourth gear,
- 70 km/h – on the fifth gear,
- 90 km/h – on the sixth gear.

The scale of the gearbox transmissions and its use on the tested section is presented in the table 3.

Tab. 3 The ranges of use of gearbox transmissions on the covered section of the road

Lp.	Speed in occurring limits km/h	Used gear	Road travelled in the speed limit in km	Structure of use of the gearbox transmi-sions in %
1	2	3	4	5
1	30	II	1,2	2,56
2	40	III	1,0	2,14
3	50	IV	14,1	30,13
4	70	V	14,5	30,98
5	90	VI	16,0	34,19
6	x	x	46,8	100,00

It results from the above, that only on the section covering in total 16,0 km the speed anticipated for the national road, that is 90 km/h was used. The degree of use of the gearbox transmissions is graphically presented on the graph 2.

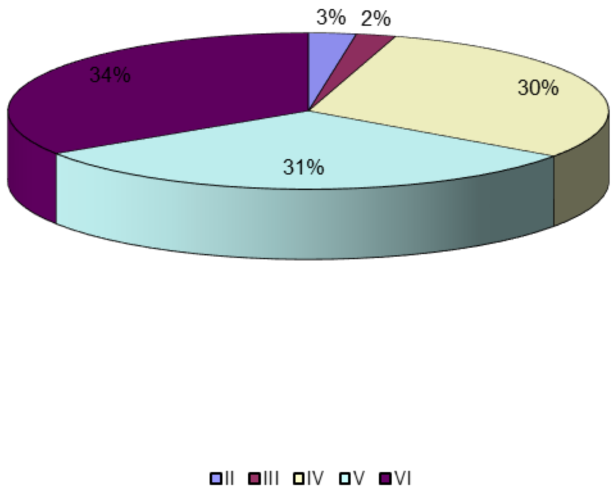

Fig. 2 The degree of use of the gearbox transmissions on the tested section

The part of the section of the road visible on the graph, travelled with the speed of 50 km/h should be considered incorrect from the point of correct passenger vehicle's exploitation, and this on account of the fact that the average at prosent for them possibility of travelling amounts to approx. 200 km/h.

CONCLUSIONS

The vehicle used for the tests has a manual gearbox having six transmissions/ six gears. The first of them, pursuant to the instructions of the producer included in the manual, is to be used at the time of starting and travelling the distance equal to the vehicle's length. and to Pierwszy z nich zgodnie ze wskazaniem producenta zawartym w instrukcji obsługi użyty ma być do ruszenia i pokonania odległości równej długości pojazdu. Then the remaining gears are used depending on conditions. Observing by a driver of the rule, that higher gears should be used what is connected with economy of drive referred to fuel consumption and the progressing degree of an engine's wearing out is a common recommendation. Considering the above as the exploitational conditioning concerning the vehicle transmitted a driver/ user/ it may be assumed, that there occurs a considerable divergence between correct exploitation of the means of transport and the road as an element of infrastructure prepared for it. The divergences prove:

- unfavourable consumption of fuel in the realized run,
- interference in a higher level than in the natural environment,
- wear and tear of an engine because of performing a higher number of work cycles,
- lower comfort of travel because of a higher level of noise generated by the engine.

It results from the above facts, that in practice each passenger vehicle in road conditions occurring in Poland is exploited at variance with the manual and a producer's instructions. Such a state of affairs undoubtedly leads to specific conduct of drivers whom commonly irregularities in conduct are being pointed out.

REFERENCES

1. User's guide of Skoda Octawia model 2010.
2. Regulation of the Minister of Transport and Maritime Economy of March 3, 1999 on technical conditions that public roads and their use should correspond to (Journal of Laws No 43, item 430 with subsequent amendments.)
3. Schwarz I., (2010)Automobil Skoda Octavia II Wyd. 2, Published by Grada Publiching, a.s., Praha.
4. Extract from the homologation for a complete vehicle, Poznań 2010.04.28.

Corresponding author:
Tadeusz Żurek, Ph.D., Faculty of Mechanical Engineering, UTP University of Science and Technology, Al. prof. S. Kaliskiego 7, 85-796 Bydgoszcz, Poland, e-mail: kolliberek@utp.edu.pl